GULF OF MEXICO MIOCENE CO_2 SITE CHARACTERIZATION MEGA TRANSECT

FINAL SCIENTIFIC/TECHNICAL REPORT (*REVISED*)

REPORTING PERIOD December 8, 2009 – September 30, 2014

PRINCIPAL AUTHORS

Timothy Meckel, PhD.
PH: 512-471-4306
tip.meckel@beg.utexas.edu

Ramon Trevino
PH: 512-471-3362
ramon.trevino@beg.utexas.edu

Report Issued December, 2014

DOE Award Number **DE-FE0001941**

The University of Texas at Austin
Jackson School of Geosciences
Bureau of Economic Geology
University Station, Box X
Austin, Texas, 78713

SUBMITTED TO

PROJECT MANAGER

Karen L. Kluger, PhD.

karen.kluger@netl.doe.gov

U. S. Department of Energy
National Energy Technology Laboratory

DISCLAIMER

ABSTRACT

This project characterized the Miocene-age sub-seafloor stratigraphy in the near-offshore portion of the Gulf of Mexico adjacent to the Texas coast. The large number of industrial sources of carbon dioxide (CO_2) in coastal counties and the high density of onshore urbanization and environmentally sensitive areas make this offshore region extremely attractive for long-term storage of carbon dioxide emissions from industrial sources (CCS). The study leverages dense existing geologic data from decades of hydrocarbon exploration in and around the study area to characterize the regional geology for suitability and storage capacity. Primary products of the study include: regional static storage capacity estimates, sequestration "leads" and prospects with associated dynamic capacity estimates, experimental studies of CO_2-brine-rock interaction, best practices for site characterization, a large-format 'Atlas' of sequestration for the study area, and characterization of potential fluid migration pathways for reducing storage risks utilizing novel high-resolution 3D (HR3D) seismic surveys. In addition, three subcontracted studies address source-to-sink matching optimization, offshore well bore management and environmental aspects. The various geologic data and interpretations are integrated and summarized in a series of cross-sections and maps, which represent a primary resource for any near-term commercial deployment of CCS in the area.

The regional study characterized and mapped important geologic features (e.g., Clemente-Tomas fault zone, the regionally extensive *Marginulina* A and *Amphistegina* B confining systems, etc.) that provided an important context for regional static capacity estimates and specific sequestration prospects of the study. A static capacity estimate of the majority of the Study area (14,467 mi^2) was estimated at 86 metric Gigatonnes. While local capacity estimates are likely to be lower due to reservoir-scale characteristics, the offshore Miocene interval is a storage resource of National interest for providing CO_2 storage as an atmospheric emissions abatement strategy.

The natural petroleum system was used as an analog to infer seal quality and predict possible migration pathways of fluids in an engineered system of anthropogenic CO_2 injection and storage. The regional structural features (e.g., Clemente-Tomas fault zone) that exert primary control on the trapping and distribution of Miocene hydrocarbons are expected to perform similarly for CCS. Industrial-scale CCS will require storage capacity utilizing well-documented Miocene hydrocarbon (dominantly depleted gas) fields and their larger structural closures, as well as barren (unproductive, brine-filled) closures. No assessment was made of potential for CO_2 utilization for enhanced oil and gas recovery.

The use of 3D numerical fluid flow simulations have been used in the study to greatly assist in characterizing the potential storage capacity of a specific reservoir. Due to the complexity of geologic systems (stratigraphic heterogeneity) and inherent limitations on producing a 3D geologic model, these simulations are typically simplified scenarios that explore the influence of model property variability (sensitivity study). A specific site offshore San Luis Pass (southern Galveston Island) was undertaken successfully, indicating stacked storage potential. Downscaling regional capacity estimates to the local scale (and the inverse) has proven challenging, and remains an outstanding gap in capacity assessments.

In order to characterize regional seal performance and identify potential brine and CO_2 leakage pathways, results from three high-resolution 3D (HR3D) seismic datasets acquired by the study using novel HR3D (P-Cable) acquisition system showed steady and significant improvements in data quality because of improved acquisition and processing technique. Finely detailed faults and stratigraphy in the shallowest 1000 milliseconds (~800 m) of data allowed for the identification and mapping of unconformable surfaces including what is probably a surface associated with the last Pleistocene glacial lowstand. The identification of a previously unrecognized (in commercial seismic data) gas chimney that was clearly defined in the 2013 HR3D survey, indicates that HR3D surveys may be useful as both a characterization tool for the overburden of a potential carbon sequestration site and as an additional monitoring tool for future engineered injection sites.

Geochemical modeling indicated that injection of CO_2 would result in minor dissolution of calcite, K-feldspar and albite. In addition, modeling of typical brines in Miocene age rocks indicate that

approximately 5% of injection capacity would result from CO_2 dissolution into the brine. After extensive searches, no rock samples of the *Marginulina* A and *Amphistegina* B seals (“caprocks”) were obtained, but analyses of available core samples of other Miocene age mudrocks (seals or caprocks) indicate that they have sealing ability sufficient for potential CO_2 storage in underlying sandstone units.

Table of Contents

List of Figures

EXECUTIVE SUMMARY

Regional studies of the near-offshore Gulf of Mexico along the Texas coast have characterized a geologic resource for CO_2 storage of State and National interest. The offshore Miocene-age stratigraphic interval of Texas provides a tremendous resource for storing anthropogenic CO_2 as a means for mitigating atmospheric emissions. Regional static capacity calculations indicate 86 Gigatonnes of CO_2 storage capacity for the Study area. While reconciling regional static capacity estimates with local dynamic assessments utilizing reservoir simulation has been challenging, this offshore region represents some of the most immediately accessible capacity for receiving industrial-scale emissions in the country. Recent infrastructure developments (onshore CO_2 pipelines) suggest this region could become a CO_2 hub capable of receiving pipeline CO_2 from other parts of the country, and indications are that the geologic storage resource could be viable for decades of utilization.

The study area extends the length of the Texas coastline, and up to 10 nautical miles offshore (Texas State-managed waters; <50 m water depth). In addition to traditional geologic characterization (identification of reservoir intervals, summary of reservoir and seal properties, regional extent, specific prospect identification), additional study effort evaluated regional sealing capability, CO_2-brine-rock geochemical interaction, best practices for site characterization, and characterization of potential fluid migration pathways for reducing storage risks by acquiring novel high-resolution 3D (HR3D) seismic data. Two independent studies subcontracted as part of the project address offshore well bore management and environmental aspects.

The primary geologic data utilized in the study were publically available but not well-integrated before completion of the current Study (e.g., thousands of well log rasters, production and micro-paleontologic data in Federal waters, formation brines dataset, etc.). Some data was leased (e.g., conventional, regional 3D seismic, acoustic well data, proprietary micro-paleontologic dataset), often with substantial cost share benefit. Characterization of the regional geology identified important geologic features (e.g., Clemente-Tomas fault zone, *Marginulina* A and *Amphistegina* B confining systems, etc.) that provided crucial context for the regional static capacity estimates as well as local dynamic capacity numerical model simulations. These various geologic data and interpretations are integrated and summarized in a series of cross-sections and maps, which represent a primary resource for any near-term commercial deployment of CCS in the area.

Analyses of available core samples of Miocene mudrocks (seals) suggest that the studied clay-rich lower Miocene mudrocks have sealing ability sufficient for potential CO_2 storage in the underlying sandstone units. The sealing capacity of the studied samples has positive correlations with clay content and calcite cementation. Clay-rich mudstone samples typically show higher capillary entry pressure and smaller pore-throat size than underlying sandstones. SEM imaging shows that claystone samples contain mostly isolated intraparticle pores, which are not effectively connected to form pore networks. A high concentration of lower Miocene hydrocarbon accumulations occurs on the hanging wall of the Clemente-Tomas fault zone where Amph B net mudstone is thick, ranging from 1,000 ft (305 m) to 3,000 ft (914 m). These natural analogs of fluid entrapment suggest that fairways characterized by a thick regional Amph B confining zone defined by net mudrock values of more than 1,000 ft (305m) might provide an excellent long-term confining mechanism for injected CO2.

Flow model simulation of fluid flow in a relatively small scale (20.51” tall by 10.39” wide (0.521 m x 0.264 m)) but high-resolution (>2M data points), 2D, digital model of a sedimentary relief peel conclude that mean grain size and sorting appear to be the key control on CO2 movement; fluid density contrast (in the expected ranges) is apparently secondary. Pressure gradients contribute to end member and transition behavior, in addition to rock properties and fluid density contrast. The pressure gradient in relative close proximity to the well (compared to the reservoir extents) can allow for fingering behavior.

As a result of batch experiments using synthetic brines (based on actual brines in Miocene age GOM units), it was determined carbon solubility trapping potential (CSTP) is most sensitive to thickness and porosity. The storage coefficient, C, appears to be one of the critical parameters for assessing CSTP in a

saline aquifer, and the most likely CSTP of the Miocene section in the study area is approximately 5% of the total CO2 storage capacity. In addition, geochemical models confirm dissolution of calcite when CO2 was injected into reservoir rock samples. The geochemical models also fit well with K concentration measurements, suggesting that K came from dissolution of K-feldspar when CO2 was injected. Modeled Na concentrations match well Na concentration measurements indicating CO2 injection leads to dissolution of albite. Si and Al are dominated by dissolution-precipitation of silicate minerals and potential secondary minerals. Proper selection of secondary minerals in the geochemical model seems very important.

During the final three years of the Study, a high-resolution 3D (HR3D) seismic acquisition (i.e., "P-Cable") system was purchased and utilized to acquire three surveys in Texas state waters (seaward from the barrier islands) of the upper Texas coast. The first two surveys were located offshore from San Luis Pass, Texas above and adjacent to a deep-seated salt dome that extends to within a few hundred feet of the modern seabed. The quality of the second survey (2013) was superior to that of the first because of advances in acquisition and processing techniques developed after the first (2012) survey. Interpretations of the 2013 survey indicate features such as a regional erosional surfaces including one possibly related to the last Pleistocene glacial lowstand. In addition, a clearly visible gas chimney emanating from the area above a deep-seated salt feature indicates natural seepage of fluids (possibly natural gas); this result suggests that HR3D surveys may be useful as both a characterization tool for the overburden of a potential carbon sequestration site and as an additional monitoring tool for future engineered injection sites. The third (2014) HR3D survey was located offshore from the High Island area, northernmost Bolivar Peninsula, an area with thousands of feet of stacked reservoir potential CO_2 sequestration. In addition, there are thick potential confining zones as shown by the presence of nearby oil and gas fields. Examples from the three HR3D surveys demonstrate that the seismic technique is capable of identifying and characterizing low-risk storage sites. When integrated with regional conventional 3D data, insight into natural fluid migration systems may distinguish entire regions as more or less prospective for future consideration for storage. HR3D (P-Cable) data are crucial for characterizing leakage pathways. It is difficult to conceive of conducting a CCS project offshore without HR3D data if they are financially obtainable.

Several sites ("leads") were characterized and CO_2 storage capacity calculated via static and dynamic methods. The site near San Luis Pass over which the 2013 HR3D survey was collected (subsequently suggesting a gas chimney) indicated dynamic capacity (i.e. using 3D fluid flow simulations) of less than 10 Mt. Pressure was the major limiting parameter for the models, and reservoir heterogeneity (e.g., mudrock baffles) and limited reservoir connectivity will probably prevent an infinitely acting system with completely open boundaries. The area associated with the Brazos Block 440-L Field was also characterized and analyzed using a static capacity method. The capacity of the entire area was estimated to be 196 Mt; whereas, the capacity of the gas structurally-controlled field area was estimated to be 14 Mt.

The Miocene of the Texas state waters, especially along the upper Texas coast, represents a region with great potential for future CO_2 sequestration development. The region has a high concentration of industrial emissions sources (e.g., power plants near large urban centers, extensive refining and petrochemical plants) as well as existing pipeline and other infrastructure in an area with significant with favorable commercial, subsurface geology, and engineering expertise.

REPORT DETAILS / SOPO TASKS

INTRODUCTION

The grant (a.k.a., DOE Award (Number DE-FE0001941) under whose auspices the following research was conducted was part of the American Recovery and Reinvestment Act of 2009, U.S. Department of Energy, National Energy Technology Laboratory Funding Opportunity Number: DE-FOA-0000033. The initial Federal award of $4,794,349 was signed on December 8, 2009. The award was subsequently augmented (September 9. 2010) with an additional Federal award of $4,668,116.

In many cases the term "Project" is used to describe a scientific effort such as that of DE-FE0001941. In the current report, the capitalized term "Study" is used to denote the entire effort undertaken to fulfill the goals and objectives of the award (grant) because it better summarizes the tremendous amount of research effort undertaken to achieve the results detailed in the current report.

The motivation for the Study arose from the various advantages presented by offshore CO_2 sequestration vs. onshore sequestration. One advantage of offshore environments is that they minimize risks to underground sources of drinking water (USDW). In addition, 1) risks to human health and safety are reduced; 2) monitoring options are readily available (e.g., high resolution 3D seismic), and 3) the surface and subsurface rights are owned by a single entity (i.e., State of Texas General Land Office - GLO), which is prepared to lease offshore storage sites.

The objectives of the proposed study were to 1) assess and analyze the existing data from historical hydrocarbon industry activities in a regional transect of the Texas Gulf Coast (Phase 1) in order to 2) verify the ability of the Miocene age rocks of the region to safely and permanently store large amounts of anthropogenic CO_2, (Phase 1) and 3) identify at least one specific site that can accept at least 30 million tons of CO_2 from future commercial CCS operations (Phase 2). As the current report details, all objectives were accomplished.

The goal of the Study was to characterize the Miocene-age geologic units throughout the submerged lands of the Texas coast and provide an assessment of specific reservoirs that are prospective for CO_2 storage. The work was designed to help meet the DOE goal of characterizing geologically representative formations that may be used to economically store anthropogenic CO_2 emissions. The Study focused efforts on Miocene–age reservoirs and confining systems on the middle and upper Texas coast, where capture and transportation are most likely to develop in the near-term (because of nearby CO_2 sources). Specific sites were studied as to their potential to store at least 30 million tons of CO_2.

In order to meet the goal and objectives of the Study, twelve tasks and various subtasks were established. The tasks were based on the FOA 0000033 "geologic storage assessment…issues that each project should, at a minimum, address." The current report sequentially describes the activities and results of each task and concomitant subtasks starting with Task 1, Project Management and ending with Task 12, Produced Fluid Management. The report also contains a Appendix A, which comprises a "Geological CO2 Sequestration Atlas for Miocene Strata..." in the northern Gulf of Mexico. In some cases (e.g., Subtasks 2.1 and 5.2) the atlas or portions of it fulfill the objective of a, respective, task. Consequently, the atlas or noted atlas section provides the task's report. Similarly, results for Subtasks 10.1, 10.2 and Task 11 are presented in Appendices B, C and D, respectively, as the tasks were conducted by subcontracted

organizations, Sandia National Laboratory (SNL) (Subtask 10.1), Environmental Defense Fund (EDF) (Subtask 10.2) and Sandia Technologies, LLC (Task 11).

Results and Discussions

Below the results and relevant discussion are presented for each task separately.

1 Task 1.0: Project Management

1.1

The current Study's generous funding (i.e., initial and augmented funding), presented tremendous research opportunities for the Gulf Coast Carbon Center (GCCC) (in the Bureau of Economic Geology (BEG) of the University of Texas at Austin) and for the Study's various partner organizations (Sandia Technologies, LLC, Environmental Defense Fund and Los Alamos National Laboratories). Not surprisingly, on such a large and long-term Study there were also management challenges, but the challenges often resulted in innovative solutions. For example, issues with the first (2012) high-resolution 3D seismic (HR3D) give rise to adjustments that resulted in using a new acquisition vessel as well as improved acquisition parameters (Task 8.0: Leakage Pathways) on the subsequent (2013 and 2014) surveys (Figure 1.1) .

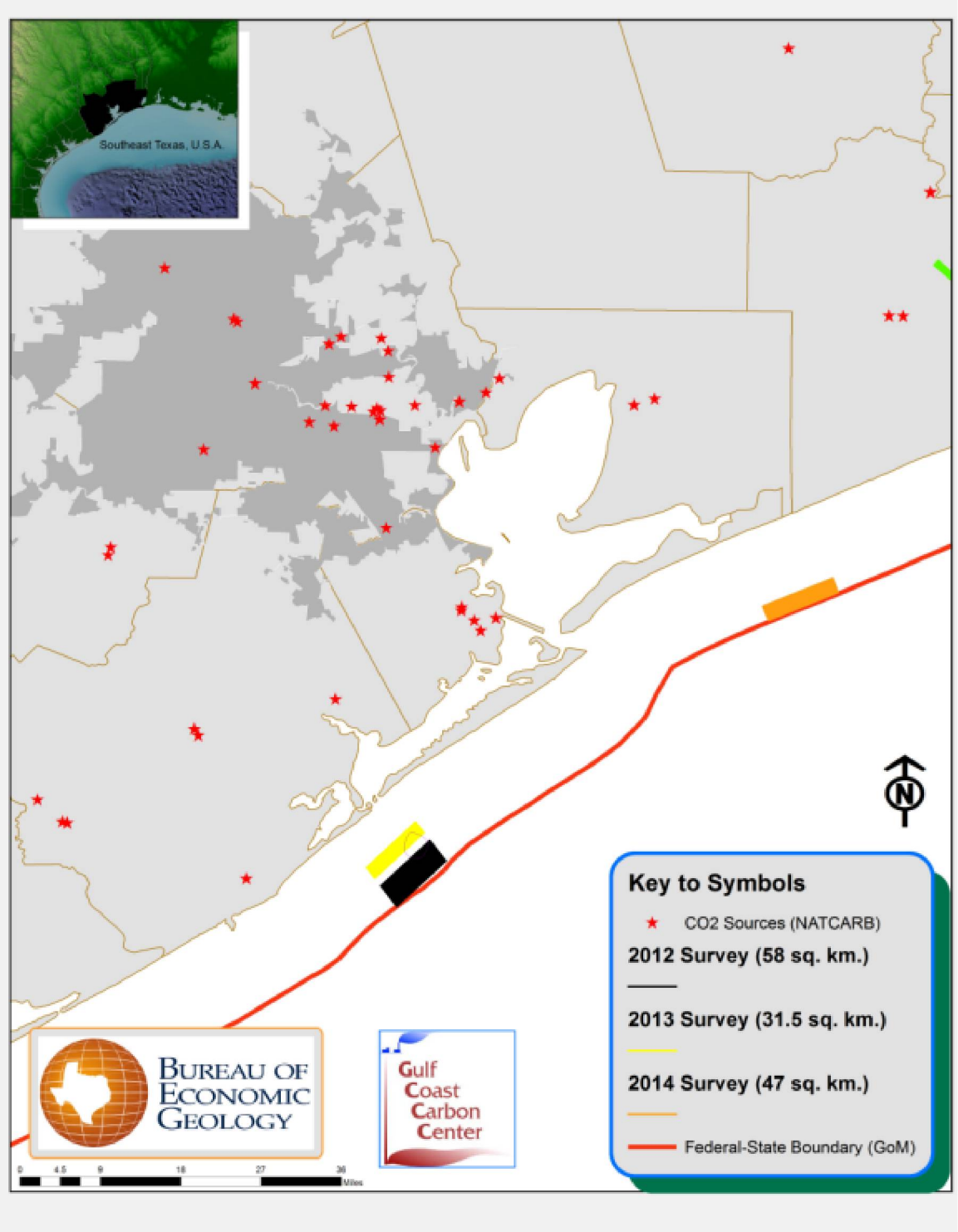

Figure 1.1: Figure 1 – A map of the southeast Texas coastal region showing the locations of three HR3D (P-Cable) surveys collected by the study. The outline of the 2012 survey is shown in black, the 2013 survey in yellow and the 2014 survey in orange. Note the outline of the city of Houston in dark gray and the boundary (red line) between State and Federal waters.

Since a significant portion of the augmented funding (see Introduction) went toward the purchase and operation of the innovative HR3D system (a.k.a. P-Cable), the HR3D system (Figure 8.1, Figure 8.2, Figure 8.3 and Figure 8.4) required significant project management time

and resources. The HR3D system was developed by P-Cable 3D Seismic, AS, http://www.pcable.com/index.php/about and was manufactured in San Jose, CA by Geometrics, Inc. The P-Cable system had been envisioned as a component of the original proposal, but it was removed before proposal submittal because its cost was greater than original available budget. Consequently, when augmented funding became available, the P-Cable system and its operation easily fit into the already existing scope and structure of the grant's research program. The original term of the Study was 36 months. After the augmented funding was secured, the Principal Investigators, Dr. Timothy A. "Tip" Meckel and Mr. Ramon Trevino, requested and received permission to extend the study for another 21 months for a total Study length of 4.75 years. The request was based on previous experience with complex field experiments (i.e., by the Gulf Coast Carbon Center at the Bureau of Economic Geology) and specifically with the expectation that the field operations related to the P-Cable 3D seismic acquisition would logistically require significantly more time. This proved to be correct as the entire system was not delivered until June 2012, only six month before the original end of the Study. Therefore, the Study's extended period of performance was definitely necessary.

The Study also established a laboratory used in high-pressure / high-temperature, rock-brine reactions (Tasks 6 and 7), which required in-depth interactions with the system designers as well as purchasing the various components. Figure 1.2 and Figure 1.3 are photos of the supercritical reaction system.

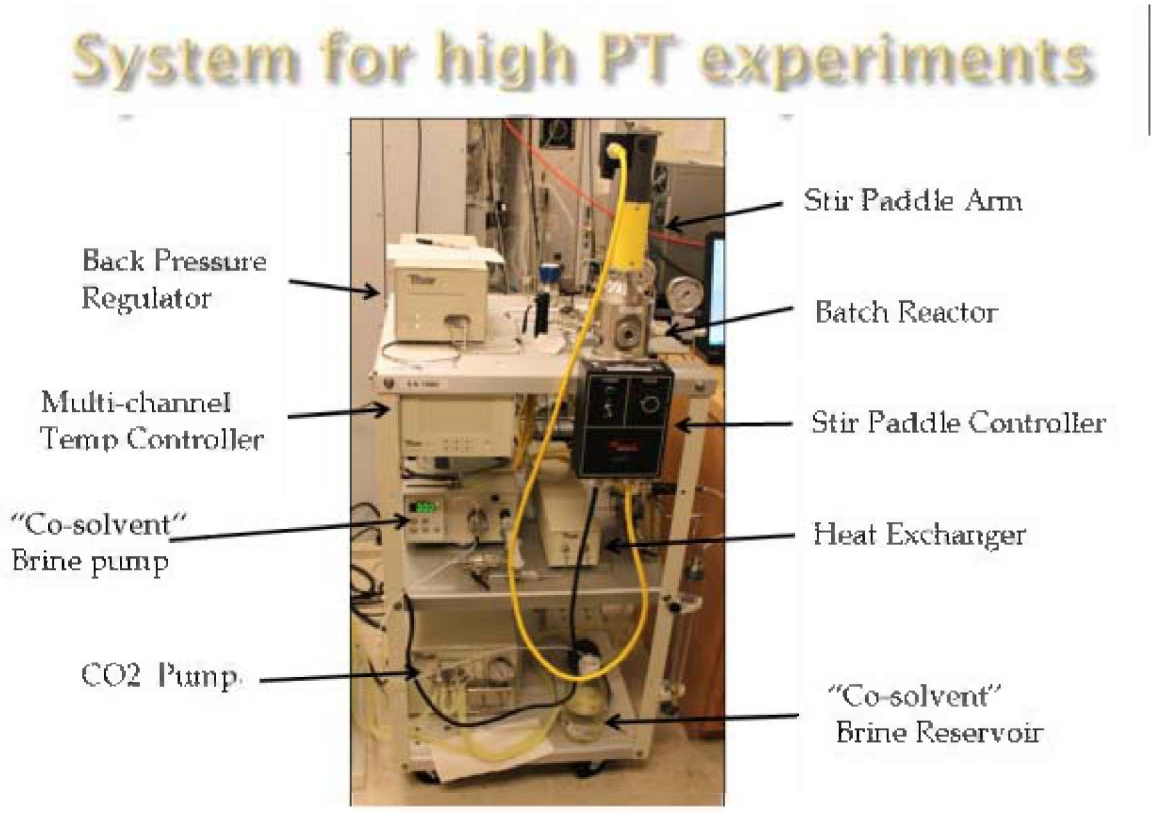

Figure 1.2: Integrated, supercritical reaction system capable of gas mixing.

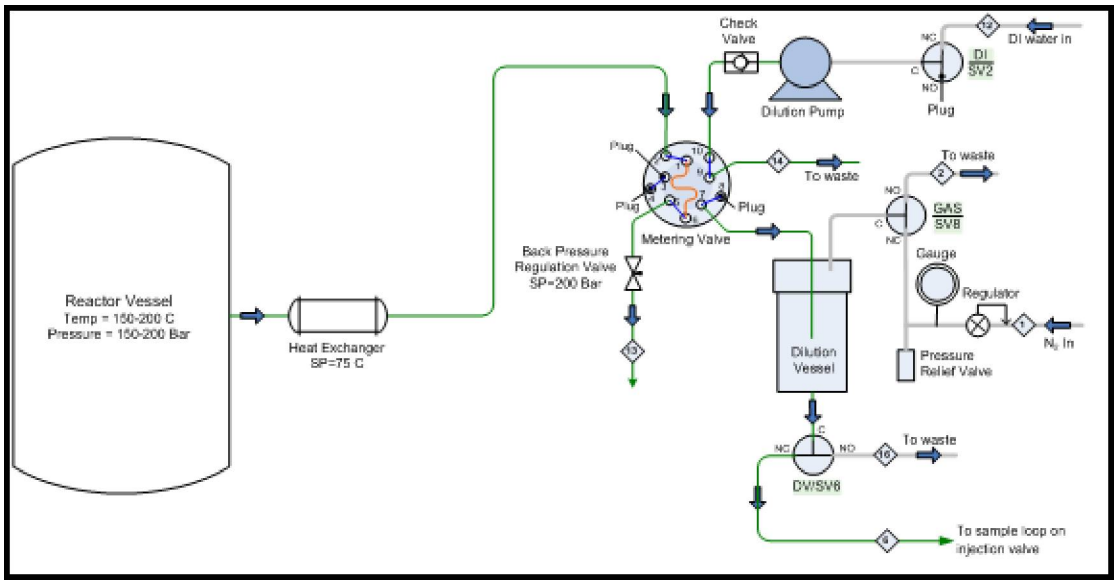

Figure 1.3: Schematic for innovative brine sampling system developed by scientists at Dionex and the BEG. The system will allow brine to be sampled directly from the reactor in a non-oxygenated setting, diluted and analyzed for anions and cations.

Tasks 2, Regional geology and significance, also required significant project management attention throughout the Study but especially in the first 2 years when data, dataset and database creation were high priorities. The task required the hiring, training and mentoring of several undergraduate research assistants. Similarly, Tasks 3, 4, 5 and 9, involved several graduate research assistants whose contributions were significant.

Throughout the study, meeting with staff, planning and directing research and reporting required time and resources. As the following detailed task-specific summaries reflect, the project management efforts yielded important research results and advances as wells as various publications.

2 Task 2.0: Regional Geology and Significance

As stated in Subtask 2.3, it is generally accepted that any geologic study should begin with a good understanding of the regional geologic setting. As the area of interest for the current study encompassed a large area (Figure 2.1), we determined that the regional geologic overview should comprise an even broader area of review. The Study area had the great advantage that oil and gas companies have explored and produced hydrocarbons for many decades in and around the study area (Figure 2.1). Consequently, the Study used the large quantities of geological data to conduct its regional geologic analysis.

2.1 Subtask 2.1: Atlas of prospective sequestration ‘plays’

This subtask composed a significant portion of the overall Study, and the data collection and database creation and maintenance formed a useful foundation for the rest of the Study. As is

enumerated in subtask 2.3, data and database management are significant and important parts of any geologic study, and in an effort of the size and scope of the current Study, they required substantial human and financial resources.

The fulfillment of Subtask 2.1, "The Geological CO_2 Sequestration Atlas for Miocene Strata Offshore Texas State Waters," is found in the Appendix A.

2.2 Subtask 2.2: Comprehensive data set of formation characteristics

Completion of this subtask over the study area and adjacent regions took several year of dedicated effort by many research assistants under the direction of researcher David Carr. Data collected included well and seismic data.

Well data collected are as follows: 12,750 wells that penetrate the Miocene; 6,893 wells in TX State waters (Figure Figure 2.1); 3,445 with well raster and/or digital logs; 424 wells with Paleontologic data; 241 with directional surveys. The foregoing wells are a subset of a much larger set of wells and well data that were assembled for the Federal Waters of the northern and western Gulf of Mexico. The total number of wells in the database is > 65,000 (Figure Figure 2.2) of which > 18,000 wells have paleontological data (i.e., paleo microfossil biozone). The well data are stored in an IHS Petra Database. The Project has access to a set of regional 2D seismic lines known as the "GulfSPAN Merge" that were made available at no cost to the project by ION Geophysical. The locations of the 2D seismic shot points were loaded into the study's PetraSeis / IHS Petra database. Some of the data were also loaded into an SMT Kingdom Suite Project for a preliminary data quality check. Although, each interpretation package provides distinct interpretation strengths, it was determined that a third, the Landmark seismic interpretation platform was the best and most robust interpretation package. Therefore, a Landmark project was established for the Project, and the 2D data were downloaded to it, and interpretation of seismic coverage of Texas State Waters and adjacent areas was undertaken.

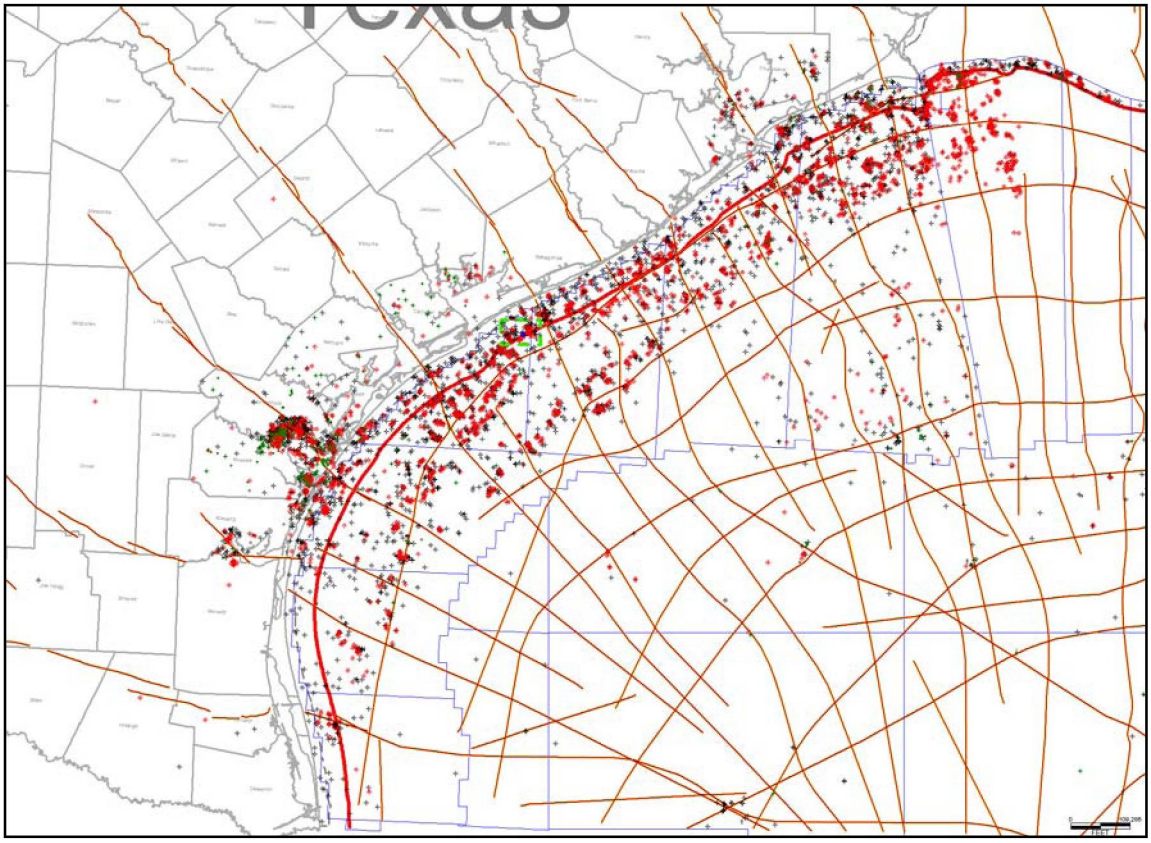

Figure 2.1: Map of the northwest Gulf of Mexico showing wells that penetrate Miocene age rocks in Texas State Waters, Texas coastal counties and Federal OCS blocks. Lines roughly orthogonal to the coast line are 2D seismic lines from the GulfSpan Merge dataset. Note the red line paralleling the coastline; offshore Texas state waters are north and west of that line and comprise the study area.

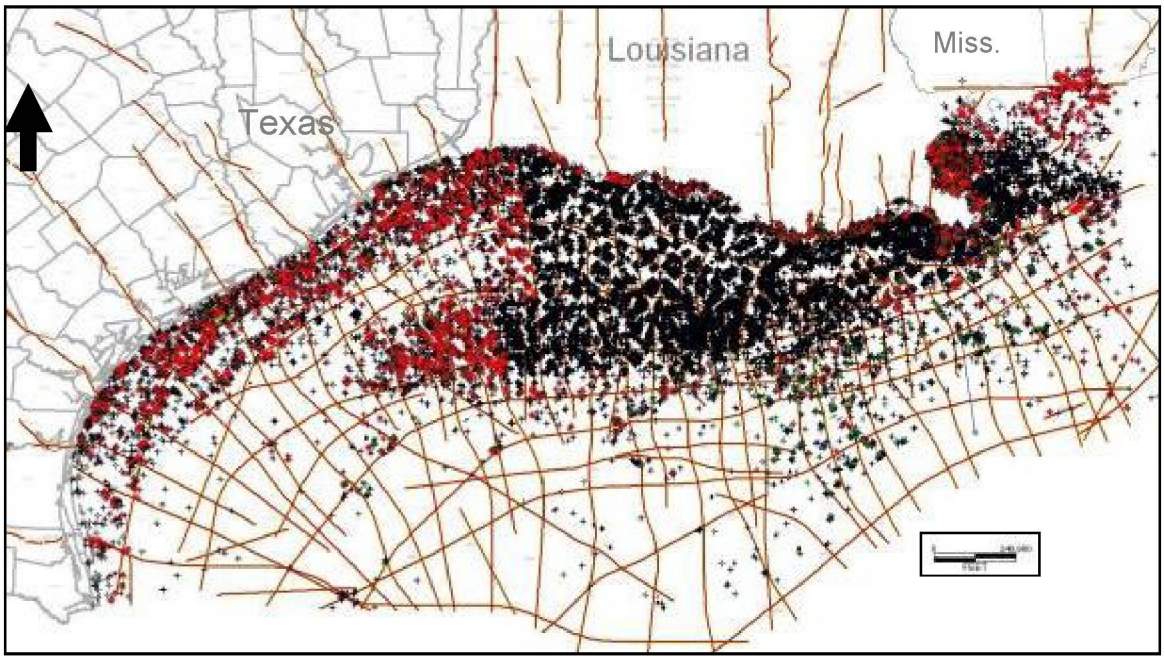

Figure 2.2: Map of the northern Gulf of Mexico showing wells that penetrate Miocene age rocks in Federal OCS blocks. Lines roughly orthogonal to the coast line are 2D seismic lines from the GulfSpan Merge dataset

Additional paleontological data were purchased in the form of the "Palcon Phase II" dataset (Pickering Enterprises). Undergraduate research assistants provided important identification information for 49 of the 307 Palcon wells in the study, which resulted in a cost savings of $1,780 off the original price (a discount of 14.5%).

A total of 778 well log rasters were added to the Petra database from the collection of the Texas General Land Office (GLO). Adding the well logs required first identifying the wells' API numbers in order to match them to the correct well information already in the database. This task involved several graduate and undergraduate research assistants. Figure Figure 2.3 shows the pertinent wells as of September 30, 2010.

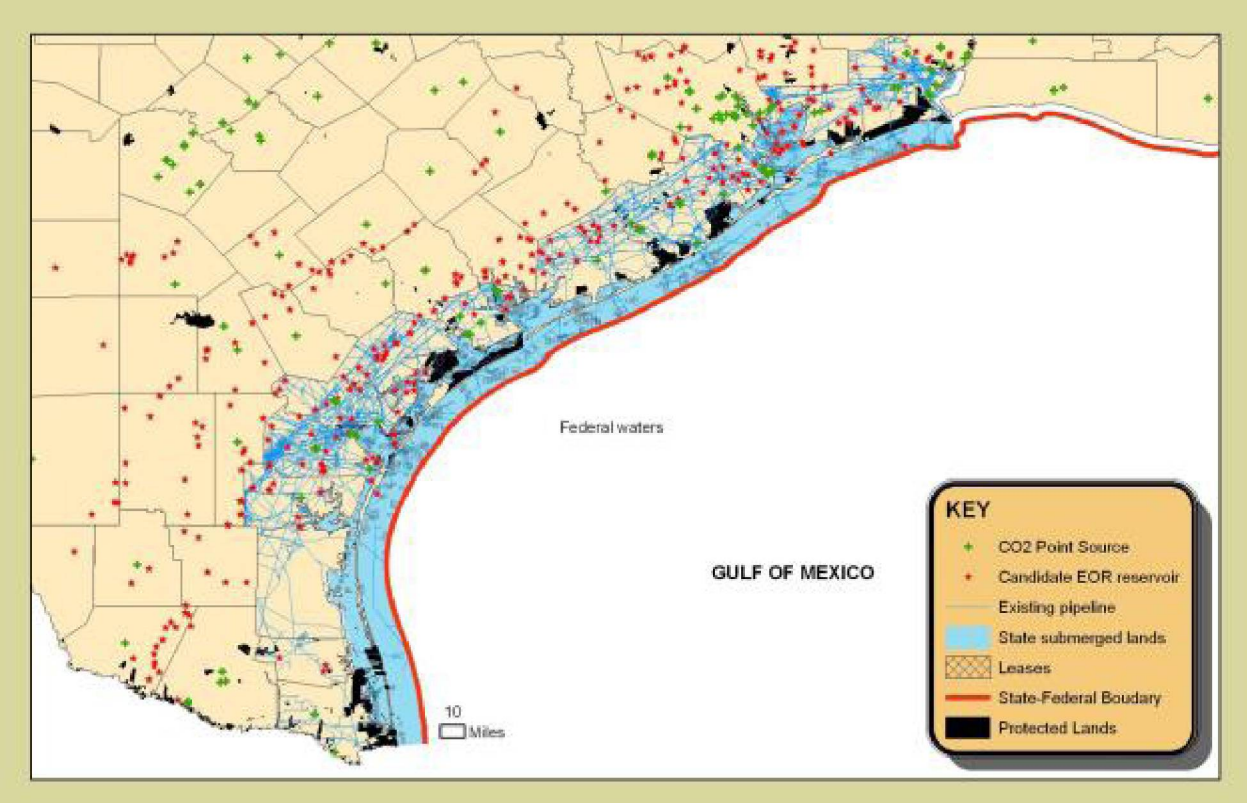

Figure 2.3: Map of the Texas coast showing the Study area (blue). The red line marks the boundary between State and Federal (Offshore Continental Shelf – OSC) waters.

The Study acquired a total of 95 velocity surveys within the High Island and OBS 3D seismic coverage areas (Figure Figure 2.4); 63 of the wells were acquired as a batch most from Petrophysics, Inc. The surveys were imported into the project's Petra database. With the addition of the new velocity surveys, there are now a total of 95 wells with velocity data in the project database (Table 2.2.1). The surveys are very important for tying wells and their data to seismic data and transferring well tops, originally picked in depth (domain), to the 3D volumes (in time domain). Similarly, the wells with velocity surveys are used to help convert the 3D volumes from time to depth (i.e., generating depth volumes, which can then be used in flow simulations).

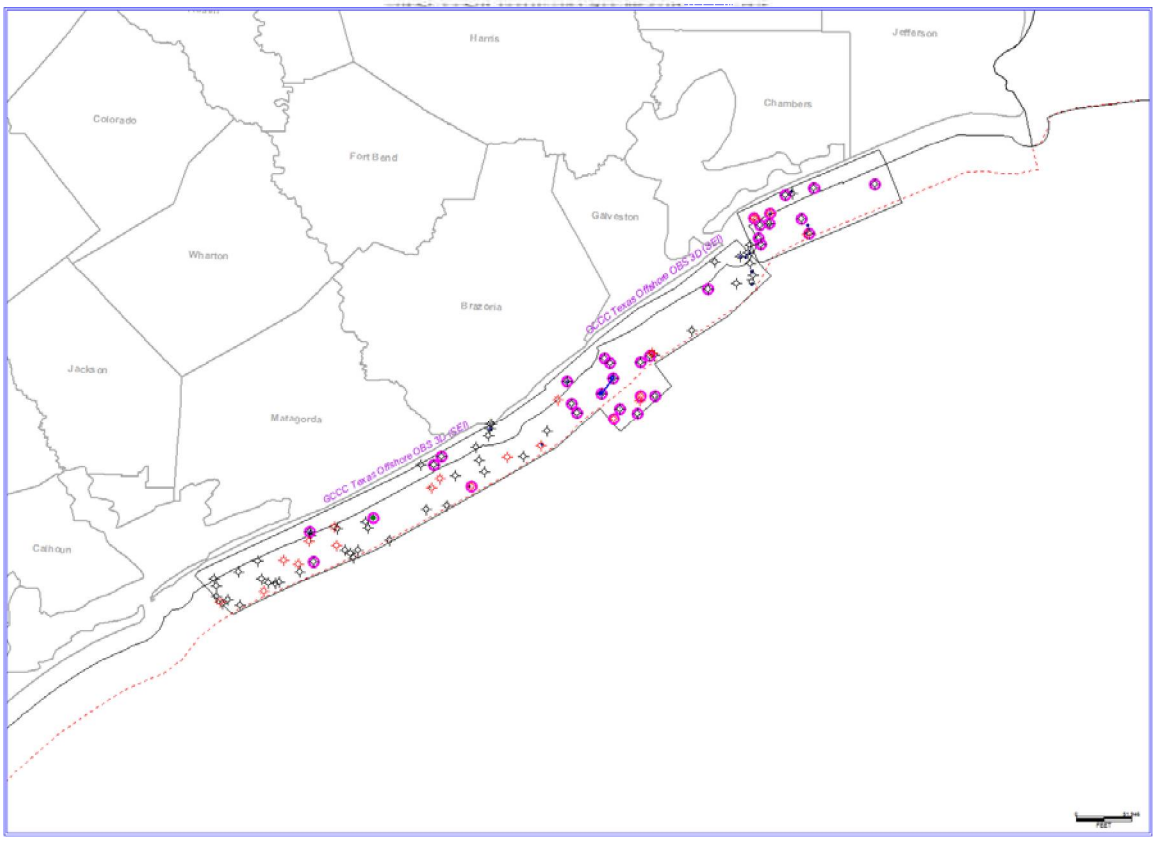

Figure 2.4: Map showing location of velocity surveys in the Study's database. Highlighted wells have velocity surveys that were acquired from various sources, non-highlighted wells denote 63 wells whose velocity surveys were purchased as a single set. See Table 2.2.1 for a list of all wells with velocity surveys.

Table 2.2.1: All wells in the database with velocity surveys. Gcvd is Gulf Coast Velocity Data and tgs is TGS NOPEC. Logdigi is a digitization company, and "in house" denotes logs digitized by the Study's research assistants.

API	Velocity type	Velocity source	Deviation survey	Deviation survey source	Existing log data in petra	Additional log data source	digitization
427064034400	Checkshot	gcvd	V		R	ihs	logdigi
427040000400	Checkshot	gcvd	D		R	ihs	logdigi
42604300120000	Checkshot	Petrophysics inc	V		R	ihs	logdigi
42604301210000	Checkshot	Petrophysics Inc	V		R	ihs	logdigi
42604301550000	Checkshot	gcvd	D		R	ihs	logdigi
42604301570000	Checkshot	gcvd	V		R	ihs	logdigi
42604301610000	Checkshot	tgs	V		R	ihs	logdigi
42703000130000	Checkshot	gcvd	V		R	Tgs	logdigi
42703000290000	Checkshot	gcvd	V		R	Tgs	logdigi
42703000380000	Checkshot	gcvd	V		R	ihs	logdigi
42703300470000	Checkshot	tgs	V		R	Tgs	logdigi
42703300590000	Checkshot	gcvd	V		R	ihs	logdigi
42704000100000	Checkshot	gcvd	V		R	Tgs	logdigi
42704000130000	Checkshot	gcvd	V		R	Tgs	logdigi
42704000160000	Checkshot	tgs	V		R	Tgs	logdigi
42704000220000	Checkshot	gcvd	V		R	Tgs	logdigi

42704000240000	Checkshot	gcvd	V		N		
42704000330000	Checkshot	tgs	V		R	Tgs	logdigi
42704300460000	Checkshot	gcvd	V		R	ihs	logdigi
42704300550000	Checkshot	gcvd	V		R	ihs	logdigi
42704300700000	Checkshot	gcvd	V		R	ihs	logdigi
42704301600000	Checkshot	tgs	V		R	Tgs	logdigi
42704301630000	Checkshot	gcvd	V		R	Tgs	logdigi
42704301700000	Checkshot	gcvd	V		R	ihs	logdigi
42704301770000	Checkshot	gcvd	V		R	ihs	logdigi
42704302760000	Checkshot	tgs	D		R	ihs	logdigi
42704302770000	Checkshot	gcvd	V		R	ihs	logdigi
42706301030000	Checkshot	gcvd	V		R	ihs	logdigi
42706301070000	Checkshot	tgs	V		R	ihs	logdigi
42706301860000	Checkshot	gcvd	D	RRC	R	ihs	logdigi
427060003700	Checkshot	gcvd	D		R+D		
427060013900	Checkshot	gcvd	D		R+D		
427064027100	Checkshot	gcvd	D		R+D		
427064010000	Checkshot	gcvd	D		R+D		
42706401330000	Checkshot	gcvd	D		R+D		
42603300230000	Checkshot	gcvd	V		R+D		
42604300180000	Checkshot	Petrophysics inc	V		R+D		
42604300190000	Checkshot	gcvd	V		R		In house
42604300240000	Checkshot	NA	V		R+D		
42604300380000	Checkshot	gcvd	V		R		In house
42605000170000	Checkshot	gcvd	V		R		In house
42605300190000	Checkshot	gcvd	V		R+D		
42605300200000	Checkshot	Gcvd	D	ihs	R+D		
42605300240000	Checkshot	gcvd	D		R+D		
42605300250000	Checkshot	gcvd	D		R+D		
42605300350000	Checkshot	gcvd	V		R+D		
42605301300000	Checkshot	gcvd	V		R+D		
42606300110000	Checkshot	gcvd	v		R+D		
42703000310000	Checkshot	tgs	v		R+D		
42703300480000	Checkshot	gcvd	v		R+D		
42703300760000	Checkshot	gcvd	V		R+D		
42703301400000	Checkshot	gcvd	V		R		In house
42703302010000	Checkshot	tgs	V		R+D		
42703302240000	Checkshot	gcvd	V		R		In house
42704000690000	Checkshot	gcvd	V		R+D		
42704300630000	Checkshot	tgs	V		R		In house
42704300680000	Checkshot	gcvd	V		R+D		
42704300780000	Checkshot	gcvd	V		R+D		
42704300930000	Checkshot	tgs	V		R+D		
42704301730000	Checkshot	tgs	V		R+D		
42704301950000	Checkshot	Tgs	V		R+D		
42704302290000	Checkshot	gcvd	V		R+D		
42704302370000	Checkshot	Petrophysics Inc	N		R		In house
42704302380000	Checkshot	gcvd	V		R+D		
42704302560000	Checkshot	Petrophysics inc	D		R+D		
42704302710000	Checkshot	Petrophysics inc	V		R		In house
42706000150000	Checkshot	gcvd	D	tgs	R+D		
42706000180000	Checkshot	gcvd	V		R+D		

42706000190000	Checkshot	gcvd	V		R+D		
42706000800000	Checkshot	Petrophysics inc	V		R+D		
42706000950000	Checkshot	gcvd	V		R+D		
42706001330000	Checkshot	gcvd	V		R+D		
42706300090000	Checkshot	tgs	V		R+D		
42706300300000	Checkshot	gcvd	V		R+D		
42706300550000	Checkshot	gcvd	D	tgs	R+D		
42706300770000	Checkshot	gcvd	V		R+D		
42706300810000	Checkshot	gcvd	V		R+D		
42706300910000	Checkshot	Petrophysics inc	V		R+D		
42706300920000	Checkshot	gcvd	V		R+D		
42706300960000	Checkshot	gcvd	V		R+D		
42706301190000	Checkshot	tgs	V		R+D		
42706301400000	Checkshot	tgs	D	tgs	R		In house
42706301440000	Checkshot	gcvd	V		R+D		
42706301520000	Checkshot	gcvd	V		R+D		
42706301570000	Checkshot	gcvd	V		R+D		
42706301590000	Checkshot	tgs	V		R		In house
42706301620000	Checkshot	gcvd	D		R+D		
42706301770000	Checkshot	gcvd	N		R+D		
42706301920000	Checkshot	gcvd	N		R+D		
42706301990000	Checkshot	gcvd	D	tgs	R+D		
42708000760000	Checkshot	gcvd	V		R+D		
42708300140000	Checkshot	gcvd	V		R+D		
42708301010000	Checkshot	gcvd	D	tgs	R		In house

Commercial 3D Seismic

In addition to well log data, the San Luis Pass Salt Dome (SLPSD) (Figure 8.5) area and a broader region of the Texas State Waters were characterized by a regional dataset of commercial 3D seismic data (**Error! Reference source not found.**) that was leased from SEI, Inc. with substantial cost share benefit to the Study. The availability of the commercial 3D seismic, provided substantially improved understanding of the subsurface to the Study's researchers.

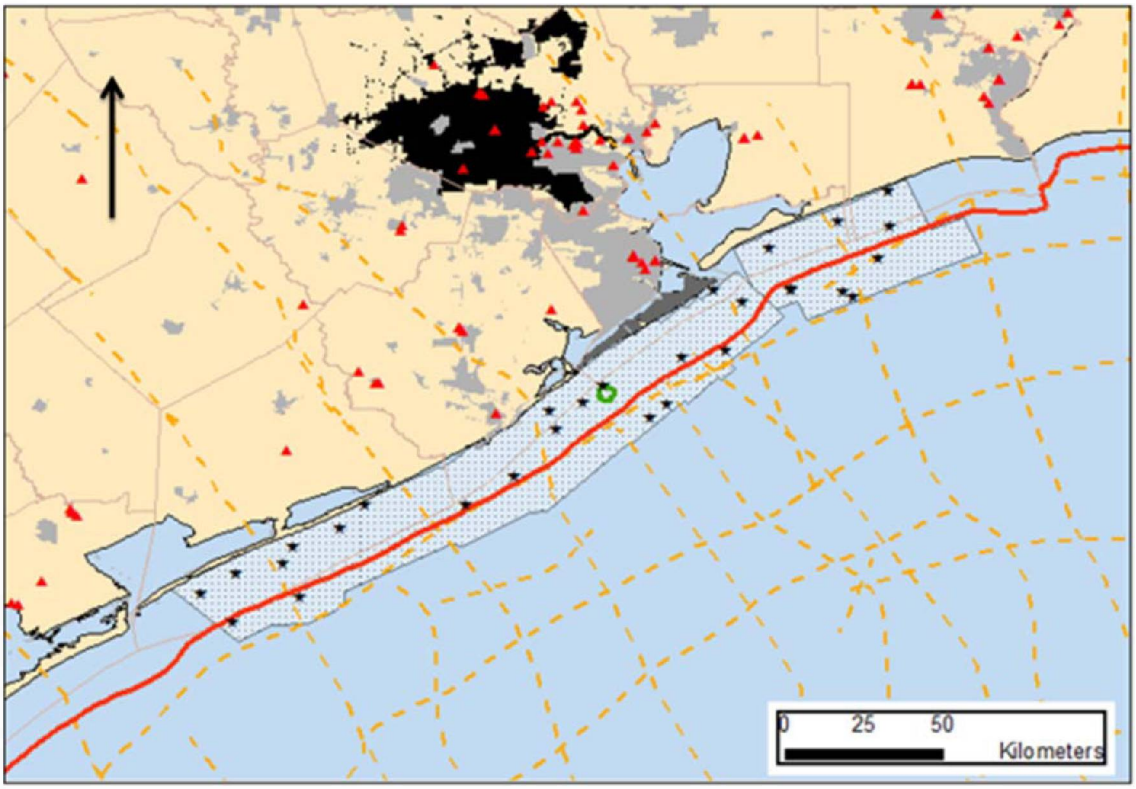

Figure 2.5: Location Map of the upper Texas coastal zone. Gray polygons in the onshore area represent urban areas, and the black polygons include portions of the Houston metro area. Stippled polygons in the near shore waters define the areal coverage of 3D seismic datasets leased for the current Study from SEI, Inc. Red triangles show locations of CO_2 sources.

2.3 Subtask 2.3: Best practices for site characterization

Database assembly and management

This task is a critical early step in any site geo-sequestration (GS) characterization effort, and even though the majority of this activity occurs early in the process it continues throughout, as new data may be discovered late in the area's analysis. In addition, processing and improvement of the existing data (e.g., digitizing, recognizing and excluding bad data points, etc.) may (and often do) take place during mature stages of data analysis and interpretation. Another important early task is to determine which subsurface geologic interpretation software package or packages best meet the projected needs of the study. In the current study, we used IHS Petra and Halliburton Landmark partly because of staff familiarity and expertise with the software but also because the former has widely recognized and superior database capability with well data and well-based interpretation; whereas, the former has similarly excellent seismic data and interpretation module capacities. Many different commercial flow simulation packages are available (e.g. Landmark Nexus; Schlumberger Eclipse, CMG GEM, TOUGH2 suite, etc), and selection of a simulation package is dependent primarily on familiarity. While most have proprietary data formats, they accept common formats (e.g. well log LAS) during model building.

I. Data Acquisition

a. Well-related data (mostly wireline well logs and biostratigraphic tops)

i. Determine data sources – There are generally two sources of well-based data: 1) those archived and held by governmental bodies, which may be available at no cost or at a nominal price, and 2) those data archived by private vendors, which charge usually cost more. The latter data may have already be improved or edited ("QC'd") by the private vendors, which may be a worthwhile investment versus conducting in-house QC.
    1. Governmental – This can include national (e.g., U.S. Federal government) and/or regional (e.g., U.S. States) departments or agencies.
    2. Industry (vendors) - Examples of these include international vendors (e.g., IHS, TGS-Nopec) national (e.g., DrillingInfo) or smaller regional / local companies (e.g., Pickering Enterprises, "Palcon" biostratigraphic data).

ii. Acquire data – Once identified, acquisition of governmental data may simply involve downloading the data to a local drive. Private vendor data acquisition may be similarly easy, and customer support should be available if problems are encountered. With governmental data user assistance can be spotty, and extra time may be needed, which should be recognized during project management planning.
    1. Select interpretation software package(s) – If a software interpretation package has not yet been selected, it should be selected at this point because the following steps require it. If digital (LAS – Log ASCII Standard) data are available, they are preferable, albeit more expensive, because they can be much more extensively utilized for quantitative log analyses. However, the overwhelming majority of wells may only have raster images available. Consequently, selecting an interpretation package that can handle rasters is imperative. Rasters can still be used for correlating and some quantitative analyses (e.g., "sand counting").
    2. QC data – quality control (QC) of the well data should always be undertaken as soon as possible. Faulty data and/or poor data quality can and often do negatively impact subsequent interpretations often resulting in incorrect interpretations. Data QC should be ongoing throughout the study and especially in the early stages.
    3. Load data – Ideally, all well data that are loaded into the selected software interpretation package are QC'd before loading, but this may not be practical. More typically, well data are loaded in their "raw" form and QC is performed as interpretation progresses from one geographic area to another.

b. Seismic data (2D and 3D)

i. Determine data sources – In general access to 2D seismic is easier to access than 3D seismic data. Similarly, older data are more accessible than newer datasets.

1. Public – Governmental agencies rarely have access to or own seismic data, but it is worthwhile to at least check some of the same agencies that archive or provide well data to the public. In rare cases, universities in the region of interest have been granted permission to use / share (usually older) seismic data.
2. Industry (vendors) – The overwhelming majority of seismic data comes from private companies. If the study is working with a petroleum company, that company is the first option; proprietary data may be available. Otherwise, vendors of speculative ("spec") data will need to be consulted.

ii. Acquire data – Seismic data are almost always leased except in the case of publically available data.
1. QC data – Seismic data should be reviewed by experienced geophysicists in order to identify non-geologic artifacts, which could, otherwise, be misinterpreted as geologic features. If necessary, should be re-processed as early as possible.
2. Select interpretation software package(s) – Several interpretation packages are available. The three dominant "families" of seismic interpretation software are Halliburton's Landmark, Schlumberger's Petrel and IHS' Kingdom, but there are others that may be more cost-effective depending on the particular requirements and needs of a project.
3. Load data – Data are usually loaded in "seg-y" format, but other formats are available. In general, loading of seismic data is much easier than loading of well data (e.g., wireline well logs, paleontological data, etc.). There may be varying degrees of difficulty with 2D seismic of different vintages, but commercial 3D seismic data are very straightforward if a minimum amount of information is included in the file.

II. Site Selection

a. **Regional Geologic interpretation** – Any site characterization study should begin and progress with a good understanding of the regional geology. As such, a robust regional geologic interpretation should be undertaken before site characterization and selection.

i. Literature review
1. Understand basin history – Geologic features that develop early in a basin's history of often affects younger geologic Systems in predictable ways. Therefore, understanding the general basin history can improve the interpretation of a specific site's geology.
2. Understand fluid systems – The fluid system of a basin is important in that it will impact the distribution of CO_2 after injection. If the basin produces petroleum, the petroleum system can be used as an analog. Understanding the shallow groundwater

systems is also important if shallow monitoring might be used during/after injection.

ii. Determine time-stratigraphic framework – Identify and incorporate regionally significant and pertinent bio-chronozones as soon as possible because they are critical for interpreting time stratigraphic units (i.e., versus lithostratigraphy, which can be misleading).

iii. Select a time-stratigraphic model – The selection of a time-stratigraphic model depends, to a large degree, on which of the main types of time-stratigraphic surfaces (i.e., transgressive surfaces of erosion, sequence boundaries or maximum flooding surfaces) is most readily identifiable. If sequence boundaries are easily recognizable sequence stratigraphy is preferable. If not, genetic stratigraphy should be considered. Similarly, if a fine-scale stratigraphic will ultimately be needed, sequence stratigraphy is preferable. If a coarser scale stratigraphic framework is acceptable either model can be used. In some basins transgressive surfaces are most prominent. Ultimately, the choice can be informed by a clear understanding of the available choices (Catuneanu et al., 2009)
    1. Sequence stratigraphy (Mitchum et al., 1977; Vail and Mitchum, 1977)
    2. Genetic stratigraphy (Galloway, 1989)
    3. Combination?
    4. Other?

iv. Determine tectonic and structural framework – As with selection of a stratigraphic model, understanding the basic tectonic framework of a basin is fundamental to an understanding of important structural elements that can have a significant impact on retention, attenuation or non-retention of injected CO_2. Following is a non-exhaustive list of items that should be understood in order to determine the viability of a region and site for engineered CO_2 storage.
    1. Dominant tectonic trends
        a. Active vs. passive margin
        b. Compressional vs. extensional terrains
        c. Mobile substrate present? If so, type is:
            i. Salt?
            ii. Fine-grained clastic ("shale")?
    2. Dominant deformation type
        a. Folding (type and prominence)
        b. Faulting (type and prominence)

v. Identify / analyze prospective regional units
    1. Reservoirs (regional saline aquifers)
        a. Below supercritical CO_2 depth?
        b. Above over-pressure depth?
            i. Analyze reservoir data
                1. Porosity

2. Permeability
3. Salinity

c. Calculate regional static capacity

2. Confining systems (seals)
   a. Identify available rock samples – Rock samples of confining zones (e.g., mudrock units, evaporates, etc.) are often difficult to obtain because the petroleum industry, from which a large proportion of whole rock samples (cores) come, has historically taken cores of reservoirs but not seal units. Nonetheless, some samples are available. If outcrops are available, use them keeping in mind that many facies of confining zone units can be easily altered by near-surface environments and may, consequently, be very different (e.g., mineralogically) in the deep subsurface.
   b. Analyze samples – The list below provides some examples of the analyses that can be used to gauge the potential suitability of confining units before new wells are drilled. Each analysis can be qualitatively or quantitatively related to retention potential.
      i. Capillary pressure properties (mercury intrusion capillary pressure analysis – MICP); These can be converted to CO_2 column height retained for the site of interest.
      ii. Scanning electron microscopy (e.g., argon-ion milled).
      iii. Clay alignment (e.g., high-resolution X-ray texture goniometry).

b. Determine potential "play" types – Using the oil and gas industry's "play" concept, determine possible geologic scenarios in the region of interest that might trap and retain CO_2 for the amount of time required (usually hundreds to thousands of years) as part of the project permitting process.
   i. If available, use petroleum fields as analogs
      1. Trap styles
         a. Structural (e.g. antiform, fault)
         b. Stratigraphic (e.g. lateral facies change)
         c. Combination
         d. Fluid drive types
            i. Open system (preferable)
            ii. Closed/Compartmentalized system (capacity-limiting parameter)
      2. Field sizes
         a. Statistically analyze accumulations

i. Known accumulations of gas and/or oil provide some basis for which seal quality and storage volumes may be assessed. Creating a cumulative distribution (CDF) plot of field sizes will highlight the largest field sizes that occur naturally, and the intended storage volumes can be compared.

ii. If no petroleum production history, determine the reason – May require examination and evaluation of surface outcrops, stratigraphic test wells, water industry data, acquisition / analysis GS-specific exploratory data (e.g., new wells, seismic data), etc. Primary reasons often relate to non-mature source rock or bypass during hydrocarbon migration.

1. Frontier area / lack of exploration? – In frontier areas with little or no petroleum exploration, items number 2-5 (immediately below) should be evaluated as precisely as possible despite (because of?) the attendant lack of petroleum industry related data.
2. Lack of hydrocarbon source? – Some basins have no organic-rich hydrocarbon source rock (e.g., high, total-organic-carbon units), or if one or more units does/do exist, they have not undergone the necessary conditions to generate hydrocarbons (Waples, 1980). Good GS candidates may, nonetheless exist.
3. Lack of confining system? – If so, is this the capacity-limiting parameter? Good GS candidates may, nonetheless exist.
4. Lack of reservoirs? – If so, is this the capacity-limiting parameter? Have potential reservoirs been overlooked? Good GS candidates may, nonetheless exist.
5. Breaching of traps? – If so, is this the capacity-limiting parameter
    a. Post petroleum migration trap breaches – subsequently "healed?" Good GS candidates may, nonetheless exist.
    b.

c. Identify *leads* (areas with good potential for CO_2 geo-sequestration) – These are specific areas that exhibit positive GS potential in terms of reservoir, confining system, structural configuration stratigraphic composition and/or reservoir drive. Closely examine the *lead* area based on the GS potential,

d. Select sites (prospects) from the most promising leads. Ranking of these sites may be achieved for a given set of priorities (e.g. volume, security, monitoring).

III. Characterize site(s) (prospects)

a. Identify risks (iterative tasks with geologic characterization of site, below). An example of risk assessment is provided by the 'Bowtie' method (e.g. Tucker et al., 2013).

i. Environmental/geologic

1. Top seal

2. Fault seal
3. Injectivity

ii. Infrastructure
1. Pre-existing well bores
2. Pipelines

iii. Economic
1. CCUS opportunities?
2. Conveniently located relative to anthropogenic source(s)

b. Interpret local well data

i. Stratigraphic
1. Incorporate biostratigraphic data
2. Identify time-stratigraphic surfaces
a. Sequence boundaries
b. Marine condensed section / maximum flooding surfaces
3. Iterate with seismic interpretation (if available)

ii. Structural
1. Identify fault cuts in wells
2. Iterate with seismic interpretation (if available)

c. Interpret local seismic data (time domain)

i. Pick / map significant seismic reflections
1. Generate time horizons

ii. Identify / define faults

iii. Iterate with well log interpretations
1. Digitize well logs (LAS – log ASCII standard) if not already done
2. Identify (purchase if necessary) well-based time-depth data
a. Acoustic (sonic) well logs
b. Check-shot data
c. VSP (vertical seismic profiles)
3. Generate time-depth tables
a. Associate with wells of utilized well logs
b. Associate time-depth tables with nearby wells
4. Import well logs into time domain.
a. Compare well-based time-stratigraphic horizons (sequence boundaries & maximum flooding surfaces) with seismic dataset.
b. Iterate - adjust wells' time-depth tables to match seismic-based with well-based interpretations.

d. Convert seismic to depth

i. Generate velocity model – utilize well-based time-depth data

ii. Apply to time volume – generate depth volume

iii. Iterate
1. Load original (depth domain) well log data.
2. Adjust or discard data from obvious data busts.

3. Update velocity model until satisfied.

e. Generate volumetrics (depth volume)
   i. Map top and base of potential reservoirs, typically using seismic amplitude minimums, maximums, or crossovers, as suggested by well log correlation.
   ii. Determine area and porosity.
   iii. Map projected CO_2 densities at reservoir depths.

f. Generate static geo-model
   i. Use mapped horizons (converted from time to depth) as a framework for discretizing/gridding reservoir volume.Selection of cell size is dependent on volume of interest and computational resources. In general coarser cell sizes allow faster run times, at the expense of spatial resolution.

g. Generate fluid flow model
   i. Injection schedule: determine injection rates for individual wells, which may require some iteration. Typically wells are assigned either a constant rate or constant downhole pressure.
   ii. Boundary conditions: Arguably the most important decision related to simulation, as it is generally unknown at the scales of most models. Well tests (e.g. pressure fall off) are typically sought to inform this decision. Prior production pressure history may also inform this decision, if the site had prior production data.
   iii. PVT table: Pressure-volume-temperature data are needed for multi-phase and compositional simulators. The research literature (e.g. Duan and Sun, 2003) provide standard equations of state that are generally used for CO_2 -brine systems. Other PVT tables are available for systems incorporating hydrocarbons, and most simulators provide their preferred PVT tables.
   iv. Multiple realizations: Significant geologic uncertainties generally exist, which can be explored with multiple realizations (e.g. stochastic) and sensitivity analyses (single- or multi-parameter). It is important to bound the range of anticipated performance, and to identify which parameters are most influential for simulation results.

h. Determine local capacity (according to preferred models / algorithms)
   i. Static - in local area use, for example, methodology of Wallace et al. (2014) or Brennan et al. (2010).
   ii. Dynamic (determine pressure regime – fluid drive – open/closed system). This is a result that comes either from analytical solutions (relatively fast) or detailed fluid flow modeling (as in part g, above).

IV. Approve or Reject Site

a. Meets capacity cutoff in anticipated timeframe?
b. Acceptable risk profile?

i. Pressure evolution through time vs. fracture pressure.
ii. Potential long-term migration and trapping mechanisms (i.e. structural, residual, local capillary, dissolution, mineralization).

c. Monitoring needs met? (not considered in this workflow)
d. Project costs acceptable? (not considered in this workflow)

3 Task 3.0: Capacity Estimates (Site)

3.1 Task 3.0: Capacity Estimates (Site)

Following is a total Miocene capacity estimate for the study area. This work was the basis for a subsequent peer-reviewed publication (Wallace et al., 2014). The workflow used to generate a regional capacity estimate for the study area required integration of a number of geological, geophysical, geochemical, and engineering tasks that culminated in application of the Goodman et al. (2011) capacity methodology to estimate **a total CO_2 storage capacity of 86 Gigatonnes**.

[1]The equation used to calculate capacity is:

$G_{CO2} = A_t \ h_g \ \Phi_t \ \rho_{CO2} \ E_{saline}$ (tonnes or metric tons),
where

A_t = geographical area defining region of CO_2 storage
h_g = gross formation thickness
Φ_t = total porosity
ρ_{CO2} = density of CO2 estimated at temperature and pressure of anticipated storage (reservoir) conditions
E_{saline} = CO2 storage efficiency factor.

An explanation of the equation and the determination its variables' values follow:

Workflow

The entire workflow involved multiple stages of data acquisition, database construction and geologic / geophysical interpretation. Steps 1 – 10 (below) were mostly completed prior to the current reporting period, but minor parts, thereof, were finalized at the beginning of the period. As such, most have been reported in previous quarterly and annual reports, but are reiterated here for the sake of clarity and completeness.

1) Constructed Petra data base consisting chiefly of well data, micropaleontologic data ('paleo'), and geophysical well logs (raster images and LAS (log ascii standard) curves).
2) Utilized paleo data to define Miocene stratigraphic boundaries.
3) Correlated top and base of Miocene in well logs guided by paleo data.
4) Tied key wells to 2-D seismic lines and interpreted Miocene stratigraphic horizons.
5) Integrated well log tops and to 2-D seismic horizons to define top and base Miocene structure and made respective structure maps.
6) Determined net reservoir sandstone cutoffs of spontaneous potential (SP) and gamma ray curves (GR) from core calibration.

7) Performed net reservoir sandstone counts from raster logs and made automated LAS sand counts within Miocene stratigraphic boundaries.
8) For LAS curves, performed cursory petrophysical analysis for normalizing SP and GR, and calculated porosity from bulk density (RHOB), and sonic (DT) curves.
9) Performed reservoir summation to count permeable net sandstone (from both raster and LAS) and determine average porosity within the sand units (from LAS only).
10) Made a regional Miocene net sandstone reservoir isopach map from net reservoir sandstone count results (from both raster and LAS).
11) Made a regional Miocene average porosity isopach map from average porosity results (from LAS only).
12) Constructed a CO_2 density vs. depth curve from regional pressure and temperature trends
13) Made a regional Miocene CO_2 density map from CO_2 density vs. depth curve.
14) Determined effective top and base suitable for CO_2 sequestration from regional pressure and temperature data and used these structural surfaces (i.e., maps), which are sub-parallel to, but slightly cross-cut Miocene stratigraphic horizons, to define the Miocene Geological Sequestration Unit (GSU).
15) We applied the NETL-MIT capacity calculation equation (MIT, 2010) to the Miocene GSU, and made a map of CO_2 capacity per square mile.
16) Finally, to obtain total Miocene capacity in the project area, we summed the capacity per square mile values.

The details of these workflow tasks and results are presented and discussed below.

Data Base

Initial information regarding Miocene chronostratigraphic units, outlines of major regional faults and other data was obtained from the Gulf Basin Depositional Synthesis (GBDS) consortium, University of Texas Institute for Geophysics (UTIG).

The digital data base was constructed in Petra, a PC-based subsurface analysis application (http://www.ihs.com/products/oil-gas-information/analysis-software/petra.aspx), as a platform for integrating and interpreting data over the Texas State Waters and adjacent onshore and Federal OCS acreage (Figure 3.16). The main well data sources were IHS Energy, BOEMRE (formerly MMS) and DrillingInfo. We have obtained well data from over 80,000 wells, including approximately 25,00 in the Miocene mapping area in and adjacent to Texas State Waters on the GOM inner shelf.

Micropaleontologic data (a.k.a. paleo), were gathered from John Pickering's PalCon 1 (onshore Texas coastal plain) and 2 (Texas State Waters) data base, the Jack Colle Collection (BEG), as well as the extensive BOEMRE (formerly MMS) paleo data base available for the immediately adjacent Federal OCS.

We obtained geophysical well logs from 5507 wells (5215 with raster images, 672 with LAS curves). Primary sources for the well logs were the Texas General Land Office (GLO), DrillingInfo, IHS Energy, A2D-TGS Nopec, and BOEMRE (formerly MMS).

ION Geophysical's GulfSPAN MERGE 2-D seismic data set was utilized to provide continuous, interwell horizon correlations, fault interpretations, and seismic stratigraphic information to supplement the log and paleo data.

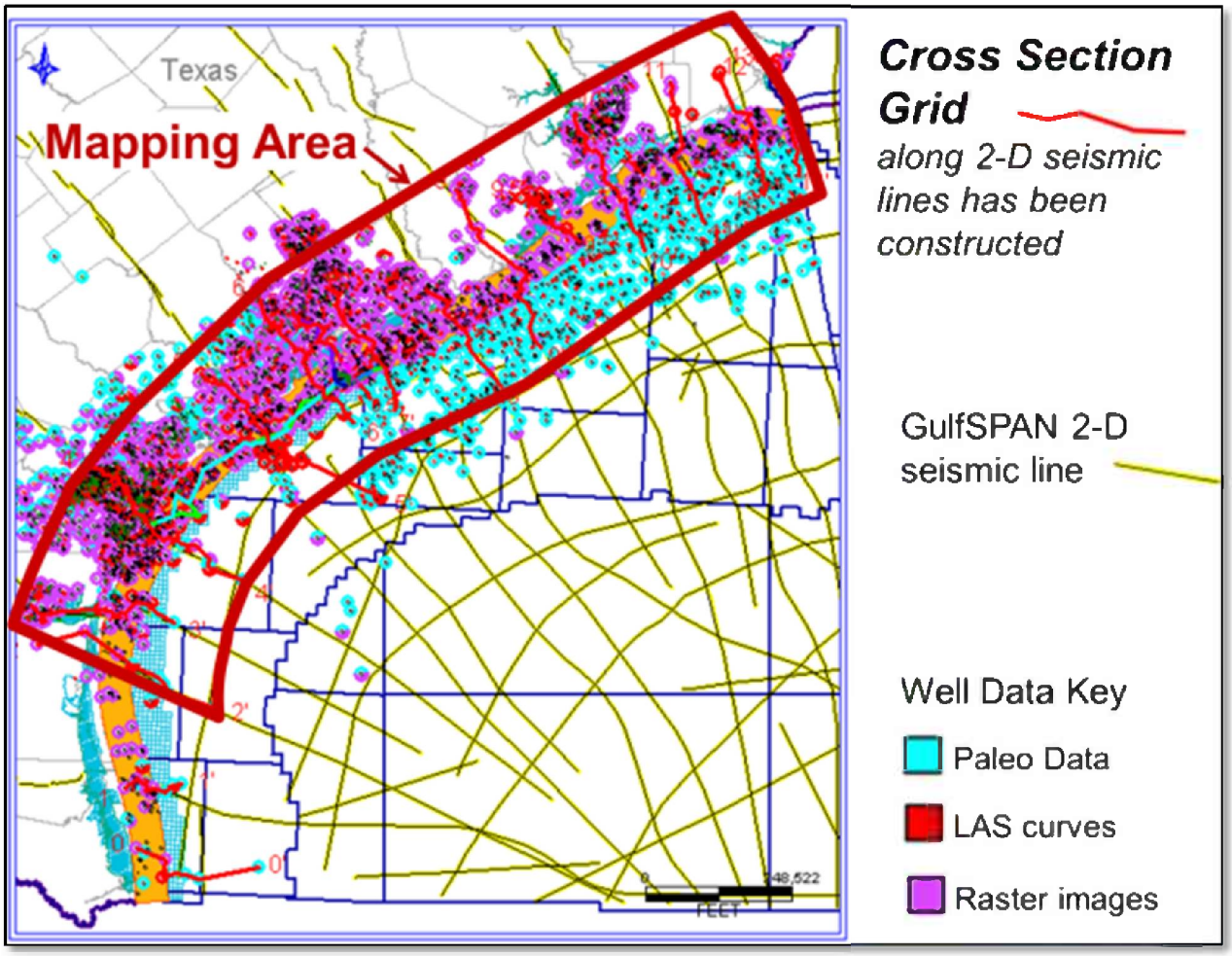

Figure 3.1: Approximately 25,000 wells shown in Texas State Waters Miocene Mapping Area. Main well data sources were IHS Energy, BOEM (formerly MMS) and DrillingInfo. Color-code indicates types of data available for specific wells shown.

Stratigraphic Framework

In order to determine gross formation thickness (h_g) for the capacity calculation equation, it was necessary to first define the stratigraphy of the pertinent Miocene geologic section. The initial mapping phase included construction of structure top and base of the Miocene. The maximum flooding surface (MFS) associated with the Anahuac Shale is marked approximately by the *Heterostegina sp.* benthic foraminiferal (foram) zone. In addition, the Anahuac itself is typically readily identified as the thick, continuous shale above the Frio Formation (Oligocene) and easy to correlate in the lower coastal plain and innermost shelf, particularly up-dip of major growth faults. Down dip, in more basinward offshore positions, the upper Oligocene and lower Miocene section, including the Anahuac thicken dramatically making it more difficult to pick the MFS.

We used the MFS associated with the paleontological markers *Robulus* "E" and/or *Bigenerina floridana* / "A" benthic foram markers to define top of the Miocene as per Lawless et al. (1997); Witrock (2002), and Hentz and Zeng (2003). The approximate top of Miocene MFS is not as well developed and thus not as easily picked as the base (Anahuac). However, we were able to correlate both the top and base Miocene with a reasonable degree of confidence by careful

examination of the wireline logs with paleo ties in cross sections and correlating the respective log signatures to wells with no paleo control. The fully interpreted cross section shown in Figure 3.2 below is an example that has been interpreted using this methodology.

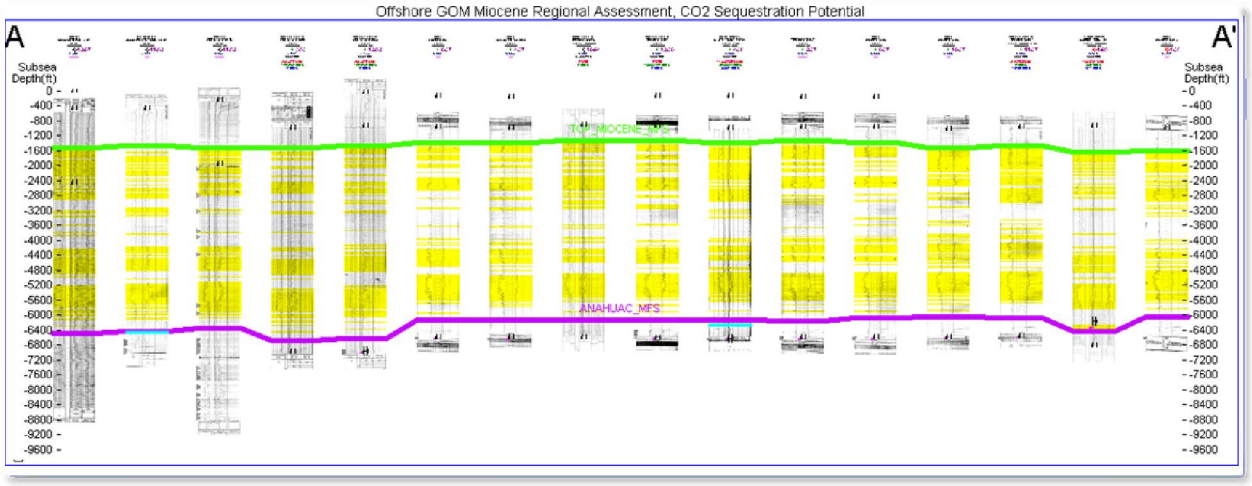

Figure 3.2: The top of Miocene horizon is shown in green, the base of Miocene in purple and selected net reservoir sandstone intervals are highlighted in yellow.

Structure Maps

The paleo-guided wireline top and base Miocene interpretations were initiated in the raster log data set; these interpretations have also been extended to include wells for which digital LAS log curves were available. The structural depths to top and base Miocene picks from both raster and LAS data sets were used to construct depth maps such as the one shown in Figure 3.3 of the area of interest (study area) analyzed for CO_2 capacity.

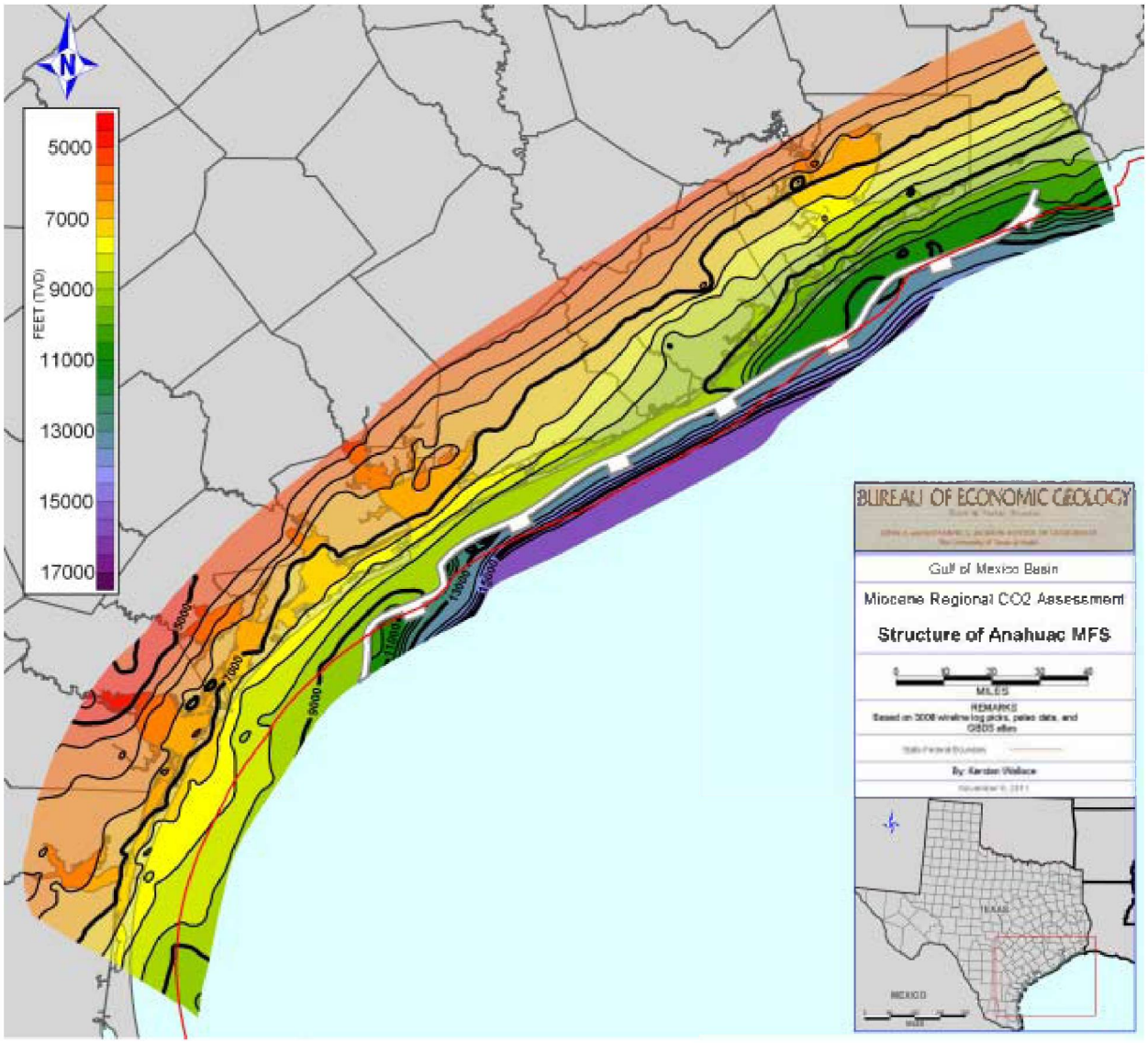

Figure 3.3: Map of true vertical (TVD) to base of Miocene (Anahuac MFS) in the area of interest (i.e., study area). The structure map is based on log picks from 3008 wells. Contour interval is 500 feet.

Petrophysical Analysis

Net Reservoir Sandstone Interpretations

SP curves were used in lieu of Gamma Ray curves as they are more abundant in the data set. Furthermore, the gamma ray does not differentiate between porous, permeable and tight (low-porosity, impermeable) sandstone and thus, is less useful for making pore-volume dependent resource estimates.

We counted net permeable reservoir sandstone from SP in two ways: (1) direct interpretation from raster images and (2) automated summation from normalized vector curves (LAS). In both cases, we used a guideline cutoff, beyond which, the SP deflection from a "shale base line" (Schlumberger, 1998a, p. 3-5) was sufficiently negative to indicate permeable sandstone. The

cutoffs for the raster sand counts were more subjective than those for the LAS curves because the interpretations SP readings directly from raster images are non-normalized and the interpreter must choose a cutoff or even multiple cutoffs within a given well, such that most of the obvious permeable sandstone can be differentiated from the impermeable rocks below the "shale base line" (Schlumberger, 1998a). Further, the cutoff line was used as a guide rather than a strict quantitative boundary, since the tops and bases of individual sandstone beds are marked by inflection points in the curves that are dependent upon bed thickness (e.g., Schlumberger, 1998, p. 3-4, Fig. 3-3). Although inflection points are typically very close to a given cutoff, they are frequently not *exactly* aligned with them such that the summation of net reservoir sandstone picked by raster inspection may vary slightly from that summed using the LAS curve of the same SP log. These differences are essentially negligible so we used LAS SP curves to automate the net reservoir sandstone picking process where data was available because it is much faster.

(1) Net Reservoir Sandstone, Raster Logs.--In wells with raster logs that span the entire Miocene, net permeable reservoir sandstone intervals were picked according to a previously defined methodology in which a simple normalization is calculated and net permeable reservoir sandstones were picked at inflection points in the SP curve using a cutoff. Figure 3.4 shows the net permeable reservoir sandstone values from 1009 wells for which raster SP curves were available over the entire Miocene interval. The net permeable sandstone composes one portion of the variable, h_g, in the capacity calculation equation.

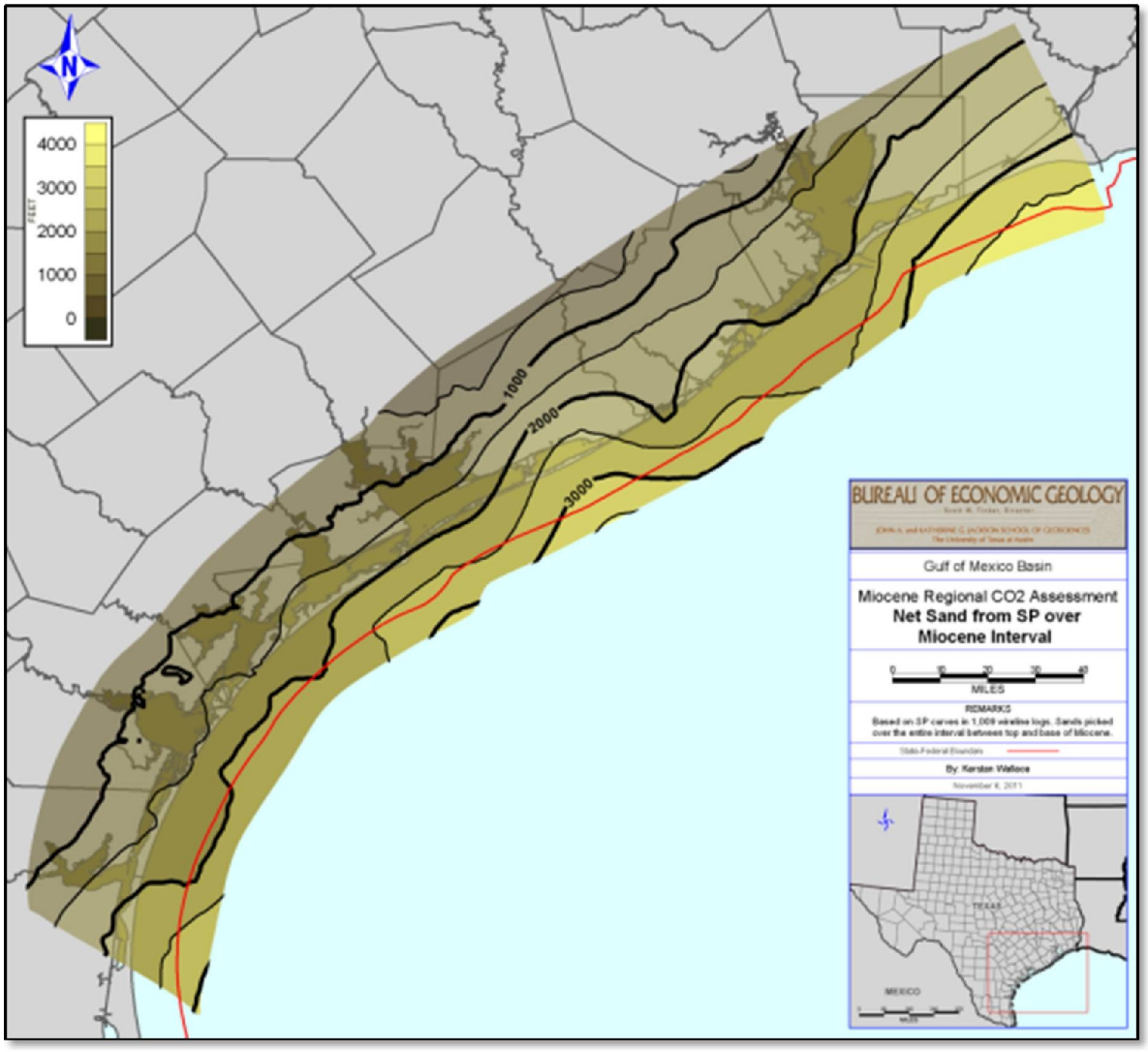

Figure 3.4: Net reservoir sandstone map for the Total Miocene interval summed from raster log interpretations from 1009 wells.

SP curves on raster logs are frequently not directly comparable to one another because differences in scales and vertical resolution make it difficult to pick net permeable reservoir sandstone in a consistent way. We developed a method using a core-log calibration as well as raster logs from various (uncored) wells that had differences in SP scale and/or resolution. The approach is to compute a simple normalization using a thick shale interval to define a maximum SP value and thick, permeable sand packages to define a minimum SP value and then apply an empirical equation to determine the SP cutoff for a particular well. The method requires that the available SP curve in the raster image covers a sufficiently large depth interval to represent enough geologic variation for determining SP_{max} and SP_{min} , and that the image has a legible scale.

Workflow steps:

(1) Make sure the log has been straightened and calibrated before proceeding.

(2) Identify thick (>20ft) shale intervals in the log until you find the one with the highest average SP value (deflection to the left); that value defines SP_{max} for the well. Limit your 'shale interval' search to shale packages that are present within the interval containing your targeted sandstones.
(3) Define SP_{min} by applying a similar process; look for a thick (>20ft), blocky sandstone package with the lowest average SP value (deflection to the right).
(4) Using the previously obtained values for SP_{min} and SP_{max}, determine the normalized cutoff value through the empirical equation from core-log calibration: $SP_{netres} = (SP_{min} + SP_{max}) * 0.53$
(5) Finally, pick the net permeable reservoir sandstone intervals using the SP_{netres} cutoff. Rather that picking all sands at the intersection of the SP curve and the Pay Pick Cutoff Indicator, use the Pay Pick Cutoff Indicator as a requirement for sands eligible to be counted. That is, if a sand layer exceeds the cutoff indicator in the negative direction, it can be counted; if not then it is ignored. To count the eligible sands, select the inflection points of the SP curve with the "Start Picking Pay Intervals" tool. In order to expedite the process, do not distinguish sand bodies as separate if the intervening shale layer does not produce an SP signature sufficient to cross back over the Pay Pick Cutoff Indicator. Examples are shown below in Figure 3.5.

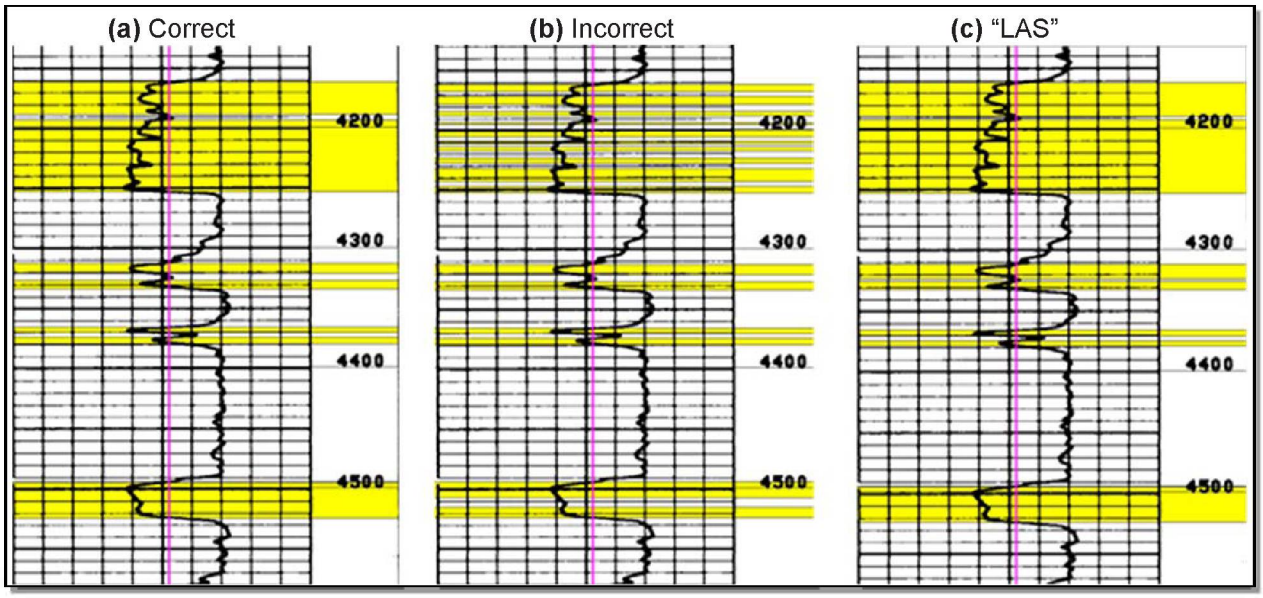

Figure 3.5: Illustrations of application of SP net permeable reservoir sandstone interpretation methodology. (a) Correct application: picked at inflection points that occur very near the SPnetres cutoff (vertical magenta line). (b) Incorrect application: Strict adherence to inflection points overcomplicates sandstone reservoir complexity. (c) "LAS": Picked strictly at intersections of the SP curve and the SP_{netres} cutoff (rather than at inflection points) results in a mechanical pick that is essentially the same way SP net permeable reservoir sandstone would be picked using computer automation on an LAS curve. Note that the differences between (a) and (c) are negligible.

Some SP logs contain scale changes that occur within the interval of interest. If the scale only changes once or twice, it is possible to simply use the workflow above separately, over each interval of consistent scale. If SP scale changes are very frequent, it may be necessary to omit the well/log from the analysis.

(2) Net Reservoir Sandstone Interpretations, LAS curves.--Spontaneous potential (SP) or gamma ray (GR) logs were used to estimate net sandstone. SP provides the most useful estimate because it qualitatively indicates permeable sandstone. The GR curve is better than SP for estimating total sandstone volume, however, the GR does not differentiate between permeable and "tight" (impermeable) sandstones that contain non-clay, pore-filling cements that diminish porosity and permeability. Because of this difference, SP curves were used where available to estimate net *permeable* reservoir sandstone in our analysis of CO_2 capacity.
SP curves were first straightened along a shale baseline in order to eliminate drift. Then the SP curves were normalized by applying a shale volume model that converts the SP curve response into a shale percentage ranging from 0% to 100% after "100% clean sand" and "100% shale" parameters are defined:

Equation 3.1-1

$$VSH_{SP} = (SP - SP_{CL}) / (SP_{SH} - SP_{CL});$$

Where,

VSH_{SP} = Shale volume from the SP curve
SP = SP curve reading (input)
SP_{CL} = SP reading in 100% clean sand (constant)
SP_{SH} = SP reading in 100% shale (constant).

Likewise, for wells lacking SP curves, the GR was substituted in a similar fashion (Equation 3.1-2 and Equation 3.1-3), using a similar shale volume method, with the addition of the non-linear Tertiary correction.

Equation 3.1-2

$$I_{GR} = (GR - GR_{CL}) / (GR_{SH} - GR_{CL});$$

Where,

I_{GR} = Gamma Ray Index: Intermediate calculation of shale volume from the GR curve
GR_{CL} = SP reading in 100% clean sand
GR_{SH} = SP reading in 100% shale.

Finally, the Tertiary non-linear correction (Larinov, 1969; Dresser, 1982; Asquith and Krygowski, 2004) was applied:

Equation 3.1-3

$$VSH_{GRc} = 0.083 * (2^{**}(3.7* I_{GR}) - 1)$$

Where,

VSH_{GRc} = Shale volume from the GR curve, corrected for overly optimistic non-linearity of Equation 3.1-2.

(3) Net Reservoir Sandstone Summation.—After determining permeable net reservoir sandstone in wells containing pertinent data (raster or LAS as described above) we summed the total footage of all the defined intervals as permeable net sandstone (total thickness in feet). The net reservoir sandstone values were gridded and contoured: Figure 3.4 is the resulting Miocene net reservoir sandstone map.

Porosity Estimates

Porosity, Φ_t , is one term in the capacity calculation equation. In order to determine porosity, well log based porosity data were used. Vector (LAS) porosity curves covering all or most of the Miocene interval were available for 86 wells in the mapping area (Figure 3.6). Sonic porosity was the favored measurement for the Miocene average porosity estimates because of the greater number of wells for which sonic data were available and also because sonic logs are not as affected by borehole rugosity as are density logs. Raster image porosity logs were also available for additional wells, but due to time/cost constraints were not utilized for porosity mapping.

Sonic porosity was calculated using the empirical, core-calibrated equation of Raymer et al. (1980):

Equation 3.1-4

$$PHIS = 0.67 * (1 - (DT_M / DT))$$

Where,

PHIS = Sonic porosity (output)
DT = Sonic log reading (input; µ-sec/ft))
DT_M = Sonic delta-t constant for rock matrix (sandstone = 55.5 µ-sec/ft)
DT_{FL}= Sonic delta-t constant for fluid (salt water = 189 µ-sec/ft)

Density porosity was calculated using (Schlumberger, 1998b, p. 5-12):

Equation 3.1-5

$$PHID = ((RHOB - RHO_M) / (RHO_{FL} - RHO_M))$$

Where,

PHID = Density porosity (output)
RHOB = Bulk density log reading, g/cc (input)
RHO_M = Matrix density constant, (input; sandstone = 2.68 g/cc)
RHO_{FL}= Fluid density constant, (input; brine = 1 g/cc)

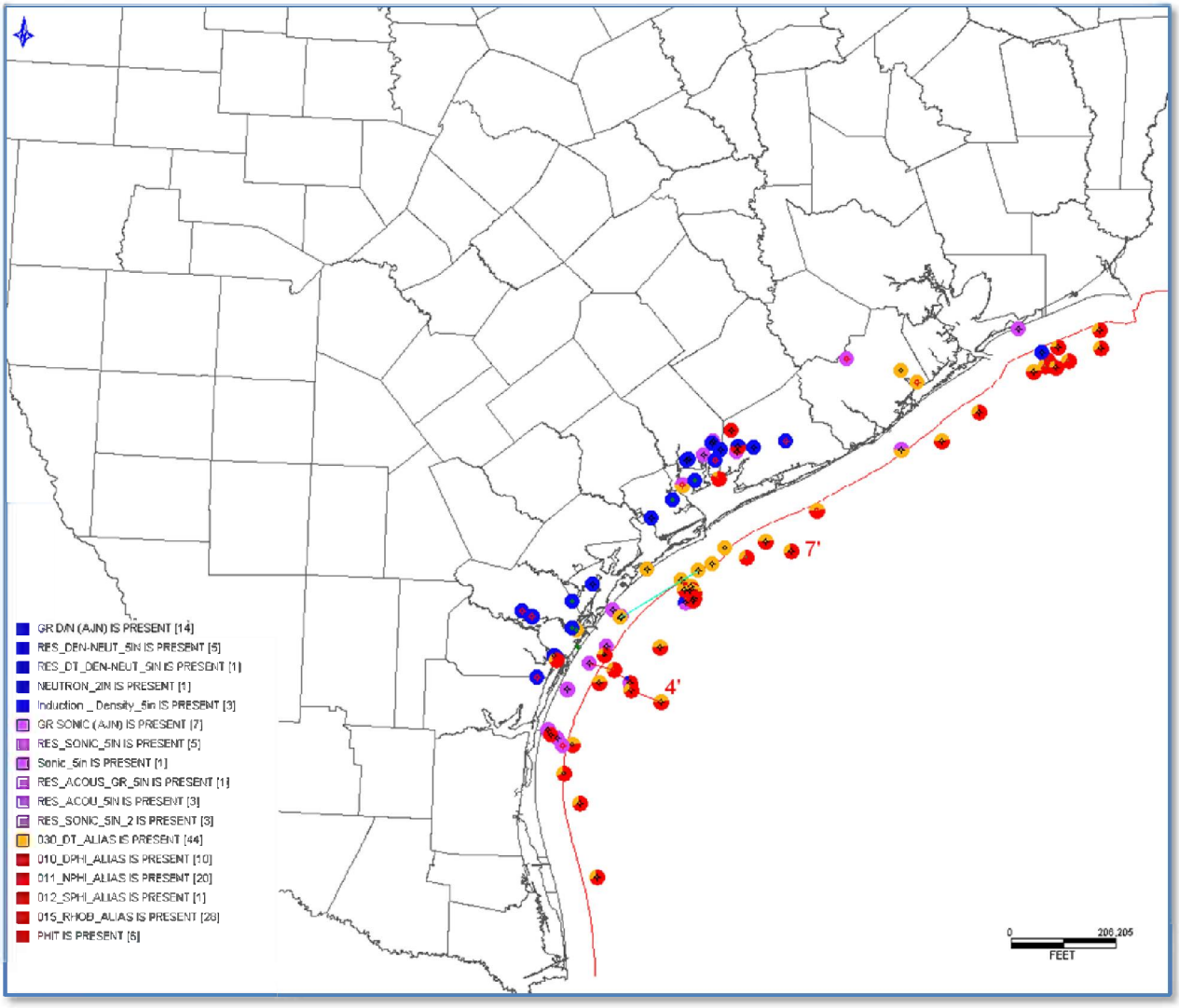

Figure 3.6: Location map showing the 86 wells for which LAS porosity curves were available over the entire Miocene interval. Blue and purple wells represent raster logs with density or sonic curves and orange and red wells represent LAS logs with density or sonic curves.

Porosity Summation — After calculating porosity from LAS curves, we performed an automated reservoir summation to calculate the average porosity within intervals previously defined (by raster or LAS methods described above) as permeable net reservoir sandstone over the entire thickness of the Miocene. The average porosity values were posted, gridded and contoured. The resulting Miocene isoporosity map is shown in Figure 3.7.

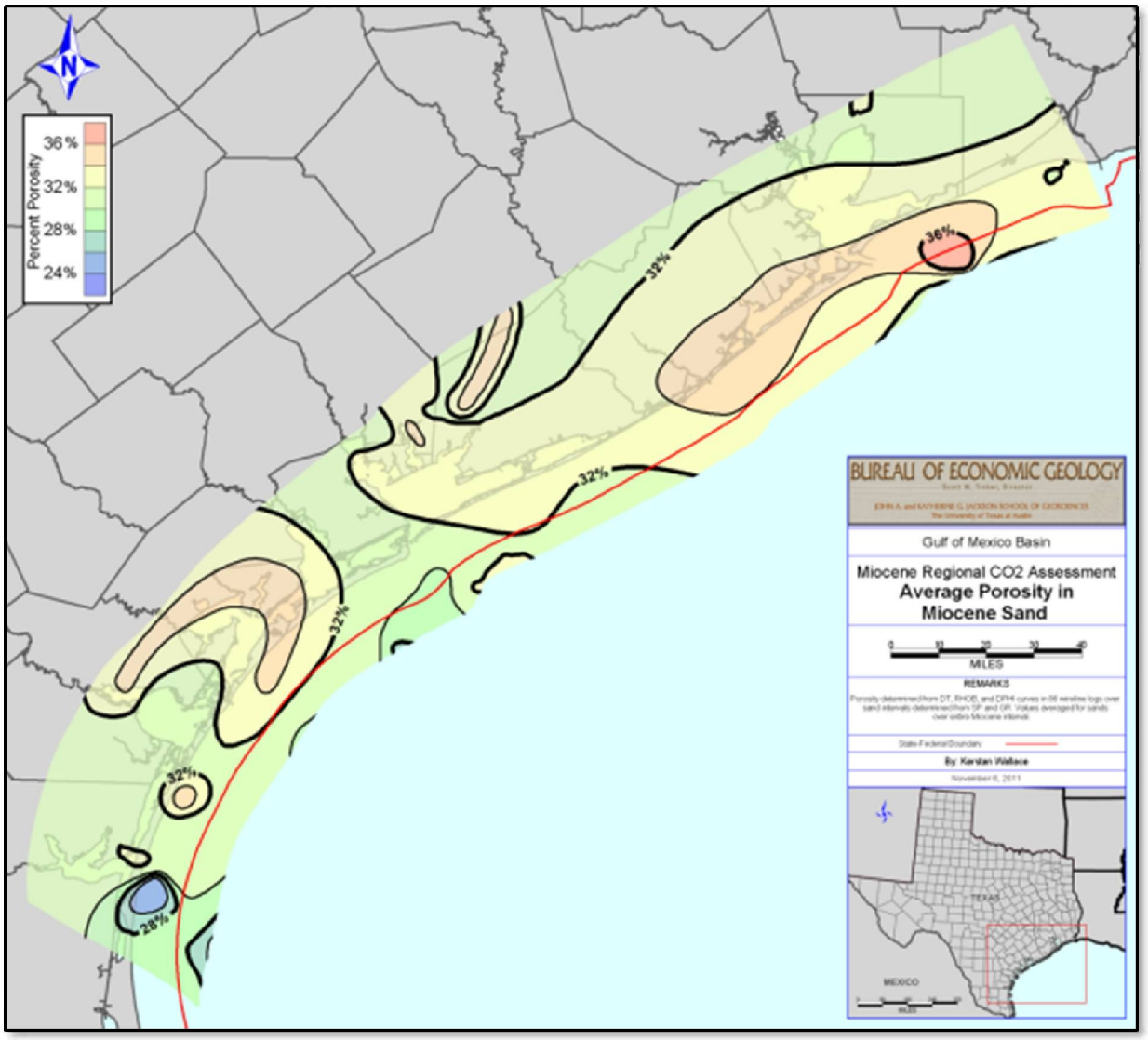

Figure 3.7: Isoporosity map, entire Miocene interval. Porosity derived from LAS curve analysis of average porosity from net permeable reservoir sandstone intervals from 86 wells shown in Figure 3.6. CI = 2% porosity units.

Capacity Calculation Interval

In order to calculate capacity, a gross formation thickness, h_g, is required for the capacity calculation equation. Though we have studied the entire Miocene interval, the capacity estimate considers only the portion that is suitable for CO_2 sequestration. Figure 3.8 is a map of the surface representing the top of overpressure in and immediately adjacent to the Study area. The top of overpressure defines, in part, the lower boundary of the capacity calculation interval. In a cross sectional view, the top of overpressure is schematically shown in Figure 3.9 (blue—top of overpressure). In some areas, the Anahuac maximum flooding surface (MFS) (Figure 3.9) is shallower than the top of overpressure. If that is the case, the Anahuac MFS defines the base of the capacity calculation interval. Therefore, the base of the capacity calculation interval is defined as the top of overpressure or the Anahuac MFS, respectively, whichever is shallower, and Figure 3.10 is the resulting depth map representing the base of the capacity estimation interval.

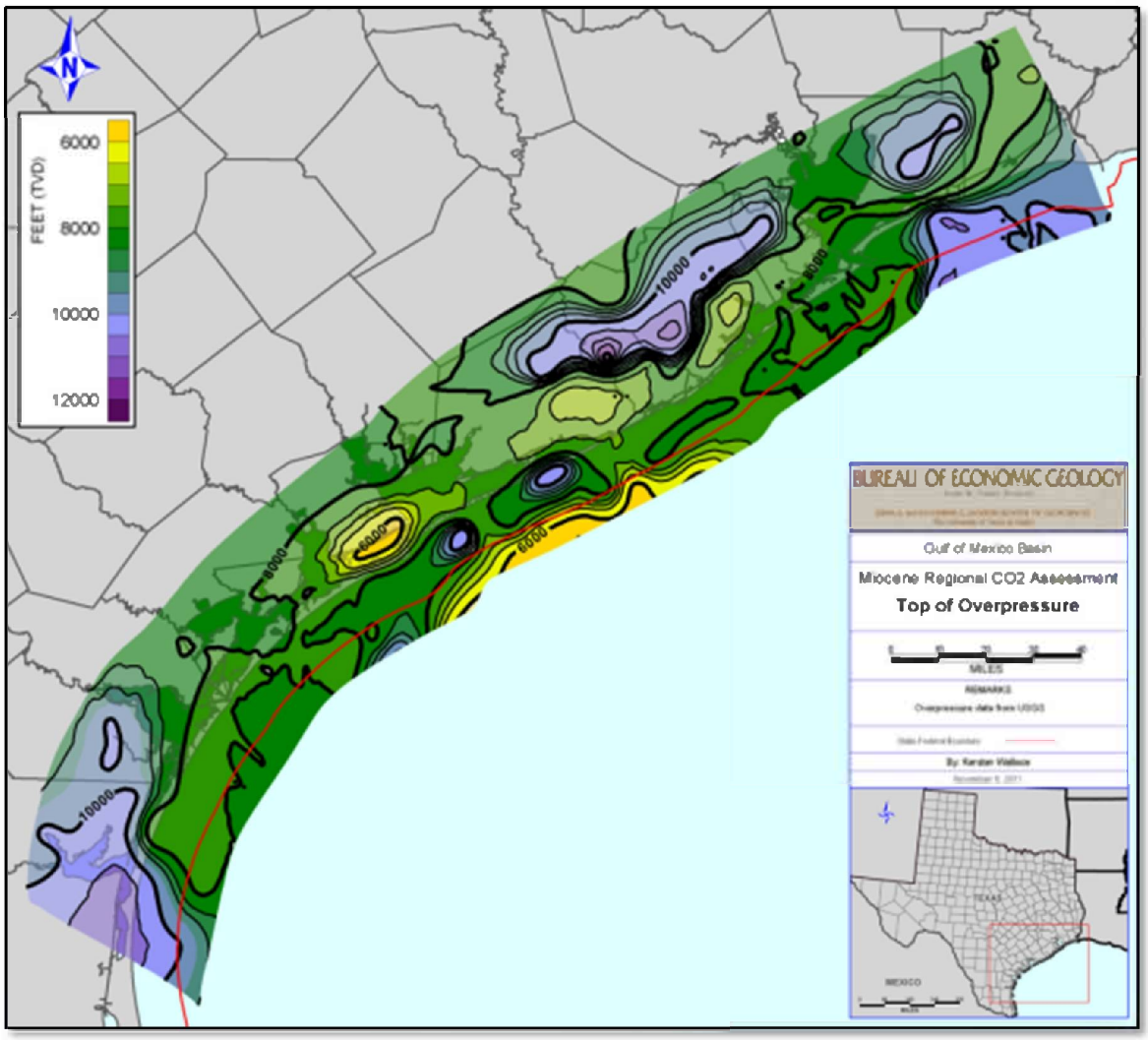

Figure 3.8: Depth to top of overpressure. The map is part of a larger USGS map (Pitman, 2011).

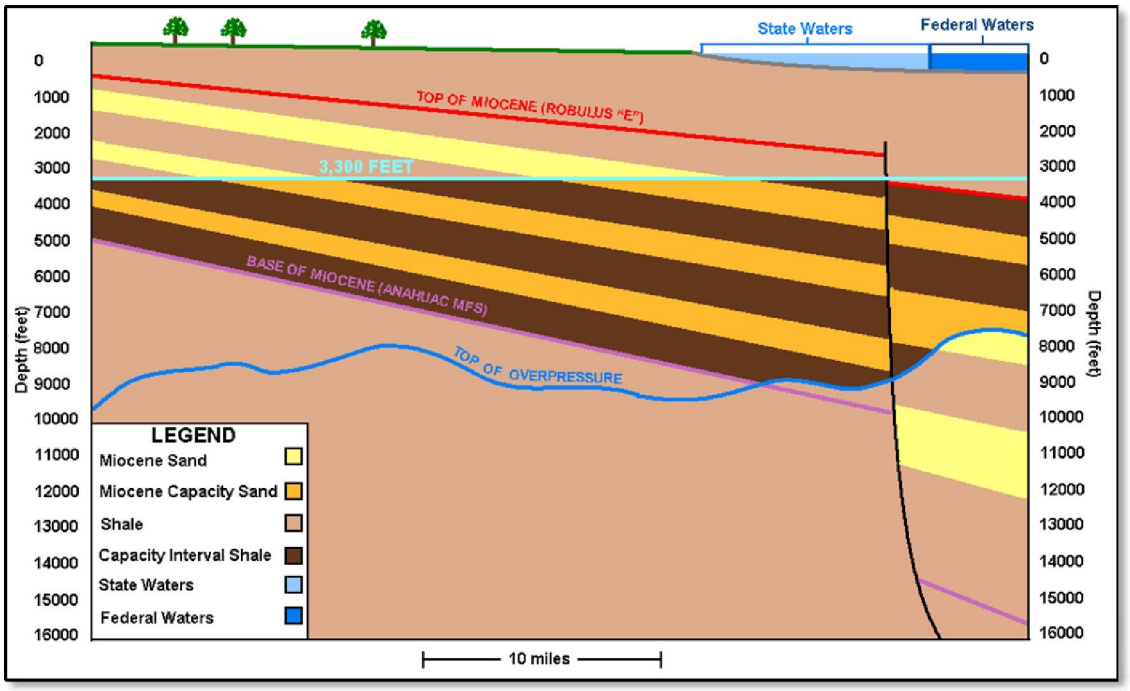

Figure 3.9: A schematic dip-oriented cross section showing the top (cyan—3300-ft constant depth) and base of the interval used for capacity calculations.

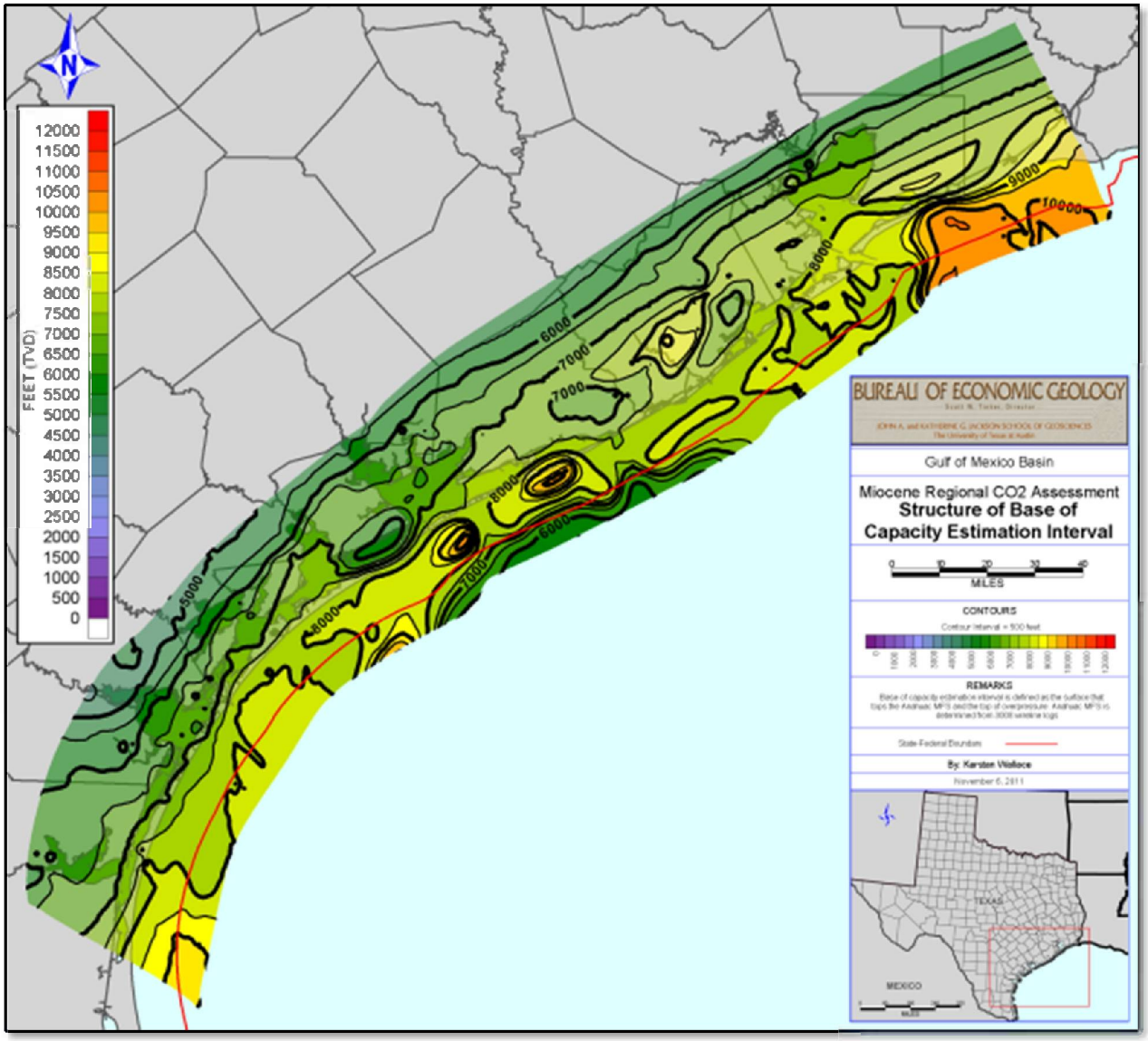

Figure 3.10: Base of capacity calculation interval defined as the top of over pressure or the Anahuac maximum flooding surface, whichever is shallower.

The upper boundary of the capacity calculation interval is defined as the depth at which CO_2 is entirely supercritical. From a CO_2 density vs. depth plot (Figure 3.11, far left), the upper boundary is determined to be 3,300 ft (1km) (i.e., below the inflection point of the curve in Figure 3.11where the rate of change of CO_2 density decreases and stabilizes with depth). Figure 3.11shows temperature and pressure trends within the Miocene section of Texas State Waters. These data were collected from 93 temperature measurements from well logs and 198 average reservoir temperature and pressure measurements from the Atlas of Northern Gulf of Mexico Gas and Oil Reservoirs (Seni et al. 1997). The average temperature trend with depth and hydrostatic pressure gradient were input into the Peng-Robinson equation of state (Peng & Robinson 1976) to solve for CO_2 fluid density with depth. The program ThermoSolver was used to quickly automate the Peng-Robinson equation of state (Barnes & Koretsky 2003). The density trend shown on the far right of Figure 3.11 was applied to the structural midpoint of the capacity calculation interval

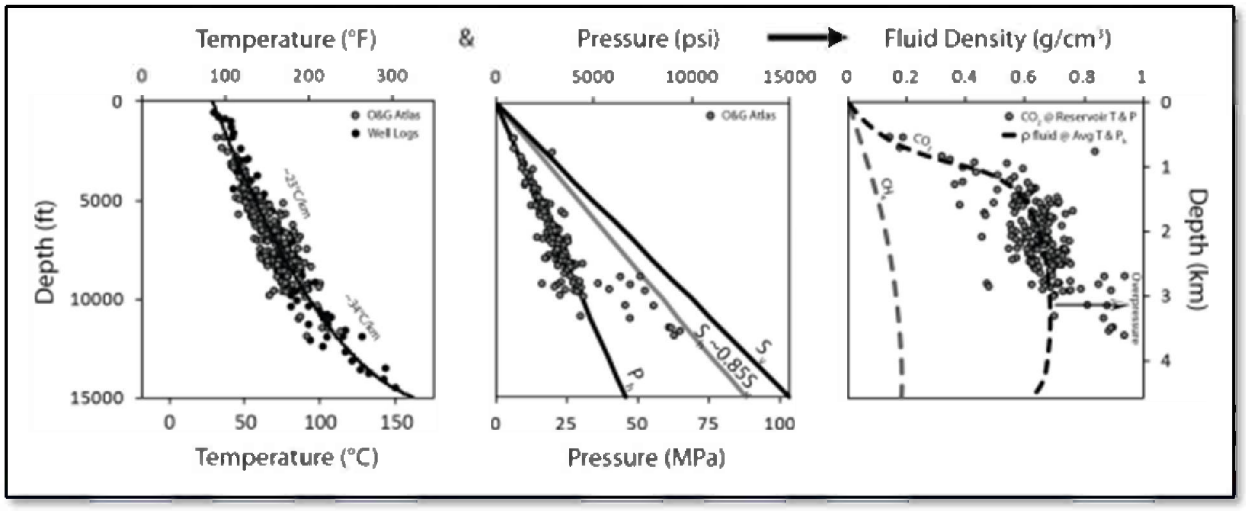

Figure 3.11: Plots of temperature and pressure, respectively, versus depth and resulting (far right) CO2 density vs. depth curve for the Miocene in the mapping area.

The density of CO2 is calculated using one of two polynomials derived from the Fluid Density vs. Depth plot (Figure 3.11). Each polynomial describes a portion of the curve within a given depth interval. The equations used are:

For 2,000-5,000 feet:
$p = 21.105x^4 - 311.51x^3 + 1637.3x^2 - 3449.5x + 2665.6$

For 5,000-10,000 feet:
$p = .475x^3 - 14.27x^2 + 147.71x + 154.92$

where:
p = density
x = depth

The input depths for the fluid density vs. depth equations (x values) used in this study comprise the depth midpoints of the capacity calculation interval (in a 1 mile x 1 mile grid) and are calculated as follows:

Input depths = (top of interval / base of interval)/2.

The resulting map of CO_2 density distribution (i.e., the variable ρ_{CO2} of the capacity calculation equation) is shown in Figure 3.12.

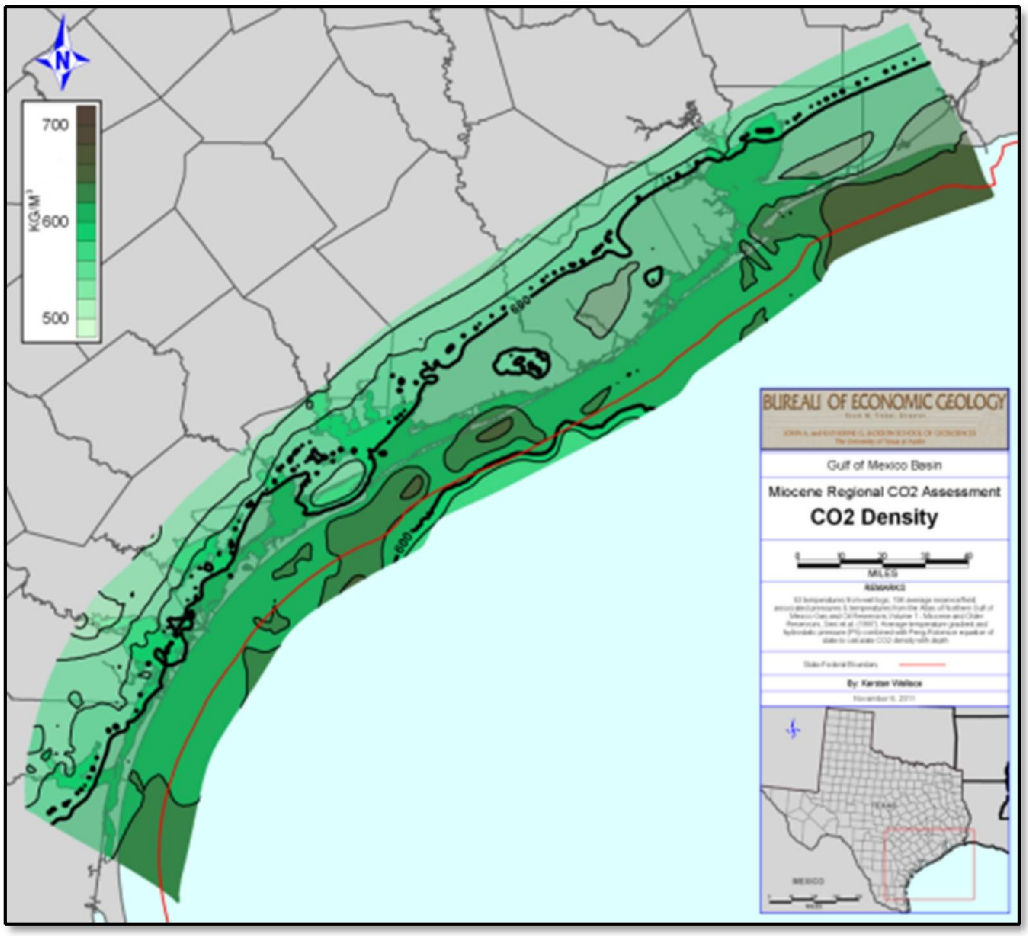

Figure 3.12: Map of calculated CO2 density in the capacity calculation interval of the Study area.

Refinement of Net Reservoir Sandstone Map.—The net reservoir sandstone map shown in Figure 3.5 was trimmed to exclude sandstone bodies -- and thus pore volume -- above 3,300 feet and beneath the base of the capacity calculation interval (Figure 3.10). Using these refined interval boundaries, the net sand counts were recalculated and mapped (Figure 3.13). The map in Figure 3.13 constitutes the gross formation thickness value, h_g, for the capacity calculation equation, Equation 6.

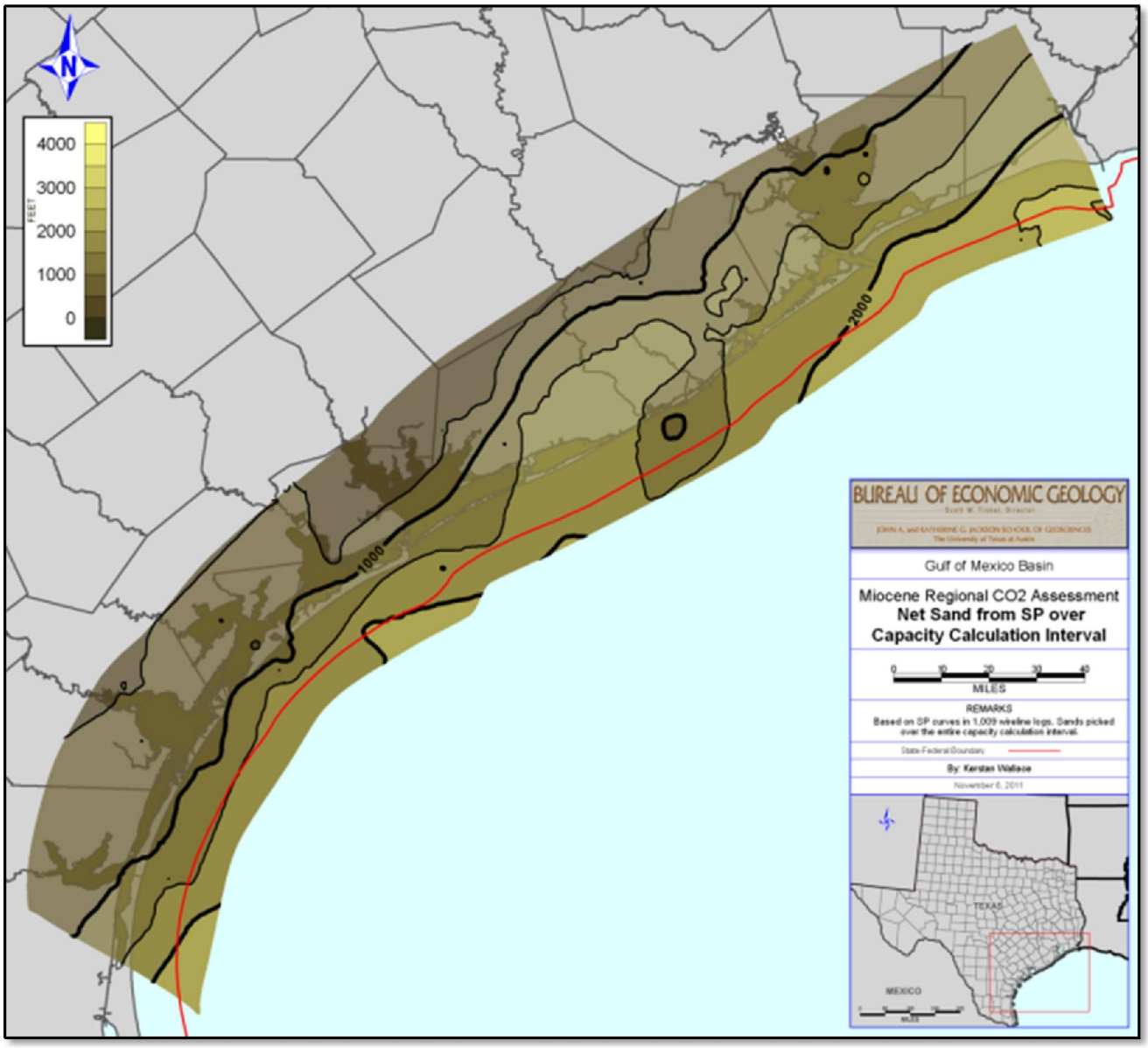

Figure 3.13: Refined net reservoir sandstone map (i.e., hg). Original map (Figure 3.5) was trimmed to exclude sandstone bodies -- and thus pore volume -- above 3,300 feet and beneath the base of the capacity calculation interval (i.e., top of overpressure or Anahuac MFS, whichever is shallower).

Capacity Calculation

As previously stated, in order to calculate capacity we applied the NETL-MIT capacity calculation equation (MIT, 2010) to our data set,

Equation 3.1-6

$$G_{CO2} = A_t \ h_g \ \Phi_t \ \rho_{CO2} \ E_{saline} \ \text{(tonnes or metric tons)},$$

where

A_t = geographical area defining region of CO_2 storage

h_g = gross formation thickness
Φ_t = total porosity
ρ_{CO2} = density of CO2 estimated at temperature and pressure of anticipated storage (reservoir) conditions
E_{saline} = CO2 storage efficiency factor.

We populated the NETL-MIT Goodman et al. (2011) equation in the following manner (Table 3.1.1) using many of the intermediate results we have discussed and illustrated above:

Table 3.1.1: Parameters used to populate the NETL-MIT (MIT, 2010) capacity calculate.

Parameter	Description	Grid or numerical used in this study
A_t	Geographical area defining region of CO2 storage	Grid size = 1 mile^2 Total area = 14,467 mi^2
h_g	Gross Formation Thickness	Refined net reservoir sandstone map (Figure 3.13)
Φ_t	Total Porosity	Isoporosity Map (Figure 3.7)
ρ_{CO2}	Density of CO2 at reservoir conditions	CO_2 density map (Figure 3.12)
E_{saline}	CO2 storage efficiency factor	E_{P50} = 0.03 (based on historical usage in the Natcarb Atlas)

The resulting maps shown in Figure 3.14 and Figure 3.15, respectively, show the CO_2 storage capacity per square mile over the project area and a detailed view illustrating individual 1 mi^2 x 1 mi^2 capacity grid cells. Each grid cell was summed over the 14,467 mi^2 project area resulting in a **total Miocene storage capacity value of 86 Gigatonnes**.

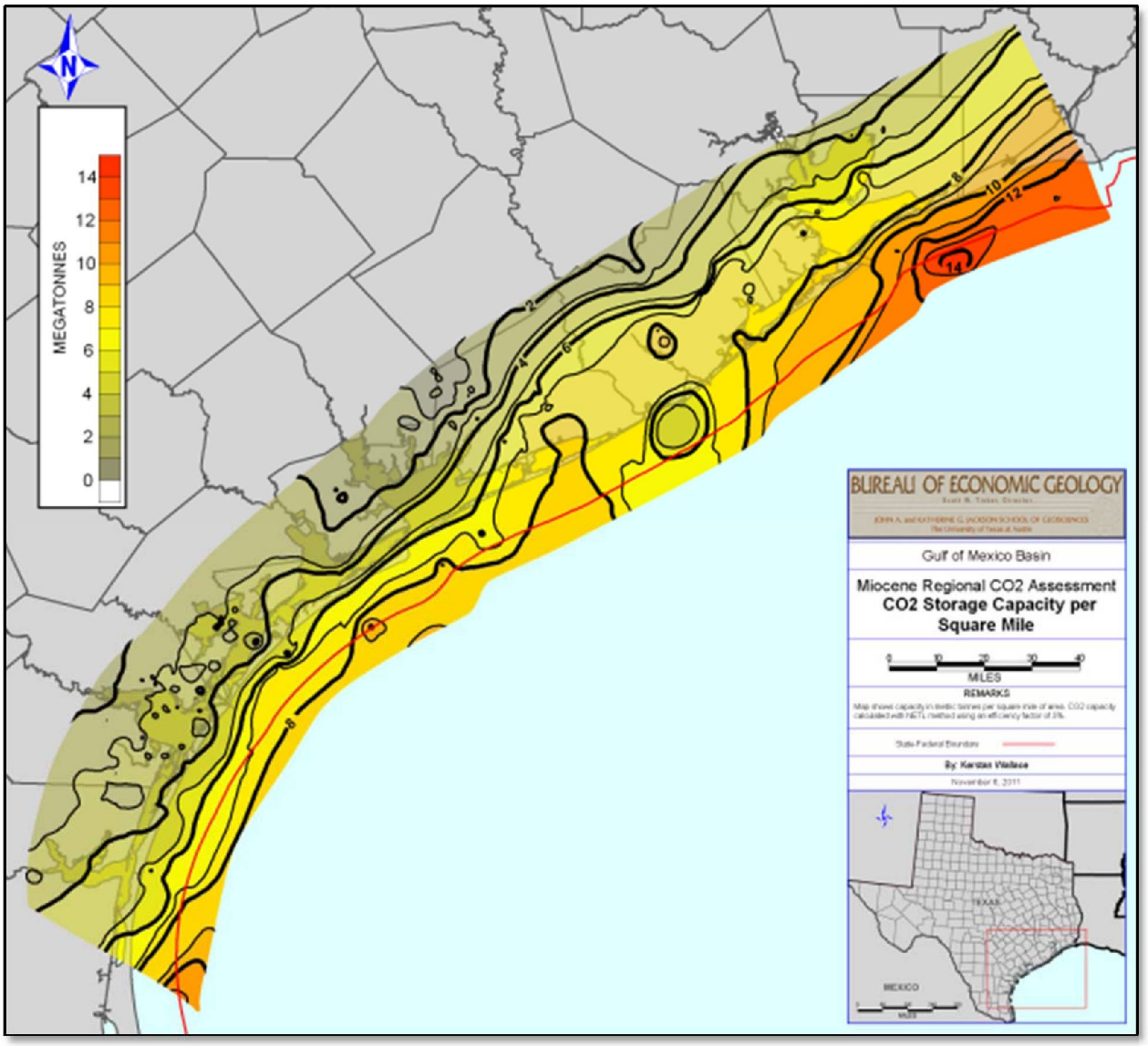

Figure 3.14: Map of capacity per square mile over the Miocene mapping area.

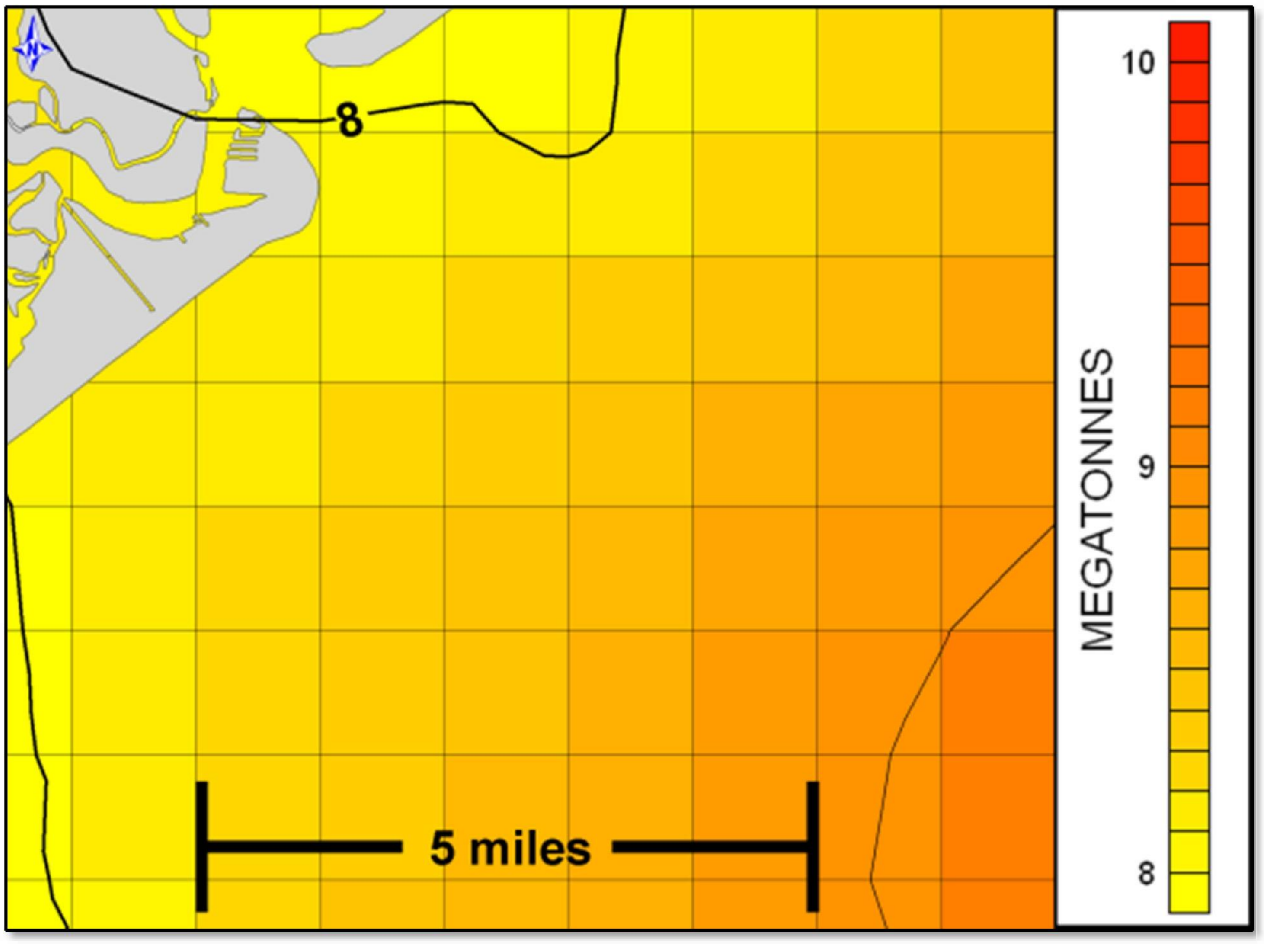

Figure 3.15: Detail from map of capacity per square mile in part of the Miocene mapping area.

3.2 Subtask 3.1: Coordination with NATCARB database

Coordination with the NATCARB Atlas and database comprised contributions to Atlases IV and V and uploading of data generated by the project. Contributions to Atlas IV included the Study's summary page (Figure 3.16) and, in addition, the maps and capacity estimates presented in Task 3.0 of the current report.

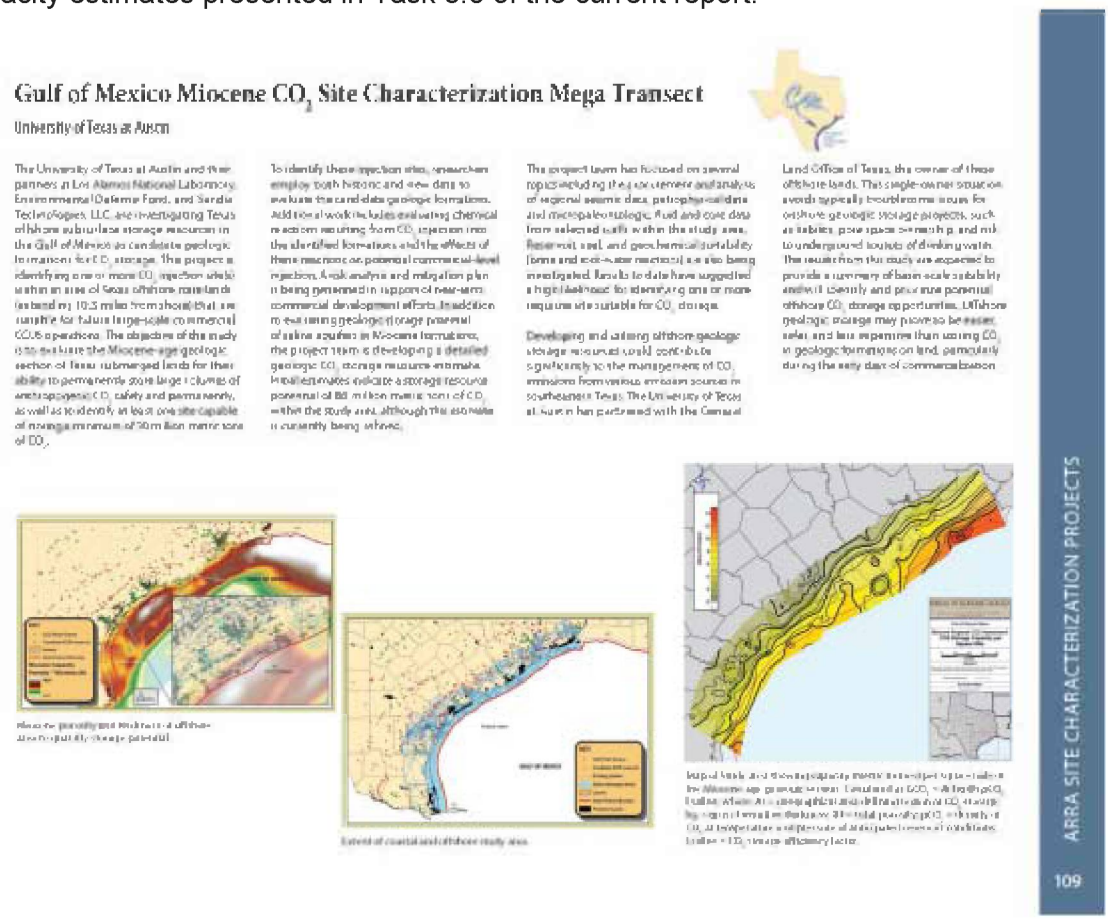

Figure 3.16: The current Study's summary page in NATCARB Atlas IV.

The contribution to NATCARB Atlas V consisted only of the study's summary page (Figure 3.17) as the capacity estimates from Atlas IV did not change.

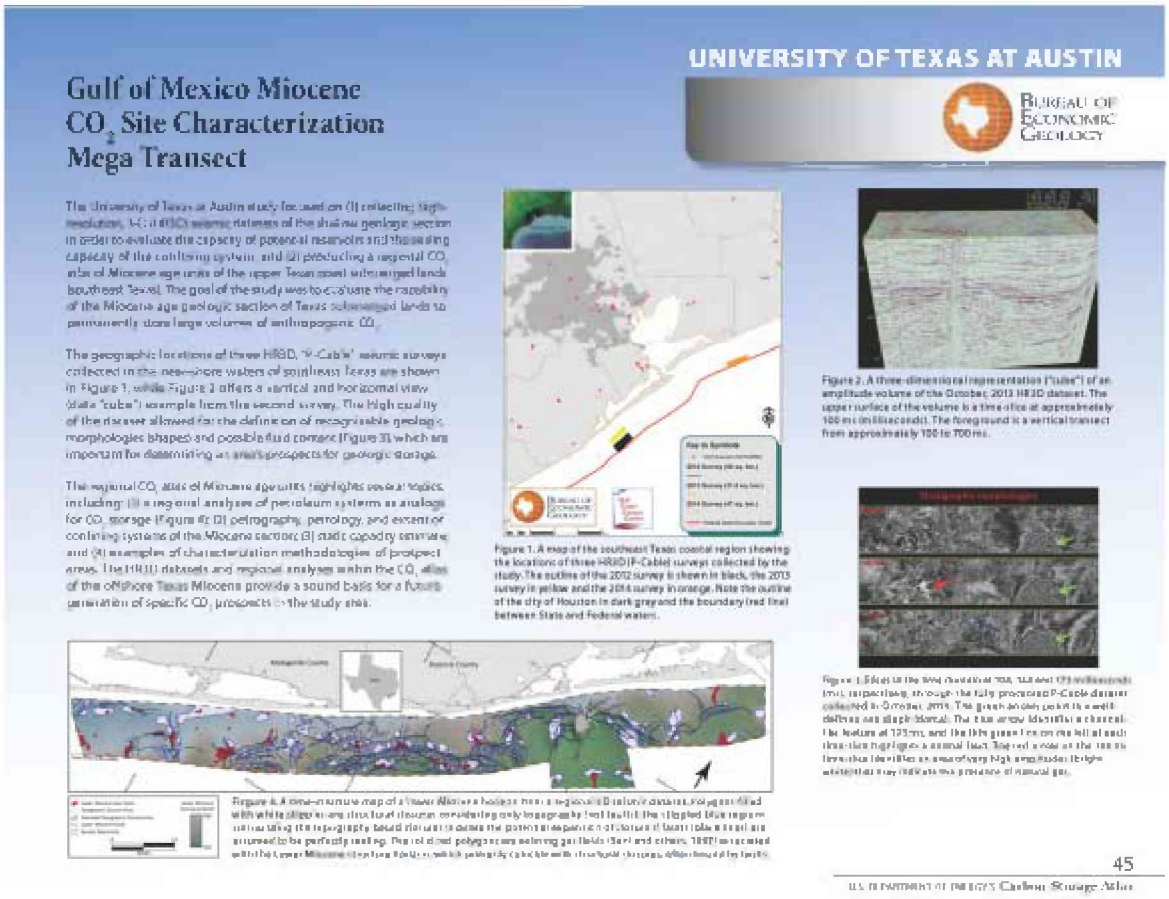

Figure 3.17: The current Study's summary page in NATCARB Atlas V.

4
Task 4.0: Injectivity (Site)

4.1
Subtask 4.1: Data collection / Analysis

The whole rock cores and core samples collected for analysis of injectivity often also served as datasets for Subtask 5.2 “Caprock Seal Capacity.” Therefore, even though specific samples belonged to a caprock interval or a reservoir unit, it was sometimes difficult to separate the analyses thereof as they belonged to the same whole core. Consequently, the reader may notice some overlap between the current Task (4) and Task 5.

Information on whole rock cores and drill cuttings from State of Texas Submerged Lands and adjacent coastal areas was obtained from the Integrated Core and Log Database (“IGOR”) of the Bureau of Economic Geology’s Core Research Center (CRC) and

Houston Research Center (HRC). Cores were examined and described at the CRC (Figure 4.1)

Figure 4.1: Dr. Jiemin Lu (left) and Dr. Tip Meckel (right) examining a Miocene age core at the Bureau of Economic Geology's Core Research Center (CRC) in Austin, TX.

A core of Miocene age rock from High Island well 24L #9 (API 427083031600) was identified and examined. The core extends from 8401 to 8761 feet for a total of 106 feet. The top of the core comprises 45 feet of calcareous mudstone. The extremely fissile mudstone is interpreted as marine shale. Below the shale are 37 feet of medium to coarse-grained sandstone, which is interpreted as fluvial channel deposits. Below the sandstone are 24 feet of interbedded shale and fine-grained sandstone of delta front deposits. The core mainly contains fissile shale and loose sandstones and is preserved in epoxy, which unfortunately makes it difficult to generate a detailed core description.

Seventeen samples were taken from the core for thin section, XRD, SEM, and other analyses. Epoxy-intruded core samples are not suitable for mercury intrusion capillary pressure (MICP) testing and porosity/permeability measurements. Samples for XRD analysis were prepared using wet-grinding in a MicroNising mill and spray dried.

An approximately 300 ft. core (6290 to 7480 ft depth) of Miocene age rock from Shell A:P Haury #3 well was examined and described. The recovery rate for the core was approximately 30%. The core comprises mudstone, siltstone and thin beds of fine-grained sandstone interpreted as deposits from a shoreface and estuarine depositional system. Thirteen samples from the Haury #3 were taken for XRD, SEM, high-resolution X-ray texture goniometry and MICP analyses. Fifteen core plugs of sandstone were taken for permeability and porosity analyses in addition to XRD and thin section

analyses. XRD analyses are underway and some quantitative results of mineralogy were acquired.

A core of Miocene age rock from the West Hastings Unit #7918 (core depths 5870 to 5950 ft.) comprises mainly medium-grained sandstones (interpreted as distributary channel fill) with interbedded mudstones (overbank and channel abandonment deposits). The core is preserved in resin and is not available for sampling.

Two other cores were identified and obtained from the BEG's HRC. They are from wells OCS-G-3733 A-6 and OCS-G-4708 #1, near Matagorda Island, in Federal waters just outside the State / Federal boundary off middle Texas Coast. Figure 4.2 shows the locations of the cores examined in the last quarter of 2010 as well as the two OCS wells. The cores were examined and logged in the first quarter of 2011.

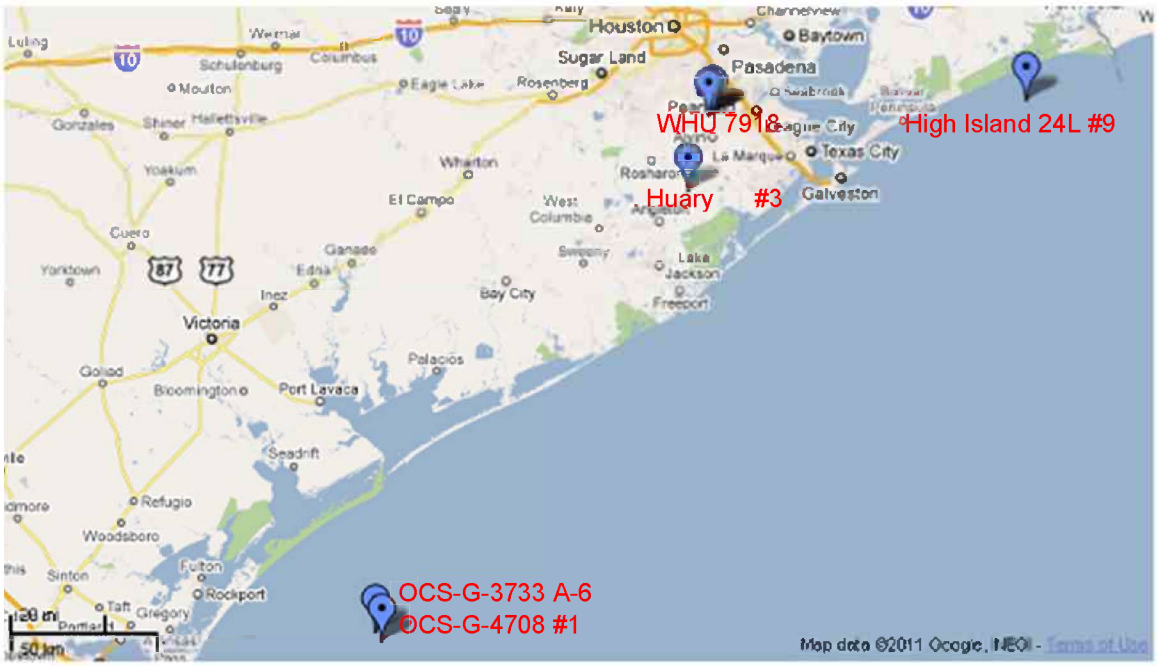

Figure 4.2: Location map of cores of Miocene age rock identified examined or requested during the last quarter of 2010.

The two cores mainly contain fine-grained sandstone facies that are interpreted as delta front deposits (Figure 4.3). The sandstone facies alternate with mudstone and siltstone that are interpreted as pro-delta deposits. The core of OCS-G-4708 #1 ranges between 10577 to 10622 feet with poor core recovery < 50%. The core mainly contains 15 ft (distributary channel) sandstone, which is overlay by a package of mudstone interbedded with fine-grained sandstone deposited in interdistributary bay environment.

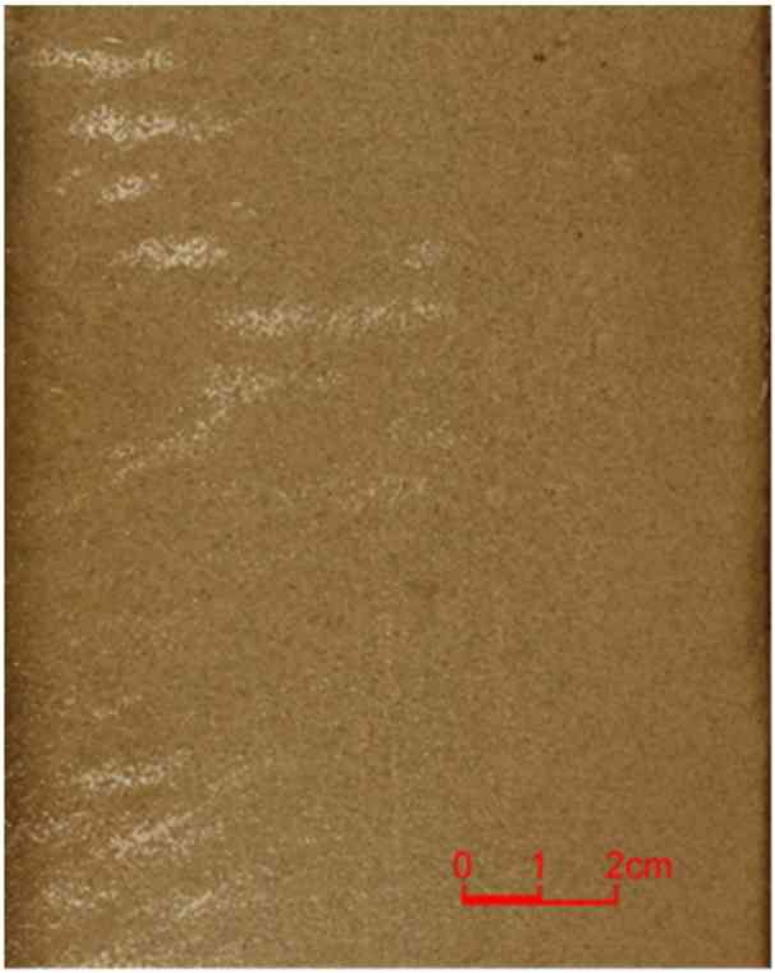

Figure 4.3: Uniform fine grained sandstone, 9128 ft, Well OCS-G-3733 A-6, Matagorda Island.

A total of 41 samples were taken from the cores for thin section and XRD mineralogical analyses. Twenty four plugs were drilled and ten sandstone plugs representing a variety of microfacies were selected for porosity/permeability tests. Eight mudstone samples, representing lithologies of potential seals were selected for mercury intrusion capillary pressure analyses. The sandstone and mudstone samples were sent out for analysis.

In addition to the OCS wells' samples, thin sections of samples from High Island 24L#9 (Figure 4.1) are being examined. Preliminary results show high porosity of the sandstones in the core (Figure 4.4). As Figure 4.4 demonstrates, primary pores in the fine-grained sandstones are mostly preserved. Quartz and calcite cementation is limited. Secondary pores derived from feldspar dissolution further enhance porosity.

The mudstone overlying the sandstones has very low porosity and contains high abundance of clay; XRD (X-Ray Diffraction) mineralogy indicates up to 40% clay content (Table 4.1.1) (Figure 4.4). XRD analyses show that the volume of calcite in the mudstone (Figure 4.5) is greater than 10 % (Table 4.1.1). Thin section examination indicates that most of the calcite occurs as cements, which should greatly reduce porosity and permeability of samples. Further petrographic studies using SEM (scanning electron microscopy) will evaluate the sealing properties of the mudstone.

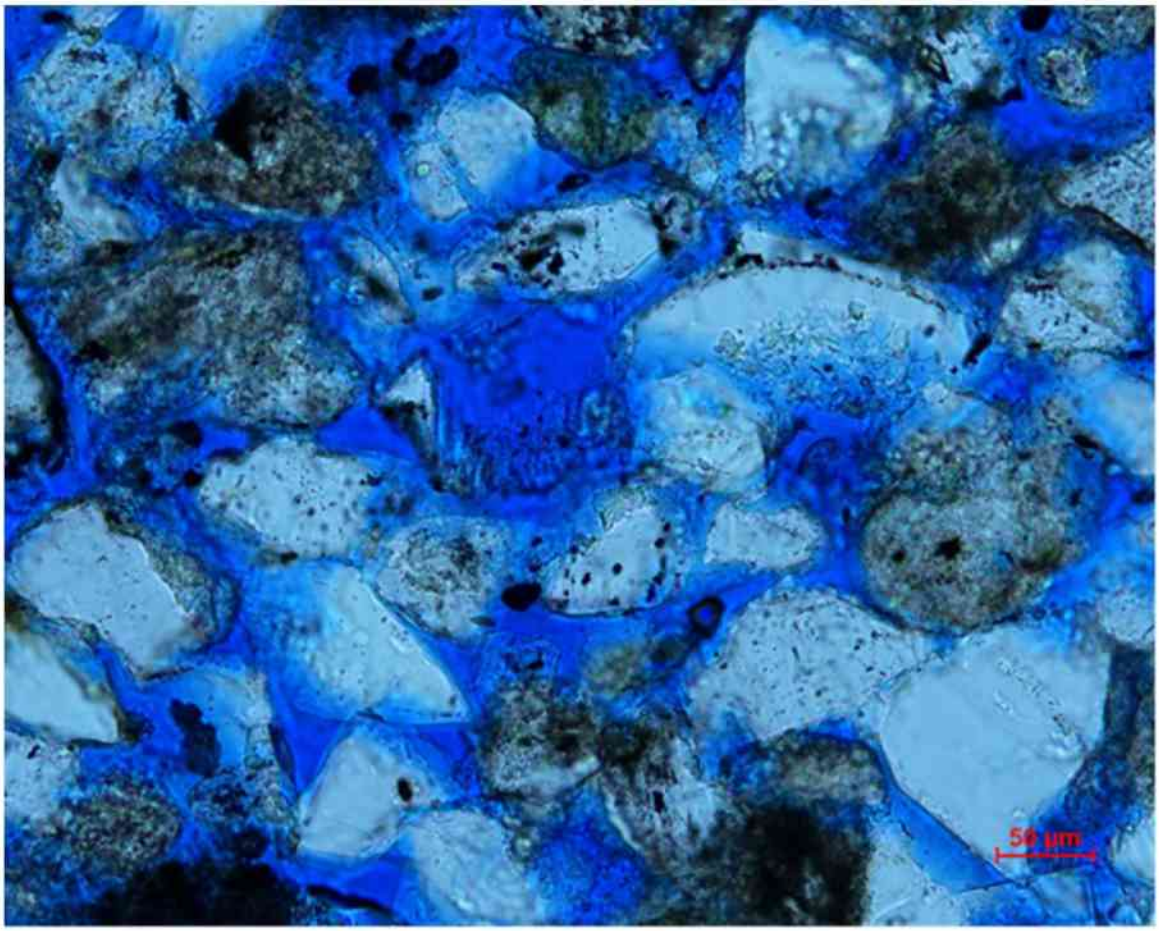

Figure 4.4: Thin section image of a fine-grained sandstone sample from the High Island 24L#9 well showing excellent porosity (~30%) from a depth of 8492 ft.

Table 4.1.1: XRD (X-ray diffraction) mineralogical composition of core samples.

Well	Depth (ft)	Quartz	Kaolinite	Calcite	Illite	Plagioclase	K-Feld
High Island 24L #9	8403.1	23.65	12.72	15.84	22.53	6.71	18.55
High Island 24L #9	8408.5	18.94	13.93	19.36	26.03	6.21	15.54
High Island 24L #9	8412.9	27.04	10.31	11.19	21.59	9.46	20.41
High Island 24L #9	8421	20.47	15.28	13.82	32.37	7.65	10.43
High Island 24L #9	8421	22.00	15.63	14.09	30.29	6.93	11.06
High Island 24L #9	8423.1	20.40	15.58	13.31	33.86	7.01	9.84
High Island 24L #9	8427.4	41.40	7.21	5.08	15.16	16.21	14.95
High Island 24L #9	8429.5	40.05	9.88	2.43	20.71	13.39	13.53
High Island 24L #9	8429.5	42.54	7.71	3.07	19.12	14.45	13.11
High Island 24L #9	8481.6	34.79	9.92	7.18	21.11	12.97	14.03
High Island 24L #9	8481.6	34.61	9.35	7.4	22.58	13.1	12.97
High Island 24L #9	8485	29.84	10.7	11.52	24.17	11.00	12.78
High Island 24L #9	8489	26.74	12.93	10.18	27.99	10.16	12.00
High Island 24L #9	8492	35.96	2.93	20.48	4.68	17.52	18.43
High Island 24L #9	8555	48.49	3.73	1.62	4.65	19.61	21.92
High Island 24L #9	8560.5	49.14	3.58	1.83	5.03	18.85	21.57

High Island 24L #9	8570.6	51.88	2.20	1.99	4.85	18.74	20.34
High Island 24L #9	8572	50.86	2.74	2.29	4.98	18.82	20.31

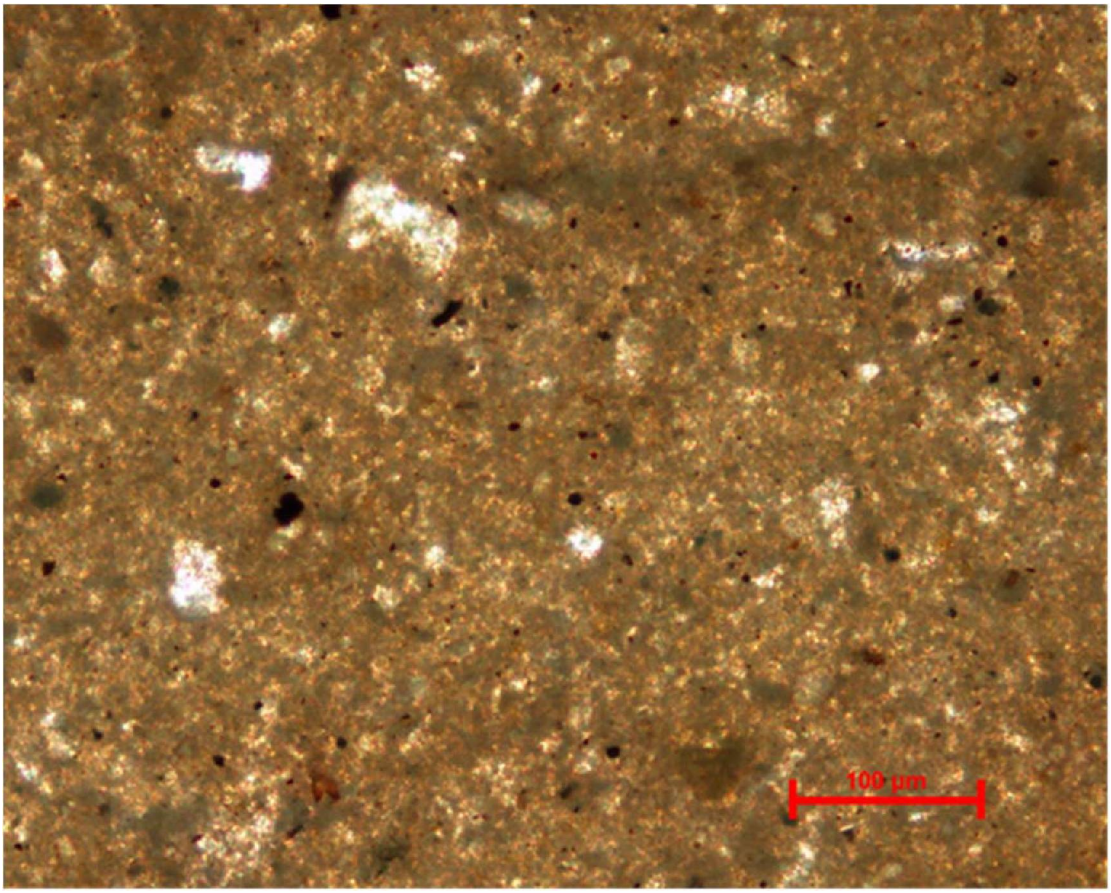

Figure 4.5: Thin section image of mudstone overlying a succession of high porosity sandstones, showing abundant clay and low porosity, therefore, high sealing capacity. 8408 ft, High Island 24L#9.

Mercury intrusion capillary pressure tests (MICP) were conducted on eight core samples from Well OCS-G-4708 #1 (427034012600) (Table 4.1.2). The samples are clay-rich siltstone, siltstone, and fine-grained sandstones from the bottom of a major mudstone layer and the underlying sandstone interval. They represent transitional lithologies from reservoir to seal.

Table 4.1.2: Samples analyzed using MICP (mercury intrusion capillary pressure) test

Sample Depth (ft)	Porosity (%)	Permeability (mD)	MICP Grain Density	Sample description
10578	6.48	0.00164	2.643	Greenish clayey siltstone, no lamination. Calcareous
10580	7.81	0.00172	2.64	Dark grey interbedded with brownish siltstone. Faint beddings. Calcareous.
10585	5.65	0.00092	2.661	Greenish clayey siltstone interbedded with brownish siltsone. Calcareous

10590	8.36	0.00205	2.69	Greeenish siltstone with abundant wood fragment. No lamination.
10597	7.04	0.00208	2.666	Greenish siltstone, calcareous, laminated.
10604	3.15	0.000145	2.665	Dark grey siltstone, no lamination.
10607	10.9	0.108	2.659	Grey fine sst. Cemented.
10609	9.32	0.00455	2.656	Grey very fine sandstone with convoluted dark grey siltstone lamina. Highly burrowed.

The samples show varied capillary entry pressure ranging from 137 to 2146 psi (Figure 4.6). At temperature 270 °F and pressure 4700 psi, they are capable of retaining a CO2 column of 13 to 243 ft before any intrusion of CO2 (Figure 4.7). The coarser-grained sandstone samples (10607 and 10609 ft) show the lowest sealing capability, while homogeneous siltstone samples (10604, 10580, and 10578 ft) show higher sealing capacity. The results suggest that the overlying mudstone sequences should have overall desirable sealing capacity.

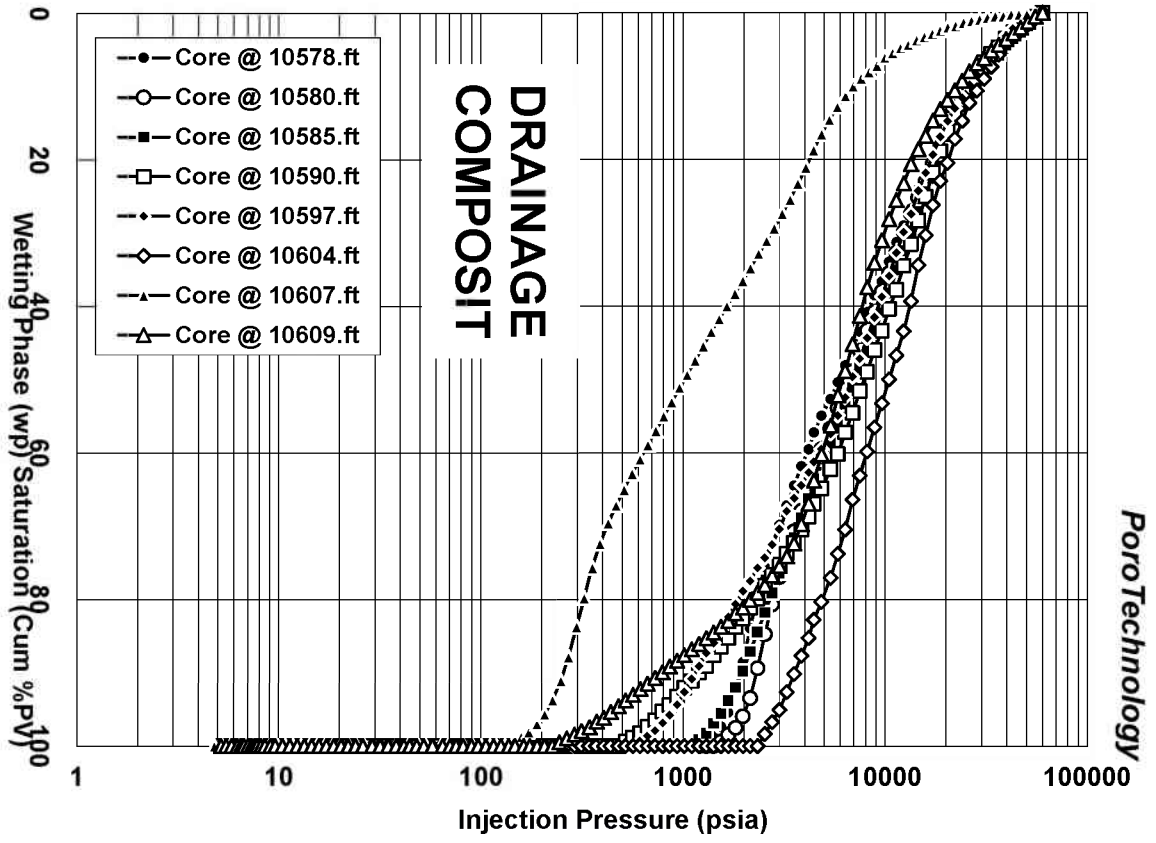

Figure 4.6: Mercury intrusion curves showng the capillary entry pressure for the samples. Sample at 10604 ft shows the highest capillary entry pressure (2146 psi), while Sample at 10607 ft shows the lowest capillarty entry pressure (137 psi).

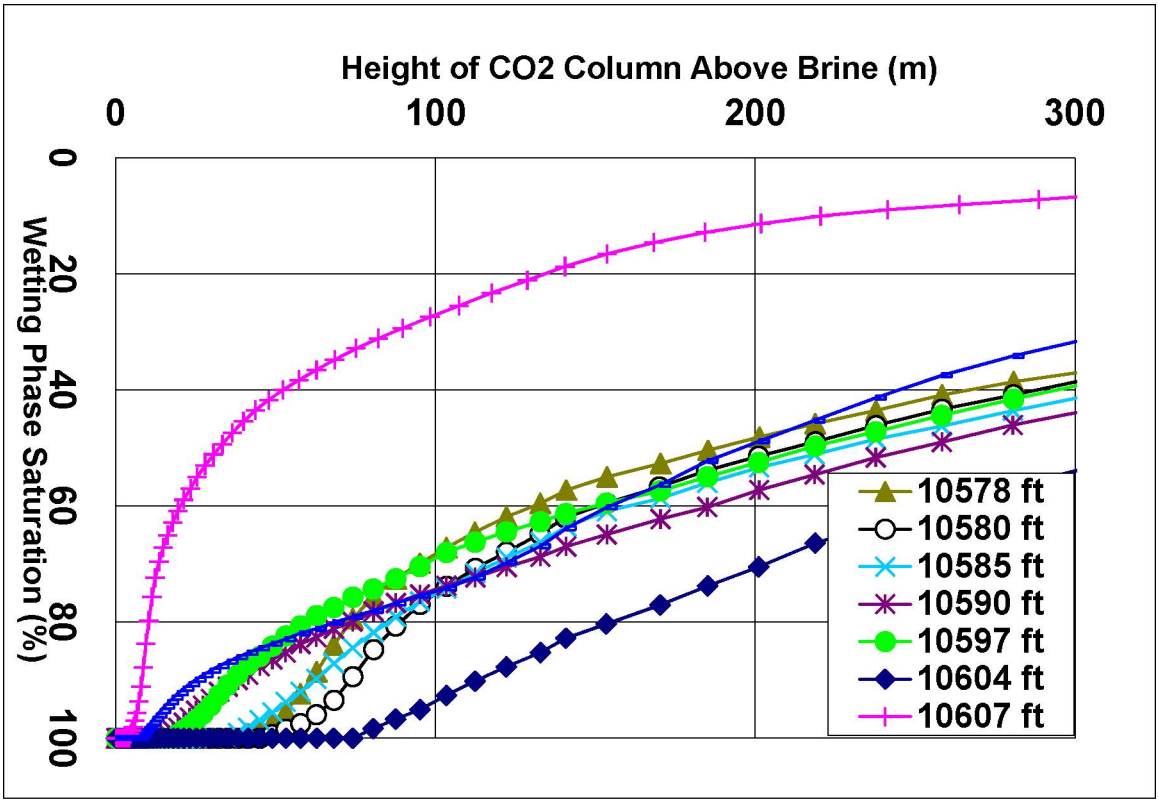

Figure 4.7: Carbon dioxide (CO2) column height calculated from mercury intrusion pressure using temperature 270 °F and pressure 4700 psi as an example.

Pore size distribution derived from mercury intrusion test is shown in Figure 4.8. Most samples have asymmetrical pore size distribution. The modal pore size is mostly in 10 - 100 nm. Porosity varies from 3 to 11 %. The pore throat size is the major factor controlling capillary trapping capacity. For example, the majority of the pores in Sample 10607 ft are larger than 500 nm, while Sample at 10604 ft has pores no larger than 100 nm.

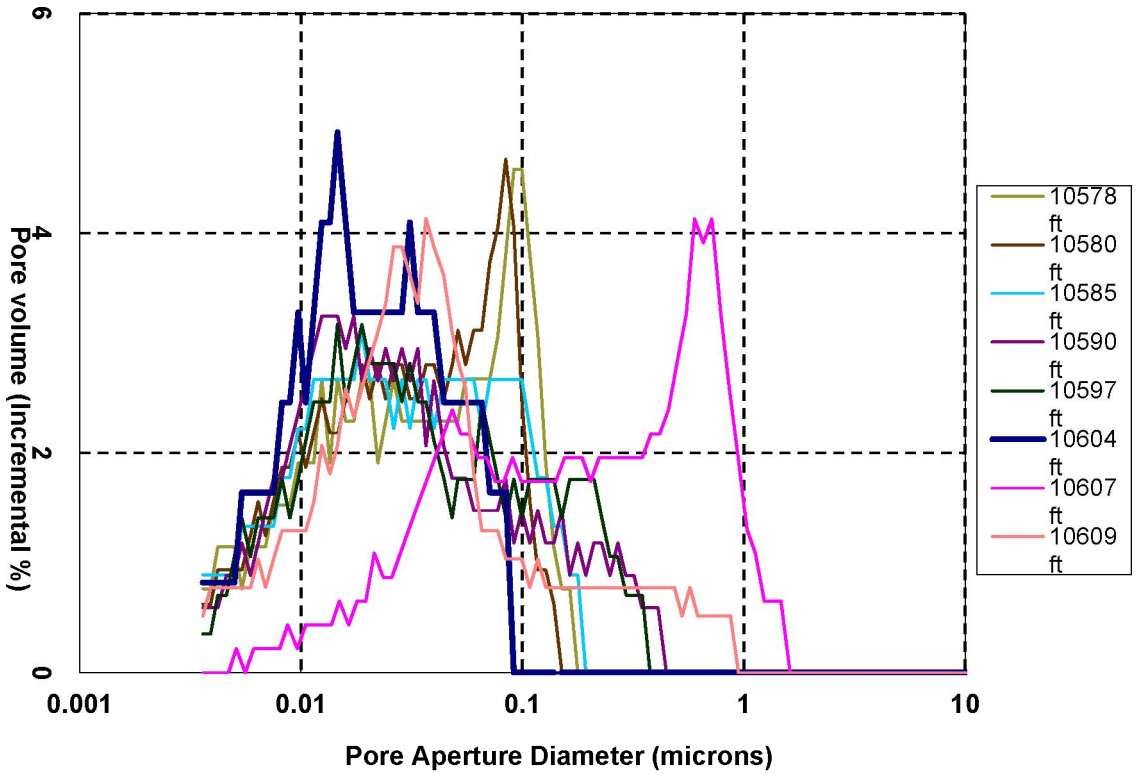

Figure 4.8: Mercury intrusion capillary pressure pore-throat–diameter distributions.

4.2 Subtask 4.2: Simulation

Results from simple dynamic analytical modeling (Jain and Bryant, 2011) of a discrete reservoir body in the Offshore Texas Miocene interval near San Luis Pass are shown in Figure 4.9. In these simulations runs are performed for 6,206 samples of porosity, permeability, and water saturation in a Gulf of Mexico Miocene gas reservoir taken from the Atlas of Northern Gulf of Mexico Gas and Oil Reservoirs (Seni et al., 1997).The average resulting capacity is found to be 30.3 megatonnes with an average fill time of 38.3 years.

Results from 3D modeling (Figure 4.10) show the final CO_2 plume distributions after 100 years of injection, along with the injection well profiles through time. The base case and 8 case variations represent the key unknown variables in the modeling study and are modeled to understand their potential impact on capacity. The 9 model cases are repeated for both a statistically heterogeneous and a seismic-based heterogeneous model (i.e., 27 models total). Figure 4.11 shows the resulting capacity for each model. It is clear that the effect of open boundaries is by far the most significant variable parameter. The primary factor influencing 3D model results is pressure. The condition that the reservoir cannot be fractured is present in each

model, and as a result, storage capacity is severely limited. The simple dynamic and 3D flow model capacity results are plotted along with area and thickness normalized regional capacity results (Figure 4.12). This graph shows the value of estimated capacity vs. the amount of effort required to produce each refinement step (in cost and time). The results indicate an 88% decrease in capacity from the initial regional estimate to the final 3D flow model results. Though this value is site specific, it highlights the necessity for the consideration of the magnitude of error that is potentially present in single value estimates of regional CO_2 storage capacity. The primary reason for the drastic difference in capacity between regional and site specific models is the consideration of pressure. The regional estimate used does not consider pressure and thus is likely overly optimistic. Consequently, understanding and predicting pressure behavior and connectivity in a reservoir is key to understanding its storage capacity for CO_2 injection.

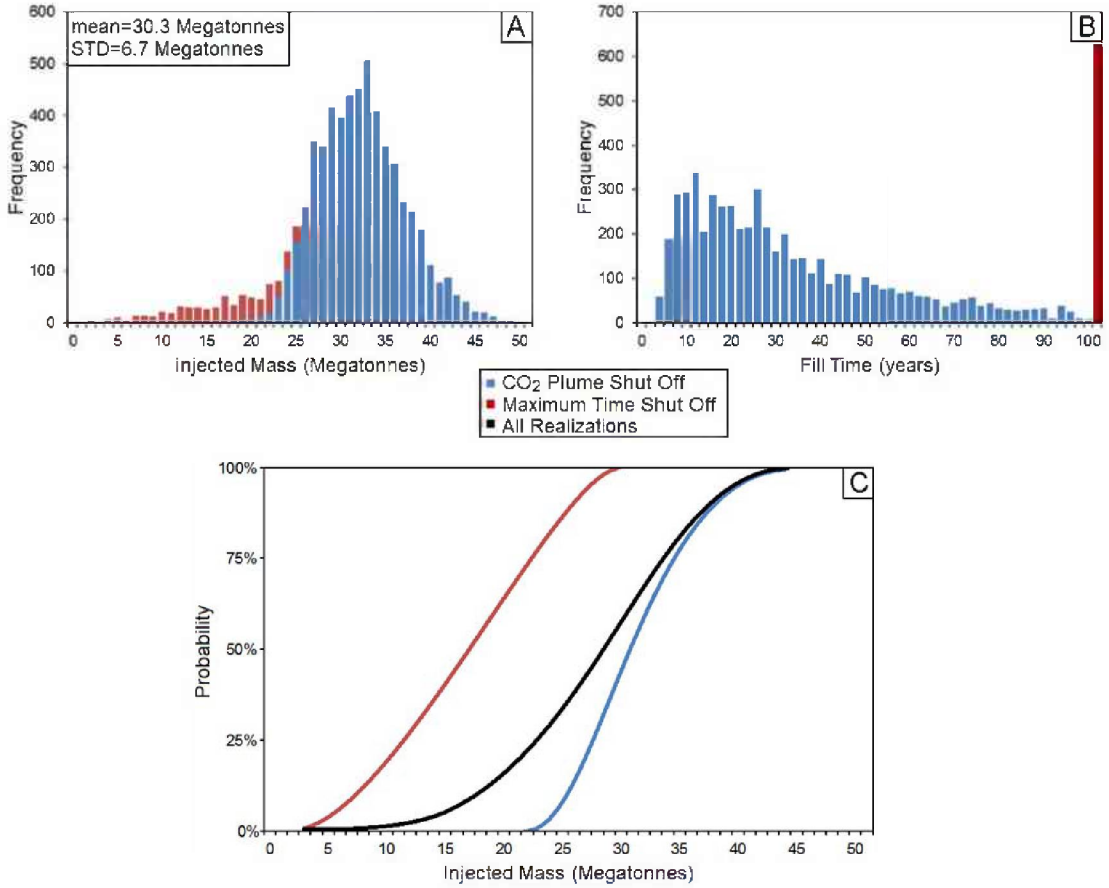

Figure 4.9: Simple analytical modeling results: Distribution of injected mass (a) and fill time (b) for model runs of 6,206 samples of porosity, permeability, and water saturation populated from the Miocene subset of the Atlas of Northern Gulf of Mexico Gas and Oil Reservoirs (Seni et al., 1997). Cumulative distribution probability plot (c) shows the probability values for both shut off flags and the probability values for all model runs combined.

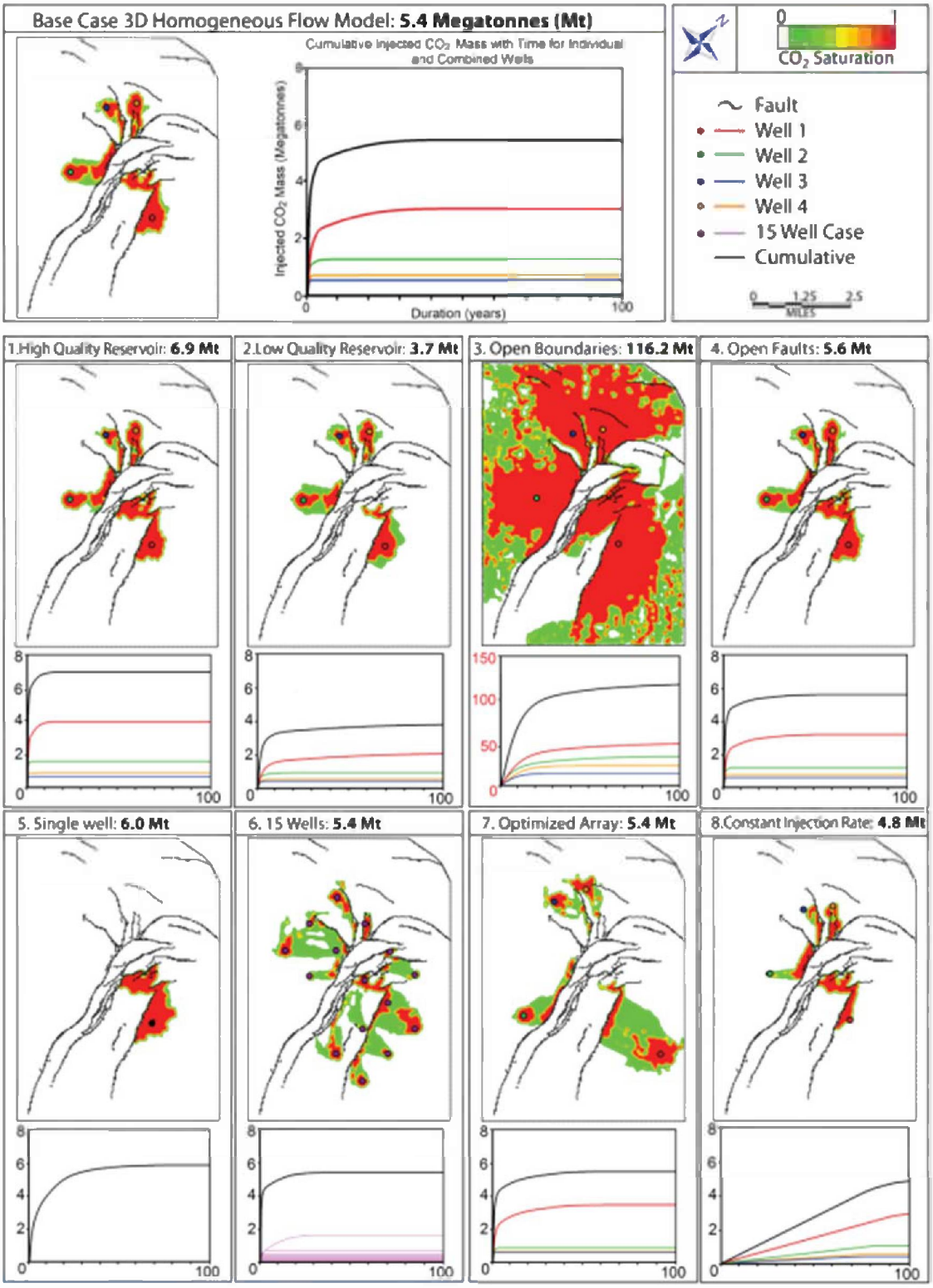

Figure 4.10: Final plume geometries at the top of the reservoir and injection profiles for cases 1-8 for homogeneous model scenario. Y-axis of all plots is injected CO2 mass (Mt) and x-axis is duration (years). Note the change in y-axis scale on case 3.

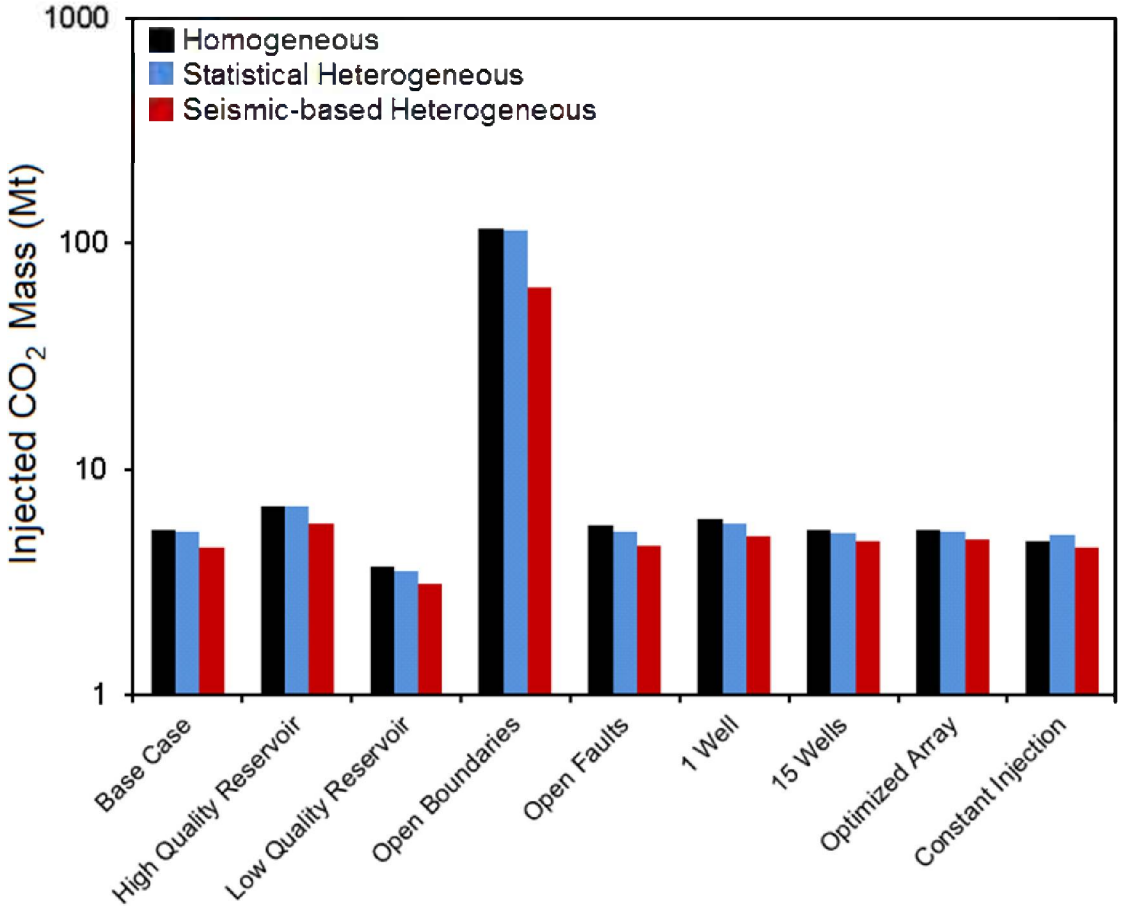

Figure 4.11: Bar graph of injected CO2 mass (Mt) for each case of homogeneous, statistical heterogeneous and seismic-based heterogeneous models. Note that the y-axis uses a logarithmic scale. In addition, note that the effect of open boundaries (case #3 in Figure 4.10) is by far the most significant variable parameter.

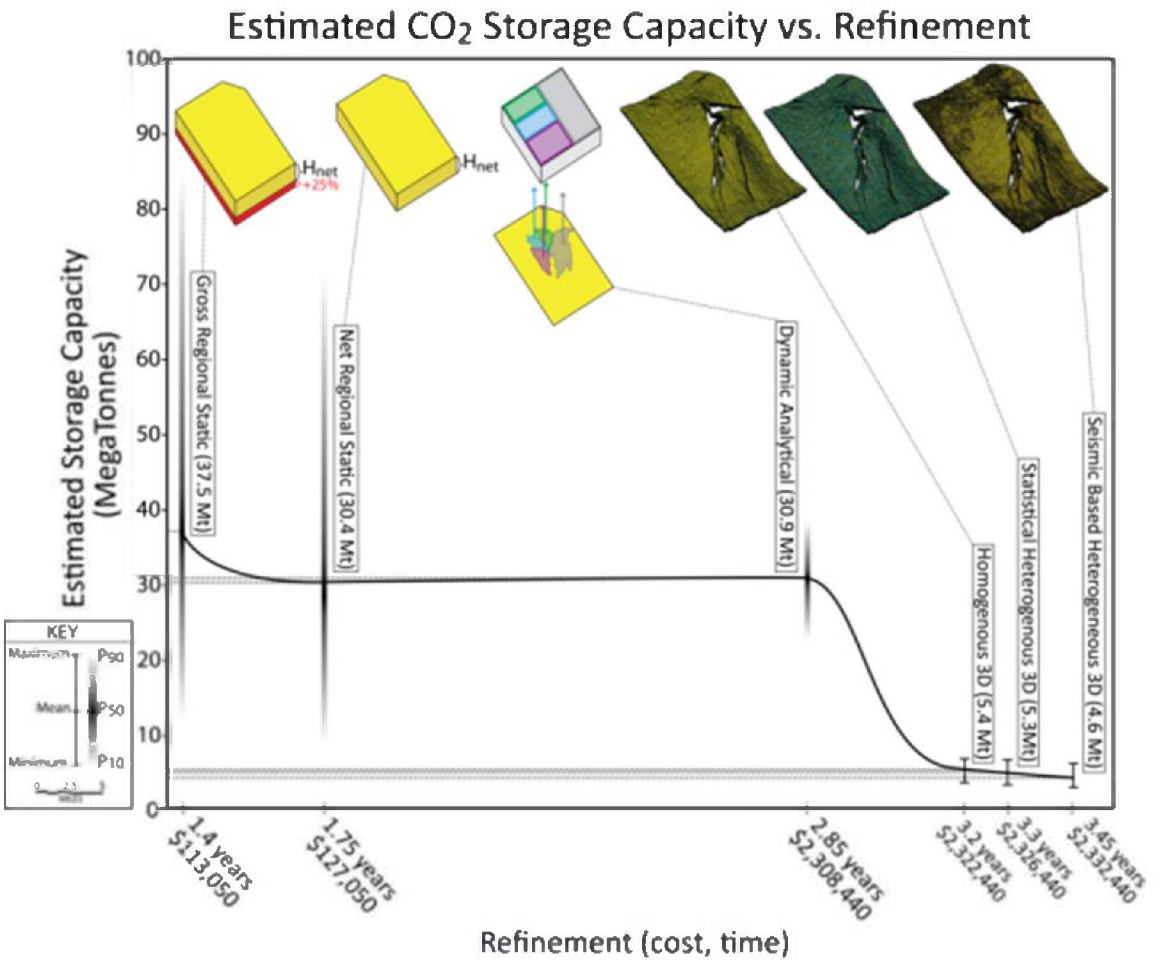

Figure 4.12: Estimated CO2 storage vs. refinement. Time and cost for each step is given on the x-axis. Vertical shading represents probability distribution and vertical bars represent the range of results. Note that the horizontal scale in the key applies to all diagrams in the upper portion of the chart.

Results and Conclusions

According to Wallace (2013) the comparative results in Figure 4.12

> "…show a decrease in estimated capacity with additional refinement, with the exception of the dynamic analytical model. The estimated capacity results from the net regional model are similar to the dynamic analytical model. Only the dynamic analytical model shows a much smaller probability range. The fluid flow assumptions in the dynamic analytical model make comparison to other capacity estimates difficult. The dynamic analytical model is known to be overly optimistic, whereas the regional and 3D flow models attempt to more accurately model capacity. The results of the dynamic analytical solution are likely highly site specific. Estimated capacity is directly related to the input area in the dynamic analytical solution. Because the fluid flow assumptions are so optimistic, the calculation can only be applied to the closure areas. In the regional and 3D flow estimates, the entire DRMA is considered either for pressure buildup or volumetric calculations. Thus, for an area where the closures were smaller relative to the study area, the dynamic analytical solution results would have a significantly different relationship to the results from regional and 3D flow models, whereas the relationship between regional and 3D models would likely be much less affected. Thus, we suggest that

the dynamic analytical solution is not ideal for capacity estimation. The added understanding by using 3D flow models is significant and the additional time and cost is relatively minor. The primary benefit of the simple dynamic model is a basic understanding of fill time.

An approximately 88% decrease in capacity is observed from the gross regional estimate to the seismic based heterogeneous models. The expected range of capacity also becomes much smaller with additional refinement, though in 3D models this is shown to be highly contingent on boundary assumptions. The reason for the large discrepancy between the gross regional model and the 3D flow models is the consideration of pressure. Pressure constraints and reservoir fracturing are not considered in the regional model, but are extremely limiting in 3D flow model simulations. The end result from the 3D modeling may not be indicative of the actual capacity of this site, however, without a better understanding of reservoir connectivity and boundary conditions, it is a reasonable estimate. Note that the maximum capacity values from 3D modeling are lower than the P10 values from the regional models. Given that the 3D models represent a possible scenario, the range in efficiency factors used in regional modeling should yield results that encompass the capacity range from 3D modeling."

In summary, utilizing regional assessments to determine feasibility for long term CCS planning, may lead to optimistic forecasts of storage potential (Wallace, 2013).

5 Task 5.0: Stratigraphic Containment (Site)

5.1 Subtask 5.1 Modeling

Research conducted for Subtask 5.1 focused on simulating fluid flow in a relatively small scale (20.51" tall by 10.39" wide (0.521 m x 0.264 m)) but high-resolution (>2M data points), 2D, sedimentary relief peel model (Figure 5.1). This work included contributions from Dr. Steve Bryant (UT-Petroleum and Geosystems Engineering faculty) and graduate student Priya Ravi Ganesh. Digital scanning of the topographic relief of the peel was conducted by Study PI, Dr. Tip Meckel, using a Suphaser 25 SP 3D laser scanner housed at the Texas Bureau of Economic Geology in Austin, TX.

The primary dataset obtained from the peel is the ranged distance between the scanner and the peel, which provided a finely-resolved topographic digital model of the peel relief. The relief of the peel is considered to be a proxy for the permeability heterogeneity of the medium. The relative elevation range is more useful to work with, so the mean ranged distance from the scanner to the specimen was subtracted from all ranged distances, thus representing topographic highs as positive values and topographic lows as negative values. An advantage of this representation of the ranged measurements is that the relative topography map can be easily converted to various permeability continuum models (Figure 5.1) for broad investigation of the effects of depositional fabric on flow processes. Initial research explored a variety of models as described below.

HIHOSS: high permeability homogeneous sandstone
- Permeability range: 1 D to 10 D

- Permeability mean: 3.6 D
- Threshold pressure range: 8 to 21 kPa (difference of about 13 kPa)

HIHESS: high permeability heterogeneous sandstone
- Permeability range: 0.01 D to 10 D
- Permeability mean: 604 mD
- Threshold pressure range: 8 to 133 kPa (difference of about 125 kPa)

MOHOSS: moderate permeability homogeneous sandstone
- Permeability range: 300 mD to 1,000 mD
- Permeability mean: 582 mD
- Threshold pressure range: 21 to 34 kPa (difference of about 13 kPa)

MOHESS: moderate permeability heterogeneous sandstone
- Permeability range: 8 mD to 1,000 mD
- Permeability mean: 131 mD
- Threshold pressure range: 21 to 145 kPa (difference of about 124 kPa)

LOHOSS: low permeability homogeneous sandstone
- Permeability range: 60 mD to 100 mD
- Permeability mean: 79 mD
- Threshold pressure range: 53 to 65 kPa (difference of about 12 kPa)

LOHESS: low permeability heterogeneous sandstone
- Permeability range: 5 mD to 100 mD
- Permeability mean: 27 mD
- Threshold pressure range: 53 to 175 kPa (difference of about 122 kPa)

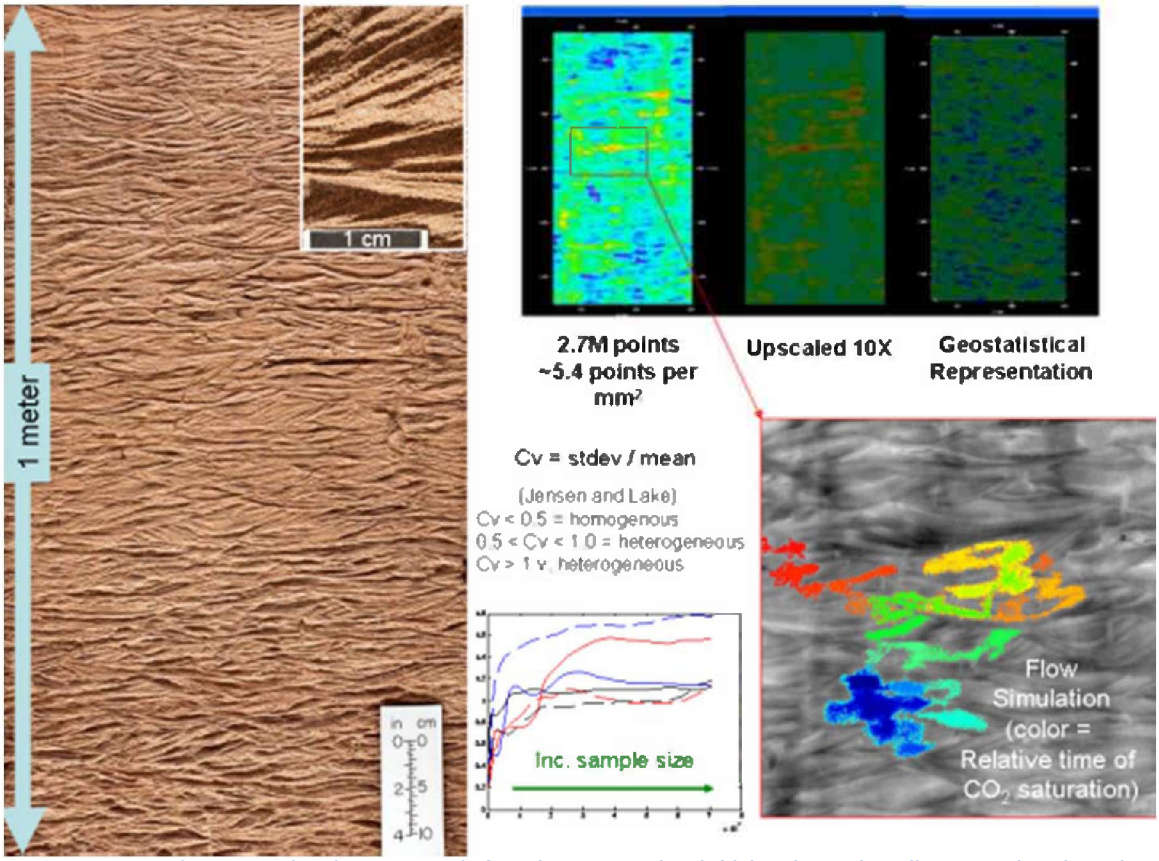

Figure 5.1: Two dimensional sedimentary relief peel specimen (on left) has been digitally scanned and used to represent various permeability fields for flow simulation to understand residual saturation (i.e. capacity) of heterogeneous media.

The dataset was input and modeled using the Permedia modeling software package (formerly MPath). For typical reservoir conditions, buoyancy and capillary forces grow dominant over viscous forces within a few hundred meters of injection wells as the injection-related pressure gradient decreases, resulting in qualitatively different plume migration regimes. A capillary channel regime arises when the capillary pressure of the leading edge of the plume and the range of threshold entry pressures within the rock at the leading edge of the plume are equivalent (Figure 5.2).

In this work we characterize capillary channel migration of CO2 in a real 2D geologic domain (1 m × 0.5 m) in which sedimentologic heterogeneity has been resolved at sub-millimeter (depositional) resolution.

When CO2 is injected into a storage reservoir during sequestration, viscous forces dominate flow behavior near the wellbore due to high injection rates and large pressure gradients. As CO2 moves into the medium, far away from the injectors, the pressure gradient from injection becomes negligible compared to buoyancy forces. Buoyancy drives plume migration through the majority of the reservoir. Flow in the migration regime depends on two factors: the capillary pressure of the leading edge of the plume (Pc) and the range of threshold entry pressures within the rock at the leading edge of the plume (Pth).

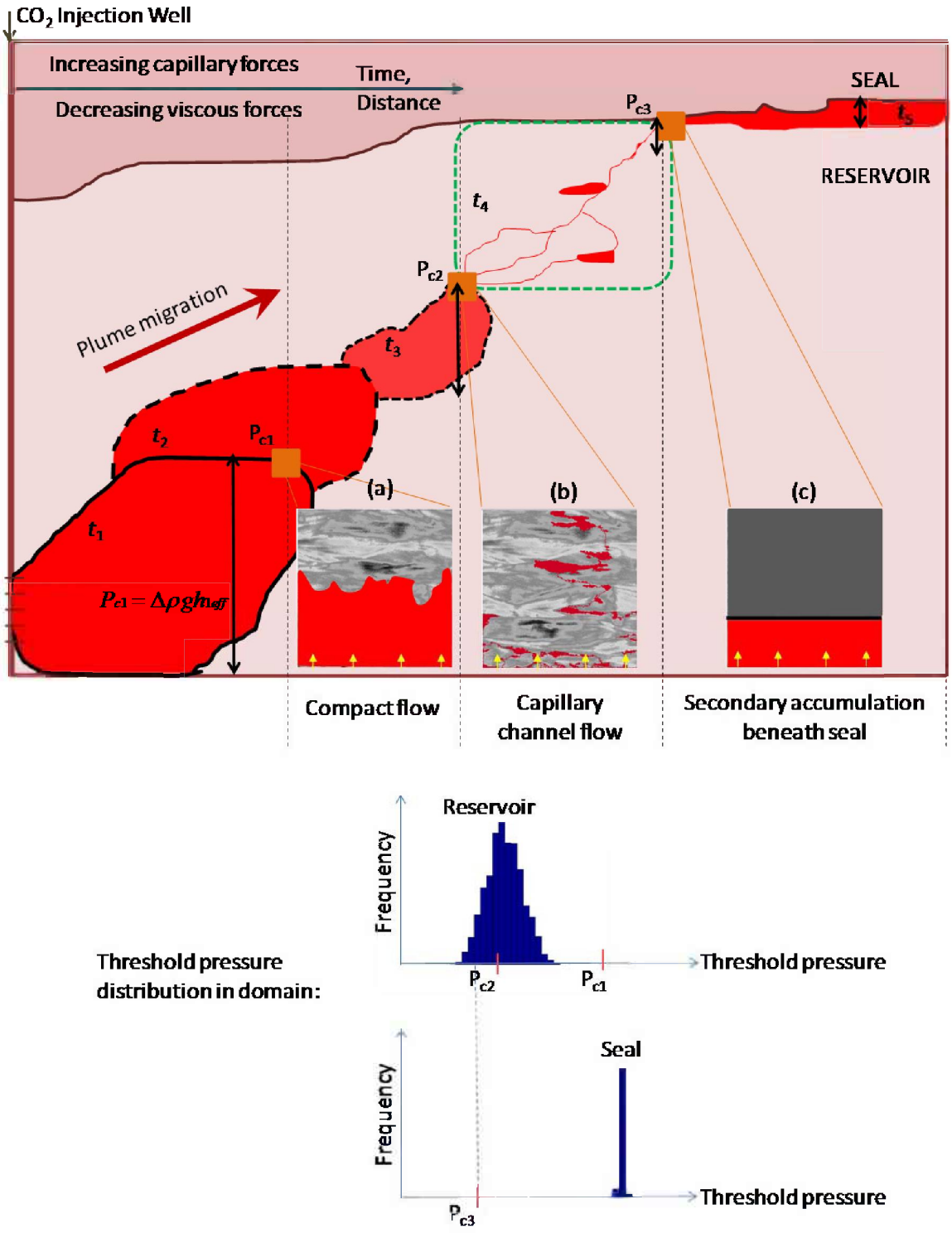

Figure 5.2: Schematic of spatial and temporal evolution of flow regimes from viscous-dominated to buoyancy/capillarity-dominated. As the mass of mobile CO2 plume moves through time (outlines of plume at times t1, t2, t3, t4 and t5 are shown) and distance in the reservoir (extreme vertical exaggeration), possible flow regimes are: (a) compact flow where Pc1 > max(Pth), (b) capillary channel flow where min(Pth) < Pc2 < max(Pth) and (c) secondary accumulation beneath a seal where Pc3 < min (Pthseal). The seal rock is a different rock type with very high threshold pressure values Pthseal compared to the reservoir rock.

The model domain is a digital representation of a physical geologic specimen. The specimen (Figure 5.3 (a)) is a vertically-oriented, quasi-2D sedimentary relief peel sample (1.0 m × 0.5 m) of alluvium extracted from the upper portions of a modern point bar of the Brazos River, Texas. Optically ranged topography of the sample surface (extent of imbibition of epoxy) and grain diameter measurements on this peel are used to build high-resolution geologic model populated with corresponding threshold pressure values calculated.

Building the geologic model

Sequential stages of building the digital model (2 million elements) are illustrated in Figure 5.3 and described as follows:

(a) Obtained peel specimen subjected to high-resolution laser scanning and imaging techniques to study epoxy imbibition and grain size distribution;
(b) Prepared digital elevation map derived from topographical variations in the peel due to epoxy imbibition;
(c) Digital high-resolution model generated representing the threshold pressure distribution of the model domain corresponding to the determined topography.

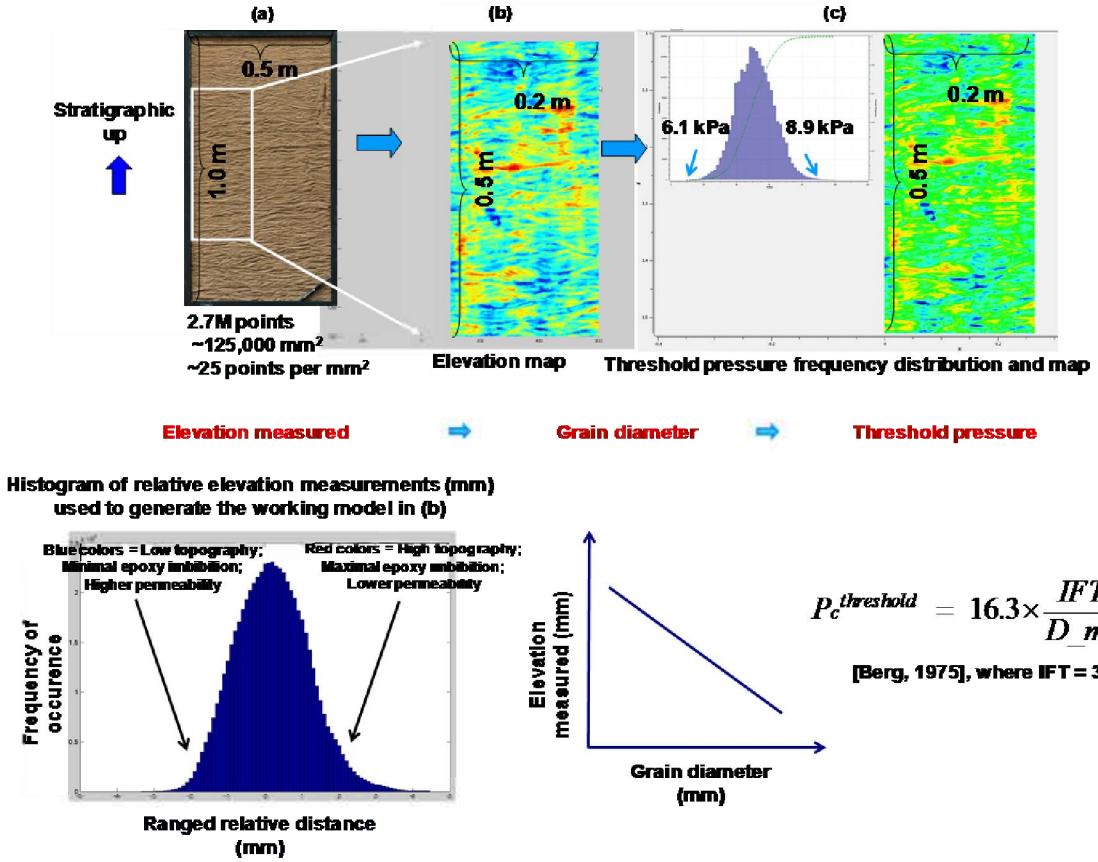

Figure 5.3: Building the geologic model domain. Higher elevations correspond with greater imbibitions as a result of smaller average grain size (hotter colors, (b) and (c)) and lower elevations correspond with lesser imbibition as a result of larger average grain size (cooler colors, (b) and (c)). For the purpose of presenting the simulation results that follow, we use the grayscale domain background where the lighter gray shades correspond to the hotter colors mapped here.

Simulation criteria

As previously reported, simulations are performed using a modified invasion percolation software, Permedia® (distributed by Halliburton).

- CO_2 is sourced from the bottom boundary of the domain as a line source.
- Periodic lateral boundaries of the domain eliminate boundary effects and artificial upward bias in plume migration for all simulation cases.
- A simulation terminates when rising CO_2 reaches the top boundary of the domain (percolation). The percentage of the domain where CO_2 is present is then calculated, as it does not increase after percolation.
- Density difference of 300 kg/m^3 between connate water and CO_2 is maintained for all simulations cases.
- Constant porosity of 20% is considered.

Simulating capillary channel flow in the peel model

We simulate buoyancy-driven migration of CO_2 in the peel model for the capillary channel migration regime. Maximum and minimum threshold pressure values of 6.1 to 8.9 kPa (mean of 7.4 kPa) are assigned to the model corresponding to the minimum and maximum grain sizes of 0.055 and 0.08 mm determined for the specimen. High-resolution simulations indicate that CO_2 migrates through the peel predominantly fingering preferentially through regions of lower threshold pressure which have an architecture defined by the depositional fabric (Figure 5.4). These capillary channels efficiently transport all CO_2 that enters the domain through a few narrow, generally vertical pathways.

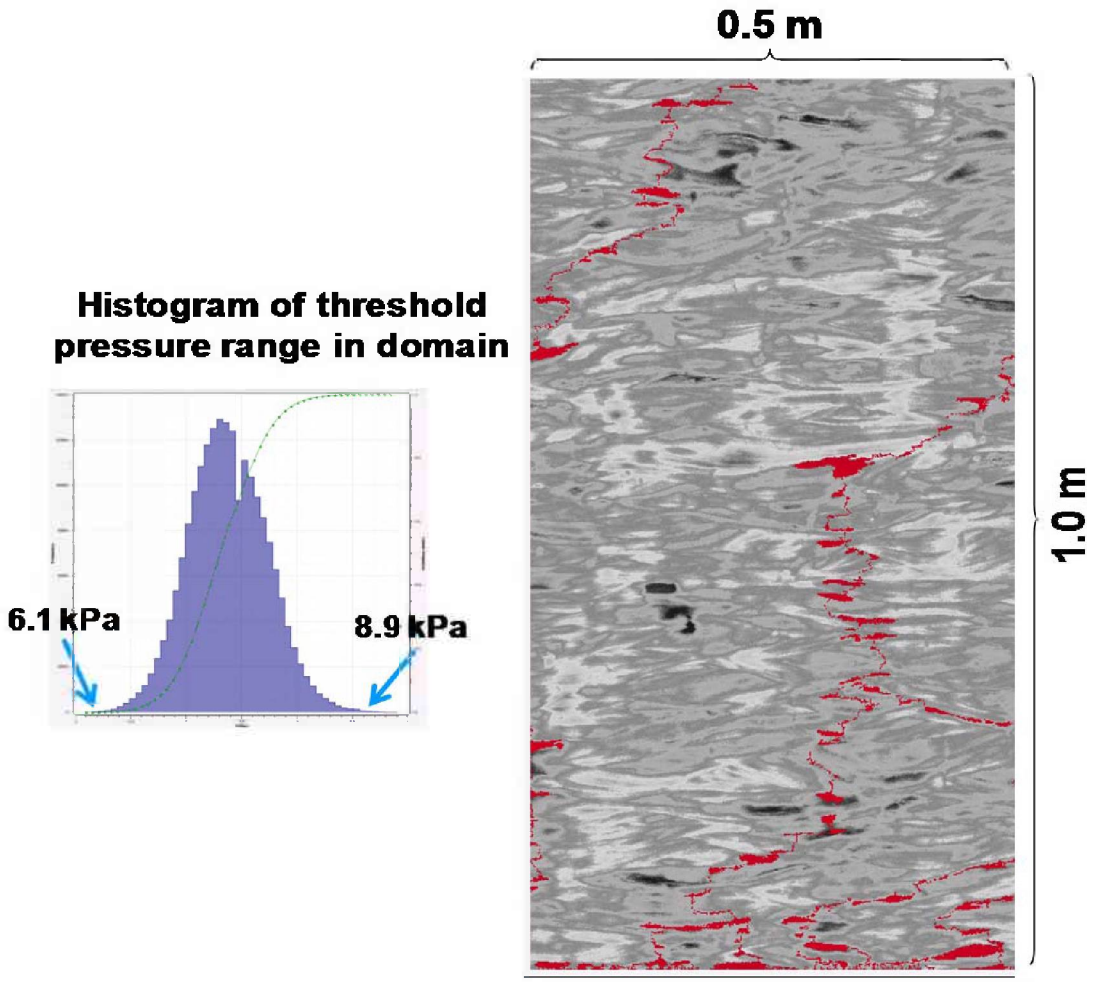

Figure 5.4: Invasion percolation simulation of CO2 migrating through the peel model. The CO2 flow pattern is characterized as 'fingering'. Only 2.86% of the model domain is saturated with CO2 at percolation. Greyscale is reflected in histogram to left.

Effect of Heterogeneity on Capillary Channels

The relevant features of heterogeneity are grain size distribution, which determines the mean and range of threshold pressures, and the correlation lengths of threshold pressures in horizontal and vertical directions. We evaluate each independently.

CASE 1: Effect of threshold pressure range on CO2 migration regime

Working model of 0.1 m × 0.1 m subsection (250000 cells) of the peel is used to resolve CO2 migration patterns while systematically varying the range of threshold pressures. This exercise provides insight into how such fabrics may influence flow in rocks with different petrophysical properties.

CO2 migration in capillary channels exhibits a transition from fingering to back-filling pattern as grain size distribution widens in the domain (Figure 5.5). Thus storage efficiency reduces as buoyancy and heterogeneity enable much CO2 to migrate longer distances with lower rock contact volume.

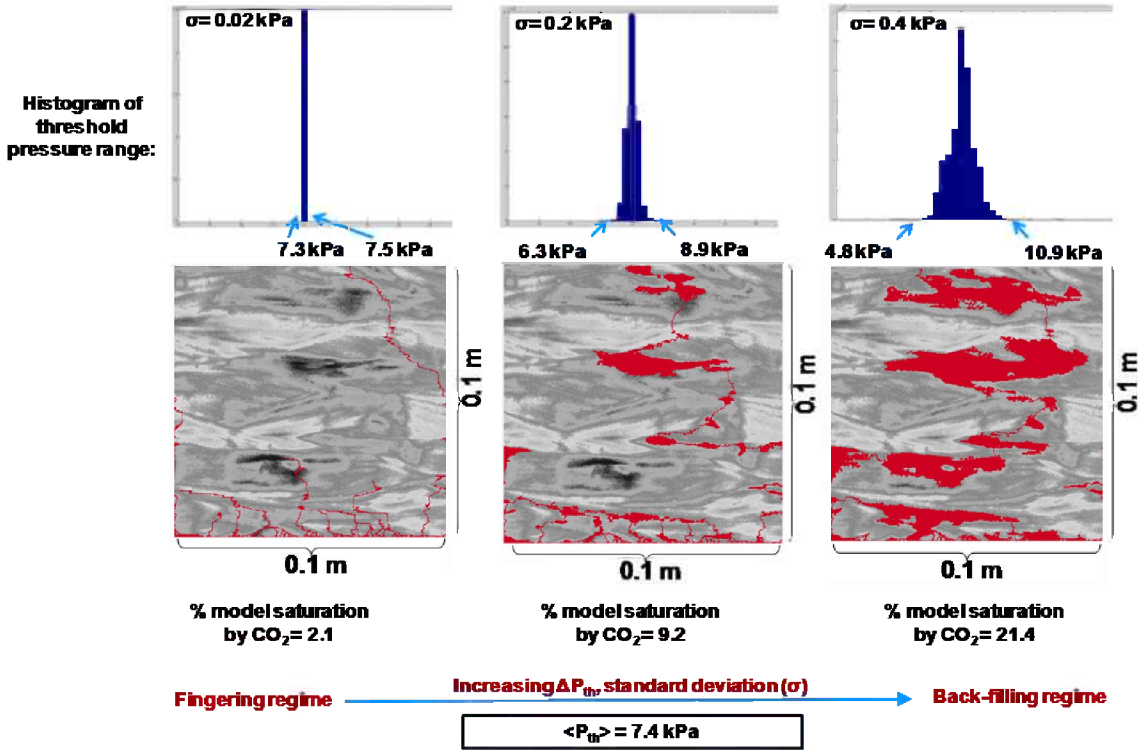

Figure 5.5: Flow transition from fingering (left) to back-filling (right) patterns occurs with increasing threshold pressure range. Mean Pth in all simulations is 7.4 kPa. Domains with wider grain size distribution cause CO2 to back-fill beneath contiguous regions of larger entry pressure, so a higher percentage of the domain becomes saturated with CO_2.

CASE 2: Effect of correlation length of threshold pressures on CO2 migration regime

The effect of varying the underlying structure (fabric) of the domain on CO2 migration is studied using geostatistical realizations of different horizontal and vertical correlation lengths of threshold pressures. Constant threshold pressure range of 6.3 – 8.9 kPa (Figure 5.5 middle panel) is used for this case.

The ratio of horizontal and vertical correlation lengths of threshold pressures in the domain influences the size of CO2 accumulations (Figure 5.6). Higher ratios of horizontal and vertical correlation lengths in the domain lead to more lateral movement of CO2 with increasing size of accumulations. Thus the tendency of CO2 to back-fill and thus contact more rock is greater as it migrates. This reiterates the importance of the underlying geologic fabric (depositional and diagenetic heterogeneity) in influencing CO2 migration regime.

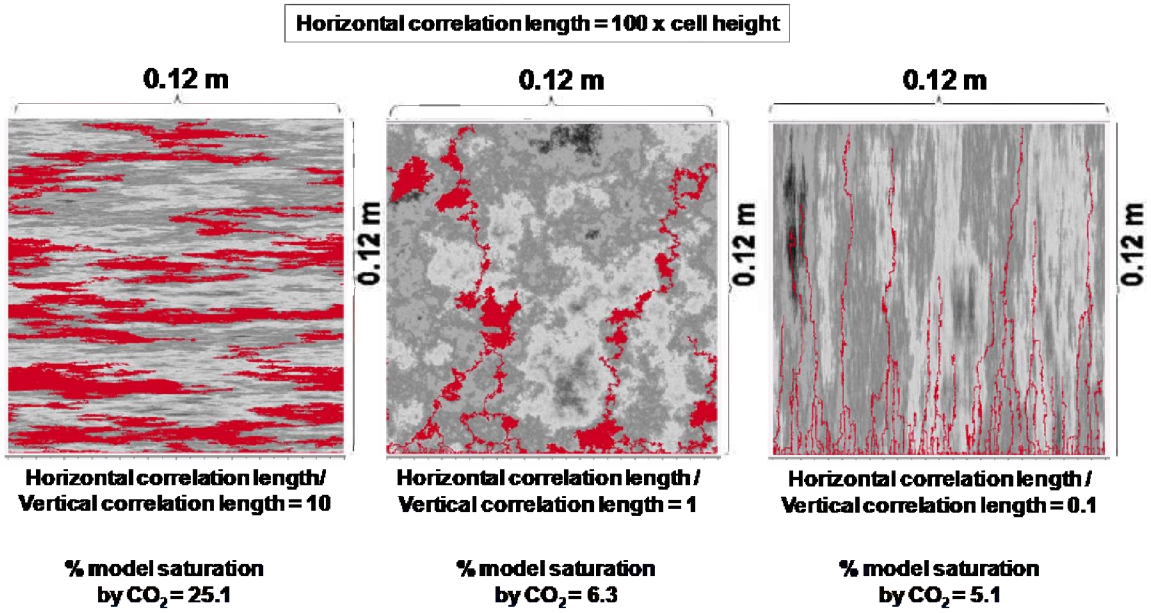

Figure 5.6: Effect of ratio of horizontal and vertical correlation lengths of threshold pressure (horizontal correlation length = 100 × constant cell dimensions) in the 250000 cells model on CO2 migration pattern.

Results and Conclusions

- The relevant physics for the migration regime we investigate is invasion percolation.
- Flow patterns within the capillary channel regime vary from finger-like structures with minimal rock contact to back-filling structures with compact volumes of saturation distributed between fingers. For this depositional fabric considered, 3% of the domain gets filled by CO_2 when it fingers while back-filling migration pattern leads to 30% saturation of the domain with CO_2.
- The storage efficiency of the capillary channel regime would be low and consequently CO_2 would also migrate greater distances than expected from models or simulations that neglect the capillary channel flow regime.
- More spatial correlation and wider grain size distributions are conducive for the back-filling migration pattern. With more compact and thus less efficient plume migration pathways, these make preferred storage sites compared to domains driving fingering migration patterns.
- Modeling the dominant flow physics at the appropriate scale is important to get valid estimates of fluid migration through formations and effective

In summary, mean grain size and sorting appear to be the key control on CO2 movement; fluid density contrast (in the expected ranges) is apparently secondary. Pressure gradients contribute to end member and transition behavior, in addition to rock properties and fluid density contrast. The pressure gradient in relative close proximity to the well (compared to the reservoir extents) can allow for fingering behavior.

The results of this research were published by Meckel et al. (2015)

5.2

Subtask 5.2: Caprock Seal Capacity

The summary and results of the Study's research on caprock seal capacity are found in chapter 3 of the Geological CO_2 Sequestration Atlas for Miocene Strata Offshore Texas State Waters, which is found in the Appendix A.

6 Task 6.0: Brine Containment

6.1 Laboratory measurements

Generation of Synthetic Brines for Batch Experiments

One of the most important initial steps in analyzing the quantitative and qualitative capacity for brines in Miocene age units of the Gulf of Mexico (GOM) to safely retain (i.e., sequester) CO_2 was to determine the composition of the brines and subsequently generate synthetic brines that could be used in batch experiments. The data sources included the USGS (United States Geological Survey) "Produced Water" database (USGS, 2002) and a paper presented by Land et al. (1988). The two data sources indicate that total dissolved solids (TDS) can be up to 274,000 mg/L with an average value of 110,000 mg/L. For Miocene age units of the GOM, Na and Cl are the two dominant ions for TDS in brine samples. Batch experiments of the current study, utilized TDS (total dissolved solids) composition for synthetic brine samples of 4000 mg/L, 110000 mg/L, 200000 mg/L, and 300,000 mg/L.)

USGS produced water Database

This database is a subset of a larger database originally provided to the USGS by GeoINFORMATION at the University of Oklahoma and can be traced to the Petroleum Laboratory at Bartlesville, Oklahoma that was originally operated by the U.S. Bureau of Mines and subsequently by the Department of Energy. In the 1980s, the database was provided to the University of Oklahoma. USGS reviewed the whole database which included 77,650 records and 102 fields. The resulting database contains 58,706 records. The revised database has 210 records from Miocene age samples. There are ~170 records with spatial coordinates which have been loaded into ARCGIS (Figure 6.1). Some records are from identical locations due to repeated sampling. The earliest samples were taken in the 1950s and the most recent sample was taken in 1980.

Land et al. (1988)

Land et al. (1988) collected 47 formation water samples from Miocene age reservoirs in offshore Louisiana and analyzed for major and minor organic and inorganic components. The Land et al. (1988) study area and locations of, respective, samples is shown in Figure 6.2. Because no exact geospatial coordinates were provided by the authors, the dataset is not shown in Figure 6.1.

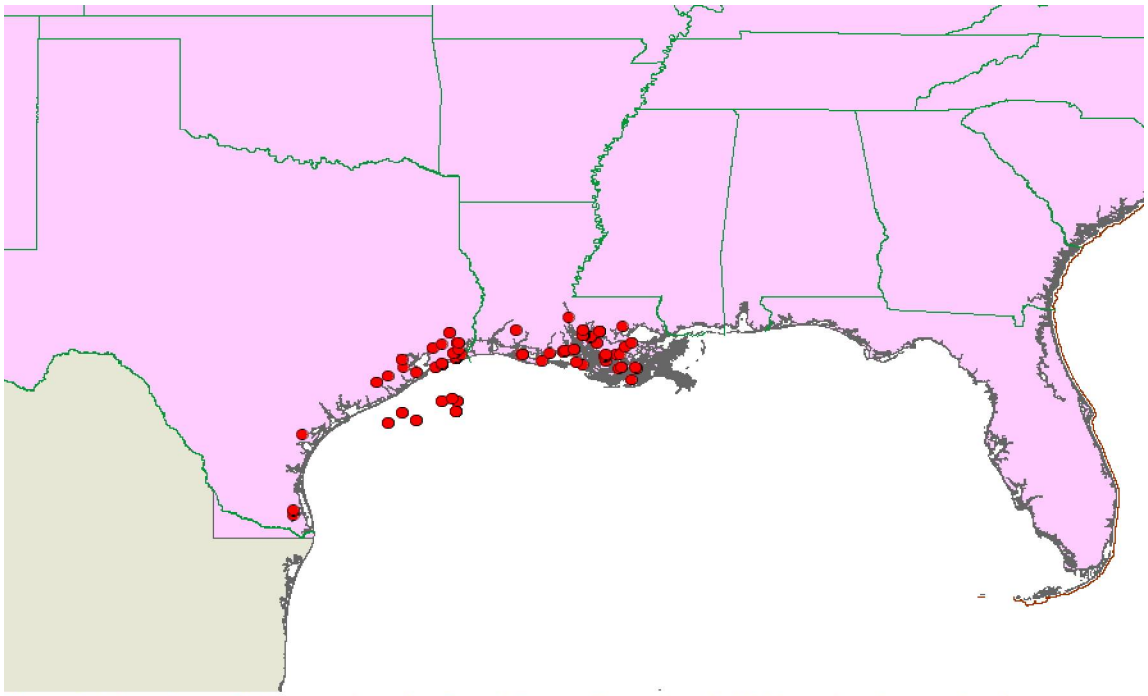

Figure 6.1: Locations of brine samples taken from Miocene formations in USGS produced water database.

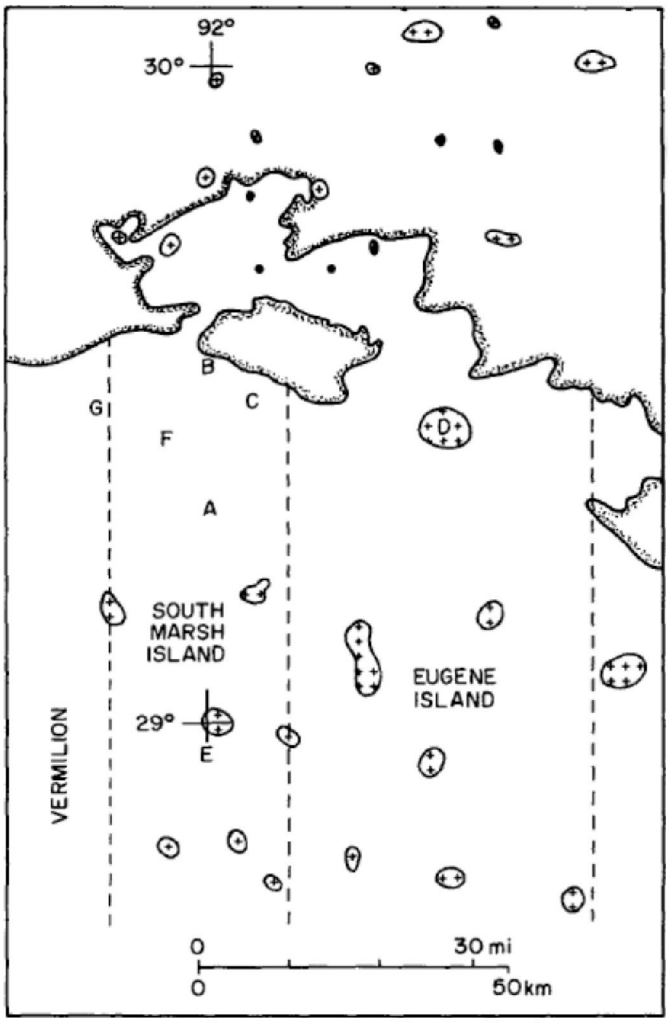

Figure 6.2: Map showing the study area of Land et al. (1988) with approximate locations of the study's brine samples.

Brine compositions

Brine compositions from the two data sources are shown in Figure 6.3 to Figure 6.8. One of the most important parameters which can affect CO_2 solubility in brine is total dissolved solids (TDS). The data indicate that TDS of Miocene formations ranges from very low up to 290,000 gm/L (Figure 6.3). However, the average TDS is about 110,000 mg/L at depth from 1000 m to 3000 m which will be considered the prime depth window for CO_2 storage formations. Maximum and minimum TDS are 274,000 mg/L and 4,070 mg/L, respectively.

Na and Cl are the two dominant ions. At depths of 1000 m to 3000 m:

1. Average Cl concentrations are 67,000 mg/L with maximum and minimum values of 168,000 mg/L and 1670 mg/L (Figure 6.4).
2. Average Na concentration is 39,126 mg/L (Figure 6.5). Maximum and minimum Na concentrations are 84600 mg/l and 1327 mg/l, respectively.

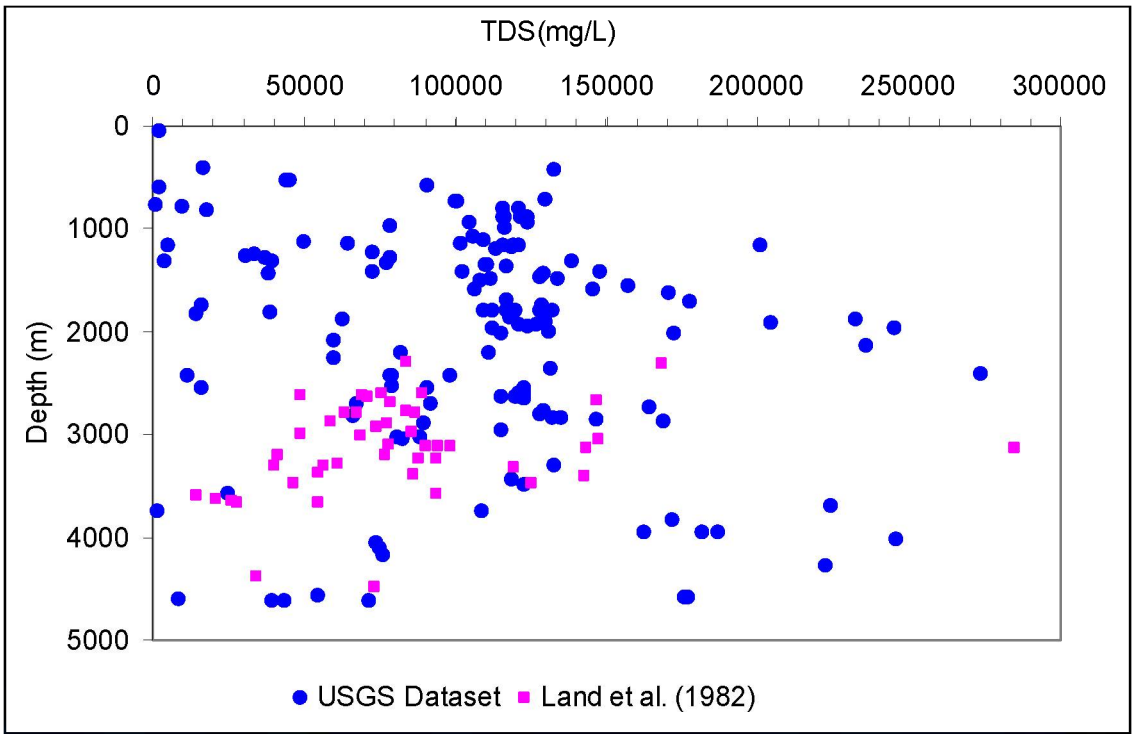

Figure 6.3: TDS versus depth (data sources: USGS produced water database (2002) and Land et al. (1988)).

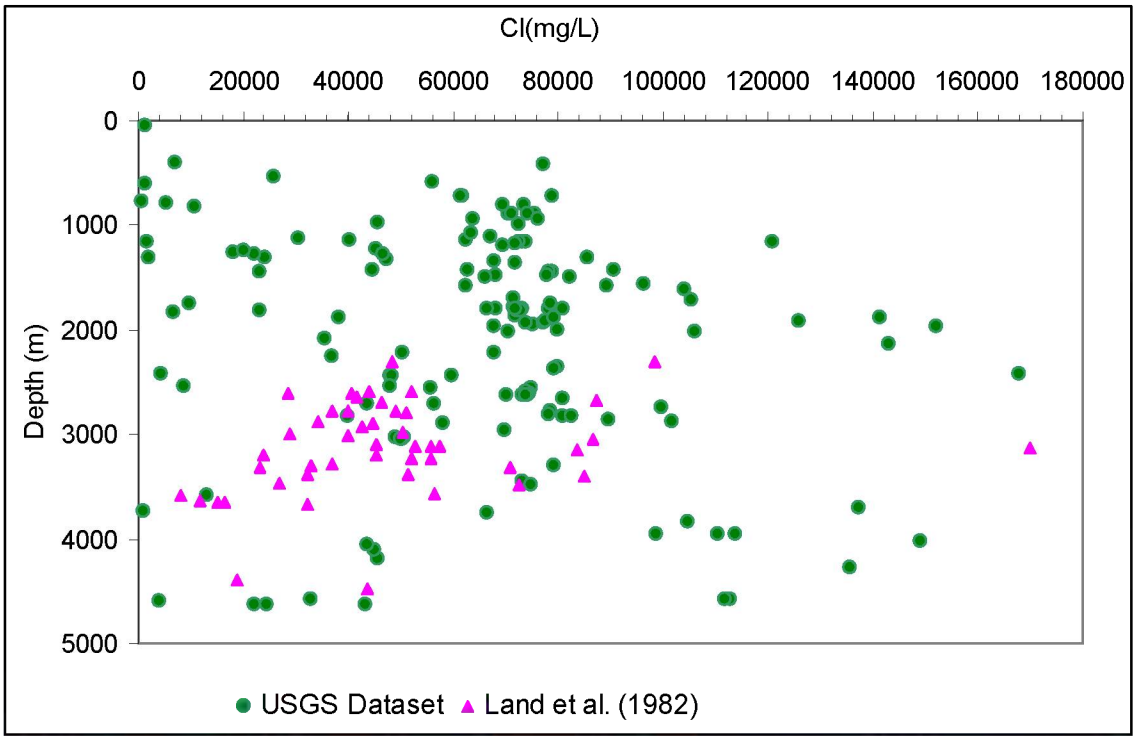

Figure 6.4: Concentration of Cl versus depth (data sources: USGS produced water database (2002) and Land et al. (1988)).

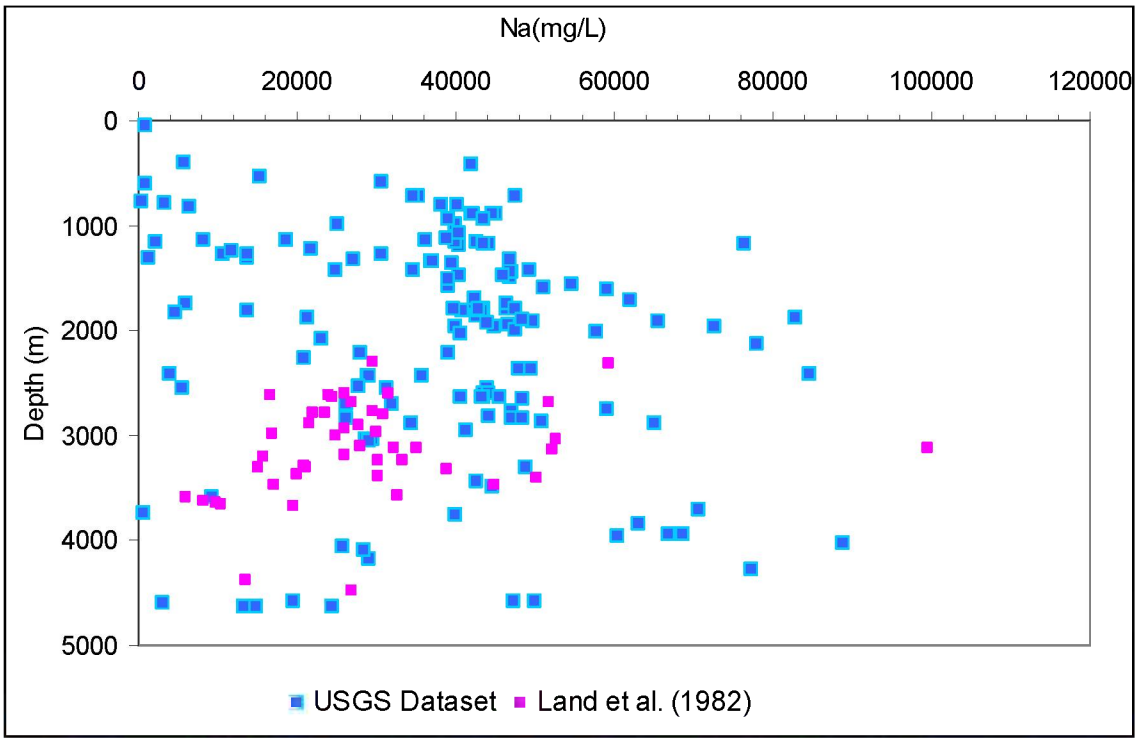

Figure 6.5: Concentration of Na versus depth (data sources: USGS produced water database (2002) and Land et al. (1988)).

Ca and Mg concentrations of most samples are less than 5000 mg/L (Figure 6.6). The average concentration of Ca+Mg is 3700 mg/L with a maximum value of 20,570 mg/L at depths of 1000 m to 3000 m.

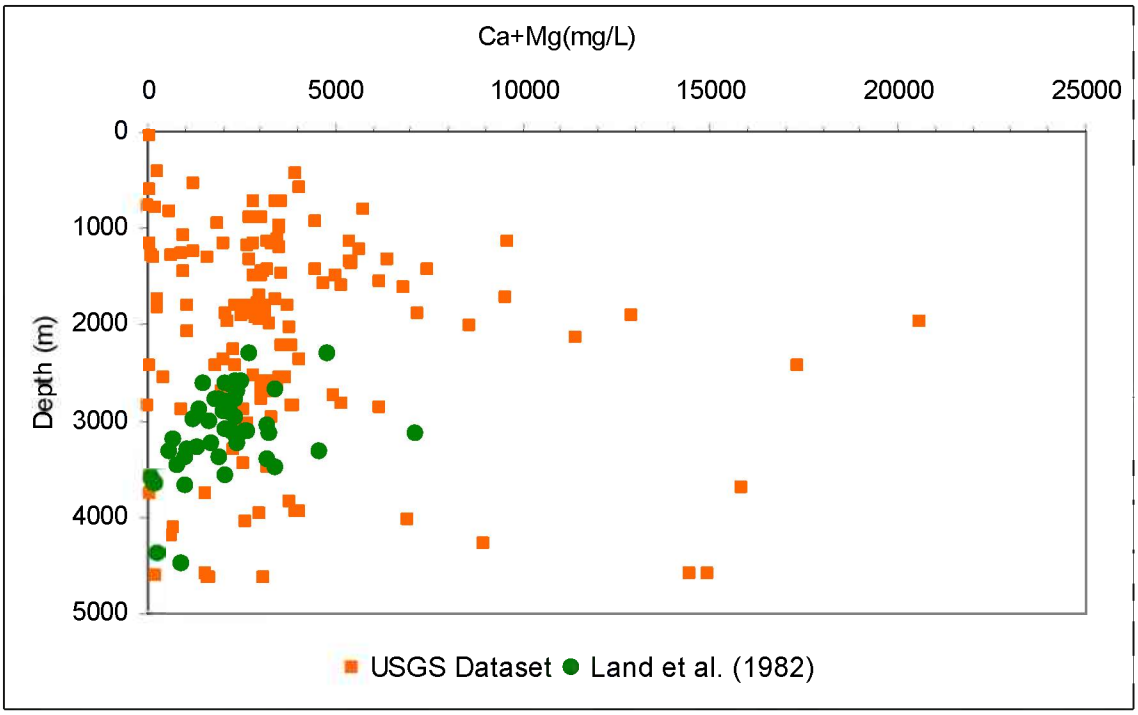

Figure 6.6: Concentration of Ca+Mg versus depth (data sources: USGS produced water database (2002) and Land et al. (1988)).

Brine Bicarbonate concentrations of most samples are less than 600 mg/L (Figure 6.7). At the depths of 1000 m to 3000 m, average bicarbonate concentration is 380 mg/L. Sulfate concentrations are shown in Figure 6.8 though it is less important for CO_2 dissolution in brine. The average value of sulfate at the depth from 1000 m to 3000 m is less than 70 mg/L.

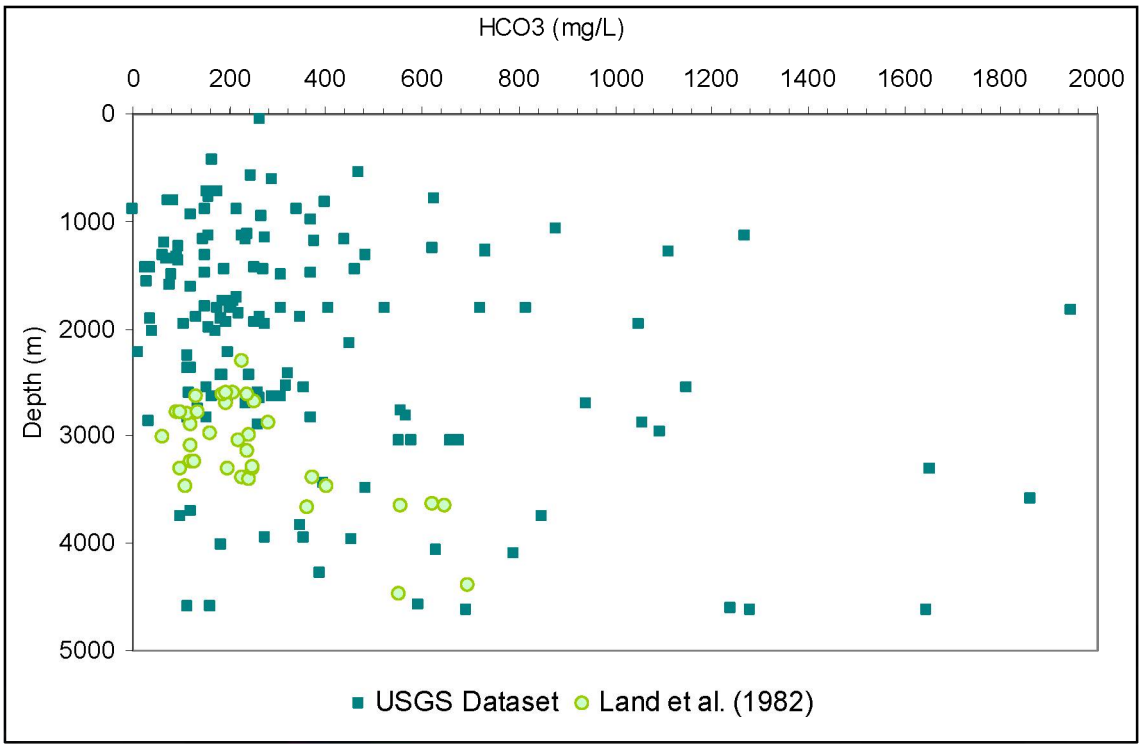

Figure 6.7: Concentration of HCO3- versus depth (data sources: USGS produced water database (2002) and Land et al. (1988)).

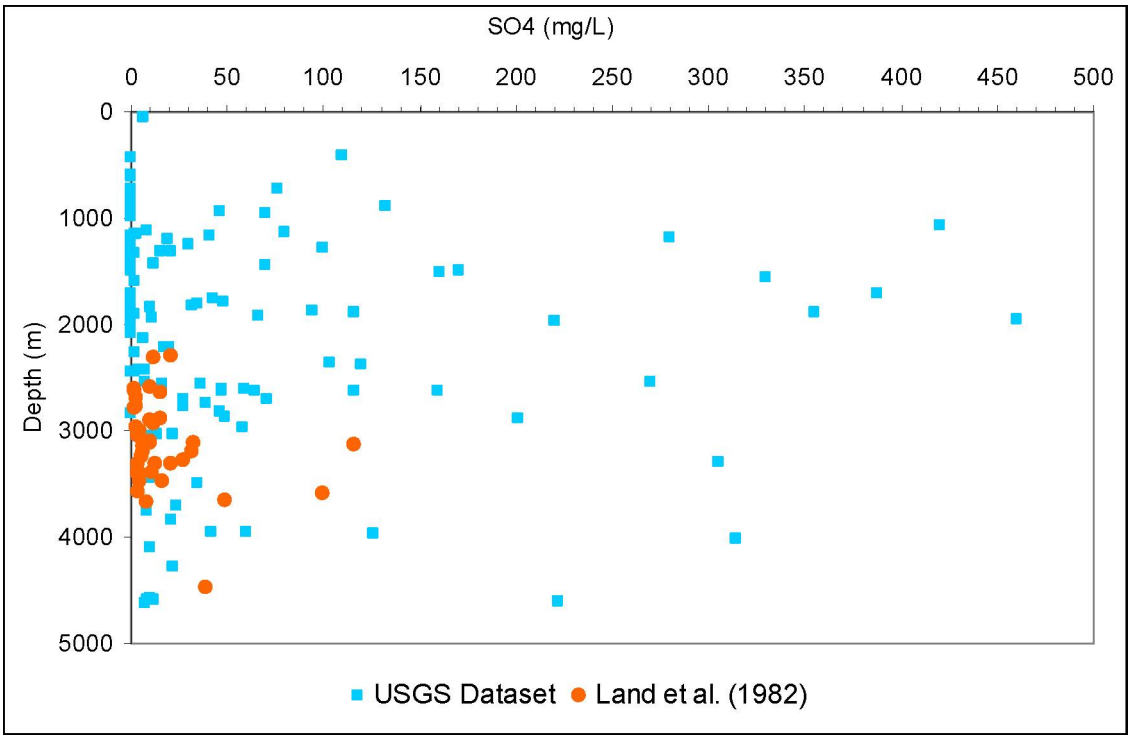

Figure 6.8: Concentration of SO4 versus depth (data sources: USGS produced water database (2002) and Land et al. (1988)).

Recommendation for synthetic brine composition

For the batch experiments, recommended TDS for synthetic brine samples is 4000 mg/L, 110,000 mg/L, 200,000 mg/L, and 300,000 mg/L. This range covers the possible TDS in Miocene formations at the expected depths of 1000 m to 3000 m.

P and T Data

Reservoir pressure for the Miocene units can vary widely with depth. Based on results of Tasks 2 and 3 pressure varies from 2215 psi to 11637 psi for the low Miocene and from 1296 psi to 16973 psi for the upper Miocene at the GOM. Therefore pressure from 2000 psi to 17000 psi was chosen for CO_2 solubility calculations.

Reservoir temperature also depends on depth and varies greatly in the Miocene age units of the GOM. Temperature ranges from 50.5 °C to 165 °C for lower Miocene and from 38 °C to 225 °C for upper Miocene based on the results of the Study's Tasks 2 and 3. Temperature from 40 °C to 230 °C was chosen for calculating CO_2 solubility.

Approach

The formulation of CO_2 solubility in brine derived by Duan et al. (2006) is used in this study since it has been used in other similar studies. The formulation is given as,

Equation 6.1-1

$$\begin{aligned}\ln m_{CO_2} &= \ln y_{CO_2}\phi_{CO_2}P - \mu^{l(0)}_{CO_2}/RT \\ &\quad -2\lambda_{CO2-Na}(m_{Na}+m_K+2m_{Ca}+2m_{Mg}) \\ &\quad -\xi_{CO2-Na-Cl}m_{Cl}(m_{Na}+m_K+m_{Mg}+m_{Ca}) \\ &\quad +0.07m_{SO4}\end{aligned}$$

where T is absolute temperature in Kelvin, P represents the total pressure of the system in bar, R is universal gas constant, m means the molality of components dissolved in water, yCO2 is the mole fraction of CO_2 in vapor phase, ϕCO_2 is the fugacity coefficient of CO_2, $\mu^{l(0)}_{CO_2}$ is the standard chemical potential of CO_2 in liquid phase, λ_{CO2-Na} is the interaction parameter between CO_2 and Na+, $\xi_{CO2-Na-Cl}$ is the interaction parameters between CO_2 and Na+, Cl^-. ϕ_{CO_2}, the CO_2 fugacity, in Equation 6.1-1, can be expressed as a function of temperature and pressure (Duan et al., 2006) Equation 6.1-1,

Equation 6.1-2

$$\begin{aligned}\phi_{CO2} &= c_1 + [c_2 + c_3T + c_4/T + c_5/(T-150)]P \\ &\quad + [c_6 + c_7T + c_8/T]P^2 \\ &\quad + [c_9 + c_{10}T + c_{11}/T]\ln P + [c_{12} + c_{13}T]/P \\ &\quad + c_{14}/T + c_{15}T^2\end{aligned}$$

Parameters used in Equation 6.1-2 are given in Table 6.1.1.

Table 6.1.1: The parameters of Eq. (2) (Duan et al., 2006).

Parameter	T-P range					
	1	2	3	4	5	6
c1	1.0000000E+00	-7.1734882E-01	-6.5129019E-02	5.0383896E+00	-1.6063152E+01	-1.5693490E-01
c2	4.7586835E-03	1.5985379E-04	-2.1429977E-04	-4.4257744E-03	-2.7057990E-03	4.4621407E-04
c3	-3.3569963E-06	-4.9286471E-07	-1.1444930E-06	0.0000000E+00	0.0000000E+00	-9.1080591E-07
c4	0.0000000E+00	0.0000000E+00	0.0000000E+00	1.9572733E+00	1.4119239E-01	0.0000000E+00
c5	-1.3179396E+00	0.0000000E+00	0.0000000E+00	0.0000000E+00	0.0000000E+00	0.0000000E+00
c6	-3.8389101E-06	-2.7855285E-07	-1.1558081E-07	2.4223436E-06	8.1132965E-07	1.0647399E-07
c7	0.0000000E+00	1.1877015E-09	1.1952370E-09	0.0000000E+00	0.0000000E+00	2.4273357E-10
c8	2.2815104E-03	0.0000000E+00	0.0000000E+00	-9.3796135E-04	-1.1453082E-04	0.0000000E+00
c9	0.0000000E+00	0.0000000E+00	0.0000000E+00	-1.5026030E+00	2.3895671E+00	3.5874255E-01
c10	0.0000000E+00	0.0000000E+00	0.0000000E+00	3.0272240E-03	5.0527457E-04	6.3319710E-05
c11	0.0000000E+00	0.0000000E+00	0.0000000E+00	-3.1377342E+01	-1.7763460E+01	-2.4989661E+02
c12	0.0000000E+00	-9.6539512E+01	-2.2134306E+02	-1.2847063E+01	9.8592232E+02	0.0000000E+00
c13	0.0000000E+00	4.4774938E-01	0.0000000E+00	0.0000000E+00	0.0000000E+00	0.0000000E+00
c14	0.0000000E+00	1.0181078E+02	7.1820393E+01	0.0000000E+00	0.0000000E+00	8.8876800E+02
c15	0.0000000E+00	5.3783879E-06	6.6089246E-06	-1.5056648E-05	-5.4965256E-07	-6.6348003E-07

Note: 1: 273 K<T<b573 K, P<P_1 (when T <305 K, P_1 equals the saturation pressure of CO_2; when 305 K<T<405 K, P1=75+(T-305)×1.25; when T >405 K, P1=200 bar.); 2: 273 K<T<340 K, P1<P<1000 bar; 3: 273 K<T <340 K, P>1000 bar; 4: 340 K<T<435 K, P1<P <1000 bar; 5: 340 K<T <435 K, P >1000 bar; and 6: T>435 K, P>P1.

Note that this method can be used to calculate CO_2 solubility in pure water and also in aqueous NaCl solution. However, this method is valid for the T-P-salinity range of 273-533 K, 0-2000 bar, 0-4.5 m NaCl. Units of pressure, temperature, and salinity for calculating CO_2 solubility in Equation 6.1-2 are bar, Kelvin (K) and molality. In the following calculation, we convert from psi (pressure) and Celsius degree (temperature) to bar and Kelvin (K), respectively, according to the following equations:

$$P(bar) = 0.0689475729 \times \mathrm{P\ (psi)}$$

$$\mathrm{T(K)} = \mathrm{T(^{\circ}C)}+273.15$$

However, converting total dissolved solid (mg/L) is based on assumptions: 1) brine salinity can be represented by NaCl; and 2) density of brine is assumed to be 1 g/cm^3.

Based on the brine data of GOM Miocene formations, Cl concentrations show a perfect linear trend with TDS of brines (Figure 6.9) which can be expressed as

$$y = 1.6404\,x$$

where x is Cl concentration and y is the TDS of brines. The R-square value approximates to 0.9983. The following equation is used to convert TDS (mg/L) to molality (mol/Kg of water)

$$molality(mol/Kg\ of\ water) = \frac{TDS(mg/L) \times 0.001}{1.6404 \times 35.4532 \times \rho}$$

where brine density, ρ is assumed to be 1 g/cm^3.

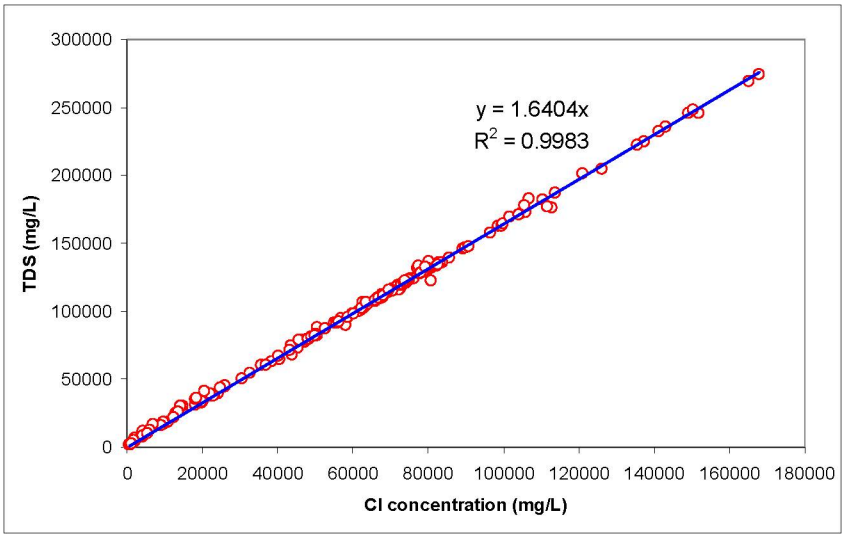

Figure 6.9: TDS versus Cl concentrations for GOM brine samples taken from the Miocene age formations.

Results

CO_2 solubility in brines from GOM Miocene age formations was calculated for temperature from 40 °C to 230 °C, pressure from 2000 psi to 17000 psi, and salinity, in terms of TDS ranging from 4000 gm/L to 250,000 mg/L and is shown in Figure 6.10 to Figure 6.17. CO_2 solubility in brine depends on pressure, temperature, and salinity. The

higher the pressure, the greater the CO_2 solubility. CO_2 solubility decreases slightly and then increases with temperature. The higher the salinity, in terms of TDS, the lower CO_2 solubility is. CO_2 solubility calculated can vary from 0.07 mol/Kg to 5.8 mol/Kg of water for the ranges of T-P-Salinity for the Miocene formation brines at the GOM.

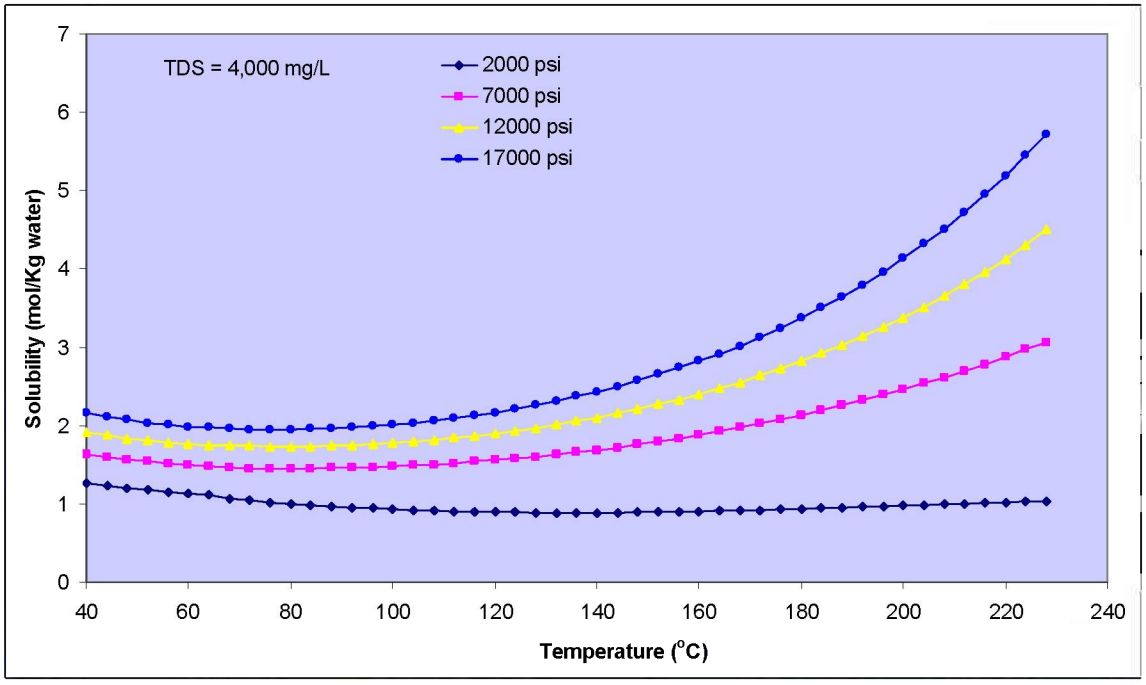

Figure 6.10: CO2 solubility versus temperature at pressures of 2000 psi, 7000 psi, 12000 psi, and 17000 psi (TDS=4000 mg/L).

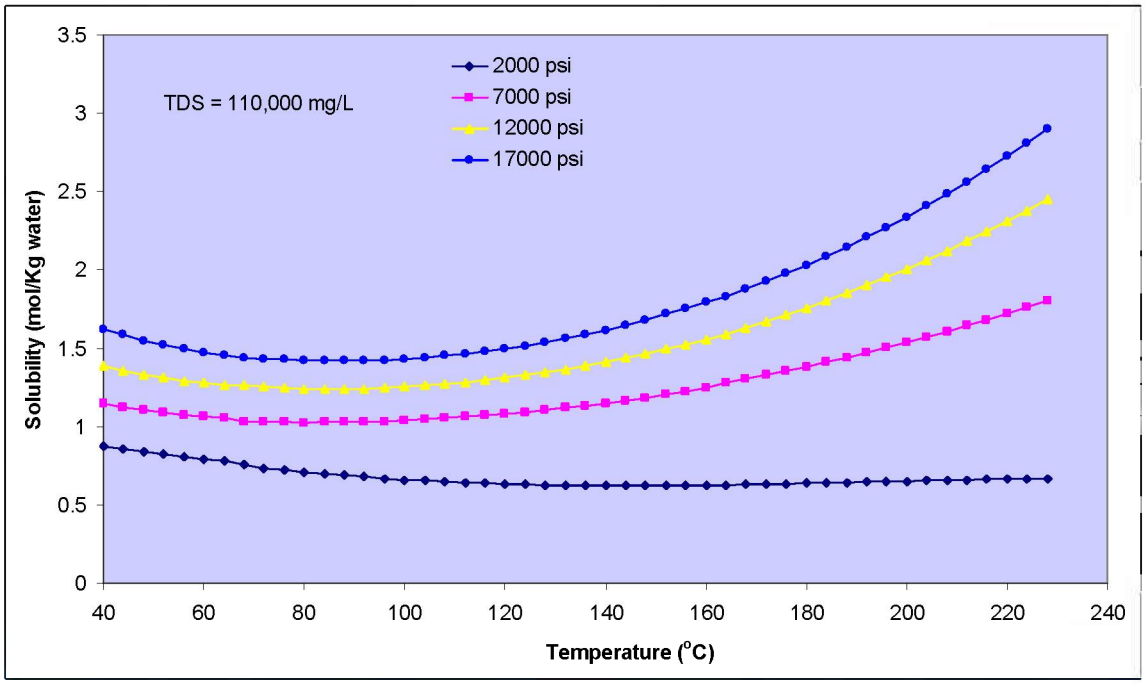

Figure 6.11: CO2 solubility versus temperature at pressures of 2000 psi, 7000 psi, 12000 psi, and 17000 psi (TDS=110,000 mg/L).

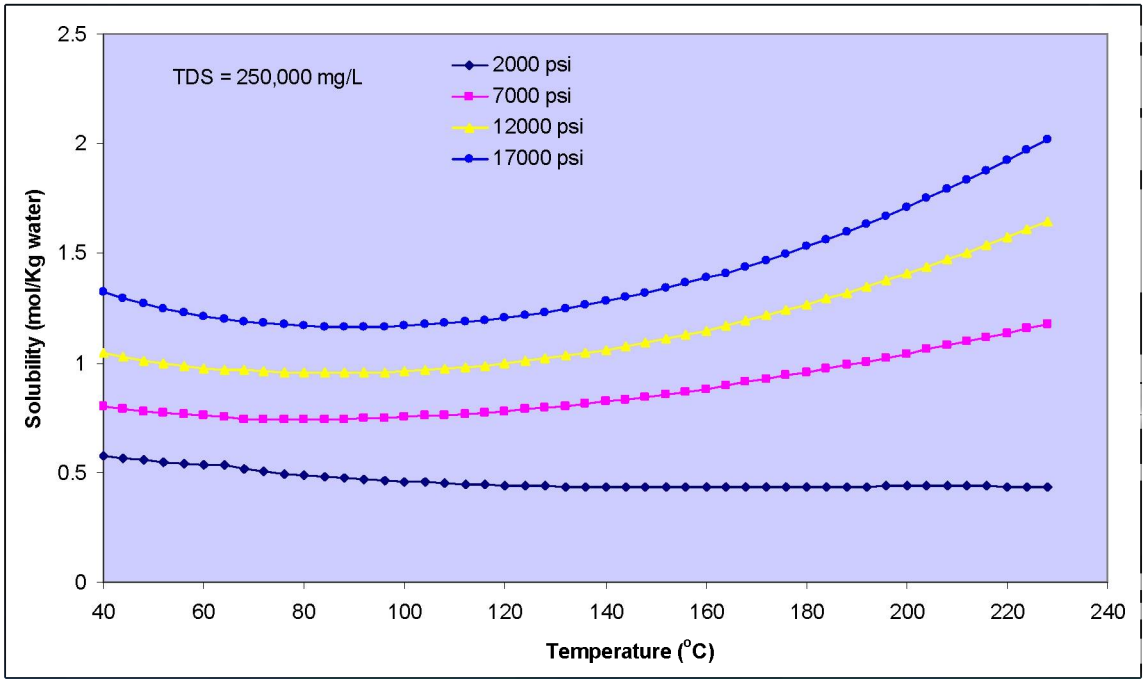

Figure 6.12: CO2 solubility versus temperature at pressures of 2000 psi, 7000 psi, 12000 psi, and 17000 psi (TDS=250,000 mg/L).

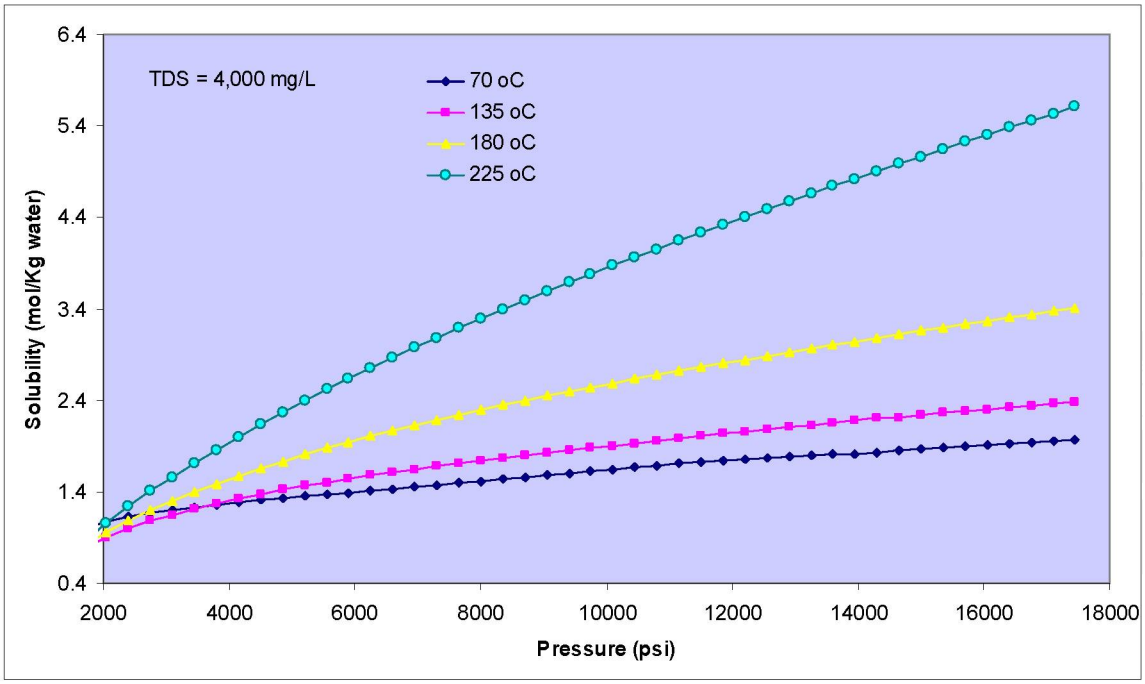

Figure 6.13: CO2 solubility versus pressure at temperatures of 70 oC, 135 oC, 180 oC, and 225 oC (TDS=4000 mg/L).

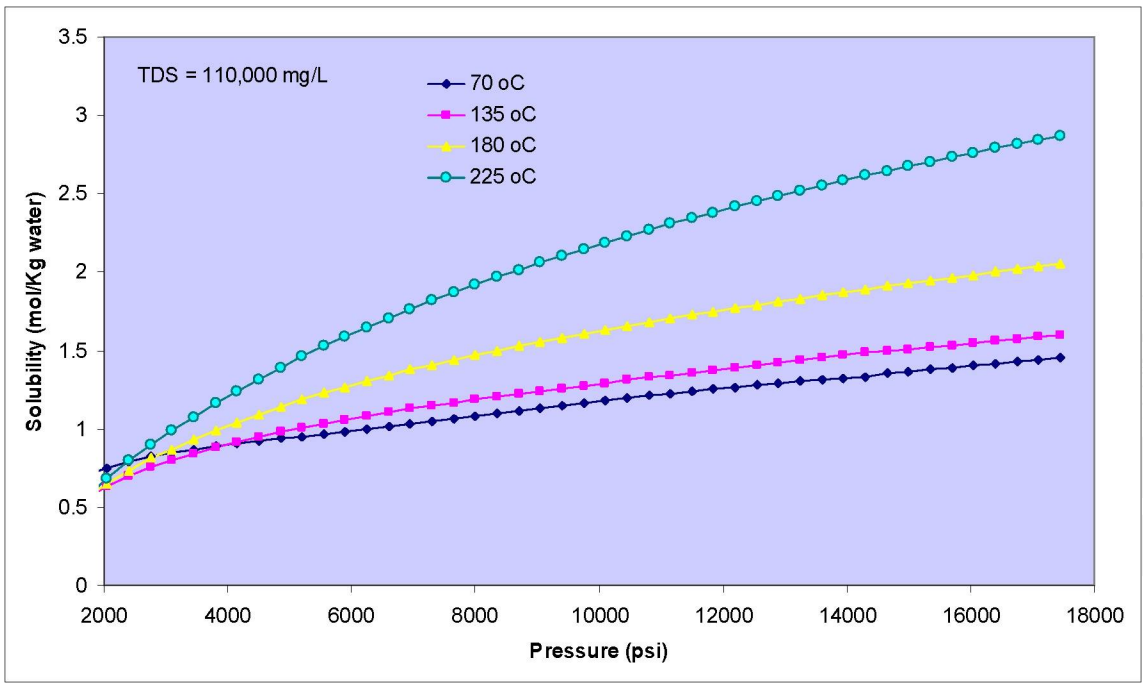

Figure 6.14: CO2 solubility versus pressure at temperatures of 70 oC, 135 oC, 180 oC, and 225 oC (TDS=110,000 mg/L).

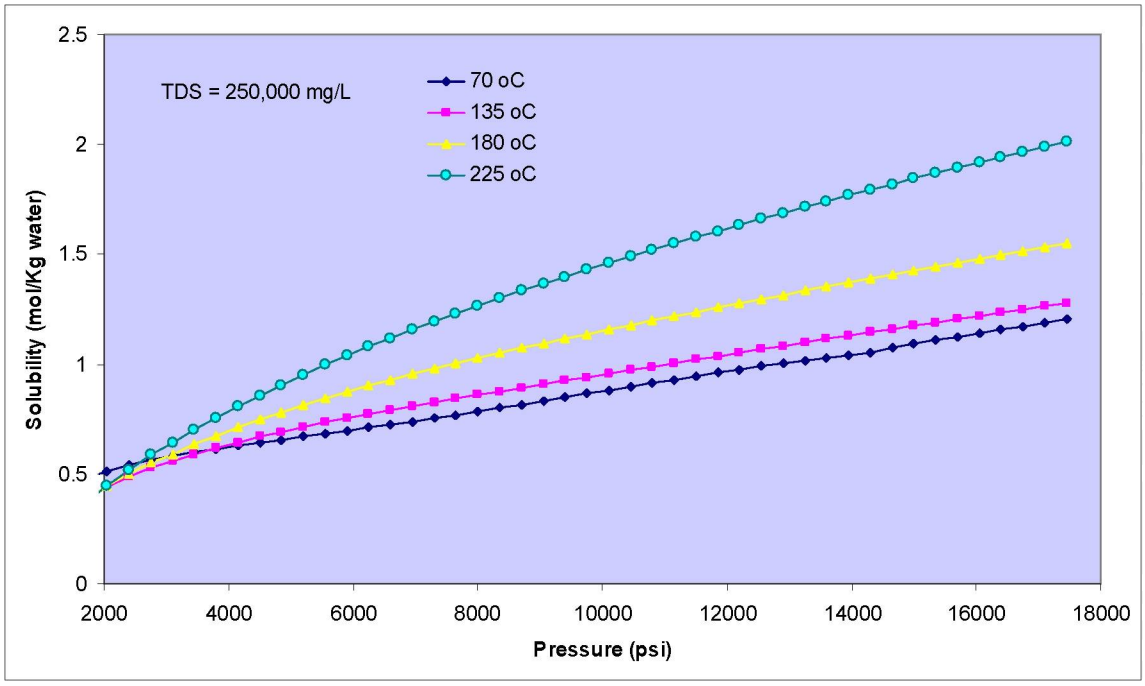

Figure 6.15: CO2 solubility versus pressure at temperature of 70 oC, 135 oC, 180 oC, and 225 oC (TDS=250,000 mg/L).

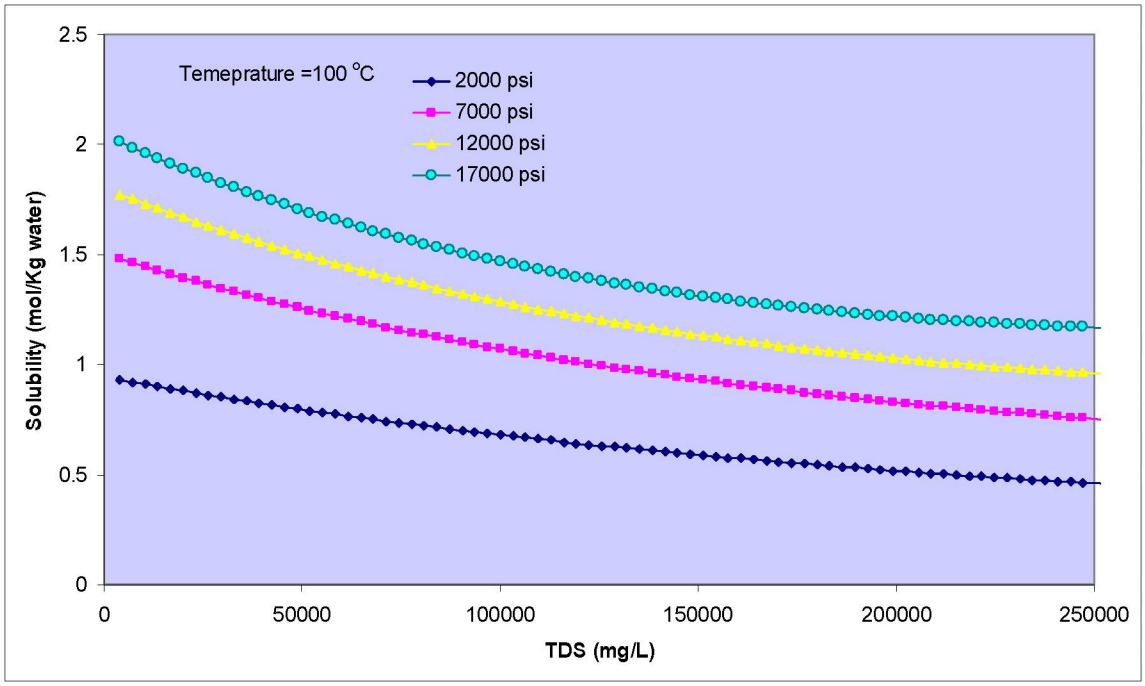

Figure 6.16: CO2 solubility versus salinity at pressures of 2000 psi, 7000 psi, 12000 psi, and 17000 psi (Temperature =100 oC).

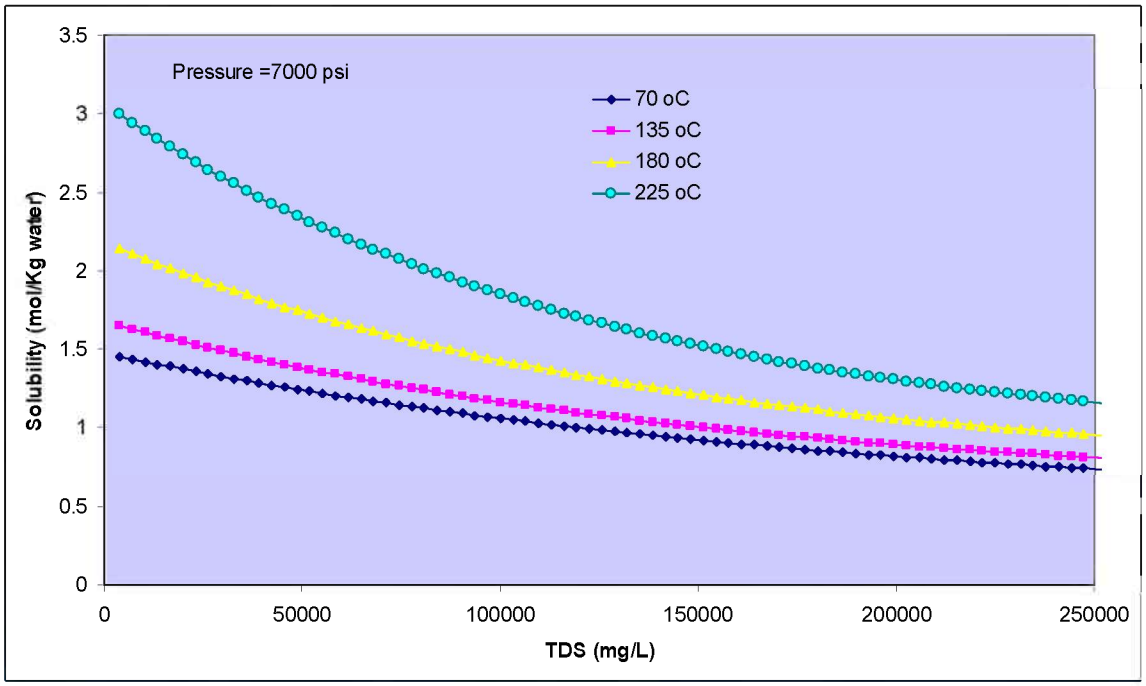

Figure 6.17: CO2 solubility versus salinity at temperatures of 70 oC, 135 oC, 180 oC, and 225 oC (Pressure = 7000 psi).

CO_2 Solubility Measurement at High Pressure and Temperature Conditions

A large degassing glass apparatus for measuring gas dissolved in brine during high pressure-temperature reaction was manufactured by the glass shop of the Chemistry Department of The University of Texas at Austin. As shown in **Error! Not a valid bookmark self-reference.**, it has been connected with vacuum line, liquid sample container, pressure gauge, gas sample container, water bath circulator, and drainage valve. Total volume of the degassing glass apparatus is 931.4ml, including a 924ml glass body and 7.4ml connection joints. The volume was determined by filling a known volume of de-ionized water into the apparatus.

Figure 6.18: Photo of degassing glass apparatus in BEG gas geochemistry laboratory.

Two sets of experiments were conducted in order to evaluate the suitable conditions for CO_2 solubility measurement by means of integrating the high temperature and pressure apparatus, liquid sampling container and degassing glass apparatus.

CO_2 solubility measurement in de-ionized water at 3000 psia and 35°C

Identification of the equilibration time for CO_2 dissolution using pressure profilse

Figure 6.19 shows the CO_2 pressure profile in the high P/T reactor during the course of reaction of CO_2 with water. The profile shows pressure variations during charging of the reactor with CO_2 using a CO_2 pump and also shows pressure drops caused when water and dissolved gas were released into the liquid sampling container. One of the key experimental elements was to quantify CO_2 dissolution by monitoring gas pressure change during the course of CO_2 dissolution into deionized water. The second element was to determine if liquid sampling reaches completion and is representative of conditions in the reactor. The top portion of Figure 6.19 shows the pressure profile during charging of the reactor to 3900 psi and pressure loss upon dissolution of CO_2 into water. The first part of the graph represents initial charging of the reactor with subsequent pump shutdown and CO_2 dissolution into deionized water due to stirring. This was a "static mode" without constant supply of CO_2 which necessitated a relatively long time to reach the equilibrium of CO_2 dissolution. We also applied the "dynamic mode" (lower portion of Figure 6.19) in which a constant CO_2 supply to the reactor was maintained with a CO_2 pump during the course of CO_2 dissolution. It was found that the

dynamic mode took a relatively short time to reach equilibrium of CO_2 dissolution. We recommend that the static mode be used at the beginning of experimental runs, and the dynamic mode can be applied to maintain CO_2 at a designated pressure after the first liquid sampling is completed. This technique allows multiple sampling events over the course of a reaction without the need for setting up new experiments for each measurement.

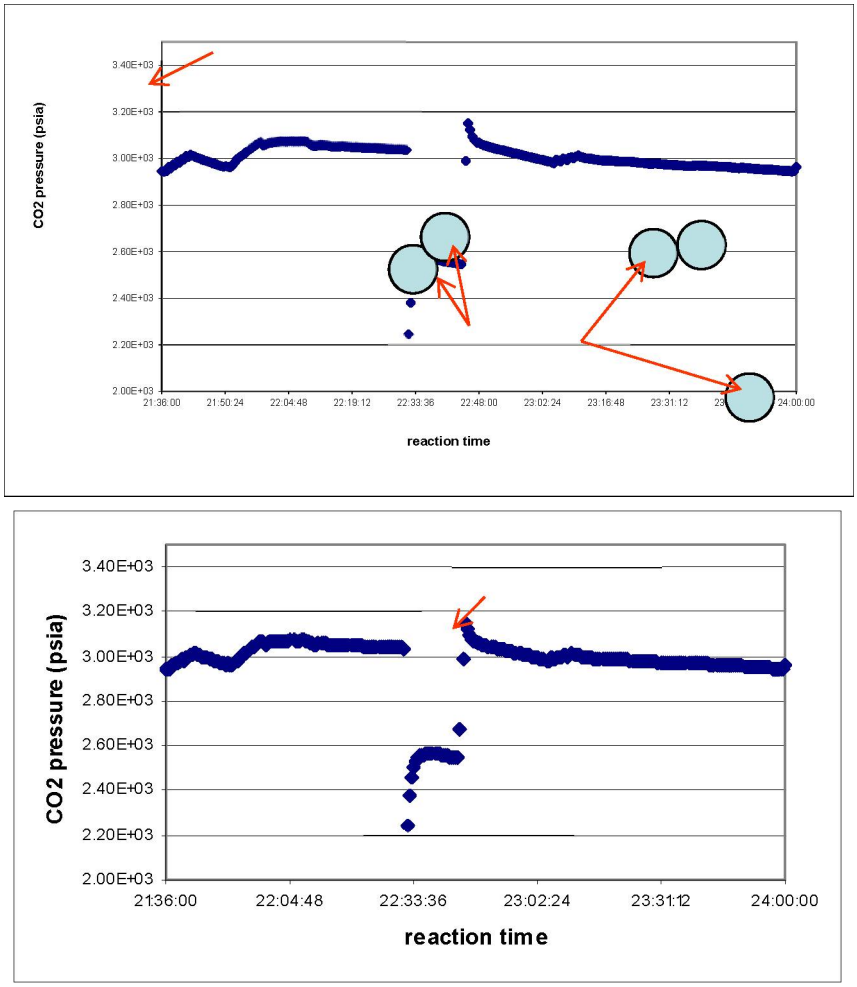

Figure 6.19: Change of CO2 pressure in the reactor over the course of CO2 dissolution and sampling.

Determine equilibration of liquid sample container through pressure profile

Figure 6.19 (bottom portion) zooms in on the pressure change in the reactor before and after taking the first liquid sample. The sampling lines connecting the reactor and the liquid container are evacuated before opening the valve between the reactor and the lines during sampling. During liquid sampling, the gas pressure in the reactor drops when the sampling lines are opened to the sampling container. When in dynamic mode, the CO_2 pump responds to the pressure drop during sampling and automatically recharges the reactor to the designated reaction pressure. Duplicate liquid samples may be taken over time for degassing measurements.

CO_2 solubility measurement through degassing samples of reacted fluids

Table 6.1.2 shows the preliminary results of the measured dissolved CO_2 amount at a total pressure of 3000 psia and 35°C. In the table, ΔP is the measured pressure difference in the gas extraction apparatus before and after degassing of CO_2 dissolved in deionized water. The term ΔW represents the measured weight of sampled fluids, which is calculated by subtracting the measured weight of the empty liquid sampling cell from that of the full liquid sampling cell after sampling. It is assumed that the reacted liquid sample totally degasses in the extraction apparatus and that the change of ΔP is entirely attributed to dissolved CO_2. Under this assumption, an extremely high CO_2 solubility measurement was obtained for sample 5 which corresponds to a relatively low CO_2 pressure of around 1.0 bar in the reactor (highlighted green in Table 6.1.2).

Table 6.1.2: Measured CO2 solubility at PCO2 = 3000psi and 35°C.

Sample ID	Reactor condition		Degassing apparatus condition				CO_2 solubility (mole CO_2/L H_2O)	
	P_{CO2} (bar)	T (°C)	ΔP (psi)	T (K)	ΔW (g)	ΔV (ml)	w/o H2O correction	w/ H2O correction
(1)	210.54	35	1.37	297.7	2.32	1.85	1.545	1.094
(2)	207.89	35	1.33	297.7	2.33	1.8	1.500	1.049
(3)	206.99	35	1.42	296.7	2.31	1.8	1.607	1.154
(4)	204.68	35	1.32	297.9	2.32	1.8	1.488	1.037
(5)	0.99	35	0.47	298.2	1.76	1.3	0.529	0.078

We collected the degassed gas of sample (5) and conducted a gas compositional analysis using the gas chromatograph (GC). Gas compositional analysis showed that CO_2 is about 14.8%, air (N_2+O_2) 0.3%. The total detected gas molar volume percent was only about 15% percent. The rest (~85%) should be water vapor, which cannot be detected with our GC configuration. Given that the total degassed pressure is 0.47psi, CO_2 partial pressure in the total degassed gas is about 0.07psi, and water vapor pressure is estimated to be 0.40 psi under the vacuum degassing apparatus configuration. The difference in the measured solubility of CO_2 in deionized water with and without the correction of water vapor pressure is significantly large (Table 6.1.2). Therefore we modified our system to minimize the contribution of water vapor pressure and accurately determine CO_2 partial pressure in the degassed gas with GC.

Helium experiment to quantify the contribution of water vapor to ΔP

Instead to loading CO_2 in the reactor, high pressure helium gas was loaded to quantify the contribution of water vapor to **ΔP.** Helium should experience only slight dissolution compared to CO_2. Table 6.1.3 summarizes our results.

Table 6.1.3: Dissolved helium measurement in deionized water at 35°C.

Sample ID	Reactor condition		Degassing apparatus condition				He solubility (mole He/L H_2O)	
	P_{He} (bar)	T (°C)	ΔP (psi)	T (K)	ΔW (g)	ΔV (ml)	w/o H2O correction	w/ H2O correction
(1)	146.57	35	0.41	295.6	2.3	1.85	5.12	0.123
(2)	133.95	35	0.45	297.4	2.3	1.85	5.59	0.621
(3)	127.05	35	0.59	297.6	11.5	10.1	1.46	0.472
(4)	113.95	35	0.56	297.5	11.5	10.8	1.39	0.397

There is a large variation in the measured helium solubility after a correction is made for water vapor assuming a constant vapor pressure of 0.4 psi for each run. This suggests the water vapor pressure might vary for each run. Therefore, we collected gas samples (1 to 4 in Table 6.1.4) to determine variations in water vapor contribution.

Table 6.1.4: GC analysis result for degassed samples in Table 6.1.3.

Sample ID	He(%)	Air(%)	Calculated H_2O vapor(%)
1	16.8	24.8	58.4
2	10.4	23.8	65.8
3	48.8	12.7	38.5
4	44.3	6.6	49.1

Based on the measured partial pressure of helium in the gas liberated from the reacted fluid, we calculated the helium solubility in deionized water at high pressure. The helium solubility ranges from 0.58 to 0.86 mole helium/liter of H_2O. It gives a reasonably consistent measurement over four runs.

1. Laboratory Experiments Data Analysis

CO_2 solubility obtained from experimental results of the current study were originally reported as molarity (moles of CO2 per liter of solution) while most CO_2 solubility data in the literature are reported in molality (moles of CO_2 per Kg of H_2O). In order to compare

the solubility data obtained in this study with that reported in the literature, solubility data in our study were converted to molality. In the following plots, the unit of CO_2 solubility is reported in molar fraction.

More data were collected from the literature and are shown in Figure 6.20-Figure 6.22. In the literature CO_2 solubility data in brines with salinities of 1.88 M and 3.4 M are very rare. Consequently, data from the literature for CO_2 solubility in brines with salinities of 1 M and 3 M are shown in Figure 6.21. Data from the literature for CO_2 solubility in brines with salinities of 3 M and 5 M are shown in Figure 6.22. The experimental results are also compared with two models in Figure 6.20-Figure 6.22. The experimental results of the current study are fairly comparable with the literature data and the model results.

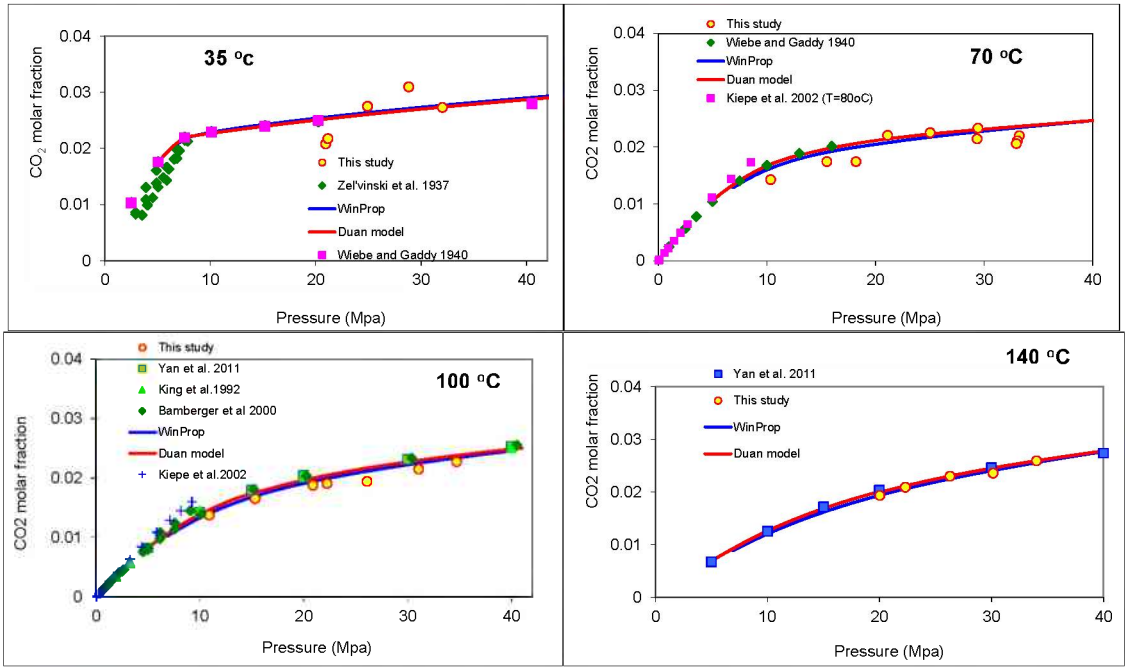

Figure 6.20: Comparison of CO2 solubility (in pure water) between experimental results obtained in this study and model results from other studies (published literature).

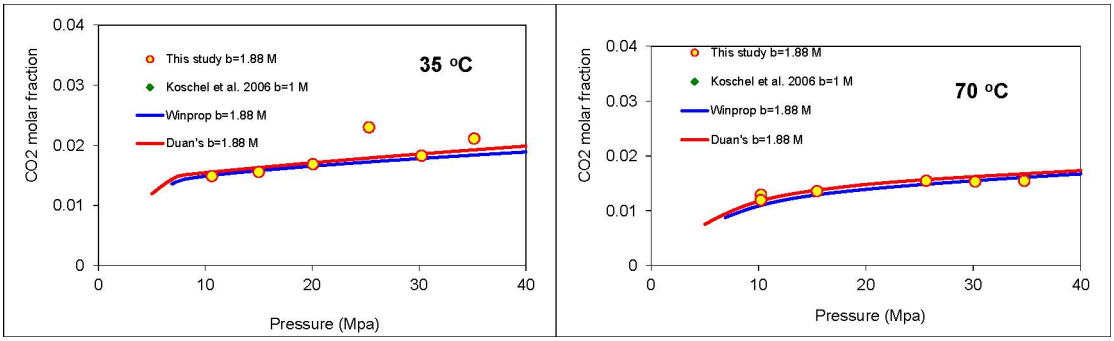

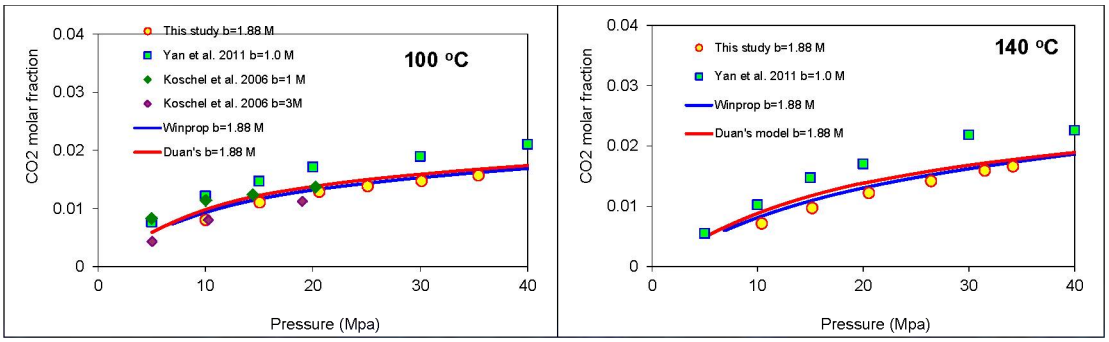

Figure 6.21: Comparison of CO2 solubility (in brine with salinity of 1.88 M) between experimental results obtained in this study and model results from other studies (published literature).

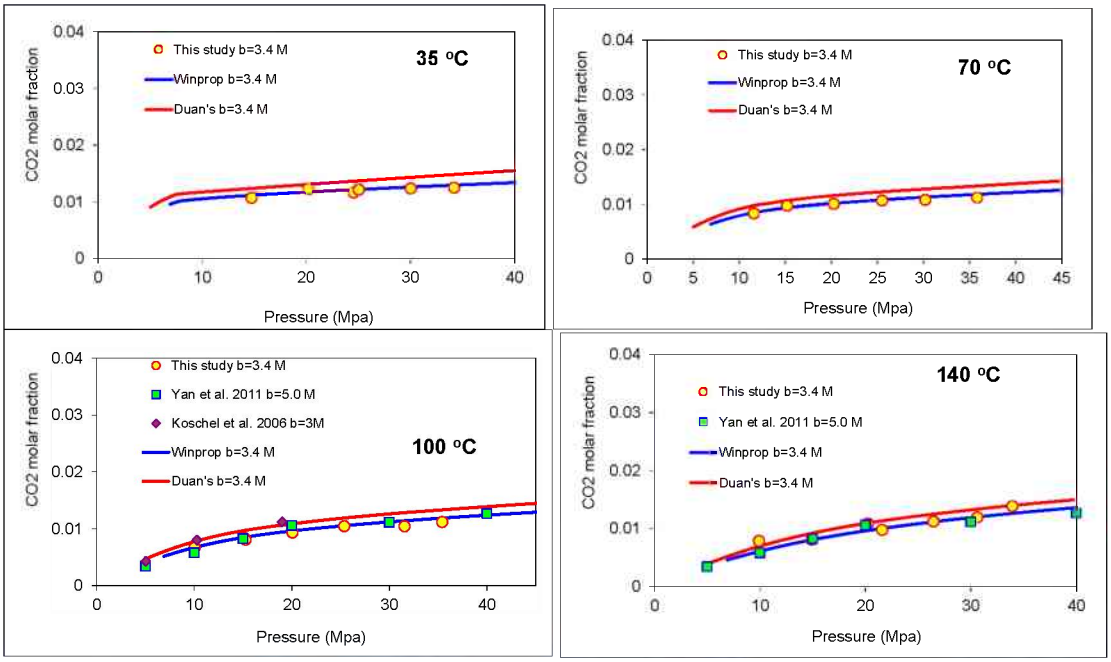

Figure 6.22: Comparison of CO2 solubility (in brine with salinity of 3.4 M) between experimental results obtained in this study and model results from other studies (published literature).

2. Brine Containment Estimate

In order to estimate the brine containment (theoretical storage in brine) in the study area, the method for calculating CO_2 storage of solubility trapping in brine proposed in (Bachu, 2007; Bachu and Adams, 2003; Bachu et al., 2003) was used. In the following, the method and results of brine containment in the study area are briefly described.

At the basin- and regional-scale, the theoretical CO_2 storage in solution can be estimated using the relation

$$M_{CO2t} = \iiint \emptyset\left(\rho_s X_s^{CO2} - \rho_0 X_0^{CO2}\right) dxdydz$$

Where ϕ is the porosity, ρ the density of brine, X^{CO2} the CO_2 solubility (mass fraction) and the subscripts 0 and s are for initial carbon content in brine before injected CO_2 dissolve in brine and carbon dioxide content at saturation, respectively.

The theoretical storage estimated for an entire aquifer is unrealistic, because it assumes that all the brine in the pore space of the entire study area can be accessed by and saturated with CO_2. Therefore, effective storage, M_{CO2e}, needs to be determined by multiplying a storage coefficient, C (Bachu et al., 2007).

$$M_{CO2e} = C \times M_{CO2t}$$

The storage coefficient, C, includes the effects of all factors that may affect the migration and dissolution of CO_2 in the study area. There is little information on what values the storage coefficient should be. Consequently, the effective storage in the study area was calculate for two values of C, 0.04 and 0.02 which are based on the results presented by Gorecki et al. (2009).

In the current study, the reservoir rock of Miocene age in the lithologic section was discretized into 14456 rectangular prisms (1 mile X 1 mile X height) (Figure 6.23). The area of interest (study area) is the identical that, which was analyzed for CO_2 capacity in Figure 3.3. Note that the height of each rectangular prism representing the thickness of Miocene sand varies spatially (Figure 6.24-A). Spatial distribution of porosity is shown in Figure 6.24-B.

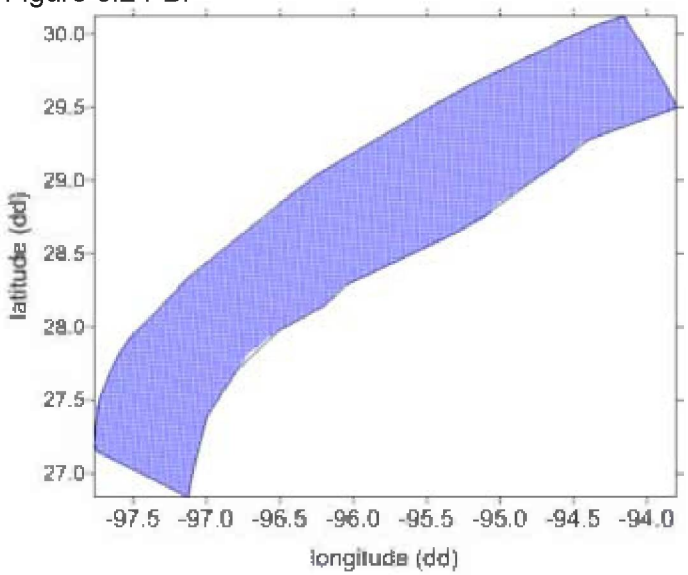

Figure 6.23: Grid (1 mile x 1 mile) of the study area (along the Texas coastal zone) used to calculate theoretical CO2 dissolution into brine (a.k.a. brine containment) in Miocene age rocks of the study area.

A.

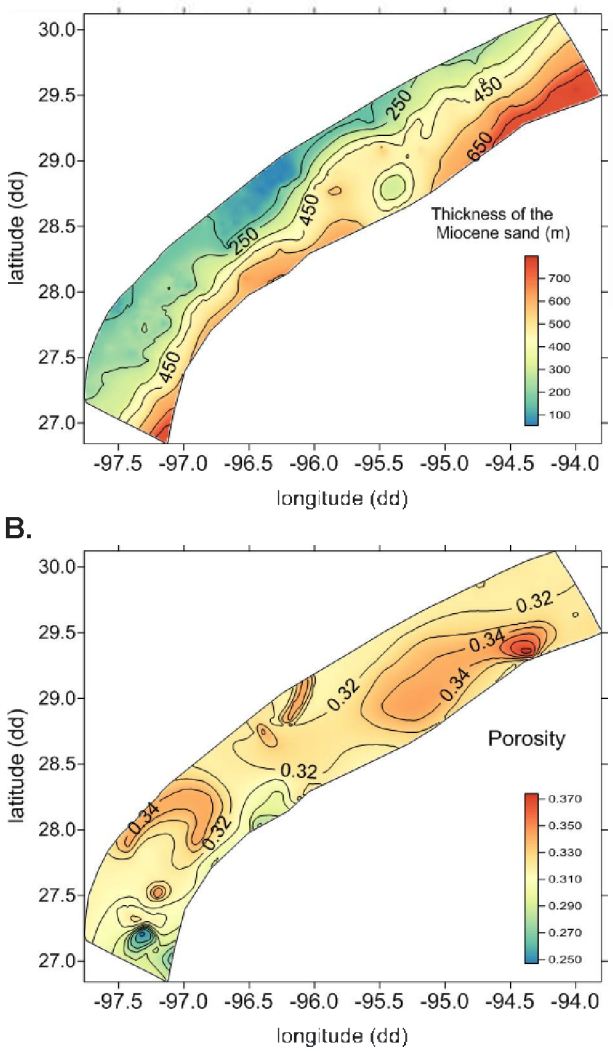

Figure 6.24: Spatial distributions in the study area (along the Texas coastal zone) of thickness of (A) Miocene net reservoir sand and (B) porosity of the study area.

Because brine density after saturation with injected CO_2 (ρ_s) and CO_2 solubility, X_S^{CO2}, is a function of pressure, temperature and salinity, it can be calculated using the models which were calibrated with laboratory experimental results in the current study (see Figure 6.20, Figure 6.21, Figure 6.22). Pressure and temperature at the depth mid-point of each rectangular prism were used to calculate brine density and CO_2 solubility (Figure 6.25 A & B, respectively). Brine salinity also shows spatial variability. However, there is not enough data in the study area to interpolate salinity data at each rectangular prism. Therefore, an average brine salinity value, 1.88 M, was assumed for all rectangular prisms in the study area. Figure 6.26 A & B, respectively, show spatial distributions of CO_2 saturated brine density and CO_2 solubility calculated from the model presented in Bachu et al. (2003). Brine density (ρ_0) was also estimated using different pressure and temperature by assuming a 1) brine salinity of 1.88 M; and 2) not considering CO_2 mass. The model of density of fresh and saline water presented by Batzle and Wang (1992) was used.

A.

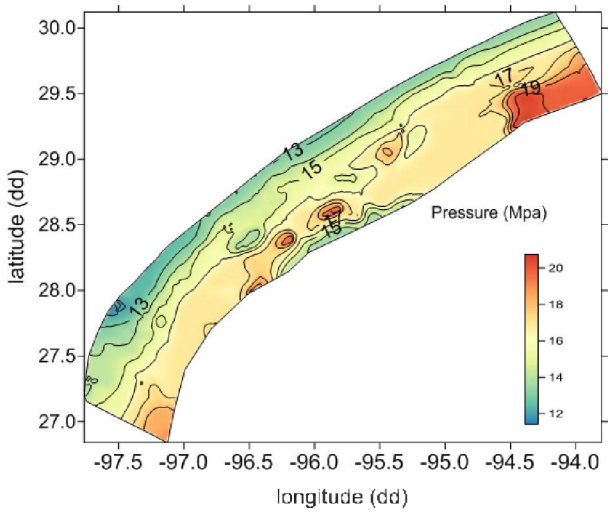

B.

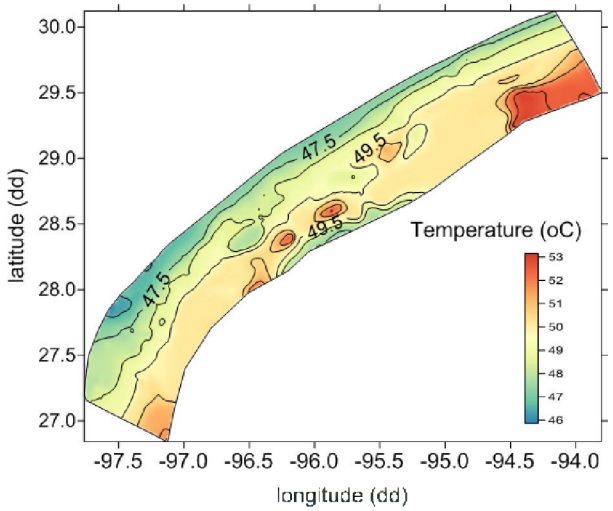

Figure 6.25: Contour maps in the study area (along the Texas coastal zone) of spatial distribution of (A) calculated pressure and (B) temperature at the depth of mid-point of each rectangular prism in the study area.

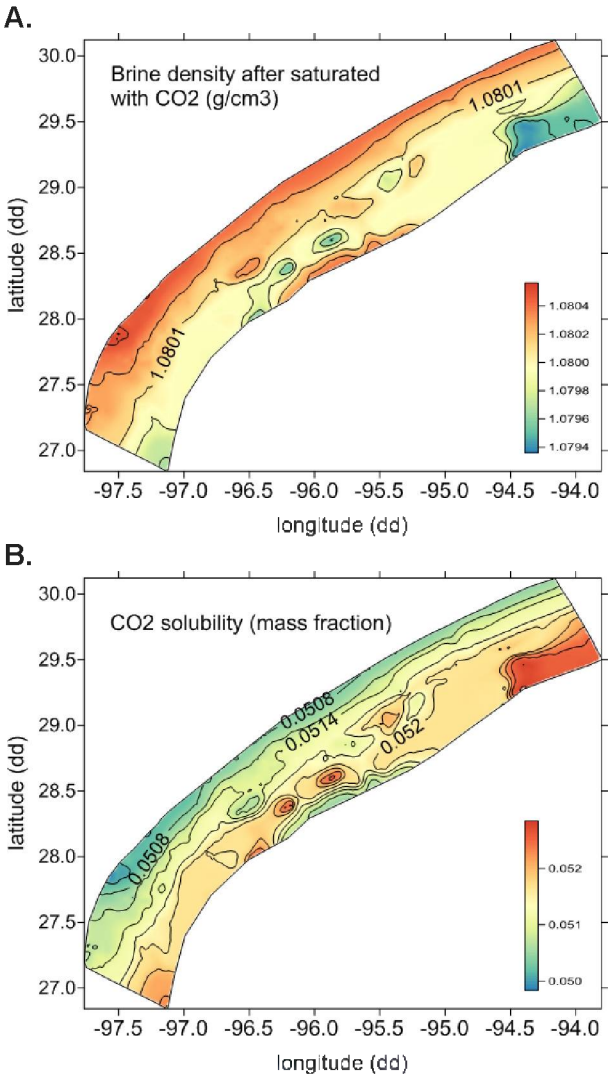

Figure 6.26: Contour maps in the study area (along the Texas coastal zone) of (A) spatial distributions of CO2 - saturated brine density and (B) CO2 solubility in the study area.

An average concentration of HCO_3 measured in brine samples was used to estimate initial CO_2 content, X_0^{CO2}. Spatial distributions of brine density and initial CO_2 content in brine before CO_2 injection are shown in Figure 6.27 A and B, respectively.

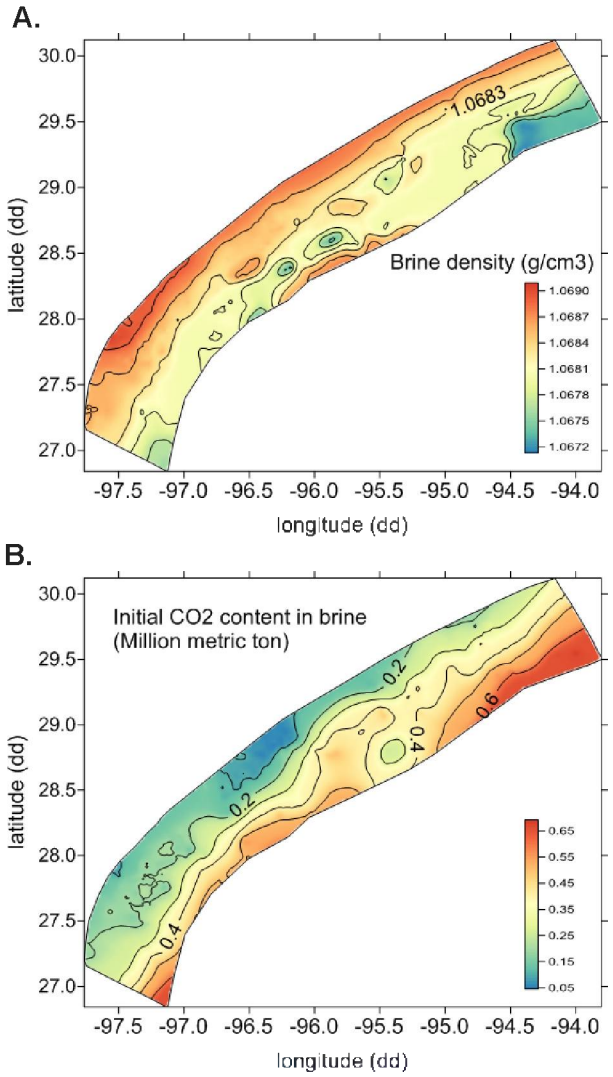

Figure 6.27: Maps of the study area (along the Texas coastal zone) of spatial distributions of (A) brine density before contact with injected CO2 and (B) initial CO2 content in brine.

The map in Figure 6.28 illustrates the calculated CO_2 dissolution storage in the Miocene age reservoir section of the study area, and Figure 6.29 shows spatial distributions of *effective* CO_2 dissolution storage using two different coefficients, C=0.04 and 0.02 based on the results presented by Gorecki et al.(2009).

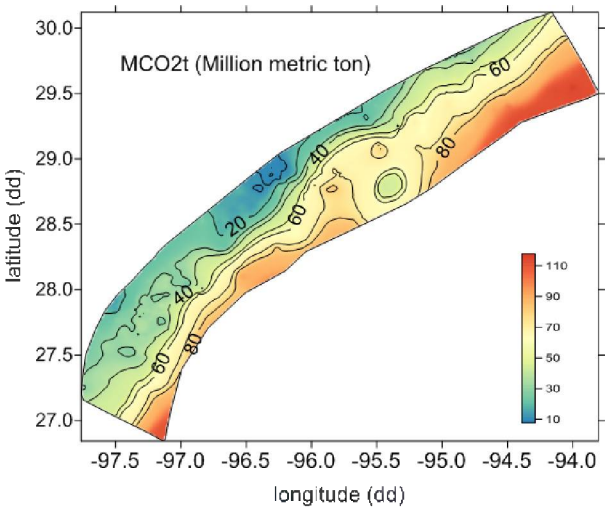

Figure 6.28: Contour map of the spatial distribution of theoretical CO2 dissolution storage in brine. The map is located on the Texas coastal zone.

A.

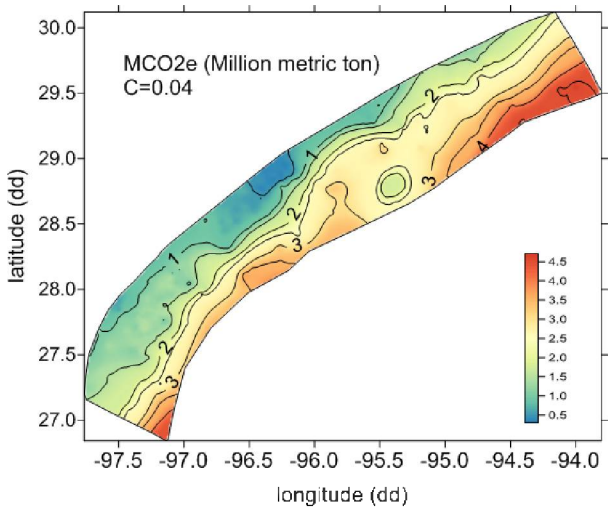

B.

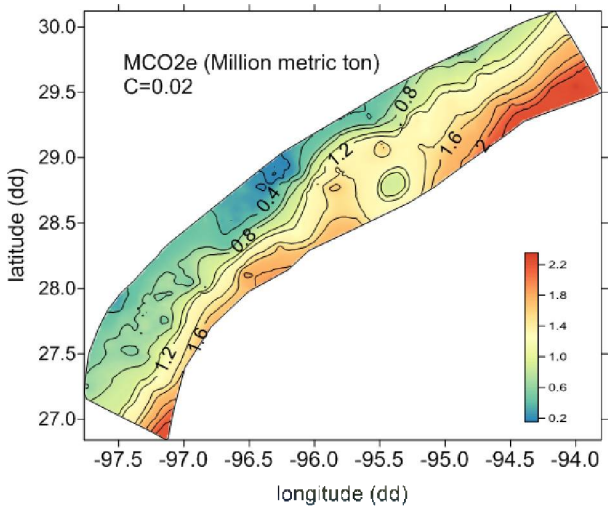

Figure 6.29: Contour maps of the study area (along the Texas coastal zone) of spatial distributions of effective CO2 dissolution storage in brine with (A) C=0.04 and (B) C=0.02.

Note that in this study, temperature and pressure were assumed uniform at each rectangular prism. However, the thickness of the rectangular prism can be up to 800 meters. Brine density after saturation with CO_2 and CO_2 solubility calculated with the pressure and temperature at the depth of middle point of the rectangular prism may not be reasonable.

Yang et al. (2014) published the results of this research and concluded that: 1) carbon solubility trapping potential is most sensitive to thickness and porosity, two of the three parameters (thickness, porosity, and area) that determine brine volume. The result suggests that the volume of available brine in the storage aquifer is a primary control and 2) the storage coefficient, C, appears to be one of the critical parameters for assessing CSTP in a saline aquifer; and 3) brine-rock-CO2 reaction experiments suggest that the most likely CO2-solubility trapping potential of the section in the area of interest (study area) is approximately 5% of the total CO_2 storage capacity calculated in Subtask 3.1.

7 Task 7.0: Mineralization Containment

Experimental Procedure

High pressure / high temperature experimental conditions are outlined in Table 6.1.1. Geochemical data were collected in several ways:

1) Initial brine concentrations were determined by mixing measured aliquots of NaCl salts, NaBr salts and deionized water. Na and Cl concentrations were outside analytical calibration on the Ion Chromatographs (IC) and the inductively coupled plasma mass spectrometer (ICP-MS). So, wet chemical procedures were used to determine initial compositions.

2) A calibrated pH meter was used to determine pH values of the brine during sampling. A Hach digital titrator using 0.1600 M H_2SO_4 was used to measure alkalinity. Because of the small volumes of brine used, 2-3 ml of reacted brine were diluted to ~30 ml using de-ionized water and the alkalinity was determined using the inflection point method calculated on the USGS alkalinity calculator.

3) Major cation and anion concentrations were measured on two Dionex ICS-1100 ion chromatographs and these analyses are indicated in the data tables by the IC heading.

4) Major and trace elemental analyses were performed on an Agilent 7500ce inductively-coupled plasma mass spectrometer (ICP-MS).

Table 6.1.1: High temperature / high pressure experimental conditions

Experiment	Temperature (C)	Pressure (bar)	Solution Properties	Rock Type	Comments
A	100	200	DI	Miocene	
B	100	200	1.88 mol/kg NaCl sol.	Miocene	
D	70	200	1.88 mol/kg NaCl sol.	Miocene	
E	100	300	1.88 mol/kg NaCl sol.	Miocene	
F	150	200	1.88 mol/kg NaCl sol.	Miocene	failed after 9 samples, Not analyzed
G	135	200	1.88 mol/kg NaCl sol.	Miocene	failed after 3 samples, Not analyzed
H	130	200	1.88 mol/kg NaCl sol.	Miocene	
L	100	200	1.88 mol/kg NaCl sol.	Miocene	Re-run of experiment B

The experimental design varied the temperature, pressure and ionic strength of the reacted solution with approximately 8 grams of Miocene rock fragments. Major cations and anions of the reaction solution were analyzed by Ion Chromatography (IC), and trace cations were analyzed on an Inductively Coupled Plasma Mass Spectrometer (ICP-MS). The majority of results have been reported in the last quarterly report, and we present selected data in graph form in this report.

The L series is a duplicate of the B series experiment and was re-run because the experimental design evolved over the course of the experiments. We re-collected the sample data so the results are more compatible with later runs. Both runs show good correlation suggesting variations in geochemistry are a result of experimental conditions and not inter-sample variability. Figures 7.1.1 show plots of reaction time vs. elemental

abundance in the reaction fluid during reaction of Miocene sediments, 1.88 Mol/L NaCl solution and super critical CO_2 at 200 bar of pressure. Plots in Figure 7.1 show a positive correlation between reaction time and elemental abundance.

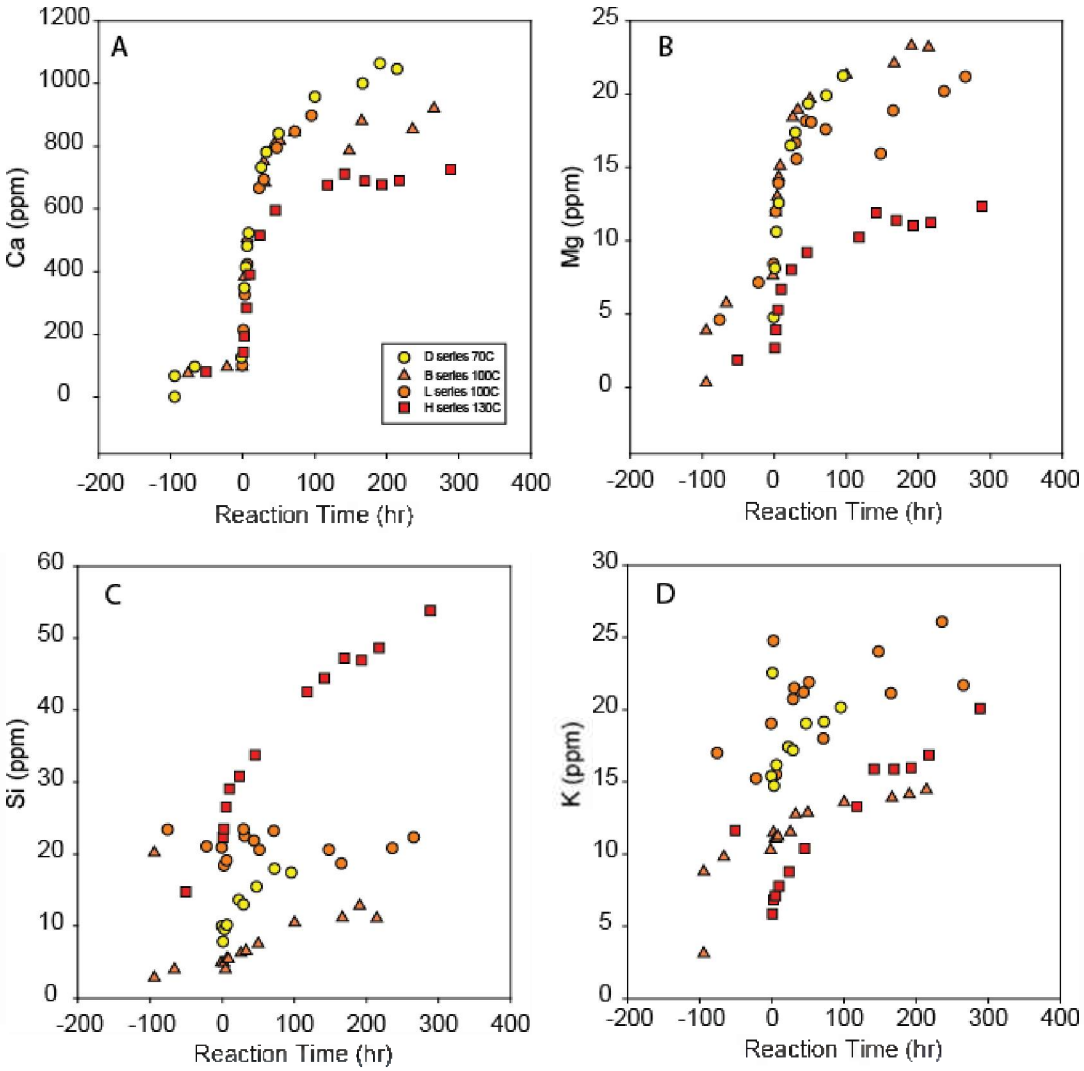

Figure 7.1: (A-D) – A) Calcium dissolution rates are highest in experiments with the lowest temperature because of higher calcite and CO2 solubility at lower temperatures. Carbonate dissolution likely controls Ca concentrations. B) Mg concentrations are also likely controlled by carbonate dissolution. C) and D) Si and K concentrations are likely controlled by K-feldspar dissolution. The silicate dissolution reactions appear to be positively correlated with reaction temperature.

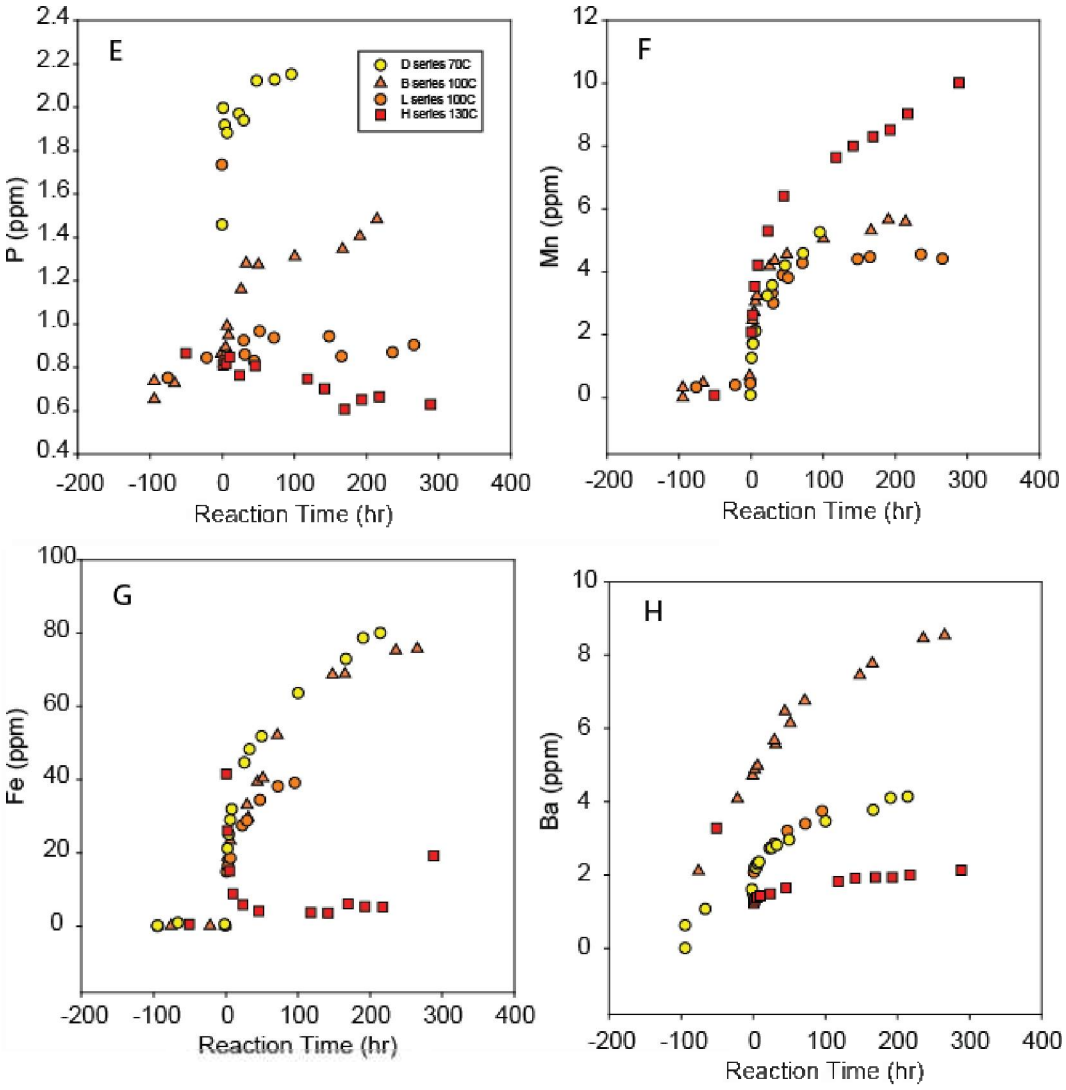

Figure 7.1.1: (E-H) – E. P concentrations are positively correlated with reaction temperatures for most experiments but the correlation is weak and the abundances stay relatively low and constant. Mn concentrations are likely controlled by both carbonate and silicate weathering. Some source of Mn from silicates is likely because Mn shows a steady increase after Ca concentrations stabilize indicate carbonate dissolution has slowed. H. Ba concentrations show the same general behavior as Ca suggesting they are controlled by carbonate dissolution. Contamination from drilling fluids is also a possibility.

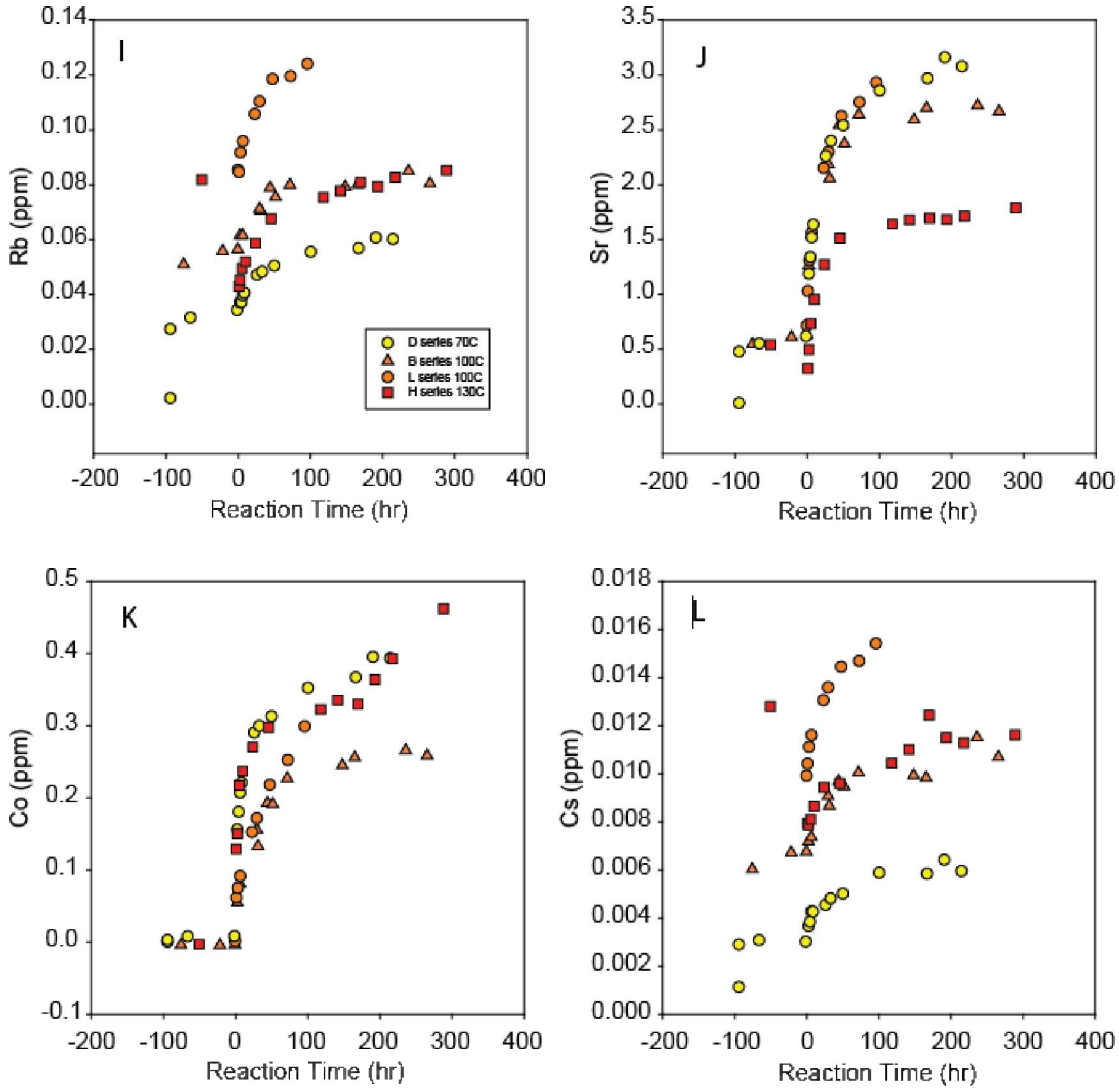

Figure 7.1.1: (I-L) – Rb, Sr, Co and Cs also show a positive correlation with reaction time. Sr is likely controlled by carbonate dissolution similarly to Ca. Rb, Co, and Cs sources are not as easy to identify. The steady increase in elemental concentrations suggests a silicate source.

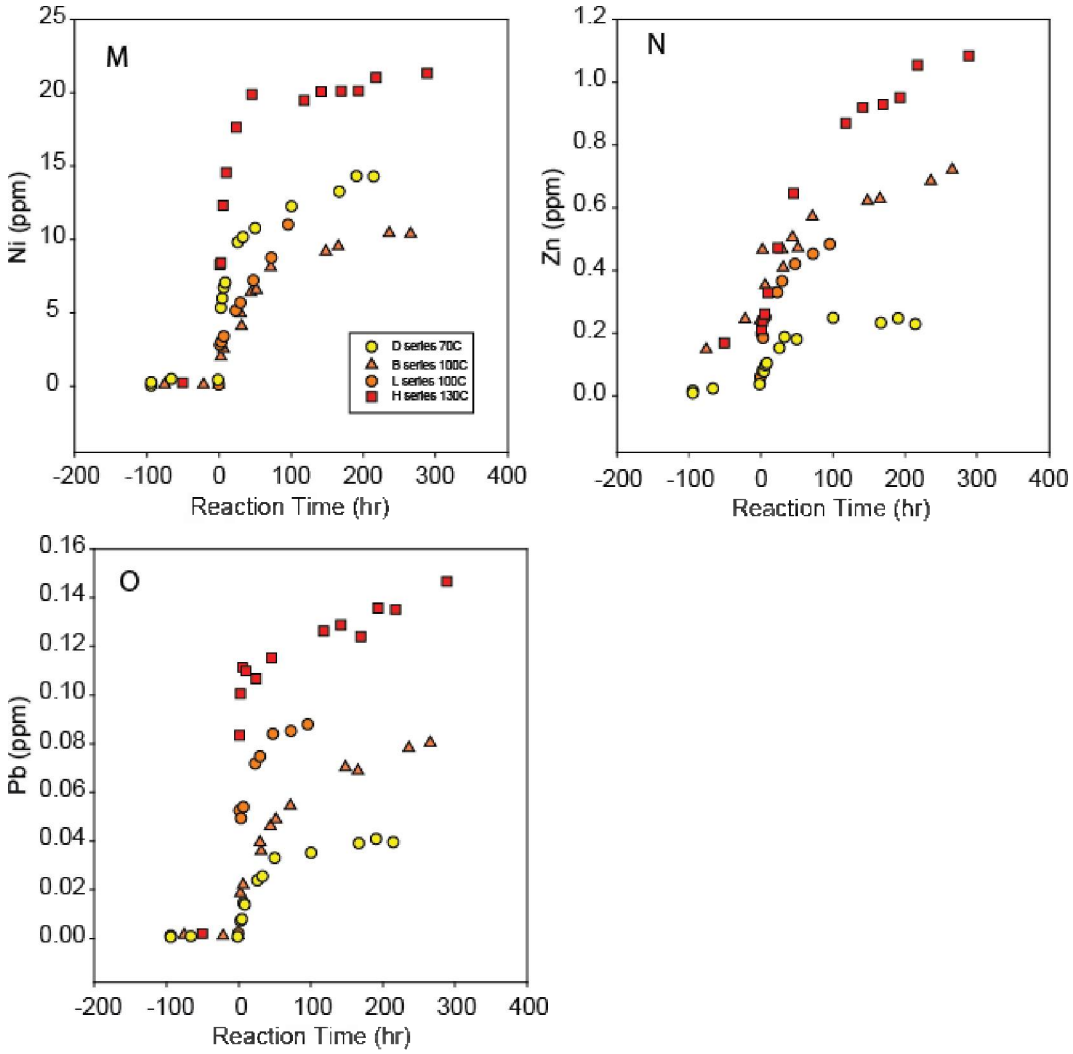

Figure 7.1.1: (M-O) – Ni and Zn concentrations are positively correlated with reaction time, however these elements have been identified as a component of the Hastalloy reaction vessel and are likely not controlled by water rock interactions. Pb may be a result of water rock interactions. The source of Pb is currently still being studied.

Plots of reaction time vs. elemental abundance in the reaction fluid during reaction of Miocene sediments, 1.88 Mol/L NaCl solution and super critical CO_2 at 200 bar of pressure. Plots in Figure 7.2 show no correlation between reaction time and elemental abundance

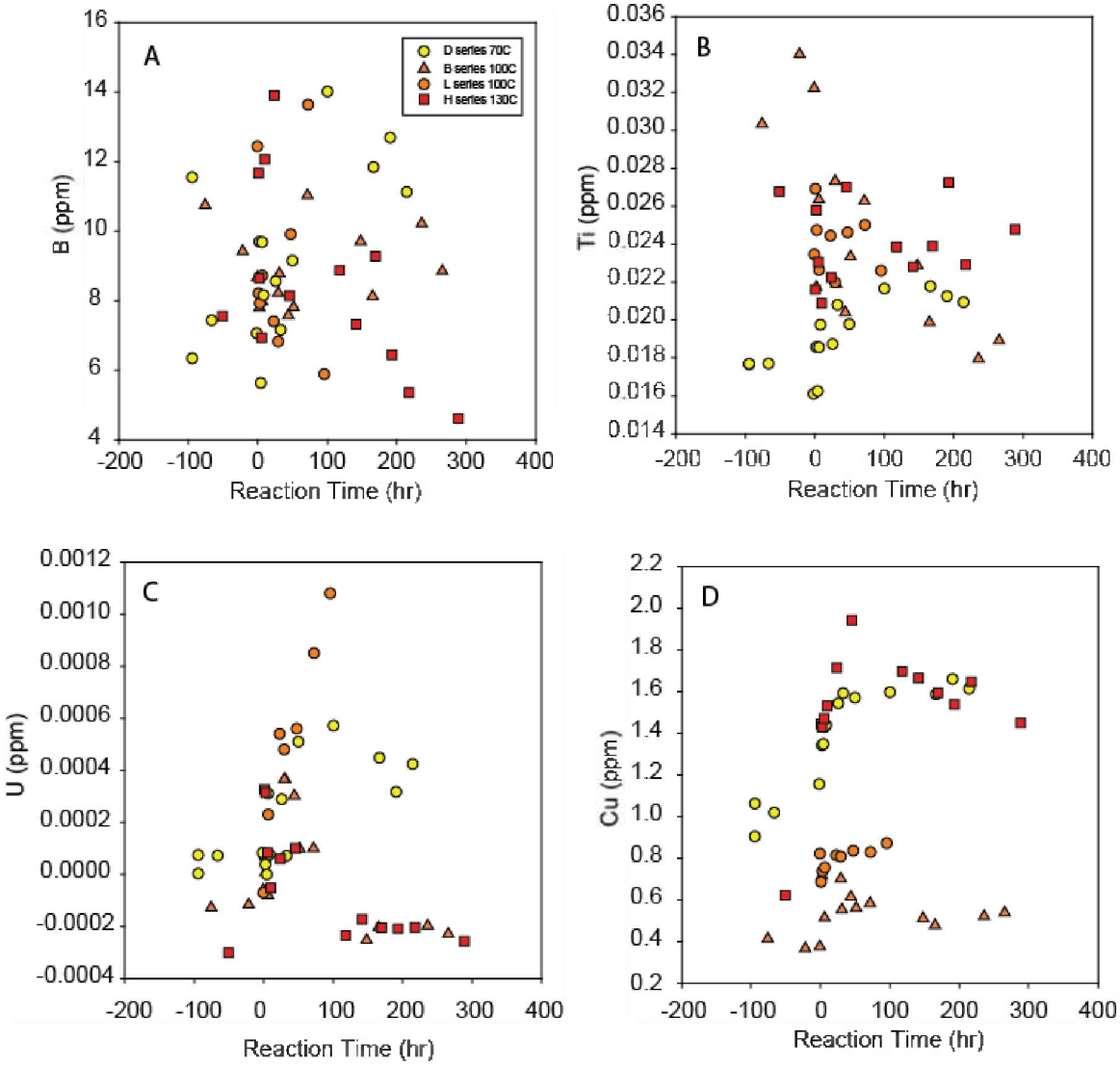

Figure 7.2: (A-D) With the exception of B these elements generally have low concentrations that are not variable over the course of the run. U has concentrations close to the detection limit as indicated by the negative concentrations.

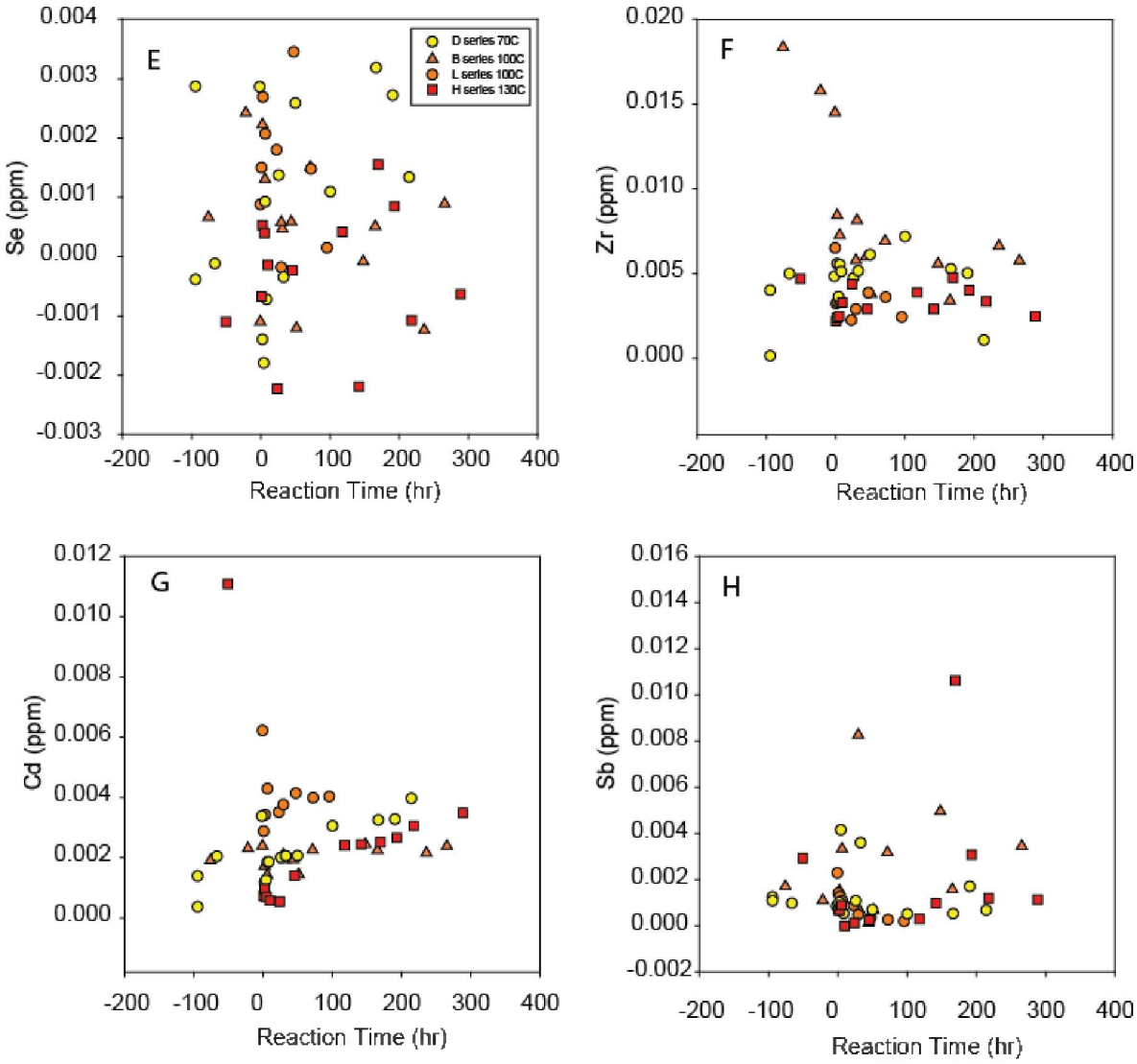

Figure 7.1.2: (E-H) – Se, Zr, Cd and Sb generally have low concentrations that do not vary significantly during the experiment.

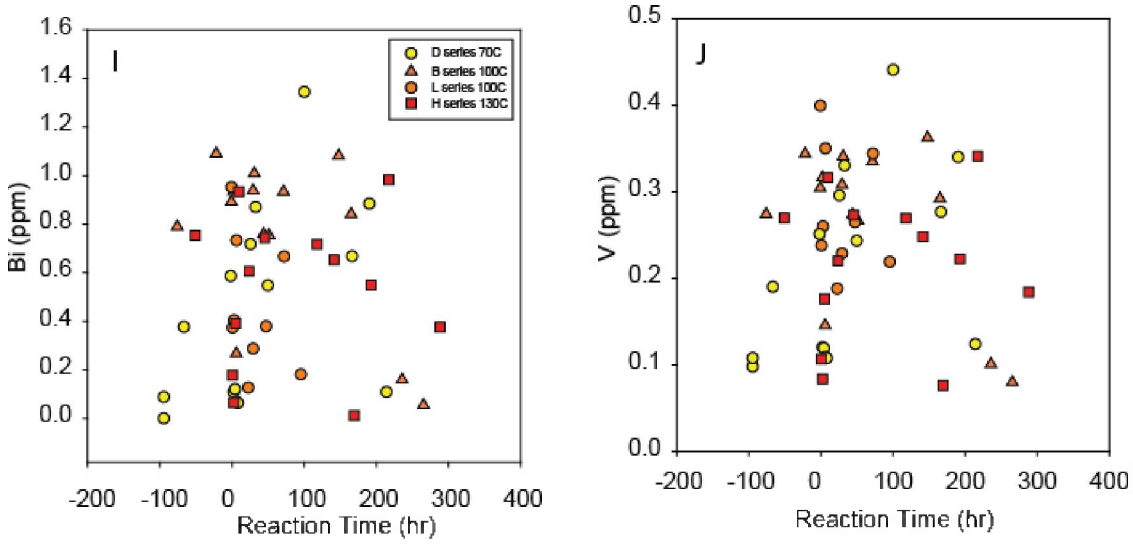

Figure 7.1.2: (I-J) – Bi and V generally have low concentrations that do not vary in a regular way with reaction time.

Figures 7.1.3 are plots of reaction time vs. elemental abundance in the reaction fluid during reaction of Miocene sediments, 1.88 Mol/L NaCl solution and super critical CO_2 at 200 bar of pressure. Plots in Figure 7.3 show a negative correlation between reaction time and elemental abundance

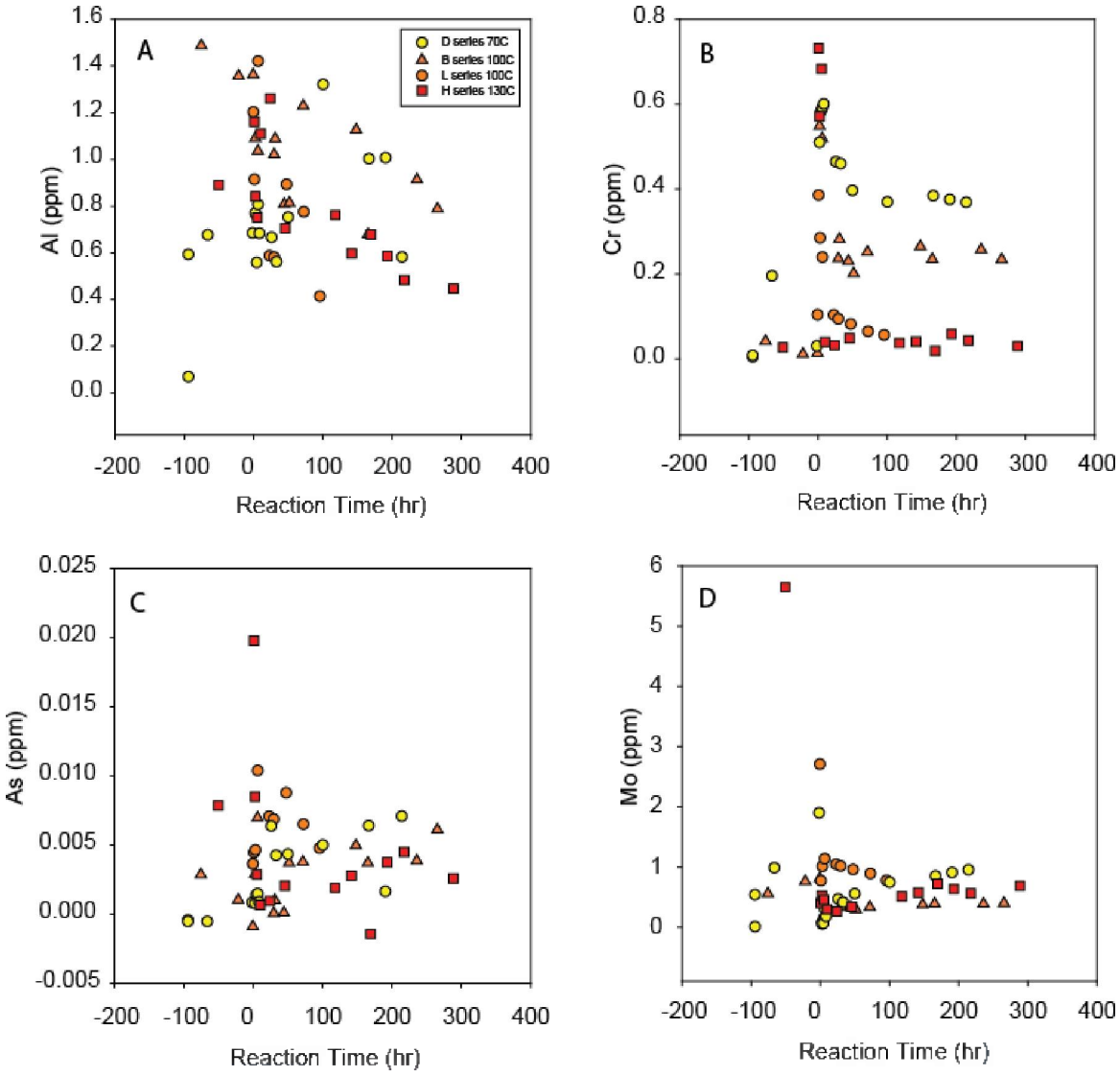

Figure 7.3: (A-D) – Al, Cr, As and Mo all show the same general behavior. These elements are initially mobilized with the introduction of the super critical CO2. These elements are insoluble at the low pH in the solution and their concentrations drop to near zero soon after the reaction starts. These elements likely sorb onto Fe coatings found in the reaction vessel and rock sample.

Figure 7.4 are plots of reaction time vs. elemental abundance in the reaction fluid during reaction of Miocene sediments, 1.88 Mol/L NaCl solution and super critical CO_2 at 100°C, pressure is varied between 200 and 300 bar of pressure

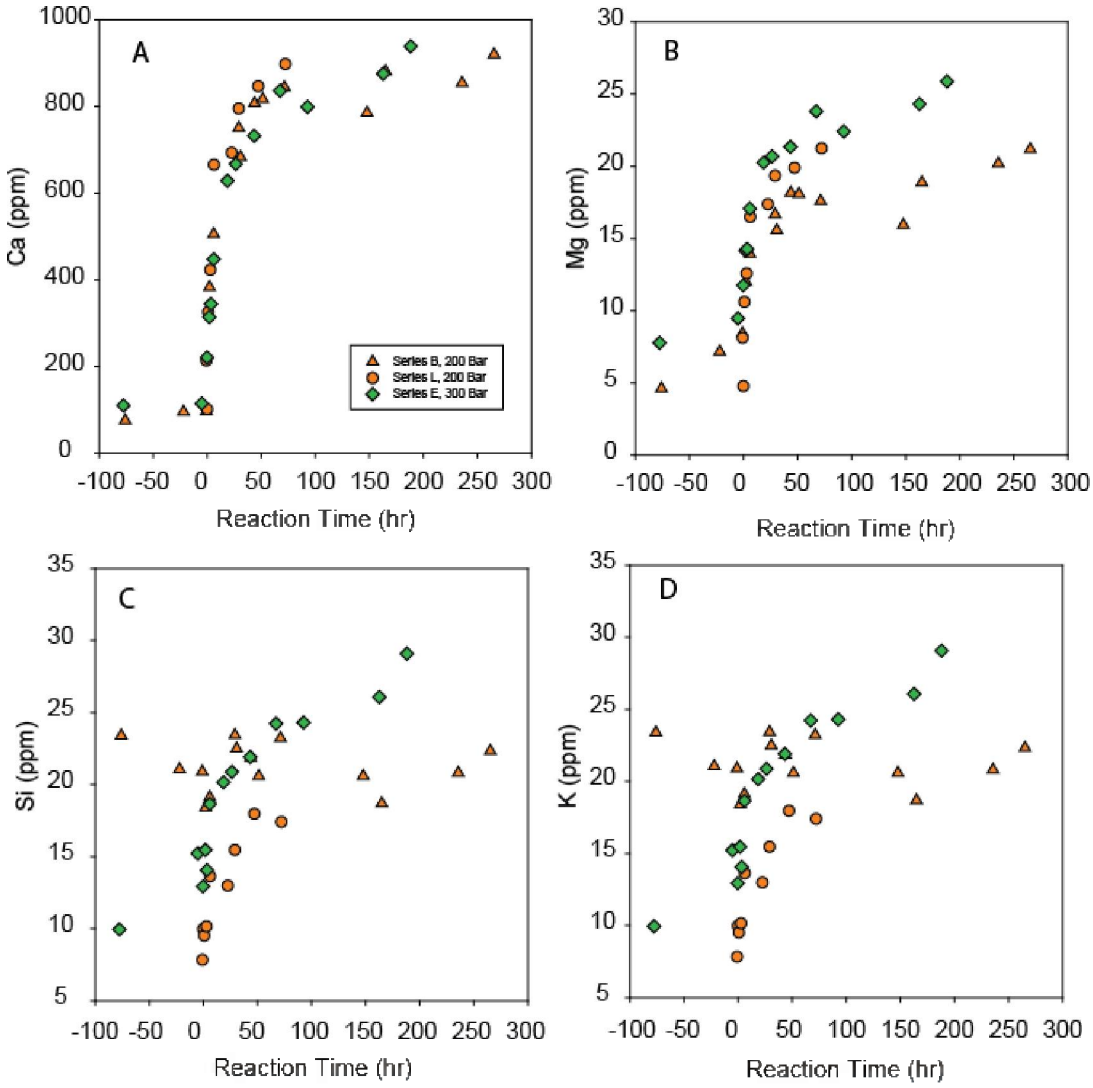

Figure 7.4: (A-D) – Plots comparing the reactions under 300 and 200 bar of pressure. The results in figure 7.4 indicate that variations in pressure do not significantly alter the reaction rates. Several, but not all, elemental systems are included. The excluded elemental systems correspond to data previously represented in Figure 7.1 – Figure 7.3.

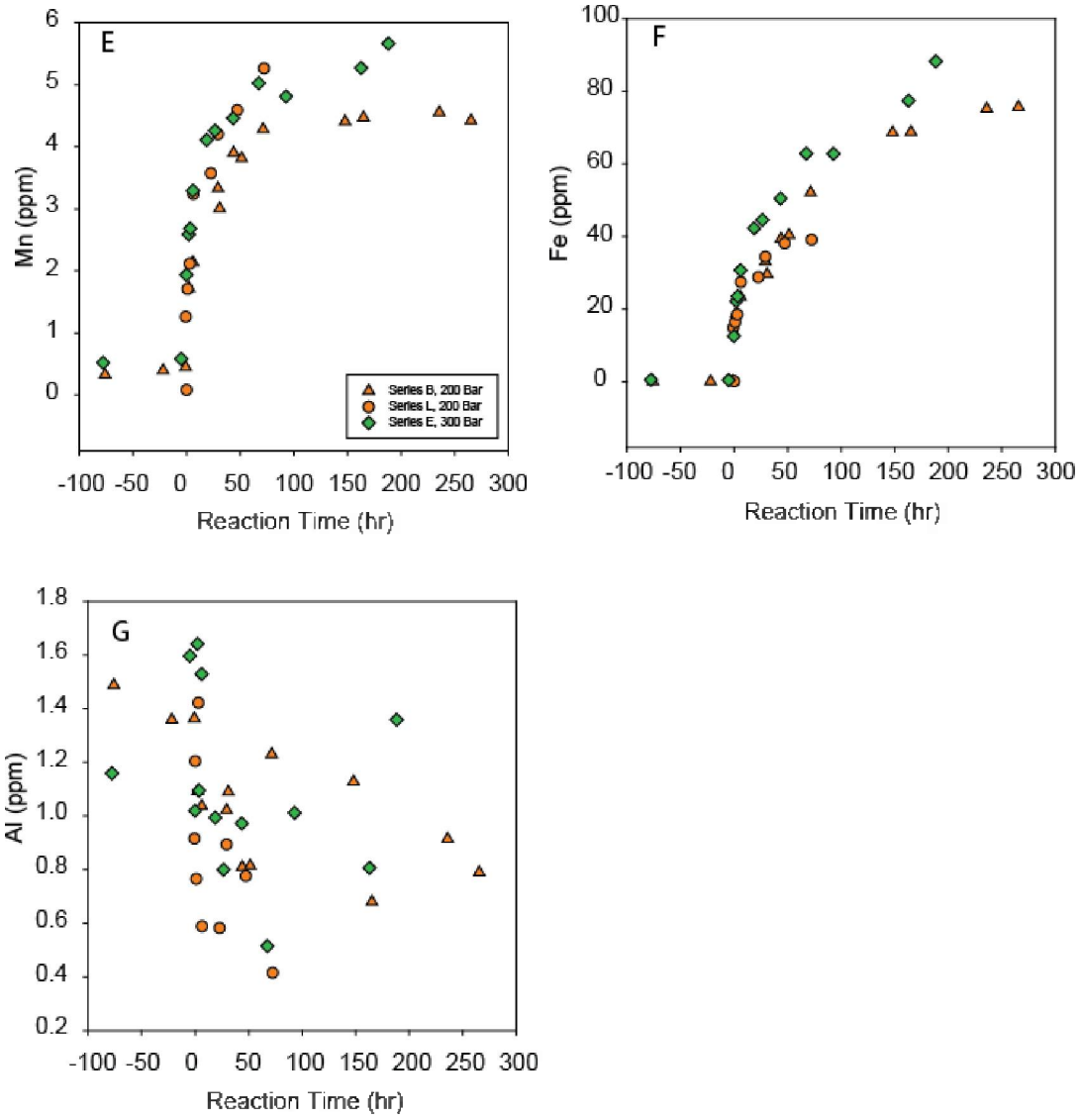

Figure 7.1.4 (E-G) – Plots comparing reactions under 300 and 200 bar of pressure, which indicate that variations in pressure do not significantly alter the reaction rates.

Figure 7.5 includes plots of reaction time vs. elemental abundance in the reaction fluid during reaction of Miocene samples, super critical CO_2 at 100°C, pressure at 200 bar of pressure. Solution chemistry is varied between de-ionized water and 1.88 Mol/L NaCl solution to assess the effect of ionic strength on reaction rates.

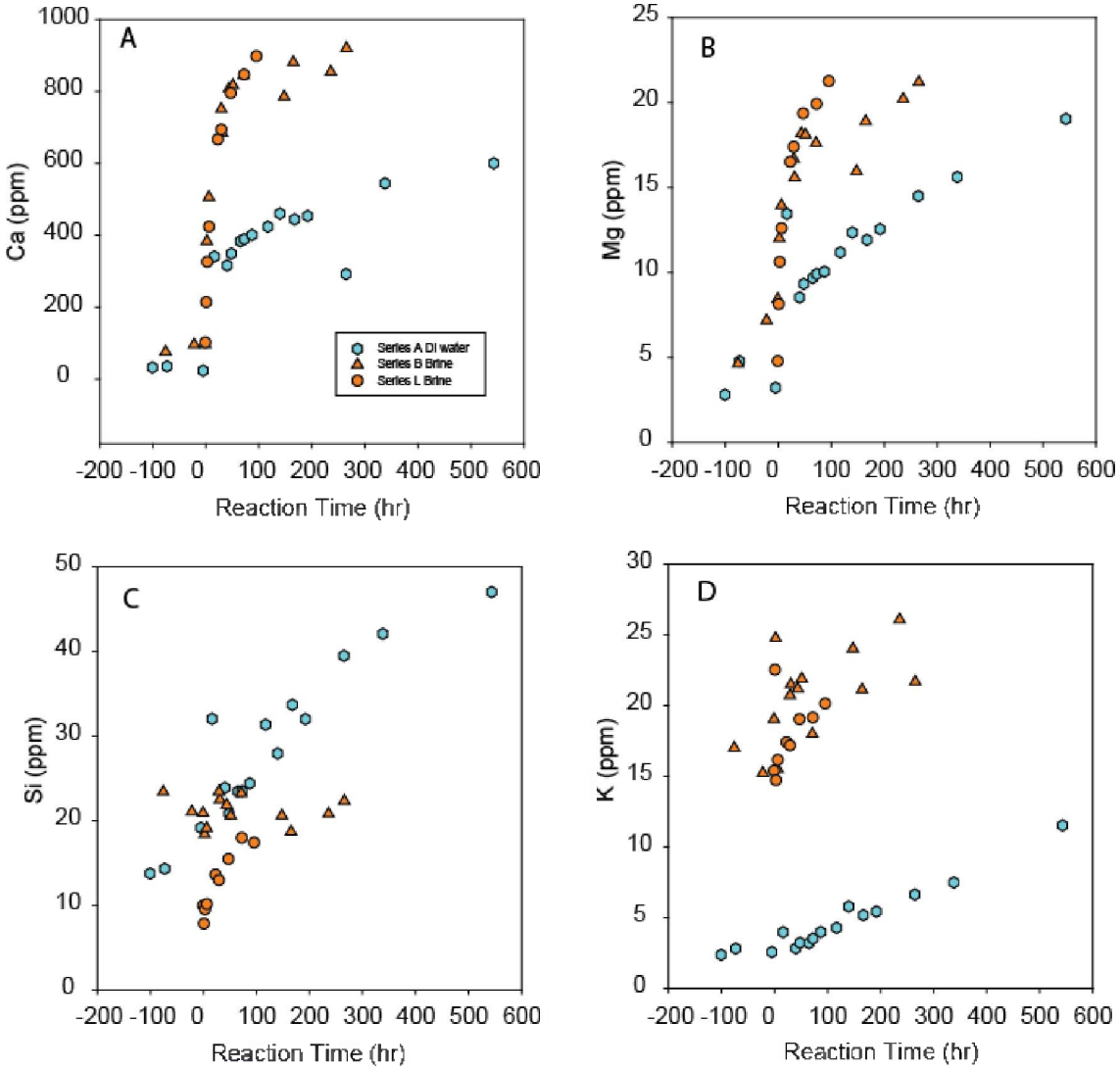

Figure 7.5: (A-D) The change in ionic strength of the reaction fluid from Di to 1.8Mol/L NaCl had a significant effect on reaction rates and Ca equilibrium concentrations in reactions controlled by carbonate dissolution seen in Ca and Mg concentrations(A and B).). The effect is lower in elements controlled by silicate dissolution, as seen in Si and K concentrations (C and D).

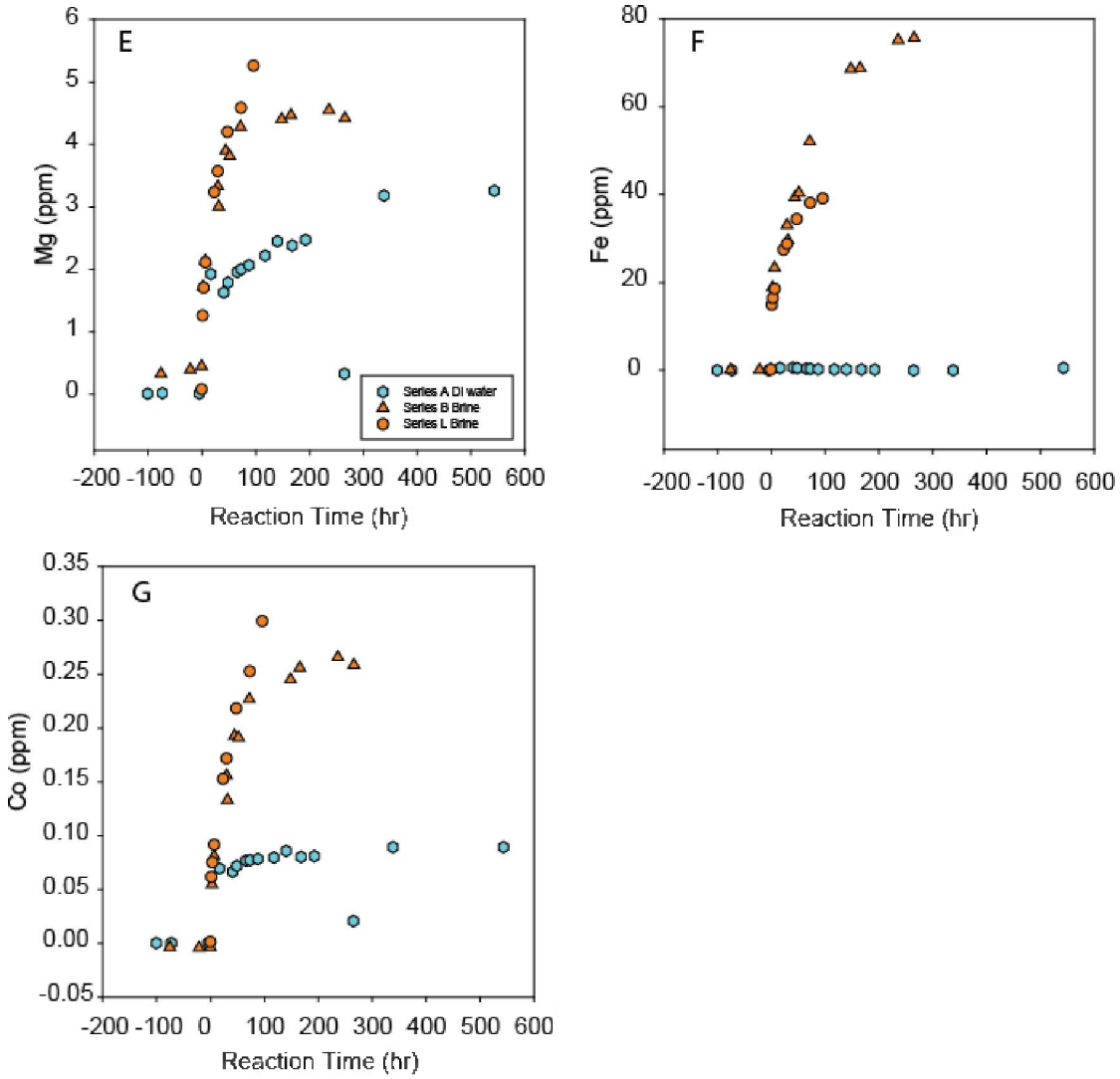

Figure 7.1.5: (E-G) Mg has high reaction rates and elemental concentrations controlled by higher carbonate dissolution in the NaCl brine. Fe has very low concentrations in the DI (de-inoized) water experiment likely due to the non-reactive nature of the reaction vessel. With the brine solution, the brine likely corroded the reaction vessel exposing reactive surfaces and higher Fe concentrations, along with Ni and Zn (not shown). Co concentrations remain relatively low and are likely controlled by silicate dissolution. CO_2 concentrations are higher in the brine solution suggesting enhanced dissolution; however Si and K concentrations do not show this increase.

The amount of calcite dissolution is greater in the brine experiment compared to the DI water case. As previously reported, calcite minerals were almost completely consumed at the reacted surface; whereas, below the surface reaction rim calcite is still abundant. EDS (electron dispersive spectrometry) scan results show that calcium content dropped significantly on the reacted sample surface (Table 6.1.2). Clearly, more calcite was consumed in the brine experiment than in the DI water experiment (i.e., 1.1% Ca remained at the reacted surface in the latter) (Table 6.1.2). The SEM observation matches well with the water chemical analyses. Calcium concentration in the brine reached 914 ppm at the end of the brine experiment compared to 544 ppm in the DI

water run. Apparently, under the reaction conditions calcite solubility is higher in brine than in fresh water.

Table 6.1.2: Chemical composition of rock sample of SEM energy dispersive spectrometry (EDS). Each result obtained from an EDS scan over an area of 1.48×1.28 cm.

	Ca %	Na %	K %	Mg %	Fe%	Ti %	Cr %
Unreacted sample							
1	4.2	1.2	1.7	0.6	5.8	0.7	
2	5.0	1.4	1.3	0.7	6.3	0.7	
3	4.9	1.2	1.4	0.6	6.3	0.8	
4	4.6	1.2	1.4	0.7	6.3	0.7	
Average	***4.7***	***1.2***	***1.4***	***0.7***	***6.2***	***0.7***	
Reacted with DI+CO_2							
Sample inside (DI+CO_2)							
1	4.8	1.4	1.8	0.9	5.9	0.8	
2	4.7	1.3	1.2	0.8	5.4	0.8	
Average	***4.8***	***1.4***	***1.5***	***0.8***	***5.7***	***0.8***	
Reacted surface (DI+CO_2)							
1	1.8	1.4	1.6		7.5	0.7	
2	0.8	1.0	1.3	0.8	7.1	0.7	0.8
3	0.7	1.0	1.1	0.8	7.5	0.7	0.6
Average	***1.1***	***1.1***	***1.3***	***0.8***	***7.4***	***0.7***	***0.7***
Reacted with brine+CO_2							
1	0.7	1.5	1.9	0.4	4.7		
2	0.5	1.2	1.9	0.3	5.6		
Average	***0.6***	***1.3***	***1.9***	***0.3***	***5.2***		
Reacted with brine+CO_2+O_2							
1	0.7	1.1	1.7	0.5	20.3	0.6	0.7
2	0.6	1.9	1.8	0.8	14.8	0.5	
Average	***0.7***	***1.5***	***1.7***	***0.7***	***17.5***	***0.6***	***0.7***

The reaction temperature had a significant effect on calcite solubility. Experiment D was run at 70^{0}C, B and L were run at 100^{0}C, and H was run at 130^{0}C. The experiment run at the lowest temperature shows the highest calcite solubility and calcite dissolution rates. The experiment run at the highest temperature shows the lowest calcite solubility and calcite dissolution rates (Figure 7.1a). The calcite solubility is likely controlled by CO_2 solubility which is higher at lower temperatures. The higher CO_2 solubility lowers pH which results in higher calcite dissolution rates and calcite solubility.

Mineral composition change

Mineral composition of the rock sample used for the reaction experiments was analyzed using the X-ray diffraction method. One of the rock samples retrieved after reaction was also analyzed using the same procedures in order to investigate potential changes in mineral composition caused by CO_2 reactions (Table 6.1.3). Together with the results of water chemistry and SEM imaging, mineralogical variations aid in determining which mineral reactions occurred during the experiments.

Sample preparation and analysis

Bulk powders of the original and reacted rock samples were prepared by means of wet grinding and spray drying. The samples were first disintegrated using a TEMA ball mill before further grinding in a McCrone Micronizing Mill. The samples were ground for 16 minutes in 0.5% (wt./vol) aqueous solution of polyvinyl alcohol to reduce particle size sufficiently to less than 10 mm. The resulted slurry samples were sprayed from top of a spray drier and dry samples were collected at the bottom. X-ray diffraction analysis was conducted on a Bruker AXS D8 diffractometer at the University of Texas at Austin. Bruker's Eva software was used to identify mineral phases. Quantitative analysis was conducted using Topas 3, a personal computer software package based on the Rietveld method (Bish, 1994). Quantitative phase analysis results from this method are accurate to within 2% absolute error.

Table 6.1.3: XRD mineral composition of the unreacted and reacted Miocene sample (Experiment B), Well Matagorda Island OCS-G-3733 A-6 (427034015800), 9205 ft.

Sample	Quartz	Kaolinite	Calcite	Illite	Plagioclase	K-feldspar	Total
Original	43.5	6.2	11.8	5.0	18.4	15.2	100.0
Reacted	49.1	4.5	9.6	5.1	18.1	13.6	100.0

XRD results show small differences between the original and reacted sample. The reacted sample shows decreases in calcite and K-feldspar abundances and increases in Kaolinite and quartz. For all minerals except quartz, changes are less than 2%, within the range of instrument error. However, quartz abundance in the reacted sample is 5.6% higher than the unreacted sample. Such a big change should be real; therefore the changes in other mineral phases may also be real. Decreases in the abundances of calcite and K-feldspar further confirm that the increases of Ca, K and alkalinity in solution during experiments were mainly caused by dissolution of calcite and K-feldspar. SEM examination of the reacted rock samples show dissolution features of calcite and feldspar minerals. Together with semi-quantitative element concentrations of X-ray Energy Dispersive Spectrometry results also show reduced Ca concentration on reacted rock surfaces. Combining all available evidence, one can easily conclude that two major mineral reactions occurred during the experiments:

$$CaCO_3 + CO_2 + H_2O \rightarrow Ca^{2+} + 2HCO_3^-$$

Equation 6.1-1

$$2KAlSi_3O_8 \text{ (K-feldspar)} + 2H^+ + H_2O \rightarrow 2K^+ + Al_2Si_2O_5(OH)_4 \text{ (kaolinite)} + 4SiO_{2(aq)}$$

Equation 6.1-2

The calcite dissolution rate is dependent on temperature and partial CO_2 pressure, with more prominent control from temperature. In the temperature range of this study, calcite dissolution rate decreases with higher reaction temperature (Figure 7.3). The difference caused by pressure variations is much smaller. In fact, calcite dissolution rates at 200 bar and 300 bar (L and E runs) are similar (Figure 7.4). Experiment B at 200 bar shows lower dissolution rates, but this experiment showed signs of leakage during the process and the results may be problematic.

Plagioclase (albite) dissolution rate is as high as K-feldspar; therefore, dissolution of plagioclase may also have occurred during the experiment as modeling results suggested. (See next section). The first reaction experiment (Experiment A) using DI water showed that Na concentrations in water increased from 24 ppm to 54 ppm during CO_2 stage. The additional sodium indicates albite dissolution. In other experiments where 1.88 molar NaCl solutions were use, no notable Na increases were observed. The modest release of sodium from albite dissolution may have been swamped by high Na concentrations in background.

Kaolinite is a usual reaction product of feldspar dissolution as Equation 6.1-1 states. However, kaolinite XRD abundance in reaction sample is not higher; in fact it is lower than the original sample. XRD analysis of clay minerals usually has higher analytic errors because it is very difficult to achieve and control random orientation of clay minerals. Therefore, it is possible that small amount of kaolinite may have precipitated during the experiment, but XRD analysis is not sufficiently precise to detect its increase. Another possible explanation is that due to slow kinetic rate, kaolinite precipitation may be limited even it is supersaturated in the solution.

Modeling approach

In this study, PHREEQC, was used to simulate brine-rock-CO_2 interactions in batch experiments under high pressure and high temperature (Parkhurst and Appelo, 1999). PHREEQC is based on an ion-association aqueous model and has capabilities for (1) speciation and saturation-index calculations; (2) batch-reaction and one-dimensional (1D) transport calculations involving reversible reactions, which include aqueous, mineral, gas, solid-solution, surface-complexation, and ion-exchange equilibria, and irreversible reactions, which include specified mole transfers of reactants, kinetically controlled reactions, mixing of solutions, and temperature changes; and (3) inverse modeling, which finds sets of mineral and gas mole transfers that account for differences in composition between waters, within specified compositional uncertainty limits (Parkhurst and Appelo, 1999).

PHREEQC generally is used for performing a wide variety of low-temperature aqueous geochemical calculations. However, it has been used to simulate water-rock-CO_2 interactions under high pressure and high temperature (Berger et al., 2009; Heeschen et al., 2011; Jacquemet et al., 2009; Koenen et al., 2011; Soong et al., 2004; Tarkowski and Uliasz-Misiak, 2007; Xie et al., 2006) as long as an appropriate geochemical database is used.

In this study, geochemical models are based on the integrated LLNL thermodynamic database, "thermo.com.V8.R6.230" (Johnson et al., 2000). The reaction constants compiled in this database can be applied to the temperature ranging from 0°C to 300°C.

However, PHREEQC simulates gas phases as ideal gases. It may lead to significant errors if total pressures of the gas phase measured in the batch experiments are directly used in PHREEQC. So in this study, we used WINPROP to calculate CO_2 gas fugacity of each batch experiment as partial pressure of CO_2 in PHREEQC. WINPROP is CMG's equation of state multiphase equilibrium property package featuring fluid characterization, lumping of components, matching of laboratory data through regression, simulation of multiple contact processes, phase diagram construction, solids precipitation, and more (CMG, 2011).

Water compositions of batch experiments (Table 6.1.4) measured immediately before CO_2 was introduced into the reactor were used as initial conditions in the models. Initial value of pH in the model is assumed to be 7 since the brine was made by adding NaCl to the distilled water. Table 6.1.4 also lists the volume of the brine and CO_2 fugacity which were used in the numerical model. CO_2 fugacity of each batch experiment was calculated using WINPROP.

Table 6.1.4: Initial water composition used in the geochemical model of 5 batch experiments.

	A	B	D	E	H
Al (moles/kgs of H_2O)	3.01E-05	5.26E-05	2.72E-05	5.92E-05	3.18E-06
Ca (moles/kgs of H_2O)	5.74E-04	2.50E-03	2.91E-03	2.87E-03	2.17E-03
Cl (moles/kgs of H_2O)	2.50E-03	1.82E+00	1.77E+00	1.83E+00	1.88E+00
K (moles/kgs of H_2O)	6.58E-05	5.07E-04	2.81E-04	3.72E-04	1.65E-04
Mg (moles/kgs of H_2O)	1.32E-04	3.61E-04	2.81E-04	3.90E-04	8.38E-05
Na (moles/kgs of H_2O)	1.06E-03	1.82E+00	1.76E+00	1.88E+00	1.88E+00
Si (moles/kgs of H_2O)	6.82E-04	7.75E-04	1.86E-04	5.42E-04	2.64E-04
pH	7	7	7	7	7
Temperature (°C)	100.0	100.0	70.0	100.0	130.0
Total Pressure (Bar)	200.0	200.0	200.0	300.0	200.0
CO2 Fugacity (atm)	120.4	120.4	97.5	152.2	138.2
Water volume (ml)	150.0	150.0	150.0	150.0	150.0
Rock samples (g)	8.0	8.0	8.0	8.0	8.0

Note: Cl- concentrations for each batch were estimated based on charge balance.

The geochemical model considers 6 primary minerals and 7 secondary minerals (Table 6.1.5). Mineral dissolution and precipitation were simulated with kinetic theory and the reaction rates are given by (Palandri and Kharaka, 2004),

$$\frac{dm}{dt} = -SA\left[\begin{array}{l} k_{acid}^{298.15K} e^{\frac{-E_{acid}}{R}\left(\frac{1}{T}-\frac{1}{298.15K}\right)} a_{H^+}^{n_1}(1-\Omega^{p_1})^{q_1} \\ +k_{neutral}^{298.15K} e^{\frac{-E_{neut}}{R}\left(\frac{1}{T}-\frac{1}{298.15K}\right)}(1-\Omega^{p_2})^{q_2} \\ +k_{base}^{298.15K} e^{\frac{-E_{base}}{R}\left(\frac{1}{T}-\frac{1}{298.15K}\right)} a_{H^+}^{n_3}(1-\Omega^{p_3})^{q_3} \end{array}\right]$$

Equation 6.1-3

where SA is reactive surface area, $k_{acid}^{298.15}$, $k_{neutral}^{298.15}$, $k_{base}^{298.15}$ are rate constants for acid, neutral and base conditions at temperature, 298.15 K, E_{acid}, $E_{neutral}$, E_{base} are activation energies (J mol^{-1}), T is the temperature (K), R is the gas constant, Ω is mineral saturation index, p and q are empirical and dimensionless parameters, a_{H+} is activity of H^+ in water and n is a parameter estimated from experiments. From Equation 6.1-3, it can be seen that mineral reaction rate includes three mechanisms. Parameters for calculating reaction rates of minerals are listed in Table 6.1.5 (Palandri and Kharaka, 2004).

The trial and error method was used to calibrate reactive surface area of minerals for each batch experiment by fitting concentrations of major ions.

Table 6.1.5: Parameters for calculating kinetic rate constants of minerals.

Mineral	Mass (%)	Neutral mechanism		Acid mechanism			Base mechanism		
		k (mol/m^2/s)	E(kj/mol)	k (mol/m^2/s)	E(kj/mol)	n_1	k (mol/m^2/s)	E(kj/mol)	n_3
primary									
quartz	43.5	1.023×10^{-14}	87.7						
kaolinite	6.2	6.918×10^{-14}	22.2	4.898×10^{-14}	65.9	0.777	8.913×10^{-18}	17.9	-0.472
Calcite	11.8	1.549×10^{-6}	23.5	5.012×10^{-1}	14.4	1.0			
Illite	5.0	1.660×10^{-13}	35	1.047×10^{-11}	23.6	0.34	3.020×10^{-17}	58.9	-0.4
K-feldspar	15.2	3.890×10^{-13}	38	8.710×10^{-11}	51.7	0.5	6.310×10^{-22}	94.1	-0.823
Albite	18.4	2.754×10^{-13}	69.8	6.918×10^{-11}	65.0	0.457	2.512×10^{-16}	71	-0.572
Secondary									
Magnesite		4.571×10^{-10}	23.5	4.169×10^{-7}	14.4	1.0			
Siderite		1.260×10^{-9}	62.76	1.590×10^{-4}	45.0	0.9			
Ankerite		1.260×10^{-9}	62.76	1.590×10^{-4}	45.0	0.9			
Downsonite		1.260×10^{-9}	62.76	1.590×10^{-4}	45.0	0.9			
Ca-smectite		1.660×10^{-13}	35	1.047×10^{-11}	23.6	0.34	3.020×10^{-17}	58.9	-0.4

Note that: all rate constants are listed for dissolution.

Preliminary modeling results

Since the rock samples are the same for the five batch experiments, the only geochemical parameter needed to be calibrated is reactive surface area. Calibrated reactive surface areas of each mineral in the five batch experiments are listed in Table 6.1.6. Because secondary minerals were not initially present in the rock samples, surface areas for those minerals are assumed to be 0.01 m^2, and no calibrations were conducted for those minerals. Reactive surface areas of primary minerals are calibrated by fitting concentrations of major ions over time with a trial-and-error method. The

reactive surface area of calcite was calibrated to fit concentration measurements of Ca and Mg (Figures 7.6-7.10). It should be noted that since Mg concentrations have a strong correlation with Ca concentrations in all five batches, Mg is consider as a replacement of Ca in the calcite molecular structure. Reactive surface areas of calcite in the B, D, E and H are very close, about 25 times the reactive surface area of calcite in the A-batch.

Table 6.1.6: Calibrated reactive surface areas of minerals at the five reactors

		A		B		D		E		H	
Mineral	mass (g)	Surface area (m^2)	Surface area (cm^2/g)	Surface area (m^2)	Surface area (cm^2/g)	Surface area (m^2)	Surface area (cm^2/g)	Surface area (m^2)	Surface area (cm^2/g)	Surface area (m^2)	Surface area (cm^2/g)
primary											
quartz	3.48	1.0E+02	2.874E+05	1.0E+02	2.874E+05	1.0E+02	2.874E+05	1.0E+02	2.874E+05	1.0E+02	2.874E+05
kaolinite	0.496	1.0E-01	2.016E+03	1.0E-02	2.016E+02	6.0E-02	1.210E+03	2.0E-02	4.032E+02	2.0E-02	4.032E+02
Calcite	0.944	4.0E-06	4.237E-02	1.0E-04	1.059E+00	2.0E-04	2.119E+00	1.5E-04	1.589E+00	1.0E-04	1.059E+00
Illite	0.4	1.0E-01	2.500E+03	5.0E-01	1.250E+04	5.0E-01	1.250E+04	5.0E-01	1.250E+04	5.0E-01	1.250E+04
Albite	1.472	5.0E-02	3.397E+02	5.0E-02	3.397E+02	5.0E-02	3.397E+02	5.0E-02	3.397E+02	5.0E-02	3.397E+02
K-feldspar	1.216	3.5E-02	2.878E+02	1.0E-01	8.224E+02	1.5E+00	1.234E+04	1.4E+00	1.151E+04	5.0E-01	4.112E+03
Secondary											
Magnesite		0.01		0.01		0.01		0.01		0.01	
Siderite		0.01		0.01		0.01		0.01		0.01	
Ankerite		0.01		0.01		0.01		0.01		0.01	
Downsonite		0.01		0.01		0.01		0.01		0.01	

Surface areas of silicate minerals are calibrated to fit concentrations of Na^+, K^+, Si, and Al^{3+} (Figure 7.6-Figure 7.10). It appears that the reactive surface areas are consistent in the five batches although reactive surface areas of K-feldspar and kaolinite showed some differences in the five batch experiments.

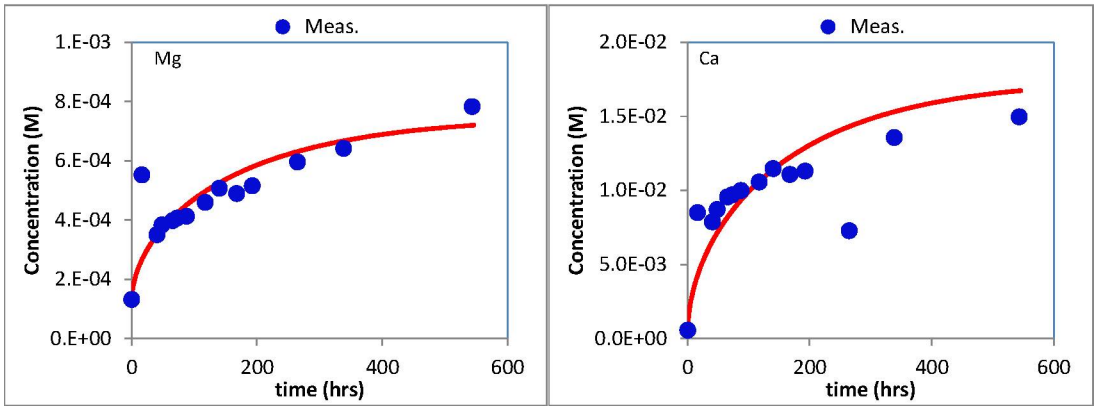

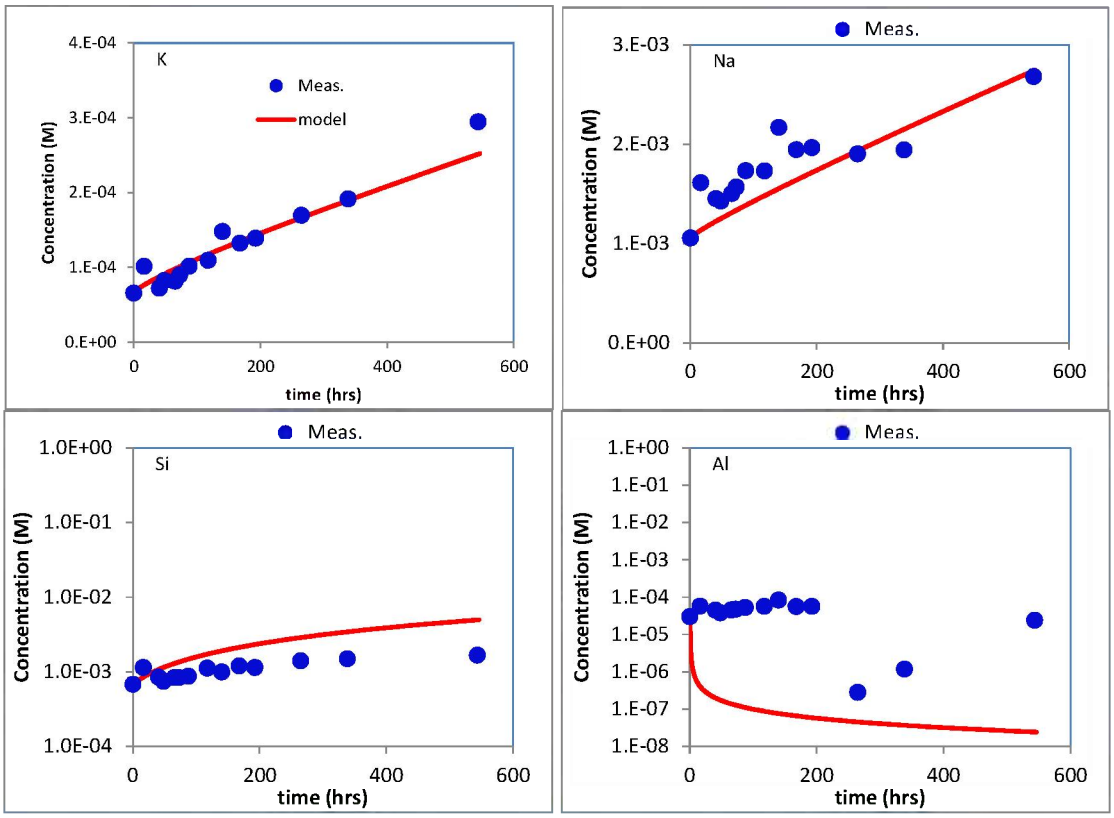

Figure 7.6: Comparison of concentrations of major ions measured and modeled for the A-batch

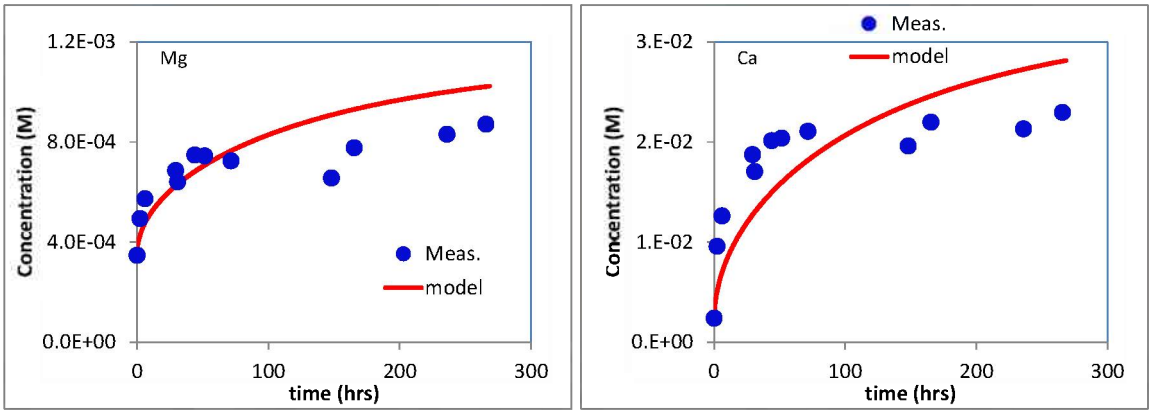

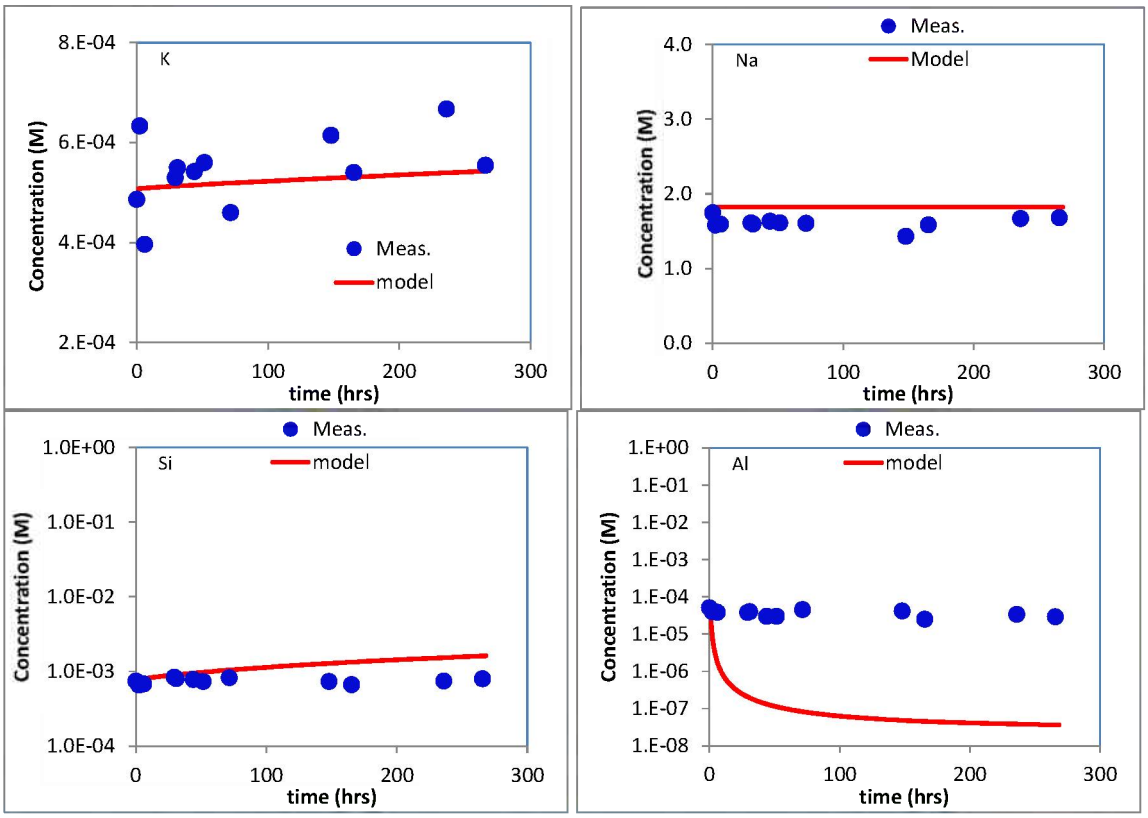

Figure 7.7: Comparison of concentrations of major ions measured and modeled for the B-batch

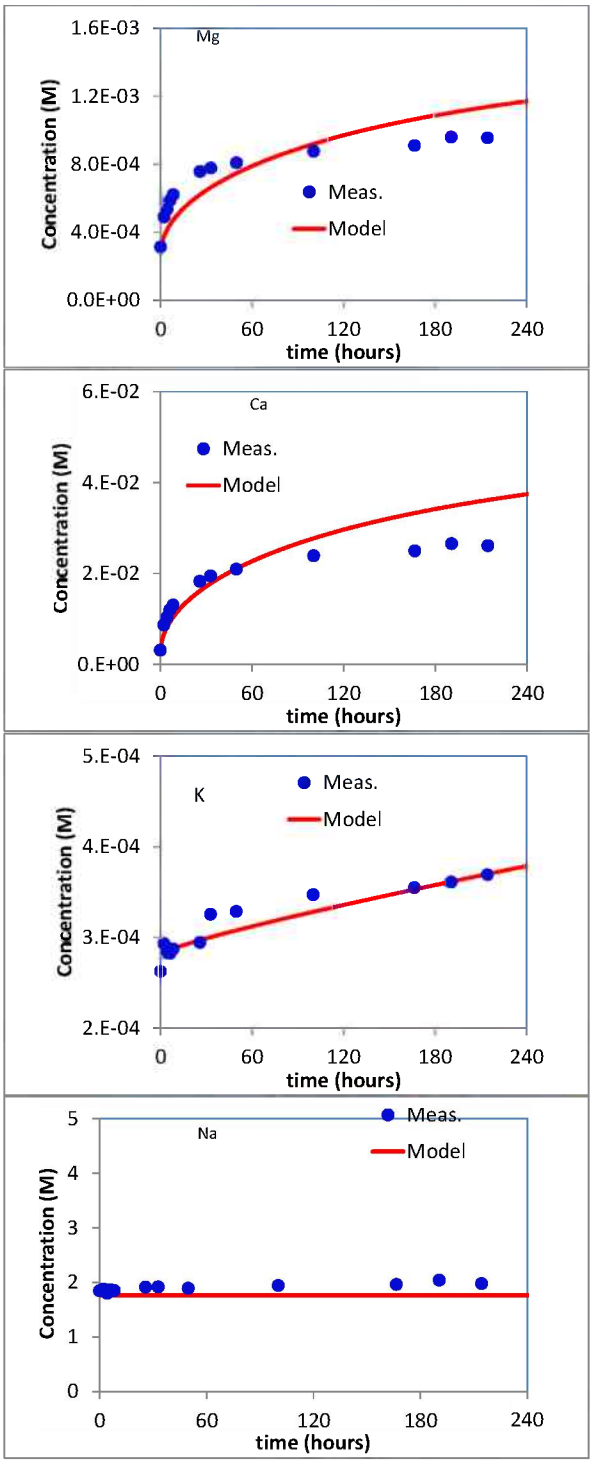
Mg
Concentration (M)
1.6E-03
1.2E-03
8.0E-04
4.0E-04
0.0E+00
Meas.
Model
0
60
120
180
240
time (hours)
Ca
Concentration (M)
6.E-02
4.E-02
2.E-02
0.E+00
Meas.
Model
0
60
120
180
240
time (hours)
K
Concentration (M)
5.E-04
4.E-04
3.E-04
2.E-04
Meas.
Model
0
60
120
180
240
time (hours)
Na
Concentration (M)
5
4
3
2
1
0
Meas.
Model
0
60
120
180
240
time (hours)

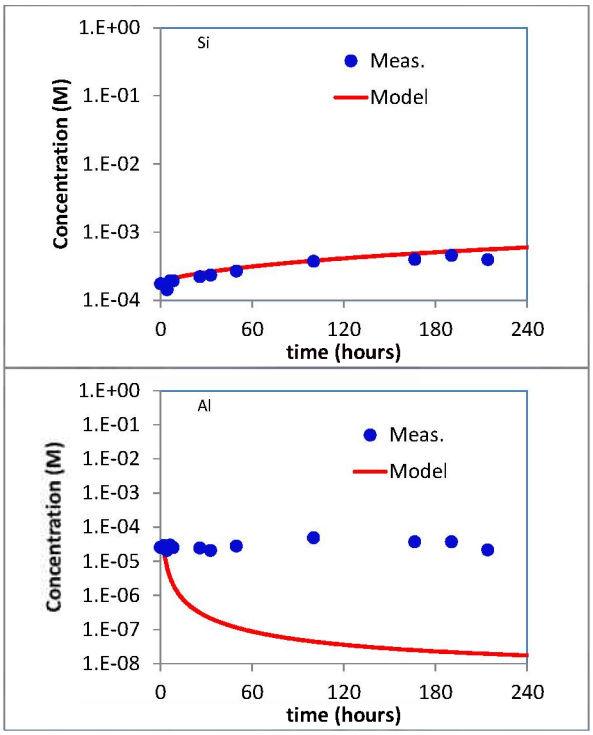

Figure 7.8: Comparison of concentrations of major ions measured and modeled for the D-batch

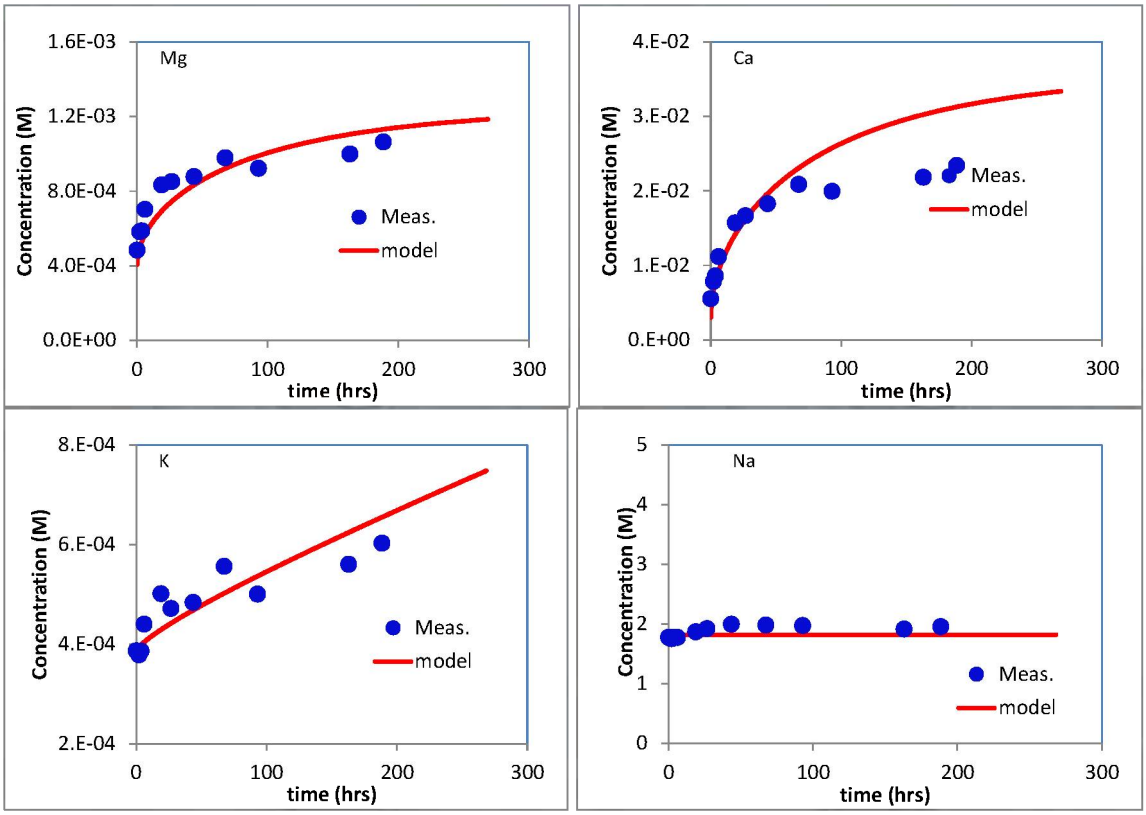

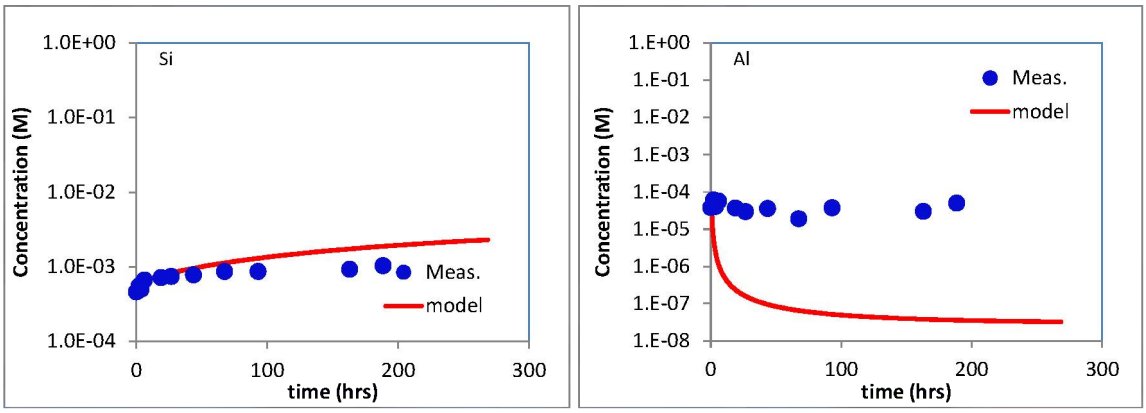

Figure 7.9: Comparison of concentrations of major ions measured and modeled for the E-batch

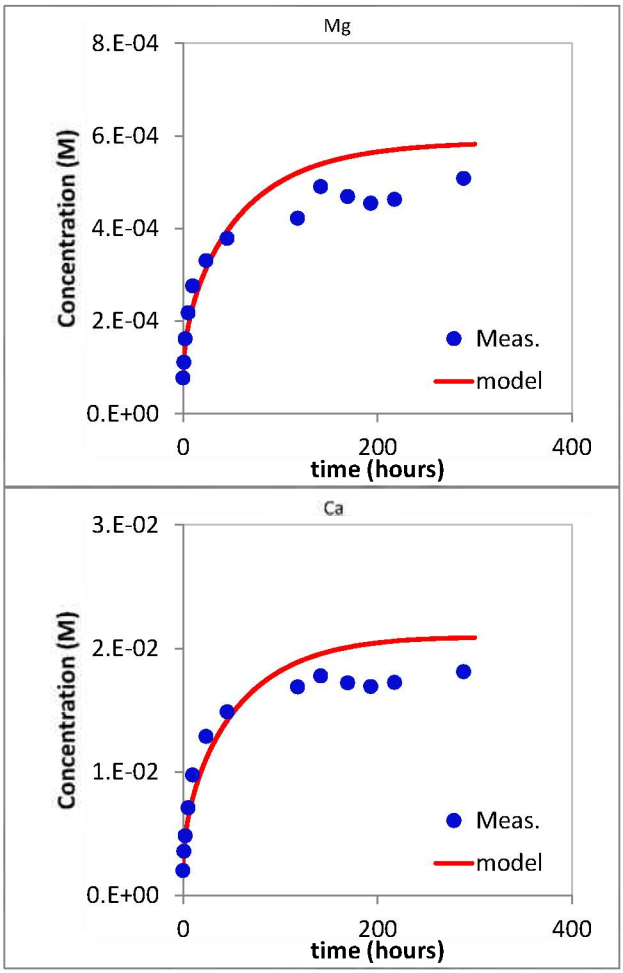

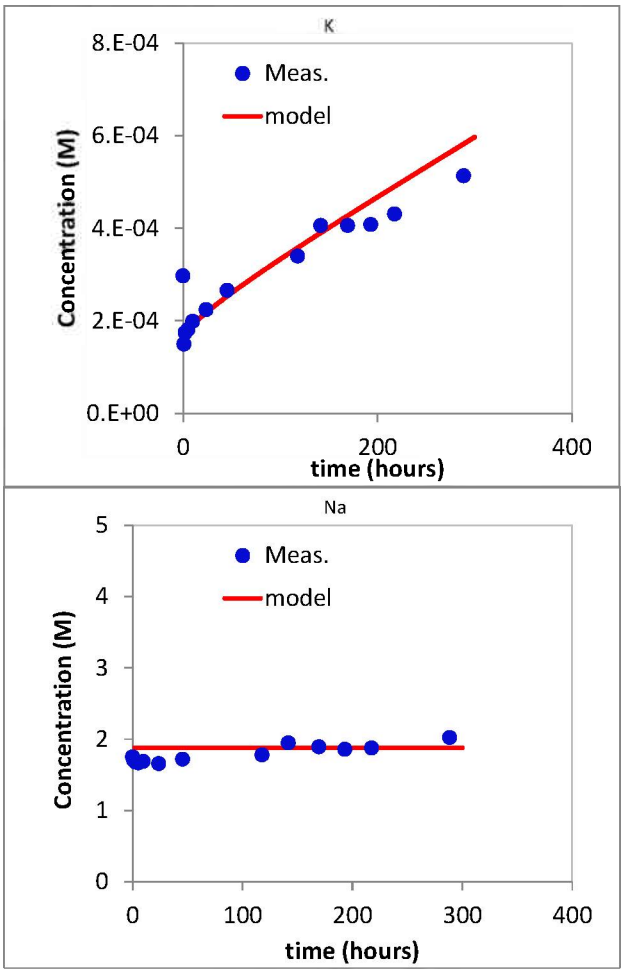
K
8.E-04
6.E-04
4.E-04
2.E-04
0.E+00
Concentration (M)
Meas.
model
0
200
400
time (hours)
Na
5
4
3
2
1
0
Concentration (M)
Meas.
model
0
100
200
300
400
time (hours)

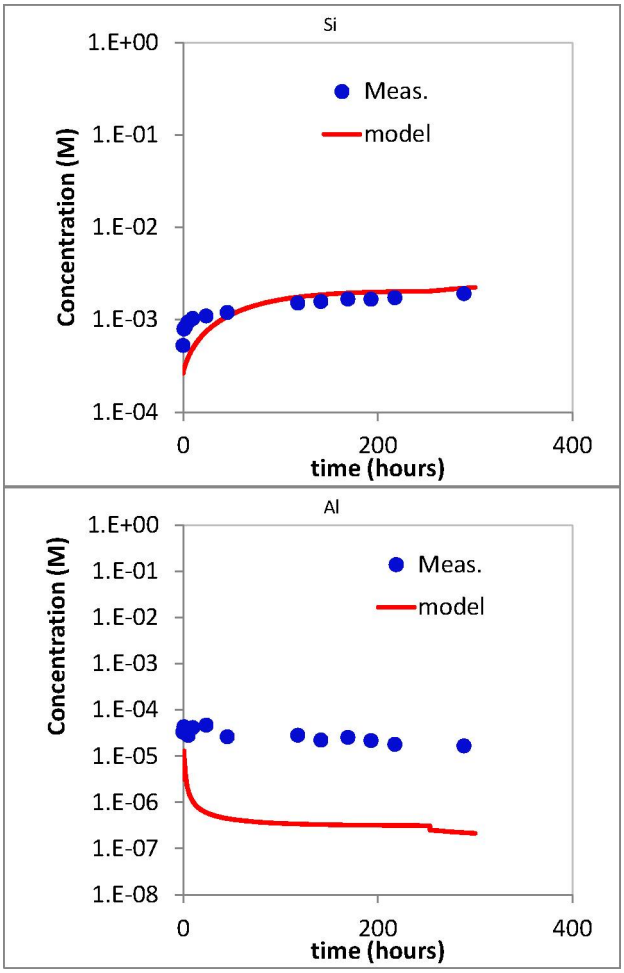

Figure 7.10: Comparison of concentrations of major ions measured and modeled for the H-batch

Generally, the geochemical models reproduced concentration measurements of Ca and Mg well (Figure 7.5), confirming dissolution of calcite when CO_2 was injected into samples of the reservoir. The geochemical models also fit well with K concentration measurements, suggesting that K came from dissolution of K-feldspar when CO_2 was injected. Modeled Na concentrations match well Na concentration measurements (Figure 7.6-Figure 7.10), indicating CO_2 injection leads to dissolution of albite. The geochemical models slightly overestimate Si concentration measurements and underestimate Al concentration measurements. Si and Al are dominated by dissolution-precipitation of silicate minerals and potential secondary minerals. Proper selection of secondary minerals in the geochemical model seems very important. Geochemical models show that Dowsonite precipitates in the B, D, E and H batch experiments (Figure 7.6), not in the A batch experiment because of higher salinity (higher Na+ concentration) and injection of CO_2 in the B, D, E and H batch experiments.

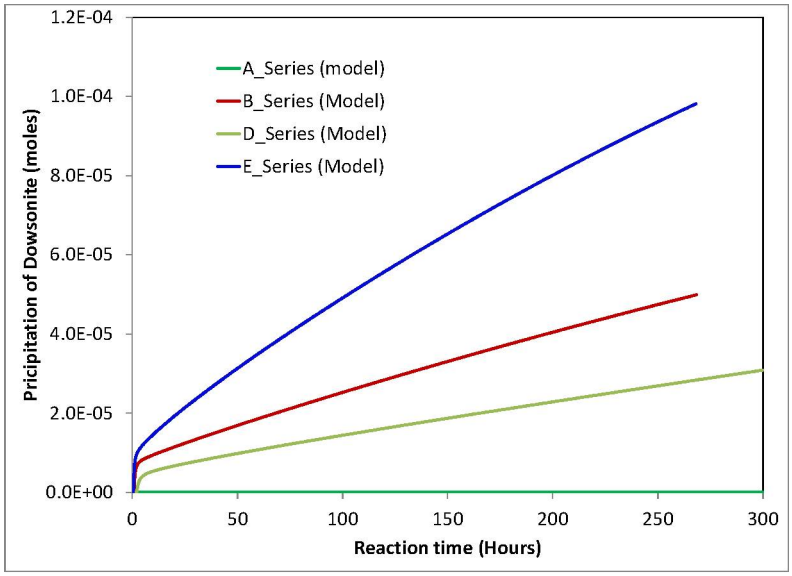

Figure 7.11: Cumulative amount of Dawsonite precipitation over the time calculated in the geochemical models.

The results of the batch experiments are also presented in Mickler (2014).

8 Task 8.0: Leakage Pathways

During the first 2 years of the Study, Task 8 consisted of considering feasibility a P-Cable system (before the augmented funding), planning, ordering and receiving the P-Cable system (Figure 8.1). During the final 2.5 year of the Study, operation of the P-Cable system and data acquisition were the primary activities associated with Task 8.

The P-Cable system allowed for the acquisition of very high-resolution 3D seismic (HR3D) of the shallowest 800 to 1500 milliseconds (ms) (approximately 1 kilometer) of the subsurface. With these data the Study's geoscientists expected to be able to analyze the shallowest section of the geologic subsurface (i.e., the overburden or confining system), which would comprise the sealing (a.k.a. "caprock") units above a potential CO_2 sequestration site. With such a dataset the stratigraphy and possibly the natural fluid flow system would be visible in unprecedented detail. The three acquired HR3D datasets met expectations, and each subsequent dataset yielded improved results as acquisition and processing techniques advanced.

Interactions between the BEG and the manufacturer, Geometrics, Inc. were initially conducted by Drs. Nathan Bangs and Matt Horbach because they had previous experience with an older version of the P-Cable. After delivery of the system, which spanned the time frame from July 2011 – June 2012, the main interactions between Geometrics and the Study were conducted by PI, Dr. Tip Meckel and co-PI, Ramon Trevino.

The first components of the system to be delivered were the paravanes (Figure 8.2). The final major components to be delivered were the four large, specialized winches (Figure 8.3), manufactured by Geometrics' subcontractor, DT Marine. After delivery of the marine components of the system, it was assembled at the BEG and tested (Figure 8.4).

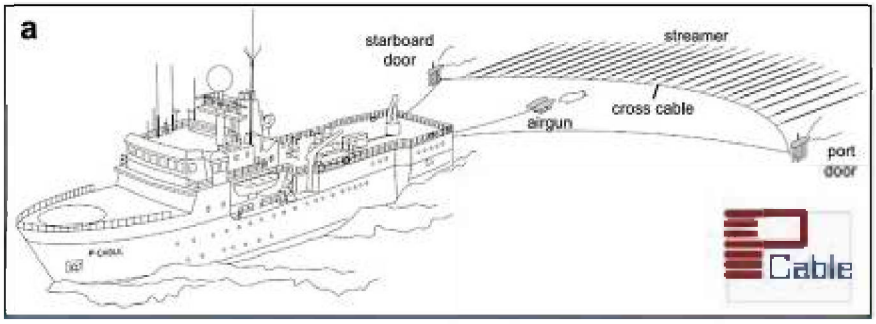

Figure 8.1: Diagram of a deployed P-Cable system. Note the starboard and port doors (another term for "paravanes").

Figure 8.2: Photo showing the starboard and port paravane doors immediately after delivery at the Bureau of Economic Geology receiving dock. Tip Meckel on the right for scale.

June 12, 2012

4 Winches purchased from DT Marine

Figure 8.3: Photograph of the four custom-designed and manufactured P-Cable winches in the manufacturing facility of DT Marine Products, Inc (Houston, TX). The photo was taken on June 12, 2012 during their inspection by Tip Meckel. Note the labels for each, respective, winch. There are two winches for the, respective, lines connected to P-Cable system paravanes (i.e., one for the port paravane and another for the starboard paravane). There is one winch for the cross-cable (aka "P-cable), and one winch for the data signal cable.

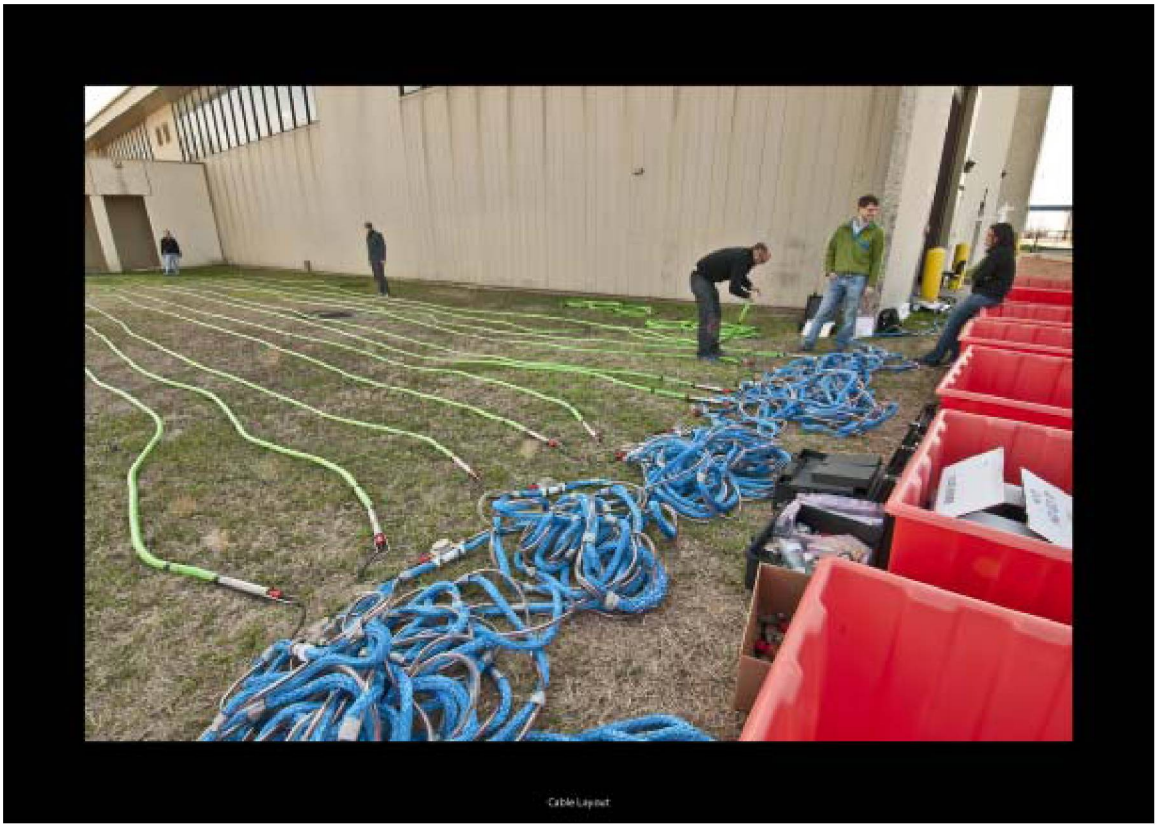

Figure 8.4: Final system assembly and powered system test.

The first and second datasets were collected during 2012 and 2013, respectively, in the area shown in Figure 8.5. The area was of great interest to the Study because of the well-known and documented presence of the San Luis Pass Salt Dome (SLPSD) a deep-seated salt dome that extends to just beneath the present seafloor. The first HR3D dataset was collected using the R/V Iron Cat (Amelia, LA) in July, 2012 Figure 8.6. As with all field operations, many issues and challenges were overcome during the 2012 HR3D acquisition, and in the end a complete seismic dataset was acquired. Initial, pre-processed results looked encouraging (Figure 8.7). However, the fully processed dataset's quality was lower than expected (Figure 8.8). The goal of the data processing was to preserve the very high frequency content (up to 200 Hz) and to image very small displacement faults and variations in stratigraphy.

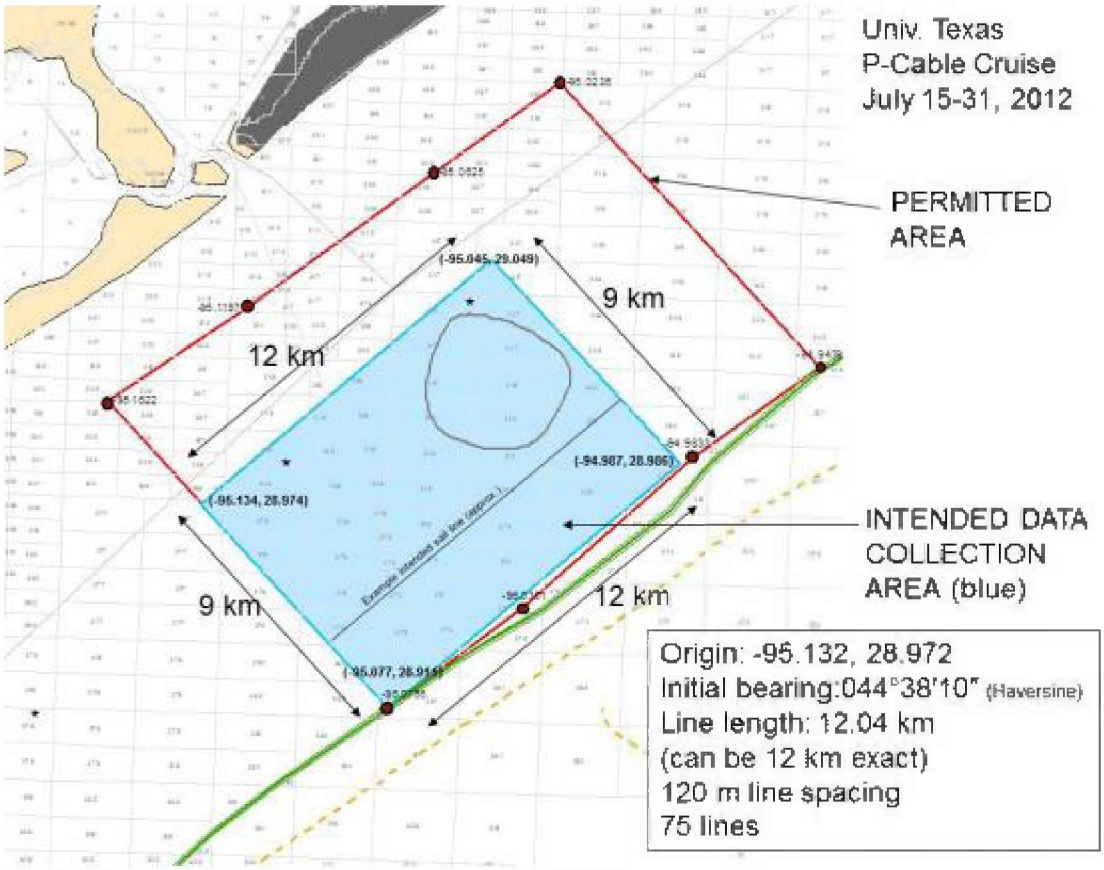

Figure 8.5: Map view of the San Luis Pass area. The southwestern end of Galveston Island is shown in dark gray. The permitted area is within the red rectangle. The survey area is within the light blue rectangle. Note the sub-circular shape in the north corner of the survey area. The shape depicts the approximate outline of the San Luis Pass Salt Dome.

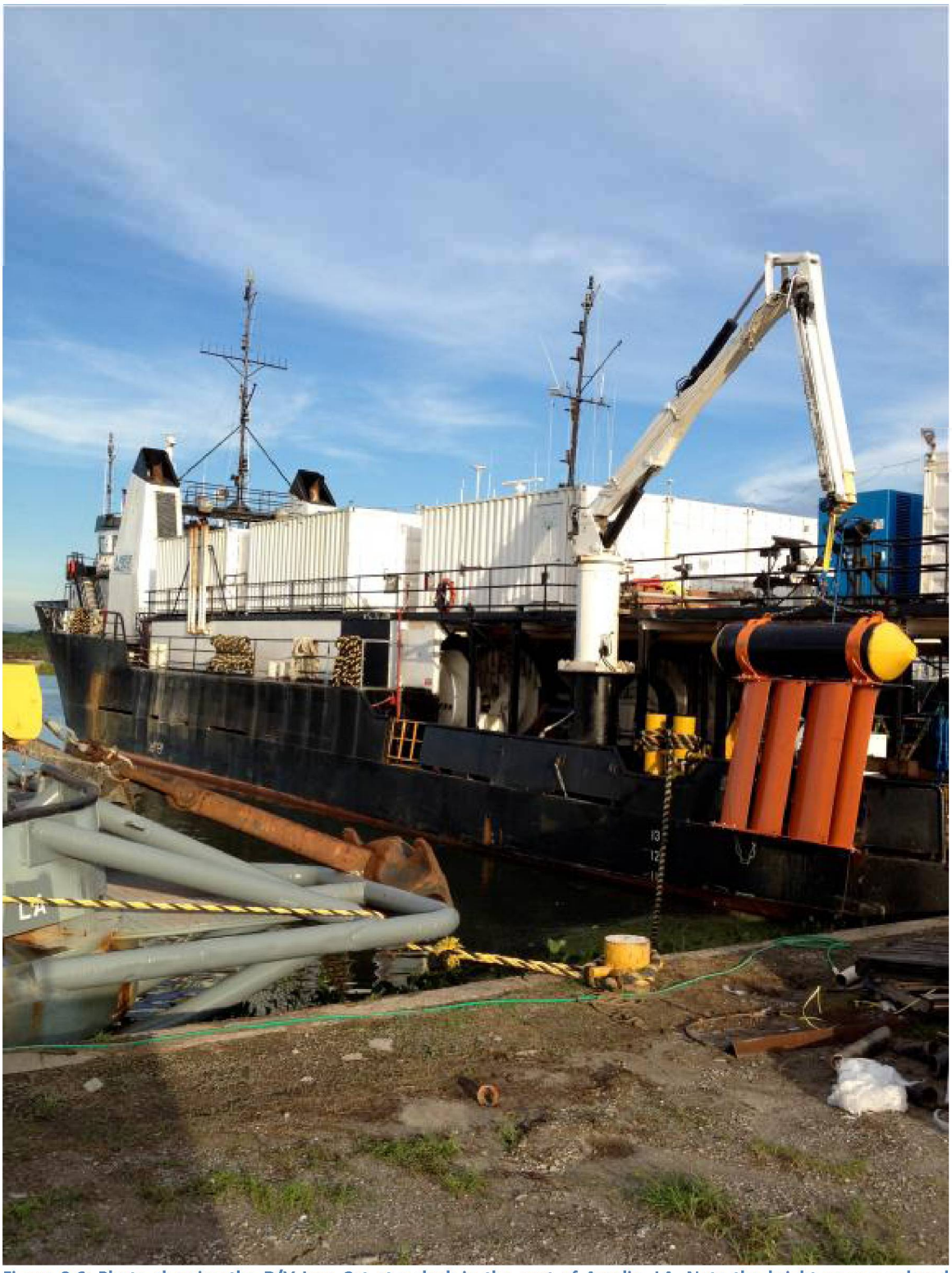

Figure 8.6: Photo showing the R/V Iron Cat at a dock in the port of Amelia, LA. Note the bright orange-colored paravanes and black and their yellow floats strapped to the side of the ship.

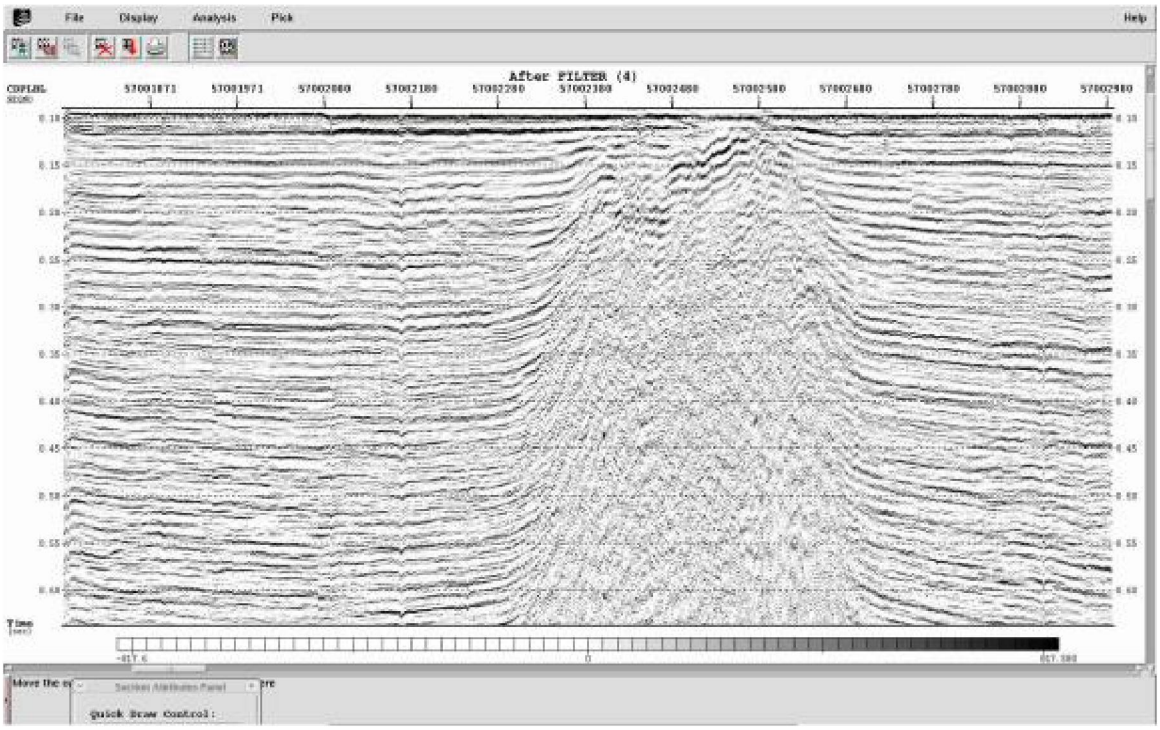

Figure 8.7: Gathers before and after moveout from sail line 5656A. Left hand side of the figure shows gathers sorted into traces from each of 20 shot with a common streamer channel (channel 70 – 75). Right hand side shows the same traces after applying a normal moveout using a velocity of 1500 m/s. At the top is a plot of the source-receiver offset in meters, and the receiver y-component position in meters. The misalignment of the traces after moveout is a function of the offset range variations. Note the large sub-vertical feature in the center and center-right of the figure; this is a seismic depiction of the SLP salt dome. The vertical scale is in time (seconds).

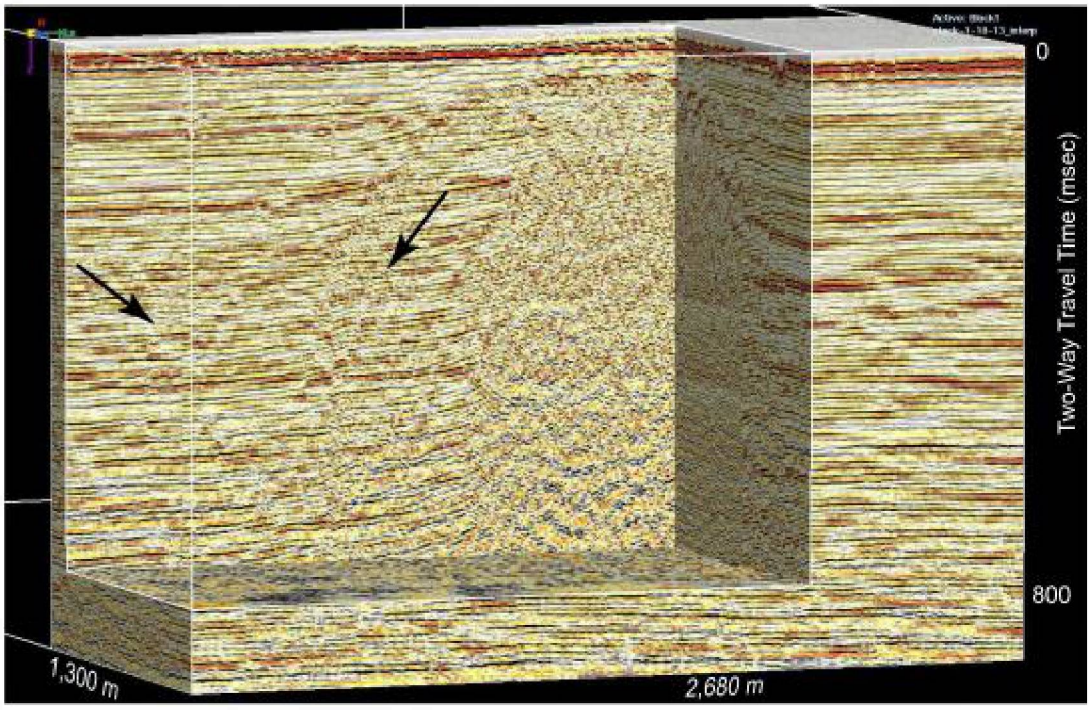

Figure 8.8: A perspective view of a piece of the 3D seismic data volume. The cube shows a cut away into the volume through the SE edge of the salt dome. The salt extends horizontally into both vertical planes and lies about 40m below the seafloor. Arrows show the orientations of two conjugate fault systems. Both of these faults have very small offsets and are identifiable by subtle changes in reflection amplitudes of horizontal strata and small vertical displacement.

Analyses of the 2012 dataset indicated that the main issues were related to incorrect navigation and/or relative timing of data from each of the successive lines. Even though most of these issues were apparently resolved, more improvement was still possible. Consequently, in the spring of 2013, field tests were undertaken to find the possible sources of error. Principal Investigator, Dr. Tip Meckel and GRA Julie Ditkof traveled to the BEG's Houston Research Center during the last week March, 2013. They conducted a 'static field test' (Figure 8.9) with navigation subcontractors and research partners NCS Subsea, Inc. The main issues were accurate absolute positioning of the receivers and sources and relative timing of data from each of the successive lines.

Figure 8.9: Static field test using the cross cable. A series of tests were conducted to verify the accuracy of algorithms used to calculate streamer receiver position during the San Luis Pass dataset acquisition in July 2012.

The static field test was conducted using the cross cable portion of the acquisition system, to which the individual streamers with receivers are attached at junction boxes during data collection. The cross cable was laid out in a field (George Bush Park) in suburban Houston. To assure accurate positioning, geodetic monuments were installed and GPS referenced. These monuments were used to survey in positions of junction boxes for various test-array geometries. Surveyed positions were taken to be 'true' positions of junction boxes, and these were compared with numerical solutions of positions calculated using only cross cable end point positions and orientation of junction boxes using the internal compass data. The latter are used to locate receivers while at sea. So, the tests conducted were meant to better-understand any sources of error in the positioning algorithm.

Cross cable geometries were constructed in the field by dragging the cross cable end points (using field vehicles) along the various separation corridors (Figure 8.2). Figure 8.11 provides an example of calculated receiver positions superimposed on a satellite image of the static field test location. The receiver positions were determined using the GPS positions of the ends of the cross cable and the junction box compass orientations.

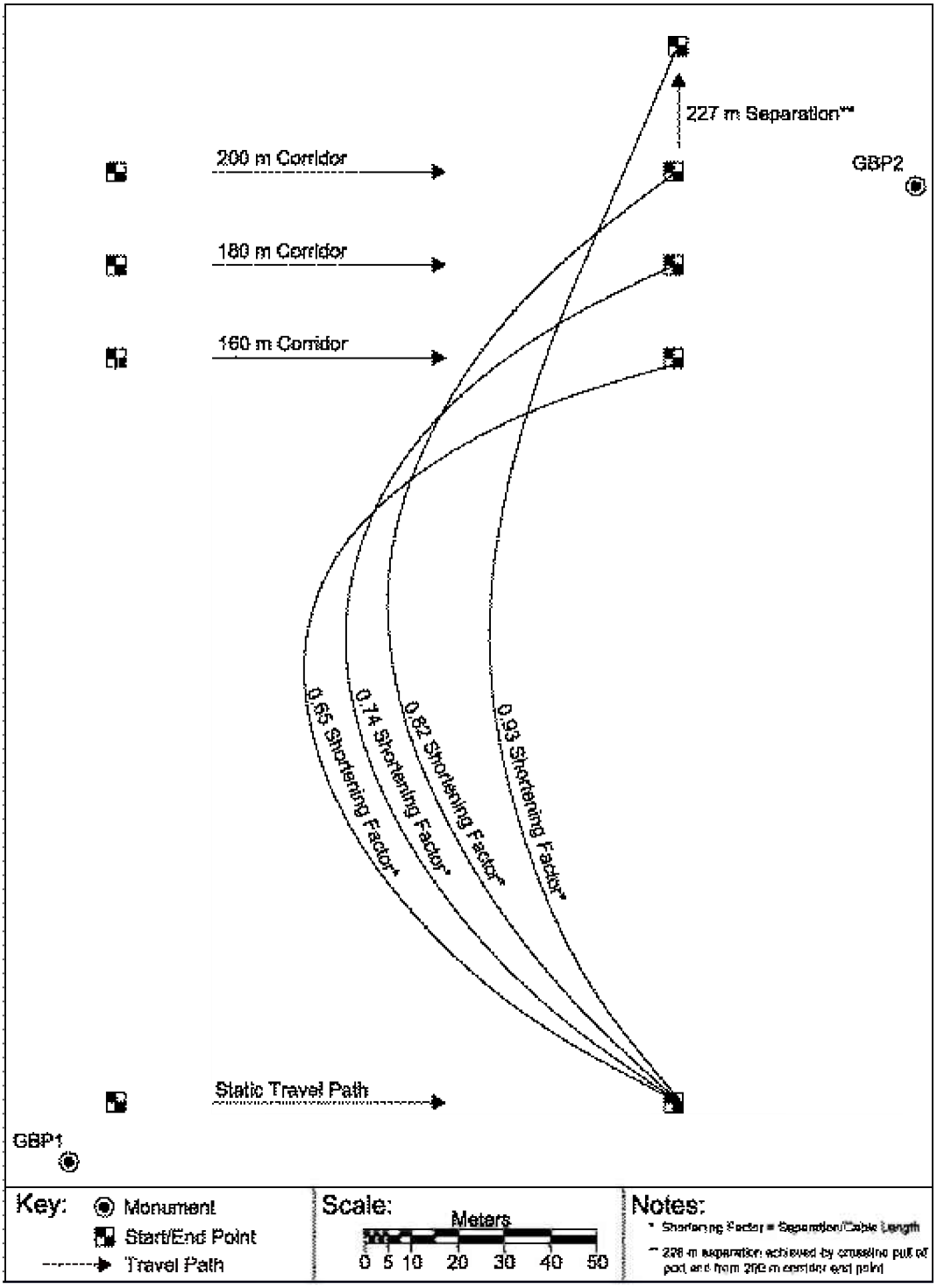

Figure 8.10: Schematic model of the static field test of the P-Cable's crossline (a.k.a., cross cable). The model shows four cross cable geometries used in the static field test. Each cable represents a different end-point separation distance and shortening factor. Shortening factor is the total cable length divided by the end-point separation for each of the four geometries investigated. Cross cable geometries were constructed in the field by dragging the cross cable end points along the various separation corridors (indicated by labeled arrows) using field vehicles.

Figure 8.11: Satellite image of the static field test location with superimposed GPS receiver positions. Blue and red points represent receiver positions determined by two, respective, algorithms. Junction box positions are calculated and then compared to known surveyed positions using a total station and established geodetic benchmarks.

A primary result from the static field test indicated that the software solution for receiver positions was robust but sensitive to the distance from the constrained GPS location of the end of the cross cable to the first junction box and tow point on the cross-cable. The conclusion is important for validating the commercial software solution for future data collection activities. A second initial result is that the offsets used for initial processing of the San Luis Pass HR3D data were less than they should have been, which likely resulted in some positioning error and affected the subsequent processing of the data. After the field test a new set of receiver locations was calculated and provided for another round of data processing. Results from one line indicated that the revised positions provided improved data quality, and the rest of the data volume was processed using the new positions.

In addition to the issues related to positioning, which the static field test addressed and corrected, there were also logistical issues with the vessel used in the 2012 survey acquisition cruise. In order to address the issues a different organization and vessel were identified and utilized for the 2013 and 2014 surveys. In both of those surveys, TDI-Brooks International, Inc. and their vessel, the R/V Brooks McCall (Figure 8.12), were incorporated into the research effort related to the P-Cable High Resolution 3D (HR3D) seismic acquisition system. Due to the time and effort required to find a new vessel and because of the logistics and scheduling conflicts, the 2013 survey was delayed by 6 months; it occurred in late October () instead of May.

Figure 8.12: Photo of the R/V Brooks McCall (TDI-Brooks International, Inc.) at it's dock in Freeport, TX on October 16, 2013 during initial installation activities for the Study's 2nd HR3D survey acquisition.

Figure 8.13: Aerial photo of the R/V Brooks McCall during active HR3D (P-Cable) seismic acqusition in the latter half of October, 2013, offshore San Luis Pass, Tx.

The data acquired in the 2013 survey were clearly improved when compared to those of the 2012 survey. From the start, data collection results were encouraging. The use of 90 cu. in. pneumatic sources instead of the 210 cu. in. sources used in 2012 appeared to qualitatively result in better data when compared to the 2012 survey (Figure 8.14).

After considerable effort, a much better array spread was achieved. In terms of paravane separation, cross-cable shape, and source receiver offsets the spread close to what the static field test data indicated would be ideal. In addition, modeling that was requested and purchased from Global Dynamics prior to the 2013 survey cruise was not a direct match, but provided good guidance and was worth the effort. In addition, specialized equipment from 3PS, Inc. (a new instrumented sheave for the signal cable winch) proved useful for tow line payout distance and real-time information during deployment/recovery. The instrumented sheave was fairly useful, but ultimately, the tension measurements were only relative. However, the data could be plotted in real time in the lab, thus somewhat reducing the possibility damaging the signal cable (a very expensive component of the system).

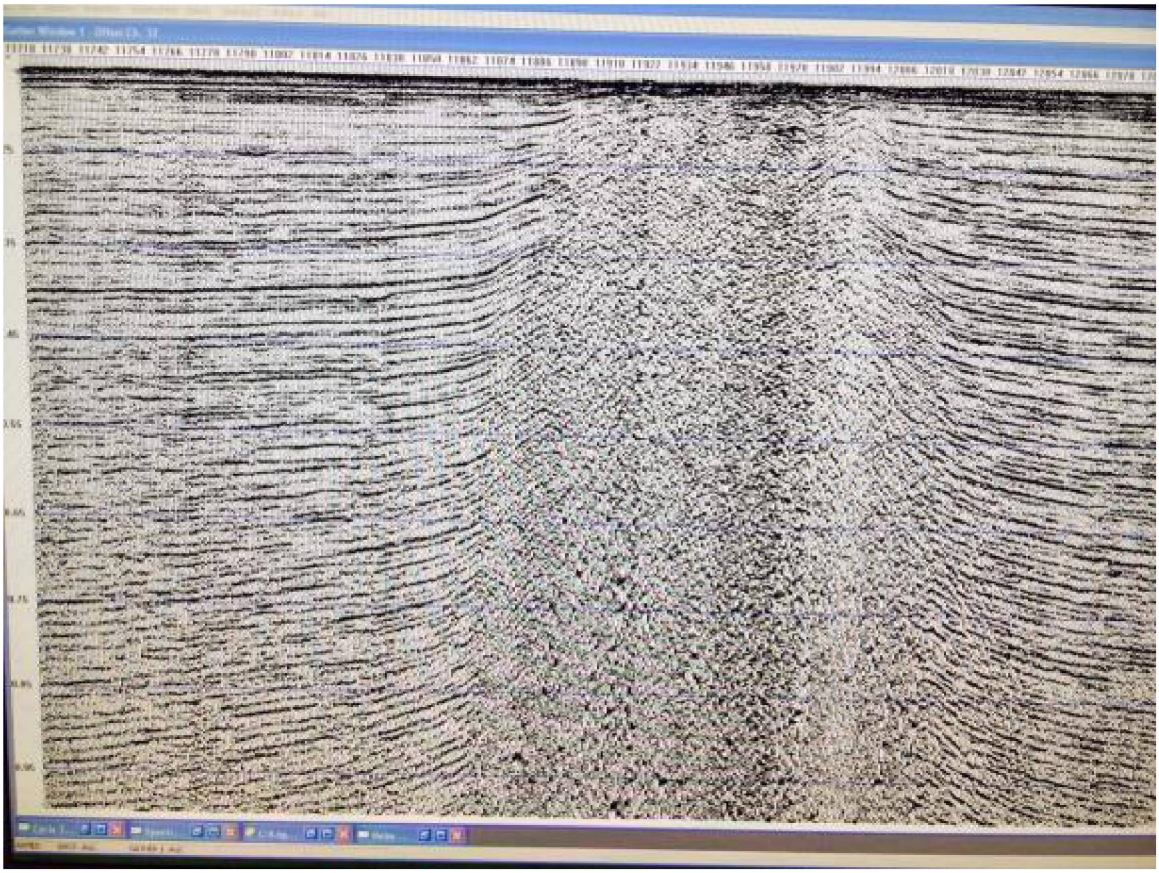

Figure 8.14: Photo of a computer monitor showing a one-channel field record over part of the San Luis Pass salt diapir.

Processing of the 2013 P-Cable dataset resulted in great improvements in data quality versus the 2012 dataset. Figure 8.15 presents three time slices from the dataset at 108, 144 and 173 milliseconds (ms), respectively and shows clearly identifiable geologic body morphologies. In each of the time slices the San Luis Pass Salt Dome is visible as the sub-circular body in the lower right-hand portion of each slice. Other visible geomorphic features include 1) a fault shown as a thin green line near the upper left corner of each time slice, 2) a low-sinuosity (fluvial?) channel (blue arrows) on 108 ms time slice and 3) a higher sinuosity channel (orange arrows) on the 173 ms time slice.

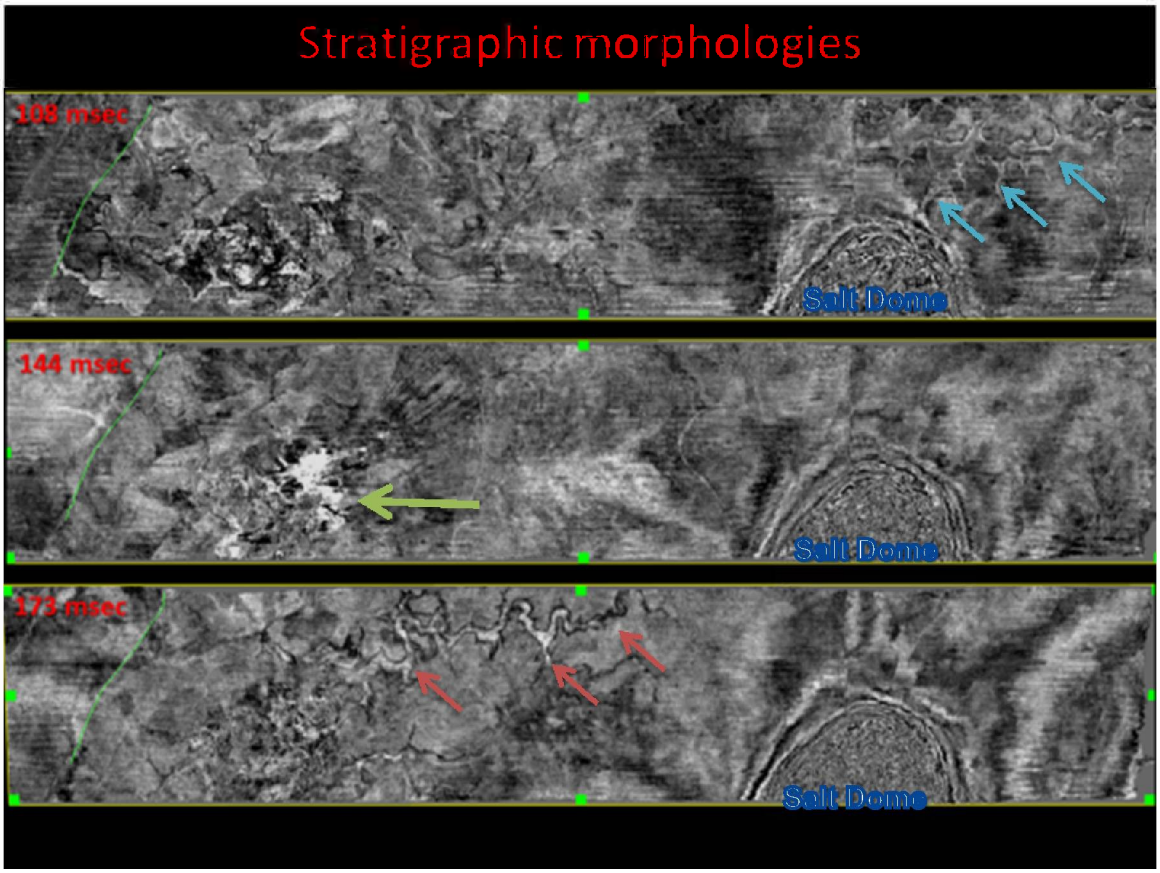

Figure 8.15: Slices in the time domain (i.e., at 108, 144 and 173 milliseconds, respectively) through the fully processed P-Cable dataset collected in October, 2013.

Figure 8.16 shows a three-dimensional amplitude volume of a portion of the October, 2013 dataset in which a time slice at approximately 100 milliseconds (ms) comprises the upper portion of the image and the foreground is a vertical slice (in the time domain) from 100 ms to approximately 700 ms. The vertical right edge of the image includes the edge of San Luis Pass Salt Dome previously noted in the horizontal time slices of Figure 8.15. Note the steep vertical nature of the salt dome.

The two light green arrows in Figure 8.16 identify a significant, previously unrecognized feature, in the San Luis Pass area. The same feature is identified by a light green arrow on Figure 8.15. In the vertical seismic view (Figure 8.16) the feature expresses itself as a dimming or blanking of the amplitudes, sometimes called wipe-out zones. In the horizontal dimension (i.e., time slice) the feature is expressed as a "bright" amplitude, the highest amplitudes in the entire volume. Note how bright the red (positive) and blue (negative) amplitudes are relative to the rest of the volume. The vertical view of this feature is typical of a "gas chimney," ((Gay et al., 2007); (Ligtenberg, 2005)) and we interpret the feature to indicate active gas migration from depth to shallower horizons.

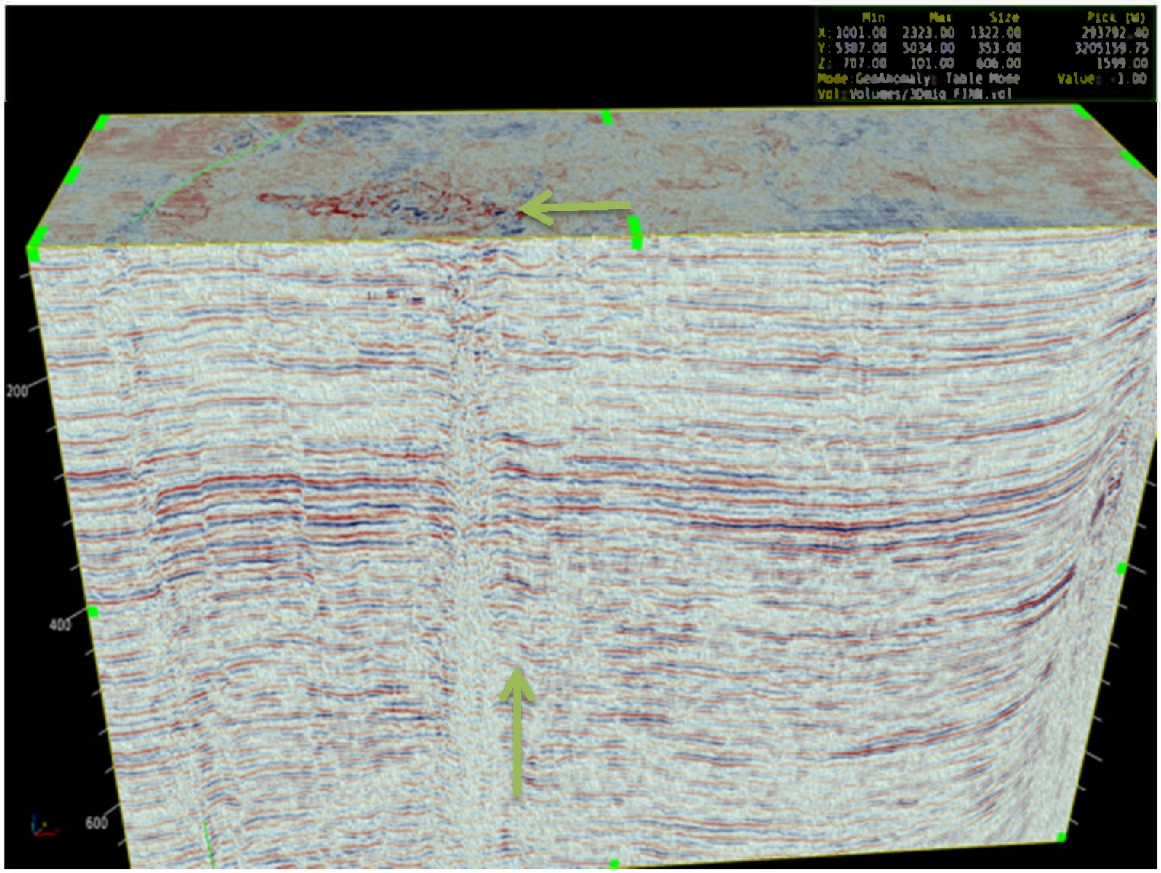

Figure 8.16: A screen capture showing a three-dimensional volume of the October, 2013 dataset. The upper surface of the volume is a time slice at approximately 100 ms. The foreground is a vertical transect from approximately 100 to 700 ms.

The high amplitudes of the gas chimney are strong enough to allow for their extraction and visualization as "geo-bodies" (Figure 8.17). Initial interpretation of the geo-bodies indicates that gas migrates laterally increasing distances with decreasing depth. The gas chimney's presence indicates that deeper potential reservoirs below the chimney's location are not good candidates for CO2 storage.

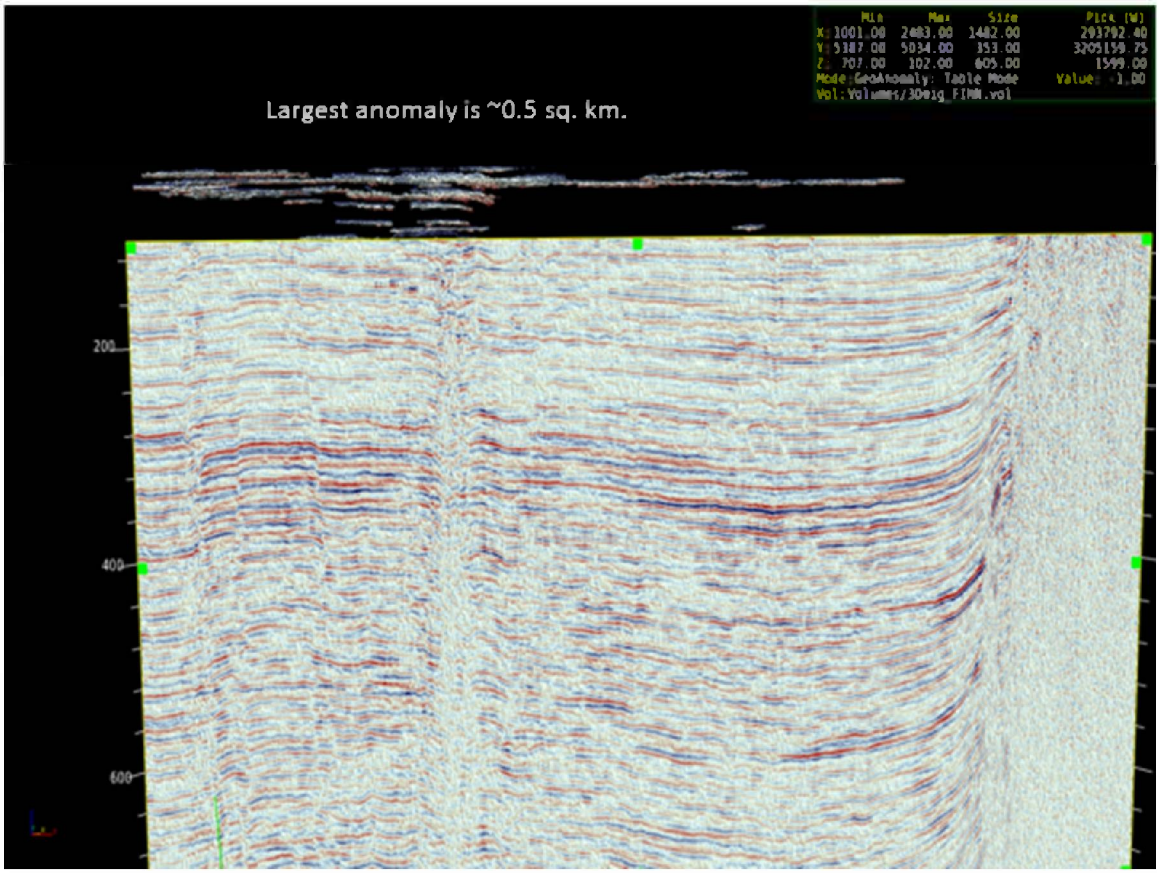

Figure 8.17: Screen capture of the same vertical seismic transect as in figure 8.7 but in this case with shallow "geo-bodies" (based on high amplitudes) extracted from the 3-D dataset.

The gas chimney identification and observations verified the initial research impetus for acquiring the P-Cable system and proved its utility and promise as a CO_2 monitoring tool. Similarly, the 2013 HR3D dataset did not confirm the initial research team's hypothesis that the San Luis Pass Salt Dome was a poor candidate for CO_2 storage. On the contrary, the dataset does not indicate any active vertical fluid migration near the salt dome. The area near the salt dome may still be prospective for CO_2 sequestration.

With the positive outcome from the 2013 survey, a new survey area was selected for the third and final (i.e., 2014) HR3D survey of the Study. Figure 8.18 shows the 2014 survey location, which was chosen because it was not near any known salt features, and there were indications from the Study's regional analyses (e.g., Figure 8.19 and Figure 8.20) that there were very thick sandstone units and potential confining zones (i.e. "caprocks"). In addition, the area encompassed historic oil and gas fields (Figure 8.19). Consequently, the new area was expected to not contain large gas chimneys.

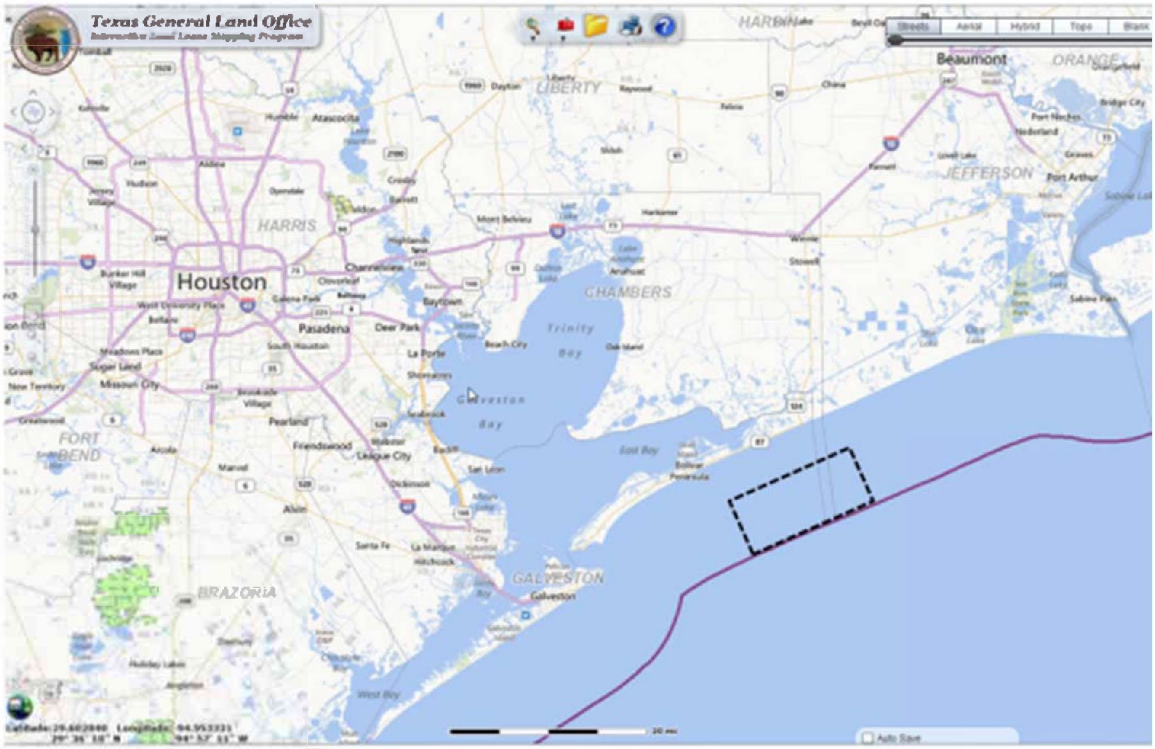

Figure 8.18: Map showing the location (within dashed rectangle) of the next (third) P-Cable cruise.

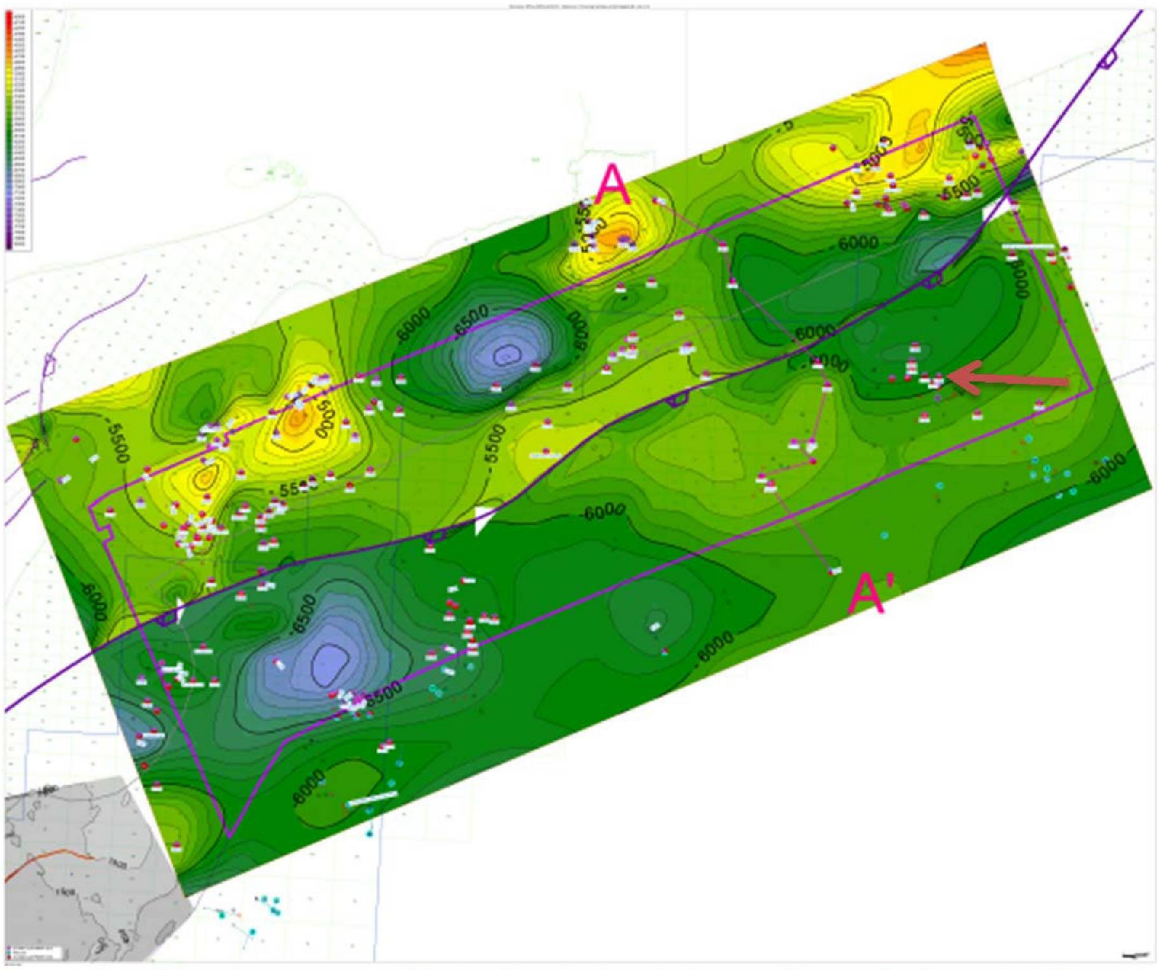

Figure 8.19: Well-based structure map of the Amphistegina B top in the area of interest for the next P-Cable survey. The area encompasses several small oil and gas field (e.g., the red arrow). Note line of section AA' for Figure 8.20.

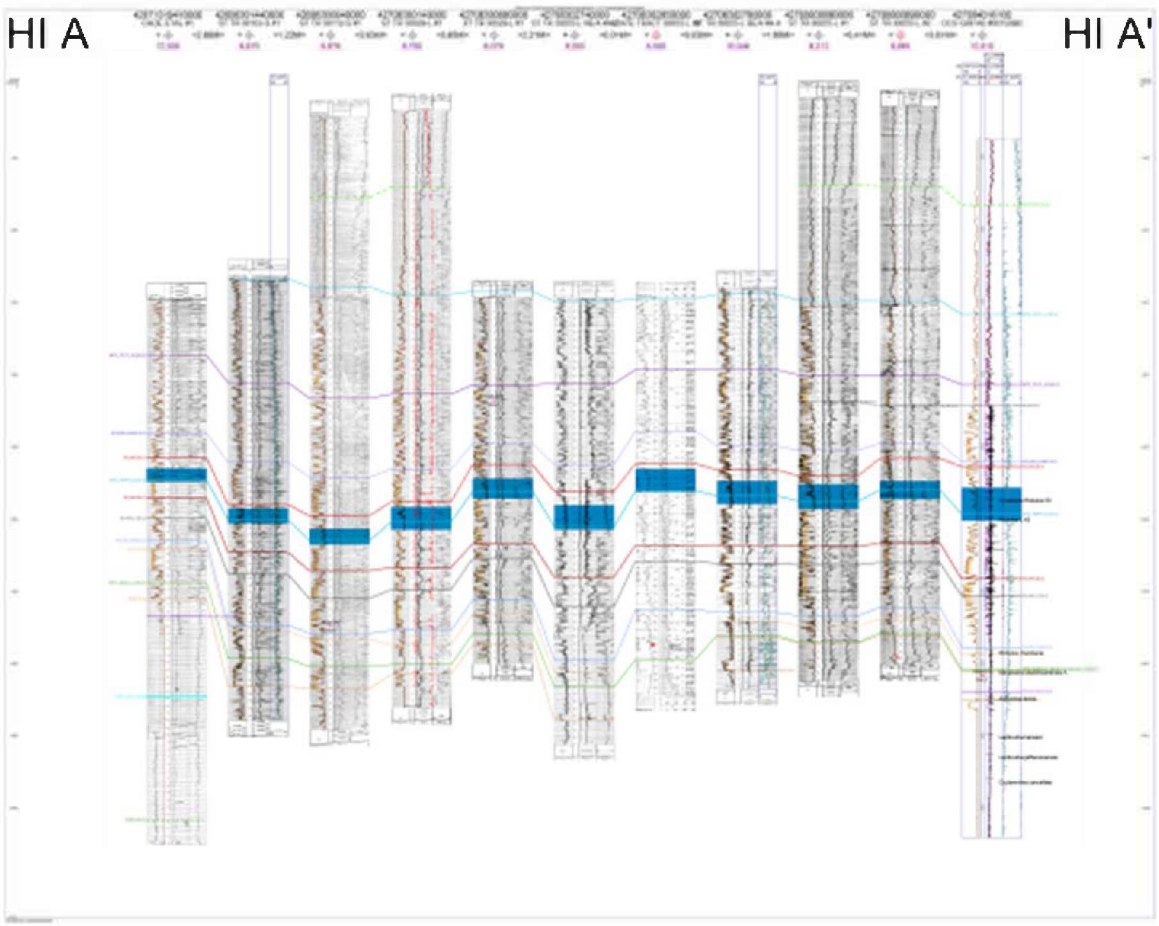

Figure 8.20: Structural cross section AA' (see Figure 8.19) in a dip direction. Note the blue shaded unit that encompasses the Amphistegina B maximum flooding surface, a potential confining unit for the underlying sandstones.

The Study's third HR3D (P-Cable) seismic survey acquisition cruise occurred in the first half of April, 2014. As with all complex field operations, there were operational challenges. However, despite recurring problems with various GPS units (e.g., starbord tripoint assembly, port paravane GPS), the P-Cable system was deployed and operational within approximately 36 hours of departing port. This was the earliest deployment of the study's three surveys. The relatively quick deployment was mostly because of the experience that the science and ship's crews had gained in previous deployments. In addition, learnings from the previous surveys was employed in the 2014 cruise. For example, the pneumatic source (airgun) compression needs had been overestimated for the single 90 cu. in. guns in the 2013 cruise. Therefore, compression were reduced from four in 2013 to three in 2014, and in the latter cruise only two compressors were used at any one time, and then only temporarily.

Several lines of good data were acquired in the first two 24 hour periods (April 3-4), but a malfunction of the signal cable required a return to port (April 5) to change out with the spare signal cable. By the evening of April 6, the system had been re-deployed, but the continued problems with GPS units delayed resumption of data acquisition until the morning of April 7. Data acquisition resumed at approximately 09:00 of April 7 and continued on a 24 hour schedule until midday on April 10.

Ultimately, the survey acquired a total of:

480 In-lines X 6.25m spacing = 3Km
2350 X-lines X 6.25m = 14.687Km

95% of the lines contained data resulting in approximately 42 sq. Km of data (Figure 8.6). Effective record for imaging was about 2.5 seconds twtt (two-way transit time) or approximately 2 Km in some areas.

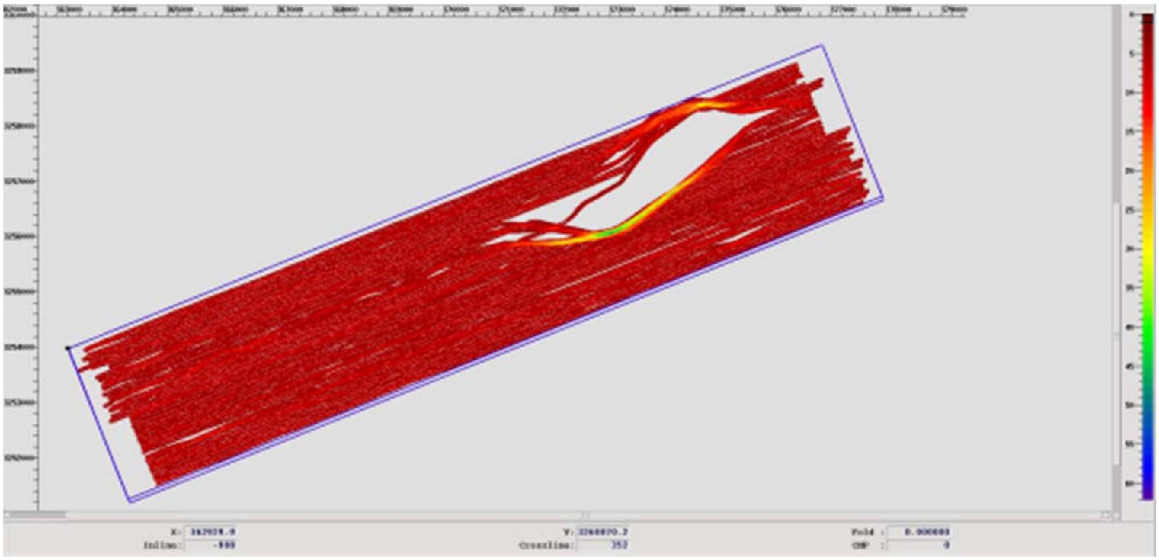

Figure 8.21: Map showing the amount of seismic fold (i.e., the number of field traces that are summed during data processing) with color (scale on the right vertical axis) indicating the number of traces per CDP (common depth point gather). The map also indicates the acquisition coverage. Note the gap in coverage (i.e., gray polygon within the red fold coverage), which is due to an existing oil well platform.

Processing

Experience from the 2012 and 2013 surveys also benefited the post-acquisition data processing. Following is a description of the initial processing stream.

The Study team's processors received the dataset on May 6, 2014 in SEGD format along with associated navigation files in UKOOA p190 format. Quality control of the data included plotting navigation lines and file comparison between observers' reports and the SEGD files. Preserving the auxiliary traces for shot signature removal, the SEGD data were read into internal ECHOS (Paradigm Software) format.

GPS errors at this stage of data collection could be analyzed using the seismic direct/refracted arrivals. This method was used in the previous P-cable projects to determine gross GPS errors. Simply applying a linear velocity (1527m/s) to the first arrivals would cause the first breaks to align about a T_0 which depends on offset and water depth. All cables and hydrophones will align if the positioning is correct. It was determined that the variation was within tolerance (1-2ms across cables) and could be corrected with static corrections or ignored.

The navigation was combined with the data using the time/date stamp, internal models for shot and receiver geometries were created and a suitable CDP (common depth

point) grid was created. A fold map was reproduced (Figure 8.21) and was compared to the navigation plots. Results were satisfactory.

SEGD auxiliary traces were again analyzed for the gun firing delay. A time shift of 98ms was determined from the onset of the first near field energy. Data is 3000ms in length with 0.5ms sampling.

Shot Domain Processing

It was determined from previous work on p-cable type surveys that mixing traces in any domain is highly likely to remove fine detail structures seen on time slices. Our goal was to maintain and improve geological details seen on time slices while adequately enhancing vertical amplitudes.

Processes in order of application

1. Trace Edits - Gross scale trace edits from observers reports and QC work.
2. Static Shift - Time shift to compensate for gun delay. Times were used from first breaks on auxiliary traces to shift the data (98ms)
3. Shot Signature Deconvolution from near field trace on auxiliary traces.
4. Secondary Signature removal using Burg spectral estimation. Process is re-entrant. Output is minimum phase wavelet. We find this two pass process works best.
5. Preliminary Velocity model was picked.
6. Spherical Divergence gain correction.
7. Ensemble equalization, compensate for shot to shot RMS amplitude variation.
8. Water bottom multiple removal (Gap deconvolution). Water depth in this area is very shallow and varies very little from 11m depths. After this point data is assumed to be zero phase.
9. Short period multiple removal using the automatic zero crossing method of gap deconvolution.
10. Wavelet shaping and noise removal.
11. Velocity model building for time migration. Very little velocity variation is seen, emphasis is on velocity model from Dix constrained velocity inversion.
12. Time Stack Volume was produced and loaded into interpretation system for preliminary work.
13. Time migration was performed on the time volume using short apertures (1.5-2 cable spreads)
14. Time migrated volume was loaded into interpretation system.
15. Amplitude adjusted volume was produced within interpretation system (AGC) to allow both Time Slice and Vertical section interpretations.

Figure 8.22 and Figure 8.23 are time slices at 124.5 and 147.5 milliseconds (ms), respectively, from an amplitude volume of the dataset, which had undergone processing steps 1-10. Similarly, Figure 8.24 and Figure 8.25 are time slices at 147 ms and 222 ms, respectively, after processing steps 1-15.

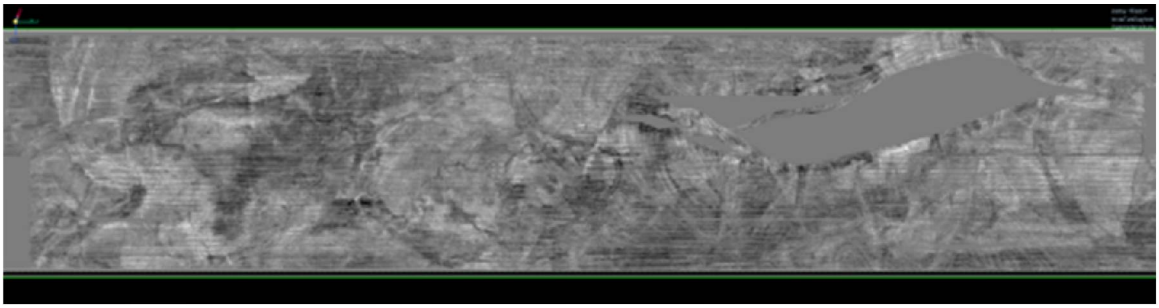

Figure 8.22: Time slice from 124.5 milliseconds (ms). The slice was taken after the volume had undergone processing steps 1-10.

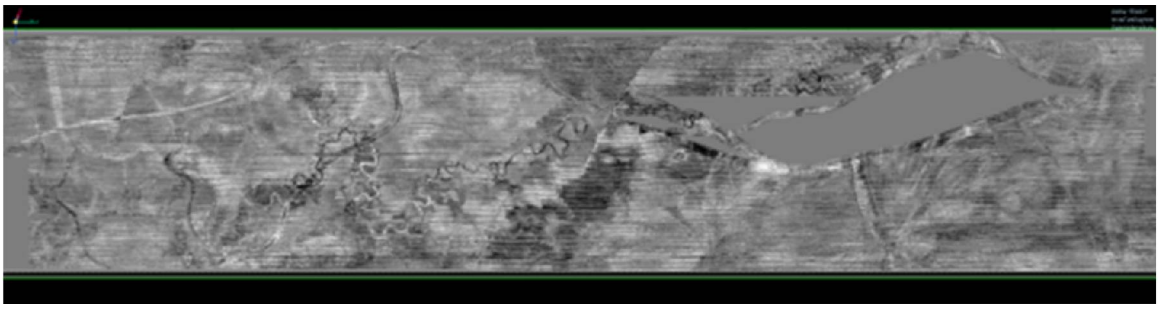

Figure 8.23: Time slice from 147.5 milliseconds (ms). The slice was taken after the volume had undergone processing steps 1-10.

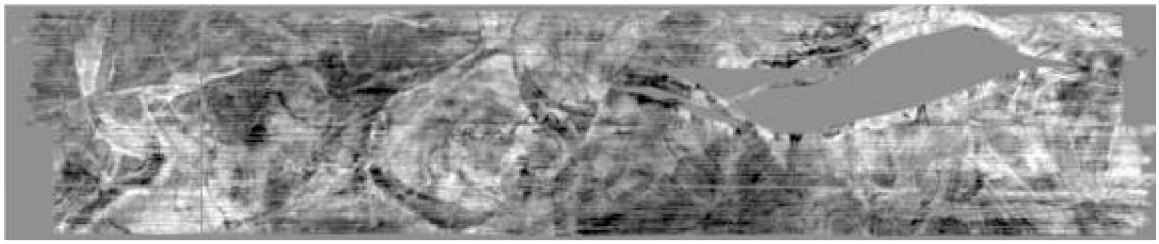

Figure 8.24: Time slice from 147 milliseconds (ms). The slice was taken after the volume had undergone processing steps 1-15 (i.e., including migration).

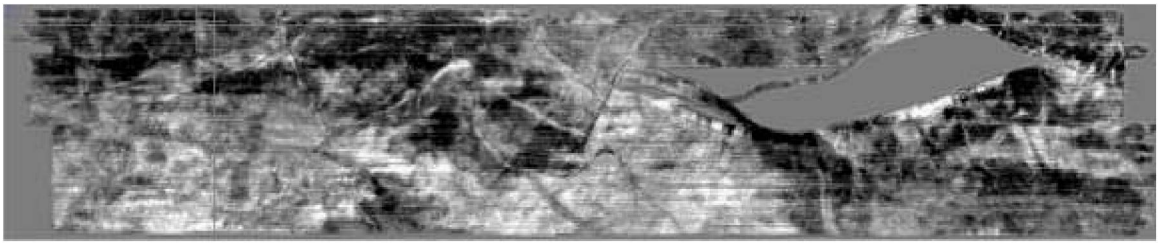

Figure 8.25: Time slice from 222 milliseconds (ms). The slice was taken after the volume had undergone processing steps 1-15 (i.e., including migration).

Processing Methodology

P-cable data have inherent qualities, which prevent a detailed velocity analysis with depth due to the short offsets. The level of detail in the data is best visualized using time slices. Picking channels or faults on a time section can be very obvious, but seeing the same geological features on a vertical section reveals only a vague impression of the 3D object.

The Study's processing needed to accent details in the time slice domain in order to preserve these features. Move out became essentially flat after about 400 ms; so,

between 0-400 some effort was made to detail the velocities. A significant inversion of the velocities occurs from water bottom to about 400ms. This is assumed to be due to unconsolidated sediments. In order to get the best details on the shallow time slices, great care was given to use the time slices as a quality control for the processing.

Earlier tests showed that mixing traces in any domain is highly likely to remove finely detailed structures visible on time slices. Tau-P, FK, array simulation, multi-trace deconvolution and other processes that mixed traces together in any domain were found to cause deterioration of the geological features in the time slice domain. Also, streamer based processing was attempted and was also found to harm the time slice resolution.

High Resolution Deconvolutional Processes for P-Cable (shot domain)

Because some processing tools caused loss of resolution, only a few strictly trace by trace processes were available to use. Fortunately most of the basic deconvolution tools can run in either multi-trace or single trace modes. A processing methodology was formulated to strictly address the convolutional model set by Robinson (1982), specifically page 228-229. The model was extended to include real world noises and systems. For example, spherical divergence is frequently not included in the convolutional model as it is usually a scalar to the observed amplitudes. The utilized software uses an offset-dependent spherical divergence correction based on Ursin (1990). This makes the term for spherical spreading dependent on the velocities of the Earth reflectivity series.

Also during the project, a new software module was released which handled the de-ghosting of the data. This made our software almost in line with the theoretical convolution model. The model is currently:

$W(t)_{obs} = [\,[E_r * W_s * Q\ * S_{geo} * N_{non}] + \text{Noise}\,] * [G_s * G_r\,] * P_r * I_r$

Where:

W(t)obs = Observed (recorded) seismic trace with no post-recording processing

E_r = Earth Reflectivity Series (Geology)

W_s = Idealized Source wavelet

Q = Absorption (Attenuation, Quality Factor)

G_r, G_s = Source and Receiver Ghosts

S_{geo} = Spherical Divergence (Geometric Spreading)

N_{non} = Non Stationary Noises, multiples, seismic interference etc.

Noise = Statistically random noises, Stationary, Ergodic Properties

P_r = Geophone or Hydrophone response as a function of frequency (Non minimum phase)

I_r = Instrument Response (Non minimum phase)

This also implies the order of processing sequences. They are :
*(trace edits and geometry applied)
1. Shot Signature deconvolution which removes $P_r * I_r$
2. De-ghosting which removes $G_s * G_r$
3. We assume statical noises are random and small (Noise)
4. Attenuation and Spherical divergence removes $Q * S_{geo}$
5. This leaves $E_r * W_s * N_{non}$ Which requires de-multiple processes on such multiples as the water bottom and periodic interbed multiples. The result should be our best approximation of the Earth Reflectivity (E_r) and be zero phase (Figure 8.26). This is also a true amplitude result, but required shot to shot variation in amplitude to be removed.

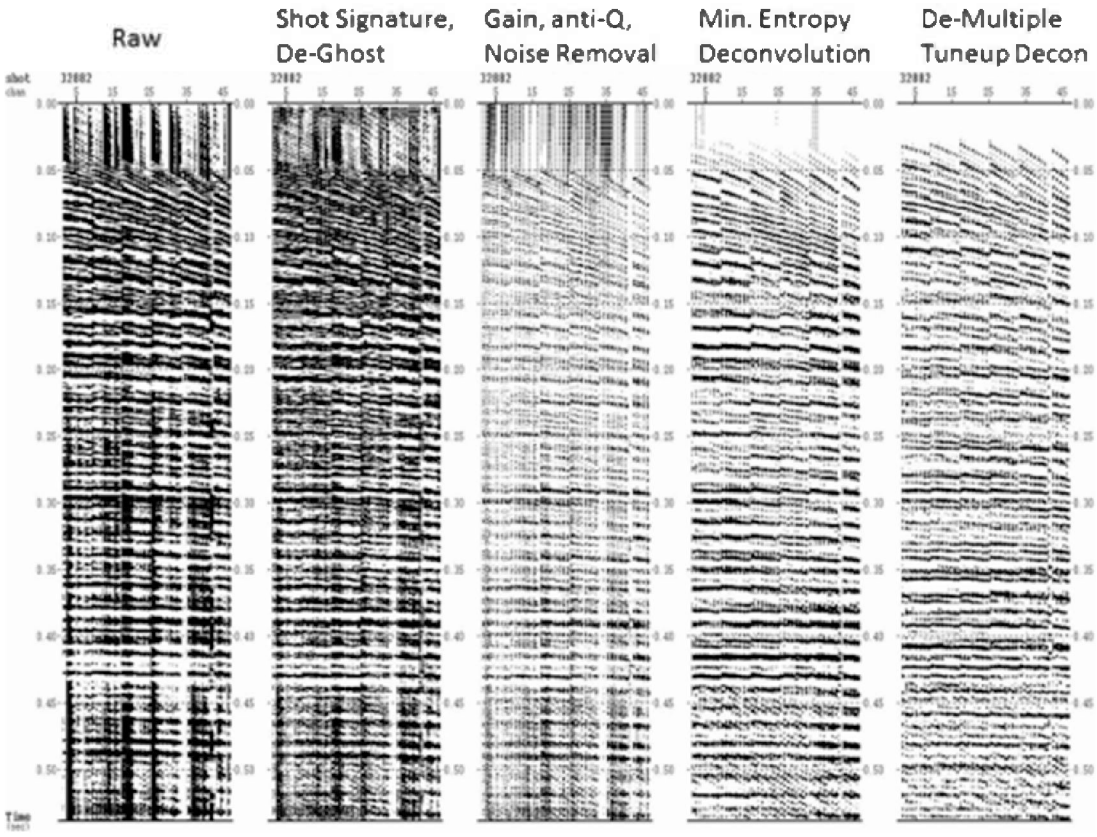

Figure 8.26: Processing example in the shot domain. This is part of one shot from raw data to final devolution. Note the earlier arrivals after Minimum Entropy Deconvolution. The arrivals correspond to the water bottom from bathymetric observations.

3D CDP based Processing

The shot data was re-organized into CDPs. Prior to stacking the data, automatic noise suppression and a gap deconvolution were applied and median stacking was used.

Processing the 3D data included

- 3D surface consistent statics corrections
- 3D surface consistent amplitude balancing
- 3D surface consistent final deconvolution
- Kirchhoff Migration, both post stack and pre-stack volumes were produced.

Resulting volumes were loaded into the interpretation software. Ongoing interpretation is currently in progress.

Summary

We have found that noise reduction techniques, which mix traces in any domain Tau-P, F-X, F-K, etc. are detrimental to the resolution of fine channel features in the Time Slice domain. This also unfortunately includes interpolation software which do not have available, thus the gaps in acquisition seen on the time slices. Resolution of the data detects channels down to the cdp bin spacing (6.25 m).

The resulting processing flow should perhaps take 3 weeks , with 1 week for quality control in the geometry, 1 week for shot domain processing and the remainder spend with 3D processes and migration. Data in the the Gulf of Mexico transition zones when collected with p-cable systems, shows fine details which conventional seismic survey cannot resolve.

9 Task 9.0: Site Selection

As outlined in Subtask 2.3, site selection and characterization is generally a process that begins with a comprehensive regional assessment and interpretation, which identifies areas of interest (a.k.a. "leads" in the terminology of the oil and gas industry). In the Study, regional assessment occurred in Task 2, but the process was iterative in so far as results from Task 2 focused efforts in Task 9 and interpretations resulting from site characterization informed Task 2. Because of the need for a robust regional assessment before site selection commenced, work on Task 9 did not begin until late 2011, two years after the Study's beginning.

Site Characterization – Conventional Datasets

A sequestration site "lead" was identified offshore from the southwest end of Galveston Island southeast of San Luis Pass. The "lead" area eventually became the focus of the first two HR3D seismic surveys (Figure 8.5). Figure 9.1 shows a map view of the lead and a well-log-based strike cross section across the area whose important geologic feature is a salt dome (a.k.a. diapir) that comes within a few hundred feet of the surface. Figure 9.2 is a well-log-based dip cross section of the same area that also schematically shows the San Luis Pass Salt Dome. Figure 9.3 is a location map that shows the line of section of the cross section in Figure 9.2.

Strike Section

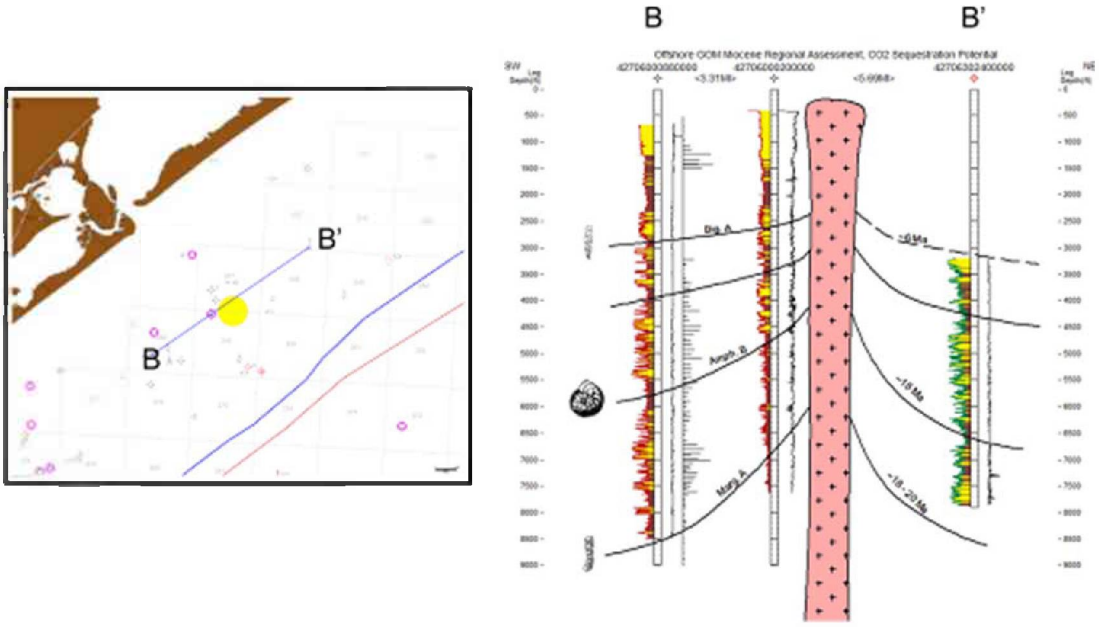

Andrew Nicholson

Sept 26, 2011

Figure 9.1: A strike cross section across the San Luis Pass, TX Salt Dome (right) and a location map and line of section (left). The figure was prepared by former graduate research assistant, Andrew Nicholson, as part of his work and research (Nicholson, 2012), which were supported by the Study.

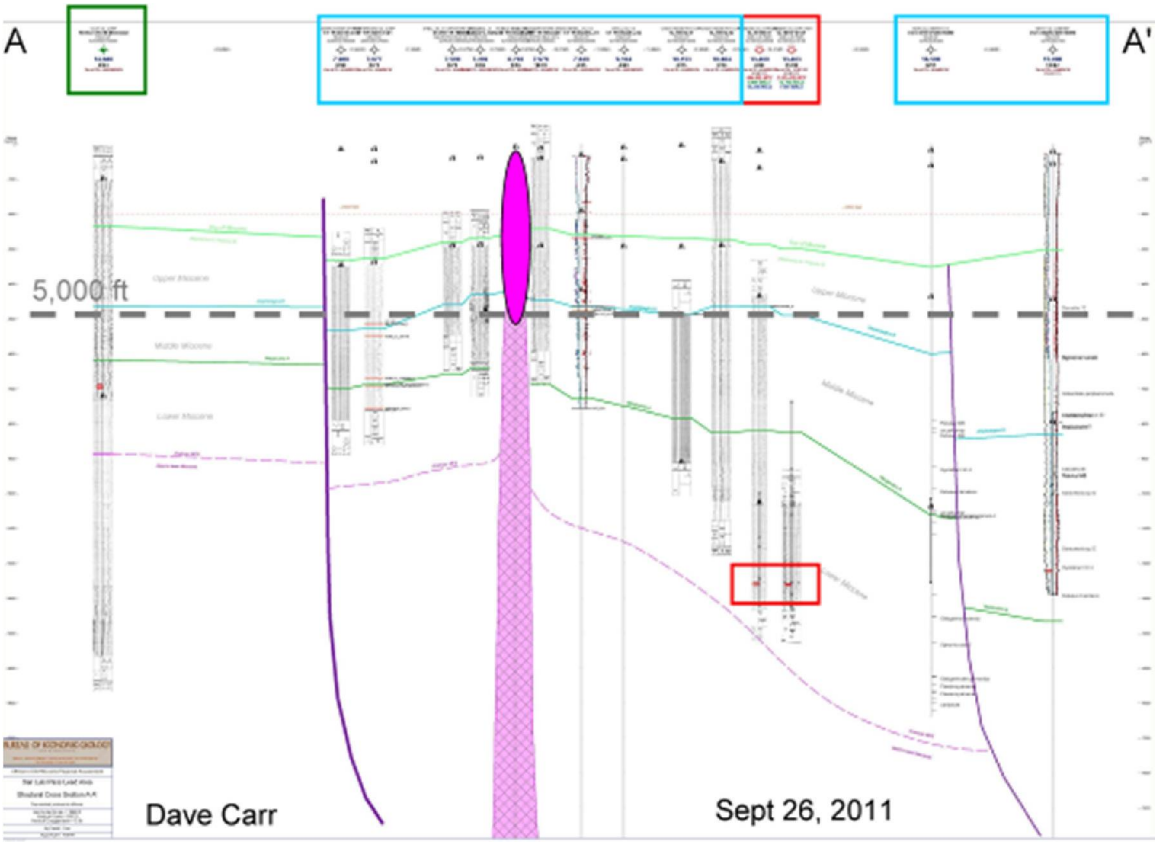

Figure 9.2: Well log based dip-oriented cross section of the San Luis, TX Pass area extending from northwest (left) to southeast (right) across the San Luis Pass Salt Dome. The line of section is orthogonal to that of Figure 9.1. David Carr was the lead researcher on Task 2 and contributed to Task 9.

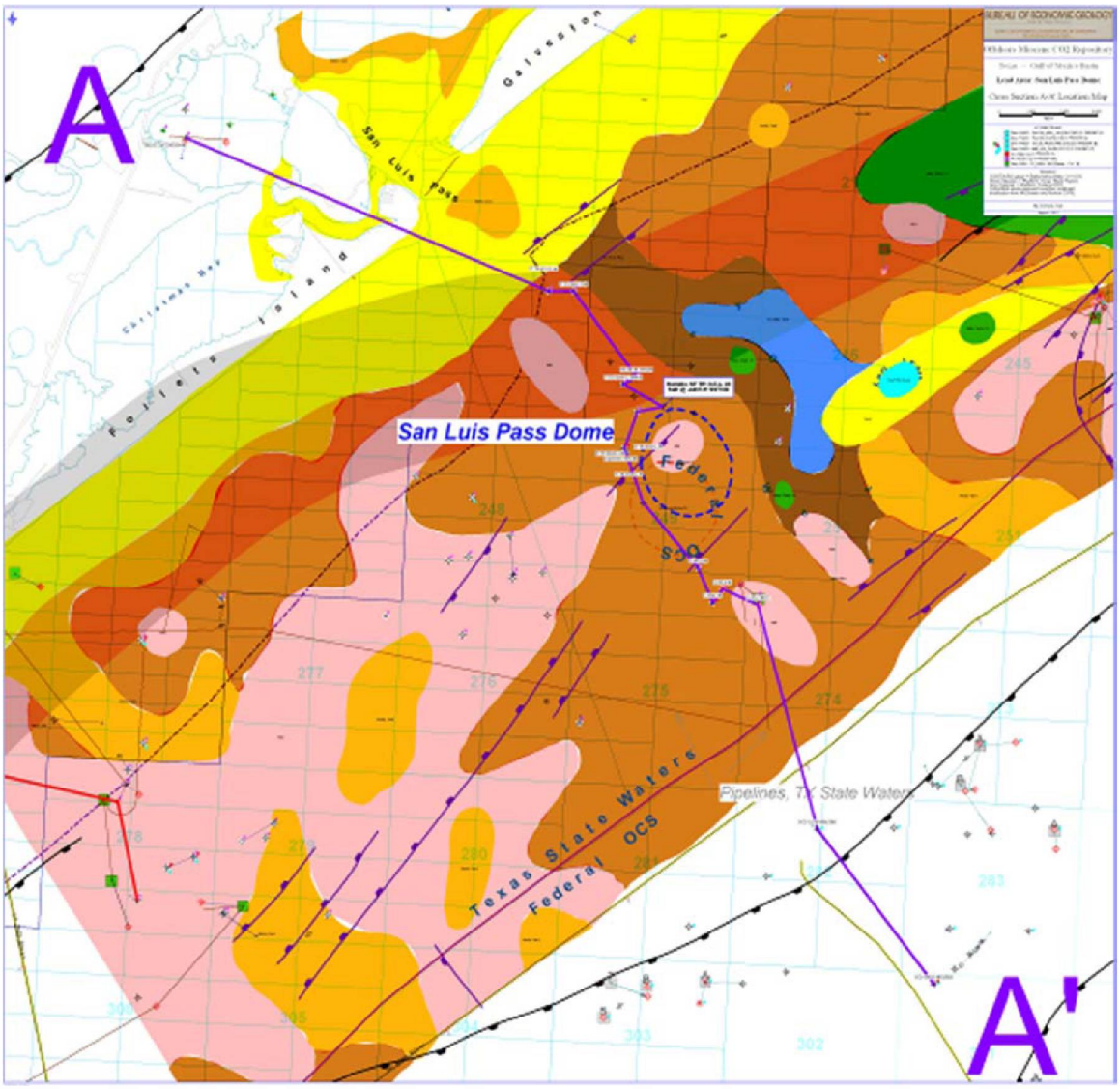

Figure 9.3: Location map of the dip cross section in figure 9.2. Note: the colored polygons in the shallow offshore waters denote different marine bottom sediment types. For example light yellow is "sand," blue is "muddy shelly sand," etc. (McGowen, 1979).

Interpretation of the regional 3D seismic data (Figure 2.5) comprised a significant portion of the regional and site characterization. Initially, most of the interpretation has been in the time domain and included both regional geology and more localized interpretations in the San Luis Pass Salt Dome prospect area.

The regional geologic foundation for the San Luis Pass area's characterization accelerated with the interpretation of a regionally extensive, high amplitude reflection above the *Marginulina "A"* and below the *Amphistegina "B"* bio-markers. The reflection was identified and mapped (in time) using the Seismworks and Geoprobe modules of the Landmark geological interpretation package. The resultant time-structure horizon, informally named "LM2" (a.k.a. Lower Miocene 2) was then exported to the Petra geologic interpretation software package where fault bounded "catchment areas" were manually defined based on fault locations and changes in horizons' dips in non-faulted

areas. Figure 9.4 shows the outlines of the catchment area polygons. Figure 9.5 shows the polygons superimposed on the time structure map of the LM2 horizon. Figure 9.6 shows well log rasters available in and around the mapped area.

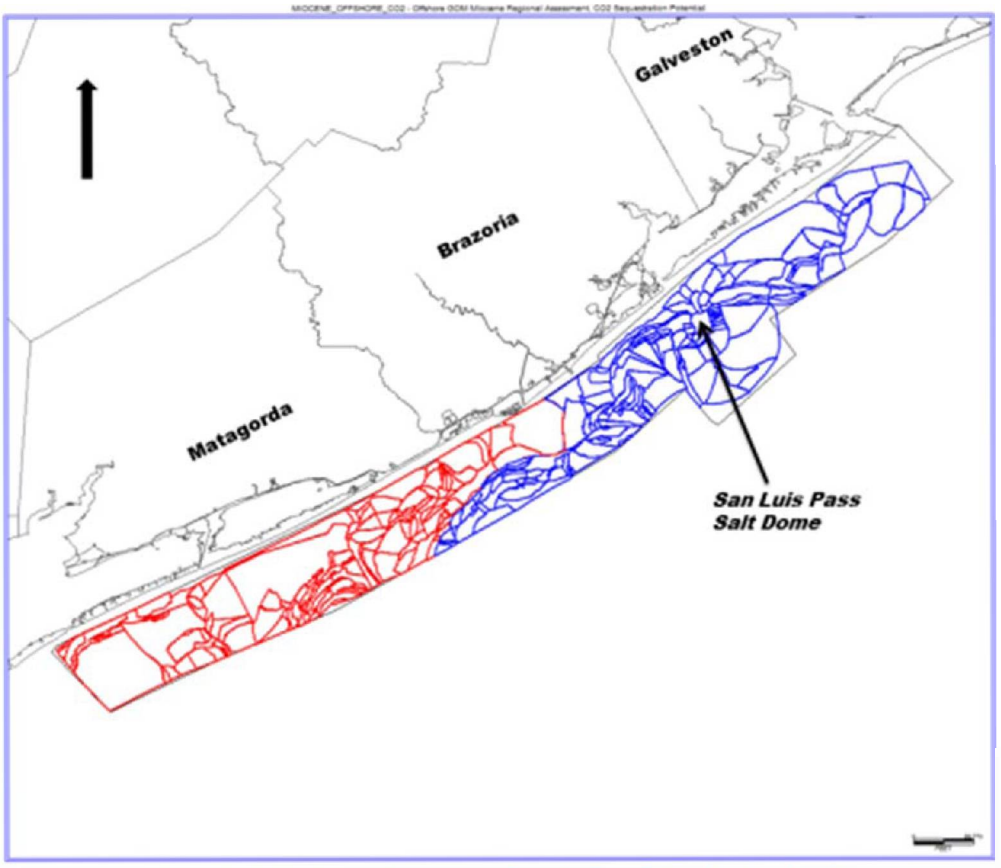

Figure 9.4: Polygons outlining fault block "catchment areas" at the "LM2" time horizon level.

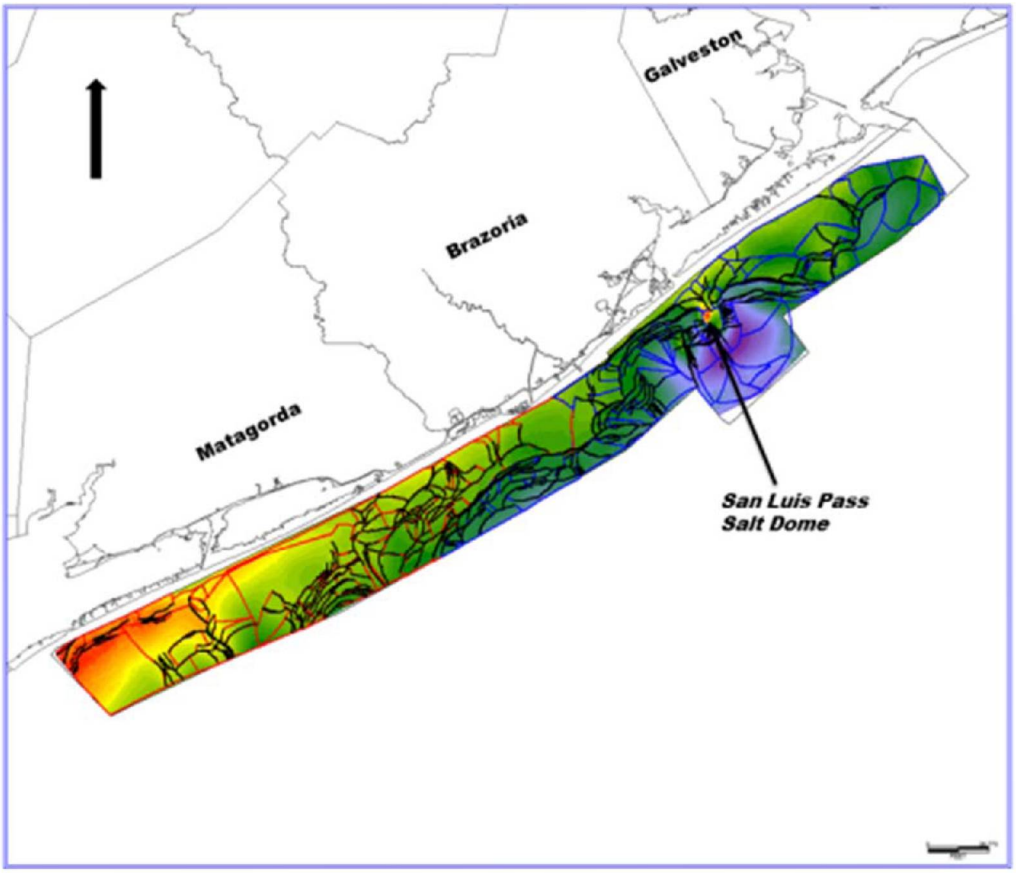

Figure 9.5: Time structure map of the "LM2" horizon with fault block "catchment area" polygons superimposed on it.

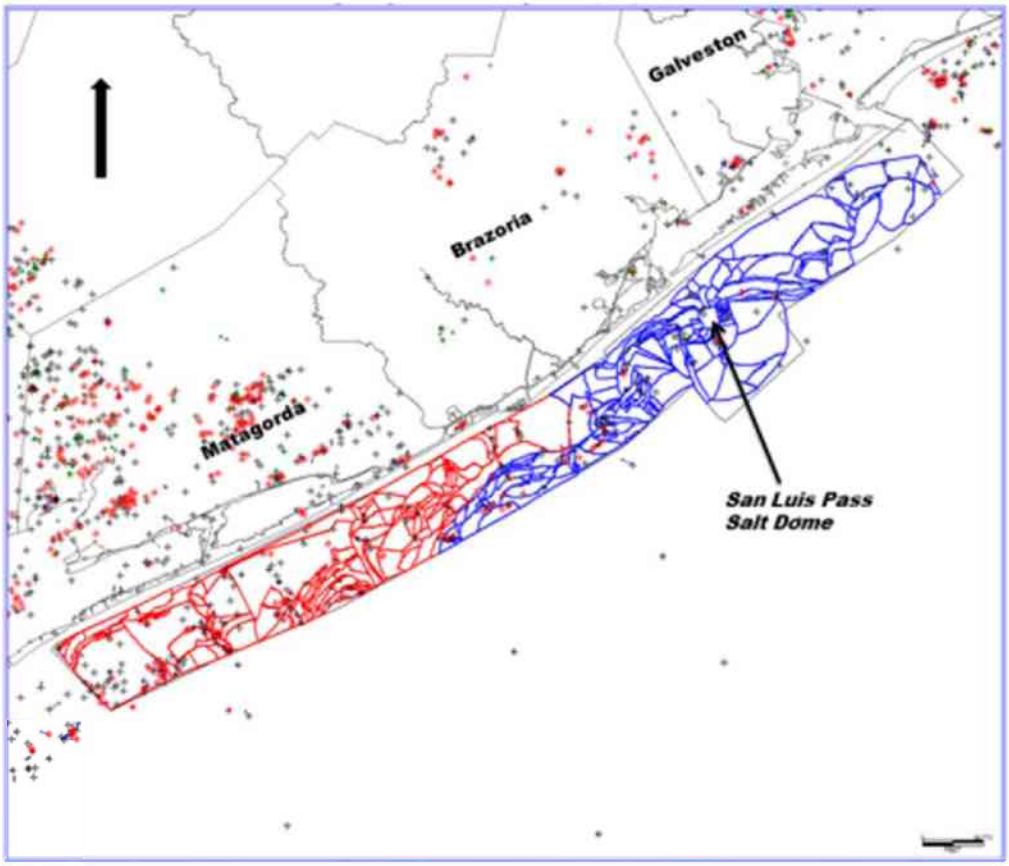

Figure 9.6: Fault block "catchment areas" at the "LM2" time horizon level and wells with rasters (red, black and green symbols) available in and around the mapped area.

For the San Luis Pass Salt Dome (SLPSD) site, depth maps were required to establish a static geologic model. Therefore, effort was directed toward the important but complicated endeavor of converting well log data to time and 3D seismic data and interpretations in the SLPSD area (Figure 9.7) to depth. To that end, deviation surveys were purchased for wells with acoustic logs in the SLPSD area. Acoustic (a.k.a. sonic) logs were used to generate synthetic seismograms and tentatively tied to the seismic time volume. Similarly, commercially available velocity (i.e., check-shot) surveys were identified, purchased, converted to digital formats (as needed), and uploaded to the Landmark OpenWorks database. An initial depth volume was generated, but was found to contain errors. Initially, the time dataset was converted to depth using a module in the Landmark software suite (i.e., TDQ). However, the result was disappointing. Later, another module, "Depth Team," was used, and it yielded much better results. The difference was that Depth Team was able to incorporate several time horizons into its calculation. The resultant depth volume from Depth Team was QC'd and deemed acceptable.

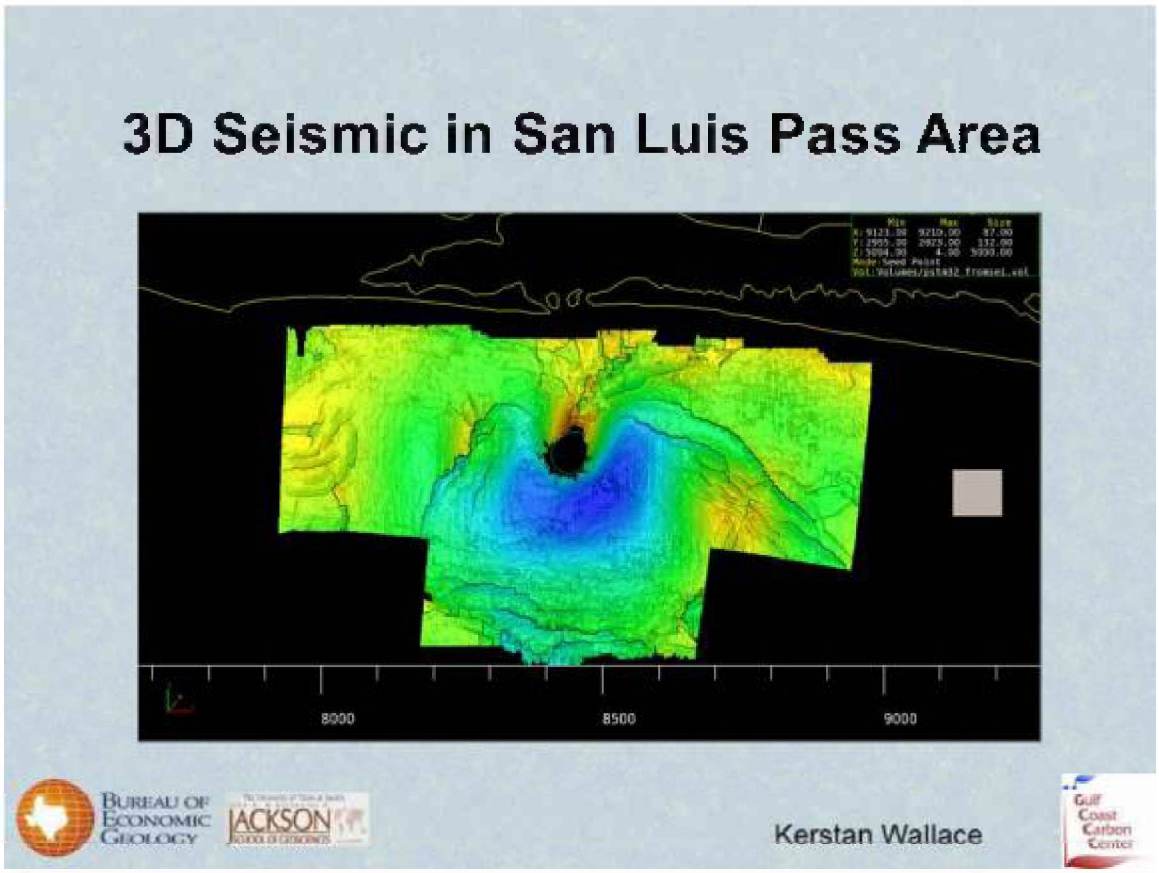

Figure 9.7: Relatively shallow time structure map from commercial seismic data. The area shown is in the offshore Texas State Waters along the southern end of Galveston Island. Note the black teardrop shaped area in the upper central portion of the colored polygon. That black teardrop shape approximates the outline of the San Luis Pass Salt Dome at the horizon level. Yellow hues denote shallower areas; whereas, dark blue hues are relatively deeper areas with green shades intermediate. The figure was prepared by former graduate research assistant, Kerstan Wallace, as part of his work and research, which were supported by the Study.

After conversion to depth of the SLPSD area's commercial seismic dataset and interpretation (Figure 9.7), the depth structure map of the LM2 horizon (Figure 9.8) was used to generate a large-scale, 3D, dynamic injection model. The model was used to obtain reasonable estimates of reservoir fill time and realistic CO_2 plume distributions. The SLPSD area was selected because of the structures observed on LM2 seismic horizon map and because of a relatively high density of available well data (Figure 9.8). A seismic reflection was selected (Appendix A, Chapter 6.2) for mapping based on log signature, amplitude, depth and seismic continuity. The reflection was very precisely mapped at the wavelet's zero crossings (i.e., both above and below the wavelet's maximum value, respectively). An RMS (root mean square) seismic attribute extraction between these two horizons is shown in Figure 9.9. Faults within the area of interest were also mapped with high precision in part, using the "semblance" (a.k.a., continuity or coherency) attribute. These input parameters structurally defined the reservoir model. The mesh fill of the reservoir model was generated in various ways to compare approaches. Some were numerically derived and some were derived through wireline log to seismic comparisons and direct sampling of seismic attribute values to a reservoir mesh. Ultimately, the modeling approach illuminated the usefulness and relative accuracy or inaccuracy of regional-scale capacity assessments. The Study's model research formed one part of Kerstan Wallace's master's thesis (Wallace, 2013).

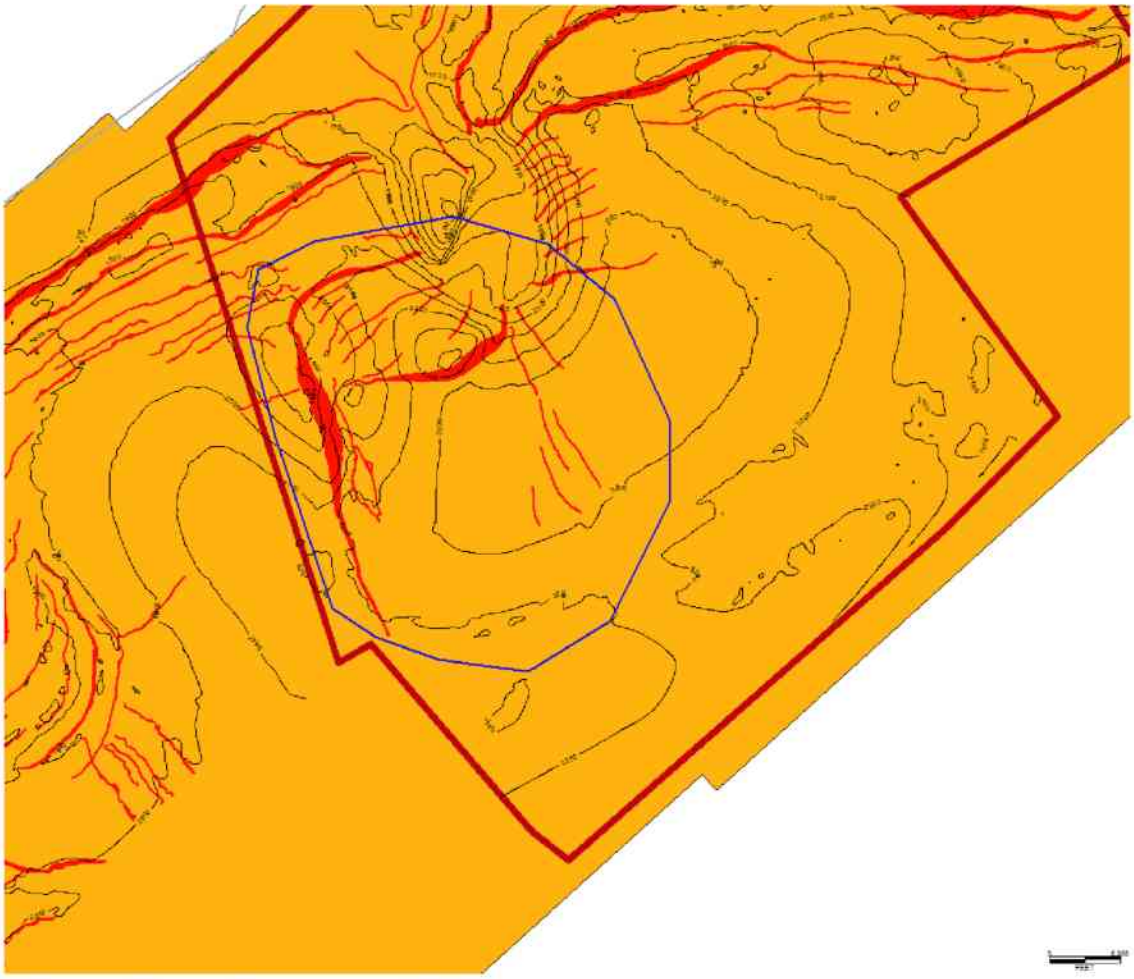

Figure 9.8: Map showing LM2 (lower Miocene 2) seismic horizon contours (black) with faults (red). The depth converted subvolume is outlined by the red polygon, and the model area is outlined in the blue polygon.

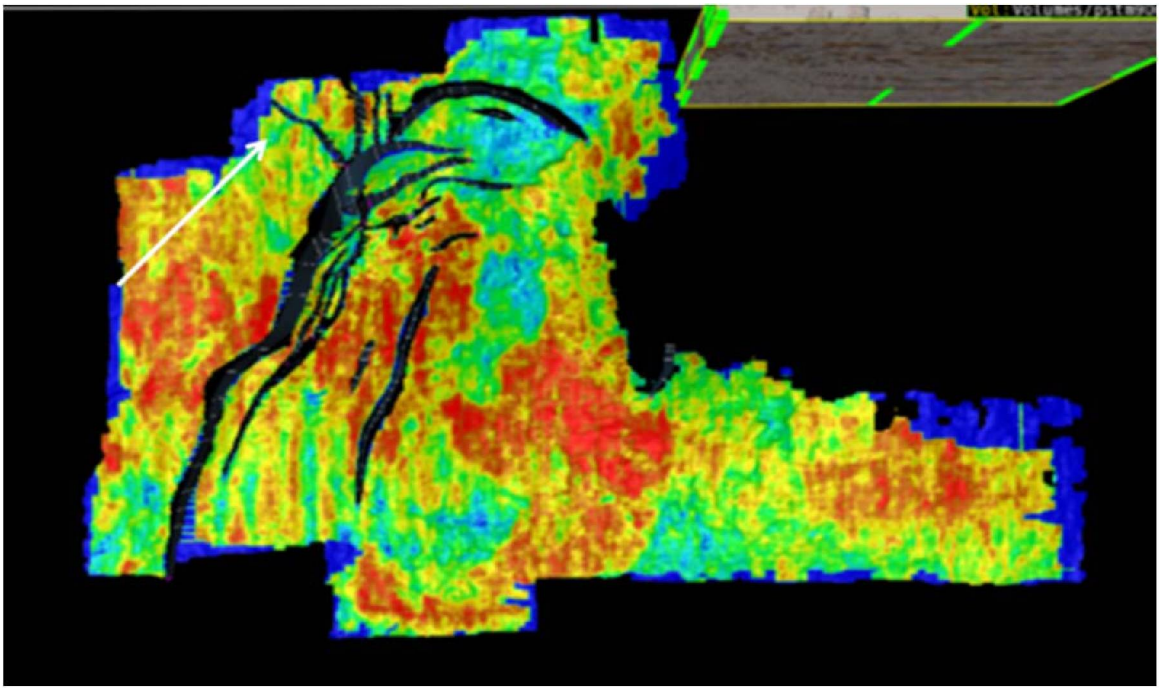

Figure 9.9: Map of the RMS (root mean square) attribute extraction between top and base of model interval. Faults are shown as dark lines.

Further detailed interpretations of the SLPSD area are found in the Appendix A, Chapter 6.2. Similarly, detailed interpretations, characterization and capacity estimations of another area related to the Brazos Block 440-L oil and gas Field

Site Characterization – HR3D Data

In addition to geologic characterization based on conventional seismic datasets, the 2013 HR3D dataset in the SLPSD area was used to interpret and analyze the shallow geologic section. As mentioned in the Task 8 section, the 2013 dataset was instrumental in highlighting a potential problem with the confining (i.e., sealing) capacity of one part of the SLPSD area (Figure 8.16 and Figure 8.17). Because of the gas chimney feature, further detailed interpretation of the shallow stratigraphy in 2013 HR3D dataset continued until the end of the Study by graduate research assistant, Francis Mulcahy. This research will compose an important part of Francis' masters' thesis.

Figure 9.10 through 9.5, which continue to show the high quality (e.g., frequency content) of the dataset. Figure 9.10 is a vertical time transect showing the five horizons mapped to date. Figure 9.11 shows the "sum negative amplitude" on a 10ms surface hung 2ms above and 8ms below the unconformity "lid" (Figure 9.12). Because there are no available cores or logs at this interval, an interpretation is based solely on morphology and geophysical attribute. Nonetheless, we interpret the most negative (i.e., colorful) attributes as indicating sand distribution.

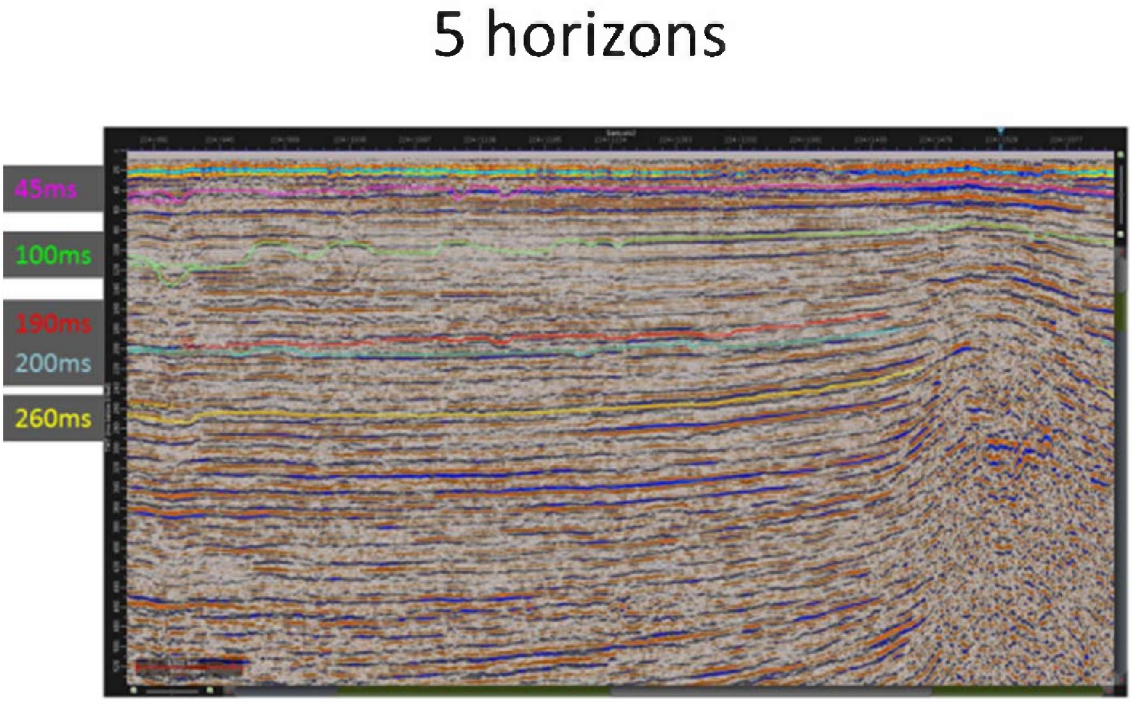

Figure 9.10: Vertical time transect of an amplitude volume of the 2013 San Luis Pass P-Cable dataset. The transect highlights the five currently mapped time horizons centered around 45, 100, 190, 200, and 260 ms (milliseconds), respectively. Note on the discordant, antiform-like feature on the right side of the figure; it is related to the San Luis Salt Dome.

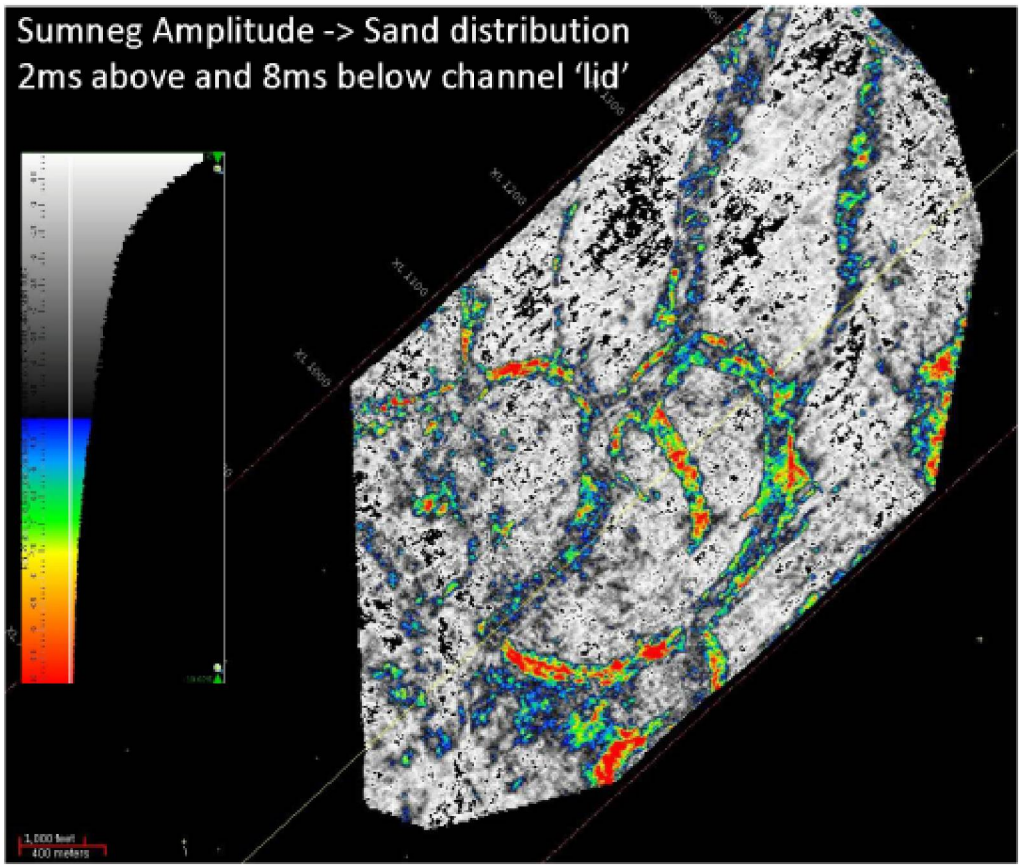

Figure 9.11: A map showing an extraction, from the "190 ms" horizon, of the sum negative amplitude attribute 10ms surface hung 2ms above and 8ms below the unconformity "lid."

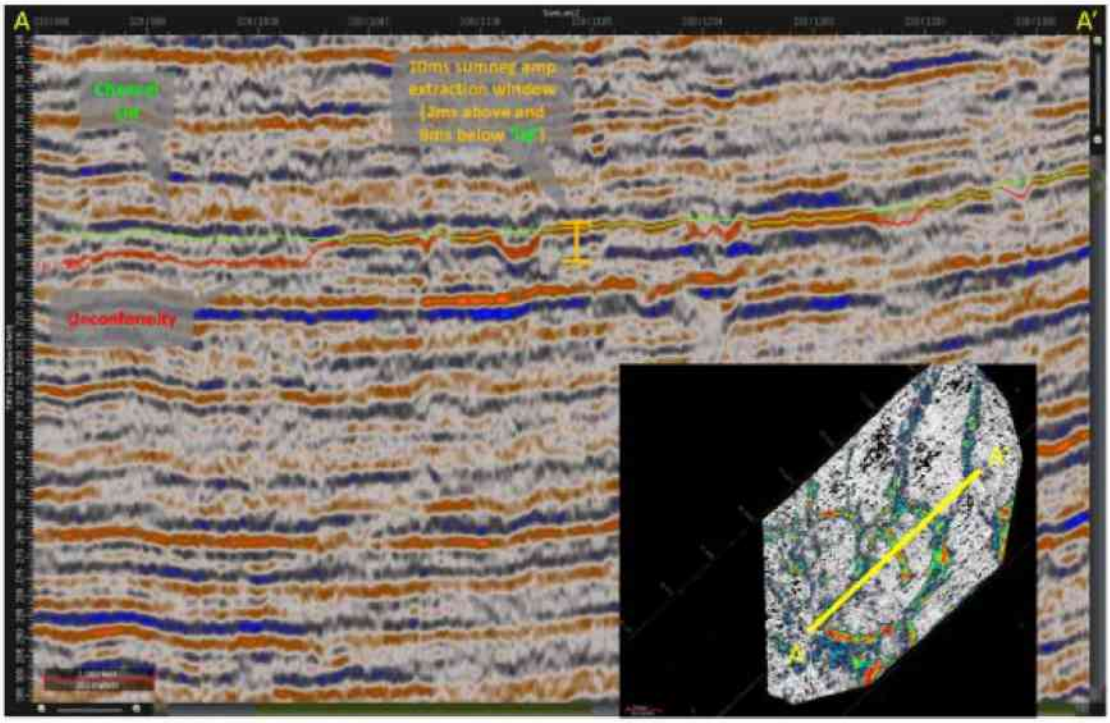

Figure 9.12: Time transect of an amplitude volume of the 2013 San Luis Pass P-Cable dataset highlighting the 190ms horizon and the "10ms sumneg amp" (sum of negative amplitudes) attribute extraction shown in the inset and in Figure 9.11.

In addition to the new horizons mentioned above, interpretation continued on the 100ms horizon (Figure 9.10). Figure 9.13, shows a contoured time structure display of the horizon and Figure 9.14 shows the time structure co-rendered with the semblance attribute.

Contoured structure

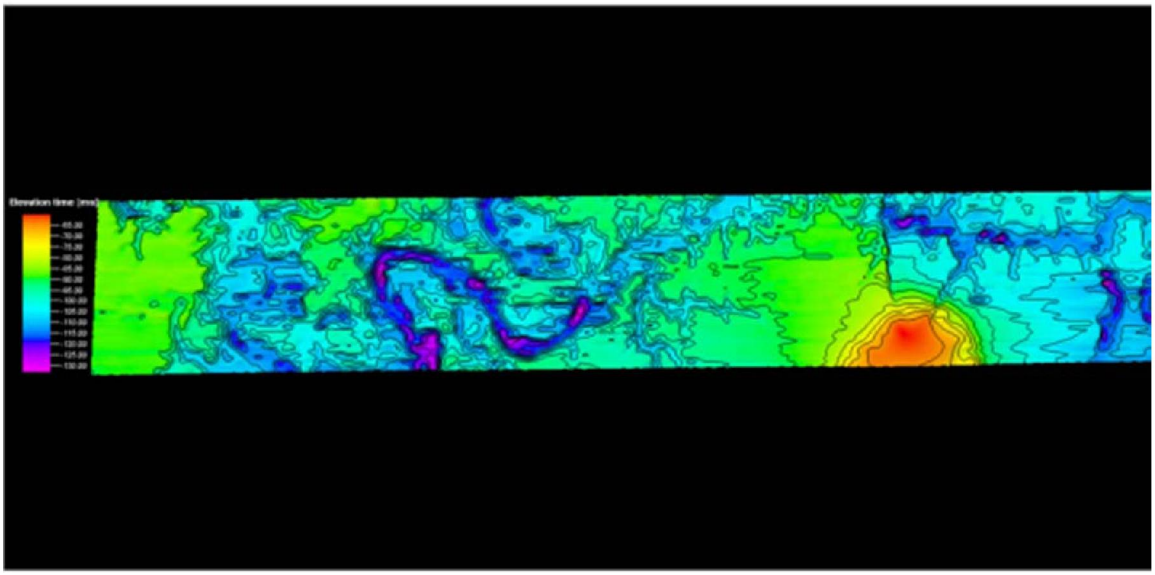

Figure 9.13: Time structure contour map of a co-rendered structure/coherency of the 100 ms horizon. The horizon is interpreted as the erosional surface generated during the Wisconsinin glacial lowstand.

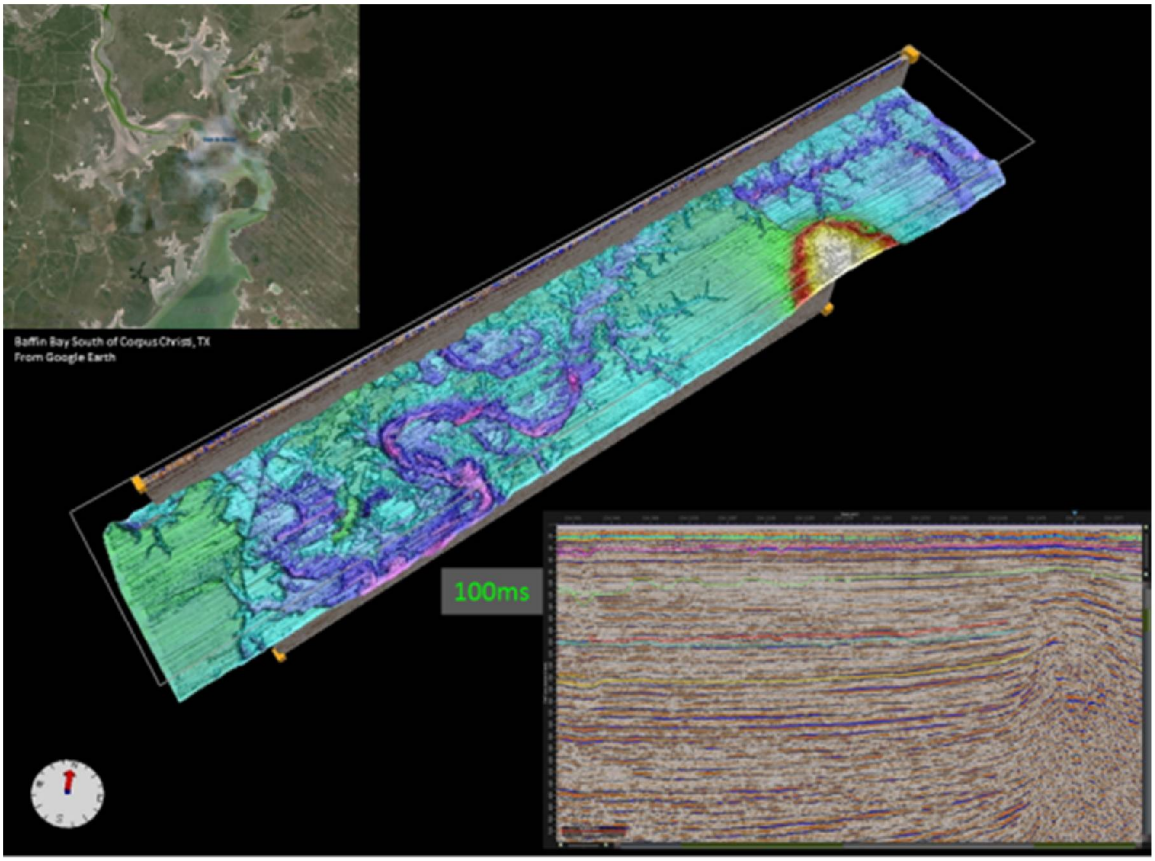

Figure 9.14: Time structure map of a co-rendered structure/semblance of the 100 ms horizon.

In Figure 9.14, note the purple colored channel feature in the lower left-hand portion of the horizon. The horizon is interpreted as the erosional surface generated during the Wisconsinin glacial lowstand. Note the lower inset showing the placement of the 100ms horizon on a vertical time transect. The upper inset is a satellite view of the Cayo del Hinoso an arm of the Baffin Bay estuary on the south Texas coast. It is proposed as a modern analog for the time structure map's channel / incision feature.

In addition to seismic mapping, wells in the seismic coverage area were analyzed to determine whether or not they could be tied to the seismic dataset. In order to accomplish accurate ties, sonic (a.k.a., acoustic or Vp) and density wireline well log data are required. The available wells only have SP (spontaneous potential) and depth measurements at the seismic data's shallow depths.

As previously mentioned, interpretation of the dataset will continue into 2015 (with support from State of Texas funding) as it will compose an important part of Francis Mulcahy's master's thesis. Similarly, it is expected that the HR3D datasets will provide future researchers many opportunities for continued investigations in the intriguing San Luis Pass Salt Dome area.

10 Task 10.0: Risk Assessment

Task 10 was conducted by two outside organizations. Los Alamos National Laboratories conducted the research on Subtask 10.1 and Environmental Defense Fund conducted the research on Subtask 10.2. As such the final research reports from each are included as separately-paginated, self-contained reports in Appendices B and C, respectively. Therefore, the, respective, reports' text, figures, tables, reference lists, etc. do not correspond to the current report's numbering scheme.

10.1 Subtask 10.1: CO2-PENS analysis

Results from this subtask are found in Appendix B.

10.2 Subtask 10.2: Identification of environmental risks specific to offshore settings

Results from this subtask are found in Appendix C.

11
Task 11.0: Well Bore Management

Task 11 was conducted by Sandia Technologies, LLC, a subcontractor. As such the final research report is included as a separately-paginated, self-contained report in Appendix D. Therefore, the report's text, figures, tables, reference lists, etc. do not correspond to the current report's numbering scheme.

11.1
Subtask 11.1: Wellbore Evaluation for Wells within Study Area

11.2
Subtask 11.2: Draft Wellbore Management Plan

12 Task 12.0: Produced Fluid Management

While there may be some beneficial use for produced fluids in certain regions (e.g. desalination in the arid western U.S.), we did not anticipate produced fluids being a significant aspect of the most prospective sites for offshore storage. Produced brine salinities would be higher than the overlying seawater, and it is preferable not to produce brine fluids in the context of offshore sequestration as there is no obvious beneficial use. For these reasons, this task was not considered in the study.

Conclusions

Regional studies of the near-offshore Gulf of Mexico along the Texas coast have characterized a geologic resource for CO_2 storage of State and National interest. The offshore Miocene-age stratigraphic interval of Texas provides a tremendous resource for storing anthropogenic CO_2 as a means for mitigating atmospheric emissions. Regional static capacity calculations indicate 86 Gigatonnes of CO_2 storage capacity for the study area. While reconciling regional static capacity estimates with local dynamic assessments utilizing reservoir simulation has been challenging, this offshore region represents some of the most immediately accessible capacity for receiving industrial-scale emissions in the country. Recent infrastructure developments (onshore CO_2 pipelines) and source-to-sink matching suggest this region could become a CO_2 hub capable of receiving pipeline CO_2 from other parts of the country, and indications are that the geologic storage resource could be viable for decades of utilization.

Primary products of the study include: regional static storage capacity estimates, sequestration "leads" and prospects with associated dynamic capacity estimates, experimental studies of CO_2-brine-rock interaction, best practices for site characterization, a large-format 'Atlas' of sequestration for the study area, and characterization of potential fluid migration pathways for reducing storage risks utilizing novel high-resolution 3D (HR3D) seismic surveys. In addition, three subcontracted studies address source-to-sink matching optimization, offshore well bore management and environmental aspects. The various geologic data and interpretations are integrated and summarized in a series of cross-sections and maps, which represent a primary resource for any near-term commercial deployment of CCS in the area.

Specific conclusions from each task follow:

TASK 2: Regional significance

The Miocene of the Texas state waters, especially along the upper Texas coast, represents a region with great potential for future CO_2 sequestration development. The region has a high concentration of industrial emissions sources (e.g., power plants near large urban centers, extensive refining and petrochemical plants) as well as existing pipeline and other infrastructure in an area with significant with favorable commercial, subsurface geology, and engineering expertise.

TASK 3: Capacity Estimates (Site)

Several sites ("leads") were characterized and CO_2 storage capacity calculated via static and dynamic methods. The site near San Luis Pass over which the 2013 HR3D survey was collected (subsequently suggesting a gas chimney) indicated dynamic capacity (i.e. using 3D fluid flow simulations) of less than 10 Mt. Pressure was the major limiting parameter for the models, and reservoir heterogeneity (e.g., mudrock baffles) and limited reservoir connectivity will probably prevent an infinitely acting system with completely open boundaries. The area associated with the Brazos Block 440-L Field was also characterized and analyzed using a static capacity method. The capacity of the entire area was estimated to be 196 Mt; whereas, the capacity of the gas structurally-controlled field area was estimated to be 14 Mt.

TASK 4: Injectivity (Site)

Core analysis and laboratory measurements indicate adequate to robust sealing capacity for the seal intervals of interest. Results from simple dynamic analytical modeling (Jain and Bryant, 2011) of a discrete reservoir body in the Offshore Texas Miocene interval near San Luis Pass. Simulations were performed for 6,206 samples of porosity, permeability, and water saturation in a Gulf of Mexico Miocene gas reservoir taken from the Atlas of Northern Gulf of Mexico Gas and Oil Reservoirs (Seni et al., 1997).The average resulting capacity is found to be 30.3 megatonnes with an average fill time of 38.3 years.

TASK 5: Stratigraphic Containment

Analyses of available core samples of Miocene mudrocks (seals) suggest that the studied clay-rich lower Miocene mudrocks have sealing ability sufficient for potential CO_2 storage in the underlying sandstone units. The sealing capacity of the studied samples has positive correlations with clay content and calcite cementation. Clay-rich mudstone samples typically show higher capillary entry pressure and smaller pore-throat size than underlying sandstones. SEM imaging shows that claystone samples contain mostly isolated intraparticle pores, which are not effectively connected to form pore networks. A high concentration of lower Miocene hydrocarbon accumulations occurs on the hanging wall of the Clemente-Tomas fault zone where Amph B net mudstone is thick, ranging from 1,000 ft (305 m) to 3,000 ft (914 m). These natural analogs of fluid entrapment suggest that fairways characterized by a thick regional Amph B confining zone defined by net mudrock values of more than 1,000 ft (305m) might provide an excellent long-term confining mechanism for injected CO_2.

Flow model simulation of fluid flow in a relatively small scale (20.51" tall by 10.39" wide (0.521 m x 0.264 m)) but high-resolution (>2M data points), 2D, digital model of a sedimentary relief peel conclude (Meckel, 2013; Meckel et al., in press) that mean grain size and sorting appear to be the key control on CO_2 movement; fluid density contrast (in the expected ranges) is apparently secondary. Pressure gradients contribute to end member and transition behavior, in addition to rock properties and fluid density contrast. The pressure gradient in relative close proximity to the well (compared to the reservoir extents) can allow for fingering behavior.

TASK 6: Brine Containment

Results from this task concluded that:

1) Carbon solubility trapping potential is most sensitive to thickness and porosity, two of the three parameters (thickness, porosity, and area) that determine brine volume. The result suggests that the volume of available brine in the storage aquifer is a primary control.

2) The storage coefficient, C, appears to be one of the critical parameters for assessing CSTP in a saline aquifer.
3) Brine-rock-CO2 reaction experiments suggest that the most likely CO2-solubility trapping potential of the section in the area of interest (study area) is approximately 5% of the total CO_2 storage capacity calculated in Subtask 3.1.

TASK 7: Mineralization Containment
Geochemical models confirm dissolution of calcite when CO_2 was injected into reservoir rock samples. The geochemical models also fit well with K concentration measurements, suggesting that K came from dissolution of K-feldspar when CO_2 was injected. Modeled Na concentrations match measured Na concentration indicating that CO_2 injection leads to dissolution of albite. Si and Al are dominated by dissolution-precipitation of silicate minerals and potential secondary minerals. Proper selection of secondary minerals in the geochemical model seems very important.

TASK 8: Leakage Pathways
HR3D (P-Cable) data are crucial for characterizing leakage pathways. It is difficult to conceive of conducting a CCS project without such data if they are financially acquirable. Examples from the three HR3D surveys demonstrate that the seismic technique is capable of identifying and characterizing low-risk storage sites. When integrated with regional conventional 3D data, insight into natural fluid migration systems may distinguish entire regions as more or less prospective for future consideration for storage.

TASK 9: Site Selection
A best practices manual outlines the recommended procedure for site selection. It is concluded that HR3D seismic data contribute overwhelmingly to the ability to adequately characterize and de-risk site selection. HR3D surveys highlight structural and stratigraphic details that can be used in simulations for forward modeling injection. In some cases, indications of natural fluid systems as visualized in HR3D data may greatly influence the ability to make strong site selection decisions.

TASK 10: Risk Assessment
A subcontractor (Los Alamos National Laboratory) completed a numerical modeling study demonstrating that the Texas Gulf Coast has significant industrial CO_2 production and geologic storage potential. The results suggest that it is not unrealistic to expect to find sites with the potential to store 30 MT of CO2, as proposed as a goal for this project.

A subcontractor (Environmental Defense Fund) completed a study anticipating the environmental risks associated with long-term offshore carbon sequestration (including the processes required to do so) and to detail policy scenarios, recommendations and technical methods to avoid or minimize those risks. The results indicate that offshore CCS is viable from an environmental perspective, but not without risk. With appropriate site selection, operational safeguards, and compliance with existing regulatory requirements and best practice methodology, long-term offshore sequestration can be performed safely and effectively and with manageable risk to the coastal environment. A series of key recommendations for further consideration were provided.

TASK 11: Wellbore Management
A subcontractor (Sandia Technologies, LLC) conducted a survey of wellbores in part of the Study area. The task report outlines a Wellbore Management Plan for locating and

evaluating artificial penetrations in a Geologic Sequestration project area subject to UIC Class VI regulations. The document presents the Wellbore Management Plan, explaining the series of steps that should be completed to ensure adequate review and evaluation of artificial penetrations. It then presents the results of the implementation of the Wellbore Management Plan in the San Luis Pass Dome area to determine if any well can serve as a conduit for the movement of borehole fluids to USDWs.

Acknowledgements

The following research assistants provided invaluable support without which the Study could not have achieved many of its objectives: Amar Amir, Nwachukwu Anyamele, Emmanuel Belostrino, Elissia Derasen, Julie Ditkof, Tyler Fritz, Brandon Johnson, Erin Miller, Priya Ravi Ganesh, Caleb Rhatigan, Tamara Sopoeva, Jordan-Leigh Taylor Rhatigan, Nolan Townsend and Wylie Walker. The research assistants gained knowledge and experience, and we greatly benefited from their excellent help.

In addition, the Study was funded by the Texas General Land Office through GLO Contract No. 10-205-000-4100, which we gratefully acknowledge.

We gratefully acknowledge ION Geophysical Corporation for complimentary access to their GulfSpan set of regional 2D seismic lines, whose high-quality data were indispensable.

We thank IHS, Inc. for access to their well and well production database via Enerdeq®. In addition we thank IHS for access to the Petra integrated geoscience software application, “a common database and interface for project and data management, well log analysis, mapping, cross-sections, seismic integration, production and reservoir analysis and 3D visualization.”

On behalf of The University of Texas at Austin, Bureau of Economic Geology, we gratefully acknowledge Halliburton’s Landmark Software and Services for access to their suite of geoscience interpretation software via the Landmark University Grant Program. Various modules of Landmark software were employed during interpretation of seismic data.

We are grateful to Hampson-Russell, a CGG company for availability and utilization of Hampson-Russell Software Services by researchers and student research assistants via the University grant program.

We thank SEI, Inc. for access to a regional 3D seismic datasets at significant cost share. The datasets were invaluable and instrumental in the regional, stratigraphic and structural understanding of the Miocene section of the Study area.

References Cited

Bachu, S., 2007, Carbon dioxide storage capacity in uneconomic coal beds in Alberta, Canada: Methodology, potential and site identification: International Journal of Greenhouse Gas Control, v. 1, p. 374-385.

Bachu, S., and Adams, J.J., 2003, Sequestration of CO2 in geological media in response to climate change: capacity of deep saline aquifers to sequester CO2 in solution: Energy Conversion and Management, v. 44, p. 3151-3175.

Bachu, S., Bonijoly, D., Bradshaw, J., Burruss, R., Holloway, S., Christensen, N.P., and Mathiassen, O.M., 2007, CO2 storage capacity estimation: Methodology and gaps: International Journal of Greenhouse Gas Control, v. 1, p. 430-443.

Bachu, S., Michael, K., and Adams, J.J., 2003, Effects of In Situ Conditions on Aquifer Capacity for CO2 Sequestration in Solution, Second Annual Conference on Carbon Sequestration: Developing & Validating the Technology Base to Reduce Carbon Intensity: Alexandria, VA, USA, NETL, p. 1-14.

Batzle, M., and Wang, Z., 1992, Seismic properties of pore fluids: Geophysics, v. 57, p. 1396-1408.

Berger, P.M., Roy, W.R., and Mehnert, E., 2009, Geochemical Modeling of Carbon Sequestration, MMV, and EOR in the Illinois Basin: Energy Procedia, v. 1, p. 3437-3444.

Bish, D.L., 1994, QUANTITATIVE X-RAY-DIFFRACTION ANALYSIS OF SOILS, 267-295 p.

Catuneanu, O., Abreub, V., Bhattacharya, J.P., Blum, M.D., Dalrymple, R.W., Eriksson, P.G., Fielding, C.R., Fisher, W.L., Galloway, W.E., Gibling, M.R., Giles, K.A., Holbrook, J.M., Jordan, R., Kendall, C., Macurda, B., Martinsen, O.J., Miall, A.D., Neal, J.E., Nummedal, D., Pomar, L., Posamentier, H.W., Pratt, B.R., Sarg, J.F., Shanley, K.W., Steel, R.J., Strasser, A., Tucker, M.E., and Winker, C., 2009, Towards the standardization of sequence stratigraphy: Earth-Science Reviews, v. 92, p. 1-33.

CMG, 2011, WinProp User's Guide – Version 2011: Calgary, Computer Modelling Group Ltd.

Duan, Z., Sun, R., Zhu, C., and Chou, I.M., 2006, An improved model for the calculation of CO2 solubility in aqueous solutions containing Na+, K+, Ca2+, Mg2+, Cl-, and SO42: Marine Chemistry, v. 98, p. 131-139.

Galloway, W.E., 1989, GENETIC STRATIGRAPHIC SEQUENCES IN BASIN ANALYSIS .2. APPLICATION TO NORTHWEST GULF OF MEXICO CENOZOIC BASIN: Aapg Bulletin-American Association of Petroleum Geologists, v. 73, p. 143-154.

Gay, A., Lopez, M., Berndt, C., and Seranne, M., 2007, Geological controls on focused fluid flow associated with seafloor seeps in the Lower Congo Basin: Marine Geology, v. 244, p. 68-92.

Goodman, A., Hakala, A., Bromhal, G., Deel, D., Rodosta, T., Frailey, S., Small, M., Allen, D., Romanov, V., Fazio, J., Huerta, N., McIntyre, D., Kutchko,

B., and Guthrie, G., 2011, US DOE methodology for the development of geologic storage potential for carbon dioxide at the national and regional scale: International Journal of Greenhouse Gas Control, v. 5, p. 952-965.

Gorecki, C.D., Sorensen, J.A., Bremer, J.M., Ayash, S.C., Knudsen, D.J., Holubnyak, Y.I., Smith, S.A., Steadman, E.N., and Harju, J.A., 2009, Development of Storage Coefficients for Determining the Effective CO2 Storage Resource in Deep Saline Formations, Development of Storage Coefficients for Determining the Effective CO2 Storage Resource in Deep Saline Formations: San Diego, California, USA.

Heeschen, K., Risse, A., Ostertag-Henning, C., and Stadler, S., 2011, Importance of co-captured gases in the underground storage of CO2 : Quantification of mineral alterations in chemical experiments: Energy Procedia, v. 4, p. 4480-4486.

Jacquemet, N., Le Gallo, Y., Estublier, A., Lachet, V., von Dalwigk, I., Yan, J., Azaroual, M., and Audigane, P., 2009, CO2 streams containing associated components--A review of the thermodynamic and geochemical properties and assessment of some reactive transport codes: Energy Procedia, v. 1, p. 3739-3746.

Jain, L., and Bryant, S.L., 2011, Time weighted storage capacity for geological sequestration, *in* Gale, J., Hendriks, C., and Turkenberg, W., eds., 10th International Conference on Greenhouse Gas Control Technologies, Volume 4: Energy Procedia, p. 4873-4880.

Johnson, J., Anderson, G., and Parkhurst, D., 2000, Database 'thermo.com.V8.R6.230,' Rev. 1.11: Livermore, Calif., Lawrence Livermore National Lab.

Koenen, M., Tambach, T.J., and Neele, F.P., 2011, Geochemical effects of impurities in CO2 on a sandstone reservoir: Energy Procedia, v. 4, p. 5343-5349.

Land, L.S., Macpherson, G.L., and Mack, L.E., 1988, The Geochemistry of Saline Formation Waters, Miocene, Offshore Louisiana: Gulf Coast Association of Geological Societies Transactions, v. 38, p. 503-511.

Ligtenberg, J.H., 2005, Detection of fluid migration pathways in seismic data: implications for fault seal analysis: Basin Research, v. 17, p. 141-153.

McGowen, J.H.a.M., R. A. , 1979, Sediment Distribution, bathymetry, faults, and salt diapirs, submerged lands of Texas, Bureau of Economic Geology, 31 p.

Meckel, T.A., Bryant, S. L. and Ganesh, P. R. , 2015, Characterization and prediction of CO2 saturation resulting from modeling buoyant fluid migration in 2D heterogeneous geologic fabrics: International Journal of Greenhouse Gas Control, v. in press.

Mickler, P.J., Yang, C., Lu J., and Lankford, K. D, 2014 Laboratory batch experiments and geochemical modelling of water-rock-super critical CO2 reactions in Gulf of Mexico Miocene rocks: Implications for future CCS projects.: Energy Procedia, v. in press.

Mitchum, R.M., Vail, P.R., and Thompson, S., 1977, Seismic stratigraphy and global changes of sea level; Part 2, The depositional sequence as a basic

unit for stratigraphic analysis: Memoir - American Association of Petroleum Geologists, p. 53-62.
Nicholson, A.J., 2012, Empirical Analysis of Fault Seal Capacity for CO2 Sequestration, Lower Miocene, Texas Gulf Coast, Unpublished Masters Thesis: Geoscience, The University of Texas at Austin, p. 88.
Palandri, J.L., and Kharaka, Y.K., 2004, A compilation of rate parameters of water-mineral interaction kinetics for application to geochemical modeling: Menlo Park, California U.S. GEOLOGICAL SURVEY, p. 70.
Parkhurst, D.L., and Appelo, C.A.J., 1999, User's guide to phreeqc (version 2)—a computer program for speciation, batch-reaction, one-dimensional transport, and inverse geochemical calculations, U.S. Geological Survey p. 310.
Robinson, E.A., 1982, Seismic Velocity Analysis and the Convolutional Model, Springer, 290 p.
Seni, S.J., Hentz, T.F., Kaiser, W.R., and Wermund Jr., E.G., 1997, Atlas of Northern Gulf of Mexico Gas and Oil Reservoirs: Austin, Texas, The University of Texas at Austin, Bureau of Economic Geology, 199 p.
Soong, Y., Goodman, A.L., McCarthy-Jones, J.R., and Baltrus, J.P., 2004, Experimental and simulation studies on mineral trapping of CO2 with brine: Energy Conversion and Management, v. 45, p. 1845-1859.
Tarkowski, R., and Uliasz-Misiak, B., 2007, Reservoir rock reaction to CO2 - An experiment to estimate their use for carbon dioxide geological sequestration needs: Gospodarka Surowcami Mineralnymi-Mineral Resources Management, v. 23, p. 109-117.
Ursin, B., 1990, OFFSET-DEPENDENT GEOMETRICAL SPREADING IN A LAYERED MEDIUM: Geophysics, v. 55, p. 492-496.
USGS, 2002, Produced waters database, Volume 2002, USGS.
Vail, P.R., and Mitchum, R.M., 1977, Seismic stratigraphy and global changes of sea level; Part 1, Overview: Memoir - American Association of Petroleum Geologists, p. 51-52.
Wallace, K.J., 2013, Use of 3-Dimensional Dynamic Modeling of CO2 Injection for Comparison to Regional Static Capacity Assessments of Miocene Sandstone Reservoirs in the Texas State Waters, Gulf of Mexico: Austin, The University of Texas at Austin.
Wallace, K.J., Meckel, T.A., Carr, D.L., Treviño, R.H., and Yang, C., 2014, Regional CO2 sequestration capacity assessment for the coastal and offshore Texas Miocene interval: Greenhouse Gases: Science and Technology, v. 4, p. 53-65.
Waples, D.W., 1980, TIME AND TEMPERATURE IN PETROLEUM FORMATION - APPLICATION OF LOPATINS METHOD TO PETROLEUM-EXPLORATION: Aapg Bulletin-American Association of Petroleum Geologists, v. 64, p. 916-926.
Xie, M., Bauer, S., Kolditz, O., Nowak, T., and Shao, H., 2006, Numerical simulation of reactive processes in an experiment with partially saturated bentonite: Journal of Contaminant Hydrology, v. 83, p. 122-147.

Yang, C.B., Trevino, R.H., Zhang, T.W., Romanak, K.D., Wallace, K., Lu, J.M., Mickler, P.J., and Hovorka, S.D., 2014, Regional Assessment of CO2-Solubility Trapping Potential: A Case Study of the Coastal and Offshore Texas Miocene Interval: Environmental Science & Technology, v. 48, p. 8275-8282.

APPENDIX A

Geological CO2 Sequestration Atlas for Miocene Strata Offshore Texas State Waters

Chapter 1: Gulf of Mexico Regional Geology

Jordan-Leigh T. Rhatigan and Ramon H. Trevino

Introduction

The initial development of the Gulf of Mexico Basin occurred during the Late Triassic and Early Jurassic periods as the North American tectonic plate separated from the South American and African plates. As rifting progressed to the Early and Middle Jurassic, basin subsidence and continental crust thinning was widespread (Salvador, 1987). It was not until the Late Jurassic, with the southward drift of the Yucatan block away from the North American plate, that the connection between the Gulf of Mexico and the Atlantic Ocean developed and allowed widespread salt deposition in the basin (Salvador, 1987). Humphris (1979) postulated the development of a spreading center during the Late Jurassic to explain the current lack of salt bodies in the central Gulf despite the existence of salt bodies in two separate yet extensive parts of the basin, hundreds of kilometers apart. In addition, during the Late Jurassic to Early Cretaceous, low sediment supply resulted in mostly carbonate deposition with some siliciclastic influx in the northern Gulf, followed by the development of carbonate platforms (Winker and Buffler, 1988).

The Early Cretaceous through the Paleocene periods were dominated by the formation of a series of basins across the Western Interior Seaway. These basins extended roughly north-south in the modern high plains of North America and were the result of Laramide orogenesis to the west (Galloway and others, 2000, 2011). High sediment yields deposited in basinal drainages in Wyoming, Colorado, and New Mexico starved the northwestern Gulf of Mexico of clastic sediment supply, resulting in mixed carbonate and siliciclastic deposition in the region. After the filling of the Laramide basins, high sediment volumes entered the northern Gulf of Mexico Basin at rates greater than 100,000 km^3/Ma, and terrigenous clastic wedges prograded basinward to the southeast (Galloway and others, 2011). The high rate of late Paleocene sediment influx via newly established river systems allowed for massive, fluvial-dominated, deltaic deposition of siliciclastics into the northwestern Gulf of Mexico Basin. This high rate of deposition caused progradation of the continental margin by tens of kilometers (Galloway and others, 2000).

During the Eocene, the delta systems' sediment-input volumes generally decreased, but during the Oligocene, sediment-input volumes again increased, especially in the Norias/Rio Grande delta systems of the modern South Texas region (Galloway and others, 2000, 2011). Volumetrically significant deposition (~55,000 km^3/Ma) of clastic sediments continued throughout the Oligocene, culminating in a significant transgression and subsequent regression that resulted in the deposition of the mudrock-dominated Anahuac unit near the end of the Oligocene. Coarse clastic deposition resumed at the beginning of the Miocene and continued throughout, "indicating ongoing active erosion in large continental drainage basins" (Galloway, 2005).

Key Regional Geologic Structures of the Northwestern Gulf of Mexico Basin

The mid-Mesozoic through Cenozoic geologic development of the Gulf of Mexico was a crucial stage of development in the formation of modern-day Texas State Waters. Two key events helped to create a geologically distinct region and play a fundamental role in the hydrocarbon trapping of the region: salt diapirism and a series of syndepositional, shore-parallel, down-to-the-basin extensional fault zones. These structures are extensive throughout the Texas State Waters and are primary controls on hydrocarbon trapping in the region (Ewing, 1991; Nehring, 1991).

Semicontinuous salt basins and salt diapirism dominate the upper Texas Coast (Houston Salt Embayment) and southwestern Louisiana (South Louisiana Salt Basin), where they constitute the primary hydrocarbon trap type. These two regions, theThe Rio Grande Embayment to the south and Houston Salt Embayment to the north, are separated by the San Marcos Arch, a broad pre–Late Jurassic, southeast-plunging structure (Ewing, 1991; Ewing and Lopez, 1991). The San Marcos Arch influences both the stratigraphy and structure of Jurassic–Miocene-age formations, extending from the Precambrian Llano Uplift to the present-day coastline of Texas (fig. 1.1). In the transition zone between the two embayments, along the distal portion of the San Marcos Arch, salt-controlled structures are absent; however, salt structures are prominent features of the northern and southern flanks of the arch near the coast (Ewing, 1991; Ewing and Lopez, 1991). Syndepositional shore-parallel growth faulting and immense sedimentation accompanied the basinward migration of the continental margin through the Cenozoic (Galloway and others, 2000; Galloway, 2008; Galloway and Ganey-Curry, 2008). Fault systems decrease in age from west to east, following the general trend of the prograding continental margin discussed below in "Miocene Regional Geology" (fig. 1.2). These major fault systems also served as significant hydrocarbon traps, discussed further in Chapter 2.

Miocene Regional Geology

Deposition

The Lower Miocene of the northwestern Gulf of Mexico Basin evolved from a Paleogene (Paleocene–Oligocene) pattern of sediment supply dominated by northwestern fluvial systems to a Neogene (Miocene–Pliocene) pattern dominated by fluvial systems entering the basin from the north (Galloway, 2005)—effectively an eastward shift of depositional axes. The trend is evident from the volumetric dominance of the Red River and Mississippi River fluvial axes of the northern edge of the basin, with the Rio Grande axis remaining as the only major fluvial axis on the western edge of the basin (fig. 1.3A). In addition, the glaciation of Antarctica affected sedimentation patterns, with early- to mid-Miocene eustatic fluctuations in sea level related to contemporaneous global climate cooling and a permanent reorganization of the Antarctic cryosphere and growth of the East Antarctic Ice Sheet (Lewis and others, 2007). During the middle Miocene, the eastward shift of depositional axes continued with the establishment of the Tennessee River axis east of the Mississippi River axis (Combellas-Bigott and Galloway, 2006) (fig. 1.3B). By the middle to late Miocene, the Tennessee and Mississippi fluvial axes merged to produce the dominant depocenter for the basin. A secondary fluvial system, the Corsair axis, located on the middle Texas coastal plain, also contributed to the sediment influx (Galloway, 2005; Galloway and others, 2011) (fig. 1.3C).

Stratigraphy

The stratigraphy of the Gulf of Mexico Basin Miocene (fig. 1.4) has been interpreted by numerous workers and subdivided in several different ways since the middle of the 20th century. According to Rainwater (1964), there was considerable debate in the early part of the 20th century as to whether the Frio Formation and the Anahuac unit were of Miocene age. Rainwater proposed that the base of the Miocene should be above the Anahuac unit, and he "arbitrarily placed the top of the Miocene at the top of a transgressive marine sequence with the foraminifera *Bigenerina cf. floridana* in the shallow neritic facies, and assemblages of other Foraminifera in the deeper marine facies."

Lithostratigraphically, the top of Anahuac is still used by some as the base of the Miocene. Based on their own work and that of others (for example, Vail and others, 1977; Berggren and others, 1985; Mitchum and others, 1990), Lawless and others (1997) published a set of "biostratigraphic and cycle

charts" that included the Miocene Series, and they recognized eight Tertiary second-order sequences, two of which included the Miocene (that is, lower and middle Miocene to lower Pliocene). Following partly on the work of Feng and Buffler (1996) and Lawless and others (1997), Galloway and others (2000) defined four basin-margin "genetic stratigraphic sequences" in the Miocene: First Lower Miocene (LM1), Second Lower Miocene (LM2), Middle Miocene (MM), and Upper Miocene (UM). The genetic stratigraphic sequences of Galloway and others (2000) were defined using "bounding marine flooding horizons" along the basin margins.

The principal sequence-stratigraphic units of the charts by Lawless and others (1997) are third-order sequences as defined by Vail and others (1977) and Posamentier and Vail (1988). Similar to Lawless and others (1997), Brown and Loucks (2009), in their Wheeler diagram, infer "13 sequences (i.e., #19–31), which are all part of Supersequence 4" and compose the Miocene of the northwest margin of the Gulf of Mexico Basin. Their sequence stratigraphic framework is based on sequence boundaries consisting of updip unconformities and correlative downdip conformities as originally defined by Mitchum and others (1977) and later refined by Mitchum and Van Wagoner (1991) and many subsequent researchers. In addition, Brown and Loucks (2009) related their sequence stratigraphic framework to established lithostratigraphy such that sequences 19 through the lower part of 23 compose the Fleming Group, and the upper part of sequence 23 through sequence 31 compose the Lagarto Formation. The useful, finer-scale sequence stratigraphic framework of Lawless and others (1997) and Brown and Loucks (2009) provides a high degree of precision often required in local areas (for example, in geologic characterization of future CO_2 geosequestration prospects) and should be considered for such detailed investigations.

For the purpose of regional correlations, the framework of Galloway and others (2000) (fig. 1.4) is preferentially utilized in the current study, in part because the two most significant potential confining zones (that is, seals or caprocks) in the Miocene of the study area are *Marginulina ascensionensis* (Marg. A) and *Amphistegina chipolensis* (Amph. B). They compose the genetic sequence boundaries of LM1 and LM2, respectively, and are laterally extensive and readily identified on available seismic reflection data and wireline well log profiles (especially when micro-paleontologic data are available). Following deposition of the LM1 and LM2 genetic sequences, a relatively brief (ca. 3 m.y.) period of deposition resulted in the middle Miocene (MM), which is capped by a transgressive shale containing either *Textularia stapperi* fauna or *Textularia W* fauna (Witrock and others, 2003). Upper Miocene (UM) deposits from the late-middle to early-late Miocene record extensive margin offlap over a period of 7 m.y. The Miocene interval is capped by a regional flooding event synchronous with the *Robulus "E"* biostratigraphic marker (Galloway and others, 2000).

Structure

The structural elements of the study area comprise regionally extensive syndepositional (that is, growth) fault zones subparallel to the basin margin (fig. 1.2, map inset A). The most regionally significant fault zones that affected the Miocene succession of the study area are the early Miocene Clemente-Tomas and the middle Miocene Corsair and Wanda systems (Galloway, 1989; Bradshaw and Watkins, 1994; McDonnell and others, 2009) (fig. 1.2B). Bradshaw and Watkins (1994) identify the relatively continuous, slightly sinuous fault trends as early Miocene and middle Miocene, respectively. The strike-parallel Clemente-Tomas fault system displaced strata by over 4,000 ft (1219 m) during deposition of the LM1 and LM2 as a result of sediment loading and salt evacuation (fig. 1.5; Winker and Edwards, 1983; McDonnell and others, 2009; Nicholson, 2012). Along the lower (that is, southern) Texas coast, the faults developed as deltas loaded the shelf edge above the mobile, fine-grained facies of the Anahuac and

caused the shelf edge to founder (Winker and Edwards, 1983). Similarly, along the upper Texas coast (that is, northern half of the growth-fault trend), foundering of the shelf edge from loading by deltas occurred, but in the latter case the mobile medium was allochthonous (presumably Louann) salt (McDonnell and others, 2009).

In some localities, the shale and salt evacuation along the Clemente-Tomas growth-fault zone resulted in a greater-than-threefold thickness increase of the LM1 in the hanging wall relative to that of the footwall. Growth faulting ceased by the LM2 regressive episode, allowing subsequent progradation of the shelf margin farther to the southeast into the Corsair growth-fault trend (Bradshaw and Watkins, 1994). The Corsair system growth faulting lasted throughout the middle to late Miocene (Vogler and Robison, 1987). The Wanda fault system of the lower Texas coast formed as a result of salt evacuation (Morton and others, 1985) approximately 12 mi (19.3 km) basinward and contemporaneous with the Corsair fault system. Twofold expansion of the upper Miocene section occurs across the Wanda fault system. Salt diapirs associated with secondary salt withdrawal along the Wanda fault zone penetrated Miocene strata (Bradshaw and Watkins, 1994). The locations of regional faults (Ajiboye and Nagihara, 2012) are shown in figure 1.2.

References

Ajiboye, O., and Nagihara, S., 2012, Stratigraphic and structural framework of the Clemente-Tomas and Corsair growth fault systems in the Texas continental shelf: Gulf Coast Association of Geological Societies Journal, v. 1, p. 107–117.

Berggren, W. A., Kent, D. V., and van Couvering, J. A., 1985, The Neogene: Part 2: Neogene geochronology and chronostratigraphy: Memoirs of the Geological Society of London, v. 10, p. 211–260.

Bradshaw, B. E., and Watkins, J. S., 1994, Growth-fault evolution in offshore Texas: Gulf Coast Association of Geological Societies Transactions, v. 44, p. 103–110.

Brown, L. F., and Loucks, R. G., 2009, Chronostratigraphy of Cenozoic depositional sequences and systems tracts: A Wheeler chart of the northwest margin of the Gulf of Mexico basin: The University of Texas at Austin, Bureau of Economic Geology Report of Investigations No. 273 , 28 p.

Combellas-Bigott, R. I., and Galloway, W. E., 2006, Depositional and structural evolution of the middle Miocene depositional episode, east-central Gulf of Mexico: AAPG Bulletin, v. 90, no.3, p. 335–362.

Ewing, T. E., 1991, Structural framework, *in* Salvador, A., ed., The Gulf of Mexico Basin: The geology of North America: Boulder, Colorado, Geological Society of America, v. J, p. 31-52.

Ewing, T. E., and Lopez, R. F., 1991, Principal structural features, Gulf of Mexico Basin, *in* Salvador, A., ed., The Gulf of Mexico Basin: The geology of North America: Boulder, Colorado, Geological Society of America, v. J, plate 2, sheet 1, scale 1:2,500,000.

Feng, J., and Buffler, R. T., 1996, Post mid-Cretaceous depositional history, Gulf of Mexico Basin, *in* Jones, J. O., and Freeds, R.L.,eds., Structural framework of the northern Gulf of Mexico: Austin, Gulf Coast Association of Geological Socieities Transactions, v 46, p 9–26.

Fillon, R. H., Lawless, P. N., Lytton, R. G., III, and others, 1997, Gulf of Mexico Cenozoic biostratigraphic and cycle charts, *in* Lawless, P. N., Fillon, R. H., and Lytton, R.G., III, Gulf of Mexico Cenozoic biostratigraphic, lithostratigraphic, and sequence stratigraphic event chronology: Gulf Coast Association of Geological Societies Transactions, v. 42, p. 271–282.

Galloway, W. E., 1989, Genetic stratigraphic sequences in basin analysis II: application to northwest Gulf of Mexico Cenozoic Basin: AAPG Bulletin, v. 73, no. 2, p. 143–154.

Galloway, W. E., 2005, Gulf of Mexico basin depositional record of Cenozoic North American drainage basin evolution: International Association of Sedimentologists Special Publication, v. 35, p. 409–423.

Galloway, W. E., 2008, Depositional evolution of the Gulf of Mexico sedimentary basin, *in* Hsu, K.J., ed., Sedimentary basins of the World, v. 5, The sedimentary basins of the United States and Canada, Miall, A. D., ed., Amsterdam, The Netherlands, Elsevier, p. 505–549.

Galloway, W. E., and Ganey-Curry, P. E., 2008, Gulf of Mexico Basin depositional synthesis (GBDS) Phase 6 Atlas, The University of Texas at Austin, University of Texas Institute for Geophysics (UTIG), 161 p.

Galloway, W. E., Ganey-Curry, P. E., Li, X., and Buffler, R. T., 2000, Cenozoic depositional history of the Gulf of Mexico basin: AAPG Bulletin, v. 84, no.11, p. 1743–1774.

Galloway, W. E., Whiteaker, T. L., and Ganey-Curry, P., 2011, History of Cenozoic North American drainage basin evolution, sediment yield, and accumulation in the Gulf of Mexico basin: Geosphere, v. 7, no. 4, p. 938–973.

Huffman, A. C., Kinney, S. A., Biewick, L. R. H., Mitchell, H. R., and Gunther, G. L., 2004, Salt diapirs in the Gulf Coast [gcdiapirg]: downloadable GIS Data, Gulf Coast Geology (GCG) Online, Miocene of

Southern Louisiana: U.S. Geological Survey, Denver, Colorado. http://gulfsci.usgs.gov/gom_ims/gcg_ims.html.

Humphris, C. C., 1979, Salt movement on continental slope, northern Gulf of Mexico: AAPG Bulletin, v. 63, no. 5, p. 782–798.

Lawless, P. N., Fillon, R. H., and Lytton, R. G., 1997, Gulf of Mexico Cenozoic biostratigraphic, lithostratigraphic, and sequence stratigraphic event chronology: Gulf Coast Association of Geological Societies Transactions, v. 47, p. 271–282.

Lewis, A. R., Marchant, D. R., Ashworth, A. C., Hemming, S. R., and Machlus, M. L., 2007, Major middle Miocene global climate change: evidence from East Antarctica and the Transantarctic Mountains: Geological Society of America Bulletin, v. 119, no. 11-12, p. 1449–1461.

Lopez, J. A., 1995, Salt tectonism of the United States Gulf Coast Basin, 2nd edition map: New Orleans Geological Society, scale 1:1,524,000.

Martin, R. G., 1980, Distribution of salt structures, Gulf of Mexico: U.S. Geological Survey miscellaneous field studies map MF-1213, scale 1:2,500,000.

McDonnell, A., Hudec, M. R., and Jackson, M. P. A., 2009, Distinguishing salt welds from shale detachments on the inner Texas shelf, western Gulf of Mexico: Basin Research, v. 21, p. 47–59.

Mitchum, R. M., Jr., and Van Wagoner, J. C., 1991, High-frequency sequences and their stacking patterns: sequence-stratigraphic evidence of high-frequency eustatic cycles: Sedimentary Geology, v. 70, p. 131–160.

Mitchum, R. M., Sangree, J. B., Vail, P. R., and Wornardt, W. W., 1990, Sequence stratigraphy in late Cenozoic expanded sections, Gulf of Mexico, *in* Perkins, J. M. A., a.B.F., ed., Sequence stratigraphy as an exploration tool: concepts and practices in the Gulf Coast: Eleventh Annual Research Conference, Gulf Coast Section SEPM Foundation, p. 237–256.

Mitchum, R. M., Vail, P. R., and Thompson, S., 1977, Seismic stratigraphy and global changes of sea level, Part 2: The depositional sequence as a basic unit for stratigraphic analysis, *in* Payton C. E., ed., Seismic stratigraphy applications to hydrocarbon exploration: American Association of Petroleum Geologists Memoirs 26, p. 53–62.

Morton, R. A., Jirik, L. A., and Foote, R. Q., 1985, Depositional history, facies analysis and production characteristics of hydrocarbon-bearing sediments, offshore Texas: The University of Texas at Austin, Bureau of Economic Geology Geological Circular v. 12, p. 512–522.

Nehring, R., 1991, Oil and gas resources, *in* Salvador, A., ed., The Gulf of Mexico Basin: The geology of North America: Boulder, Colorado, Geological Society of America, v. J, p. 445–494.

Nicholson, A. J., 2012, Empirical analysis of fault seal capacity for CO_2 sequestration, lower Miocene, Texas Gulf Coast: The University of Texas at Austin, Master's thesis, 88 p.

Posamentier, H. W., and Vail, P. R., 1988, Sequences, systems tracts, and eustatic cycles: AAPG Bulletin, v. 72, no.2, p. 237–237.

Rainwater, E. H., 1964, Regional stratigraphy of the Gulf Coast Miocene: Gulf Coast Association of Geological Societies Transactions, v. 14, p. 81–124.

Salvador, A., 1987, Late Triassic-Jurassic paleogeography and origin of Gulf of Mexico Basin: AAPG Bulletin, v. 71, no. 4, p. 419–451.

Vail, P. R., Mitchum, R. M., Todd, J. M., Widmier, J. M., Thompson, S., III, Sangree, J. B., Bubb, J. N., and Hatlelid, W. G., 1977, Seismic stratigraphy and global changes of sea level, *in* Payton C. E., ed., Seismic stratigraphy applications to hydrocarbon exploration: American Association of Petroleum Geologists Memoirs 26, p. 49–212.

Vogler, H. A., and Robison, B. A., 1987, Exploration for deep geopressured gas-Corsair trend, offshore Texas: AAPG Bulletin, v. 71, no.7, p. 777–787.

Winker, C. D., and Buffler, R. T., 1988, Paleogeographic evolution of early deep-water Gulf of Mexico and margins, Jurassic to Middle Cretaceous (Comanchean): AAPG Bulletin, v. 72, no. 3, p. 318–346.

Winker, C. D., and Edwards, M. B., 1983, Unstable progradational clastic shelf margins, *in* Stanley, D. J., and Moore, G. T., eds., The shelf break: critical interface on continental margins: SEPM Special Publication, v. 33, p. 139–157.

Witrock, R. B., Nixon, L. D., Post, P. J., and Ross, K. M., 2003, Biostratigraphic chart of the Gulf of Mexico offshore region, Jurassic to Quaternary: New Orleans, Louisiana, U.S. Department of the Interior, Bureau of Ocean Energy Management.

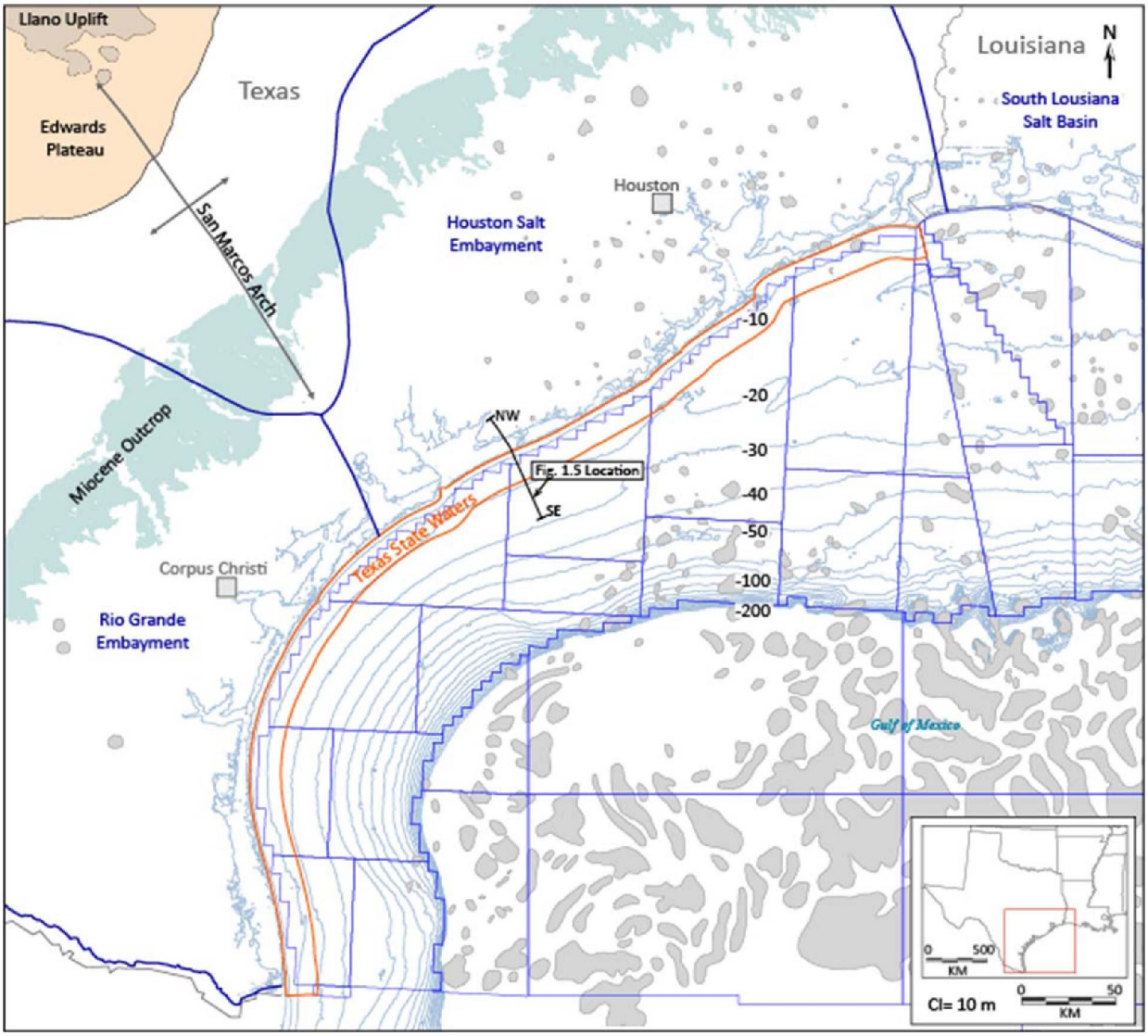

Figure 1.1. Map of Texas Gulf Coast showing the current study area; Texas State Waters (orange outline); bathymetry (contour interval = 10 m) to the present-day shelf margin at 200 m; Miocene outcrop belt; location of major Texas and southern Louisiana salt basins, regional tectonic features, and major salt bodies shown as gray polygons (modified from Martin, 1980; Ewing and Lopez, 1991; Lopez, 1995; Huffman and others, 2004); and figure 1.5 cross-section location.

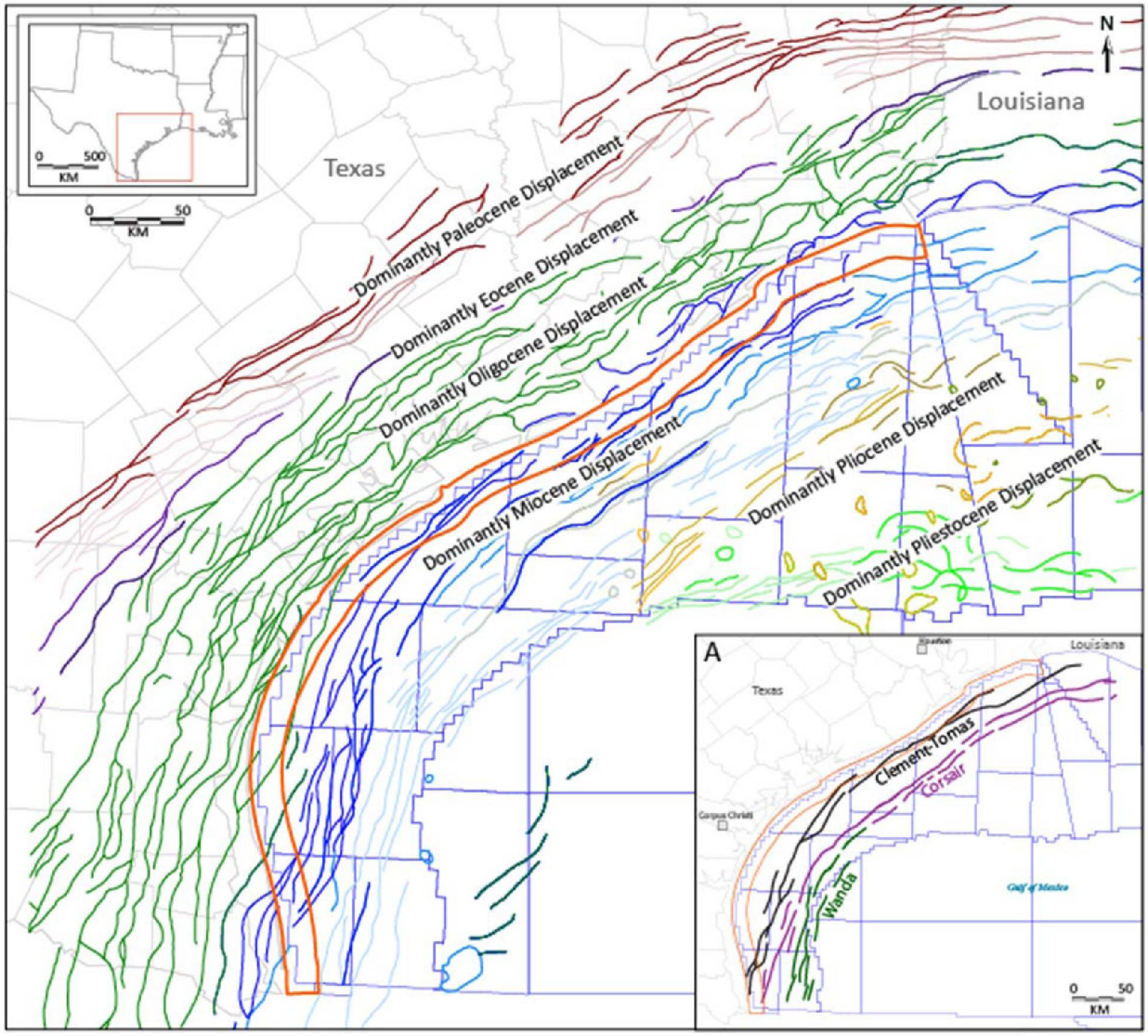

Figure 1.2. Map of the Texas Gulf Coast showing the major Cenozoic fault zones. The age of these approximately shore-parallel, syndepositional, extensional faults is marked by their respective dominant displacement (modified from Galloway and others, 2000; Galloway, 2008; Galloway and Ganey-Curry, 2008). Inset map A highlights Miocene-age fault zones (black, Clemente-Tomas; purple, Corsair; green, Wanda) (modified from Ajiboye and Nagihara, 2012).

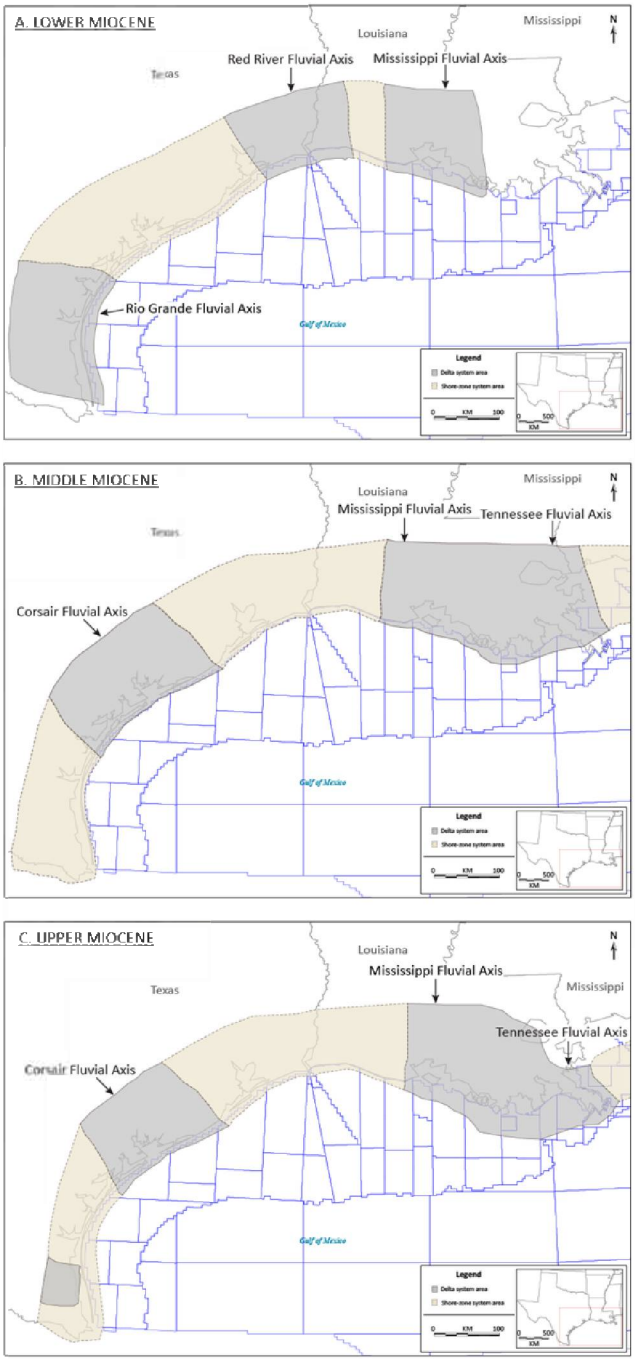

Figure 1.3. Simplified outlines of deltaic and shore-zone depositional systems of the (a) Lower, (b) Middle, and (c) Upper Miocene. Principal fluvial axes operating during each depositional episodes listed (modified from Galloway, 2005).

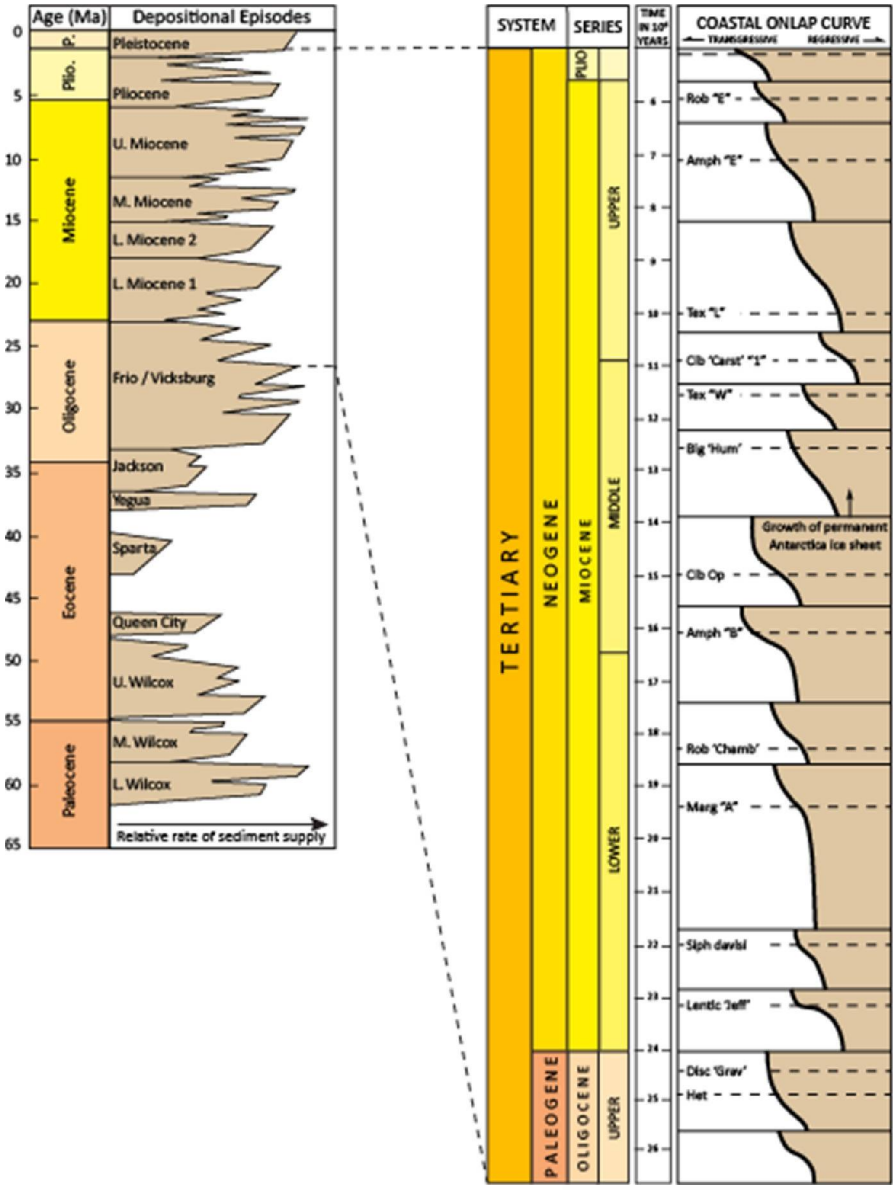

Figure 1.4. Stratigraphic column of major Tertiary depositional episodes And Miocene detailed coastal onlap curve (right) with abbreviations of key benthic foraminiferal biochronozones (such as “Marg. A” and “Amph. B”) (modified from Fillon and others, 1997; Galloway and others, 2011).

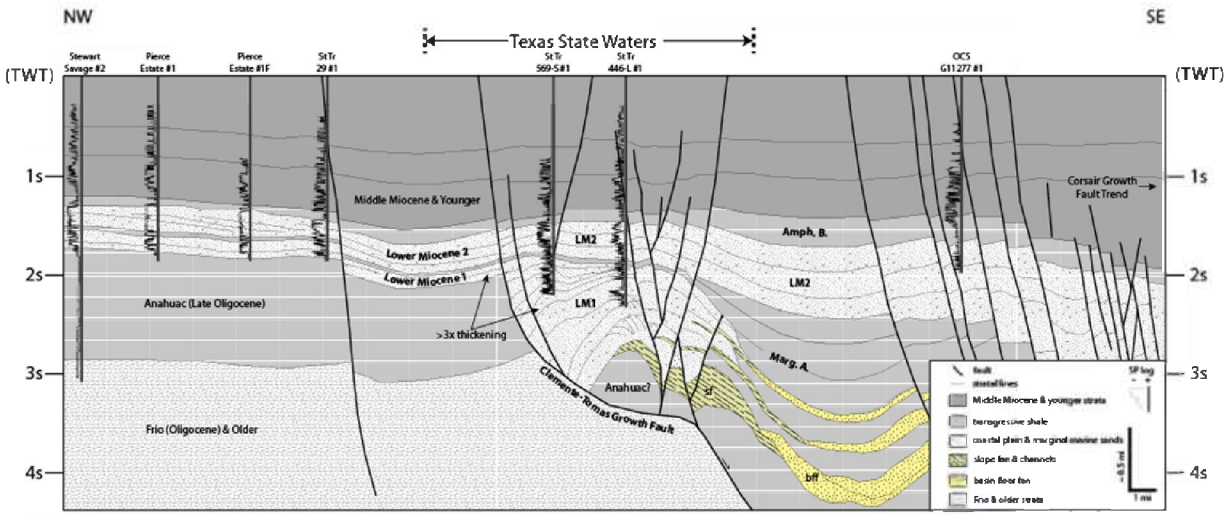

Figure 1.5. Dip-oriented structural cross section (from Nicholson, 2012). Intrepreted 2D seismic line (from ION Geophysical). Location shown in Figure 1.1.

Chapter 2: Implications of Miocene Petroleum Systems for Geologic CO_2 Sequestration beneath Texas Offshore Lands

Jordan-Leigh T. Rhatigan[1] and T. A. Meckel[1]

[1]Gulf Coast Carbon Center, Texas Bureau of Economic Geology, The University of Texas at Austin

Introduction

Carbon capture and storage (CCS) remains one of the most viable options for near-term mitigation of industrial-scale CO_2 emissions. Much research effort has focused on the viability and long-term storage capability of individual hydrocarbon reservoirs and on the use of CO_2 for enhanced oil recovery (EOR). While regional capacity studies have been undertaken for years (Elewaut and others, 1996; Brennan and others, 2010; NETL, 2012), such volumetric analyses rarely incorporate perspectives provided by the petroleum systems of those basins. This study uses petroleum-system analysis as the departure point for informing regional aspects of subsurface CO_2 storage such as volumetric retention (storage capacity) and seal performance. A review of Miocene-age oil and gas fields of the Texas State Waters and their relationship with regionally extensive fault zones indicates that reservoirs are sealed sufficiently enough to contain abundant hydrocarbons. Future commercial carbon capture and storage could take advantage of these data-rich fields by considering them as initial targets for CCS.

This study focuses on the viability of charged and uncharged closures of specific stratigraphic intervals and structural settings in Texas State Waters that represent prospective storage sites. Initially, we provide a summary of historically produced Miocene-age hydrocarbon reservoirs and their relationship with existing regional structures (e.g., the Clemente-Tomas Fault system), which makes inferences about storage capacity and long-term sealing potential, focusing on the most promising geologic settings. Next, a rough quantification of potential storage capacity in Miocene-age depleted gas reservoirs is presented, using a simple methane (CH_4) gas to CO_2 subsurface volume replacement for each reservoir. Results suggest that anticlinal closures with and without associated faulting represent the largest potential CO_2 storage capacity of the trap types identified. However, only the largest 10% of the existing gas fields in state waters are likely to be volumetrically significant storage targets for industrial-scale emissions, unless structures can retain additional volume beyond historical accumulation size. For this reason, a regional structural-closure analysis of a lower Miocene stratigraphic horizon was conducted to identify potential for additional storage in large closures that may be underfilled or uncharged but may otherwise represent excellent prospective storage sites.

Data

Analysis presented in this study focuses on the robust quantitative data available from decades of exploration and production of hydrocarbon-bearing reservoirs in the Gulf of Mexico Basin. This study integrates published data and comprehensive digital databases from a 181,000-km^2 coastal area from Texas to Alabama. The area contains 1,357 major Miocene oil and gas fields, but only 109 of the fields in Texas State Waters are of Miocene age. Use of GIS technology facilitates evaluating relationships among sets of specific field parameters such as trap type, reservoir geology, drive mechanism, and size of hydrocarbon accumulations.

Miocene oil and gas field data and key regional geologic structures (e.g., faults or salt bodies) from published GIS data sets were compiled into a comprehensive digital interface using both ArcGIS and IHS Petra. Oil and gas field data sources include the *Atlas of Northern Gulf of Mexico Gas and Oil Reservoirs* (Seni and others, 1997), *Atlas of Major Texas Gas Reservoirs* (Kosters and others, 1989), *Atlas of Major Texas Oil Reservoirs* (Galloway and others, 1983), *Reservoirs and Petroleum Systems of the Gulf Coast* (Pitman, 2009), and Bureau of Ocean Energy Management (BOEM) data from the Federal offshore Outer Continental Shelf (BOEM, 2006).

Data were used to generate a variety of maps, incorporating all pertinent regional geologic structures and hydrocarbon occurrences to illustrate the regional trends of the Miocene petroleum systems and other field properties (e.g., depositional environment, trap type, drive type) that may provide useful insight into CO_2 sequestration potential. Given the current study's focus on Texas State Waters for CO_2 storage, the material presented here will concentrate only on the innermost portion of the Gulf of Mexico Outer Continental Shelf (OCS) offshore Texas (fig. 2.1).

Summary of the Miocene Petroleum System

Most Miocene-age oil and gas production in the Gulf Coast of Texas occurs in lower Miocene reservoirs. Numerous lower Miocene oil and gas accumulations cover a broad swath of offshore Texas, mostly the innermost Federal OCS but also the central part of Texas State Waters (Ewing, 1991; Ewing and Lopez, 1991). Gas fields dominate along the middle and south Texas coast, whereas oil accumulations are more prevalent along the upper Texas coast (fig. 2.1). The Texas gulf coast is dominated by large-scale Cenozoic-growth fault zones, but the Oligocene and Miocene fault zones are the most relevant to this study, as fault-controlled trapping of Miocene hydrocarbons is prevalent (Galloway, 1986; Berg and Avery, 1995; Galloway and others, 2000; Galloway, 2008; Galloway and Ganey-Curry, 2008). The largest lower Miocene hydrocarbon volumes are found in gas accumulations in the offshore region and are mostly trapped in the early–middle Miocene faulted regions. Along the upper Texas coast and southwestern Louisiana, where oil accumulations are commonly dominant, fluids were trapped in salt-controlled traps associated with piercement salt diapirs (Martin, 1980; Nehring, 1991; Lopez, 1995; Huffman and others, 2004).

Early–middle Miocene hydrocarbon accumulations migrated progressively to stratigraphically younger units from west to east, following the trend of terrigenous clastic depocenters basinward (Galloway, 1989; Galloway and others, 2000; Galloway, 2005). What little middle Miocene production occurs in onshore Texas is limited to the southeastern part of the Houston Salt Embayment. The greatest middle Miocene hydrocarbon volumes are, as in the lower Miocene, gas accumulations found in the offshore region. A small cluster of fields are related to the regional highs associated with the San Marcos Arch on the central coast (fig. 2.1). Maps made as part of the study, but not presented here for brevity, indicate that Middle Miocene oil and gas accumulations along the upper Texas coast and southwestern Louisiana coast show very limited geographic movement through the early to middle Miocene, a pattern that differs from trapped hydrocarbons in the central and southern portions of Texas. Limited basinward shifting of fields is likely explained by the vertical migration of fluids—commonly associated with piercement salt diapirs—which provide the dominant trapping mechanism for both oil and gas accumulations along the upper Texas coast and southwestern Louisiana coast.

Upper Miocene accumulations, dominantly oil, are almost entirely restricted to Louisiana, the exception being an isolated cluster of gas fields in the Federal OCS waters approximately 100 km south of Houston. Salt domes of this region provide the primary trapping mechanism for the majority of hydrocarbon accumulations; however, fault- and stratigraphy-

controlled traps have also been identified. The late Miocene stratigraphy has contributed negligibly to oil and gas production in Texas, including in Texas State Waters. Thus, our focus remains on the depleted hydrocarbon fields in the lower- and middle-Miocene chronostratigraphic intervals, the relationships between regional geologic features and hydrocarbon accumulations, and the implications for identifying suitable CO_2 storage sites.

Regional Structural Controls on Hydrocarbon Trapping

The Cenozoic structural and stratigraphic development of the northern Gulf of Mexico Basin is dominated by passive margin progradation of dominantly clastic sediments with attendant salt diapirism and regionally extensive fault zones (Winker and Edwards, 1983; Galloway, 1989; Kosters and others, 1989; Bradshaw and Watkins, 1994; Seni and others, 1997; Galloway and others, 2000; Galloway, 2005; McDonnell and others, 2009). It has been well documented that the regional and local structures largely influence the size and location of hydrocarbon accumulation along the margin of the Gulf of Mexico Basin (Ewing, 1991; Nehring, 1991).

The large-scale extensional faulting along the Texas and southwestern Louisiana coasts occurred predominantly during the late Oligocene and early Miocene and appears to control the distribution of volumetrically significant hydrocarbon accumulations in Miocene reservoirs. For example, the strike-parallel Clemente-Tomas growth fault zone, a prominent structural feature of the lower Miocene stratigraphic interval, has as much as several thousand feet of displacement, depending on geographic location and depth (Winker and Edwards, 1983; Bradshaw and Watkins, 1994; McDonnell and others, 2009; Ajiboye and Nagihara, 2012). All known major Miocene oil and gas fields (Galloway and others, 1983; Kosters and others, 1989; Seni and others, 1997) coincide with regions dominated by Oligocene and Miocene fault displacement (fig. 2.1). The boundary between the two faulted regions is marked by the gray dashed line in figure 2.1. The region updip (landward) of this line is dominated by Oligocene-age faulting (green shading), whereas the downdip (seaward) region is dominated by Miocene-age faulting (blue shading). Growth faults are characterized by the age of the most pronounced differential growth (qualitatively determined for each unit using thickness maps, seismic lines, or cross sections). Although pronounced differential growth may have occurred during a particular time period, it does not exclude fault reactivation or growth in other time periods (Galloway and others, 2000; Galloway, 2008; Galloway and Ganey-Curry, 2008).

The majority of Miocene accumulations occur offshore and downdip of the schematic boundary separating the Oligocene- and Miocene-age faulted regions. Only minor accumulations are noted updip despite the occurrence of porous and permeable Miocene sandstones and numerous hydrocarbon traps in older horizons on the footwall of regional growth faults (e.g., the Wilcox, Frio, and Yegua formations). Hydrocarbon occurrence updip of the zone of Miocene-age faulting is likely associated with fluid migration from the prolific underlying Oligocene Frio Formation and/or vertical migration associated with salt structures of the upper Texas coast and even older, deeper units. This observation suggests that late Oligocene–early Miocene faults acted as a regional barrier for hydrocarbons, preventing large-scale updip migrations of fluids, likely from Cretaceous and lower Tertiary sources much farther basinward, into the onshore Texas Gulf Coast region (Kennicutt and others, 1992; Wagner and others, 1994; Hood and others, 2002). As fluids migrated updip out of the central basin, they encountered the Miocene-age faults and were trapped in preexisting structures, preventing larger onshore accumulations (Galloway, 1986; Berg and Avery, 1995).

There is a significant volumetric difference in cumulative gas production between the two distinct updip and downdip regions. For the onshore updip region we estimate 2.3 TcfgEQ (trillion cubic feet of gas equivalent), and for the downdip offshore region, 57.1 TcfgEQ (fig. 2.1). These estimates support the premise that future large-volume CO_2 injections into the Miocene reservoirs of Texas State Waters might also be similarly confined in the downdip, mostly offshore region. In the upper Texas coast region, the Clemente-Tomas fault zone occurs very close to the location of the present-day shoreline and potential industrial CO_2 emissions sources.

Relationship between Hydrocarbons and Trap Types

Assessing the relationship between trap types and their associated hydrocarbon accumulation volumes provides a basis for determining whether (1) particular trap types may be preferable for future CO_2 sequestration sites, and (2) some trap types appear to be problematic with respect to poor overall volumetric retention. To assess this, a cumulative distribution function (CDF) plot of the occurrence of gas field size was generated for all reservoirs in the OCS database (N=10,283; BOEM, 2006), as well as for just those of Miocene age (N=3,932; fig. 2.2). The distribution of Miocene-age field size is essentially identical to that of the larger population, including reservoirs of all ages, throughout the Gulf of Mexico, which indicates that the Miocene accumulations are no different in primary occurrence characteristics (sizes and trap types) than the reservoir population as a whole.

The cumulative distribution curves for individual trap types were similarly plotted and conform to the curve for the entire population (fig. 2.2). Some of the curves are populated with fewer data (e.g., N=42 for updip pinch-out traps) and have a less smooth shape, but adhere to the overall population trend. Such conformance demonstrates that no single trap type is any more or less likely than another to have a large (or small) accumulation. Stated another way, large accumulations are not associated with any specific trap type, and accumulations of all sizes are equally likely to occur in any of the structural trap settings. Since many of the trap types represented involve faulting, the conformance is a strong indirect indication that fault seals, as a population, do not inherently limit accumulation size (see also Chapter 4). Individual field analysis may indicate that a fault seal is a controlling factor, but this does not occur often enough to become apparent in the CDF plots. If faulting were a primary limitation to accumulation size, CDF curves for those trap types would be shifted toward the left, indicating an overall inability to trap large volumes.

A histogram of the dominant trap types for the Miocene oil and gas fields of the Texas State Waters is shown in figure 2.3 (N=148 reservoirs). Fluid-trapping mechanisms are dominantly fault and salt controlled, with fewer occurrences of stratigraphically controlled types. Lower Miocene traps are largely fault controlled (45% faulted anticline, 30% rollover anticline into growth fault). Rollover anticlines are most common in the lower Miocene, where fault offsets and growth strata on downthrown blocks are largest (Galloway, 1986; Berg and Avery, 1995). Fault-controlled traps (i.e., 40% faulted anticline, 20% normal fault) remain dominant during the middle Miocene. However, minor salt-controlled traps (11% sediment overlying dome) have been documented for fields located along the upper Texas and southwestern Louisiana coasts.

Accumulations in the upper Miocene are negligible and restricted to a small portion of the Federal OCS, approximately 20 miles beyond the Texas State Waters. Although fault-controlled traps (i.e., 27% faulted anticline, 17% normal fault) are again dominant, numerous salt domes (i.e., 17% sediment overlying dome, 10% flank trap associated with salt diapirs) off the coast of southwestern Louisiana provide approximately 25% of the fluid traps documented.

Stratigraphic traps are noted for approximately 15% of the upper Miocene fields, though these traps are geographically restricted to the southeast Louisiana coast.

These observations suggest that, while all trap types may be equally suitable for consideration for CCS, specific structural settings (trap types) are more common for natural hydrocarbon accumulation. Based on the dominance of faulted traps in hosting gas accumulations, and the observation that such faulted traps are capable of retaining even the largest volumes observed naturally (fig. 2.2), these settings appear highly prospective for CCS.

Relationship between Hydrocarbons and Depositional Environments

Miocene hydrocarbon reservoirs in Texas State Waters (N=148) were analyzed according to interpreted depositional environments because depositional environments are a primary control on both reservoir characteristics (e.g., permeability, continuity) and overlying seal thickness and quality. The most numerous hydrocarbon accumulations occur within shore-zone (57%) and wave- and fluvial-dominated deltaic (35%) depositional systems, with minor occurrences in sandy shelf complexes (fig. 2.4). The largest individual fields occur in more homogeneous depositional systems (e.g., strand-plain/barrier-island complexes and large deltas).

Appreciating these generalized relationships between size and depositional environment is an important consideration for CCS; as the trends suggest which depositional environments may similarly be most prospective for CO_2 injection, further research can be focused on those reservoir types. The fact that the majority of the Miocene accumulations are in shore-zone and deltaic systems may simply reflect their volumetric dominance in the stratigraphic section. On the other hand, it may suggest an underlying consistency of the vertical association of good reservoir properties with continuity and overlying seal quality. Likely it is some combination of frequency of occurrence and quality of geology.

Relationship between Hydrocarbons and Drive Mechanism

Figure 2.5 presents a histogram of reservoir-production drive type for Miocene fields of Texas State Waters. Water drive is the most reported reservoir drive mechanism. However, partial-water, pressure-depletion, and combination drive mechanisms are also well represented in the available data set. The largest accumulations are associated with strong water drive, which is the most efficient fluid displacement type of drive mechanism (Sills, 1992).

The fraction of reservoir pore space saturated with water as well as production drive mechanisms are critical parameters for CO_2-evaluating sequestration prospects because storage capacity is heavily dependent on an understanding of reservoir boundary conditions and efficient water displacement during injection. The importance of open-versus-closed boundary conditions at potential CO_2 sequestration sites has been debated by many (Chadwick and others, 2010; Dooley and Davidson, 2010; Ehlig-Economides and Economides, 2010). However, historical oil and gas production has proven that the reservoirs studied typically have open boundaries, allowing for some amount of communication with surrounding rock media and thus negating most arguments for a closed-boundary scenario.

Typical reservoirs fall between the hydrostatic and fracture pressure gradients (~85% lithostatic), with the majority near hydrostatic pressure gradient (~0.433 psi/ft). This, in combination with the dominance of water drive mechanisms documented for these reservoirs (Sills, 1992), suggests that the Miocene portion of Texas State Waters is relatively well connected hydrologically. Open hydrologic conditions are extremely beneficial for CO_2 injection because they increase injectivity and reduce pressure elevation, thereby increasing capacity and decreasing fill time (Miller, 2012; Wallace, 2013). The widespread occurrence of water drive is

significant for CO_2 storage because it is an indirect indication that the reservoirs have strong communication over geologic timescales with associated brine aquifers, suggesting that pressure elevation from engineered injections may be manageable.

Integrating the information on trap type, depositional environment, and drive type from gas-accumulation settings, obvious initial targets for CCS are shore-zone (strand plain and barrier island) and large deltaic-reservoir systems that are involved in fault-bound anticlines or rollover anticlines with strong associated water drive. Because of the relatively low sediment supply (compared to the Mississippi River system further east in Louisiana) and active fault positions during the Miocene, these settings occur in relatively narrow, shore-parallel trends (Kiatta, 1971). As an example, one of the larger offshore Miocene-age gas fields, El Gordo, occurs in delta-fan sediments of a compartmentalized anticline set up by a large-offset growth fault (Seni and others, 1997). Although onshore, another example of such a favorable environment is described by Ambrose (1990) for brine disposal into a Miocene barrier island, fluvial and deltaic complex.

Caveats of Using a Petroleum Systems Approach for Informing CCS

There are some significant caveats in the approach pursued in this research. Most notably, there are distinct differences between how hydrocarbons accumulate naturally and how CO_2 behaves during engineered injection. The most important of these differences is the time frame of accumulation, or the rate of "charge." Natural accumulations evolve over geologic time, while injections occur over decades. Experience in enhanced oil recovery with CO_2 indicates that injected CO_2 generally has poor sweep efficiency because of reservoir heterogeneity. Thus, there is some hazard in making an assumption that reservoir saturations for injected CO_2 will be as high as those for natural accumulations. One strategy for overcoming the poor sweep efficiency of CO_2 is to inject low on structures and allow the CO_2 to rise buoyantly into the trap, attempting to mimic natural migration and accumulation.

A second major caveat of using petroleum systems analysis to guide CCS prospects is that hydrocarbons occur naturally in only a very small proportion of the stratigraphy. An important question relates to whether this is because (1) these are the only suitable retention sites, or (2) a more nuanced relationship exists between migration pathways and structure, such that much of the stratigraphy is bypassed. In either case, CCS can initially be considered for a much larger proportion of the available stratigraphy, and many settings likely exist that were not part of the hydrocarbon system but that have favorable geology and structure. These brine-filled reservoir systems may largely be untested for retention of buoyant fluids. However, the insights learned from adjacent production settings may allow reservoir and/or seal characteristics to be correlated with some confidence, perhaps verified in part with logs from dry exploration wells.

A third fundamental caveat is that settings other than those with structural closure can be considered for CO_2 storage. The various trapping mechanisms for CO_2 indicate that local capillary and residual phase trapping (Saadatpoor and others, 2009) can both be significant for immobilization of CO_2. Thus, some storage could occur on dipping stratigraphy without structural closure (Hovorka and others, 2006). The majority of stratigraphy in most basins represents this setting without structural closure (typically considered fetch areas for accumulations). However, the early CO_2 storage sites are likely to be those with defined closure for reasons related to uncertainty reduction of plume evolution, liability, and insurability.

CH_4–CO_2 Volumetric Replacement Assessment

Depleted gas fields are particularly attractive for CO_2 storage because of their proven seals for a more buoyant gas phase. First-order questions are: What volumes of storage are achievable by simply "refilling" depleted gas fields to their historic accumulation size? How does this storage-capacity estimate compare to the projected emissions of anthropogenic CO_2 to be sequestered? A volume-replacement exercise was conducted in order to rapidly and simply estimate the potential CO_2 storage capacity of Miocene gas reservoirs.

Available field data for Miocene gas reservoirs from the Texas State and Federal OCS Waters (Seni and others, 1997; BOEM, 2006) were subdivided into individual gas reservoirs, where a reservoir is defined as a single accumulation of gas held by a trapping structure and seal to impede further migration, while a field is a grouping of several reservoirs located on a single geologic feature or otherwise closely related (Seni and others, 1997; Levorsen, 2001). For each reservoir, original gas in place (OGIP) volumes were calculated for all Miocene gas reservoirs using equation 1:

$$OGIP = \frac{CUMG * B_g}{RFG} \qquad (1)$$

where CUMG is the cumulative gas production, B_g is the reservoir volume factor for gas for each reservoir, and RFG is the recovery efficiency of gas. The B_g parameter was calculated and used to convert given surface volume to subsurface volumes (Garb and Smith, 1987; Metcalfe, 1987; Sustakoski and Morton-Thompson, 1992). The surface-to-subsurface volume parameter, B_g, is a critical parameter to consider when converting from subsurface volumes to sequestration capacity estimates, as gases compress to reservoir pressure and temperature conditions (Brennan and others, 2010; Miller, 2012; Blondes and others, 2013).

Conversion of the calculated OGIP volume to the equivalent CO_2-saturated pore space was calculated using reservoir-specific and depth-related conditions (e.g., pressure and temperature). The CO_2 density for each gas reservoir was determined by using the method described in Nicholson (2012) after the Peng and Robinson (1976) equation of state incorporating reservoir-specific pressures and temperatures. Subsequently, the CO_2 density was multiplied by the OGIP volume to obtain a potentially sequestered mass of CO_2 in each Miocene gas reservoir. The calculations assume that the residual water saturation (R_{sw}) for hypothetical CO_2 injections was equivalent to natural methane accumulations, which may be optimistic (see above) but a reasonable first-order approximation. All mass values are presented in metric Megatonnes (Mt; standard mass measurement for CO_2 storage). The English Megaton equivalent is approximately 10% greater. For reference, typical emissions from a 500 mW electrical utility are on the order of 3 Mt per year.

OGIP (CH_4) volumes and the corresponding mass of CO_2 are shown for different trap style and drive type in figures 2.3 and 2.5 (note log scale). As discussed above, water drive mechanism and faulted anticline and rollover anticline into growth-fault trap types occurred most frequently and account for the greatest volumes of methane gas. Of primary interest, calculated conversions confirm that the largest CO_2 masses are also correlated with these settings. Of secondary interest, variation in the magnitude differences between OGIP and CO_2 mass are a function of reservoir-specific conditions given for each of the 148 Miocene gas reservoirs included in the analysis. Recall that methane (CH_4) density varies only slightly with depth (0.0–0.2 g/cm^3), while the density of CO_2 rapidly increases with depth until it reaches a steady range between 0.6 and 0.7 g/cm^3 below 3,200 ft. At depth, typically greater than 2,600 ft where high reservoir pressure (>1,000 psi) and temperature (>88°F) exist, the CO_2 phase changes from gaseous to supercritical (Bachu, 2000).

The cumulative frequency distributions of gas reservoir sizes in Miocene-age reservoirs from both the Texas State Waters (solid lines) and the Federal OCS (dashed lines) are shown in figure 2.6. Most Miocene-age gas reservoirs of the Texas State Waters are smaller than 1000 MMcf (million cubic feet), which is relatively small in the context of the greater Gulf of Mexico and global basins. Curves illustrating the converted CO_2 masses for these same gas reservoirs are also displayed, using the scale at the top of the diagram. While the total converted CO_2 mass for all gas reservoirs studied in the Texas State Waters is an impressive 554 Mt CO_2, only the largest 10% of those fields are greater than 10 Mt each. It is extremely unlikely that investment would be made to develop a CO_2 storage site less than 10 Mt, as that does not represent a volume attractive for long-term, industrial-scale injection. Those smaller sites are suitable for demonstration projects. Only sites in the 50–100 Mt range are likely to be economically developed for industrial-scale storage, and data indicate that there are few depleted gas fields of that size in the Texas State Waters.

A distinct divergence between the CH_4 and CO_2 distribution curves for Texas State Water reservoirs (two solid curves in fig. 2.6) occurs in volumes exceeding 100 MMcf. Smaller reservoirs tend to be located at shallower depths, where the difference between the density of CH_4 and CO_2 is less pronounced. The larger reservoirs are typically found at deeper depths, where the density difference between methane and CO_2 is much greater. This density difference explains the divergence of the cumulative distribution curves. It is likely that if a single conversion factor existed to replace CH_4 with CO_2 in a reservoir, the distribution curve of CO_2 would more closely parallel (and not diverge from) the OGIP distribution curve. However, inherent variations in pressure, temperature, and behavior of CO_2 in the subsurface all directly correspond to the differences noted in this CH_4–CO_2 volume replacement.

The cumulative distribution curve for the Federal OCS reservoir size distribution (black dashed line in fig. 2.6) is very similar in shape to that of the Texas State Waters, but the volume of OGIP in the Federal OCS is two orders of magnitude greater. This reflects the much larger sample size for the Federal OCS (>10,000 reservoirs versus <150). It is possible that these different distribution curves could signal potential reservoir size limitations resulting from limited sample population and restricted region of study, fluid-migration timing and distance from source, and/or quality of seals, but determining this would require further in-depth reservoir analysis. However, based on the conversion of OGIP to CO_2 mass for the Texas State Waters, it is likely that if the same fluid replacement exercise were completed for the 10,000 gas reservoirs of the Federal OCS, the result would be a distribution curve with volumetric curve shifts similar to what is observed for Texas State Waters (rightmost red dashed curve in fig. 2.6). The exact shape and magnitude of that distribution would be dependent on reservoir-specific temperature and pressure, which was not undertaken because of the primary focus of this study on Texas State Waters. However, experience doing those calculations for the Texas State Waters suggests that CO_2 storage capacity in the Federal OCS historic gas reservoirs could be roughly 10–100's Mt of CO_2 per reservoir. These likely represent economic storage development sites in the context of offshore storage.

Structural Closure Analysis

While it is obvious from figure 2.6 that the majority of offshore CO_2 storage in the Gulf of Mexico resides in the OCS, there may be some potential for storage in the Texas State Waters that the prior analysis of depleted gas fields fails to identify. One of the primary conclusions of

the prior structural analysis is that the majority of prospective CO_2 storage in depleted gas fields occurs in faulted anticline settings. Historic methane accumulation in these settings suggests that fault seal is not a primary limiting factor in natural accumulation size (or these faulted fields would not exist; fig. 2.2; Sales, 1997) and, by inference, in engineered CO_2 injections. This conclusion is consistent with top- and fault-seal analysis done for specific parts of the Texas State Waters study area (Nicholson, 2012; Chapters 3 and 4, this volume). The results suggest that top and fault seals can likely hold higher column heights of CO_2 than can known natural gas accumulations, and that there may be potential to inject larger volumes of CO_2 into many structures, provided the structural closure exists. Recall that hydrocarbon accumulations only occupy a tiny fraction of the total stratigraphy available. That is, the cumulative CO_2 mass distribution curve (solid red line in fig. 2.6) could be shifted farther to the right, allowing for larger total capacity in depleted gas fields by incorporating the downdip water leg of those reservoirs. To investigate this potential, a closure analysis was conducted for a typical lower Miocene stratigraphic horizon and compared to the footprint of known gas fields.

The stratigraphic horizon used in the analysis was derived from a continuous integrated 3D seismic volume covering the upper portion of the Texas State Waters from central Matagorda County to the north end of Galveston Island (fig. 2.7). While it is difficult to maintain consistent stratigraphic position over such a large area in a time seismic volume, biostratigraphic well data constrained by checkshots were utilized where possible. The interpreted horizon very closely represents the subsurface structure that exists in the lower Miocene (LM2) interval in the region. The major elements of the structure extend vertically upward toward the upper Miocene, and some of the major faults extend into the Plio-Pleistocene stratigraphy (Nicholson, 2012). It is therefore reasonable that this horizon reflects major structure for the hydrocarbon system at the time of charge throughout much of the lower Miocene section, making it sensible to vertically project all lower Miocene reservoirs onto this surface for generalized analysis.

The geographic footprint of the Miocene gas fields (red shapes in fig. 2.7) is derived from the *Atlas of Major Texas Gas Reservoirs* (Kosters and others, 1989). These boundaries are largely schematic but are constrained when possible with known detailed structure maps of fields and hydrocarbon-water contact elevations. So, while the outlines are not exact, they are a reasonable estimate of the extent of the fields and are suitable for the qualitative analysis undertaken here.

In this study, major potential storage compartments for the Miocene interval in the Texas State Waters have been identified using traditional petroleum systems concepts like structural closure, “fill and spill,” and “fetch area” (Nicot and Hovorka, 2009). Fetch areas are analogous to watersheds in surface-water drainage basins in that any migrating fluid within a fetch area is likely to remain in that fetch area because of structural considerations. While watersheds are separated by topographic maxima, fetch areas for buoyant fluids are separated by topographic minima and can include boundary zones created by faults. Fetch areas represent regions within which any injected CO_2 would tend to migrate strictly under buoyancy forces until immobilized via dissolution, capillary trapping, free-phase structural accumulation, or likely some combination of these. The updip area in which an accumulation occurs is defined as the structural closure and is often a subset of the fetch area (Nicot and Hovorka, 2009).

The primary inputs into fetch-and-closure analysis are the time-structure horizon of the lower Miocene derived from continuous 3D seismic data and interpreted fault polygons (fig. 2.7). The structure horizon can be analyzed spatially (topographically) to define the closure areas, with column height filled to spill point (white regions in fig. 2.7). A primary observation is that

most of the historic gas fields are located on those identified structural closures, although some identified closures do not host hydrocarbon accumulations. Both productive and barren settings represent prospective CO_2 storage targets, although the closures without accumulations are potentially untested with respect to buoyant fluid retention (or they represent leaky systems).

Also note that most of those closures are fault bound. When faults (black traces in fig. 2.7) are assumed to be completely sealing, the closures (mapped to spill point) enlarge to various degrees (blue regions in fig. 2.7). While this fault performance is unlikely to uniformly be the case (and may not be valid at any particular site), the analysis of Chapter 4 suggests that the fault seal is fairly robust (again noting that most hydrocarbon accumulations are fault bound). This increase in the closure area beyond the footprint of the gas accumulations represents the additional area that may be available for CO_2 storage, if the geology (reservoir continuity and faults) will retain larger accumulations than the gas fields represent. Reasons for this underfilling of closures may relate to charge history and/or dynamically held accumulations (seal integrity). Underfilling suggests that the CO_2 masses calculated by volumetric replacement may represent capacity minimums because the original methane accumulations are smaller than their native closures. Additional column height may be possible, and the cumulative distribution function of CO_2 mass for Texas State Waters (fig. 2.6) may theoretically be movable to the right, increasing total capacity. Quantifying the amount of that shift would require individual field analysis and would be most sensible to assess in detail only for the largest fields.

Conclusions

Miocene gas fields of the Texas State Waters represent demonstrable locations of buoyant fluid trapping, natural analogs for engineered CO_2 injections, and prospective storage targets. From this assessment of the Miocene petroleum systems, we conclude that the regional structural features that exert primary control on the trapping and distribution of Miocene hydrocarbons should perform similarly for CCS. Approximately shore-parallel, early Miocene fault zones, such as the Clemente-Tomas in offshore Texas State Waters, typically mark the landward extent of Miocene hydrocarbon accumulations and likely prevented large hydrocarbon volumes from moving into updip traps onshore. Because dominant Miocene-age displacement along regionally extensive growth faults is primarily responsible for hydrocarbon trapping, CO_2 injected into Miocene-age reservoirs of the Texas State Waters also has high potential for regional entrapment in the offshore setting.

Miocene-age gas reservoirs predominantly occur in faulted anticline and rollover anticline trap types with water drive mechanisms, which contain the largest OGIP volumes among all gas fields analyzed in this study. Depositional environments including shore-zone (strand plain and barrier island) and large deltaic-reservoir systems host most of the largest gas fields. These characteristics are therefore the most prospective for near-term CO_2 sequestration targets.

Miocene oil and gas fields are aerially smaller than their typically much larger structural closure areas. As such, existing Miocene gas volumes likely represent CO_2 capacity minima. Within Texas State Waters, depleted gas fields alone will not provide enough capacity for commercial-scale CO_2 sequestration. The volume of the Miocene gas fields converted to CO_2-saturated pore space equates to approximately 550 Mt of CO_2, but only the largest 10% of fields have CO_2 capacities greater than 10 Mt each. Industrial-scale CCS will require storage capacity comprising both the well-documented Miocene hydrocarbon fields and their larger closure and fetch areas, as well as barren (unproductive, brine-filled) closures. A regional structural-closure analysis helps identify those locations. The potential for building CO_2 column heights greater

than those of natural petroleum accumulations indicates that fault and top-seal analyses are critical for understanding long-term CO_2 storage potential at individual sites.

References

Ajiboye, O., and Nagihara, S., 2012, Stratigraphic and structural framework of the Clemente-Tomas and Corsair growth fault systems in the Texas continental shelf: Gulf Coast Association of Geological Societies Journal, v. 1, p. 107–117.

Ambrose, W. A., 1990, Facies heterogeneity and brine-disposal potential of Miocene barrier-island, fluvial, and deltaic systems: examples from northeast Hitchcock and Alta Loma Fields, Galveston County, Texas: The University of Texas at Austin, Bureau of Economic Geology Geological Circular 90-4, p. 35.

Bachu, S., 2000, Sequestration of CO_2 in geologic media: criteria and approach for site selection in response to climate change: Energy Conversion and Management, v. 41, no. 9, p. 953–970.

Berg, R. R., and Avery, A. H., 1995, Sealing properties of tertiary growth faults, Texas Gulf-Coast: AAPG Bulletin, v. 79, no. 3, p. 375–393.

Blondes, M. S., Brennan, S. T., Merrill, M. D., Buursink, M. L., Warwick, P. D., Cahan, S. M., Cook, T. A., Corum, M. D., Craddock, W. H., DeVera, C. A., Drake, R. M., II, Drew, L. J., Freeman, P. A., Lohr, C. D., Olea, R. A., Roberts-Ashley, T. L., Slucher, E. R., and Verala, B. A., 2013, National assessment of geologic carbon dioxide storage resources—methodology implementation: U.S. Geological Survey Open-File Report 2013-1055, 26 p., http://pubs.usgs.gov/of/2013/1055/.

Bradshaw, B. E., and Watkins, J. S., 1994, Growth-fault evolution in offshore Texas: Gulf Coast Association of Geological Societies Transactions, v. 44, p. 103–110.

Brennan, S. T., Burruss, R. C., Merrill, M. D., Freeman, P. A., and Ruppert, L. F., 2010, A probabilistic assessment methodology for the evaluation of geologic carbon dioxide storage: U.S. Geological Survey Open-File Report 2010-1127, 31 p., http://pubs.usgs.gov/of/2010/1127.

Bureau of Ocean Energy Management (BOEM), 2006, Sand-level data as of January 1, 2006: Atlas of Gulf of Mexico Gas and Oil Sands Data: Bureau of Ocean Energy Management, U.S. Department of the Interior, http://www.data.boem.gov/homepg/data_center/gandg/gandg.asp.

Chadwick, A., Smith, D., Hodrien, C., Hovorka, S., Mackay, E., Mathias, S., Lovell, B., Kalaydjian, F., Sweeney, G., Benson, S., Dooley, J., 2010, Zero Emissions Platform: The realities of storing carbon dioxide: A response to CO_2 storage sapacity issues raised by Ehlig-Economides & Economides: European Technology Platform for Zero Emission Fossil Fuel Power Plants, p. 9.

Dooley, J.J., and Davidson, C.L., 2010. PNNL: A Brief Technical Critique of Ehlig-Economides & Economides 2010: Sequestering Carbon Dioxide in a Closed Underground Volume, 2010. U.S. Department of Energy, p. 12.

Elewaut, E., van der Straaten, R., Koelewijn, D., Baily, H. E., Holloway, S., Barbie, J., Lindeberg, E., Moller, H., and Gaida, K. H., 1996, Inventory of the theoretical CO_2 storage capacity of the European Union and Norway, *in* The Underground Disposal of Carbon Dioxide, final report of JOULE II Project no. Ct92-0031.

Ehlig-Economides, C., and Economides, M.J., 2010, Sequestering carbon dioxide in a closed underground volume: Journal of Petroleum Science and Engineering, v. 70, no. 1-2, p. 118-125.

Ewing, T. E., 1991, Structural framework, *in* Salvador, A., ed., The Gulf of Mexico Basin: The geology of North America: Boulder, Colorado, Geological Society of America, v. J, p. 31–52.

Ewing, T. E., and Lopez, R. F., 1991, Principal structural features, Gulf of Mexico Basin, *in* Salvador, A., ed., The Gulf of Mexico Basin: The geology of North America: Boulder, Colorado, Geological Society of America, v. J, plate 2, sheet 1, scale 1:2,500,000

Galloway, W. E., 1986, Growth faults and fault-related structures of prograding terrigenous clastic continental margin: Gulf Coast Association of Geological Societies Transactions, v. 36, p. 121–128.

Galloway, W. E., 1989, Genetic stratigraphic sequences in basin analysis II: application to northwest Gulf of Mexico Cenozoic Basin: AAPG Bulletin, v. 73, no. 2, p. 143–154.

Galloway, W. E., 2005, Gulf of Mexico Basin depositional record of Cenozoic North American drainage basin evolution: International Association of Sedimentologists Special Publication, v. 35, p. 409–423.

Galloway, W. E., 2008, Depositional evolution of the Gulf of Mexico sedimentary basin, *in* Hsu, K. J., ed., Sedimentary basins of the world, v. 5, The sedimentary basins of the United States and Canada, Miall, A. D., ed., Amsterdam, The Netherlands, Elsevier, p. 505–549.

Galloway, W. E., Ewing, T. E., Garrett, C. M., Tyler, N., and Bebout, D. G., 1983, Atlas of major Texas oil reservoirs: The University of Texas at Austin, Bureau of Economic Geology, 139 p. plus plates.

Galloway, W. E., and Ganey-Curry, P. E., 2008, Gulf of Mexico Basin depositional synthesis (GBDS) Phase 6 Atlas, The University of Texas at Austin, University of Texas Institute for Geophysics (UTIG), 161 p.

Galloway, W. E., Ganey-Curry, P. E., Li, X., and Buffler, R. T., 2000, Cenozoic depositional history of the Gulf of Mexico basin: AAPG Bulletin, v. 84, no. 11, p. 1743–1774.

Garb, F. A., and Smith, G. L., 1987, Estimation of oil and gas resources, *in* Bradley, H. B., ed., Petroleum engineering handbook: Richardson, Texas, Society of Petroleum Engineers, p. 40-1 to 40-38.

Hood, K. C., Wenger, L. M., Gross, O. P., and Harrison, S. C., 2002, Hydrocarbon systems analysis of the northern Gulf of Mexico: delineation of hydrocarbon migration pathways using seeps and seismic imaging, *in* Schumacher, D., and LeSchack, L. A., eds., Subsurface exploration case histories: applications of geochemistry, magnetics, and remote sensing: AAPG Studies in Geology No. 48 and SEG Geophysical References Series No. 11, p. 25–40.

Hovorka, S. D., et al., 2006, Measuring permanence of CO_2 storage in saline formations: the Frio experiment: Environmental Geosciences, v. 13, no. 2, p. 105–121.

Huffman, A. C., Kinney, S. A., Biewick, L. R. H., Mitchell, H. R., and Gunther, G. L., 2004, Salt diapirs in the Gulf Coast [gcdiapirg]: downloadable GIS data: Gulf Coast Geology (GCG) Online, Miocene of Southern Louisiana: U.S. Geological Survey, Denver, Colorado. http://gulfsci.usgs.gov/gom_ims/gcg_ims.html.

Kiatta, H. W., 1971, The stratigraphy and petroleum potential of the lower Miocene, offshore Galveston and Jefferson Counties, Texas: Gulf Coast Association of Geological Societies Transactions, v. 21, p. 257–270.

Kennicutt, M. C., II, McDonald, T. J., Comet, P. A., Denoux, G. J., and Brooks, J. M., 1992, The origins of petroleum in the northern Gulf of Mexico: Geochimica et Cosmochimica Acta, v. 56, no. 3, p. 1259–1280.

Kosters, E. C., Bebout, D. G., Seni, S. J., Garrett, C. M., Jr., Brown, L. F., Jr., Hamlin, H. S., Dutton, S. P., Ruppel, S. C., Finley, R. J., and Tyler, N., 1989, Atlas of major Texas gas reservoirs: The University of Texas at Austin, Bureau of Economic Geology, 161 p. plus plates.

Levorsen, A. I., 2001, Geology of petroleum, 2nd edition: Tulsa, Oklahoma, The AAPG Foundation, 724 p.

Lopez, J. A., 1995, Salt tectonism of the United States Gulf Coast Basin, 2nd edition map: New Orleans Geological Society, scale 1:1,524,000.

Martin, R. G., 1980, Distribution of salt structures, Gulf of Mexico: U.S. Geological Survey miscellaneous field studies map MF-1213, scale 1:2,500,000.

McDonnell, A., Hudec, M. R., and Jackson, M. P. A., 2009, Distinguishing salt welds from shale detachments on the inner Texas shelf, western Gulf of Mexico: Basin Research, v. 21, p. 47–59.

Metcalfe, R. S., 1987, Gas properties and correlations, *in* Bradley, H. B., ed., Petroleum engineering handbook: Richardson, Texas, Society of Petroleum Engineers, p. 20-1 to 20-18.

Miller, E. N., 2012, A question of capacity assessing CO_2 sequestration potential in Texas offshore lands: The University of Texas at Austin, Master's thesis, 119 p.

National Energy Technology Laboratory (NETL), 2012, The United States 2012 Carbon Utilization and Storage Atlas, 4th Edition, U.S. Department of Energy, Office of Fossil Energy, 129 p.

Nehring, R., 1991, Oil and gas resources, *in* Salvador, A., ed., The Gulf of Mexico Basin: The geology of North America: Boulder, Colorado, Geological Society of America, v. J, p. 445–494.

Nicholson, A. J., 2012, Empirical analysis of fault seal capacity for CO_2 sequestration, lower Miocene, Texas Gulf Coast: The University of Texas at Austin, Master's thesis, 88 p.

Nicot, J.-P., and Hovorka, S., 2009, Leakage pathways from potential CO_2 storage sites and importance of open traps: case of the Texas Gulf Coast, *in* Grobe, M., Pashin, J. C., and Dodge, R. L., eds., Carbon dioxide sequestration in geological media—state of the science: AAPG Studies in Geology 59, p. 321–334.

Peng, D., and Robison, D. B., 1976, New two-constant equation of state: Industrial & Engineering Chemistry Fundamentals, v. 15, no. 1, p. 59–64.

Pitman, J. K., 2009, Reservoirs and petroleum systems of the Gulf Coast, AAPG Datapages, GIS Open Files, American Association of Petroleum Geologists, http://www.datapages.com/Partners/AAPGGISPublicationsCommittee/GISOpenFiles/ReservoirsandPetroleumSystemsoftheGulfCoast.aspx

Saadatpoor, E, Bryant, S. L., Sepehrnoori, K, 2009, New trapping mechanism in carbon sequestration, Transport in Porous Media, v. 82, no. 1., p 3–17.

Sales, J. K., 1997, Seal strength vs. trap closure—a fundamental control on the distribution of the oil and gas, *in* Surdam, R. C., ed., Seals, traps, and the petroleum system: AAPG Memoir 67, p. 57–83.

Seni, S. J., Hentz, T. F., Kaiser, W. R., and Wermund, E. G., Jr., 1997, Atlas of northern Gulf of Mexico gas and oil reservoirs: Volume 1. Miocene and older reservoirs: The University of Texas at Austin, Bureau of Economic Geology, 199 p.

Sills, S. R., 1992, Drive mechanisms and recovery: Part 10. Reservoir engineering methods, *in* Morton-Thompson, D., and Woods, A. M., eds., Development geology reference manual: AAPG Methods in Exploration Series No. 10, p. 518–522.

Sustakoski, R. J. and Morton-Thompson, D., 1992, Reserves estimation: Part 10. Reservoir engineering methods, *in* Morton-Thompson, D., and Woods, A. M., eds., Development geology reference manual: AAPG Methods in Exploration Series No. 10, p. 513–517.

Wagner, B. E., Sofer, Z., and Claxton, B. L., 1994, Source rock in the Lower Tertiary and Cretaceous, deep-water Gulf of Mexico: Gulf Coast Association of Geological Societies Transactions, v. 44, p. 729–736.

Wallace, K. J., 2013, Use of 3-dimensional dynamic modeling of CO_2 injection for comparison to regional static capacity assessments of Miocene sandstone reservoirs in the Texas state waters, Gulf of Mexico: The University of Texas at Austin, Master's thesis, 137 p.

Winker, C. D., and Edwards, M. B., 1983, Unstable progradational clastic shelf margins, *in* Stanley, D. J., and Moore, G. T., eds., The shelf break: critical interface on continental margins: SEPM Special Publication, v. 33, p. 139–157.

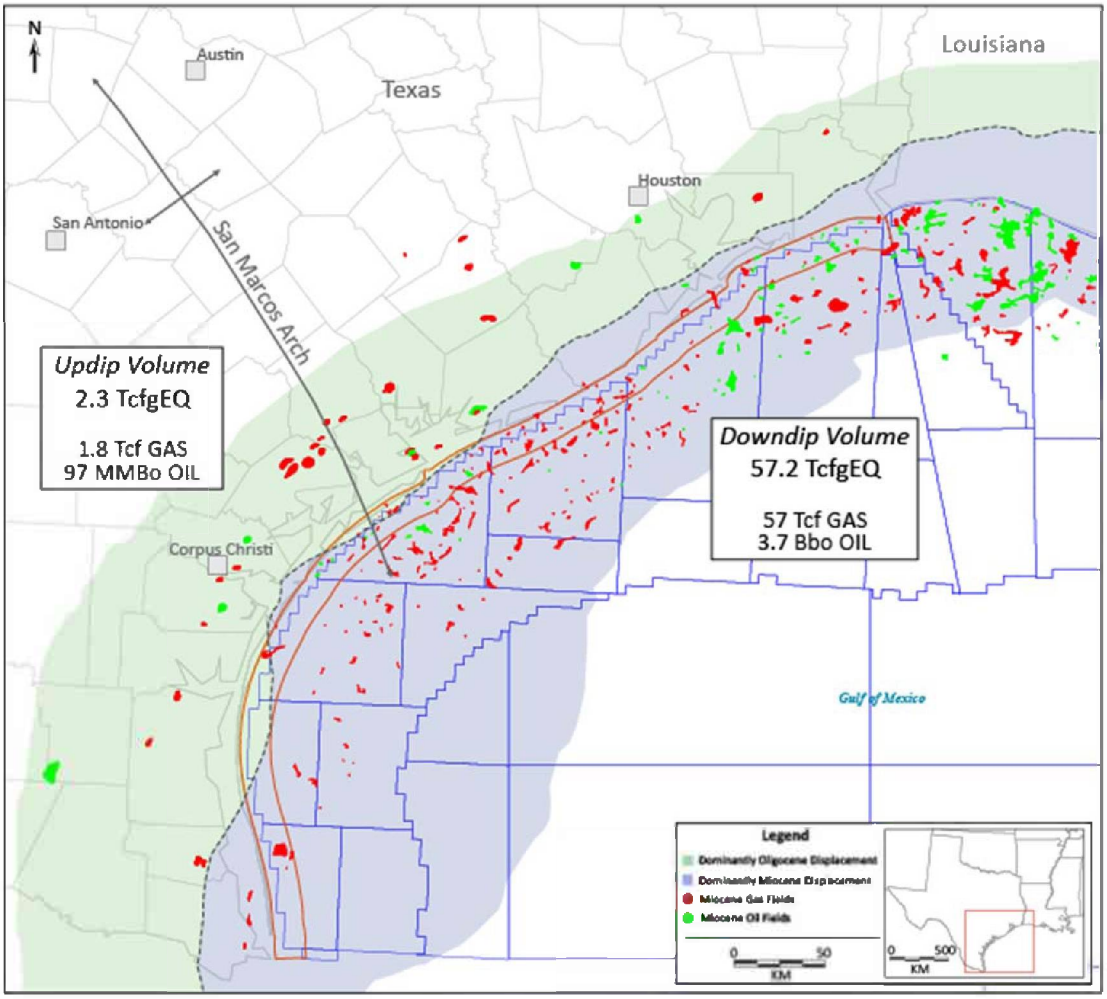

Figure 2.1. Miocene oil and gas fields populate two distinct fluid-trapping regions where Oligocene and Miocene fault displacement dominate (see fig. 1.2, this volume, for detailed fault zone locations). The gray dashed line marks a general boundary between regions of dominantly Miocene displacement to the southeast and dominantly Oligocene displacement to the northwest. During the Miocene, there was minor reactivation of Oligocene growth faults. The accumulations associated with Miocene growth faulting are volumetrically larger than those associated with Oligocene faults (modified from Galloway and others, 1983; Kosters and others, 1989; Ewing and Lopez, 1991; Seni and others, 1997; Galloway and others, 2000; Galloway, 2008; Galloway and Ganey-Curry, 2008). Note that hydrocarbon dominates in the downdip region, suggesting regional Miocene-age fault seal for much of the region.

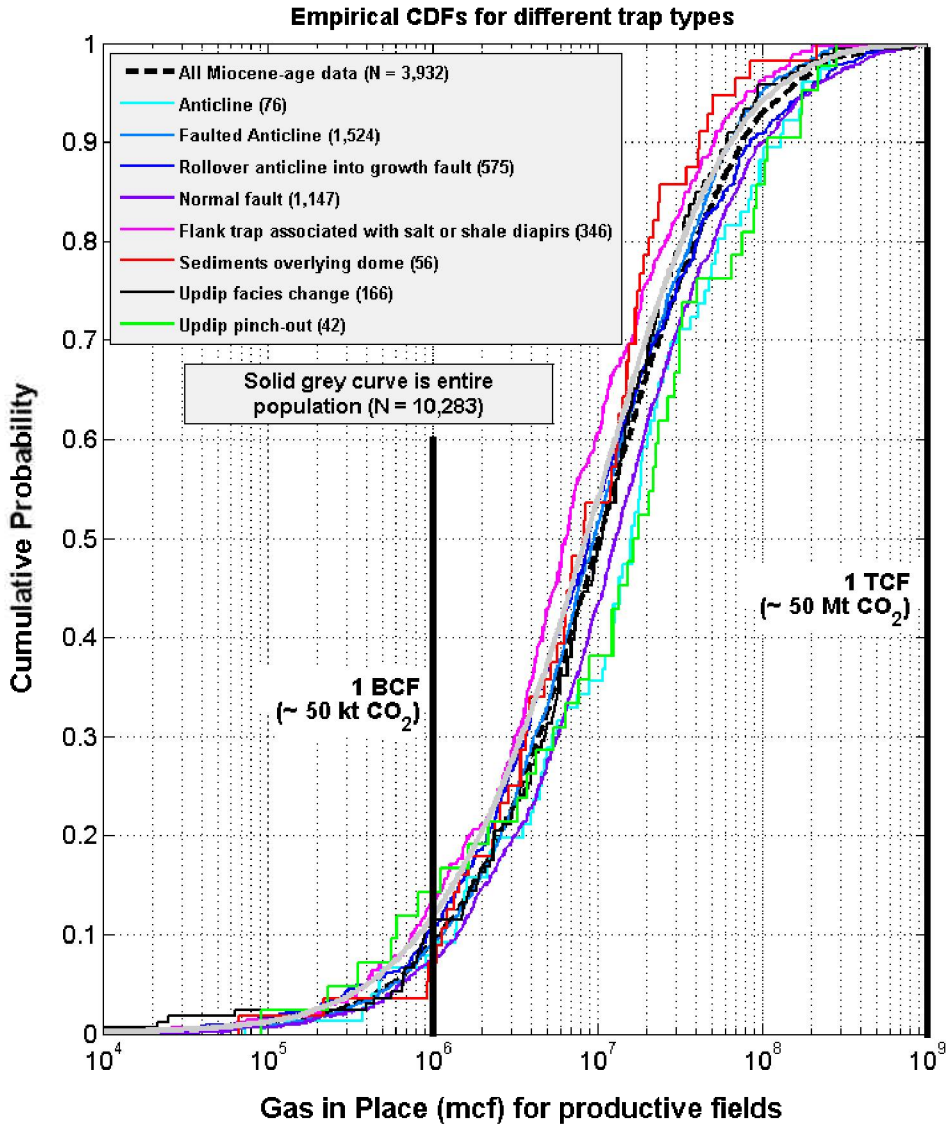

628

629 **Figure 2.2.** Cumulative distribution functions (CDF) for gas reservoir sizes in the Federal Outer Continental Shelf (OCS)
630 database. Data are represented as an entire population (N=10,283) and as a subset of only Miocene-age reservoirs
631 (N=3,932). The Miocene-age gas fields are further broken down into individual trap types. Data indicate that Miocene
632 reservoirs are fundamentally similar in size distribution to the population of all productive gas reservoirs in the Gulf of
633 Mexico. Individual trap type curves are very similar in distribution to the curves for the larger populations, indicating
634 that trap type does not exert a large control on gas-field size distribution. Reasons for a limit on the largest field sizes
635 of around 1 TCF are unknown and could relate to charge history or to fundamental retention characteristics of the
636 basin. Maximum field size is important for CO_2 storage, as it suggests that the largest individual engineered CO_2
637 accumulations possible may be on the order of 50 Mt.

638

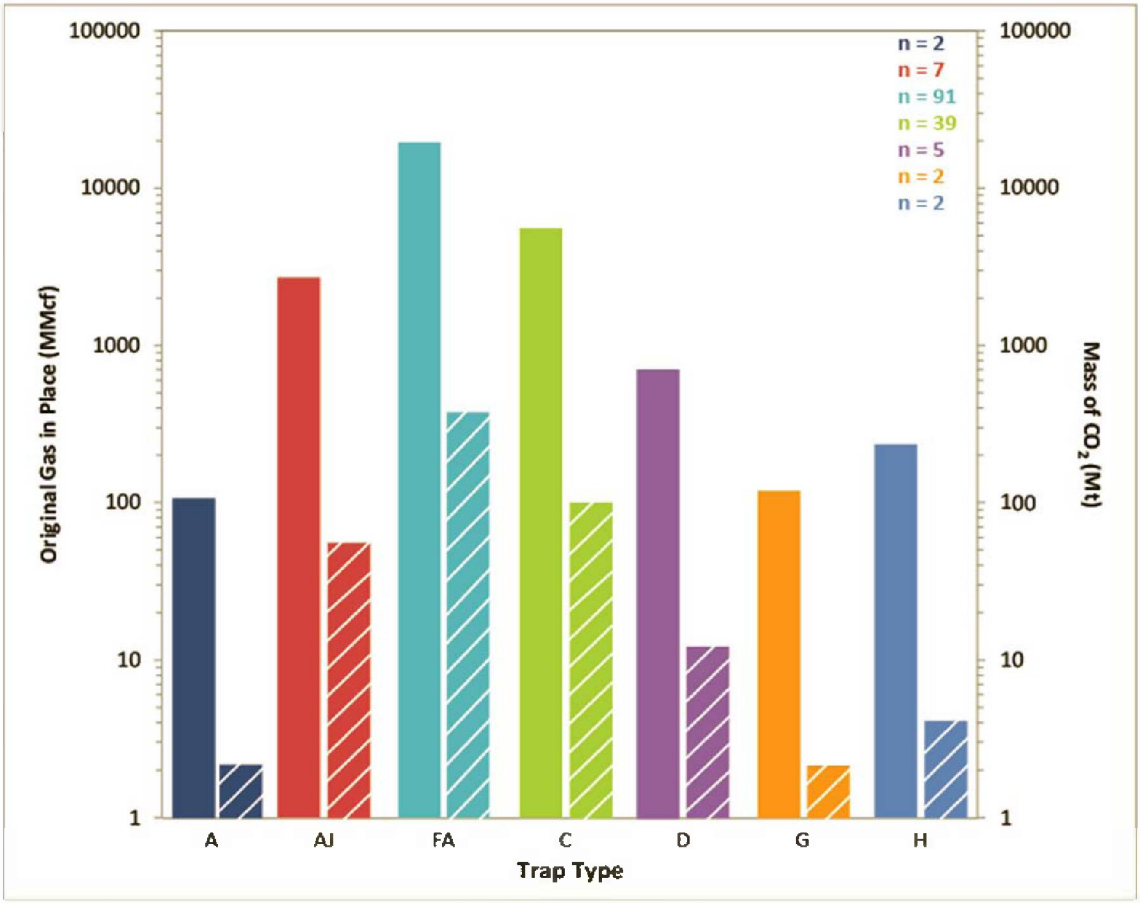

Figure 2.3. Histogram showing the relationship of trap type, original gas in place (OGIP), and estimated mass of CO_2 in Miocene-age gas reservoirs, Texas State Waters (N = 148 reservoirs). Column color denotes reservoir-specific trap types (A, Anticline; AJ, Anticline with updip facies change; FA, Faulted anticline; C, Rollover anticline into growth fault; D, Normal fault; G, Flank trap associated with shale or salt diapirs; H, Sediment overlying dome)(Seni and others, 1997). Solid-colored columns denote the sum of original gas in place by volume (MMcf), and patterned columns denote the sum of the mass of CO_2 (Mt) of individual gas reservoirs used in the CH_4–CO_2 volume replacement exercise. Reservoirs with faulted anticline and rollover anticline in growth fault occur most frequently and account for the majority of OGIP volume and potential storage capacity for CO_2.

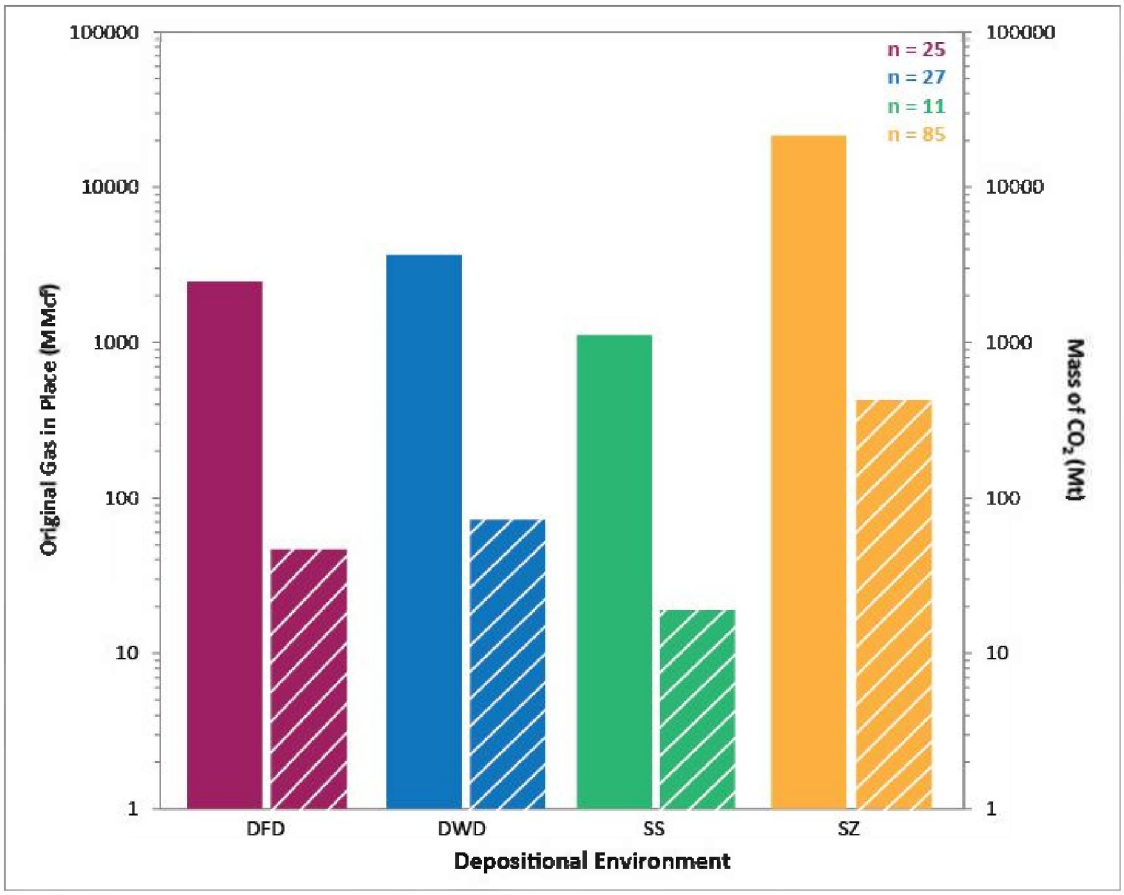

Figure 2.4. Histogram showing the relationship of interpreted depositional environments, OGIP (CH_4), and predicted mass of CO_2 in Miocene-age gas reservoirs, Texas State Waters. Column color denotes interpreted depositional environments (DFD, Fluvial-dominated deltaic; DWD, Wave-dominated deltaic; SS, Sandy shelf; SZ, Shore zone) (Seni and others, 1997; Galloway and others, 2000). Solid-colored columns denote the sum of OGIP by volume (MMcf), and patterned columns denote the sum of the calculated mass of CO_2 (Mt) of individual gas reservoirs (n = 148) as presented in the CH_4–CO_2 volume replacement exercise. Reservoirs are dominantly hosted within shore zone (57%) and deltaic (35%) depositional systems.

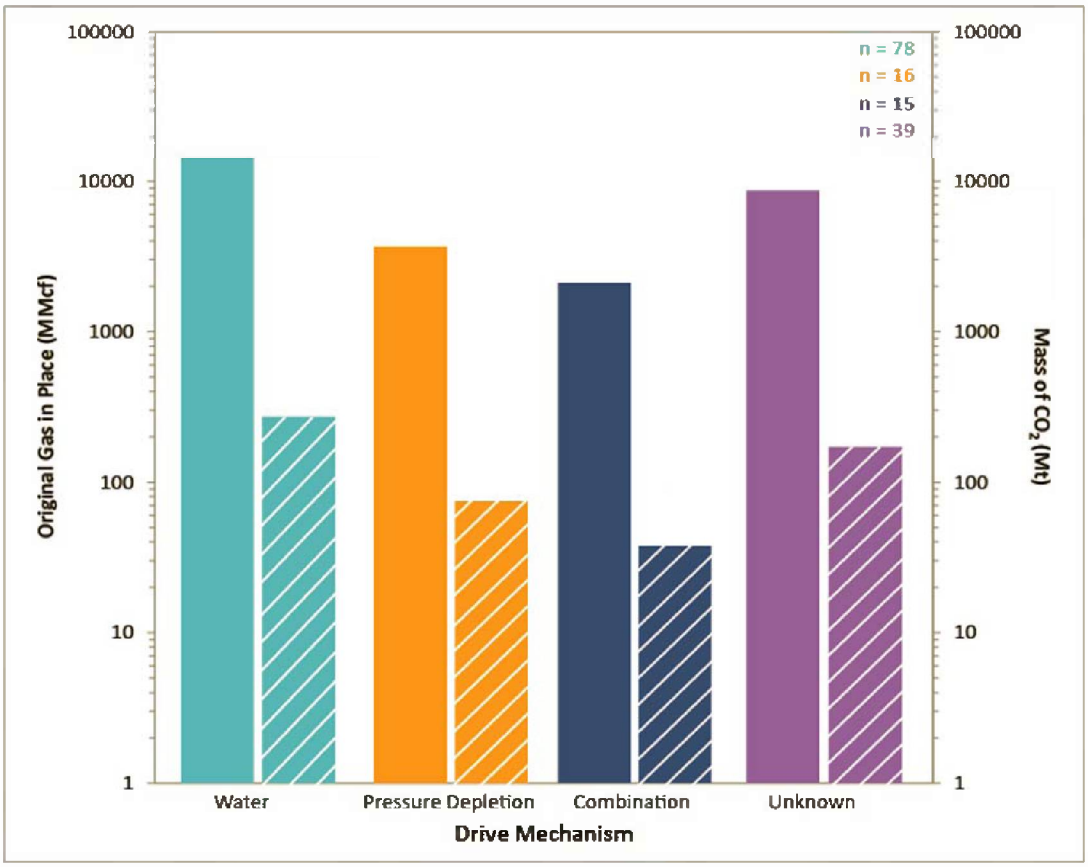

Figure 2.5. Histogram showing the relationship of drive mechanisms, OGIP (CH_4), and predicted mass of CO_2 in Miocene-age gas reservoirs, Texas State Waters. Column color denotes reservoir-specific drive mechanisms (Seni and others, 1997). Solid-colored columns denote the sum of OGIP by volume (MMcf), and patterned columns denote the sum of the mass of CO_2 (Mt) of individual gas reservoirs (n = 148) as presented in the CH_4–CO_2 volume replacement exercise. Reservoirs with water drive mechanism occur most frequently and account for the majority of OGIP volume and mass of CO_2.

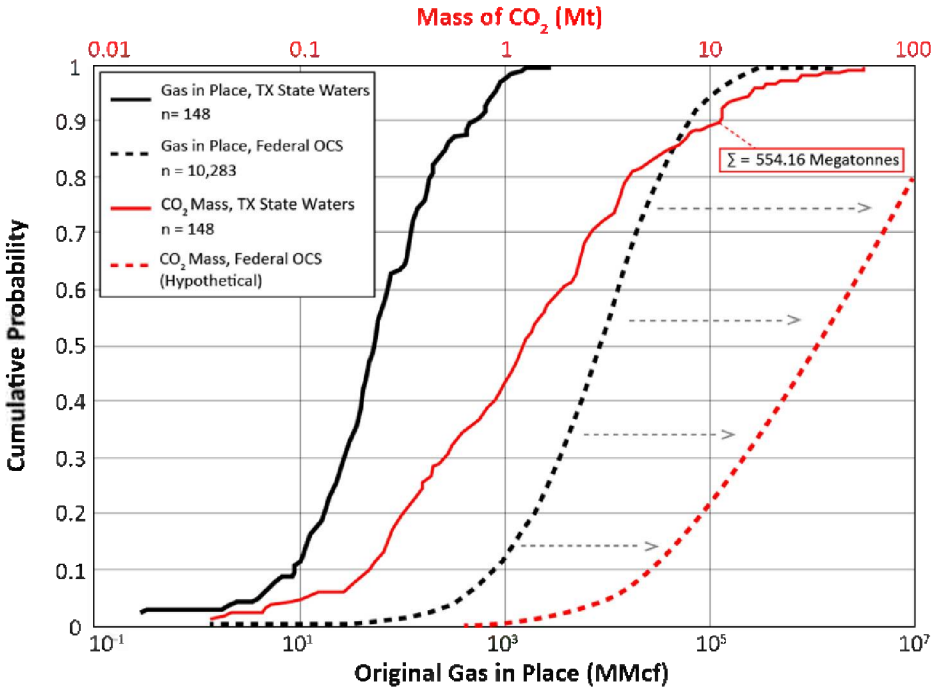

Figure 2.6. Cumulative distribution plot of OGIP (MMcf) for Miocene gas reservoirs, Texas State Waters (black line) and Federal OCS (black dashed line) (Seni and others, 1997; BOEM, 2006). The mass of CO_2 (red curves; Megatonnes on top axis) was derived by the conversion of OGIP volumes to CO_2-saturated pore space using reservoir-specific parameters and assuming residual water saturation similar to gas accumulations.

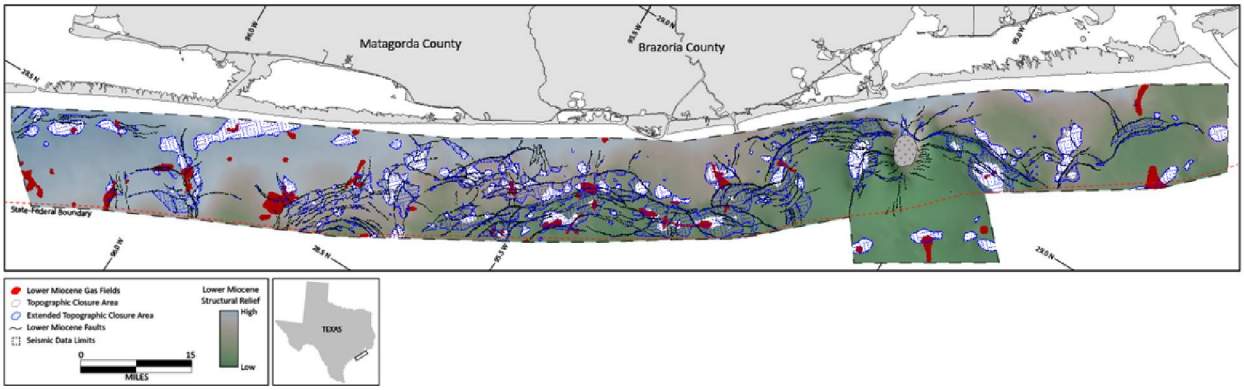

Figure 2.7. A structural analysis of Miocene-age stratigraphy in a portion of the Texas State Waters. Background colors indicate interpreted structural relief based on TWTT (sec) of a lower Miocene (LM2) horizon (Nicholson, 2012). White stippled shapes are structural closures (filled to spill point) considering only topography (not faults); the blue stippled regions surrounding the topography-based closures indicate the potential expansion of closure (again, filled to spill point) if faults (black lines) are assumed to be perfectly sealing. The solid red shapes are existing lower Miocene gas fields (Seni and others, 1997) associated with the LM2 structural horizon. Note that these primarily coincide with structural closures, often bound by faults. Not all closures have hydrocarbon accumulations, but those that do are largely under-filled with respect to total potential closure (with or without faults). Both observations suggest opportunities for CO_2 storage.

Chapter 3: Evaluation of Lower Miocene Confining Units for CO_2 Storage, Texas Offshore Waters, Northern Gulf of Mexico, USA

Jiemin Lu, David L. Carr, Ramon Trevino, Jordan-Leigh T. Rhatigan, and Reynaldy Fifariz[1]

[1]Gulf Coast Carbon Center, Bureau of Economic Geology, The University of Texas at Austin, Austin, TX, USA

Introduction

A basic requirement for any engineered carbon geosequestration operation is the presence of one or more rock strata above the injection zone that will, for a prescribed period of time (usually hundreds to thousands of years), attenuate the effects (fluid displacement, pressure increase) of injected CO_2. Such strata are variously referred to as caprocks, seals, or confining zones ("confining system" in the aggregate). For the purposes of the current discussion, the term "confining zone" or "confining system" is preferred, since it is based on the current Environmental Protection Agency (EPA) regulations under the Safe Drinking Water Act, Class VI wells (http://water.epa.gov/type/groundwater/uic/upload/UIC_GS_poster_508_Final_4-27-11.pdf). In the Gulf of Mexico Basin, confining zones overwhelmingly comprise mudrock (i.e., mudstone, siltstone, and shale) units with low permeability, most marine in origin. The ability of the confining system and individual confining zones to attenuate the effects of CO_2 injection is variously referred to as the attenuation, sealing, or trapping ability.

A topic that is not part of the current study is geomechanical deformation. Nonetheless, geomechanical deformation of a confining system due to a pressure increase from CO_2 injection can be an important part of the overall attenuation capability of a confining system. The topic is extensively addressed in the scholarly literature (e.g., Johnson and others, 2005; Morris and others, 2011; Kim and Hosseini, 2014).

A number of factors affect the ability of confining zones to attenuate CO_2 movement and pressure perturbation. The factors include the confining unit's rock texture, mineralogy, fabric alignment, abundance of bioclastic and organic material, diagenesis, macroscale sedimentary fabrics, burrows, and fractures, as well as the presence in the unit of laminae with high permeability (Katsube and Williamson, 1994; Dewhurst and others, 1998, 1999; Bolton and

others, 2000; Day-Stirrat and others, 2011; Schneider and others, 2011). On larger scales, the confining zones can be breached by (stratigraphic) lateral discontinuities, fracture networks, and faults. (The latter two topics are discussed in Chapter 4 of this volume.) We, herein, present our analyses of small-scale parameters based on analyses of samples from drill cores, as well as of a large-scale characterization of a major regional confining zone based on geophysical well logs and 3D seismic data. The large-scale analysis encompasses correlation of chronostratigraphic surfaces and focuses on the *Amphistegina B* (informally called the "Amph B") bio-chronostratigraphic zone. The analysis and entailed measurement of isopach values in 558 wells within a 2,671 mi^2 (6,918 km^2; approx. 1.7M acres) area centered on the Texas State Waters approximately 64 km (40 mi) south of Houston (fig. 3.1). The extent of the study area was largely determined by the location of a 3D seismic data set that provided continuous coverage of a 115 mi- (185 km-) long subset of the area analyzed by wireline well-log data.

Approach

In this study, core samples of potential seal of Miocene age were analyzed using a number of techniques. Confining-zone fluid-attenuation capacity and pore-throat size distribution were measured using mercury intrusion capillary pressure (MICP) tests. Other methods (thin-section petrography, scanning electron microscopy, X-ray diffraction, and high-resolution X-ray texture goniometry) were used to characterize texture, nanopore distribution, mineralogy, and fabric alignment. The probable controls of confining-zone quality were identified, and the relationship between confining-zone capacity and its controlling factors is discussed. The data sets summarize confining-zone properties of various microfacies present in the core samples; they do not, however, represent all of the confining-zone facies of Miocene age, owing to the scarcity of cores.

A critical challenge, not addressed here, lies in upscaling confining-zone capacity at core scale to that of the whole confining system. We did not attempt upscaling per se, but instead constructed a "net mudrock" isopach map of the Amph B regional confining zone (fig. 1.4, Chapter 1 of this volume). The Amph B is a thick, widespread marine shale unit that caps the lower Miocene. In offshore Texas State Waters, the Amph B confining unit is relatively easy to identify and correlate in both well logs and seismic. Miocene production and geological

information for the offshore Texas State Waters compiled by Seni and others (1997) indicates that 82% of gas production (2.8 trillion cubic feet of gas [Tcfg] of total 3.4 Tcfg) and 95% of oil production (41.5 million barrels of oil [MMBO] of total 43.8 MMBO) were produced from underlying lower Miocene reservoirs. This information suggests that the Amph B acted as a major regional seal for trapping migrating hydrocarbon fluids in underlying lower Miocene sandstone reservoirs (Chapter 2, this volume). Likewise, there may be large-scale potential for confining CO_2 in lower Miocene reservoirs in areas overlain by substantial thicknesses of Amph B confining shale.

We correlated key chronostratigraphic surfaces that define the Amph B confining-zone unit in 712 wells within 42,261 km^2 (16,317 mi^2) of total study area. Next, we utilized spontaneous potential curves to estimate the net mudstone isopach values for each well. Finally, we constructed an isopach map of the net mudstone Amph B values to determine the aerial distribution of the confining zone.

Small-Scale Confining Properties: Analysis of Cores

There are relatively few available Miocene cores, particularly whole cores, in Texas offshore waters; this is especially true for mudrock intervals, which are historically assiduously avoided by oil and gas companies. If whole cores are taken at all in the relatively expensive offshore operating realm, most petroleum operators core reservoir sandstone units because their objectives are analyses of potential reservoirs. Mudrock cores are typically available where core point was "missed" (i.e., the top of the sandstone target was incorrectly predicted) or from relatively thin mudrock interbeds that occur within sand-prone reservoir zones. In addition, portions of the Miocene interval are typically poorly consolidated, and it is difficult to recover intact cores in good condition. Thus, the offshore Miocene core record is biased toward samples from deeper lower Miocene intervals that have been subjected to a greater degree of compaction and cementation than those overlying intervals of approximately 3300–10,000 ft (Chapter 5, this volume). We nonetheless studied the few available lower Miocene cores to gain insights into Miocene rocks, which appear to be comparable to the shallower units in most other characteristics (e.g., mineralogic provenance, depositional environments) and should inform sequestration potential in a general way.

Three whole cores from Miocene-age units were studied in detail: two from the Federal OCS Matagorda Island Area—the OCS-G-3733 A-6 (API: 427034015800) and OCS-G-4708 #1 (API: 427034012600)—and the other from Texas State Waters, the High Island 24L #9 (API: 427083031600) (fig. 3.1). The three cores are from depths near or below the base of the desired capacity interval, which is defined as the top of overpressure (Pitman, 2011). Of the three, the latter two cores contain mudstone facies and were analyzed as potential confining zones (fig. 3.1).

Core Analyses and Interpretation

The core of well OCS-G-4708 #1, between 10,577 and 10,622 ft, is from the lower Miocene and shows a generally upward-fining character from fine-grained sandstone to interbedded silty claystone and siltstone (fig. 3.2). It exists at a transition from an underlying sandstone interval to a major mudstone succession.

The core of well High Island 24L #9 on the upper Texas coast (fig. 3.1) belongs to the *Siphonina davisi* (Siph davisi) biochronozone (fig. 1.4, Chapter 1 of this volume). The sandstone portion of the cored interval is hydrocarbon-productive. The core extends from 8,401 to 8,761 ft deep, with a total recovery of 106 ft. The upper portion of the core comprises 45 ft of fissile, calcareous mudstone and siltstone. The extremely unconsolidated nature of the upper portion prevented analysis of the interval for anything except X-ray diffraction mineralogy.

X-ray Diffraction Mineralogy

X-ray diffraction (XRD) analysis results of samples from well OCS-G-4708 #1 and High Island 24L #9 are shown in Table 3.1. Generally, mudstone samples contain less than 35% quartz; high clay content, up to 50%. Sandstone samples have more quartz and less clay. The mudstone in the latter core contains higher clay content. High clay abundance tends to lead to high sealing capacity of the mudstone interval in the High Island core.

Table 3.1. XRD mineralogical composition of core samples. Mudstone samples marked in green; sandstone samples, in orange.

Depth (ft)	Quartz	Kaolinite	Calcite	Illite	Albite	K-feldspar	Chlorite	Total
Well OCS-G-4708 #1, Matagorda Island, API: 427034012600								
10578	29.1	13.1	16.0	7.6	10.5	12.5	11.2	100.0
10580	22.9	14.1	16.7	11.8	8.0	14.4	12.2	100.0
10585	22.8	16.9	20.8	8.0	8.6	12.1	10.9	100.0
10590	28.1	13.5	19.2	4.3	13.3	8.8	12.8	100.0
10597	28.6	12.5	14.3	8.5	11.2	13.0	11.8	100.0
10604	27.8	11.6	23.2	6.1	9.7	11.9	9.6	100.0
10607	37.2	5.2	26.5	3.2	15.7	10.2	2.1	100.0
10609	33.6	8.7	14.0	8.4	13.7	11.6	10.0	100.0
10612	41.5	4.1	20.1	3.9	15.3	11.5	3.6	100.0
10613.2	45.6	2.5	18.3	4.3	15.0	10.0	4.4	100.0
10618.8	40.0	3.3	20.8	5.2	16.0	9.5	5.2	100.0
Well High Island 24L #9, API: 427083031600								
8403.1	23.7	12.7	15.8	22.5	6.7	18.6		100.0
8408.5	18.9	13.9	19.4	26.0	6.2	15.5		100.0
8412.9	27.0	10.3	11.2	21.6	9.5	20.4		100.0
8421	20.5	15.3	13.8	32.4	7.7	10.4		100.0
8421*	22.0	15.6	14.1	30.3	6.9	11.1		100.0
8423.1	20.4	15.6	13.3	33.9	7.0	9.8		100.0
8427.4	41.4	7.2	5.1	15.2	16.2	15.0		100.0
8429.5	40.1	9.9	2.4	20.7	13.4	13.5		100.0
8429.5*	42.5	7.7	3.1	19.1	14.5	13.1		100.0
8481.6	34.8	9.9	7.2	21.1	13.0	14.0		100.0
8481.6*	34.6	9.4	7.4	22.6	13.1	13.0		100.0
8485	29.8	10.7	11.5	24.2	11.0	12.8		100.0
8489	26.7	12.9	10.2	28.0	10.2	12.0		100.0
8492	36.0	2.9	20.5	4.7	17.5	18.4		100.0
8555	48.5	3.7	1.6	4.7	19.6	21.9		100.0
8560.5	49.1	3.6	1.8	5.0	18.9	21.6		100.0
8570.6	51.9	2.2	2.0	4.9	18.7	20.3		100.0
8572	50.9	2.7	2.3	5.0	18.8	20.3		100.0

*Repeat measurements demonstrate reproducibility of method.

Petrography and Diagenesis

Silt and sand grains from the core of well OCS-G-4708 #1 are mostly subangular and poorly–moderately sorted (fig. 3.3A). Quartz, plagioclase, K-feldspar, and fossil and rock fragments are the major framework grains. Calcite is abundant. Trace amounts of dolomite and ankerite were detected by scanning electron microscope (SEM) analysis. Metamorphic and volcanic rock fragments, usually deformed and altered, compose up to 5% of the sample. Chlorite, illite, and kaolinite are the major clay minerals. Major diagenetic events include compaction (fig. 3.3B), carbonate cementation (fig. 3.3C), clay precipitation (fig. 3.3D, E), and mineral dissolution (fig. 3.3F).

Capillary Pressure Properties—Mercury Intrusion Test

MICP analyses were conducted on the OCS-G-4708 #1 core. The samples showed varied capillary entry pressure ranging from 137 to 2146 psi. At a temperature of 270°F and a pressure of 4700 psi, for example, they are capable of retaining a CO_2 column of 13 to 243 ft before any intrusion of CO_2 (fig. 3.4).

Most samples show asymmetrical pore-size distribution (fig. 3.5). The modal pore size is mostly in the 10–100 nm range. Porosity varies from 3 to 11%. The pore throat size is the major factor controlling capillary-trapping capacity. A negative correlation exists between porosity/permeability and calcite abundance (fig. 3.6A, B). Higher abundance of calcite correlates with higher cementation, which results in higher CO_2 trapping capacity. There is a negative correlation between permeability and clay content, with the outlier of the highly cemented sample from 10,604 ft (fig. 3.6C). Similarly, mercury entry pressure is also correlated to total clay content (fig. 3.6D).

Pore Characterization—Scanning Electron Microscope on Ion-Milled Surface

Argon-ion milled samples were examined using SEM analyses. In the claystone samples, most pores resolved by SEM (1s–100s nm) consist of intragranular pores derived from mineral dissolution or crystal defection, which are mainly associated with feldspar (fig. 3.7A, B) and carbonate grains (fig. 3.7C, D). Most pores appear to be isolated within individual mineral grains and not connected to an effective porosity network. The abundant clay particles greatly reduce primary intergranular porosity and diminish the connections of the pore network.

Clay Alignment—High-Resolution X-ray Texture Goniometry

The high-resolution X-ray texture goniometry (HRXTG) method was used to measure the alignment of mudstone phyllosilicates. The degree of alignment of previously identified phyllosilicates is determined by pole-figure scan (Ho et al., 1995). More highly aligned fabrics yield pole figures that can be contoured as concentric rings (e.g., fig. 3.8A); completely random or isotropic fabrics yield figures that have no poles (e.g., fig. 3.8B). The degree of particle

alignment is expressed as maximum pole densities in multiples of a random distribution (m.r.d.) (Wenk, 1985), where higher values reflect higher degrees of alignment and potentially higher trapping capacity. Results are shown in Table 3.2.

Table 3.2. Maximum intensity in m.r.d. for illite–smectite and chlorite + kaolinite peaks; calculated d-spacing for illite–smectite and chlorite + kaolinite

Sample ID	Depth (m)	Max. intensity m.r.d. "I–S" or mica	Max. intensity m.r.d. "C + K"
1	10578	2.75	2.26
2	10580	2.66	2.22
3	10585	4.81	3.33
4	10590	2.13	1.9
5	10597		2.15
6	10604		1.97
7	10607	1.74	1.72
8	10609	2.04	1.81

A positive relationship exists between total clay content and clay fabric intensity (fig. 3.9A). The degree of phyllosilicates alignment is higher with lower detrital mineral content (quartz + plagioclase + K-feldspar) (fig. 3.9B). Clay fabric intensity has a negative relationship with porosity and a positive relationship with permeability derived from MICP (fig. 3.9C, D). However, the correlation is not strong because of other controlling factors such as carbonate cementation and laminations.

Large-Scale Analysis: *Amphistegina B* Regional Confining Zone

Measuring small-scale lithologic properties provides insight and predictability about a potential confining zone's ability to attenuate (i.e., trap) fluids, including CO_2. The scarcity of rock samples from mudrock units (i.e., confining zones) required use of available samples for small-scale analyses. However, the availability of wireline well logs and 3D seismic data (along the upper Texas coast) permit regional (i.e., large-scale) analysis of confining zones, independent of rock-sample availability. A primary large-scale property of a potential confining zone is the

zone's thickness. The general hypothesis is that thicker confining zones attenuate CO_2 movement or migration better than thinner units with equivalent small-scale properties.

A mudrock unit informally called the "Amph B" and encompassing the *Amphistegina B* bio-chronostratigraphic zone is the thickest and most extensive regional confining zone in the Miocene section of the upper Texas coast. The Amph B records a major transgressive event in the northwest Gulf of Mexico Basin that marks the end of the early Miocene (Galloway, 1989). The event is estimated to have occurred approximately 16 MYBP (Galloway, 1989; Fillon and others, 2000; Brown and Loucks, 2009), before the initial development of the West Antarctic Ice Sheet (Galloway, 2001). The *Amphistegina B* transgression interrupted episodes of sandstone-dominated deltaic and shore-zone progradation near the end of the early Miocene and at the beginning of the middle Miocene (Galloway, 1989).

In the central and upper Texas offshore area, nearly all hydrocarbon production from Miocene-age units underlies the Amph B, attesting to its trapping capability (Chapter 2, this volume). Determining the thickness of the Amph B confining zone in the study area is one readily available way to broadly identify potentially favorable CO_2 geosequestration fairways. In general, a thicker section of Amph B is preferable to a thinner section because areas with thinner Amph B may present greater opportunities for fluid seepage through the unit.

Construction of Amph B Net Mudrock Isopach Map

Two available data sets, 3D seismic and geophysical well logs, were used to determine an Amph B isopach over a portion of the study area (fig. 3.1). The overall geographic coverage of geophysical well logs is much greater than that of the 3D seismic, but the seismic provides much better spatial data coverage in the area where it is available. Where seismic data are unavailable,

well logs provide precise vertical resolution of net mudrock isopach values at specific locations. Marine mudrock/shale zones tend to exhibit a high degree of lateral continuity, especially when compared to sandstone units, because they resulted from relatively low depositional energy over broad areas; this fact lends confidence to well control-based net mudrock isopach mapping on a regional scale. Both data sets offer complementary information about the thickness of the Amph B confining zone. Where both are available, a seismic isopach integrated with well log data is preferable.

Geophysical Well Logs: Stratigraphic Definition of the Amph B Confining Zone

Stratigraphic correlations were made of the following key chronostratigraphic (fig. 3.10) surfaces in available geophysical well logs:

- Amph B maximum flooding surface ("MFS_Amph_B")
- Overlying sequence boundary ("SB_M08")
- Underlying sequence boundary ("SB_M09")

The Amph B maximum flooding surface was initially identified in wells for which both geophysical well logs and micropaleontological reports were available by inferring that the likely position of the maximum flooding surface is located in highly organic, low-energy mudrocks where there is a confluence of low spontaneous potential, maximum gamma ray (if available), and minimum resistivity response (Mitchum and others, 1993) in the vicinity of Amph B micropaleontological interpretations (fig. 3.10). After initial identification, the Amph B maximum flooding surface was correlated throughout the well data set.

Identification of the surface was relatively straightforward in the Texas State Waters of the upper coast, north of Matagorda County, but as the overall Miocene section thins southward

onto the San Marcos Arch (fig. 1.1, Chapter 1 of this volume), the presence of sandstone interbeds makes correlation more difficult. Likewise, correlation difficulty increases landward/updip, particularly across the Clemente-Tomas fault zone (fig. 3.1). In general, confidence in Amph B correlations and in the determination of isopach values is highest on the hanging wall of the Clemente-Tomas fault zone, where the Amph B confining zone expands significantly. This high-confidence area effectively coincides with the Texas State Waters north of Calhoun County (fig. 3.1).

Geophysical Well Logs: Estimation of Net Mudrock

We identified net mudrock intervals and counted (summed) them using spontaneous potential (SP) curves from 712 wells (map of well control shown in fig. 3.1). The top of the target Amph B confining unit was defined as Miocene sequence boundary 8 (SB_M8) and the base as Miocene sequence boundary 9 (SB_M9) (fig. 3.10). The Amph B maximum flooding surface (MFS_Amph_B) approximately bisects the unit. Prior to running the automated summations in *Petra*™ (IHS Energy), the SP curves were straightened along a shale baseline (i.e., the consistently less negative SP values associated with impermeable mudrock/shale intervals) in order to eliminate downhole drift and/or scale shifts, and were rescaled from -100 to 0 millivolts (mv). From the straightened, normalized SP curves, we defined net mudrock intervals to be where the normalized SP reading was greater than -35 mv (brown-shaded zones in fig. 3.10). The net mudrock values were plotted on the map, gridded at a 1-km (3,081-ft) spacing, and contoured at a 152-m (500-ft) interval (fig. 3.12).

3D Seismic

Figure 3.1 shows an outline of the portion of the study area in which the isopach of the Amph B was assessed with 3D seismic data in addition to wireline well log data. The 3D seismic data set "Texas Offshore OBS" was leased from SEI, Inc., and the central area selected because of the high quality of continuous interpretable seismic reflections (yellow polygon in fig. 3.1). Three seismic horizons were interpreted in the time domain: (1) Top of LM2 (Chapter 1, this volume), (2) Top Amph B Shale, and (3) Top of Miocene. The horizons roughly correspond to sequence stratigraphic surfaces shown in figure 3.11; Base LM2 corresponds to SB_M09, and Top Amph B Shale to SB_M08.

In addition to seismic horizons, more than 40 faults were also interpreted and used to determine Amph B areal thickness. Landmark's DecisionSpace® software was used in the gridding process, with appropriate parameters (e.g., cell size, rotation, cleaning area) to generate faulted seismic surfaces within a 3D framework. The surfaces and faults were converted to depth as a whole such that the 3D framework included the integration of horizons and faults; thus, the faults' displacements were incorporated into the surfaces. The 3D framework was, subsequently, converted from two-way time (time domain) to the depth domain using imported velocity model parameters from Landmark's DepthTeam Express®. The velocity model utilized five horizons and check-shot data from 13 wells in the central area. After the 3D framework was converted to depth, faulted depth structure maps of each horizon were generated, and isopach maps were calculated. The thickness between Top Amph B Shale and Top of LM2 represents the Amph B thickness in the central area (fig. 3.13).

Results

Amph B Confining Zone Isopach Map

Mapping confidence is highest within the Texas State Waters, where there is relatively dense well control and continuous 3D seismic data (fig. 3.1). Error is greatest on the landward and seaward edges of the Texas State Waters (Fig. 3.1), where there is less well control. Although there was better well coverage landward of the Texas State Waters, accurate stratigraphic correlations were more difficult because the Miocene section thins dramatically on the footwall (0–500 ft; 0–152 m) vs. the hanging wall (1000–2,500 ft; 305–762 m) of the Clemente-Tomas fault (fig. 3.12).

Several major observations can be made from the Amph B mudrock isopach patterns in figure 3.12:

1. An abrupt regional thickness increase occurs on the hanging wall of the Clemente-Tomas fault in the central and upper Texas offshore.
2. Locally, there are abrupt variations in the vicinity of structural highs and lows, primarily in the upper Texas offshore. Most of these are related to salt movement that is prevalent in this area ("Houston Salt Embayment," Chapter 1, this volume).
3. Regional thinning to the southwest reflects the presence of the San Marcos Arch (Chapter 1, this volume).
4. Regional thickening occurs southward from the San Marcos Arch into the Rio Grande Embayment (Chapter 1, this volume).

The abrupt thickness increase that occurs on the hanging wall of the Clemente-Tomas growth fault indicates that significant fault movement occurred during the early Miocene. The vertical

seismic section in figure 3.11 clearly demonstrates early Miocene movement on the Clemente-Tomas fault: from left to right in the hanging wall (labeled "Undifferentiated Lower Miocene" immediately beneath the Amph B sequence), strata thicken markedly toward the fault. Local thickness variations are inferred to be accommodation responses to faults and/or underlying salt movement during early Miocene sedimentation. The influence of salt movement is most evident in the northeast part of the study area, especially in the Amph B net mudrock isopach pattern around the San Luis Pass Dome area (location of dome shown in fig. 3.1; fig. 3.11; Chapter 6, this volume). The Miocene thins southward onto the San Marcos Arch, and despite the relative lack of data in far South Texas, the Amph B sequence clearly thickens south to the Mexican border.

Figure 3.13 shows the Amph B net mudrock isopach map in grayscale, with the addition of all major hydrocarbon-producing reservoirs of lower Miocene age reported by Seni and others (1997). The map shows that most of the lower Miocene fields occur downdip from and are associated with the Clemente-Tomas fault. Also, this area coincides with thicker (> 500 ft; 152.4 m) Amph B net mudrock isopach. The pattern in the central part of the Texas offshore, where a number of larger lower Miocene fields are tucked into the curve of the southern terminus of the Clemente-Tomas fault zone, is particularly striking. These central coast features (i.e., faults, thick confining shale) are located immediately downdip of a major regional high, the San Marcos Arch (Chapter 1, this volume). The relatively high concentration of lower Miocene fields in this central offshore area may owe its existence to trapping by the Clemente-Tomas fault zone in conjunction with the associated thick Amph B confining strata that occur there.

It is fortuitous that the thickened Amph B confining mudrock on the Clemente-Tomas hanging wall is located proximal to many CO_2 sources. The natural analogue provided by lower

Miocene hydrocarbon accumulations suggests that this large fairway might also provide an excellent long-term trapping mechanism for injected CO_2.

Comparison of Amph B Isopach Seismically Derived Isopach

We noticed that the Amph B mudrock is readily observable as a thick transparent zone in 3-D seismic vertical sections under Texas State Waters (Fig. 3-11). Easy seismic identification of the unit facilitated relatively rapid interpretation of bounding key surfaces. We performed a quick experiment to test the utility of using seismic to quickly measure thickness distribution as a proxy for confining seal potential, and/or provide information for areas lacking well control. A small pilot area of 596 km^2 (230 mi^2) in the middle of the offshore Texas State Waters project area was chosen for the test (Figs. 3-1, 3-14). Key Amph B bounding key surfaces were interpreted, depth converted and isopach was calculated by grid subtraction.

The general pattern of the seismic-derived isopach (Fig. 3-14a) is similar to that estimated from well control (Fig. 3-14b) in general pattern and is quantitatively within an order of magnitude. However, in detail, the seismic isopach is consistently approximately -4x the absolute thickness of the Amph B mudrock seal as determined by the SP curve over the Amph B sequence and contains much higher horizontal resolution than the well control estimate, which was made from vastly sparser horizontal data control, i.e., available well control (Fig. 3-1). There are several possible reasons for the discrepancy between the magnitude Amph B mudrock seal isopach estimates from these two independent data sets, including seismic horizon interpretation error and depth conversion error, especially across faults, well-log interpretation and normalization errors. However, the main reason for differences in the two isopach estimates is

probably because the well control estimate was made over a thicker overall stratigraphic interval (i.e. the whole Amph B sequence from SB_M09 to SB_M08). As such, it includes some impermeable non-mudrock interbeds as well as mudrock interbeds the occur within sandier units that are concentrated at the top and the base of the Amph B sequence.

Nonetheless, we feel that the trend similarity, and quantitative order-of-magnitude agreement of these two isopachs indicate that seismic can indeed provide a reasonable, quick estimate at a high horizontal resolution for assisting assessments of the sealing potential of regionally extensive confining units.

Conclusions

Core-based analyses suggest that the studied clay-rich lower Miocene mudrocks have sealing ability sufficient for potential CO_2 storage in the underlying sandstone units. The sealing capacity of the studied samples has positive correlations with clay content and calcite cementation. Clay-rich mudstone samples typically show higher capillary entry pressure and smaller pore-throat size than underlying sandstones. SEM imaging shows that claystone samples contain mostly isolated intraparticle pores, which are not effectively connected to form pore networks. The multiple data sets suggest that the studied mudstone unit is compacted sufficiently enough to provide adequate seal for up to 240 ft of CO_2 column. However, it is noteworthy that lower Miocene mudrocks in Texas State Waters are shallower than the studied core and that their fluid attenuation capacity may be affected by more primary pores and less cementation and mineral dissolution.

The Amph B transgressive mudrock unit is a proven confining zone for lower Miocene natural hydrocarbon accumulations in the area. We recognized and mapped the Amph B in geophysical well logs in a large study area of 42,261 km^2 (16,317 mi^2) centered on the offshore Texas State Waters and also in a regional 3D seismic data set of 625 km^2 (241 mi^2). The Amph B net mudstone thickness varies from zero to 1524 m (5,000 ft) in the project area.

A high concentration of lower Miocene hydrocarbon accumulations occurs on the hanging wall of the Clemente-Tomas fault zone where Amph B net mudstone is thick, ranging from 1,000 ft (305 m) to 3,000 ft (914 m). These natural analogs of fluid entrapment suggest that fairways characterized by a thick regional Amph B confining zone defined by net mudrock values of more than 1,000 ft (305m) might provide an excellent long-term confining mechanism for injected CO_2.

References

Bolton, A. J., Maltman, A. J., and Fisher, Q., 2000, Anisotropic permeability and bimodal pore-size distributions of fine-grained marine sediments: Marine and Petroleum Geology, v. 17, p. 657–672.

Brown, L. F., Jr., and Loucks, R. G., 2009, Chronostratigraphy of Cenozoic depositional sequences and systems tracts: a Wheeler chart of the northwest margin of the Gulf of Mexico basin: The University of Texas at Austin, Bureau of Economic Geology Report of Investigations No. 273, 28-p. + chart.

Day-Stirrat, R. J., Schleicher, A. M., Schneider, J., Flemings, P. B., Germaine, J. T., and van der Pluijm, B. A., 2011, Preferred orientation of phyllosilicates: effects of composition and stress on resedimented mudstone microfabrics: Journal of Structural Geology, v. 33, no. 9, p. 1347–1358, doi:10.1016/j.jsg.2011.06.007.

Dewhurst, D. N., Aplin, A. C., and Sarda, J-P., 1999, Influence of clay fraction on pore-scale properties and hydraulic conductivity of experimentally compacted mudstones: Journal of Geophysical Research, v. 104, p. 29261–29274.

Dewhurst, D. N., Aplin, A. C., Sarda, J-P., and Y. Yang, 1998, Compaction driven evolution of porosity and permeability in natural mudstones: an experimental study: Journal of Geophysical Research, v. 103, p. 651–661.

Fillon, R. H., and Lawless, P. N., 2000, Lower Miocene–early Pliocene deposystems in the Gulf of Mexico, regional sequence relationships: Gulf Coast Association of Geological Societies Transactions, v. 50, p. 411–428.

Galloway, W. E., 1989, Genetic stratigraphic sequences in basin analysis I: architecture and genesis of flooding-surface bounded depositional units: American Association of Petroleum Geologists Bulletin 73, p. 125–142.

Galloway, W. E., 2001, Cenozoic evolution of sediment accumulation in deltaic and shore-zone depositionals systems, Northern Gulf of Mexico Basin: Marine and Petroleum Geology, v. 18, p. 1031–1040.

Ho, N. C., Peacor, D. R., and van der Pluijm, B. A., 1995, Reorientation mechanisms of phyllosilicates in the mudstone-to-slate transition at Lehigh Gap, Pennsylvania: Journal of Structural Geology, v. 17, p. 345–356.

Johnson, J. W., Nitao, J. J., and Morris, J. P., 2005, Reactive transport modeling of cap rock integrity during natural and engineered CO_2 storage, *in* Thomas, D. C., and Benson, S. M., eds., Carbon dioxide capture for storage in deep geologic formations, v. 2, p. 787–813.

Katsube, T. J., and Williamson, M. A., 1994, Effects of diagenesis on clay nanopore structure and implications for sealing capacity: Clay Minerals, v. 29, p. 451–461.

Kim, S., and Hosseini, S. A., 2014, Above-zone pressure monitoring and geomechanical analyses for a field-scale CO_2 injection project in Cranfield, MS: greenhouse gases: Science and Technology, v. 4, no. 1, p. 81–98.

Mitchum, R. M., Sangree, J. B., Vail, P. R. and Wornardt, W. W., 1993, Recognizing sequences and systems tracts from well logs, seismic data, and biostratigraphy: examples from the late Cenozoic of the Gulf of Mexico: Chapter 7: Recent applications of siliciclastic sequence stratigraphy, *in* Weimer, P., and Posamentier, H. eds., Siliciclastic sequence stratigraphy: recent developments and applications: Tulsa, Oklahoma, American Association of Petroleum Geologists, p. 163–197.

Morris, J. P., Hao, Y., Foxall, W., and McNab, W., 2011, A study of injection-induced mechanical deformation at the In Salah CO_2 storage project: International Journal of Greenhouse Gas Control, v. 5, no. 2, p. 270–280.

Pitman J. K., 2011, Reservoirs and petroleum systems of the Gulf Coast: depth to top overpressure. Online, available at: http://www.datapages.com/Services/GISUDRIL/OpenFiles/ReservoirsandPetroleumSystemsoftheGulfCoast. aspx [March 1, 2013].

Schneider, J., Flemings, P. B., Day-Stirrat, R. J., and Germaine, J. T., 2011, Insights into pore-scale controls on mudstone permeability through resedimentation experiments, Geology, v. 39, no. 11, p. 1011–1014, doi:10.1130/G32475.1.

Seni, S.J., T.F. Hentz, W.R. Kaiser, and E. G. Wermund, Jr. (eds.), 1997, Atlas of northern Gulf of Mexico gas and oil reservoirs: Volume 1. Miocene and older reservoirs. Texas Bureau of Economoic Geology, Gas Research Institute, Department of Energy, and Minerals Management Service, 199 p. plus plates and CD-Rom.

Wenk, H. R., 1985, Measurement of pole figures, *in* Wenk, H. R., ed., Preferred orientation in deformed metals and rocks: an introduction to modern texture analysis: Orlando, Florida, Academic Press, p. 11–48.

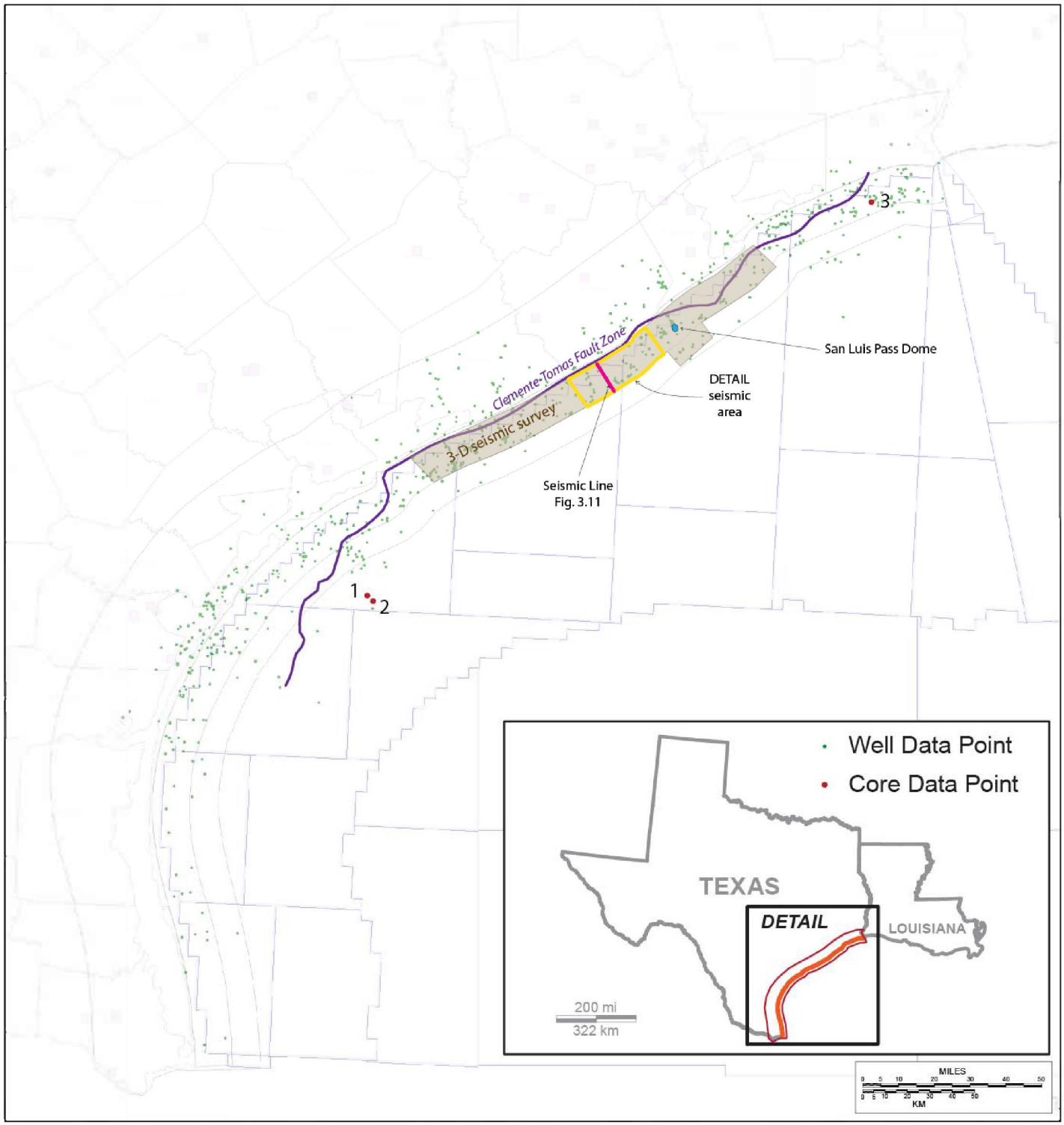

Figure 3.1. Location of Miocene cores studied and outline of Amph B isopach mapping area. OCS-G-4708 #1 ("2") and High Island 24L #9 ("3") cores were studied as potential seals; OCS-G-3733 A-6 ("1") core was examined as storage candidate. Green dots represent 712 wells used to construct Amph B net shale isopach map.

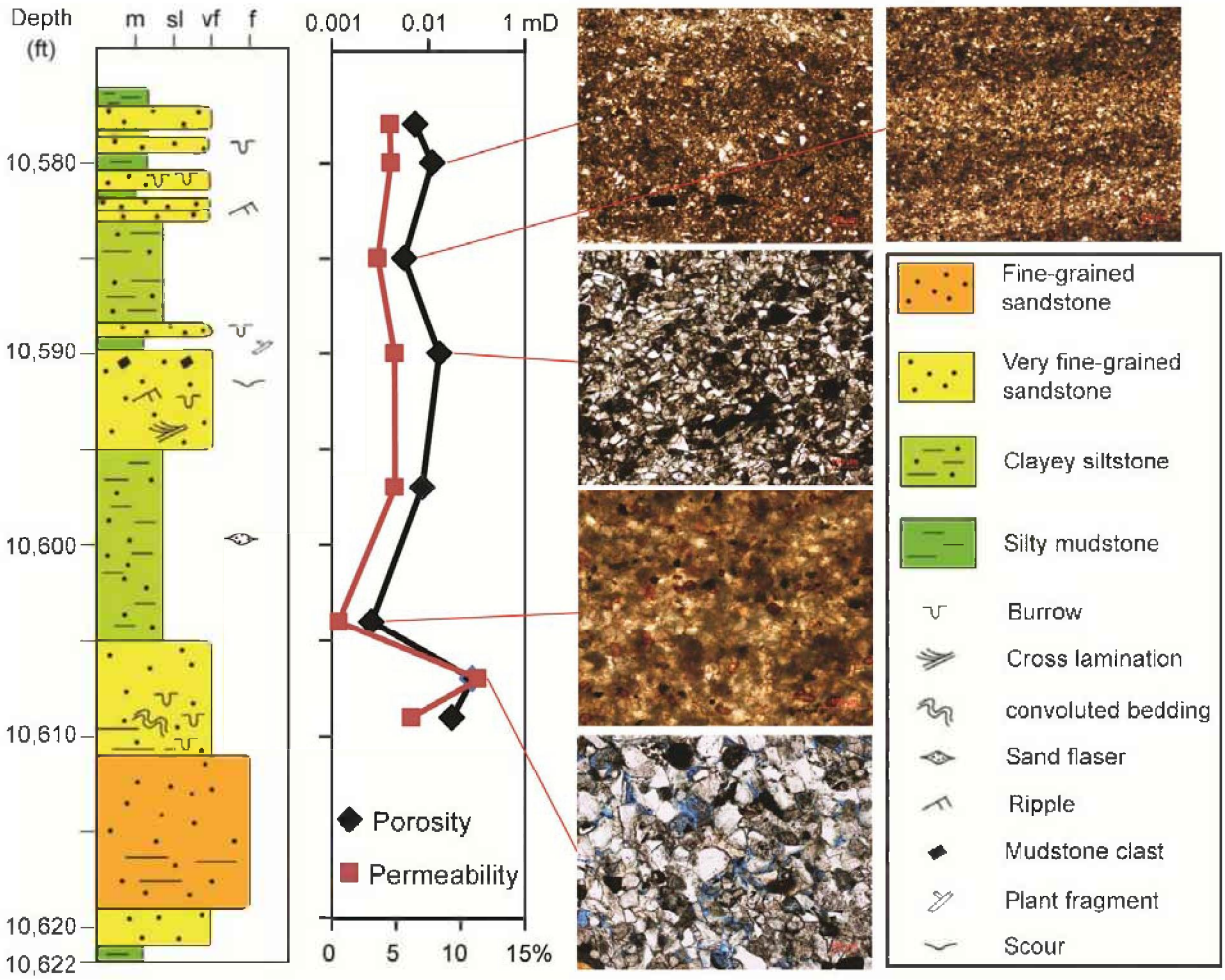

Figure 3.2. Description and data from OCS-G-4708 #1 core, depths from 10,577 ft to 10,622 ft, Matagorda Island Area Federal OCS (well 2, fig. 3.1). Log at left shows average grain size, lithology, and sedimentary structures. Porosity and permeability determined by mercury intrusion capillary pressure (MICP) tests shown in the middle. Thin section photomicrographs from representative facies are shown at right.

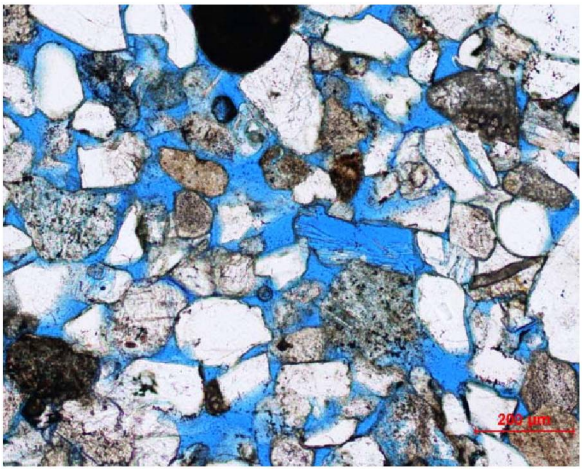

Figure 3.3A. Fine-grained sandstone poorly sorted, moderately rounded. Secondary pores present derived from grain dissolution. 10612.5 ft, OCS-G-4708 #1.

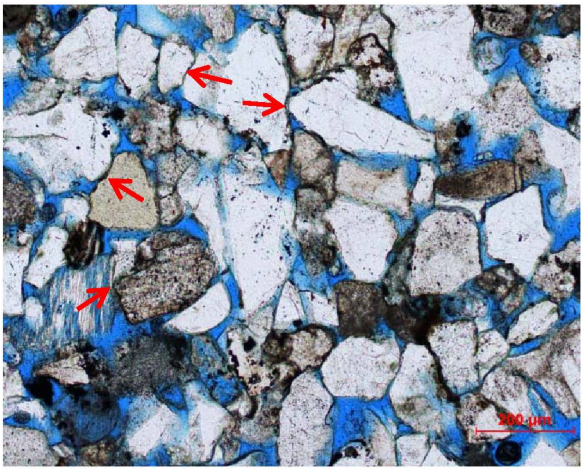

Figure 3.3B. Compaction-related grain deformation and pressure dissolution (arrows). 10612.5 ft, OCS-G-4708 #1.

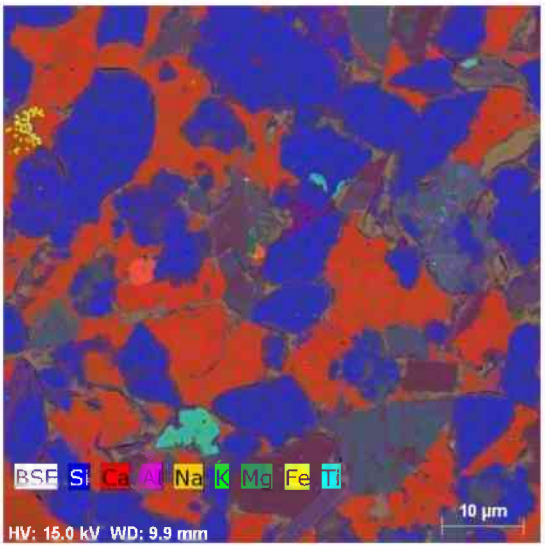

Figure 3.3C. Siltstone. Abundant calcite cements diminish porosity and permeability. Porosity: 3.1 %; permeability: 0.0001 mD. 10604 ft, OCS-G-4708 #1.

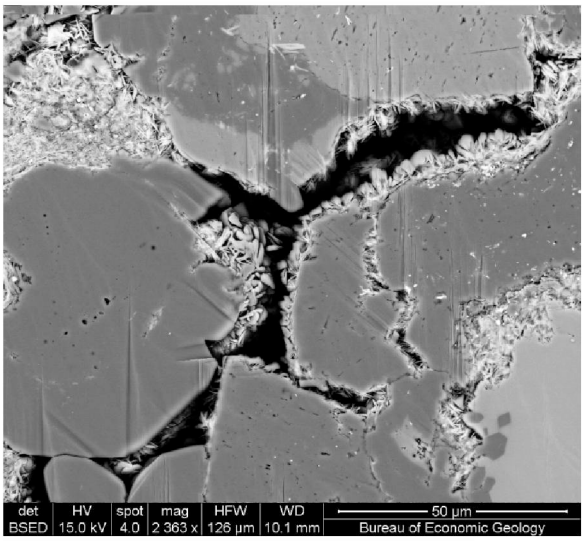

Figure 3.3D. Chlorite coatings around quartz and feldspar grains and pore-filling chlorite. 10607 ft, OCS-G-4708 #1. Porosity: 10.9%; permeability: 0.11 mD.

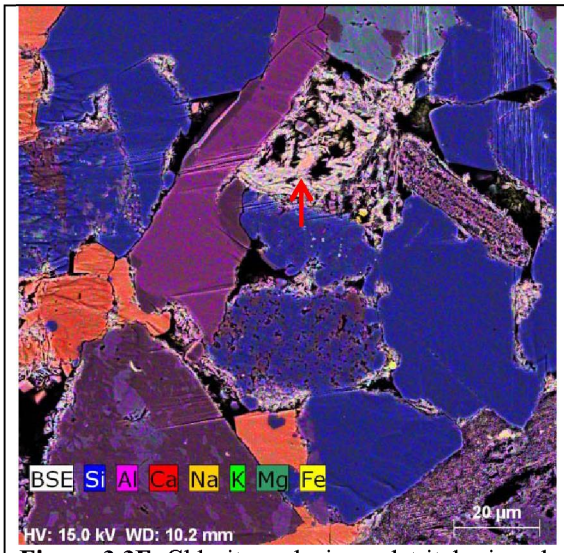

Figure 3.3E. Chlorite replacing a detrital mineral grain

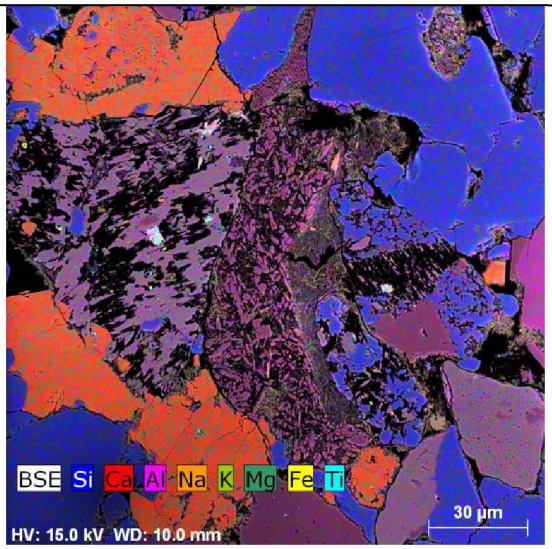

Figure 3.3F. K-feldspar and albite grains partially

(arrow). 10607 ft, OCS-G-4708 #1.	corroded to form secondary porosity. 10607 ft, OCS-G-4708 #1.

Figure 3.4. Carbon dioxide (CO_2) column height calculated from mercury intrusion entry capillary pressure at 275°F (135°C) temperature and 4700 psi (32.4 MPa) pressure. Samples from well OCS-G-4708 #1 (well 2, fig. 3.1).

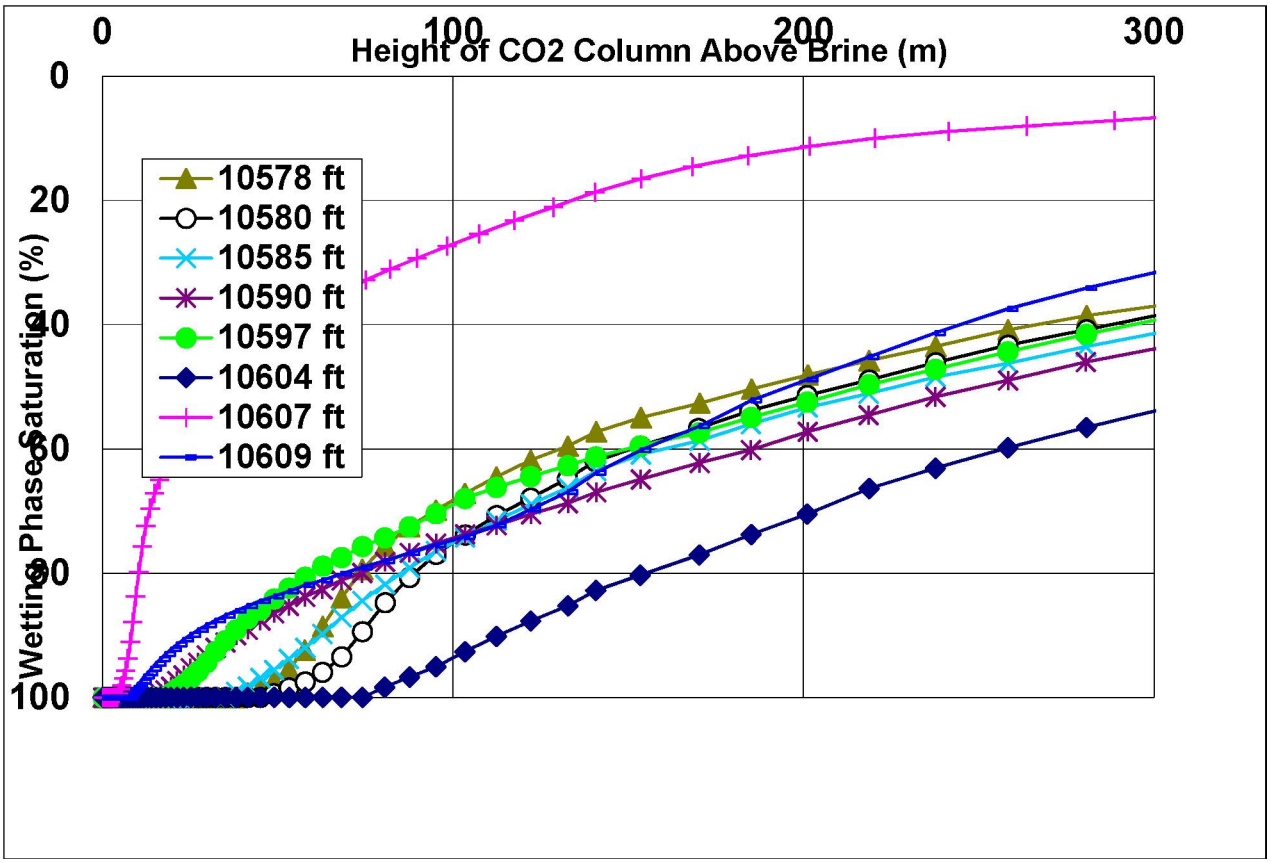

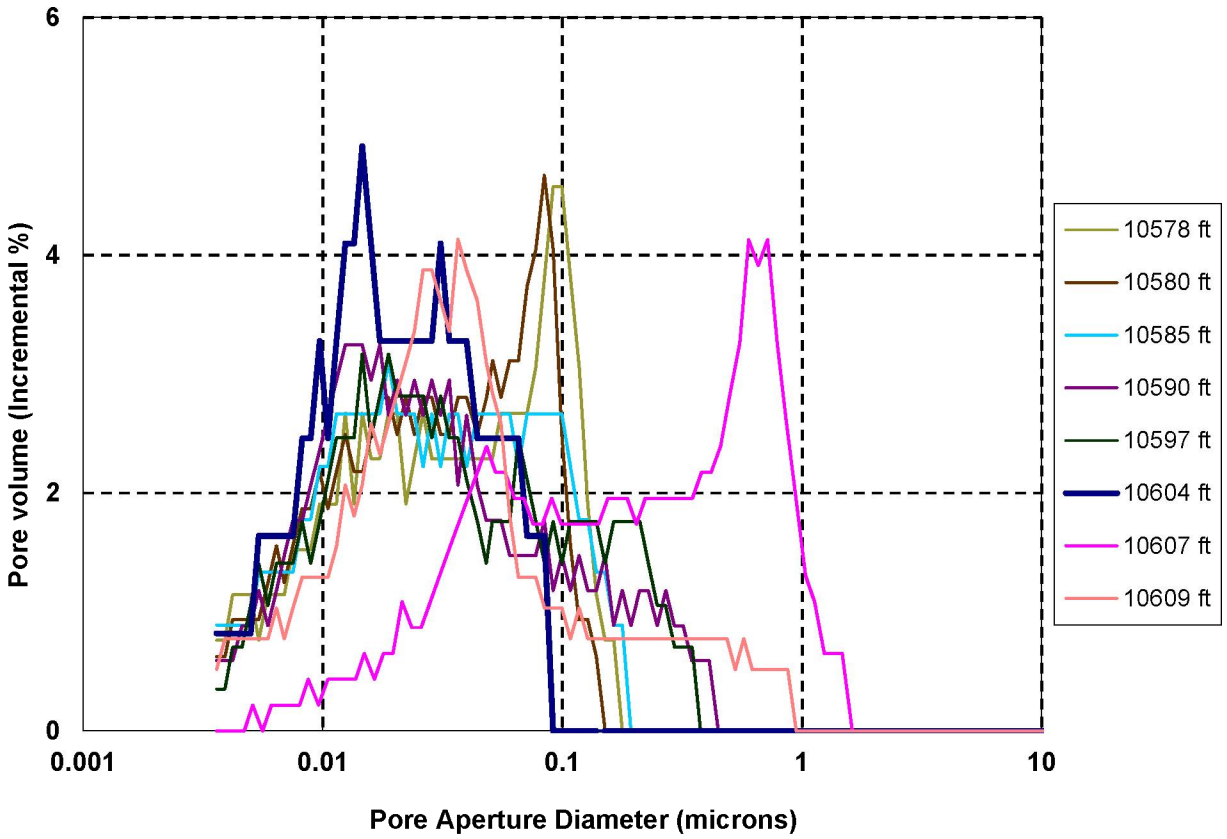

Figure 3.5. Mercury intrusion capillary pressure pore-throat-diameter distributions. Samples from well OCS-G-4708 #1 (well 2, fig. 3.1).

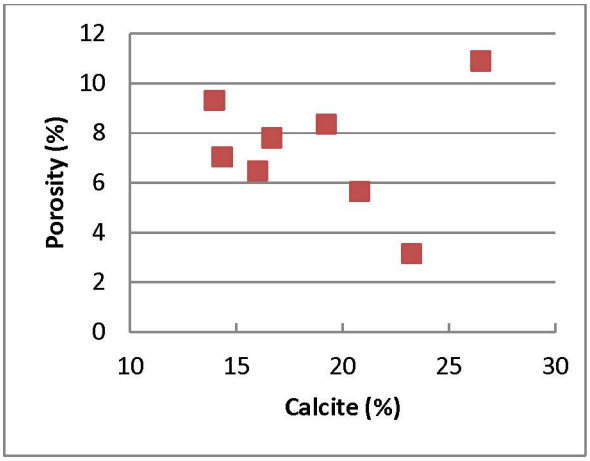

Figure 3.6A. Porosity vs. calcite abundance of the MICP test samples of well OCS-G-4708 #1, showing decreasing porosity with higher calcite abundance.

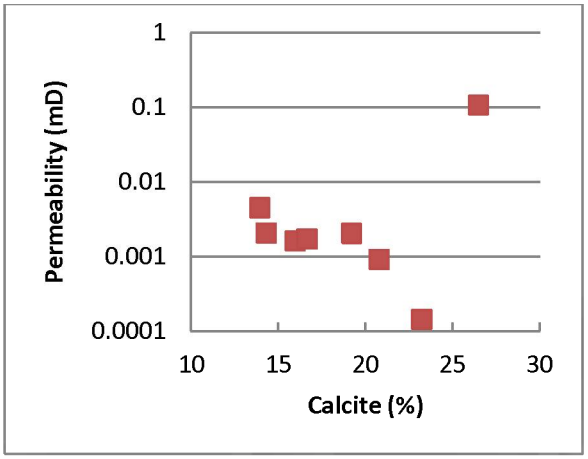

Figure 3.6B. Permeability vs. calcite abundance of the MICP test samples of well OCS-G-4708 #1, showing decreasing permeability with higher calcite abundance.

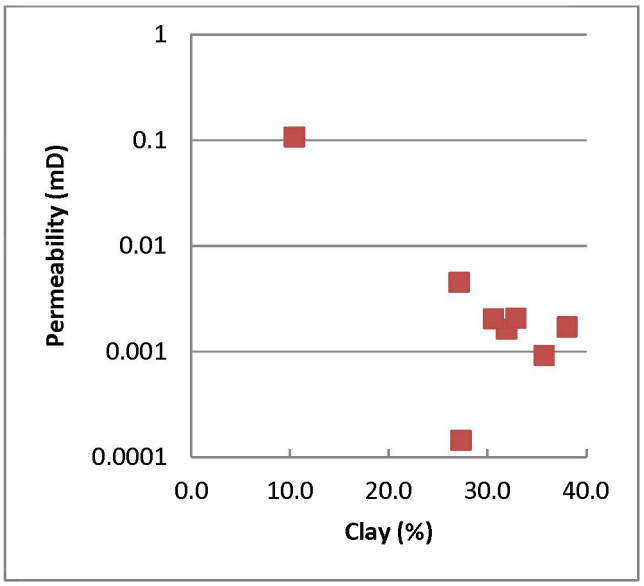

Figure 3.6C. Permeability vs. clay abundance of the MICP test samples of well OCS-G-4708 #1, showing decreasing permeability with higher clay abundance.

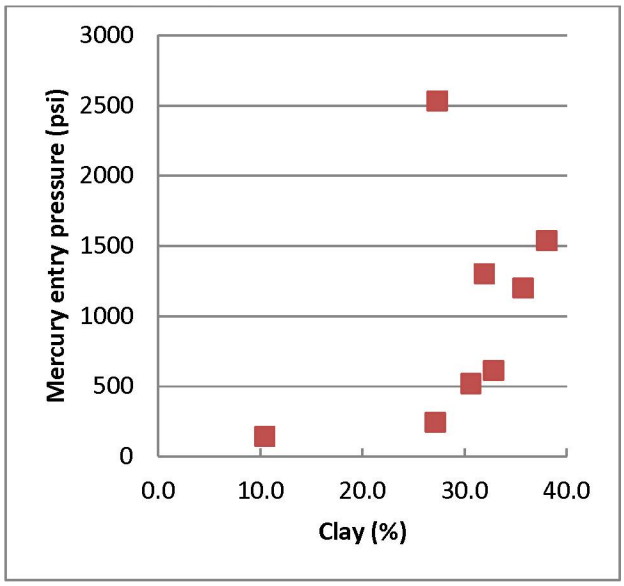

Figure 3.6D. Mercury entry pressure vs. clay abundance of the MICP test samples of well OCS-G-4708 #1, showing increasing entry pressure with higher clay abundance, with two sandstone outliers.

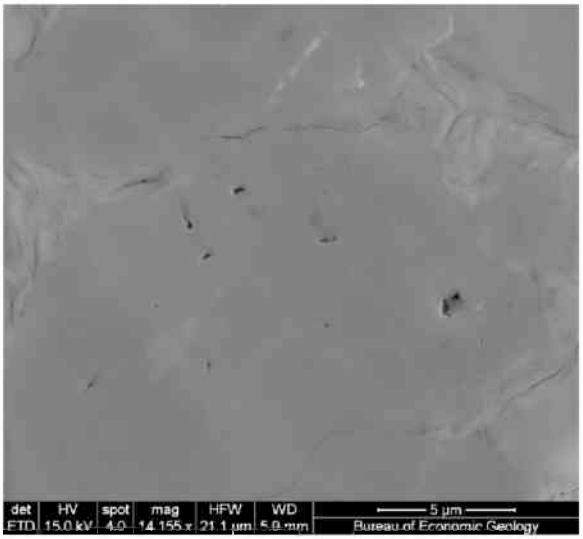

Figure 3.7A. Intragranular pores in an albite grain. SE image of ion-milled sample. 10578 ft, OCS-G-4708 #1. Porosity: 6.5%; permeability: 0.002 mD.

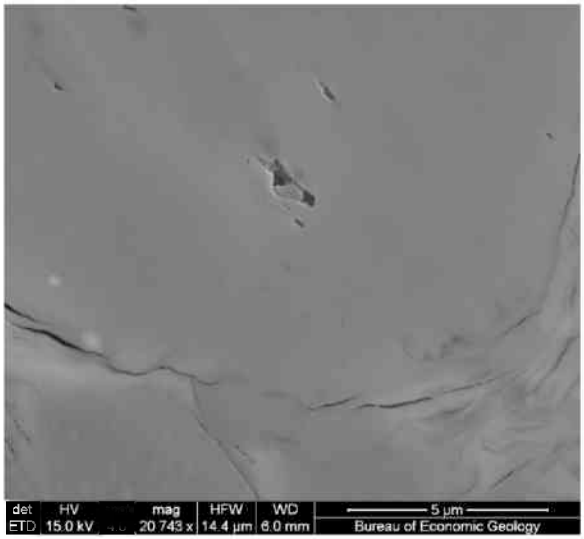

Figure 3.7B. Intragranular pores in a K-feldspar grain. SE image of ion-milled sample. The largest pore is over 1.5 µm in size. 10578 ft, OCS-G-4708 #1.

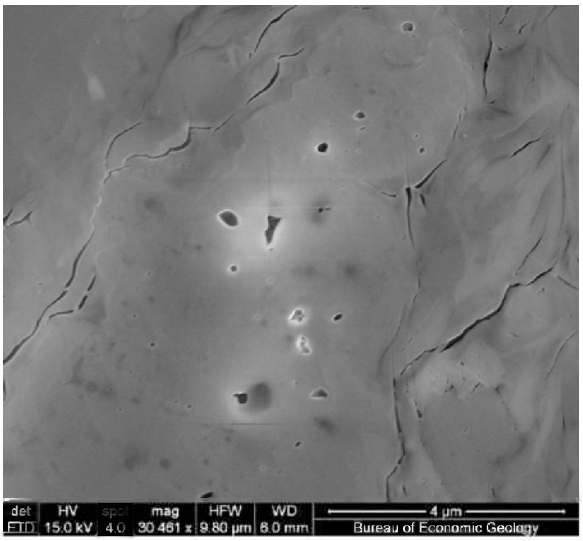

Figure 3.7C. Intragranular pores in a calcite grain. SE image of ion-milled sample. 10578 ft, OCS-G-4708 #1. Porosity: 6.5%; permeability: 0.002 mD.

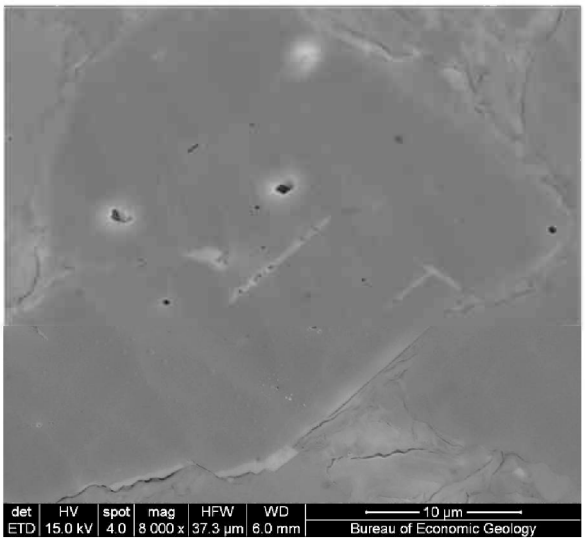

Figure 3.7D. Intragranular pores up to 1 µm in size in a detrital dolomite grain. SE image of ion-milled sample. 10578 ft, OCS-G-4708 #1.

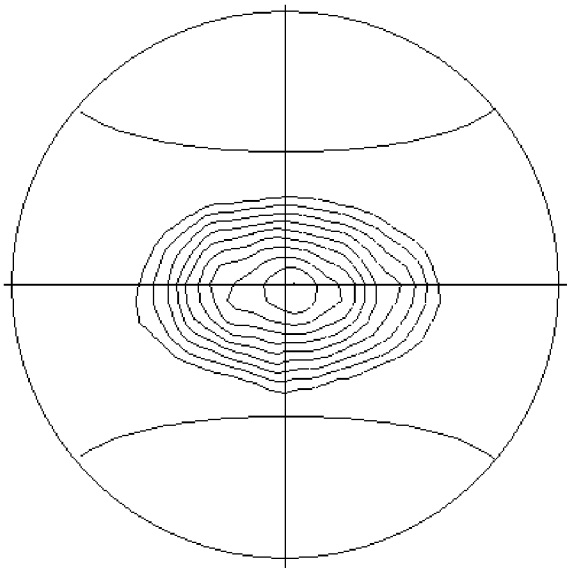

Figure 3.8A. Pole figure of I-S, 2.75 m.r.d., 10578 ft.

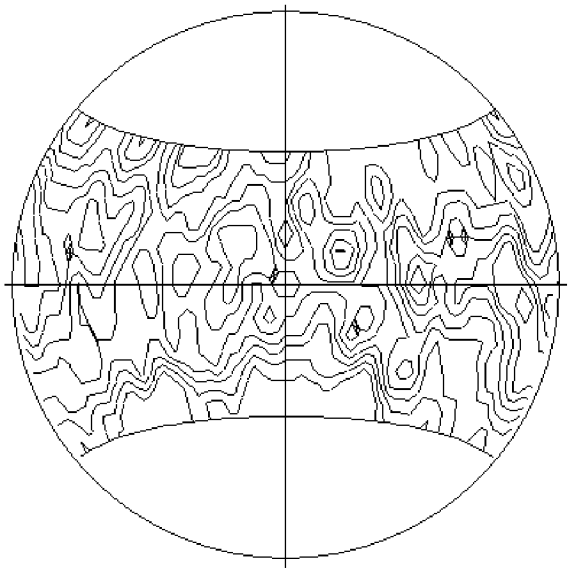

Figure 3.8B. Pole figure of mica, 1.74 m.r.d., 10607 ft.

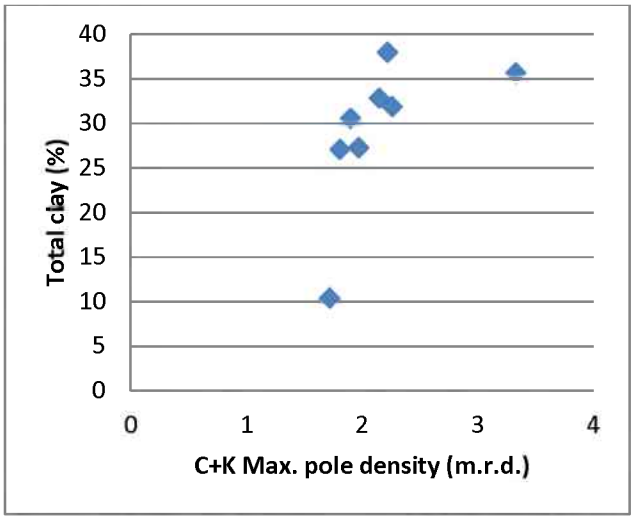

Figure 3.9A. Correlation between chlorite + kaolinite (C+ K) alignment (m.r.d.) and total clay abundance.

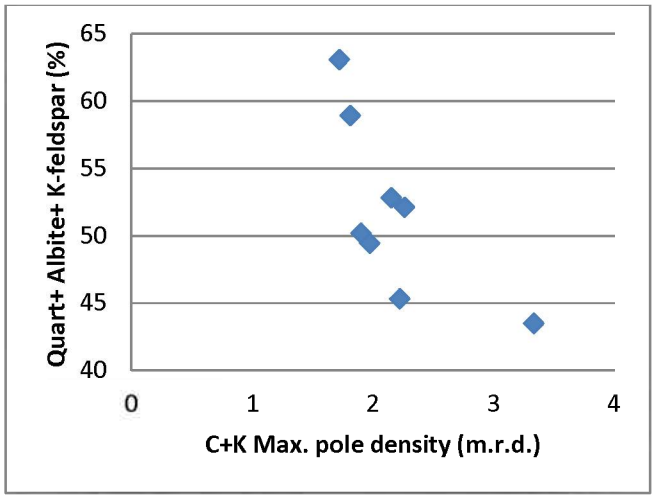

Figure 3.9B. Correlation between chlorite + kaolinite (C+ K) alignment (m.r.d.) and whole-rock abundance of detrital grains (quartz + albite + K-feldspar).

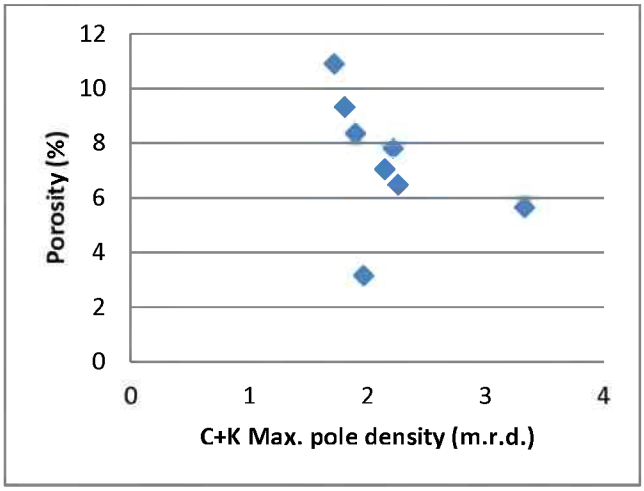

Figure 3.9C. Correlation between chlorite + kaolinite (C + K) alignment (m.r.d.) and porosity.

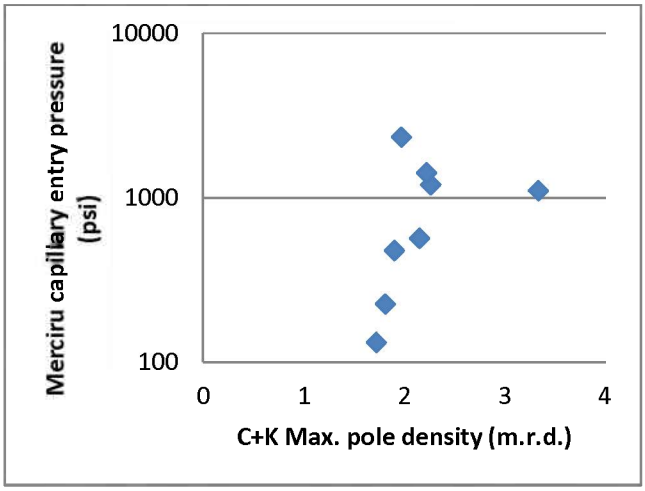

Figure 3.9D. Correlation between chlorite + kaolinite (C+ K) alignment (m.r.d.) and mercury entry pressure.

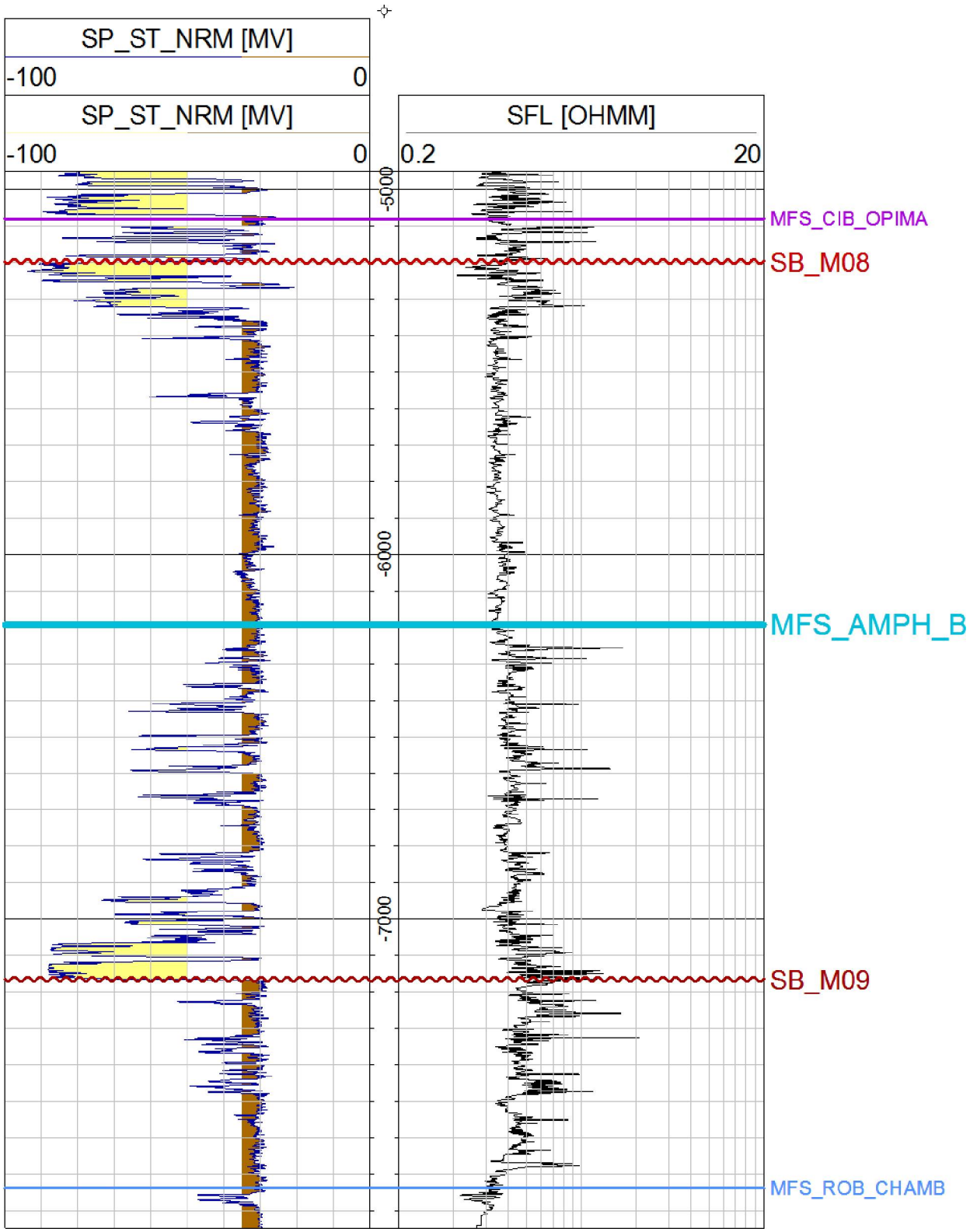

Figure 3.10. Representative geophysical well log from Texas State Waters area (Trans Ocean Oil, SL 70526 #1, API # 42706300860000) showing key chronostratigraphic surfaces and > -35 mv cutoff defining net mudrock (brown shading). Yellow shading represents net sandstone reservoir defined by < -50 mv cutoff (Chapter 5, this volume). Shallow resistivity (SFL) is black curve in right track. Key chronostratigraphic surface interpretations shown are labeled at far right (see text for explanation).

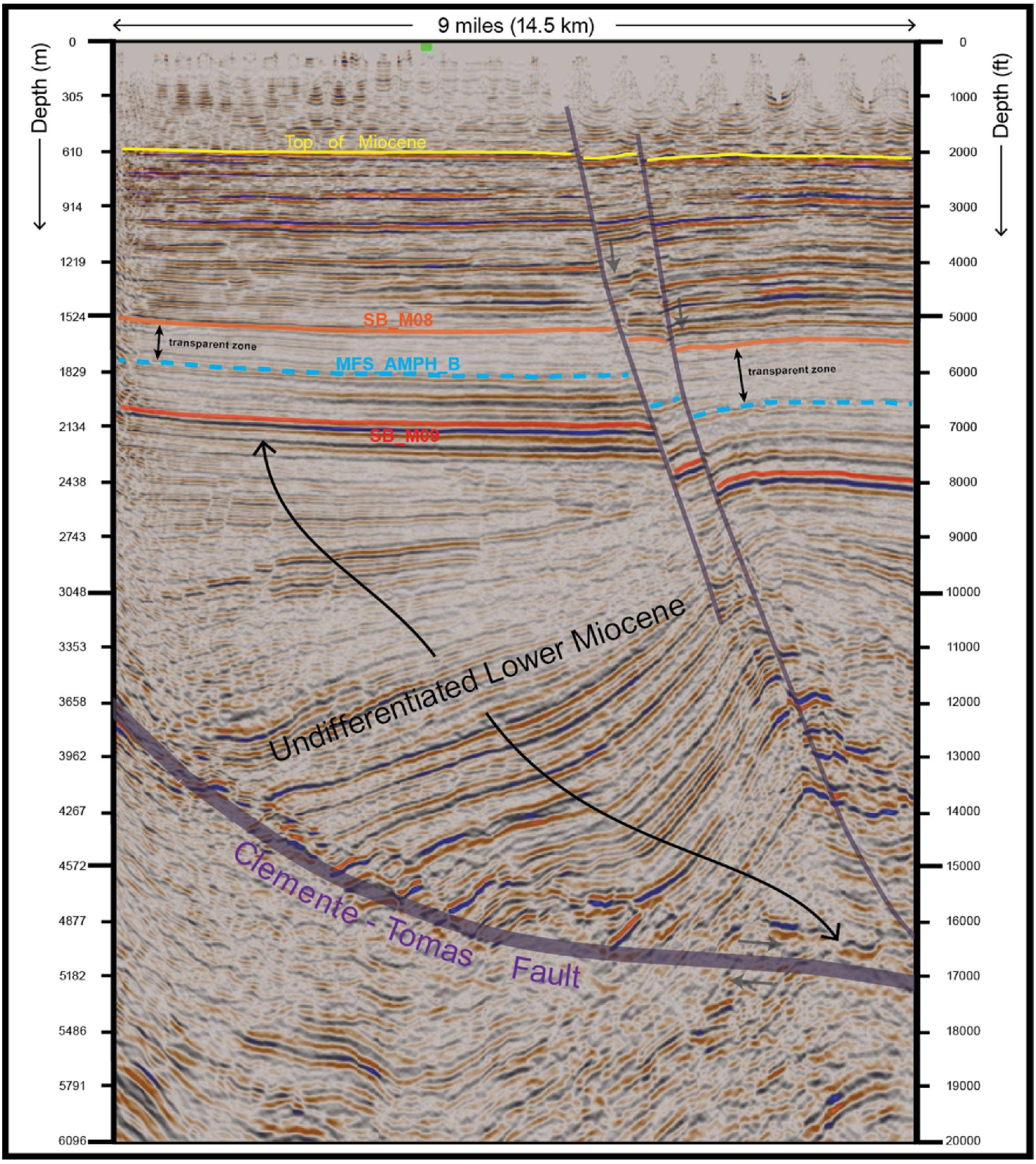

Figure 3.11. Dip-oriented, vertical 3D seismic section, depth domain; approximate location of line shown in figure 3.1. The section profiles most of the 10-mile swath of Texas State Waters. Far right (seaward) edge of the graphic is coincident with the Federal OCS boundary. The Amph B sequence is bounded by orange and red sequence boundaries SB_M08 and SB_M09, respectively.

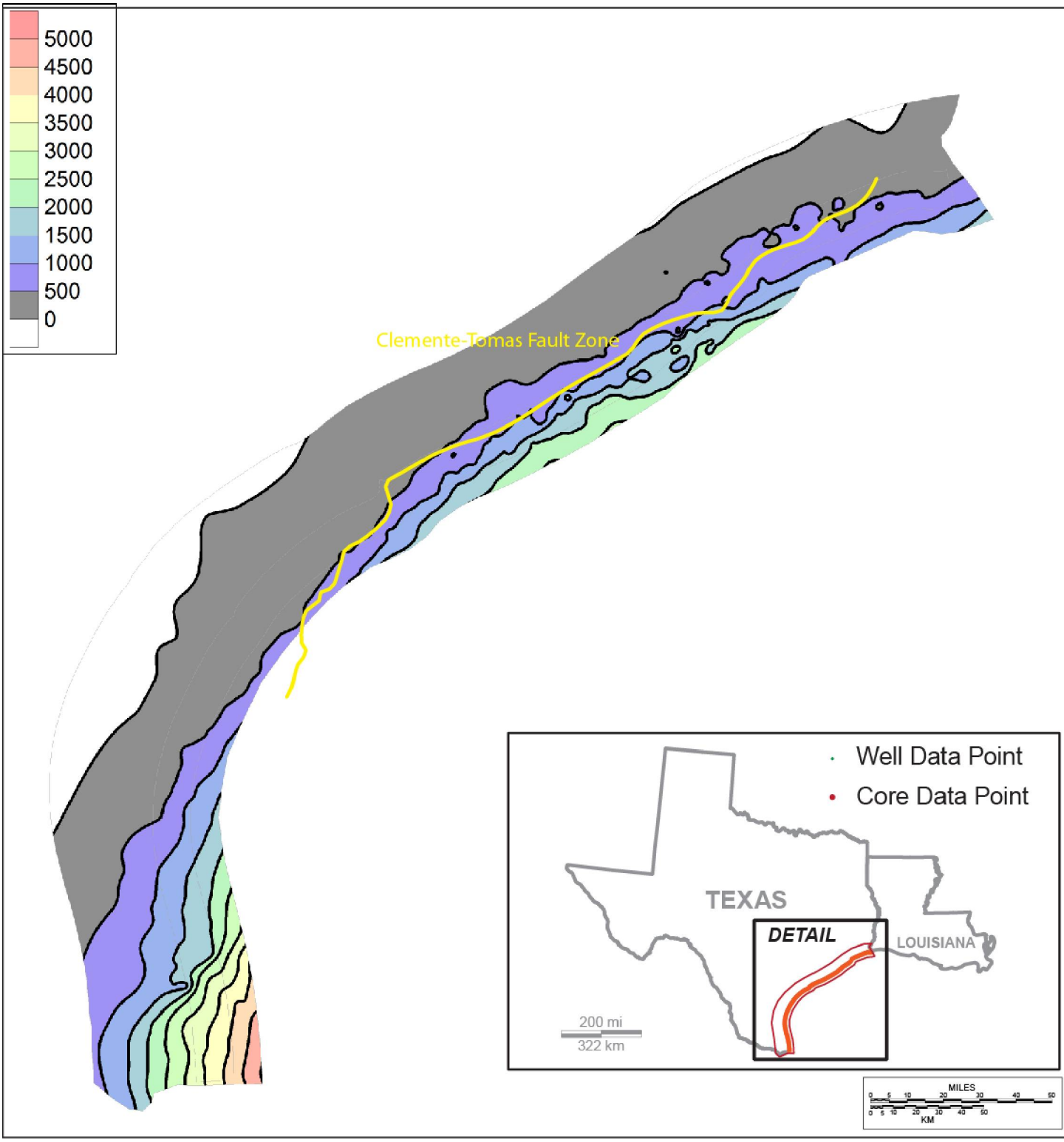

Figure 3.12. Amph B net mudrock isopach map derived from geophysical well logs (SP curves). CI = 500 ft. Locations for 712 wells used to construct the map are shown in figure 3.1. Dark red polygon represents the outline of the entire study area; orange polygon outlines the offshore Texas State Waters.

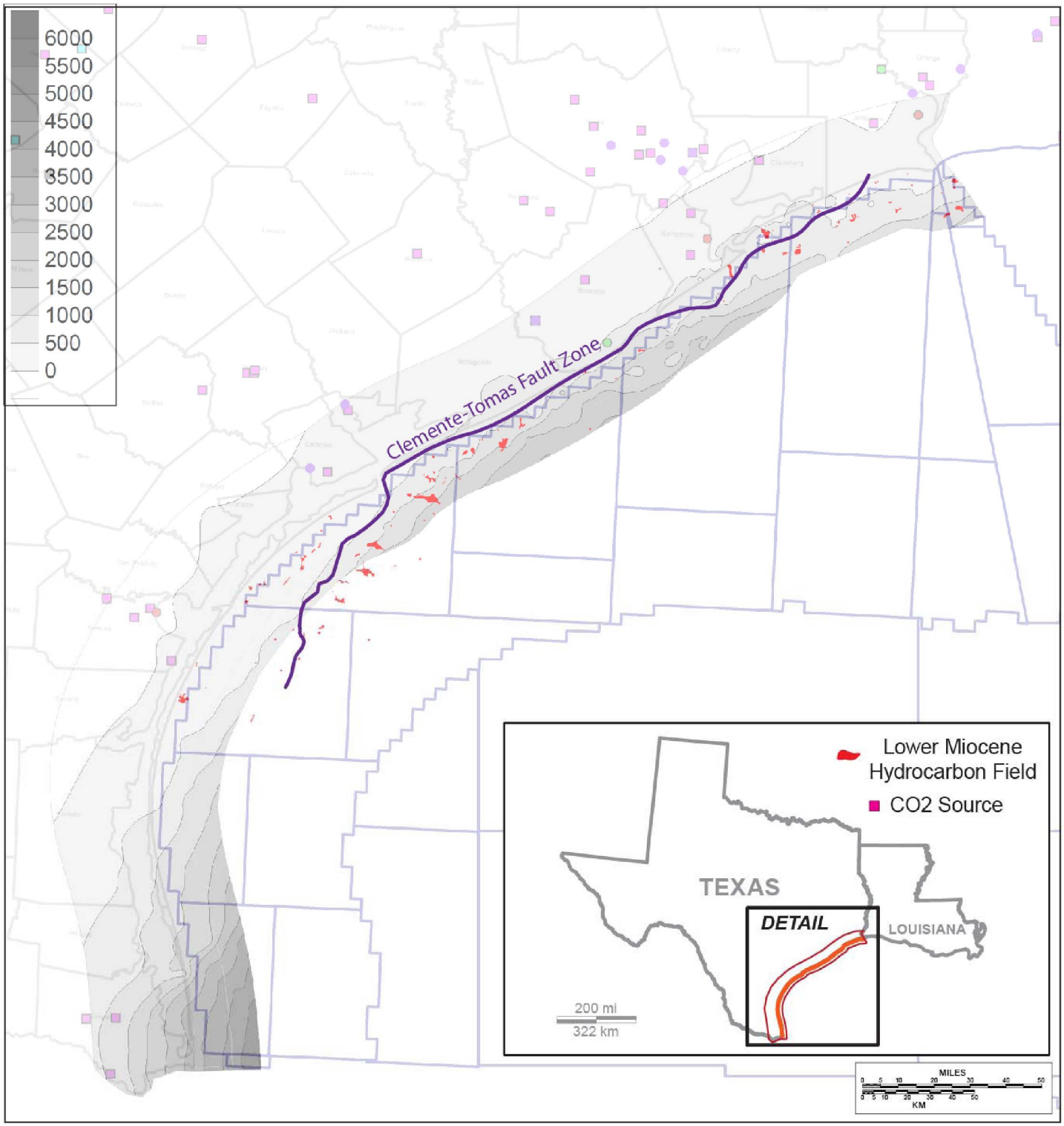

Figure 3.13. Major lower Miocene–age hydrocarbon reservoirs of offshore Texas. Amph B net mudrock isopach map from figure 3.12 is shown in grayscale, CI = 500 ft. Locations for 712 wells used to construct the map are shown in figure 3.1. Dark red polygon represents the outline of the entire study area; orange polygon outlines the offshore Texas State Waters.

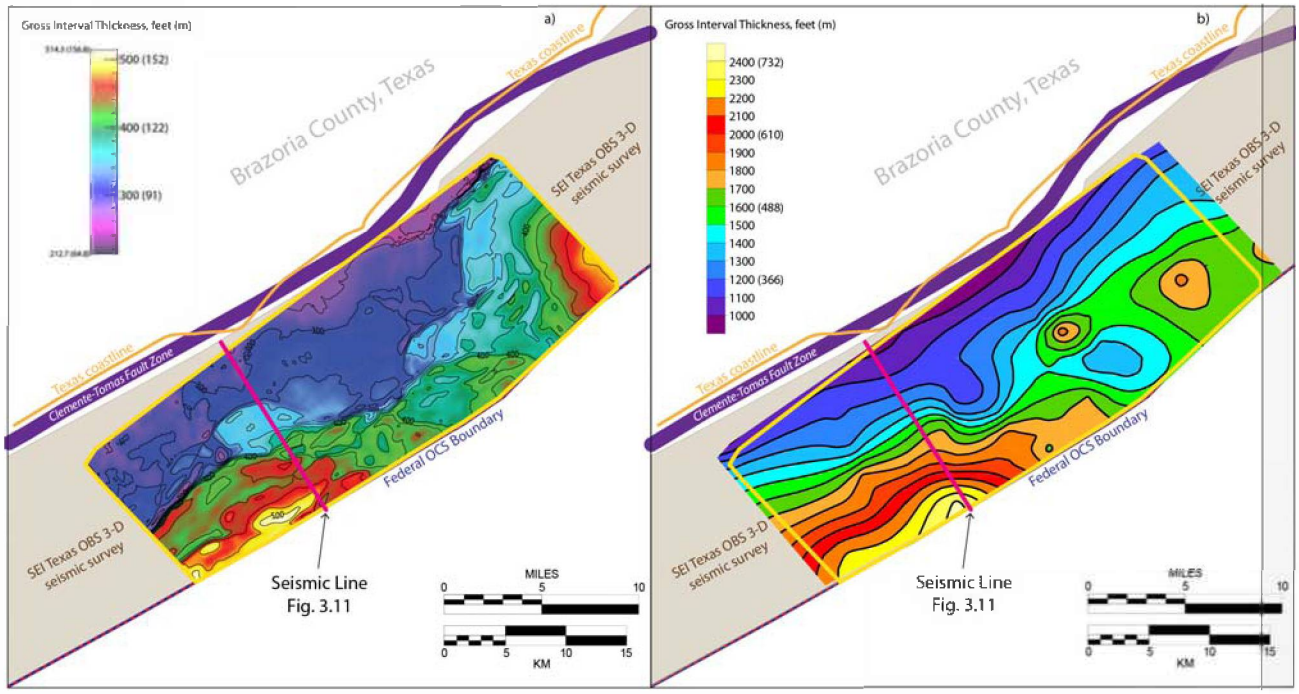

Figure 3.14. Amph B mudrock isopach map derived from a) 3D seismic interpretation nad b) well control only.

CHAPTER 4: Fault Seal Properties for CO_2 Sequestration, Offshore Texas Miocene

A.J. Nicholson, T. A. Meckel, J. Liu, and R. Trevino

Gulf Coast Carbon Center, Bureau of Economic Geology, The University of Texas at Austin, Austin, TX, USA

ABSTRACT

The Gulf Coast of Texas has been proposed as a high capacity storage region for geologic sequestration of anthropogenic CO_2. The Miocene section within the Texas State Waters is an attractive near-offshore alternative to onshore sequestration. However, the stratigraphic targets of interest and prior hydrocarbon accumulations highlight a need to understand and potentially utilize abundant fault-bounded structural traps. Regional capacity estimates in this area have previously focused on simple volumetric estimations or more sophisticated fill-to-spill scenarios with faults acting as no-flow boundaries. Capacity estimates that ignore the static and dynamic sealing capacities of faults may therefore be inaccurate. A comprehensive fault seal analysis workflow for CO_2-brine membrane fault seal potential has been developed for geologic site selection in the Miocene section of the Texas State Waters. Traditional top seal analysis (x-ray diffraction and mercury-injection capillary entry pressure) and capacity estimation is performed on a stratigraphically equivalent Miocene whole core for comparison. To reduce uncertainty of fault performance, a fault seal calibration has been performed on 6 Miocene natural gas traps in the Texas State Waters in order to constrain the capillary entry pressures of the modeled fault gouge. Results indicate that calculated membrane fault seal capacity for the Lower Miocene section agree with published global fault seal databases. Faults in the area can therefore serve as effective seals for CO_2, as suggested by natural hydrocarbon accumulations. However, fault seal capacity is generally an order of magnitude lower than top seal capacity in the same stratigraphic setting, making the requirement to understand local fault seal capacity as important as defining regional top seal capacities.

INTRODUCTION

The Texas Gulf Coast contains many point sources of anthropogenic carbon dioxide (CO_2) emissions such as refineries, petrochemical plants, coal and natural gas power plants, and cement factories. Recent estimates by the United States Geological Survey highlight the Gulf of Mexico as one of the most prospective for large-scale storage. In addition, the region exemplifies both historic and active hydrocarbon exploration, which provides abundant data on the local stratigraphy that can be used for carbon sequestration. The thick (5,000 – 15,000') clastic Miocene section, with porous (>25% porosity) reservoirs and numerous regional seals, is readily available for commercial CO_2 sequestration or enhanced oil recovery (EOR) operations in the Texas State Waters (TSW).

The State Waters provide a common lessor for mineral ownership and the lack of potable groundwater resources mitigates the risk of USDW (protected underground source of drinking water) contamination. Shallow water depth (<100') can aid surface monitoring efforts (von Deimling et al., 2010). Data from natural gas fields in Miocene reservoirs can be used as analogs prior to site selection for brine storage. An estimated 2.5 Gt or greater capacity resides in Gulf Coast EOR candidate fields (Holtz et al., 2005), while annual CO_2 emissions from the Gulf Coast region (Texas, Louisiana, and Mississippi) are ~1Gt per year (Ambrose et al., 2009). Thus, although EOR offers a needed early economic driver for CO_2 capture, compression, and transmission, brine storage will eventually need to be utilized to achieve long-term significant reduction in Gulf Coast emissions through time.

Capacity estimation is a critical aspect of both local and regional sequestration site selection. Bradshaw et al. (2007) point out that many studies have focused on estimating regional capacity using simple pore-volume calculations. More advanced calculations use no-flow boundary conditions for faults and evaluate structural fill-to-spill capacity (Nicot et al., 2006). While treating faults and top seals as no-flow boundaries may be sufficient for first attempts at regional capacity estimates, site specific capacity estimates must consider the petrophysical properties of faults and their effect on CO_2 capacity over geologic time scales. Fill-to-spill capacity modeling estimates, which represent the upper end member of potential CO_2 storage capacity in a stratigraphic unit will likely over predict the long term CO_2 capacity of faulted basins. Historic natural gas field data in Miocene age reservoirs within the State Waters (Seni et al., 1997) provide natural analog data to perform empirical fault seal calibration that can be used in both regional and site specific CO_2 storage capacity estimates for fault-bound traps. Core data are used to calibrate potential top seal capacity.

Membrane fault seal capacity modeling is hypothesized to lower estimates of CO_2 storage capacity when compared with fill-to-spill capacity modeling. In order to

assess the relative importance of CO_2 fault seal capacity, regional fluid property trends are assessed, fault bound natural gas accumulations are calibrated with estimated fault rock properties, empirical fault seal capacity is compared with core-derived top seal capacity from a stratigraphically equivalent section, and a workflow is developed to empirically estimate the effect of membrane fault seal capacity compared with fill-to-spill capacity over geologic time scales.

REGIONAL GEOLOGY

This study focuses on the Texas State Waters within the 10 mile wide tract of submerged land paralleling the Texas coastline (Figure 1). Data available for mapping and characterization include a Seismic Exchange, Inc. (SEI) 3D seismic dataset, ION Geophysical GulfSPAN 2D seismic data, synthetic seismograms and check shot surveys, and numerous well log and paleontological databases.

The present-day Gulf of Mexico is a passive margin created by seafloor spreading during the Middle Jurassic through Early Cretaceous. Late Cretaceous through Paleocene Laramide basin formation across the Inner Cretaceous Seaway initiated high potential sediment yield within internal drainages in Wyoming, Colorado, and New Mexico, effectively starving the Northern Gulf of Mexico sediment supply. This initial meager sediment supply resulted in mixed carbonate and siliciclastic deposition in the Gulf of Mexico region. After many of the Laramide basins were filled in the latest Cretaceous and Paleocene, spillways developed and drainages gathered so that, from late Paleocene, high sediment volume rates (>100,000 km^3/Ma) entered the Northern Gulf of Mexico basin and terrigenous clastic wedges prograded basinward to the southeast. This drainage system from the northwest, as well as others from the north and northeast, continued to reach the Gulf waters through the Pleistocene (Galloway et al., 2011). The Lower Miocene interval of the Northwestern Gulf of Mexico formed two porous, siliciclastic progradational wedges that are available for CO_2 sequestration within the Texas State Waters (Figure 2). The regressive Lower Miocene 1 (LM1) and Lower Miocene 2 (LM2) siliciclastic wedges that extend seaward from the Texas coastline are underlain by a major transgressive flooding surface represented lithologically by the late Oligocene Anahuac shale (Rainwater, 1964; Galloway, 1989). The thick (>1000') Anahuac section that strikes parallel to the present day coastline is downthrown thousands of feet by the Clemente-Tomas fault system, a Lower Miocene, linked growth fault succession (Galloway, 1989; Bradshaw and Watkins, 1994; McDonnell et al., 2009). Along the southern half of the Texas coastline these growth faults are caused by deltaic sand-loading and shelf-edge foundering of the mobile Anahuac shale (Winker and Edwards, 1983). The northern half of the growth fault succession paralleling the Texas coastline and into Louisiana is caused by evacuation of allocthonous salt (presumably Louann salt) from the previous Late Oligocene Anahuac shelf edge (McDonnell et al., 2009). The shale and salt evacuation along the Clemente-Tomas growth fault

system resulted in a more than threefold increase in the hanging wall sediment thickness relative to the footwall of the LM1 in some localities (Figure 2). Growth faulting ceased by the LM2 regressive episode of shelf growth, allowing progradation of the shelf margin farther to the southeast and into the Corsair growth fault trend (Bradshaw and Watkins, 1994).

The Galloway (1989) classification scheme is used to distinguish the top LM1 and the top LM2 regressive episodes based on benthic foraminifera data. The *Marginulina ascensionensis* (Marg. A.) shale defines the top of the LM1 depositional episode and the *Amphistegina chipolensis* (Amph. B) shale defines the top of the LM2 depositional episode. The entire Lower Miocene succession spans in age from roughly 24-16 Ma (Galloway, 1989). Both the LM1 and LM2 intervals provide prospective reservoirs and seals for CO_2 sequestration within the Texas State Waters.

PROSPECTIVE SEQUESTRATION PLAYS AND FAULT DISTRIBUTION

While there is considerable pore space available for CO_2 sequestration in Miocene brine reservoirs in the Texas State Waters, many sub-regional (site scale) structural boundaries exist (e.g. faults). A structure map of the top of the Lower Miocene 2 indicates that fault surfaces mapped in seismic data bound even the largest potential sites and often cut through structural highs (Figure 3A). Prospective sequestration sites for the LM2 horizon are growth-faulted shelf-edge rollover anticlines, transverse grabens, faulted syncline mini-basins, and piercement salt domes. The transverse grabens are formed from corrugations in the Clemente-Tomas fault system inherited from previous Oligocene detachments (Trevino and Vendeville, 2008; McDonnell et al., 2010). For the LM1 horizon the dominant play type is rollover anticlines formed during the regional growth faulting phase of the Clemente-Tomas linked growth fault (McDonnell et al., 2010). Existing natural gas fields from the LM2 and the upper portion of the LM1 conform to faulted structural features rather than stratigraphy (Figure 3B). This suggests that understanding fault seal, regardless of the play type chosen, is critical.

Near-surface (sea floor) penetrating faults (Figure 3C) extend to the upper limits of seismic resolution (< 0.3s, or < ~850 ft) and are a concern for CO_2 storage in that they provide a potential leakage pathway to the sea floor. It is known that faults can act as both seals and conduits for fluid (Weber et al., 1978; Bouvier et al., 1989; Alexander and Handschy, 1998; Davies et al., 2003). In a worst-case scenario, fault parallel flow (i.e. vertically and laterally along a fault, as opposed to across-fault flow) could occur in a continuous leak from the injection interval to the surface or out of a containment structure if they are not sealing. A fault seal

calibration is necessary to understand both the degree to which faults are likely to seal and the petrophysical properties of the sealing fault-rock.

FACTORS LIMITING HYDROCARBON ACCUMULATIONS: SEAL CAPACITY

Lateral seals (e.g. faults) and top seals are important boundaries for fluid entrapment and it is important to understand the different categories of mechanisms that can limit the size of a trapped fluid accumulation over both geologic time scales (thousands of years) and sequestration time scales (decades to centuries). Buoyancy force created between the less dense immiscible hydrocarbon (non-wetting phase) and brine (wetting phase) is the dominant mechanism driving secondary migration (both lateral and vertical) of hydrocarbons (Thomas et al., 1968; Schowalter, 1979). The main static mechanisms limiting hydrocarbon accumulation size are structural spill and faulted self-juxtaposition of reservoir sands, top seal and fault seal capillary entry pressure (Schowalter, 1979), and top seal and fault seal mechanical failure (Handin et al., 1963; Jaeger and Cook, 1969).

Structural spill occurs when the buoyant fluid fills the entire structural relief of the trap and the trap cannot reatin any more buoyant fluid. Juxtaposition spill occurs when the trapped fluid fills to the tip of a fault (zero displacement point), or where the reservoir regains self-juxtaposition (Allan, 1989), but the structural spill could still hold more buoyant fluid (Figure 4A). Across-fault juxtaposition of sand-on-sand or sand-on-shale does not necessarily mean those contacts are leak points or seals, respectively. Fault rock (or fault gouge) material will exist between the juxtaposition, and this will determine the degree of seal or lack thereof. Traps limited by structural or juxtaposition leak imply the top seals have the ability to withstand larger column heights.

Capillary (membrane) fault seal and top seal (Figure 4B) become a potential controlling factor when traps are not filled to either the structural spill or the juxtaposition leak point (Schowalter, 1979). In the case that fault seal or top seal are the limiting factor, capillary entry pressure (P_{ce}) of the top seal lithology or fault rock determines the maximum supported column height. Traps in which fluids have exceeded the capillary entry pressure of the seals will remain sealing once enough fluid has migrated out of the trap to regain equilibrium capillary pressures (Thomas et al., 1968), i.e. when the buoyancy pressure (BP) is once again below the capillary entry pressure.

Fracturing of the reservoir and top seal can occur (Figure 4C) if the total pore pressure, or reference pore pressure (RPP, equal to or greater than hydrostatic pore pressure) plus buoyancy pressure, exceeds the minimum principal horizontal stress (S_h). Pore pressure limits from a South Texas study of overpressured oil

and gas fields by Engelder and Leftwich Jr. (1997), particularly from Oligocene (Frio) examples in the Redfish Bay area, show that pore pressure never exceeded values of 80-90% of lithostatic stress (S_v), providing an approximation for S_h. The Engelder and Leftwich Jr. (1997) study provides a good methodology for estimating S_h in the absence of leakoff tests by using existing pore pressure data.

Preexisting faults can also reactivate (Figure 4C) at lower pore pressures (the critical pore pressure, S_c) than required to hydraulically fracture the top seal (Finkbeiner et al., 2001). Leakage by fault reactivation has been documented in field studies (Wiprut and Zoback, 2000; Lyon et al., 2005), but it is difficult to distinguish from leakage by hydraulic fracturing. Fault reactivation occurs when the total pore pressure causes the differential principal stresses to intersect the Mohr-Coulomb failure envelope of a preexisting fault (Finkbeiner et al., 2001). Reactivation is considered in greater detail below. Because fault reactivation and hydraulic fracturing of the reservoir are limiting factors for CO_2 sequestration that can be addressed with pressure management and modeled for the short-term injection time scales, long term storage of CO_2 adjacent to faults requires focusing on fault seal and top seal capillary entry pressures.

FAULT ROCK TYPES AND DETERMINATION

Fault gouge in clastic sedimentary systems, much like its host rock, shows variations in both lithology and petrophysical properties. Before assessing the prediction of fault rock lithology and petrophysical properties in the subsurface it is important to understand the main categories of fault rock as summarized in Fisher and Knipe (1998). Outcrop and thin section photographs (Figure 5) illustrate the fault rock classification (Yielding et al., 2010).

Cataclasites and Disaggregation Zones

Cataclasites occur in porous, clay free sandstones during faulting (Fisher and Knipe, 1998) and are often referred to as deformation bands. Deformation bands form as single shear bands (mm to cm scale width), evolve into zones of deformation bands, and may eventually result in a slip plane (Antonellini and Aydin, 1994). These bands are the result of grain crushing, rotation, and sliding due to mechanical compaction at grain-to-grain contacts (Milliken and Reed, 2002). Cataclasis results in loss of permeability and porosity relative to the host rock from which they were formed due to both mechanical and enhanced chemical compaction (Antonellini and Aydin, 1994; Milliken and Reed, 2002).

Disaggregation zones are similar to cataclasites, with throws on the order of millimeters to centimeters, but are formed under low mean effective stress conditions (either shallow burial or low effective stress while lacking cementation) and therefore do not involve grain crushing (Sperrevik et al., 2002).

Phyllosilicate Framework Fault Rocks

Phyllosilicate Framework Fault Rocks (PFFR) are classified as having 15-40% phyllosilicates (e.g. chlorite, illite, smectite, kaolinite, etc.) and form by deformation induced mixing of impure (clay content >0%) sandstones and siltstones (Fisher and Knipe, 1998). PFFRs have been documented in Gulf of Mexico strata as old as Eocene (Smith, 1980; Berg and Avery, 1995), and based on data introduced in a later chapter, are the dominant sealing fault rock type for the Texas Gulf Coast Miocene strata.

Shale Smears

Shale smears are continuous zones of ductilely deformed clay-rich host rock (>40% phyllosilicates) entrained parallel to the fault (Fisher and Knipe, 1998). Shale smear length and continuity is proportional to the source bed thickness and inversely proportional to the amount of throw along the fault. Mechanisms for shale smearing include abrasion of clay grains by juxtaposed sandstone during faulting, shearing, and to a lesser extent, injection of shale beds along the fault (Lindsay et al., 1993).

Takahashi (2003) advanced the understanding of shale smear continuity through lab experiments by showing that the ratio of fault throw to source bed thickness required to maintain continuous smears increases with increasing effective normal stress. Therefore, in normal stress regimes, as depth increases without an increase in overpressure, longer and more continuous shale smears can be maintained. Shale smears were shown to have a reduction in permeability relative to the original host rock within the initial faulting regime (Takahashi, 2003). This is consistent with porosimetry tests of shale smears by Eichhubl et al. (2005) relative to their host rock. The reduced permeability of the experimental smears was maintained until they became discontinuous and entrained cataclasites, causing recovered permeability that steadily increased with increasing throw (Takahashi, 2003). Because fault-rock bulk permeability is inversely proportional to capillary entry pressure (Sperrevik et al., 2002), it can be inferred from the experimental regimes of Takahashi (2003) that as shale smears become discontinuous and enter into the fault-rock classification realm of PFFRs, the fault rock will have lower capillary entry pressures as more silt and sand-sized particles are entrained in the fault gouge.

While many fault rock types have been categorized in outcrop and core, a predictive approach needs to be introduced to assess fault-rock type and petrophysical properties in the subsurface prior to CO_2 injection.

FAULT SEAL PREDICTION IN THE SUBSURFACE - THE SHALE GAUGE RATIO

Outcrop and core studies have shown that increasing percent phyllosilicates entrained within the fault gouge increases the capillary entry pressure (Figure 6) and decreases the bulk permeability (Gibson, 1998; Sperrevik et al., 2002; Eichhubl et al., 2005). The capillary entry pressure, and therefore sealing capacity, shows a linear increase with increasing percent phyllosilicates (termed V_{cl}). This deterministic fault seal approach from whole core studies cannot be accurately applied in the subsurface unless mineralogical analysis of the host rock is available and estimations of the amount of clay entrained in the fault can be calculated. This is difficult to use for predicting fault seal capacity prior to drilling a well or choosing an appropriate storage site.

Previous algorithms for estimating fault rock heterogeneity in the subsurface provided a qualitative assessment using throw and bed thickness, only estimating the ability of a shale bed to form a continuous smear (Bouvier et al., 1989; Lindsay et al., 1993). The more widely accepted Shale Gouge Ratio (SGR) of Yielding et al. (1997) provides a quantitative approach that relies on both fault throw and bed thickness, as well as incorporating the estimated amount of clay within host rock to determine the clay content of fault gouge:

$$SGR = \frac{\sum(V_{cl} * \Delta z)}{throw} \quad (1)$$

SGR at any point along a fault plane is the summation of the estimate of percent shale in an individual bed (V_{cl}) times the bed thickness (Δz) across the throw window, divided by the *throw*, resulting in a unit-less estimate of the percent shale in the fault gouge.

The SGR, prior to calibration with subsurface pressure data, has been shown to be an effective qualitative predictor for sealing versus non-sealing faults (Yielding, 2002). SGR data from the fault bounded reservoirs of both sealing and non sealing faults show that SGR values of approximately 15-20% are the cutoff for sealing versus non-sealing faults.

However, to approach quantitative fault seal predictions in the subsurface, estimates of SGR must be calibrated to natural accumulations of oil and gas and their associated fluid properties. Before calibrating fluid properties to fault rock properties, it's important to understand what governs the membrane sealing capacity of fault rock.

BUOYANCY PRESSURE AND CAPILLARY ENTRY PRESSURE

Fluids of interest for fault seal calibration, such as methane, oil, and CO_2, are less dense than brine and therefore migrate vertically and laterally through rocks, exerting a buoyant force. Buoyancy pressure is the force exerted by the density

contrast between the wetting phase and the non-wetting phase, in this case assumed to be either brine-CO_2 or brine-methane:

$$P_b = (\rho_w - \rho_f) * 0.433 * H \ , \qquad (2)$$

where P_b is the buoyancy pressure (psi), ρ_w is brine density (g/cm^3), ρ_f is the density of the buoyant fluid (g/cm^3), and H is total column height (ft) (Schowalter, 1979). Buoyancy pressure increases by increasing column height, decreasing depth within a fixed column height, or increasing wetting (water) and non-wetting phase density contrast (Figure 9). The confining geologic units that trap the buoyant fluid (i.e. top seal and fault seal) restrict fluid movement due to the capillary forces associated with the smaller pore throat radii typical in seals. The capillary entry pressure for the fault-rock or top seal with cylindrical pore throats is governed by a variation of the Laplace law:

$$P_{ce} = \frac{2\sigma cos(\theta)}{r} * 0.145 \ , \qquad (3)$$

where P_{ce} is the capillary entry pressure (psi), σ is interfacial tension (mN/m) between the wetting and non-wetting phase, θ is the wettability (degrees), expressed as the contact angle between the wetting and non-wetting phase and the solid pore throat, and r is mean interconnected pore throat radius (μm) (Purcell, 1949; Schowalter, 1979). For static, trapped methane fields from the Lower Miocene in the Gulf Coast under near-hydrostatic conditions, it is assumed that the buoyancy pressure (P_b) exerted by the trapped methane column equals the limiting seals capillary entry pressure (P_{ce}):

$$P_b = P_{ce} \qquad (4)$$

This is only the case if the rate of charge does not exceed the rate of leakage by capillary flow and the methane column is not limited by structural spill, juxtaposition spill, mechanical top seal failure, or fault reactivation. If the methane column is limited by any of the spill or failure mechanisms, then the buoyancy pressure of that methane column represents a minimum estimate of the fault seal or top seal capillary entry pressure.

Buoyancy pressures exerted from different fluid column heights at varying reservoir depths (varying temperatures and pressures) require normalization. Fluid properties affecting buoyancy pressure and capillary entry pressure, such as fluid density, interfacial tension, and contact angle, have been shown to vary for the same fluid type depending on temperature, pressure, and brine salinity (Firoozabadi and Ramey, 1988; Argaud, 1993; Chalbaud et al., 2006; Chiquet et al., 2007b).

FLUID PROPERTIES AND THEIR EFFECT ON CAPILLARY ENTRY PRESSURE

Column heights composed of the same fluid (e.g. methane) that are representing the capillary entry pressure of the fault gouge or top seal must be normalized if their buoyancy pressures are measured at varying depths in the subsurface (varying temperatures and pressures). Therefore, an understanding of modeled fluid properties based on regional temperature, pressure and salinity trends is necessary for predicting the sealing capacity of faults and top seals.

Temperature and Pressure

Regional temperature and pressure data have been compiled from wells and produced fields within the Miocene section of the Texas State Waters. Ninety three wireline temperature measurements (uncorrected for time since circulation) and 198 average reservoir temperature measurements (Seni et al., 1997) show an approximately 23°C/km gradient within the Miocene section (Figure 11A). Temperature gradients begin to increase around 14,000ft where wells begin to penetrate the insulating Anahuac shale on the footwall of the Clemente-Tomas fault system. Average temperature for the region can be expressed by the equation:

$$T = 0.602D^2 + 4.158D + 98.49 \quad , \tag{5}$$

where T is temperature (°F) and D is depth (kilo-feet). This temperature trend is consistent with findings from nearby offshore geothermal studies (Nagihara, 2010).

Average initial reservoir pressure (Seni et al., 1997) trends for all Miocene reservoirs within the State Waters are shown to be hydrostatic until depths of approximately 9,000ft. This depth is geographically variable and should only be used as a rule of thumb. The overburden stress, or S_v for normal-fault stress regimes, is assumed to be an average of 1 psi/ft. In the absence of conventional stress magnitude measurements, such as leakoff tests (Hickman and Zoback, 1983), the overpressured reservoirs provide a reasonable estimate for the minimum principal stress magnitude of 85% S_v. These values are consistent with the findings of Engelder and Leftwich Jr. (1997).

Fluid Density

The average temperature trend with depth and hydrostatic pressure gradient were input into the Peng-Robinson equation of state to solve for CO_2 fluid density with depth (Peng and Robinson, 1976). The program ThermoSolver™ was used to automate the Peng-Robinson equation of state (Barnes and Koretsky, 2003) resulting in average density trends with depth for both CO_2 and methane (Figure 11C). CO_2 density rapidly increases with depth until it reaches a steady range

between 0.6 and 0.7 g/cm^3 below 1km depth. Maximizing CO_2 density can greatly increase storage capacity and should be considered when choosing a sequestration site. Calculated CO_2 density at field-specific measured Miocene reservoir temperature and pressures (Seni et al., 1997) show that when overpressure is taken into account, as opposed to hydrostatic pressure, CO_2 density can approach 0.9 g/cm^3 (grey dots, Figure 11C).

Buoyancy pressure and fluid gradients are normally obtained from in-situ measurement of reservoir pressures at varying depth increments. These measurements are used to demonstrate reservoir connectivity (or lack thereof). In the absence of such data, the temperature and initial reservoir pressure can be used to calculate a fluid density using the Peng-Robinson equation of state. This is only effective for pure fluids such as methane and CO_2. The calculated methane density and known, mapped column heights can then used to calculate buoyancy pressure (Equation 2).

Interfacial Tension

The interfacial tension (or attraction) between two immiscible fluids is a key parameter in Equation (3). The higher the interfacial tension between two fluids, the more attracted they are and the more pressure is required to displace the wetting fluid. In other words, higher interfacial tension yields a higher sealing capacity (when all other external factors are constant). Macleod (1923) used the Van der Waals' equation assumption that force of attraction falls off with the 4th power of the distance between molecules. He found that the surface tension of a liquid and its vapor is dependent upon the empirical formula:

$$C = \frac{\sigma}{(\rho_l - \rho_v)^4} \quad , \tag{6}$$

where C is a constant, σ is the surface tension of a pure compound, and ρ_l and ρ_v are the liquid and vapor densities, respectively. Surface tension is directly proportional to the density difference between the two fluids. Therefore, as the density difference decreases, the interfacial tension between two immiscible fluids decreases.

Experimental findings on methane-brine interfacial tensions (Hough et al., 1951; Jennings and Newman, 1971) were analyzed by Firoozabadi and Ramey (1988) and, using Equation (6) for an initial evaluation, interfacial tension (IFT) was shown to vary with both density contrast ($\Delta\rho$) as well as reduced temperature (T_r). Reduced temperature is a dimensionless scaling factor:

$$T_r = \frac{T}{T_c} \quad , \tag{7}$$

where T is the measured temperature of the gas or supercritical fluid and T_c is the critical temperature at which point a fluid becomes supercritical (Peng and Robinson, 1976). T_c for CH_4 and CO_2 are 190.15K and 304.15K, respectively (Atkins and Jones, 2005). Using the relationships between $\Delta\rho$ and T_r established Firoozabadi and Ramey (1988), as well as the interfacial tension measurements from Jennings and Newman (1971) and Sachs and Meyn (1995), the following equation for pure water-methane interfacial tension was fit to the data in Figure 11D:

$$\frac{\sigma^{0.25}}{\Delta\rho} T_r^{0.3125} = 3.2562 * \Delta\rho^{-0.82} \quad (8)$$

Therefore, given the density contrast between the wetting and non-wetting phase of a reservoir, and the temperature of the reservoir, the interfacial tension of methane-brine can be calculated at depth using the temperature and pressure trends.

Brine-CO_2 interfacial tensions cannot be estimated using $\Delta\rho$ and T_r alone. The effects of CO_2 solubility and, to a lesser extent, salinity must be taken into account (Chalbaud et al., 2006; Chiquet et al., 2007b) (Figure 11E). IFT experiments consider varying reservoir temperatures, pressures, and salinities, and therefore varying CO_2 densities and CO_2-saturated brine densities. The empirical equation from Chalbaud et al. (2006) to predict CO_2-brine IFT is:

$$\sigma_{CO2} = \sigma_{plateau} + (1.255X_{NaCl}) + [(\frac{P}{M}) * \Delta\rho]^{4.718} * T_r^{1.0243} \quad , \quad (9)$$

where $\sigma_{plateau}$ is 26 mN/m; X_{NaCl} is the NaCl molality equivalent of the target brine reservoir; P, the parachor number, is a scaling constant of 82; M is molar mass equal to 44.01 g/mol; $\Delta\rho$ is the density difference between the CO_2-saturated brine and the CO_2; and T_r is the reduced temperature. Salinity is taken into consideration within Equation (9) for CO_2, but not in Equation (8) for methane. Adding the effect of salinity for methane is discussed in a subsequent section.

Both methane and CO_2 density increase with depth (increasing temperature & pressure) and therefore the density difference between brine (nearly incompressible) and the buoyant fluid decreases. As the density difference decreases, the interfacial tension should decrease (Equation 6). Therefore, both methane-brine and CO_2-brine interfacial tensions decrease with depth as expected (Figure 11).

Using the average temperature and pressure curves (Figure 11), it should be noted that the error caused by CO_2 solubility on the $\Delta\rho$ calculation will never be more than 5% (Chiquet et al., 2007b). Still, it is something to take into consideration for settings with extremely saline brines.

Salinity

The CO_2 IFT experiments of Chalbaud et al. (2006) showed that with increases in brine molality (XNaCl), the CO_2-brine IFT also increased. Since the Firoozabadi and Ramey (1988) correlation uses experiments that were done on CH4-pure water IFT, an inquiry into the error owing to salinity on CH4-brine IFT calculations is warranted. The free cations at the water interface with CH_4 will increase the ratio of charge to cation surface area that the water 'feels' and thus increases the surface tension (Argaud, 1993).

Argaud (1993) found the relationship between cation molality and IFT increase to be linear for a range of molalities. The simple linear function for X_{NaCl} is:

$$\delta\sigma = 1.63X_{NaCl} \ , \qquad (10)$$

where the increase in IFT ($\delta\sigma$) is 1.63 mN/m per molal NaCl (X_{NaCl}). Maximum NaCl molality from the USGS Produced Waters Database (Breit, 2006) for Gulf Coast Miocene brines in Texas is 1.63m (Appendix B). Samples from the database for this region have a maximum depth of about 8,200ft. Using 1.63m as the maximum X_{NaCl} (Equations 8, 9 & 10), it can be seen that variations in salinity have a minor effect of up to a few units of IFT (Figure 11F).

Contact Angle

Contact angle between brine and the non-wetting fluid can vary with non-wetting fluid type, pressure, salinity, and mineralogy of the seal (Chiquet et al., 2007a; Espinoza and Santamarina, 2010). Experimental contact angle studies between supercritical CO_2 and brine have been compared with theoretical calculations (Meckel, 2010) to determine that a θ of 30° is a fair approximation for most modeling. In this paper, contact angle will remain at 0° (considered optimistic) for both CO_2-brine and CH_4-brine, but it should be noted that changing θ from 0° to 30° for CO_2-brine will yield a smaller $\cos(\theta)$, from 1 to 0.866, respectively (i.e. a 13.4% reduction in sealing capacity).

Mercury-Air Normalization

If the buoyancy pressure of a methane column acting on a fault is considered to reflect the capillary entry pressure of the fault, then the capillary entry pressure must be converted to mercury-air capillary entry pressure before it can be compared with similar or different fluids at varying depths (i.e. different interfacial tensions).

Fluids have different capillary entry pressures for the same pore throat diameter based on their varying interfacial tensions (Equation 2). Buoyancy pressures from different Miocene methane-brine columns must be normalized to a common standard, such as mercury-air, in order to compare the sealing capacity of different fault-rock and top seal over varying depths:

$$P_{chw} = \frac{\sigma_{hw} * \cos(\theta_{hw})}{\sigma_{ma} * \cos(\theta_{ma})} P_{cma} \quad (11)$$

where P_{chw} is the hydrocarbon-water capillary entry pressure, P_{cma} is mercury-air capillary entry pressure, σ_{hw} is the hydrocarbon-water interfacial tension, σ_{ma} is the mercury-air interfacial tension (480 dyne/cm), θ_{hw} is the hydrocarbon-water contact angle (usually considered to be 0° in water-wet rocks), and θ_{ma} is the mercury-air contact angle (40°) (Schowalter, 1979).

CALIBRATING THE QUANTITATIVE FAULT SEAL FAILURE ENVELOPE

Having established the fluid properties and theory behind the capillary entry of varying fault gouge, the estimations of clay content in fault gouge calculated by the shale gauge ratio (SGR) must first be calibrated to field data in order to ultimately calculate and compare membrane fault seal and fill-to-spill CO_2 capacity estimates. Quantitative fault seal analysis using various algorithms, especially the SGR, have been most readily applied in the Gulf of Mexico (Alexander and Handschy, 1998; Davies et al., 2003; Kim et al., 2003), the North Sea (Freeman et al., 1998; Ottesen Ellevset et al., 1998; Harris et al., 2002; Childs et al., 2002; Færseth et al., 2007; Bretan et al., 2011), the Otway Basin (Lyon et al., 2005), the North West shelf of Australia (Jones and Hillis, 2003), and the Niger Delta (Bouvier et al., 1989; Jev et al., 1993).

The Global Fault Seal Calibration

Global comparisons of fault seal have been developed over the last two decades (Figure 13) (Yielding, 2002; Bretan et al., 2003; Yielding et al., 2010). The global fault seal data points were determined from over 10 fault bound reservoirs (Graham Yielding, Badleys Geoscience, personal communication, 2012) using field data (V_{sh} logs, structural models, fluid contacts, and pressure gradients). For a given value of SGR (calculated) along a fault there is an associated buoyancy pressure (extrapolated from measured pressure data) acting on the same point of the fault within the hydrocarbon reservoir interval. This provides many data points for a single fault bound trap, but only one true weak point, or the highest ratio of buoyancy pressure and SGR. The dashed lines in Figure 13 represent the fault seal failure envelopes bounding the weak point values. Most importantly, the fault seal failure envelopes represent a quantitative calibration of the

maximum amount of buoyancy pressure for a particular fluid that a given value of SGR can seal (Bretan et al., 2003). The fault seal failure envelope equations (linear, similar to the deterministic data presented in Figure 6) allow for the prediction of maximum buoyancy pressure, and therefore maximum column height, that an untested fault block could sustain. The different colored dashed lines represent a given reservoir depth interval as defined by the author (blue: <3.0km, red: 3.0-3.5km, and green >3.5km). Equations for the less than 3km and greater than 3.5km depth lines are given, respectively,

$$(<3.0\text{km})\ BP = 0.175 * SGR - 3.5 \quad (12)$$
$$(>3.5\text{km})\ BP = 0.150 * SGR + 1.9\ , \quad (13)$$

where the maximum *BP* (buoyancy pressure, bars) that a fault segment with a given *SGR* is able to withstand is a linear fit and increases with increasing SGR (Yielding et al., 2010). These equations are then converted to PSI (1bar = 14.503psi):

$$(<3.0\text{km})\ BP = 2.538 * SGR\ -\ 50.76 \quad (14)$$
$$(>3.5\text{km})\ BP = 2.175 * SGR\ +\ 27.55\ , \quad (15)$$

and normalized to mercury-air capillary entry pressure so that fluids from different depths can be compared. This is not explicitly shown by Yielding et al. (2010) since there is no mention as to what fluid types (oil, gas, or both) were used for their global calibration. However, it is stated that a 10x multiplier can be applied to normalize the published equations to mercury-air (Yielding et al., 2010) based on Equation (11), and yields the following equations:

$$(<3.0\text{km})\ BP_{ma} = 25.38 * SGR\ -\ 507.6 \quad (16)$$
$$(>3.5\text{km})\ BP_{ma} = 21.75 * SGR\ +\ 275.5\ , \quad (17)$$

where BP_{ma} is the mercury-air equivalent buoyancy pressure, or maximum sealing capillary entry pressure according to Equation (4). Equations (16) and (17) from the global dataset will be compared to the calibration from the local Miocene data. Depth relationships to membrane fault seal capacity, as presented by the Yielding et al. (2010) fault seal failure envelopes, are variable, depending on fluid properties (Firoozabadi and Ramey, 1988; Chalbaud et al., 2006), across fault pressure differences (Underschultz, 2007), and depth (effective stresses) at time of faulting (Sperrevik et al., 2002; Takahashi, 2003). Owing to this variability it is suggested that the SGR always be calibrated to the basin, and more specifically, the target reservoirs of interest.

Fault Seal Calibration Workflow for Historic Natural Gas Fields

SGR is normally calculated using field scale, 3D-seismic-derived structural models of fault & stratigraphic data in conjunction with pressure data from wells within different fault blocks. This application is time consuming and normally utilized over many years of exploration and development with contributions from many disciplines. In an effort to reduce the duration of these analyses and still effectively calibrate a fault seal failure envelope for a desired basin, an older methodology (with established concepts) is applied to historic field publications for the results shown below. SGR can still be calculated as long as structure maps exist with fluid contacts (for calculating column height and fault throw) and original reservoir pressure & temperature data exist (for calculating methane density). An atlas of field maps and reservoir properties is available for fields in the Texas State Waters (Seni et al., 1997). One-dimensional triangle diagrams can be used to calculate SGR as it varies along a fault with known offsets (Knipe, 1997; Childs et al., 2002) by using a base stratigraphic column from an unfaulted gamma ray (GR) log converted to volume shale (V_{sh}). Converting GR to V_{sh} gives a reliable estimate of the amount of clay within the stratigraphy:

$$V_{sh} = \frac{GR - GR_{min}}{GR_{max} - GR_{min}}, \tag{18}$$

where GR is the measured GR, GR_{min} is the average GR response of clean sandstones, and GR_{max} is the average GR response of shale (Bhuyan and Passey, 1994). It is recommended that the 10th percentile GR value be used for GR_{min} and the 90th percentile GR value be used for GR_{max} for stratigraphic intervals spanning thousands of feet. The Brazos Block 440 Field B-sand (Figure 14) (Lane and Pace, 1998) is one of four fields evaluated for SGR calibration. Two of the gas columns (northern and southern fault block) within the field are evaluated.

Methane density is calculated from Peng and Robinson (1976) using the average reservoir temperature and pressure. Methane density and column height are then applied to Equation (2) to calculate the buoyancy pressure exerted by the methane column at the crest of the structure, a better assumption weak-leak point test than across-fault differential pressure (Fisher et al., 2001). The buoyancy pressure is then converted to mercury-air equivalent pressure (Equation 11) which plots on the Y-axis of the fault-seal failure plot (Figure 13).

V_{sh} is then calculated for the unfaulted, representative stratigraphic section using a GR log. V_{sh} is evaluated using a standard triangle diagram (Figure 15 for the Brazos Block 440 B-sand) to calculate SGR (Equation 1) at the crest of the structure (maximum column height). Four other methane columns from fields within the Texas State Waters were evaluated (Appendix C) using this workflow (Figure 16A).

Calibration Results

Fault-bounded methane columns at reservoir depths less than 3.0km depth (blue triangles, Figure 16A, left) correlate to the global fault-seal failure envelope of Yielding et al. (2010). This correlation shows that for the Miocene section in the Texas State Waters, the less than 3.0km fault seal failure envelope (Equation 16) can be used to estimate membrane fault seal capacity. The single fault bounded methane column from a depth greater than 3.0km (green triangle, Figure 16A, left) corresponds to a reservoir depth between 3.0-3.5km, and incidentally it falls in the middle of the $\leq$3.0km line and >3.5km line of Yielding et al. (2010), showing an increase in sealing capacity for the same SGR with increasing depth. Fault-bounded methane column heights for 11 reservoirs $\leq$3.0km and 10 reservoirs >3.0km (Figure 16A, right) either lack detailed across-fault mapping or a GR log for calculation of SGR. All column height data are listed in Appendix D. A general increase in column height gives justification to the increase of sealing capacity of faults with depth.

Top seal capacity is necessary to incorporate into robust capacity estimation models (Divko et al., 2010), however, fault seal is often ignored while preference is given to top seal investigations. Top seal values (10% MICP) from 6 LM1 mudstone and siltstone mercury-injection capillary pressure (MICP) tested lab samples (10,578-10,604' depth, or 3.225-3.233 km, well OCS-G-4708#1) are shown on the rightmost vertical axis of Figure 16A (Jiemin Lu, Bureau of Economic Geology, personal communication, 2011). The lowest two top seal values are from siltstone samples (1103 psi and 1200 psi) and are still more effective seals than most of the $\leq$3.0km fault seals. This shows that natural accumulations of methane in fault bounded traps are critically limited by the sealing capacity of faults, not top seal capacity.

However, top seal capacity can be a limiting factor, no matter how large the fault sealing capacity is (Figure 16B). Indeed, one of the methane columns appears to be limited by top seal (Middle Bank Reef 6000' reservoir, SGR=64, BP_{ma}=510 psi, Appendix C). Five of the six methane columns analyzed correlate with published fault seal failure envelopes and are interpreted to be fault seal limited (Figure 16C).

Shale smears can have a higher sealing capacity than the host-rock shale it was derived from owing to shearing (Takahashi, 2003; Eichhubl et al., 2005). However, empirical subsurface field observations (Figure 16A) show that the column heights sealed are lower than the stratigraphically equivalent top seal. Since shale smears increase the sealing capacity of fault rock relative to their host rock (Eichhubl et al., 2005), the faults would likely have an average sealing potential equivalent to the average top seal values if they were smears. Since they are lower than the equivalent top seals, and fall in the range of deterministic PFFR

seal capacity (Figure 6), these calibrated data suggest that PFFRs, not shale smears, are the dominant sealing fault rock type.

FAULT SEAL VARIATION WITH DEPTH

Global depth relationships for fault seal capacity have shown a general increase with depth (Sperrevik et al., 2002; Yielding et al., 2010), but the preliminary sorting of Gulf of Mexico Miocene data (Figure 16) show a disagreement with using discrete depth cutoffs (e.g. >3.0 km values). The 27 aforementioned fault-bound methane column heights and buoyancy pressures were sorted based on the average pool depth of the reservoir (Figure 17). Methane IFT for each specific reservoir temperature, pressure, and methane density was calculated (Equation 8) and then each buoyancy pressure was converted to mercury-air equivalent pressure (Equation 11 with a contact angle of 0°) (Figure 17 and Appendix D). These data (depth versus column height) show a trend of increasing fault-seal capacity with depth.

Column height data must be considered in the context of the percent overpressure (Figure 17) of the reservoir in question due to potential across-fault pressure sealing capacity support (Brown, 2003):

$$\%\, Overpressure = \left(\frac{IP - P_{hydro.\ equiv}}{S_{v\ equiv} - P_{hydro.\ equiv}}\right) x\ 100\ , \qquad (19)$$

where IP (psi) is the initial reported reservoir pressure, $P_{hydro.\ equiv}$ (psi) is the hydrostatic equivalent pressure of the average reservoir depth (0.445 psi/ft), and $S_{v\ equiv}$ is the estimated overburden pressure at the average reservoir depth (1.0 psi/ft). Without detailed pressure data from the field it is impossible to tell if the increasing column heights with depth are the result of across-fault pressure support, or hydrodynamic seal (Schowalter, 1979; Watts, 1987; Losh et al., 1999; Davies et al., 2003; Brown, 2003; Underschultz, 2007). The increasing fault seal capacity can be attributed more accurately to increased mechanical compaction and cementation (Lander and Walderhaug, 1999) with depth, as well as potentially increased depth (or more accurately, increased effective stress) at time of faulting (Sperrevik et al., 2002; Takahashi, 2003).

While the depth trend for fault seal may potentially be a problem at great depths, economic sequestration of CO_2 will likely target shallow reservoirs (i.e. <3km) and therefore the fault seal calibration (Equation 16) can be used to model fault bound traps for CO_2 sequestration within the Lower Miocene of the Texas State Waters. Further investigations of depth relationships on fault seal capacity are not delineated.

MODELING MEMBRANE FAULT SEAL FOR A POTENTIAL SEQUESTRATION PROJECT

Potential CO_2 sequestration prospects (Figure 3A) highlight the need for membrane fault seal modeling in order to assess site specific CO_2 capacity. The piercement salt diapir adjacent to San Luis Pass, Galveston (Figure 1) has been chosen for modeling due to its proximity to anthropogenic CO_2 sources. The southeast fault block of the LM2 horizon (Figure 18) has been chosen as the potential sequestration target due to its potential ability to structurally contain migrating fluids, lack of near-surface penetrating faults, a thick (>500ft) Amph. B. top seal, and an average reservoir depth (7,500ft) for maintaining dense, supercritical CO_2. The southeast fault block is bound on the west by the A Fault and to the north by the B Fault (Figure 18). The average dip of 16° on the structure allows for some certainty that the fluids would migrate toward the NW to the top of the structure. The LM2 horizon (Figure 19, also used for V_{sh} calculations) is interpreted to pinchout at 6400' based on seismic lap relationships onto the salt.

Buoyancy pressure profiles (Figure 20) are used to perform static trap capacity estimates for buoyant fluids (Bretan and Yielding, 2005). In buoyancy pressure profiles, the fault, separating a charging trap and an uncharged brine (Figure 20A), is progressively filled (A→C) to the limits of the estimated fault gouge capillary entry pressure. Fault rock properties (SGR) vary with depth along a single fault (Figure 20B). These fault derived SGR values, adjacent to the reservoir contact with the fault, are converted to the appropriate capillary entry pressure (Figure 20C) for the charging fluid (Equations 11 & 16).

The progressively modeled charges (A→C) create fluid columns with increasing buoyancy pressure (Equation 2) until the buoyancy pressure (column C, Figure 20C) eventually equals the capillary entry pressure of the fault rock, representing the exact weak point on the fault.

The workflow applied to the depth-converted 3D seismic volume to map the fault properties required to calculate the SGR requires mapping of the faults and stratigraphic horizons, calculation of Vsh distribution along the fault, and calculating the throw distribution along the fault from the mapped horizons (Figure 21). The SGR values from the LM2 reservoir interval only (adjacent to the footwalls of both the A and B Faults) are calculated and implemented into the following workflow to convert SGR to CO_2-capillary entry pressures.

Static CO2-Brine Membrane Fault Seal Workflow Summary

The SGR values must first be converted to mercury-air equivalent capillary entry pressures (Equation 16). Average temperature for the reservoir crest is calculated (Equation 5), reservoir pressure is assumed to be hydrostatic, and the average CO_2 density is calculated using the Peng-Robinson equation of state for the estimated temperature and pressure. CO_2 IFT is then calculated (Equation 9). The mercury-

air converted SGR data points are then converted to CO_2 equivalent capillary entry pressures using the calculated CO_2-brine IFT, a contact angle of 0°, and a maximum Miocene salinity value of 1.63m (Equation 11).

Only the SGR values from the footwalls of the A Fault (blue line) and B Fault (red line), LM2 horizon, are considered (Figure 22A). Simulated buoyancy pressures from increasing CO_2 column heights are overlain on the mercury-air equivalent capillary entry pressures to create a buoyancy pressure profile (Figure 22B). Buoyancy pressures are calculated (Equation 2) using the calculated average CO_2 density of 0.62 g/cm^3 at the reservoir crest depth (6,400') and a brine density of 1.02 g/cm^3. Assumed geologic time scales allow for equilibration (Equation 4) of the injected fluid (i.e. no mechanical leakage).

Fault Seal Capacity vs. Fill-to-Spill Capacity

The modeled 450 foot CO_2 column height (Figure 22B) reaches the limit of capillary membrane seal of the B Fault. Therefore, the B Fault is the weak-leak point, and the maximum potential CO_2 column height sealed over geologic time is estimated to be 450 ft. The area that this column height would occupy (from top structure at 6,400' to 6,850', green dashed line, Figure 18) is 175 acres. The area associated with a model that fills this trap from fill-to-spill (red dashed line, Figure 18) is 2,760 acres. The fill-to-spill model would overestimate the CO_2 storage capacity by 15.77 times. This is, however, a more extreme example with relatively steep dips where the area increases exponentially down structure. Traps that have shallower dips and become more confined down structure would have less pronounced differences between membrane seal capacity to structural spill capacity and could even yield the same result, or zero difference.

FAULT SLIP STABILITY

While membrane fault seal capacity is important for long term containment modeling for CO_2 sequestration, it is also important to model the prospective site for pressure fluctuations to avoid fault reactivation or hydraulic fracturing of the seal. Case studies show that increases in pore pressure from injection of salt water brine adjacent to a fault can reactivate the fault and create small magnitude (M ~2.5 - 3.0) earthquakes (Raleigh et al., 1976; Frohlich et al., 2011). While most faults in the unconsolidated sediments of the Gulf of Mexico have been shown to move by aseismic creep (Frohlich, 1982), regional studies have shown that fault reactivation can lead to hydrocarbon leakage along the fault (Finkbeiner et al., 2001) at potentially high rates (Losh et al., 1999).

The principal stress directions for normal faulting are S_v (σ_1) > S_H (σ_2) > S_h (σ_3), where S_v is the vertical stress, S_H is the maximum principal horizontal stress, and S_h is the minimum principal horizontal stress. These principal stresses create shear stress (τ) parallel to the fault plane and normal stress (σ_n) perpendicular to the fault plane (Figure 23A). The differential stress ($\sigma 1$-$\sigma 3$) defines the diameter of the Mohr circle and the shear stress and normal stress define the Coulomb failure envelope:

$$\tau = C + \mu(\sigma_n - P_{f)} \ , \qquad (20)$$

where C is cohesion (psi), or the inherent shear strength of the fault gouge, μ is the coefficient of static friction, and P_f is the pore fluid pressure (Jaeger and Cook, 1969; Byerlee, 1978). Cohesion of fault gouge is often considered to be negligible.

The coefficient of static friction of fault gouges largely depends on the composite mineralogy of the gouges. Values of 0.6 are reasonable estimates for μ (Shimamoto and Logan, 1981). Increased pore fluid pressure can cause the Mohr circle to move towards, and potentially intersect, the Coulomb failure envelope (Figure 23B). When P_f is increased enough to cause the shear stress on a fault plane to intersect the failure envelope, reactivation of a preexisting fault occurs.

In the absence of 4-arm dipmeter data used for borehole breakout analysis (Moos and Zoback, 1990), regional fault strike statistics (Figure 24) are being substituted to determine the orientation of the principal horizontal stresses. Average fault strike from 297 faults, each broken into 500-foot spacing in map view in order to negate bias towards smaller fault traces, yielding 8003 total measurements. These fault strikes have a mean azimuth of 54.1°. This azimuth roughly parallels the coastline and agrees with onshore determinations of the maximum principal horizontal stress azimuth (Zoback and Zoback, 1980).

Using C=0, μ=0.6, σ_1=1.0 psi/ft, σ_3 = 0.85 psi/ft, P_f = 0.445 psi/ft, and an S_H (σ_2) azimuth of 54.1°, the fault slip stability for the A Fault and B Fault have been calculated (Figure 25), respectively, for a depth of -6,600ft (just below the top LM2 reservoir). Since S_H could not be modeled, the two extremes for values of S_H in a normal stress regime ($S_v > S_H > S_h$) are modeled: $S_H = S_h$ and $S_H = S_v$. Regardless of which portion of the fault is most susceptible to slip as a function of increased pore pressures from injection of CO_2, it should be noted that these pore pressure elevations are at minimum ~2500psi, which is two order of magnitude larger than the buoyancy pressure required to overcome the capillary entry pressure of the same faults (Figure 22B). The maximum sustainable pore pressures estimated from fault slip stability analysis should be used as guidelines for best practices in monitoring pressure increases due to CO_2 sequestration.

Modeling of the fault slip stability can have significant error due to unpredictable variations in μ, C, or local stress states (Dewhurst and Jones, 2002). However, even if the critical pore pressure is exceeded, generating aseismic earthquakes in unconsolidated sediment may not equate to fluid leakage, and if leakage does occur, may only produce flow rates within the upper range of fault zone permeabilities (Wilkins and Naruk, 2007). If uncemented PFFRs or clay smears are the sealing mechanisms, reactivation and displacement may further shear the fault gouge instead of creating a conduit for flow. For example, surface penetrating faults adjacent to an exploration target are often considered to be a detrimental factor that equates to a dry hole. However, fields within the deepwater Gulf of Mexico have surface penetrating faults with active scarps and the same faults trap considerable hydrocarbon columns at depth (Nicholson et al., 2012).

VARIABILITIES IN THE SGR CALCULATION - SOURCES OF ERROR AND CAUSE FOR CONCERN

V_{cl} Calibration

One difficulty with empirical V_{sh} calculations is the consistency of methodology in determining the volume of shale (Bretan et al., 2003). V_{sh} determined from log suites attempt to measure the relative percentages of clay minerals in the rock. However, as can be seen from the effects of cataclasis (in the absence of clay minerals), fault seal is dependent upon maximum interconnected pore throat diameter (Equation 3). In siliciclastics this is primarily dependent on the direct relationship between mineralogy and grain size (pore throat size).

Lateral Stratigraphic Heterogeneity

Lateral stratigraphic heterogeneities can create lateral variability in the SGR calculation for a fault. However, for faults with throws that are orders of magnitude higher than the variable bed thickness in question, small scale

stratigraphic heterogeneities become negligible. This effect can be a concern in highly channelized depositional settings, such as in channelized fluvial or turbidite deposits.

Structural Interpretation from Seismic

Faults are often interpreted on seismic data as single continuous planes, when in reality they can exist as complex anastomosing slip surfaces. Fault tip bifurcations can cause splays and multiple closely spaced fault steps (Wehr et al., 2000; Koledoye et al., 2003). Fault steps can completely alter SGR calculations (Færseth et al., 2007). However, large, seismic scale faults (>100's ft throw) can reduce this uncertainty. Fault steps can also cause blocks of host rock sandstone to be incorporated into the fault core (Loveless et al., 2011). Sandstone boudinaged in the fault gouge cannot be predicted by the SGR algorithm and can provide a potential leakage pathway (Wehr et al., 2000; Færseth et al., 2007).

Seismic Resolution and the Fault Damage Zone

The SGR methodology applies to the fault core itself, or the area between the main slip surfaces. The fault damage zone, or the area flanking the fault core which contains numerous small faults, is often the leakage pathway in carbonate fault rocks, whereas the fault core itself is sealing (Agosta et al., 2007). Siliciclastic faults have been suggested to show similar fault core and fault damage zone geometries, however cataclasites occur in the damage zone instead of fractures (Loveless et al., 2011). Fault statistics can be used to constrain the minimum resolvable fault dimensions and their relationship to other studies of normal faults. Maximum fault trace versus maximum fault displacement data for 297 faults from the LM2 horizon show good agreement with the fault-growth models (F'=3 GPa shear modulus) of Walsh and Watterson (1988) (Figure 26). The important data missing owing to limits in seismic resolution are faults with traces less than 100-200 meters and below (small fault throws). Could these small faults act as the main conduits for leakage? Even if small, seismically irresolvable faults are a potentially dominant leakage mechanism, they are highly unlikely to be both continuous and surface penetrating. Most likely these small damage zone faults will act as inter-formational leakage mechanisms from the injection reservoir to the next structurally higher reservoir. Acquiring higher resolution seismic surveys for shallower targets can help mitigate this concern.

Small Throw on Faults

The SGR has been shown to properly estimate the amount of clay in the fault gouge on large faults (100's m) in the subsurface and even in outcrop (Foxford et al., 1998). Conversely, the SGR for faults with small throw (< 10m), thinly bedded host rock shales (~1-2m), and a high degree of smear have been shown to underestimate the amount of clay in the fault gouge as well as underestimate the sealing potential (Eichhubl et al., 2005). SGR has also been shown to

overestimate the sealing potential of faults with small throw within sandy reservoir intervals thicker than the throw window (Nicholson et al. 2012).

DISCUSSION

While static membrane seal capacity of faulted traps has been shown (e.g. San Luis Pass salt dome) to result in smaller column heights (smaller storage areas) than fill-to-spill modeling of faulted traps on a site specific scale, faulting on a regional scale may actually increase storage potential. For example, if no faults were to exist around the San Luis Pass salt dome, the entire column height required to fill the structure would be limited by the top seal capillary entry (assuming pore pressure is monitored and does not exceed S_h or S_c). However, by introducing faulted compartments the structure of the newly formed traps may have (a) shallower relief, (b) the ability to trap many more, smaller accumulations with a net increase in capacity, and (c) the ability to increase residual trapping by increasing the number of catchments.

Faulted compartments can also increase the capacity volume owing to the rate of charge of the trap. Thus far, time has been referenced only as 'geologic time,' a very ambiguous number, but one that refers to the time scales for which the system can equilibrate to the membrane seal (capillary entry) capacity. This equilibration is the basis for the exploration-style fault seal methodology used for calibration from natural hydrocarbon accumulation. However, if the fault-bound trap is charged with CO_2 to the point where capillary entry pressure is overcome and hydraulic leakage (Watts, 1987) begins to occur, yet reservoir pressure is managed so as not to overcome the fracture or fault-reactivation gradient, time becomes a critical factor in containment. What if the time scale for the equilibration of capillary sealing is 1 million years, but the time interval of interest for CO_2 containment is only 10,000 years? In this scenario the relative permeability (to CO_2) of the fault and the fault core thickness become the necessary properties to map and simulate. If CO_2 takes 10,000 years to reach the sea floor by upward fault-parallel migration from the injected fault block that has now been slowly filled-to-spill, then the area associated with the fill-to-spill structure is a more accurate assessment of present-day usable capacity. The path forward for modeling fault-bound trap capacity is to use the presented workflow to model fault rock petrophysical properties to be used in a dynamic injection-leak model. Using an SGR fault model converted to CO_2-brine capillary entry pressure, the fault rock mercury-air capillary entry pressure to bulk permeability workflow of Sperrevik et al. (2002), and the relative permeability curves for fault rocks and CO_2 of Tueckmantel et al. (2012), simulations of fault-parallel flow from the injection reservoir to the sea floor can model the time scales for CO_2 leakage from the reservoir to out-of-zone compartments or the sea floor. This will provide a worst-case minimum estimate of storage time.

The static SGR calculated column height workflow is put forth as an empirical methodology to estimate risk in fault bound traps and predict realistic, pre-injection CO_2 capacities. The proposed dynamic fault slip stability and dynamic fault migration workflows are meant to act as guidelines for more detailed CO_2 capacity and containment modeling. However, it should be noted that no field studies or subsurface projects exist on active, purely CO_2-brine injection sites along the Gulf Coast to test the presented fault seal analyses. It is suggested that moving forward, small, field scale tests be conducted in the subsurface on faulted compartments (using both injection and across-fault monitoring wells) to test the principles of pre-injection fault seal prediction prior to the commencement of commercial scale CO_2 injection into fault bound brine reservoirs.

CONCLUSIONS

Regional play concepts have been established for CO_2 sequestration in the Lower Miocene stratigraphy of the Texas State Waters. All dominant play types involve fault-bounded traps. Regional natural gas trends conform with faulted structures and show that treating faults as no-flow boundaries (fill-to-spill modeling) is not accurate and fault rock properties must be used in modeling long term CO_2 sequestration capacity.

A workflow has been established to calibrate membrane fault seal capacity. Regional temperature, pressure, and salinity data are compiled and used to calculate fluid properties such as fluid density and interfacial tension variability with depth. These fluid properties allow for the calibration of Miocene age fault bound methane columns to calculated fault rock properties (SGR). Fault seal analysis for the Miocene section along the Texas State Waters agrees with published global fault seal databases, but may not be applicable for reservoirs deeper than 3km. Stratigraphically equivalent top seal capacity can be expected to be an order of magnitude higher than fault seal capacity, showing that faults are the limiting factor for capacity estimation for the reservoir studied.

The methane fault seal calibration can be converted to CO_2 equivalent capillary entry pressure for site specific capacity modeling. Modeled results for membrane fault seal capacity at the SE block of the San Luis Pass salt dome, LM2 reservoir, show a large decrease in long term capacity compared with fill-to-spill (structural closure) modeling.

Regional fault mapping and pressure data provide context for the regional state of stress orientation and magnitude, respectively. Fault slip stability modeling shows that pressure increases two orders of magnitude greater than the buoyancy pressure retained over geologic time scales are required to potentially cause fault reactivation and leakage. There is no certainty that fault reactivation will cause

leakage, but these pressure increases provide a good estimate for the maximum allowable increase in reservoir pressure during short-term injection time scales.

Membrane fault seal and fault slip stability workflows established for the Lower Miocene in the Texas State Waters can be used to quantify column heights and storage capacities for both site specific and regional capacity estimations.

References

Agosta, F., M. Prasad, and A. Aydin, 2007, Physical properties of carbonate fault rocks, fucino basin (Central Italy): implications for fault seal in platform carbonates: Geofluids, v. 7, p. 19-32.

Alexander, L. L., and J. W. Handschy, 1998, Fluid flow in a faulted reservoir system: Fault trap analysis for the Block 330 field in Eugene Island, South Addition, offshore Louisiana: Aapg Bulletin-American Association of Petroleum Geologists, v. 82, p. 387-411.

Allan, U. S., 1989, Model for hydrocarbon migration and entrapment within faulted structures: AAPG Bulletin, v. 73, p. 803-811.

Ambrose, W. A., C. Breton, M. H. Holtz, V. Nunez-Lopez, S. D. Hovorka, and I. J. Duncan, 2009, CO2 source-sink matching in the lower 48 United States, with examples from the Texas Gulf Coast and Permian Basin: Environmental Geology, v. 57, p. 1537-1551.

Antonellini, M., and A. Aydin, 1994, Effect of faulting on fluid-flow in porous sandstones - petrophysical properties: AAPG Bulletin, v. 78, p. 355-377.

Argaud, M. J., 1993, Predicting the interfacial-tension of brine/gas (or condensates) systems: Advances in Core Evaluation Iii - Reservoir Management: Reviewed Proceedings of the Society of Core Analysts Third European Core Analysis Symposium, v. 3, 147-174 p.

Atkins, P. W., and L. L. Jones, 2005, Chemical Principles, The Quest for Insight: New York, W.H. Freeman and Company.

Barnes, C., and M. Koretsky, 2003, ThermoSolver (Version 1.0), http://cbee.oregonstate.edu/education/Thermosolver/, John Wiley & Sons, Inc.

Berg, R. R., and A. H. Avery, 1995, Sealing properties of tertiary growth faults, Texas Gulf-Coast: AAPG Bulletin, v. 79, p. 375-393.

Bhuyan, K., and Q. R. Passey, 1994, Clay estimation from GR and neutron-density porosity logs: SPWLA 35th Annual Logging Symposium.

Bouvier, J. D., C. H. Kaarssijpesteijn, D. F. Kluesner, C. C. Onyejekwe, and R. C. Vanderpal, 1989, 3-Dimensional seismic interpration and fault sealing investigations, Nun River Field, Nigeria: AAPG Bulletin, v. 73, p. 1397-1414.

Bradshaw, B. E., and J. S. Watkins, 1994, Growth-fault evolution in offshore Texas: Gulf Coast Association of Geological Societies Transactions, v. 44, p. 103-110.

Bradshaw, J., S. Bachu, D. Bonijoly, R. Burruss, S. Holloway, N. P. Christensen, and O. M. Mathiassen, 2007, CO2 storage capacity estimation: Issues and development of standards: International Journal of Greenhouse Gas Control, v. 1, p. 62-68.

Breit, G., 2006, Produced Waters Database, USGS.

Bretan, P., and G. Yielding, 2005, Using buoyancy pressure profiles to assess uncertainy in fault seal calibration: AAPG Hedberg Series, v. 2, p. 151-162.

Bretan, P., G. Yielding, and H. Jones, 2003, Using calibrated shale gouge ratio to estimate hydrocarbon column heights: AAPG Bulletin, v. 87, p. 397-413.

Bretan, P., G. Yielding, O. M. Mathiassen, and T. Thorsnes, 2011, Fault-seal analysis for CO2 storage: an example from the Troll area, Norwegian Continental Shelf: Petroleum Geoscience, v. 17, p. 181-192.

Brown, A., 2003, Capillary effects on fault-fill sealing: AAPG Bulletin, v. 87, p. 381-395.

Byerlee, J., 1978, Friction of rocks: Pure and Applied Geophysics, v. 116, p. 615-626.

Chalbaud, C., M. Robin, and P. Egermann, 2006, Interfacial tension data and correlations of brine-CO2 systems under reservoir conditions: SPE Annual Technical Conference and Exhibition.

Childs, C., Ø. Sylta, S. Moriya, J. J. Walsh, and T. Manzocchi, 2002, A method for including the capillary properties of faults in hydrocarbon migration models: Norwegian Petroleum Society Special Publications, v. 11, p. 127-139.

Chiquet, P., D. Broseta, and S. Thibeau, 2007a, Wettability alteration of caprock minerals by carbon dioxide: Geofluids, v. 7, p. 112-122.

Chiquet, P., J.-L. Daridon, D. Broseta, and S. Thibeau, 2007b, CO2/water interfacial tensions under pressure and temperature conditions of CO2 geological storage: Energy Conversion and Management, v. 48, p. 736-744.

Davies, R. K., L. J. An, P. Jones, A. Mathis, and C. Cornette, 2003, Fault-seal analysis South Marsh Island 36 field, Gulf of Mexico: AAPG Bulletin, v. 87, p. 479-491.

Dewhurst, D. N., and R. M. Jones, 2002, Geomechanical, microstructural, and petrophysical evolution in experimentally reactivated cataclasites: Applications to fault seal prediction: AAPG Bulletin, v. 86, p. 1383-1405.

Divko, L. M. G., J. Hamilton, and G. W. O'Brian, 2010, Evaluation of the regional top seal for the purpose of geologic sequestration in the Gippsland Basin, Southeastern Australia, AAPG Annual Convention & Exhibition, New Orleans, LA.

Eichhubl, P., P. S. D'Onfro, A. Aydin, J. Waters, and D. K. McCarty, 2005, Structure, petrophysics, and diagenesis of shale entrained along a normal fault at Black Diamond Mines, California—Implications for fault seal: AAPG Bulletin, v. 89, p. 1113-1137.

Engelder, T., and J. T. Leftwich Jr., 1997, A pore-pressure limit in overpressured South Texas oil and gas fields, *in* R. C. Surdam, ed., Seals, traps, and the petroleum system: AAPG Memoir 67, p. 255-267.

Espinoza, D. N., and J. C. Santamarina, 2010, Water-CO2-mineral systems: Interfacial tension, contact angle, and diffusion-Implications to CO2 geological storage: Water Resources Research, v. 46.

Færseth, R. B., E. Johnsen, and S. Sperrevik, 2007, Methodology for risking fault seal capacity: Implications of fault zone architecture: AAPG Bulletin, v. 91, p. 1231-1246.

Finkbeiner, T., M. Zoback, P. Flemings, and B. Stump, 2001, Stress, pore pressure, and dynamically constrained hydrocarbon columns in the South Eugene Island 330 field, northern Gulf of Mexico: AAPG Bulletin, v. 85, p. 1007-1031.

Firoozabadi, A., and H. J. Ramey, 1988, Surface-tension of water-hydrocarbon systems at reservoir conditions: Journal of Canadian Petroleum Technology, v. 27, p. 41-48.

Fisher, Q. J., S. D. Harris, E. McAllister, R. J. Knipe, and A. J. Bolton, 2001, Hydrocarbon flow across faults by capillary leakage revisited: Marine and Petroleum Geology, v. 18, p. 251-257.

Fisher, Q. J., and R. J. Knipe, 1998, Fault sealing processes in siliciclastic sediments: Geological Society, London, Special Publications, v. 147, p. 117-134.

Foxford, K. A., J. J. Walsh, J. Watterson, I. R. Garden, S. C. Guscott, and S. D. Burley, 1998, Structure and content of the Moab Fault Zone, Utah, USA, and its implications for fault seal prediction, *in* G. Jones, Q. J. Fisher, and R. J. Knipe, eds., Faulting, Fault Sealing and Fluid Flow in Hydrocarbon Reservoir, v. 147, London Geological Society Special Publication, p. 87-103.

Freeman, B., G. Yielding, D. T. Needham, and M. E. Badley, 1998, Fault seal prediction: the gouge ratio method: Geological Society, London, Special Publications, v. 127, p. 19-25.

Frohlich, C., 1982, Seismicity of the central Gulf of Mexico: Geology, v. 10, p. 103-106.

Frohlich, C., C. Hayward, B. Stump, and E. Potter, 2011, The Dallas-Fort Worth earthquake sequence: October 2008 through May 2009: Bulletin of the Seismological Society of America, v. 101, p. 327-340.

Galloway, W. E., 1989, Depositional framework and hydrocarbon resources of the early miocene (Fleming) episode, Northwest Gulf-Coast Basin: Marine Geology, v. 90, p. 19-29.

Galloway, W. E., T. L. Whiteaker, and P. Ganey-Curry, 2011, History of Cenozoic North American drainage basin evolution, sediment yield, and accumulation in the Gulf of Mexico basin: Geosphere, v. 7, p. 938-973.

Gibson, R. G., 1998, Physical character and fluid-flow properties of sandstone-derived fault zones: Geological Society, London, Special Publications, v. 127, p. 83-97.

Handin, J., R. V. Hager Jr., M. Friedman, and J. N. Feather, 1963, Experimental deformation of sedimentary rocks under confining pressure: AAPG Bulletin, v. 47, p. 717 - 755.

Harris, D., G. Yielding, P. Levine, G. Maxwell, P. T. Rose, and P. Nell, 2002, Using Shale Gouge Ratio (SGR) to model faults as transmissibility barriers in reservoirs: an example from the Strathspey Field, North Sea: Petroleum Geoscience, v. 8, p. 167-176.

Hickman, S. H., and M. D. Zoback, 1983, The interpretation of hydraulic fracturing pressure-time data for in situ stress determination, Hydraulic Fracturing Stress Measurements: Washington, D.C., National Academy Press.

Holtz, M. H., V. Lopez Nunez, and C. Breton, 2005, Moving Permian Basin technology to the Gulf Coast: the geologic distribution of CO2 EOR potential in Gulf Coast reservoirs: West Texas Geological Society Publication #05, v. 115, p. 11.

Hough, E. W., M. J. Rzasa, and B. B. Wood, 1951, Interfacial tensions at reservoir pressures and temperatures; apparatus and the water-methane system: AIME Petroleum Transactions, v. 192, p. 57-60.

Jaeger, J. C., and N. C. W. Cook, 1969, Fundamentals of rock mechanics (third edition): London, Chapman & Hall.

Jennings, H. Y., and G. H. Newman, 1971, Effect of temperature and pressure on interfacial tension of water against methane-normal decane mixtures: Society of Petroleum Engineers Journal, v. 11, p. 171-175.

Jev, B. I., C. H. Kaarssijpesteijn, M. Peters, N. L. Watts, and J. T. Wilkie, 1993, Akaso field, Nigeria - use of integrated 3-D seismic, fault slicing, clay smearing, and rft pressure data on fault trapping and dynamic leakage: AAPG Bulletin, v. 77, p. 1389-1404.

Jones, R. M., and R. R. Hillis, 2003, An integrated, quantitative approach to assessing fault-seal risk: AAPG Bulletin, v. 87, p. 507-524.

Kim, J. W., R. R. Berg, J. S. Watkins, and T. T. Tieh, 2003, Trapping capacity of faults in the Eocene Yegua Formation, East Sour Lake field, southeast Texas: AAPG Bulletin, v. 87, p. 415-425.

Knipe, R. J., 1997, Juxtaposition and seal diagrams to help analyze fault seals in hydrocarbon reservoirs: AAPG Bulletin, v. 81, p. 187-195.

Koledoye, B. A., A. Aydin, and E. May, 2003, A new process-based methodology for analysis of shale smear along normal faults in the Niger Delta: AAPG Bulletin, v. 87, p. 445-463.

Lander, R. H., and O. Walderhaug, 1999, Predicting porosity through simulating sandstone compaction and quartz cementation: AAPG Bulletin, v. 83, p. 433-449.

Lane, R. F., and R. C. Pace, 1998, Brazos 440-L Field, Offshore Texas: GCAGS Special Publication, p. 27-36.

Lindsay, N. G., F. C. Murphy, J. J. Walsh, and J. Watterson, 1993, Outcrop studies of shale smear on fault surfaces: International Association of Sedimentologists Special Publication, v. 15, p. 113-123.

Losh, S., E. Eglinton, M. Schoell, and J. Wood, 1999, Vertical and lateral fluid flow related to a large growth fault, South Eugene Island Block 330 field, offshore Louisiana: AAPG Bulletin, v. 83, p. 244-276.

Loveless, S., V. Bense, and J. Turner, 2011, Fault architecture and deformation processes within poorly lithified rift sediments, Central Greece: Journal of Structural Geology, v. 33, p. 1554-1568.

Lyon, P. J., P. Boult, R. R. Hillis, and S. D. Mildren, 2005, Sealing by shale gouge and subsequent seal breach by reactivation: a case study of the Zema Prospect, Otway Basin, *in* P. Boult, and J. Kaldi, eds., Evaluating Fault and Cap Rock Seals: AAPG Hedberg series, The American Association of Petroleum Geologists, p. 179-197.

Macleod, D. B., 1923, On a relation between surface tension and density: Transactions of the Faraday Society, v. 19, p. 38.

McDonnell, A., M. R. Hudec, and M. P. A. Jackson, 2009, Distinguishing salt welds from shale detachments on the inner Texas shelf, western Gulf of Mexico: Basin Research, v. 21, p. 47-59.

McDonnell, A., M. P. A. Jackson, and M. R. Hudec, 2010, Origin of transverse folds in an extensional growth-fault setting: Evidence from an extensive seismic volume in the western Gulf of Mexico: Marine and Petroleum Geology, v. 27, p. 1494-1507.

Meckel, T., 2010, Capillary seals for trapping carbon dioxide (CO2) in underground reservoirs, *in* M. M. Matroto-Valer, ed., Developments and innovation in carbon dioxide (CO2) capture and storage technology, v. 2 Woodhead Publishing Series in Energy, p. 185-202.

Milliken, K. L., and R. M. Reed, 2002, Internal structure of deformation bands as revealed by cathodoluminescence imaging, Hickory Sandstone (Cambrian), Central Texas: Gulf Coast Association of Geological Societies Transactions, v. 52, p. 725-736.

Moos, D., and M. D. Zoback, 1990, Utilization of observations of well bore failure to constrain the orientation and magnitude of crustal stresses - application to continental, deep-sea drilling project, and ocean drilling program boreholes: Journal of Geophysical Research-Solid Earth and Planets, v. 95, p. 9305-9325.

Nagihara, S., 2010, Characterization of the sedimentary thermal regime along the Corsair growth-fault zone, Texas continental shelf, using corrected bottomhole temperatures: AAPG Bulletin, v. 94, p. 923-935.

Nicholson, A. J., S. J. Wilkins, C. Contrino, J. Termina, M. Hertz, and H. Dembicki, 2012, Fault and top seal strength at Nansen Field, East Breaks, Gulf of Mexico: AAPG Annual Convention & Exhibition.

Nicot, J. P., S. D. Hovorka, P. R. Knox, and T. Naing, 2006, Area of review: how large is large enough for carbon storage?: UIC Conference of the Groundwater Protection Council.

Ottesen Ellevset, S., R. J. Knipe, T. Svava Olsen, Q. J. Fisher, and G. Jones, 1998, Fault controlled communication in the Sleipner Vest Field, Norwegian Continental Shelf; detailed, quantitative input for reservoir simulation and well planning: Geological Society, London, Special Publications, v. 147, p. 283-297.

Peng, D., and D. B. Robinson, 1976, New 2-constant equation of state: Industrial & Engineering Chemistry Fundamentals, v. 15, p. 59-64.

Purcell, W. R., 1949, Capillary pressures - their measurements using mercury and the calculation of permeability therefrom: AIME Petroleum Transactions, v. 186, p. 39-48.

Rainwater, E. H., 1964, Regional stratigraphy of the Gulf Coast Miocene: Gulf Coast Association of Geological Societies Transactions, v. 14, p. 81-124.

Raleigh, C. B., J. H. Healy, and J. D. Bredehoeft, 1976, Experiment in earthquake control at Rangely, Colorado: Science, v. 191, p. 1230-1237.

Sachs, W., and V. Meyn, 1995, Pressure and temperature-dependence of the surface-tension in the system natural-gas water - principles of investigation and the first precise experimental-data for pure methane water at 25-degrees-c up to 46.8-MPa: Colloids and Surfaces a-Physicochemical and Engineering Aspects, v. 94, p. 291-301.

Schowalter, T. T., 1979, Mechanics of secondary hydrocarbon migration and entrapment: AAPG Bulletin, v. 63, p. 723-760.

Seni, S. J., T. F. Hentz, W. R. Kaiser, and E. G. Wermund, eds., 1997, Atlas of northern Gulf of Mexico gas and oil reservoirs, v. 1, The University of Texas at Austin, Bureau of Economic Geology, 199 p.

Shimamoto, T., and J. M. Logan, 1981, Effects of simulated fault gouge on the sliding behavior of Tennessee Sandstone - non-clay gouges: Journal of Geophysical Research, v. 86, p. 2902-2914.

Smith, D. A., 1980, Sealing and nonsealing faults in Louisiana Gulf Coast Salt Basin: AAPG Bulletin, v. 64, p. 145-172.

Sperrevik, S., P. A. Gillespie, Q. J. Fisher, T. Halvorsen, and R. J. Knipe, 2002, Empirical estimation of fault rock properties: Norwegian Petroleum Society Special Publications, v. 11, p. 109-125.

Streit, J. E., and R. R. Hillis, 2004, Estimating fault stability and sustainable fluid pressures for underground storage of CO2 in porous rock: Energy, v. 29, p. 1445-1456.

Takahashi, M., 2003, Permeability change during experimental fault smearing: Journal of Geophysical Research-Solid Earth, v. 108.

Thomas, L. K., D. L. Katz, and M. R. Tek, 1968, Threshold pressure phenomena in porous media: Society of Petroleum Engineers Journal, v. 8, p. 174-&.

Trevino, R. H., and B. C. Vendeville, 2008, Origin of coast-perpendicular extensional faults, western Gulf of Mexico: The relationship between an early-stage ridge and a late-stage fault: AAPG Bulletin, v. 92, p. 951-964.

Tueckmantel, C., Q. J. Fisher, T. Manzocchi, S. Skachkov, and C. A. Grattoni, 2012, Two-phase fluid flow properties of cataclastic fault rocks: Implications for CO2 storage in saline aquifers: Geology, v. 40, p. 39-42.

Underschultz, J., 2007, Hydrodynamics and membrane seal capacity: Geofluids, v. 7, p. 148-158.

von Deimling, J. S., J. Greinert, N. R. Chapman, W. Rabbel, and P. Linke, 2010, Acoustic imaging of natural gas seepage in the North Sea: Sensing bubbles controlled by variable currents: Limnology and Oceanography-Methods, v. 8, p. 155-171.

Walsh, J. J., and J. Watterson, 1988, Analysis of the relationship between displacements and dimensions of faults: Journal of Structural Geology, v. 10, p. 239-247.

Watts, N. L., 1987, Theoretical aspects of cap-rock and fault seals for single-phase and 2-phase hydrocarbon columns: Marine and Petroleum Geology, v. 4, p. 274-307.

Weber, K. J., G. Mandl, W. F. Pilaar, B. V. F. Lehner, and R. G. Precious, 1978, The role of faults in hydrocarbon migration and trapping in Nigerian growth fault structures, Offshore Technology Conference, Houston, TX.

Wehr, F. L., L. H. Fairchild, M. R. Hudec, R. K. Shafto, W. T. Shea, and J. P. White, 2000, Fault seal: contrasts between the exploration and production problem, *in* M. R. Mello, and B. J. Katz, eds., AAPG Memoir 73: Petroleum Systems of South Atlantic Margins, p. 121 - 132.

Wilkins, S. J., and S. J. Naruk, 2007, Quantitative analysis of slip-induced dilation with application to fault seal: AAPG Bulletin, v. 91, p. 97-113.

Winker, C. D., and M. B. Edwards, 1983, Unstable progradational clastic shelf margins: SEPM Special Publication 33, p. 139-157.

Wiprut, D., and M. D. Zoback, 2000, Fault reactivation and fluid flow along a previously dormant normal fault in the northern North Sea: Geology, v. 28, p. 595-598.

Yielding, G., 2002, Shale Gouge Ratio - calibration by geohistory: Norwegian Petroleum Society Special Publications, v. 11, p. 1-15.

Yielding, G., P. Bretan, and B. Freeman, 2010, Fault seal calibration: a brief review: Geological Society, London, Special Publications, v. 347, p. 243-255.

Yielding, G., B. Freeman, and D. T. Needham, 1997, Quantitative fault seal prediction: AAPG Bulletin, v. 81, p. 897-917.

Zoback, M. L., and M. Zoback, 1980, State of stress in the conterminous United States: Journal of Geophysical Research, v. 85, p. 6113-6156.

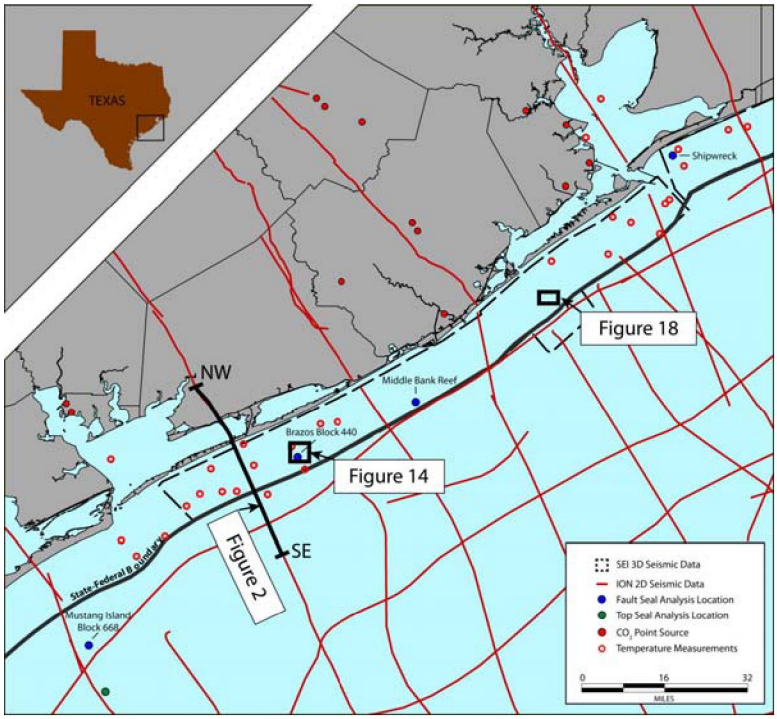

Figure 1. Data and figure locations, upper Texas Gulf Coast.

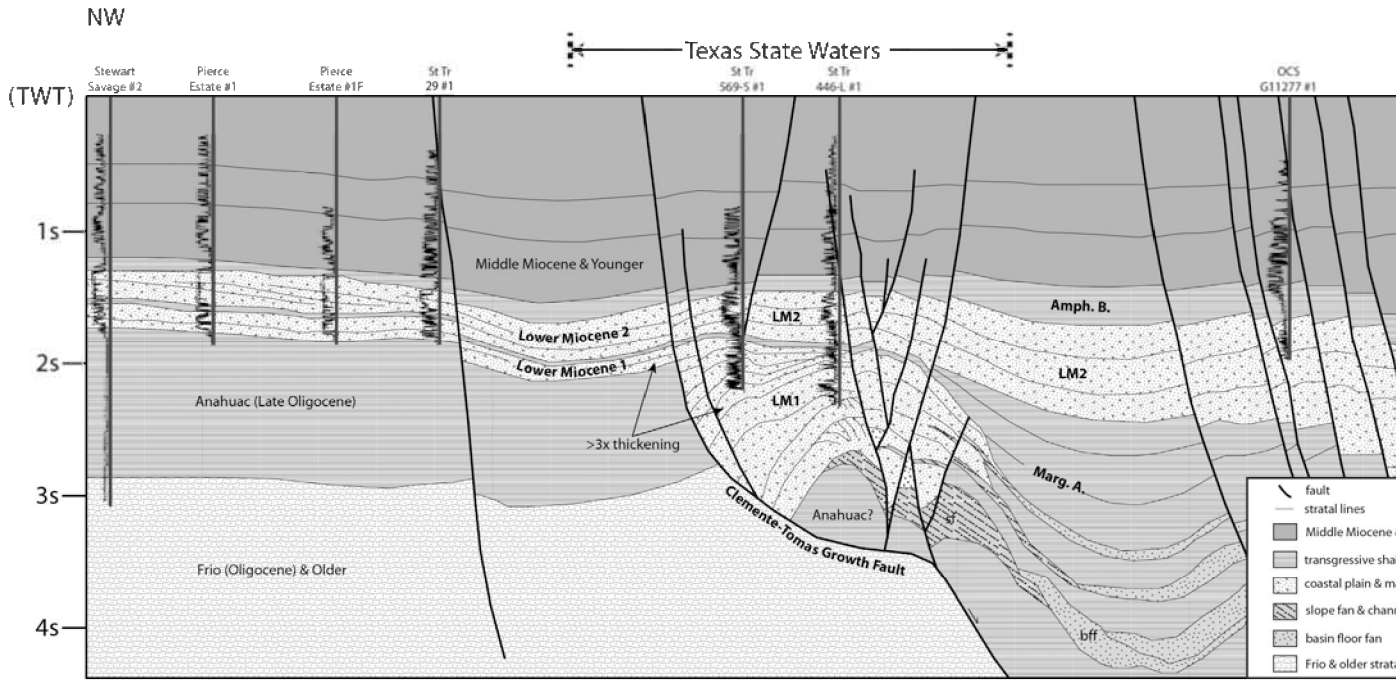

Figure 2. Dip-oriented structural cross section. Interpreted from ION 2D geophysical line. Location shown in Fig. 1. The portion covering the Texas State Waters is indicated.

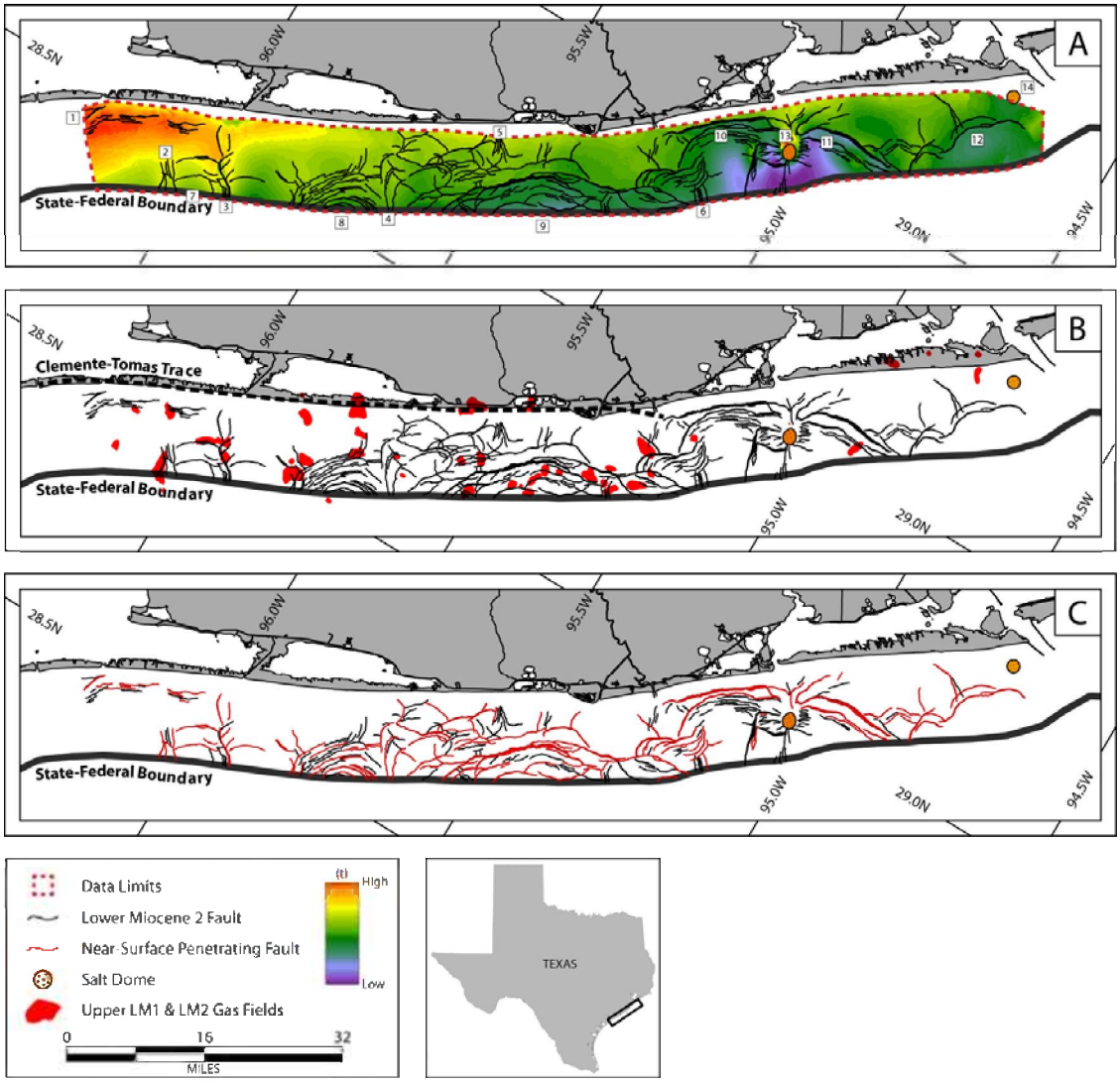

Figure 3. Structure, faulting, and natural gas accumulations of the Lower Miocene. (A) Time structure map and sequestration play types for the LM2: (1) rollover anticlines; (2-6) transverse grabens; (7-12) faulted synclinal minibasins; (13-14) piercement salt domes. (B) LM2 fault polygons overlain with upper LM1 and LM2 gas field polygons. (C) 'Near-seafloor' penetrating faults outlined with red fault polygons.

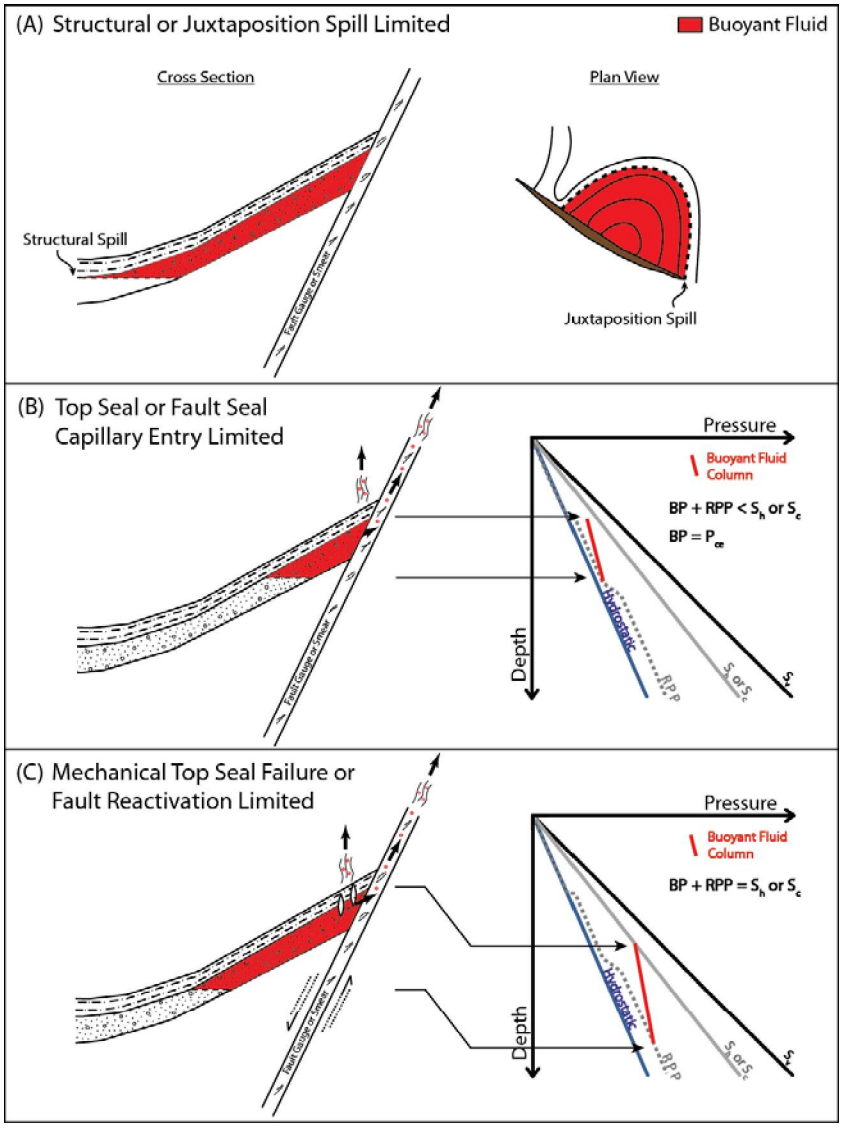

Figure 4. Mechanisms that limit natural accumulations. (A) Structural and self-juxtaposition spill limited. (B) Top seal or fault seal capillary entry limited. When the buoyancy pressure (BP) equilibrates to the capillary entry pressure (P_{ce}) of the fault rock or top seal, but the reference pore pressure (RPP; or overpressured brine) and buoyancy pressure does not exceed the depth equivalent minimum principal horizontal stress (S_h; or fracture gradient) or critical stress (S_c; or fault reactivation pressure). (C) Mechanical top seal failure ($BP+RPP=S_h$) or fault reactivation ($BP+RPP=S_c$) limited.

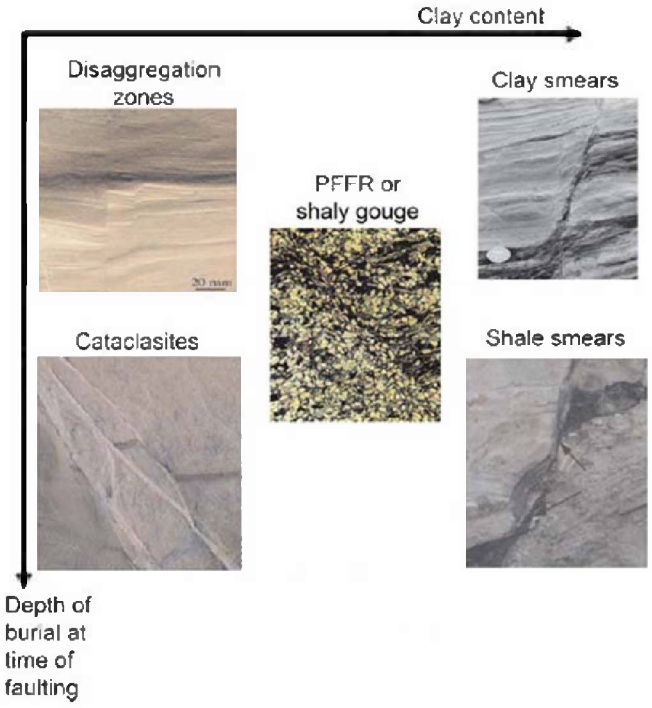

Figure 5. Fault rock types. Modified from Yielding et al. (2010)

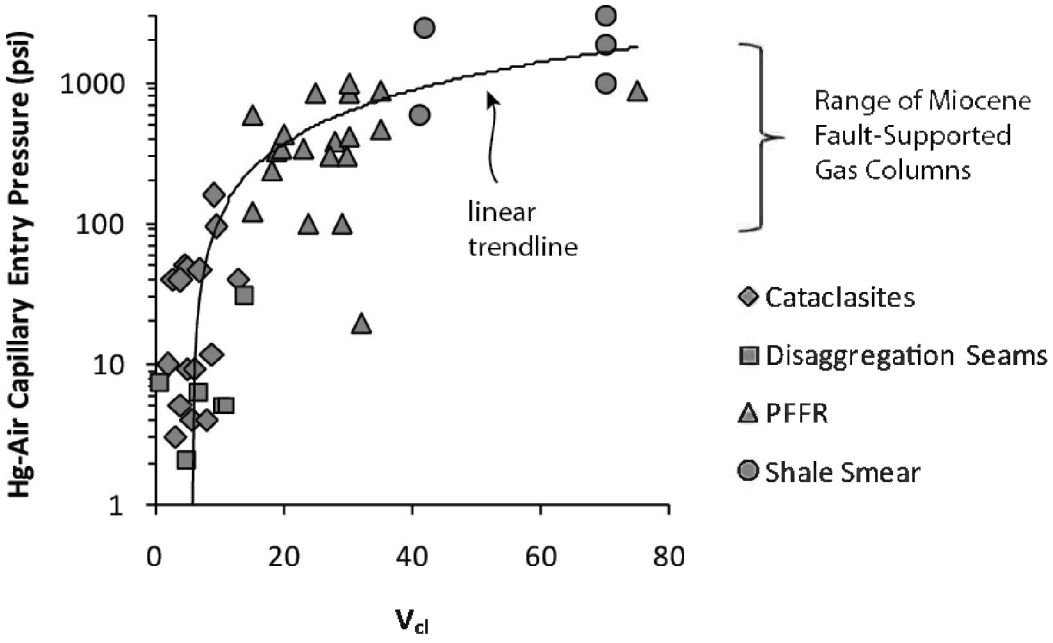

Figure 6. Deterministic fault seal literature review. Data are plotted on a semi-log plot to illustrate the order of magnitude scatter in the cataclasites and phyllosilicate framework rocks (PFFR). Mercury-air (Hg-Air) capillary entry pressure tests are performed perpendicular to the fault plane and the percent phyllosilicates (V_{cl}) in the fault gouge are measured by x-ray diffraction techniques. Data points for fault gouge from normal faults are taken from Gibson (1998), Sperrevik et al. (2002), and Eichhubl et al. (2005).

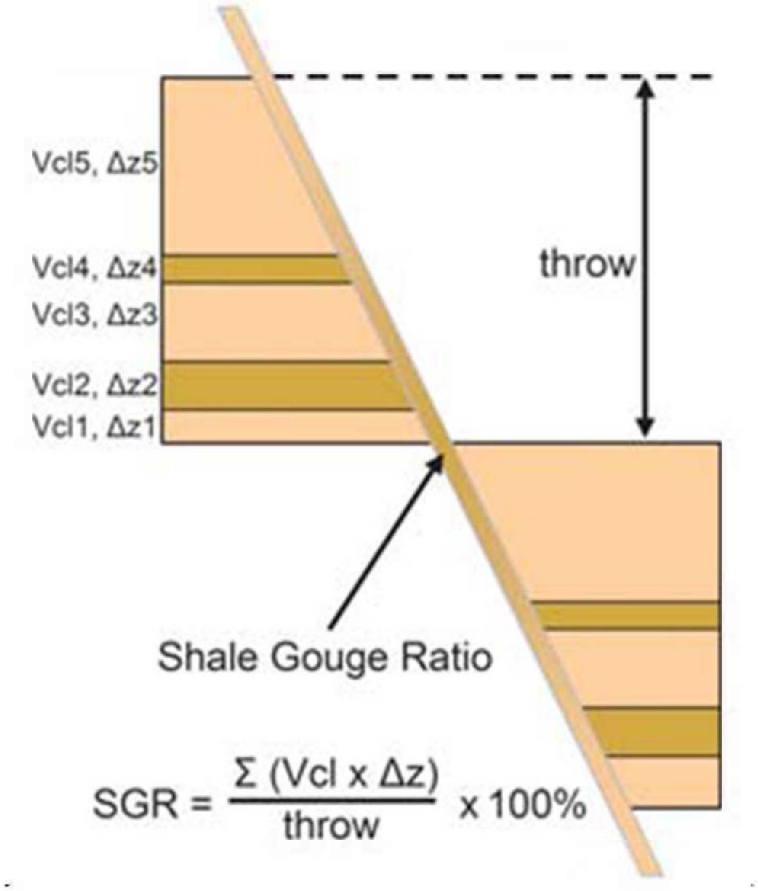

Figure 7. Shale gouge ratio (SGR). Modified from Yielding et al. (2010).

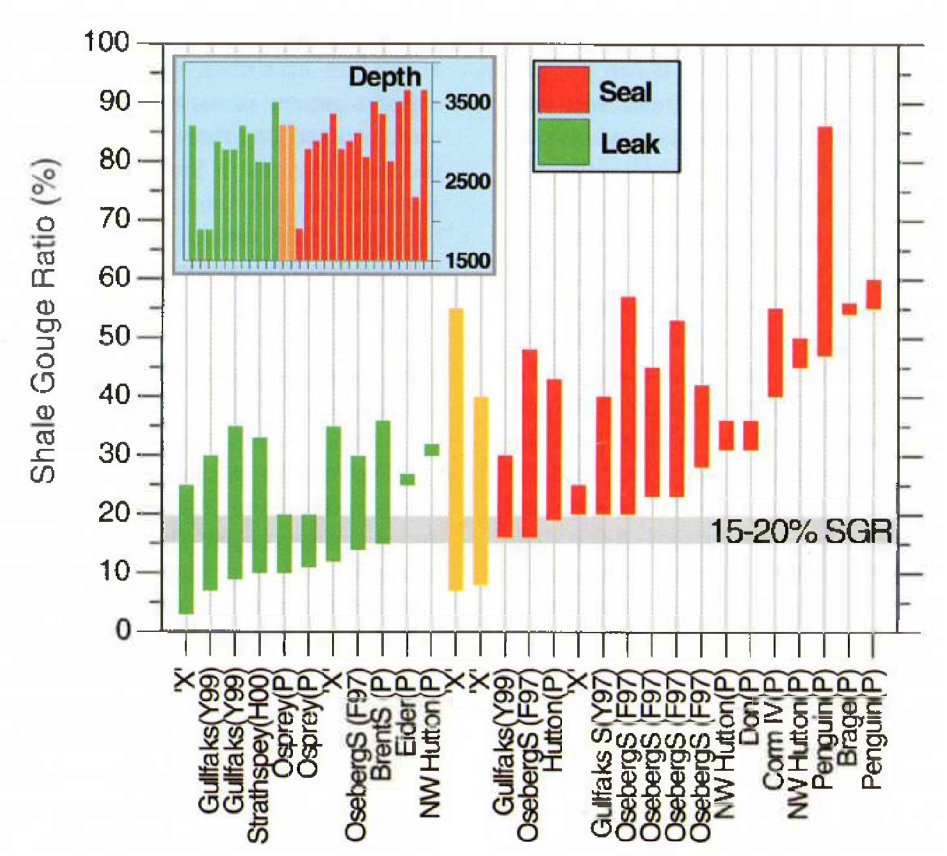

Figure 8. Qualitative use of the SGR. SGR shows sealing vs leaking faults from various North Sea fields. Image from Yielding (2002).

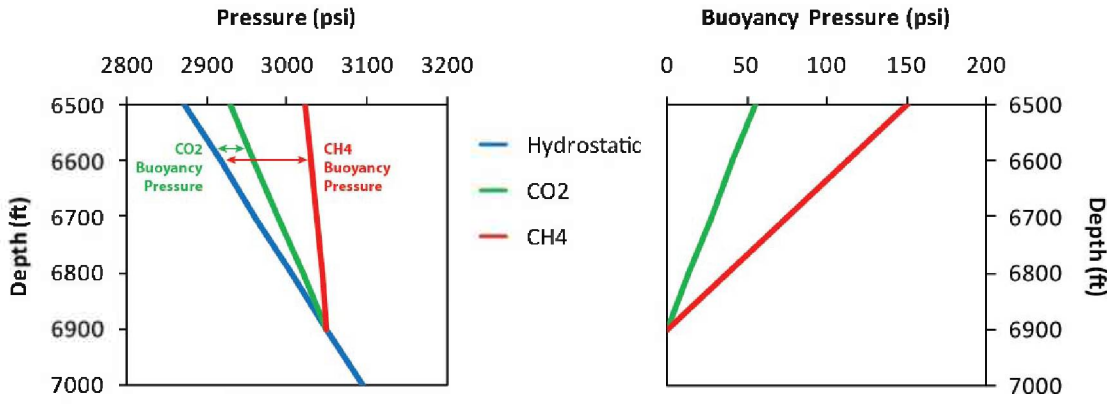

Figure 9. Hypothetical buoyancy pressure. Hypothetical pressure vs depth profile (left) illustrating the different pressure trajectories due to buoyancy for CO_2 (ρ = 0.7 g/cm^3), and CH4 (ρ = 0.15 g/cm^3). Brine density is 1.05 g/cm^3. Buoyancy pressure versus depth (right) for the same pressure profile.

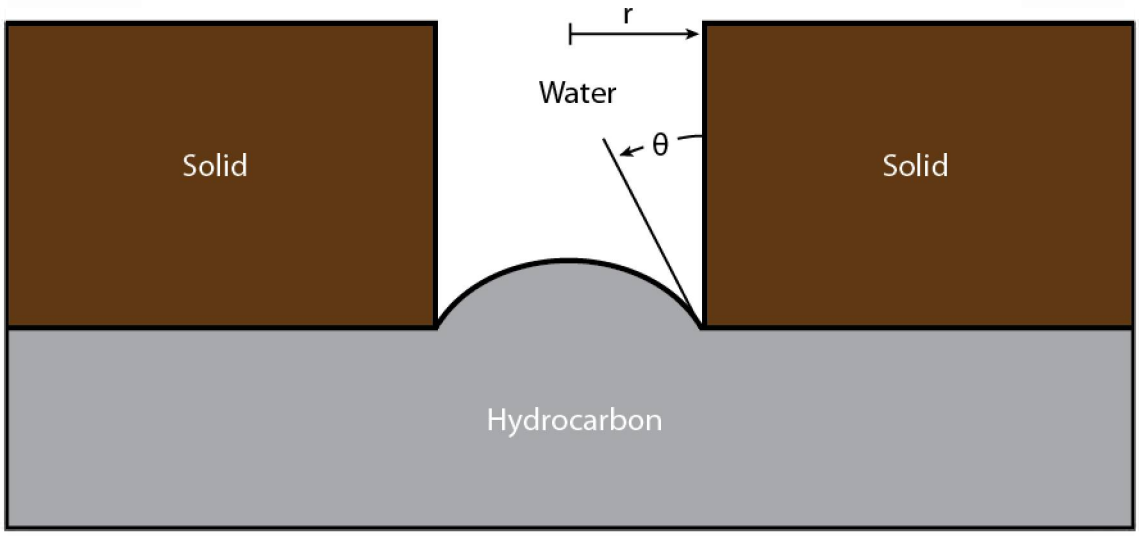

Figure 10. Capillary entry schematic. The hydrocarbon (non-wetting) and water (wetting) form a contact angle (θ) with the solid substrate. Pore throat radius is represented as 'r.' Image modified after Schowalter (1979).

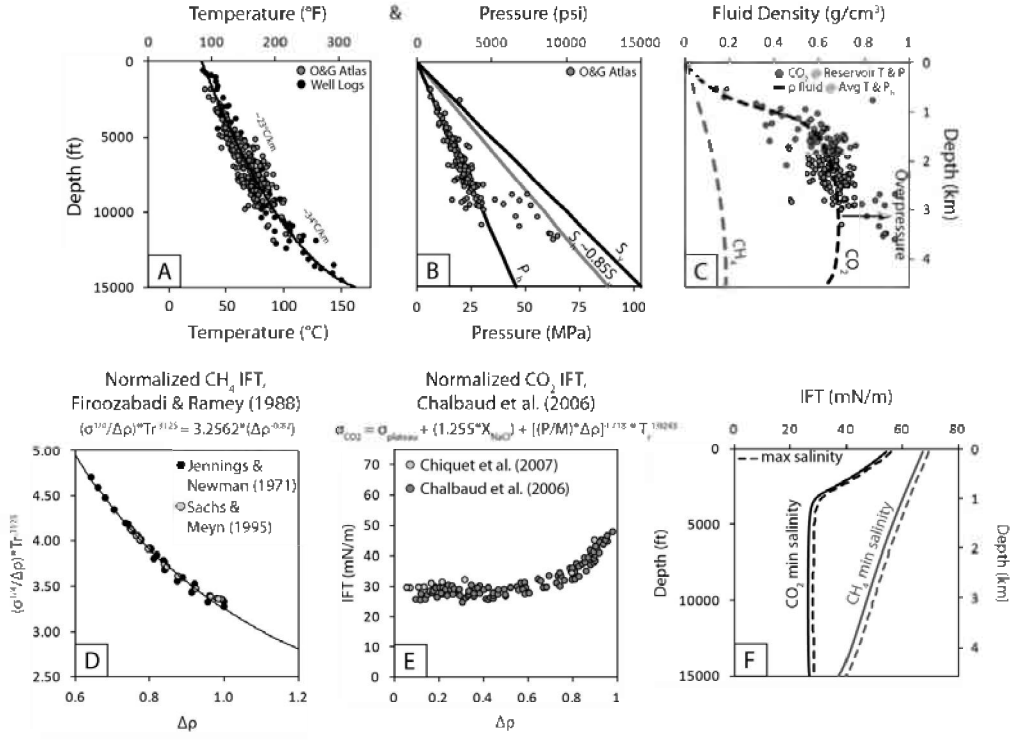

Figure 11. Temperature, pressure, density, and interfacial tension trends with depth.

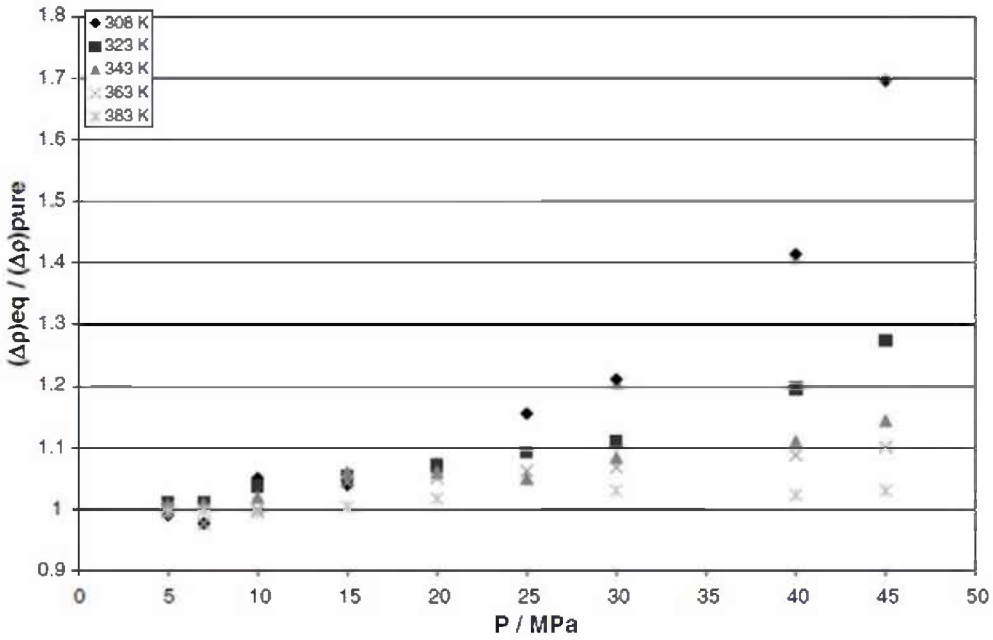

Figure 12. Ratio of CO_2-brine density in equilibrium and pure CO_2 density (y-axis) vs. pressure (x-axis) for varying reservoir scale temperatures. Image from Chiquet et al. (2007b).

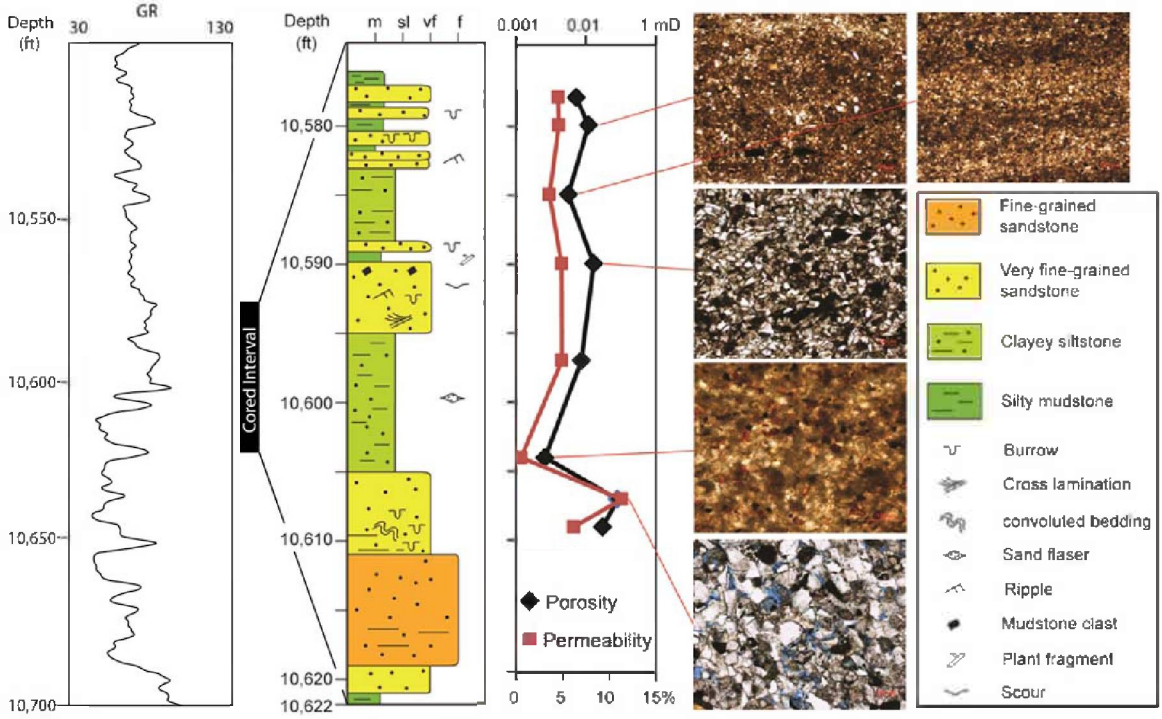
Depth (ft)
GR
30
130
10,550
10,600
10,650
10,700
Cored Interval
Depth (ft)
m
sl
vf
f
10,580
10,590
10,600
10,610
10,620
10,622
0.001
0.01
1 mD
Porosity
Permeability
0
5
10
15%
Fine-grained sandstone
Very fine-grained sandstone
Clayey siltstone
Silty mudstone
Burrow
Cross lamination
convoluted bedding
Sand flaser
Ripple
Mudstone clast
Plant fragment
Scour

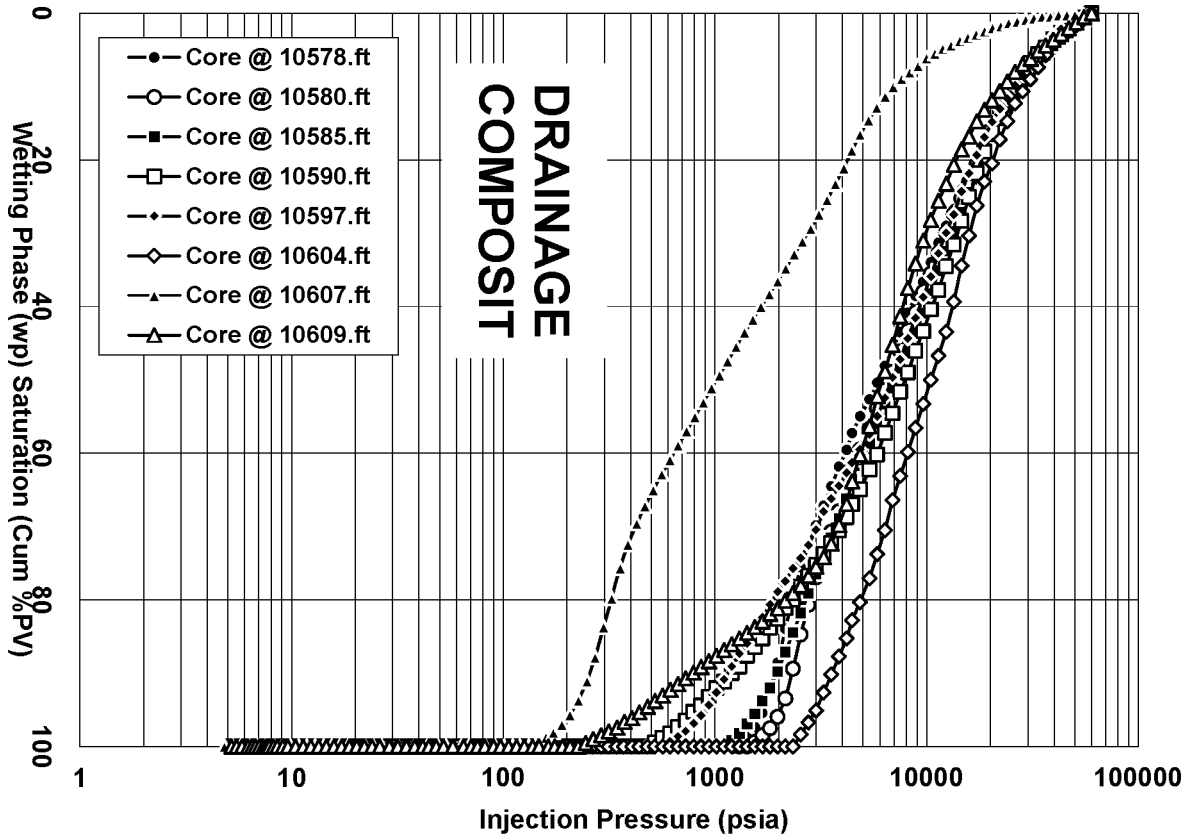
DRAINAGE
COMPOSIT
Core @ 10578.ft
Core @ 10580.ft
Core @ 10585.ft
Core @ 10590.ft
Core @ 10597.ft
Core @ 10604.ft
Core @ 10607.ft
Core @ 10609.ft
Wetting Phase (wp) Saturation (Cum %PV)
0
20
40
60
80
100
1
10
100
1000
10000
100000
Injection Pressure (psia)

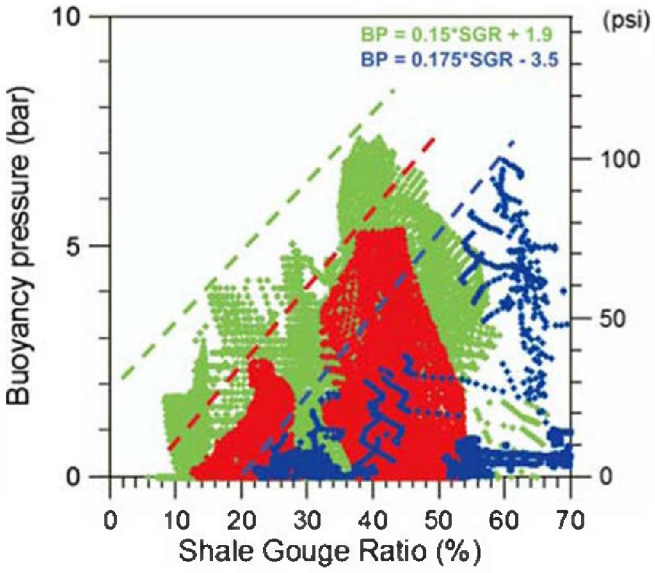

Figure 13. Global fault seal calibration database. Dashed lines represent fault seal failure envelopes. Colors represent depths of sealing faults: blue (< 3km), red (3 - 3.5km), and green (>3.5km). Image from Yielding et al., (2010).

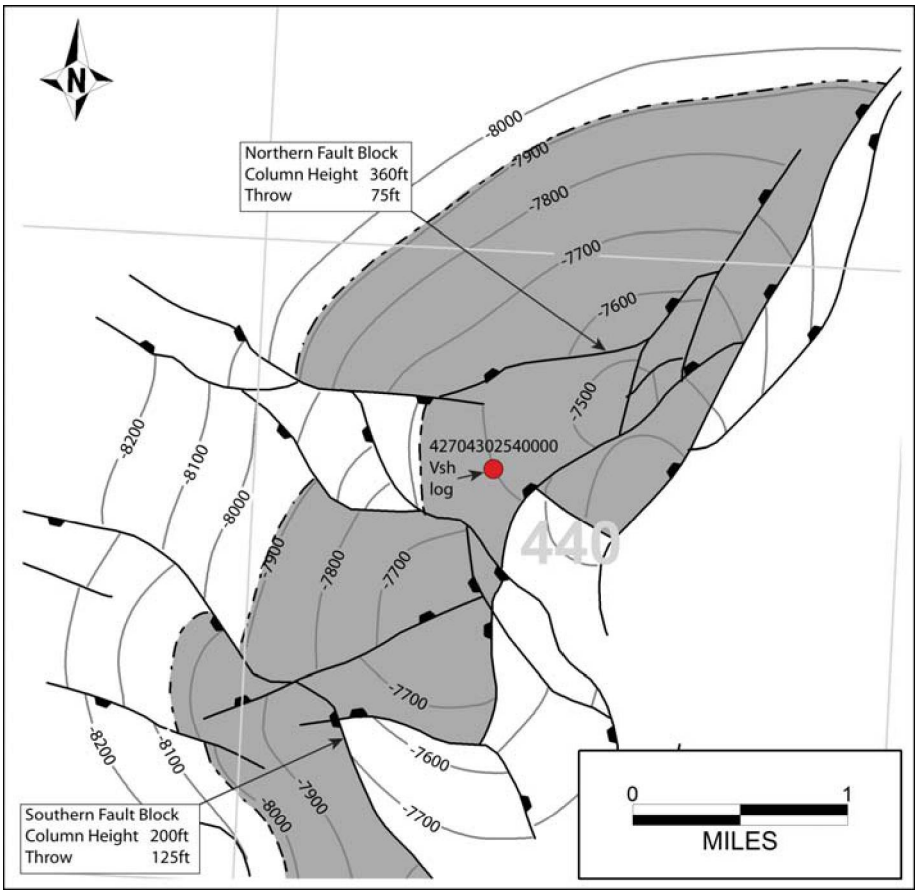

Figure 14. Structure map of the Brazos Block 440 B sand. Modified from Seni et al. (1997).

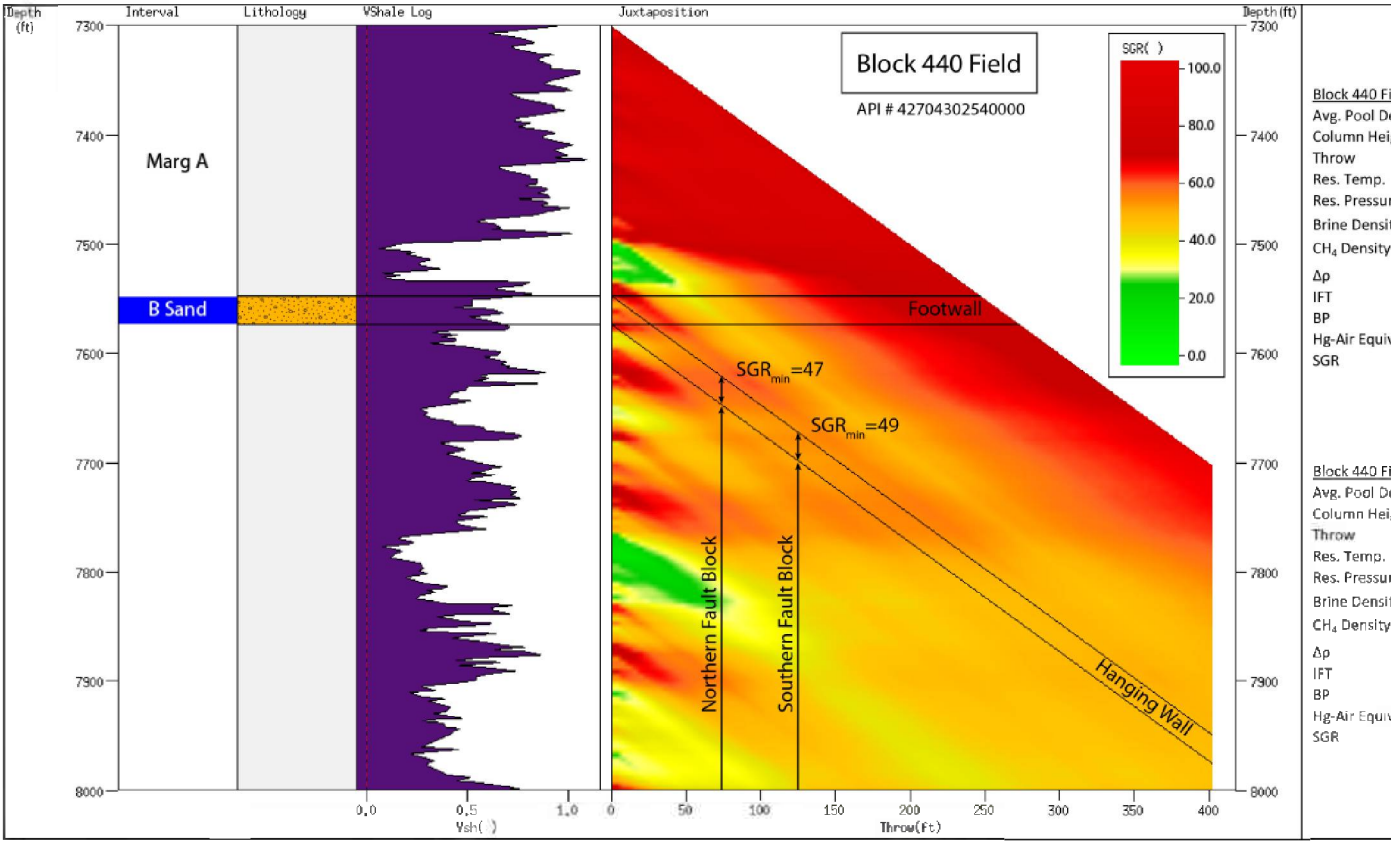

Figure 15. Triangle diagram for the Brazos Block 440 B sand.

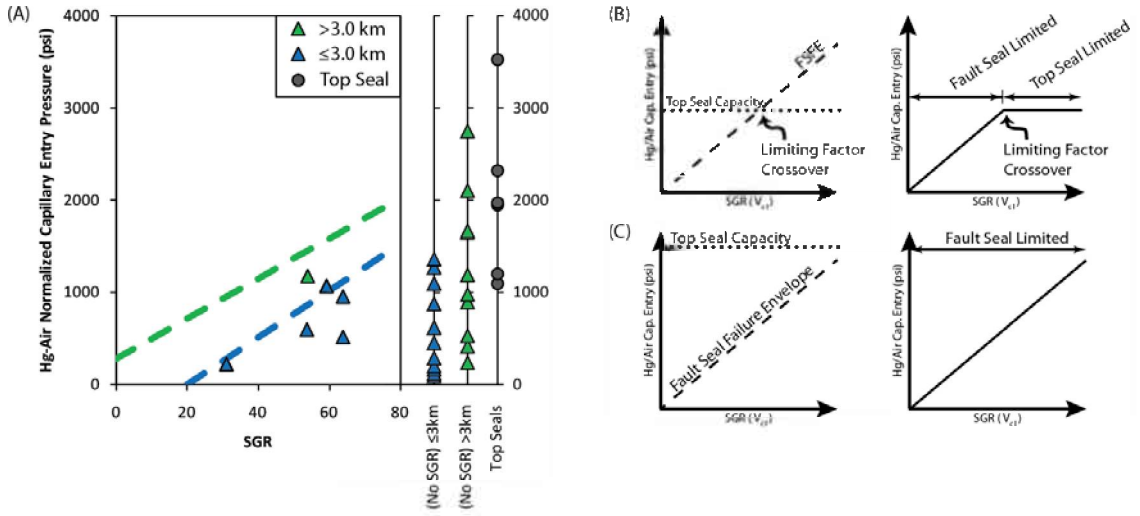

Figure 16. Calibrated Lower Miocene fault seal & top seal. (A) Calibrated fault seal failure envelope. The blue dashed line and green dashed line correspond to Equations (16) and (17), respectively, from the global fault seal database. Blue and green triangles correspond to data points ≤3.0km and >3.0km, respectively. Column heights lacking SGR calculations are displayed on two vertical axes (≤3.0km & >3.0km). Top seal mercury injection capillary pressure data are plotted on the rightmost vertical axis. (B) Schematic diagram in which top seal capacity limits the fault bound column height. (C) Schematic diagram similar to (A), where the fault seal is the dominant limiting factor on sealing capacity.

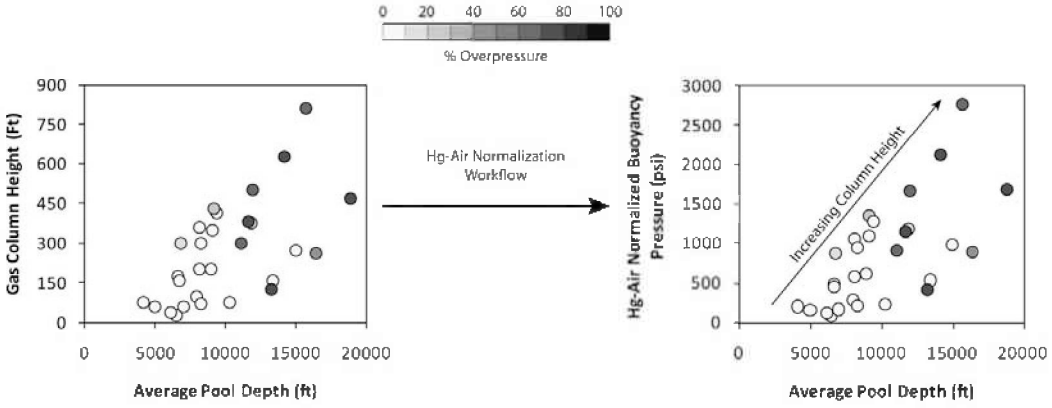

Figure 17. Fault bound column heights trends with depth. 27 fault supported column heights (left) converted to mercury-air equivalent buoyancy pressures (right). Data points are shaded by % overpressure.

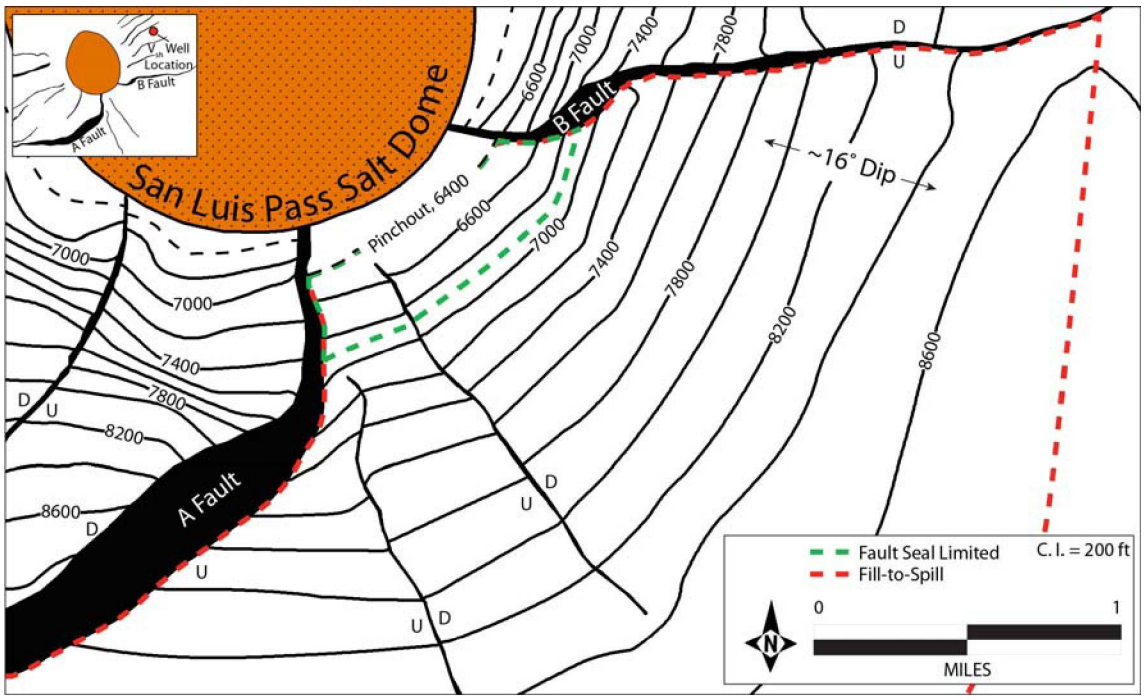

Figure 18. San Luis Pass salt dome, LM2 structure map, SE fault block. Dashed green line represents the limit of membrane fault seal for the LM2 reservoir in the footwall of the B Fault (Area = 175 acres). Dashed red line represents the limits of 'fill-to-spill' for the structure (Area = 2760 acres).

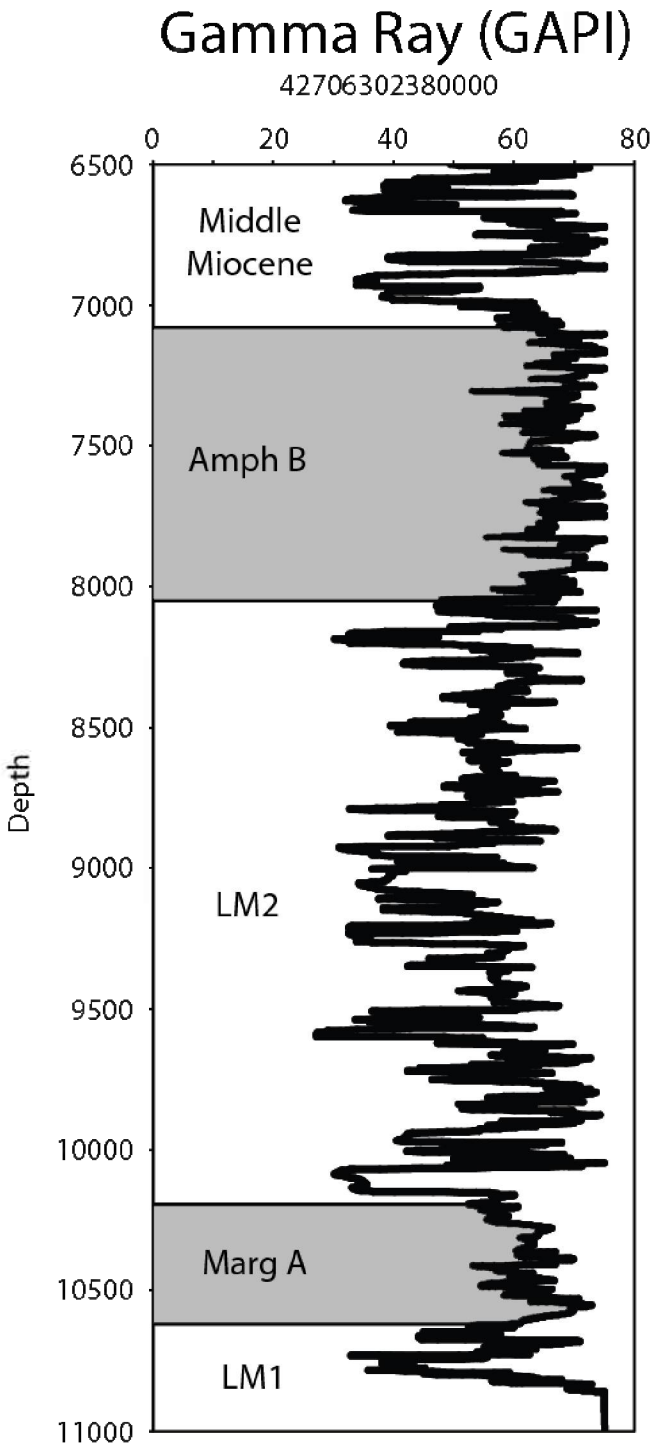

Figure 19. Gamma ray well log type section for the Lower Miocene 1 & 2, San Luis Pass.

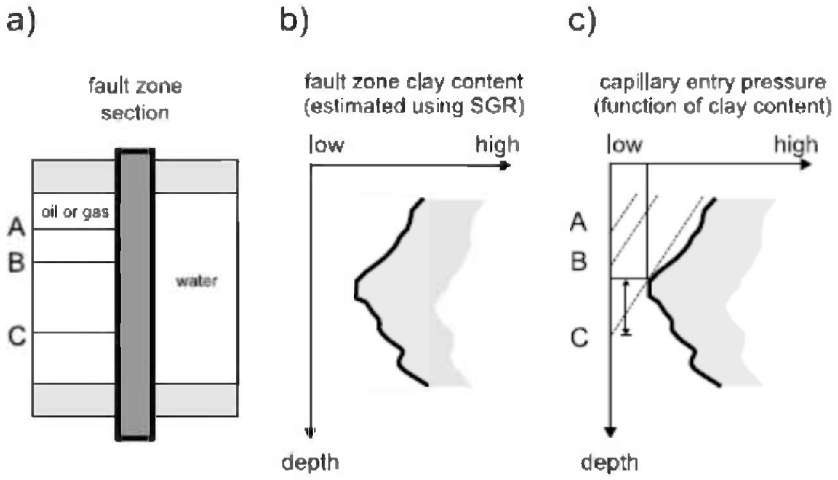

Figure 20. Buoyancy pressure profile schematic. See text for discussion. (a) Fault zone separates a progressively charging trap (A→C) on the left hand side from a water bearing reservoir on the right hand side. (b) The SGR values of the fault zone as they vary with depth. (c) The SGR have been converted to P_{ce} and the pressure exerted by the buoyant columns with depth is represented by A→C, with C representing the maximum column height supported (BP=P_{ce}) by the fault zone properties. Image from Bretan and Yielding (2005).

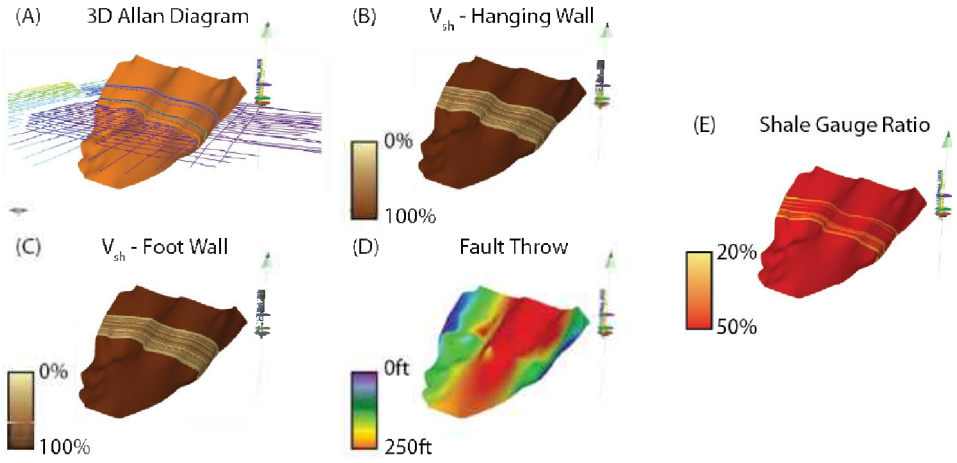

Figure 21. Schematic 3-dimensional fault modeling workflow (A→E). (A) Allan diagrams (Allan, 1989) are constructed from fault and horizon data. (B,C) V_{sh} is calculated for the hanging wall and footwall. (D) Fault throw is modeled from the Allan diagram. (E) Shale gouge ratio is computed from V_{sh} distribution and fault throw.

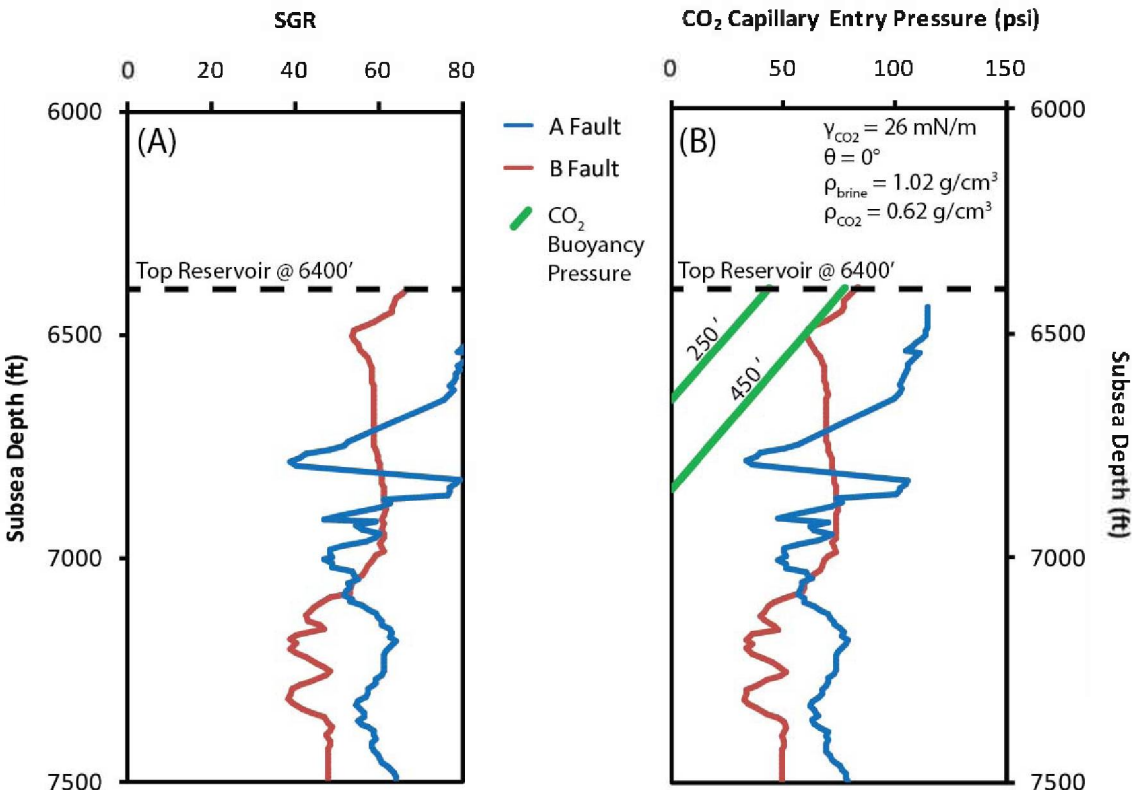

Figure 22. Buoyancy pressure profile LM2, SE fault block, San Luis Pass salt dome. (A) LM2 reservoir interval SGR values from the footwall of both the A Fault and B Fault. (B) Buoyancy pressure profile created from (A) using the workflow: P_{cma} = 25.382 (SGR) - 507.63 and average CO_2 fluid properties from the top-reservoir depth of 6400 ft.

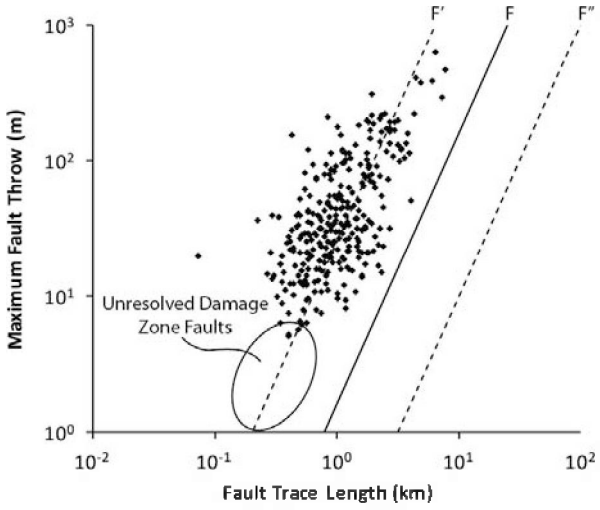

Figure 26. Fault trace length vs maximum fault throw, LM2 horizon. The data are from a regionally depth converted seismic volume and therefore have a minor amount of inherent error from time-to-depth conversion.

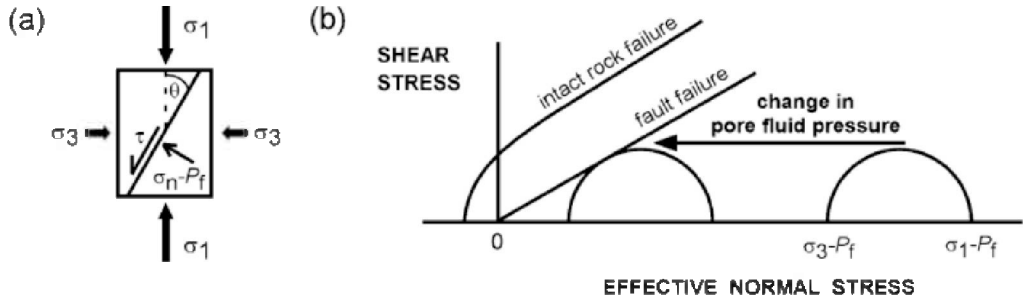

Figure 23. Fault slip stability schematic. (a) Two-dimensional graphic of vertical (σ_1 for normal stress regimes) and horizontal (σ_3) stresses acting on an angled (θ) fault plane to create shear stress (τ) and normal effective stress (σ_n-P_f). (b) Mohr-Coulomb diagram showing the effects of a change in fluid pressure on the effective differential stress. Image from Streit and Hillis (2004).

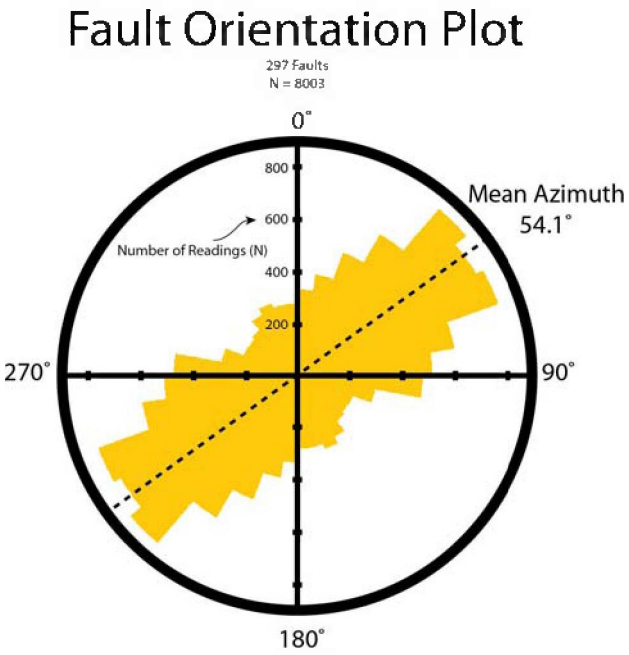

Figure 24. Regional fault strike rose diagram. Fault orientation plot of 297 faults mapped on the LM2 horizon. Each fault is broken into segments at 500' lateral intervals and the average strike is measured to reduce the bias of smaller faults, resulting in 8003 measurements. Mean azimuth of the fault segments is 54.1°.

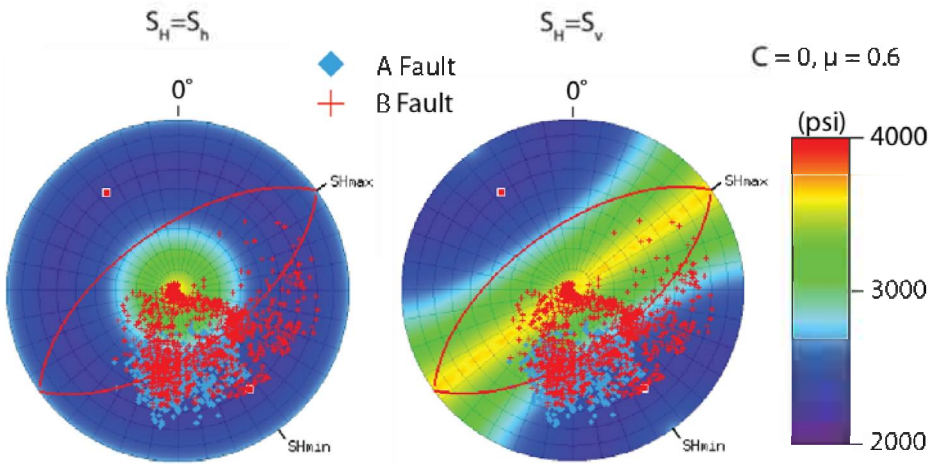

Figure 25. Fault slip stability plots for the A Fault and B Fault. Depth modeled: 6,600ft. Poles to the planes of the A Fault and B Fault are plotted on a lower hemisphere projection. Since there is uncertainty in the value of S_H, the two possible extremes were modeled: (left) $S_H=S_h$ and (right) $S_H=S_v$.

Chapter 5. Regional CO_2 Static Capacity Estimate, Offshore Miocene of Texas State Waters

David L. Carr, Kerstan J. Wallace, Andrew J. Nicholson, and Changbing Yang, Gulf Coast Carbon Center, Bureau of Economic Geology, The University of Texas at Austin, Austin, TX, USA

Introduction

Geologic sequestration of carbon dioxide (CO_2) into saline aquifers has been proposed as a potentially viable method for reducing atmospheric greenhouse gas emissions and has been shown to be possible with existing technology (Gale and others, 2001; Holloway, 2001; Tsang and others, 2002; Bachu, 2003; Bachu and Gunter, 2003; Lackner, 2003; Eiken and others, 2011). Estimates of CO_2 storage potential have been generated for many sedimentary basins worldwide using a method that consists of a discounted pore-volume calculation. The current estimate of total CO_2 storage capacity for North America is between 1160 and 3500 gigatonnes (Gt) (DOE, 2010). According to the Environmental Protection Agency (EPA, 2013), CO_2 emissions in Texas are the highest of any state in the United States. The proximity of many CO_2 point sources along the Texas coast highlights the potential advantage of CO_2 geosequestration (GS) in geologic reservoirs of the coastal region (fig. 5.1). Consequently, one objective of the study resulting in the current atlas was to perform and present a static regional capacity estimate for a large portion of the Miocene-age stratigraphic interval of the offshore Texas State Waters to quantify the potential CO_2 storage resource.

Offshore Texas Miocene Suitability for Sequestration

The Gulf of Mexico has been an active target for oil and gas production for over 70 years and, as a result, is densely populated with subsurface data. From this dense data set, the offshore Miocene stratigraphy is known to typically exhibit thick sandstone intervals with high porosity and permeability, trapping mechanisms, and seals. The following properties all indicate potentially high CO_2 storage volumes and overall positive GS feasibility for offshore Texas State Waters Miocene units:

- High porosity values (e.g., Seni and others, 1997: 28.2% average, range 5.2%–38%, n = 102 offshore Texas State Waters Miocene fields) in log and core observations from multiple, stacked reservoir sandstones (up to 244 m thick) provide very large pore volumes for potential CO_2 storage.
- High permeability (e.g., Seni and others, 1997: 338 md average, range 16 md–1600 md, n = 15 offshore Texas State Waters Miocene fields) observed in offshore Miocene sandstones suggests favorable injectivity with slow pressure build-up.
- Thick mudrock intervals, such as the *Amphistegina B* (Amph B) unit (see Chapter 3, this volume), provide low-permeability regional seals that have proven to be adequate for gas trapping on geologic time scales.
- Structural deformation from salt tectonism and extensional growth faulting has created numerous effective trap types observed throughout the region.
- Approximate depths to the top of the Miocene interval range from approximately 328 m (1000 ft) in the vicinity of the San Marcos Arch and increase, to 1220 m (4,000 ft) in the

Rio Grande Embayment to the southwest, and to 1,044 m (3,425 ft) at the Louisiana border.

- Approximate depths to the base of the Miocene range from 4,270 m (14,000 ft) near the Rio Grande Embayment to 2,130 m (7,000 ft) on the offshore salient of the San Marcos Arch, seaward of Corpus Christi Bay, to 4875 m (16,000 ft) at the Louisiana border.
- Proximity of offshore Miocene reservoirs to multiple point sources of high CO_2 emission along the Texas coast reduces transportation costs, and the existing offshore pipeline infrastructure facilitates the use of offshore reservoirs as CO_2 sinks (fig. 5.1).
- Environmental risks of sequestration are lower given the lack of potable groundwater.
- Single landowner (State of Texas) simplifies land rights and liabilities assessment.

Numerous depleted oil and gas fields in the offshore Miocene may serve as initial storage or enhanced recovery targets.

Methodology

North American CO_2 capacity was examined by seven Regional Carbon Sequestration Partnerships (RCSP) supported by the U.S. Department of Energy (DOE) (Litynski and others, 2008). Similarly, European capacity for CO_2 storage was examined as part of the GeoCapacity program (Vangkilde-Pedersen and others, 2009). These studies are typically performed by multiplying gross pore volume by CO_2 density and an efficiency factor. Goodman and others (2011) proposed the following equation for determining CO_2 storage resource mass estimates (G_{CO_2}) in saline formations:

$$G_{CO_2} = A_t \, h_g \, \varphi_{tot} \, \rho E_{saline} \qquad (1)$$

where,

A_t = Total area

h_g = Gross thickness

φ_{tot} = Total porosity

ρ = CO_2 density

E_{saline} = Storage efficiency factor

The storage efficiency factor (E) is determined at different probability values and for various lithologies through Monte Carlo simulation using field data from multiple oil and gas reservoirs in basins around the world. According to Goodman and others (2011), the efficiency factor considers

(1) net-to-total area—the fraction of the area that is suitable for CO_2 storage;

(2) net-to-gross thickness—the fraction of the interval with sufficient porosity and permeability to serve as an adequate CO_2 reservoir;

(3) effective-to-total porosity—the fraction of the pore space that is connected;

(4) volumetric displacement efficiency—the fraction of the reservoir volume accessible to CO_2 as a result of the density contrast between CO_2 and connate water;

(5) microscopic displacement efficiency—the fraction of pore space that is occupied by immobile, residual fluids.

Using ranges of observed and hypothesized values for each of these parameters, Goodman and others (2011) propose a set of efficiency factors, ranging from 0.4 to 5.5%, for use in saline aquifers in sandstone, limestone, or dolomite reservoirs and for probability values of P_{10}, P_{50}, or P_{90} (table 5.1).

Table 5.1. Goodman and others (2011) table of saline formation efficiency factors

Lithology	P10	P50	P90
Clastics	0.51%	2.00%	5.40%
Dolomite	0.64%	2.20%	5.50%
Limestone	0.40%	1.50%	4.10%

The regional capacity assessments provided by the DOE RCSP are obtained using the methodology discussed above with assumed E values. These studies serve as the current primary basis for the estimate of total North American CO_2 storage capacity and, in turn, imply the feasibility for widespread carbon capture and storage (CCS) development in the United States.

For the current study, we utilized the net reservoir sandstone refinement (equation 1) proposed by Wallace and others (2014):

$$G_{CO_2} = A_t \, \mathbf{h_{net}} \, \varphi_{tot} \, \rho E_{saline} \qquad (2)$$

where,

$\mathbf{h_{net}}$ = Net reservoir sandstone thickness

(all other variables identical to equation 1)

By picking sandstone intervals in wireline logs, uncertainty in the net-to-gross ratio consideration of the efficiency factor is significantly reduced, and one aspect affecting potential error in the regional assessment can be tested. More detailed explanation of specific methodologies and calculations used in this regional static capacity estimate can be found in Wallace and others (2014).

Workflow

Following the methodology above, we calculated capacity for each square kilometer (0.3861 mi^2) of the study area using gridded input maps generated from well-log interpretations. To accomplish the mapping tasks, we built a Petra™ software (IHS Energy) database containing petroleum well, wireline-log, and paleontological data. We also integrated information from previous studies into the Petra™ electronic database, most notably works by Dr. William E. Galloway and associates (e.g., Galloway, 2001) from the Gulf Basin Depositional Synthesis (GBDS) group at the University of Texas Institute for Geophysics, and Dr. Janet K. Pitman's (2011; U.S. Geological Survey) GIS release of the Top of Overpressure map for the northern Gulf of Mexico Basin, which was modified from Wallace and others (1981).

Study Area and Data Set

The 42,261 km^2 (16,317 mi^2) Total Project Area is within the dark red polygon in figure 5.1. The area is large; in fact, it is larger than the total areas of several U.S. states, including Maryland, Hawaii, Massachusetts, Vermont, New Hampshire, New Jersey, Connecticut, Delaware, and Rhode Island (U.S. Census Bureau, 2010). The focal point of this study was the offshore Texas State Waters (orange polygon in fig. 5.1). Although it is a subset of the overall project area, the offshore Texas State Waters area is also comparatively large, at 9,875 km^2 (3,813 mi^2), which would submerge an area larger than Delaware or Rhode Island. The basinward extent of the project area is approximately (+/- 0.5 km) 10 km seaward from the Texas State Waters–Federal Outer Continental Shelf (OCS) boundary. Landward and updip, the project area extends (+/- 0.5 km) 40–50 km (approx. 25–30 mi) from the Texas shoreline.

Our northern Gulf of Mexico Petra™ database contains approximately 90,000 wells. For making the capacity estimate, we high-graded this data set to 3,184 wells, located in and/or

adjacent to the Total Project Area (fig. 5.1), for which wireline-log data were available. Table 5.2 lists the specific types and quantities of data utilized. Many wells in the offshore realm were directionally drilled; it is thus necessary to obtain directional surveys in order to make accurate interpretations of true vertical depth.

Both raster logs and Log ASCII Standard (LAS) files were used to make stratigraphic picks and identify net sandstone reservoir intervals from which we subsequently made maps. Well logs run in petroleum exploration and production wells in the Gulf of Mexico typically contain full lengths (entire depth of well) of spontaneous potential (SP) and resistivity curves, +/- sonic (acoustic) curves. Porosity log suites—which commonly include gamma ray (GR), bulk density, density porosity, and neutron porosity curves—are typically run over shorter intervals, where there are known reservoirs or potential reservoir-bearing zones. Raster logs, which are scanned images of paper copies of well logs, were the primary source for making stratigraphic correlations. Raster logs were also used for making, predominantly from the SP response, net reservoir sandstone counts, which can provide an excellent qualitative indication of porous and permeable reservoir rocks. Digital well logs, frequently referred to as LAS curves, of key wells were either purchased commercially or digitized in-house from raster-log images. The digital logs were also used for net reservoir sandstone summations as well as for average porosity determination.

Paleontological (paleo) reports were used to improve the accuracy of stratigraphic correlations. Paleo reports are primarily composed of depth interpretations of key benthic foraminifera that are tied to geologic time zones within the Miocene and throughout the Tertiary section in the Gulf of Mexico. The greatest concentrations of benthic microfossils are typically

found in mudrock units that represent flooding/maximum flooding events. The reports are based on drill-cuttings data collected at 9-m (30-ft) intervals from the circulating mud system at the well site. As such, paleo-report interpretations are subject to human error and dilution from mixing of cuttings and wellbore slough. Typically, we used paleo picks, rather than "golden spike" ground truth, as broad guidelines when correlating.

Seismic data (not shown in this chapter but featured prominently in others of this volume) and paleo reports were used to guide stratigraphic correlations.

Table 5.2. Description of data set used to make the capacity estimate

Data Type	Number of Wells Total Project Area	Number of Wells Offshore Texas State Waters	Major Data Source(s)
Wells	3,184	672	IHS Energy, DrillingInfo
Directional Surveys	364	112	U.S. Bureau of Ocean Energy Management (BOEM), IHS Energy,Texas Railroad Commission (TXRRC)
Raster-Log images	2,900	587	Texas General Land Office (GLO), DrillingInfo, Texas Bureau of Economic Geology (BEG), BOEM, TXRRC, IHS Energy,TGS-Nopec
LAS Log Curves	2,142	610	In-house digitizing of raster images; IHS Energy,TGS-Nopec
Spontaneous Potential (SP)	1,186	585	In-house digitizing of raster images
Gamma Ray (GR)	330	116	In-house digitizing of raster images; IHS Energy,TGS-Nopec
Density and/or Sonic Porosity	292	106	IHS Energy,TGS-Nopec
Paleo Reports	386	114	BOEM (2010), Pickering Enterprises "PaLCon"
Seismic Data	na	na	Ion Geophysical (2D seismic); Seismic Exchange, Inc. (SEI)

Miocene Stratigraphic Boundaries and Structure

Galloway and others (2000) defined the top of the Miocene as a "flooding event associated with the *Robulus E* biostratigraphic top or, in parts of the basin where *Rob. E* is not picked, the slightly older *Bigenerina A* marker" (fig. 5.2). Our offshore Texas paleo data (BOEM, 2010) contained about three times more *Bigenerina A* picks than *Robulus E* picks, so we opted to define the Miocene top using the *Bigenerina A* maximum flooding surface to facilitate consistency (fig. 5.2). Updip and landward onshore, the top of the Miocene is much more difficult as the section thins and becomes dominated by more heterogeneous fluvio-deltaic and fluvial facies.

The base of the Miocene is relatively easier to pick in the offshore Texas State Waters since it is marked by the Anahuac Shale (latest Oligocene), which overlies the prolific onshore Texas hydrocarbon producer, the Frio Formation. The *Discorbis gravelli* biostratigraphic zone approximately marks the Anahuac second-order maximum flooding and correlates to a strong warming event within the larger-scale cooling inferred to have taken place from the late Oligocene through early Miocene (Fillon and others, 1997; Fillon and Lawless, 2000; Trevino and others, 2003). The Anahuac maximum flooding surface (MFS) provided a consistent, reliable marker just beneath the Miocene interval, so we used it to define the base of the Miocene (fig. 5.2). Downdip, across the Clemente-Tomas fault zone, the Anahuac is deep, greatly expanded, and only rarely penetrated by wellbores. In these areas, most prominently in the upper (northeast) and far south Texas coastal offshore, we relied upon "Top Oligocene" contours, provided to us by Gulf Basin Depositional Synthesis (GBDS), that are similar to those published

by Galloway (2001). Updip and landward, the Anahuac can be correlated but, as with the top Miocene pick, with less confidence as the section thins and becomes dominated by more heterogeneous fluvio-deltaic and fluvial facies.

Structure maps of the top and base of the Miocene, constructed using the stratigraphic markers described above, are presented in figure 5.3A and B, respectively. Pitman's (2011) "Top of Geopressure" contours were imported into our Petra™ database and were gridded and contoured (fig. 5.3C).

Miocene Capacity Interval

Because of the greater volumetric efficiency of storing CO_2 in a supercritical or dense phase (Elewaut, 1996), the top of the Miocene capacity interval (CI) (fig. 5.4) is defined as either the top of the Miocene section or 3,300-ft (1,005-m) depth, whichever is deeper. The 3,300-ft depth is the upper limit of the zone in which CO_2 behaves as a supercritical fluid (fig. 5.5). The base of the Miocene CI is defined as either the base of the Miocene section or the top of overpressure zone, whichever is shallower. Regional overpressure is typically encountered at depths of approximately 8,000–10,000 ft (2,438–3,048 m) in the study area (Wallace and others, 1981; Pitman, 2011).

Capacity Calculations: Inputs

Using the subsurface data set, we were able to map the parameters required to input to the Wallace and other (2014) capacity equation (equation 2). To automate the calculation process, the senior author created a computer program (a Petra™ "Grid Model Calc Transform") to calculate CO_2 capacity from four basic input maps:

(1) Depth to top of CI

(2) Depth to base of CI

(3) Net reservoir sandstone isopach of CI

(4) Average porosity of CI

Figure 5.6 shows the input maps used to calculate net regional capacity for the Miocene in the project area. The following section explains how we constructed the maps.

Depth Mapping and Determination of CO2 Density

Nicholson (2012) compiled temperature and pressure data from wells and produced fields in Miocene strata in the Texas State Waters and applied the Peng-Robinson equation of state to determine regional CO_2 fluid density with depth (Fig. 5.5). We used this relationship to calculate CO_2 fluid density at the midpoint depth of the Miocene CI for each grid. The midpoint depth was derived by subtracting the top of CI depth map from the base of CI depth map.

The depth to the top of the Miocene CI (fig. 5.6A) is the result of integrating the top Miocene (*Bigenerina A*) structure map (fig. 5.3A) where it exceeded 3,300 ft (1,005 m). The stratigraphic top of Miocene is shallower than 3,300 ft in most of the project area; the only exceptions are small areas on the far upper coast and in far south Texas (fig. 5.6A). Thus, the depth to top of the Miocene CI is 3,300 ft throughout most of the project area (gray area in fig. 5.6A).

The depth to base of the Miocene CI (fig. 5.6B) map was created by integrating the base of the Miocene structure (Anahuac MFS as discussed above; converted to depth) map and Pitman's (2011) "Top of Geopressure" map. The two grids were compared at each location, and the shallower value was taken to represent the depth to base of the Miocene CI. The resulting

map (fig. 5.6B) ranges from 4,000 ft (1,220 m) in the San Patricio County/Corpus Christi Bay Area to a maximum of about 11,000 ft (3,350 m) in far south Texas and offshore of the far upper coast bordering Louisiana.

Net Reservoir Sandstone Interpretations

We interpreted net reservoir sandstones and counted (summed) the intervals over the Miocene CI in 1,876 wells (fig. 5.6C). SP curves were the favored and primary data source utilized to identify and quantify net reservoir sandstone within the Miocene CI. The GR curve does not differentiate between porous (permeable) and tight (low-porosity, impermeable) sandstone and, thus, slightly overestimates net reservoir sandstone; it was, nonetheless, useful in a few wells where no SP was available. SP curves were first straightened along a shale baseline in order to eliminate downhole drift and/or scale shifts. Then, the SP curves were normalized to a scale from -100 to 0 millivolts (mv). Likewise, for wells lacking SP curves, the GR curve was normalized using a shale volume method (e.g., Asquith and Krygowski, 2004).

We counted net permeable reservoir sandstone from SP in two ways: (1) direct interpretation from raster images, and (2) automated summation from straightened, normalized vector SP curves (LAS). In both cases, we used a guideline cutoff, beyond which the SP deflection from a "shale base line" (Schlumberger, 1998a) was sufficiently negative to indicate permeable sandstone. The cutoffs for the raster sand counts were more subjective than those for the LAS curves because the interpretations of SP readings directly from raster images are non-normalized and the interpreter must choose a cutoff or even multiple cutoffs within a given well, such that most of the obvious permeable sandstone can be differentiated from the impermeable rocks below the "shale base line" (Schlumberger, 1998a).

Further, the cutoff line was used as a guide rather than as a strict quantitative boundary, since the tops and bases of individual sandstone beds are marked by inflection points in the curves that depend upon bed thickness (e.g., Schlumberger, 1998). Although inflection points are typically very close to a given cutoff, they are frequently not *exactly* aligned with them such that the summation of net reservoir sandstone picked by raster inspection may vary slightly from that summed using the LAS curve of the same SP log. These differences are essentially negligible so we used LAS SP curves to automate the net reservoir sandstone-picking process, where data was available because it is much faster, reproducible, and less prone to user error and/or bias.

For straightened, normalized SP curves, we defined net reservoir sandstone to be where the SP reading was less than -50 mv. For shale volume curves from the GR, we used a less-than-50% cutoff to define net reservoir sandstone.

Porosity Estimation

Vector (LAS) porosity curves covering all or most of the Miocene interval were available for 230 wells in the mapping area (fig. 5.6D). Sonic porosity was the favored measurement for the Miocene average-porosity estimates because of the greater number of wells for which sonic data were available and also because sonic logs are not greatly affected by borehole rugosity, as are density tools. Raster porosity logs were also available for additional wells, but because of time/cost constraints were not utilized for porosity estimation.

Sonic porosity was calculated using the empirical, core-calibrated equation of Raymer et al. (1980):

$$PHIS\_SS = 0.67 * (1 - (DT_M / DT)) \quad (3)$$

where,

PHIS = Sonic porosity, sandstone matrix

DT = Sonic log reading (μ-sec/ft)

DT_M = Sonic delta-t constant for rock matrix (sandstone = 55.5 μ-sec/ft)

DT_{FL}= Sonic delta-t constant for fluid (salt water = 189 μ-sec/ft).

Density porosity was calculated using Schlumberger (1998b):

$$PHID\_SS = ((RHOB - RHO_M) / (RHO_{FL} - RHO_M)) \quad (4)$$

where,

PHID = Density porosity (decimal)

RHOB = Bulk density log reading (gm/cm^3)

RHO_M = Matrix density constant, sandstone = 2.65 gm/cm^3

RHO_{FL}= Fluid density constant, brine = 1.0 gm/cm^3.

The number and aerial distribution of porosity data points was not as robust compared to the net reservoir sandstone data set in the project area, so we supplemented our own log measurements with 67 average reservoir-porosity values published for producing oil and gas fields (Galloway and others, 1983; Kosters and others, 1989; Seni and others, 1997; BOEM, 2010). Most of these are located in South Texas, where our data set is relatively thin compared to that of the upper Texas coast (e.g., fig. 5.1).

Reservoir Summations

After determining permeable net reservoir sandstone in wells containing pertinent data (raster or LAS, as described above), we used the computer to sum the total footage of all the

intervals we defined as permeable net sandstone (total thickness in feet) within the Miocene CI. The net reservoir sandstone values were gridded and contoured. The resulting Miocene isoporosity map is shown in figure 5.6C.

Similarly, after calculating porosity from LAS curves, we performed an automated reservoir summation to calculate the average porosity within intervals previously defined (by raster or LAS methods described above) as permeable net reservoir sandstone over the Miocene CI. The average porosity values were posted, gridded, and contoured. The resulting Miocene isoporosity map is shown in figure 5.6D.

Results: Miocene Static Capacity Estimate

Table 5.3 lists quantitative and statistical results of the capacity estimate for the median (P_{50}) case. The aerial distribution of capacity shown in figure 5.8 displays the potentially storable volumes of CO_2 per square kilometer in the project area, using the methodology of Wallace and others (2014) (equation 2). Over the 42,261 km^2 (16,317 mi^2) Total Project Area, an estimated 124.9 Gigatonnes (Gt) of CO_2 can potentially be stored within the Miocene CI (fig. 5.8A). Over the 9,875 km^2 (3,813 mi^2) of offshore Texas State Waters that lie within the Total Project Area, we estimate 30.1 Gt of CO_2 can potentially be stored within the Miocene CI (fig. 5.8B).

Table 5.3. Summary statistics of the CO_2 capacity estimate results (P_{50})

Property	Total Project Area	Offshore Texas State Waters
Area	42,261 km^2 (16,317 mi^2)	9,875 km^2 (3,813 mi^2)
Estimated CO_2 Capacity (P_{50})	124.9 Gt CO_2/km^2	30.1 Gt CO_2/km^2

Average	*2.99 Mt CO^2/km^2*	*3.09 Mt CO^2/km^2*
Range	*0 to 8.7 Mt CO^2/km^2*	*0 to 7.42 Mt CO^2/km^2*
Standard Deviation	*1.46 Mt CO^2/km^2*	*1.41 Mt CO^2/km^2*
Statistical *n* (number of measured grid cells)	41,777	9,767

We did not use our grid model to calculate P_{10} and P_{90} but rather our P_{50} estimate, employing a simple proportional calculation using (1) efficiency factors for clastic reservoirs—i.e., 0.51% and 5.4% for P_{10} and P_{90}, respectively (table 5.1; Goodman and others, 2011)—and, (2) our P_{50} capacity estimates and the efficiency factors we used to derive them (P_{50} E_{Saline}= 2%). For the Total Project Area, P_{10} CO_2 Capacity is 31.7 Gt CO_2, and P_{90} CO_2 Capacity is 336.2 Gt CO_2 (equations 5 and 6, respectively):

$$\mathbf{P_{10}}\ CO_2\ \text{Capacity} = (0.0051/0.02) * 124.5\ \text{Gt}\ CO_2 = \mathbf{31.7\ Gt\ CO_2} \quad (5)$$

$$\mathbf{P_{90}}\ CO_2\ \text{Capacity} = (0.054/0.02) * 124.5\ \text{Gt}\ CO_2 = \mathbf{336.2\ Gt\ CO_2}. \quad (6)$$

Likewise, for the offshore Texas State Waters, P_{10} CO_2 Capacity is 7.7 Gt CO_2 and P_{90} CO_2 Capacity is 81.3 Gt CO_2 (equations 7 and 8, respectively):

$$\mathbf{P_{10}}\ CO_2\ \text{Capacity} = (0.0051/0.02) * 124.5\ \text{Gt}\ CO_2 = \mathbf{7.7\ Gt\ CO_2} \quad (7)$$

$$\mathbf{P_{90}}\ CO_2\ \text{Capacity} = (0.054/0.02) * 124.5\ \text{Gt}\ CO_2 = \mathbf{81.3\ Gt\ CO_2}. \quad (8)$$

Comparison of Capacity Estimate to other U.S. and International Estimates

We reviewed published capacity estimates for North America (United States and Canada) and for the world in order to put our results into perspective. DOE (2012) North American capacity estimates are provided in table 5.4 and capacity estimates for various regions of the world, in table 5.5.

A glance at the DOE (2012) P_{10} and P_{90} CO_2 capacity estimates for U.S. states and Canadian provinces shown in table 5.4 illustrates that the Miocene of the Texas coast and State Waters is significant compared to other entire states/provinces. Only the top 11 states/provinces and the U.S. Federal OCS have P_{90} CO_2 capacity estimates that exceed estimates for the Miocene of the Total Project Area. The P_{10} CO_2 capacity estimates in table 5.4 vary less systematically than the P_{90} values; overall, they also illustrate that P_{10} CO_2 capacity estimates for the Miocene of the Total Project Area are also comparable to estimates made for the top third of other states/provinces.

Internationally, our CO_2 capacity estimates compare favorably to those published for entire countries. The P_{10} and P_{90} CO_2 capacity estimates for the offshore Texas State Waters are of similar magnitude or exceed the bottom half of capacity estimates made for other entire states/provinces (cf., table 5.4). The high-side estimates (P_{90}) for the offshore Texas State Waters compare favorably to estimates made for northern Europe, Norway, and the state of Queensland, Australia.

Table 5.4. DOE (2012a) CO_2 capacity estimates, U.S. states and Canadian provinces; Gt = 10^9 tonnes

Rank	State/Province	P_{10} Estimate (Gt CO_2)	P_{90} Estimate (Gt CO_2)
1	U.S. Federal OCS	489.8	6,440.1
2	Texas	443.8	4,329.9
3	Louisiana	169.5	2,104.0
4	Mississippi	145.0	1,185.0
5	Montana	84.6	912.7
6	Alabama	122.5	694.4
7	Wyoming	72.7	684.9
8	Florida	102.7	555.0
9	Washington	36.6	496.7
10	California	33.9	420.6
11	New Mexico	42.8	359.1
12	Colorado	37.6	357.2
13	Oklahoma	57.0	244.6
14	Utah	25.5	240.9
15	Georgia	145.3	159.1
16	North Dakota	67.1	147.5
17	Alberta	41.8	131.2
18	Saskatchewan	38.7	121.9
19	Illinois	10.0	116.8
20	Nebraska	23.8	113.2
21	Oregon	6.8	93.7
22	Kansas	10.9	86.3
23	Indiana	32.0	68.2
24	Arkansas	6.2	63.7
25	Michigan	19.1	47.2
26	South Carolina	30.1	34.2
27	South Dakota	8.8	24.0
28	Pennsylvania	22.1	22.1
29	Alaska	8.6	19.8
30	North Carolina	1.3	18.4
31	West Virginia	16.7	16.7
32	Ohio	13.5	13.5
33	Kentucky	2.92	7.65
34	New York	4.64	4.64
35	British Columbia	0.91	3.86
36	Tennessee	0.43	3.86
37	Manitoba	1.72	3.52
38	Virginia	0.44	2.91
39	Maryland	1.86	1.93
40	Arizona	0.13	1.17
41	Idaho	0.04	0.39
42	Missouri	0.01	0.17
43	Iowa	0.01	0.05
44	Delaware	0.04	0.04
na	North America Total	2,379.8	20,352.7

Table 5.5. CO_2 capacity estimates, various regions of the world; Gt = 10^9 tonnes

Geographical Region	CO_2 Capacity Estimate	Reference	Methodology	Comments
World	1,678–11,100 Gt	Benson and others (2005)	Various, a broad compilation of what appear to be theoretical static volumetric estimates	Sum of depleted hydrocarbon fields, saline aquifers, and unmineable coal seams; upper estimate includes 10^4 Gt for saline aquifers, which is uncertain.
Mexico	100 Gt	DOE (2012b)	Static volumetric	Theoretical CO_2 storage resource estimate for saline aquifers in nine assessed geological provinces. Includes onshore and offshore areas adjacent to and under Gulf of Mexico waters.
Northern Europe	49 Gt	Höller and Viebahn (2011)	Static volumetric	Includes countries where German CO_2 emissions could possibly be stored: Germany, Netherlands, France, Denmark, Norway, UK, Poland. Most of this capacity (36 Gt) is from offshore North Sea of Norway and the UK.
Norway	72 Gt	Halland and others (2011)	Static volumetric	All capacity is located offshore. Sum of saline aquifers and petroleum field related capacity.
Queensland, Australia	53 Gt	Bradshaw and others (2010)	Static volumetric	Estimate is based on calculation of conservative maximum theoretical storage volumes accounting for the extent of highly prospective reservoir-seal intervals in “high-prospectivity” basins.
China	3,160 Gt	Li and others (2009)	Static volumetric	Onshore and offshore

Conclusions

Using a large and robust subsurface data set covering 42,261 km^2 (16,317 mi^2) of coastal Texas and the adjacent offshore ("Total Project Area"), including the immediately adjacent 9,875 km^2 (3,813 mi^2) of the offshore Texas State Waters, we have demonstrated that the Miocene sandstone-bearing interval presents a world-class opportunity for geological CO_2 sequestration. Using a modified NETL-DOE static CO_2 "net"-capacity estimate methodology (Goodman and others, 2011; Wallace and others, 2014), we estimate P_{50} net capacity for the Miocene sandstone-bearing interval in the Total Project Area to be 124.5 Gt CO_2. In the smaller offshore Texas State Waters, which is a subset of the Total Project Area, we estimate P_{50} net capacity for the Miocene interval to be 30.1 Gt CO_2.

Our offshore Texas Miocene CO_2 capacity estimates are noticeably high compared to many estimates from other states and countries (Tables 5.4 and 5.5). This is due to the unusually large pore volumes offered by the thick, high net-to-gross, and high porosity Miocene strata of the northern Gulf of Mexico Basin which are geologically young and typically only mildly altered compared to those of many areas, e.g., Europe, Australia, or South Africa. Future, more detailed studies that consider confining and fault seal capabilities, and dynamic parameters will undoubtedly whittle down our estimates.

Although our calculations in this paper do not include detailed reservoir, seal, or trap analyses, the Miocene of the northern Gulf of Mexico is well documented and well understood such that we feel confident that it provides excellent CO_2 sequestration potential. Multiple stacked reservoir sandstones with high porosity and permeability provide very large pore volumes for potential CO_2 injection and storage. Thick mudrock intervals provide low-permeability regional seals that have proven to be adequate for natural-gas trapping on geologic

time scales. Structural deformation from salt tectonism and extensional growth faulting has created numerous effective trap types that are observed throughout the region. Approximate depths to the top of the Miocene interval lie at favorable drilling depths of 1000 m (3300 ft) and typically contain a 300–600-m (1000–2000-ft) thickness of stacked sandstone reservoir intervals.

Coastal Texas is particularly well positioned to capitalize on the Miocene geological CO_2 sequestration opportunity. Multiple CO_2 point sources either immediately overlie (onshore) or are relatively close to adjacent offshore. This proximity, as well as the existing offshore pipeline infrastructure, facilitates use of offshore reservoirs and may potentially reduce transportation costs. Numerous depleted offshore Miocene oil and gas fields may be available for initial storage and/or enhanced recovery targets. More than 60 years of offshore oil and gas exploration and production in the region have generated robust data sets, facilities infrastructure, geological and engineering knowledge, and general cultural acceptance of offshore subsea and subsurface operations.

In addition to the above, the offshore Texas State Waters provide two more distinct advantages when compared to onshore geological CO_2 sequestration sites: (1) environmental risks of sequestration are lower, given the lack of potable groundwater; and (2) the "single landowner" (i.e., State of Texas) status allows for simpler land rights and liabilities assessment. The Federal OCS waters also possess the advantages of "single landowner" and lack of potable groundwater. Further, the plethora of oil and gas accumulations that have been discovered and produced from Miocene and other Tertiary sandstone reservoirs further offshore in the Federal OCS suggests that future work to detail CO_2 capacity there would be fruitful.

Acknowledgments

This research was supported by the National Energy Technology Laboratory (NETL), the United States Department of Energy (DOE), and the Texas General Land Office (GLO). We thank the Bureau of Ocean Energy Management (BOEM; formerly Minerals Management Service) for providing a wealth of digital data (e.g., well information, directional surveys, paleo reports, and reservoir properties) free and available for download. Dr. William E. Galloway's deep knowledge of Gulf of Mexico geology sedimentary helped point us to the Miocene interval. Dr. Galloway's associates Patty Ganey-Curry and John Snedden of the Gulf Basin Depositional Synthesis group, University of Texas Institute for Geophysics, lent contextual mapping information that made our interpretations and products stronger.

References

Asquith, G., and Krygowski, D., 2004, Basic well log analysis: AAPG Methods in Exploration 16, p. 31–35

Bachu, S., 2003, Screening and ranking of sedimentary basins for sequestration of CO_2 in geologic media in response to climate change: Environmental Geology, v. 44, p. 277–289.

Bachu, S., and Gunter, W. D., 2003, Acid gas injection in the Alberta Basin, Canada: a CO_2 storage experience: Geological Society of London Special Publications, v. 233, p. 225–234.

Benson, S., P. Cook, and others, 2005, Chapter 5: Underground geological storage, *in*: IPCC, 2005: IPCC Special Report on Carbon Dioxide Capture and Storage. Prepared by Working Group III of the Intergovernmental Panel on Climate Change [Metz, B., O. Davidson, H. C. de Coninck, M. Loos, and L. A. Meyer (eds.)]. Cambridge University Press, Cambridge, United Kingdom and New York, NY, USA, 442 pp., p. 195–276.

Bradshaw, B. E., Spencer, L. K., Lahtinen, A., Khider, K., Ryan, D. J., Colwell, J. B., Chirinos, A., Bradshaw, J., Draper, J. J., Hodgkinson, J., and McKillop, M., 2010, An assessment of Queensland's CO_2 geological storage prospectivity—the Queensland CO_2 Geological Storage Atlas, The 10th International Conference on Greenhouse Gas Control Technologies (GHGT-10).

Bureau of Ocean Energy Management (BOEM; formerly Minerals Management Service), 2010, Paleontologic Information, Releasable Paleo Reports (downloaded ACSII data set files): https://www.data.boem.gov/homepg/data_center/paleo/paleo.asp [accessed 1/11/2010 and 4/17/2013]

DOE (U.S. Department of Energy), 2010 carbon sequestration atlas of the United States and Canada online: National Energy Technology Laboratory, 3rd Ed. Available at http://www.netl.doe.gov/technologies/carbon_seq/refshelf/atlas/index.html [accessed 1 March 2013]

DOE (U.S. Department of Energy), 2012a, Carbon utilization and storage atlas of the United States: National Energy Technology Laboratory, 4th Ed. Available at http://www.netl.doe.gov/technologies/carbon_seq/refshelf/atlas/index.html [accessed 1 March 2013]

DOE (U.S. Department of Energy), 2012b, North American Carbon Storage Atlas: National Energy Technology Laboratory, 1st Ed. Available at http://www.netl.doe.gov/research/coal/carbon-storage/cs-global/nacap [accessed July 2, 2012]

Eiken, O., Ringrose, P., Hermanrud, C., Nazarian, B., Torp, T. A., and Høier, L., 2011, Lessons learned from 14 years of CCS operations: Sleipner, In Salah, and Snøhvit: Energy Procedia, v. 4, p. 5541–5548.

Elewaut, E., van der Straaten, R., Koelewijn, D., Baily, H. E., Holloway, S., Barbier, J., Lindeberg, E., Moller, H., and Gaida, K. H., 1996, Inventory of the theoretical CO_2 storage capacity of the European Union and Norway, *in* The Underground Disposal of Carbon Dioxide, final report of JOULE II project no. Ct92-0031.

EPA (U.S. Environmental Protection Agency), Inventory of U.S. greenhouse gas emissions and sinks 1990–2010 http://www.epa.gov/climatechange/ghgemissions/usinventoryreport.html [accessed 1 March 2013]

Fillon, R. H., and Lawless, P. N., 2000, Lower Miocene–early Pliocene deposystems in the Gulf of Mexico: regional sequence relationships: Gulf Coast Association of Geological Societies Transactions, v. 50, p. 411–428.

Fillon, R. H., Lawless, P. N., and Lytton, R. G., III, 1997, Gulf of Mexico Cenozoic biostratigraphic and cycle charts, *in* Lawless, P. N., Fillon, R. H., and Lytton, R. G., III, Gulf of Mexico Cenozoic biostratigraphic, lithostratigraphic, and sequence stratigraphic event chronology: Gulf Coast Association of Geological Societies Transactions, v. 47, p. 271–282.

Gale, J., Christensen, N. P., Cutler, A., and Torp, T. A., 2001, Demonstrating the potential for geologic storage of CO_2: the Sleipner and GESTCO projects: Environmental Geoscience v. 8, p. 160–165.

Galloway, W. E., 2001, Cenozoic evolution of sediment accumulation in deltaic and shore-zone depositional systems, Northern Gulf of Mexico Basin: Marine and Petroleum Geology, v. 18, p. 1031–1040.

Galloway, W. E., Ewing, T. E., Garrett, C. M., Tyler, N., and Bebout, D. G., 1983, Atlas of major Texas oil reservoirs: The University of Texas at Austin, Bureau of Economic Geology Special Publication, 139 p. plus plates.

Galloway, W. E., Ganey-Curry, P., Li, X., and Buffler, R. T., 2000, Cenozoic depositional evolution of the Gulf of Mexico Basin: AAPG Bulletin, v. 84, p. 1743-1774.

Galloway W. E., Whiteaker, T. L., and Ganey-Curry, P., 2011, History of Cenozoic North American drainage basin evolution, sediment yield, and accumulation in the Gulf of Mexico basin: Geosphere, v. 7, p. 938–973.

Goodman, A., Hakala, A., Bromhal, G., Deel, D., Rodosta, T., Frailey, S., Small, M., Allen, D., Romanov, V., Fazio, J., Huerta, N., McIntyre, D., Kutchko, B., and Guthrie, G., 2011, U.S. DOE methodology for the development of geologic storage potential for carbon dioxide at the national and regional scale: International Journal of Greenhouse Gas Control, v. 5, no. 4, p. 952–965.

Halland, E.K , W.T. Johansen, and F. Riis (Eds.), 2011, CO_2 Storage Atlas, Norwegian North Sea: Norwegian Petroleum Directorate, Stavanger, Norway; 72 p. Available at http://www.npd.no/Global/Norsk/3-Publikasjoner/Rapporter/PDF/CO2-ATLAS-lav.pdf [accessed January 26, 2012]

Höller, S., and Viebahn, P., 2011, Assessment of CO_2 storage capacity in geological formations of Germany and Northern Europe: Energy Procedia 4, GHGT-10; Elsevier Ltd., p. 4897–4904.

Holloway, S., 2001, Storage of fossil fuel derived carbon dioxide beneath the surface of the earth: Annual Review of Energy and the Environment, v. 26, p. 145–166.

Kosters, E. C., Bebout, D. G., Seni, S. J., Garrett, C. M., Jr., Brown, L. F., Jr., Hamlin, H. S., Dutton, S. P., Ruppel, S. C., Finley, R. J., and Tyler, Noel, 1989, Atlas of major Texas gas reservoirs: The University of Texas at Austin, Bureau of Economic Geology, 161 p.

Lackner, K. S., 2003, A guide to CO_2 sequestration: Science, v. 300, no. 5626, p. 1677–1678.

Li, X., Wei, N., Liu, Y., Fang, Z., Dahowski, R.T., Davidson, C.L., 2009, CO_2 point emission and geological storage capacity in China: Energy Procedia v. 1, p. 2793–2800.

Litynski, J. T., Plasynski, S., McIlvried, H. G., Mahoney, C. and Srivastava, R. R., 2008, The United States Department of Energy's regional carbon sequestration partnerships program validation phase: Environment International, v. 34, p. 127–138.

Nicholson, A. J., 2012, Empirical analysis of fault seal capacity for CO_2 sequestration, lower Miocene, Texas Gulf Coast: The University of Texas at Austin, Master's thesis, 88 p. http://repositories.lib.utexas.edu/handle/2152/ETD-UT-2012-05-5606.

Pitman, J. K., 2011, Reservoirs and petroleum systems of the Gulf Coast: depth to top overpressure 2011 [map] http://www.datapages.com/Services/GISUDRIL/OpenFiles/ReservoirsandPetroleumSystemsoftheGulfCoast.aspx [accessed 1 March 2013]

Raymer, L. L., Hunt, E. R. and Gardner, J. S., 1980, An improved sonic transit time-to-porosity transform: SPWLA 21st Annual Logging Symposium, July 8–11, p. 1–12.

Schlumberger, 1998a, Chapter 3: Spontaneous potential and natural gamma ray logs, *in* Log interpretation principles/applications, Schlumberger Wireline & Testing, Sugar Land, Texas, 11 p.

Schlumberger, 1998b, Chapter 5: Porosity logs, *in* Log interpretation principles/applications, Schlumberger Wireline & Testing, Sugar Land, Texas, 24 p.

Seni, S. J., Hentz, T. F., Kaiser, W. R., and Wermund, E. G., Jr. (eds.), 1997, Atlas of northern Gulf of Mexico gas and oil reservoirs: Volume 1, Miocene and older reservoirs, Texas Bureau of Economoic Geology, Gas Research Institute, Department of Energy, and Minerals Management Service, 199 p. plus plates and CD-Rom.

Trevino, R. H., Loucks, R. G., Brown, L. F., Jr., and Remington, R. L., 2003, General geology of the mid-Tertiary Block 889 field area, offshore Mustang Island, Texas: Gulf Coast Association of Geological Societies Transactions, v. 53, p. 802–814.

Tsang C. F., Benson, S. M., Kobelski, B., and Smith, R.E., 2002, Scientific considerations related to regulation development for CO_2 sequestration in brine formations: Environmental Geology, v. 42, p. 275–281.

U.S. Census Bureau, 2010, State Area Measurements and Internal Point Coordinates. Available at https://www.census.gov/geo/reference/state-area.html [accessed September 5, 2014]

Vangkilde-Pedersen, T., Anthonsen, K. L., Smith, N., Kirk, K., Neele, F., van der Meer, B., Gallo, Y. L., and others, 2009, Assessing European capacity for geological storage of carbon dioxide—the EU GeoCapacity project: Energy Procedia, v. 1, p. 2663–2670.

Wallace, K. J., Meckel, T. A., Carr, D. L., Treviño, R. H., and Yang, C., 2014, Regional CO_2 sequestration capacity assessment for the coastal and offshore Texas Miocene interval: greenhouse gases: Science and Technology, v. 4, no. 1, p. 53–65.

Wallace, R. H., Jr., Wesselman, J. B., and Kraemer, T. F., 1981, Occurrence of geopressure in the Northern Gulf of Mexico Basin: Fifth Conference on Geopressured-Geothermal Energy, U. S. Geological Survey Map.

Chapter 5 Figures

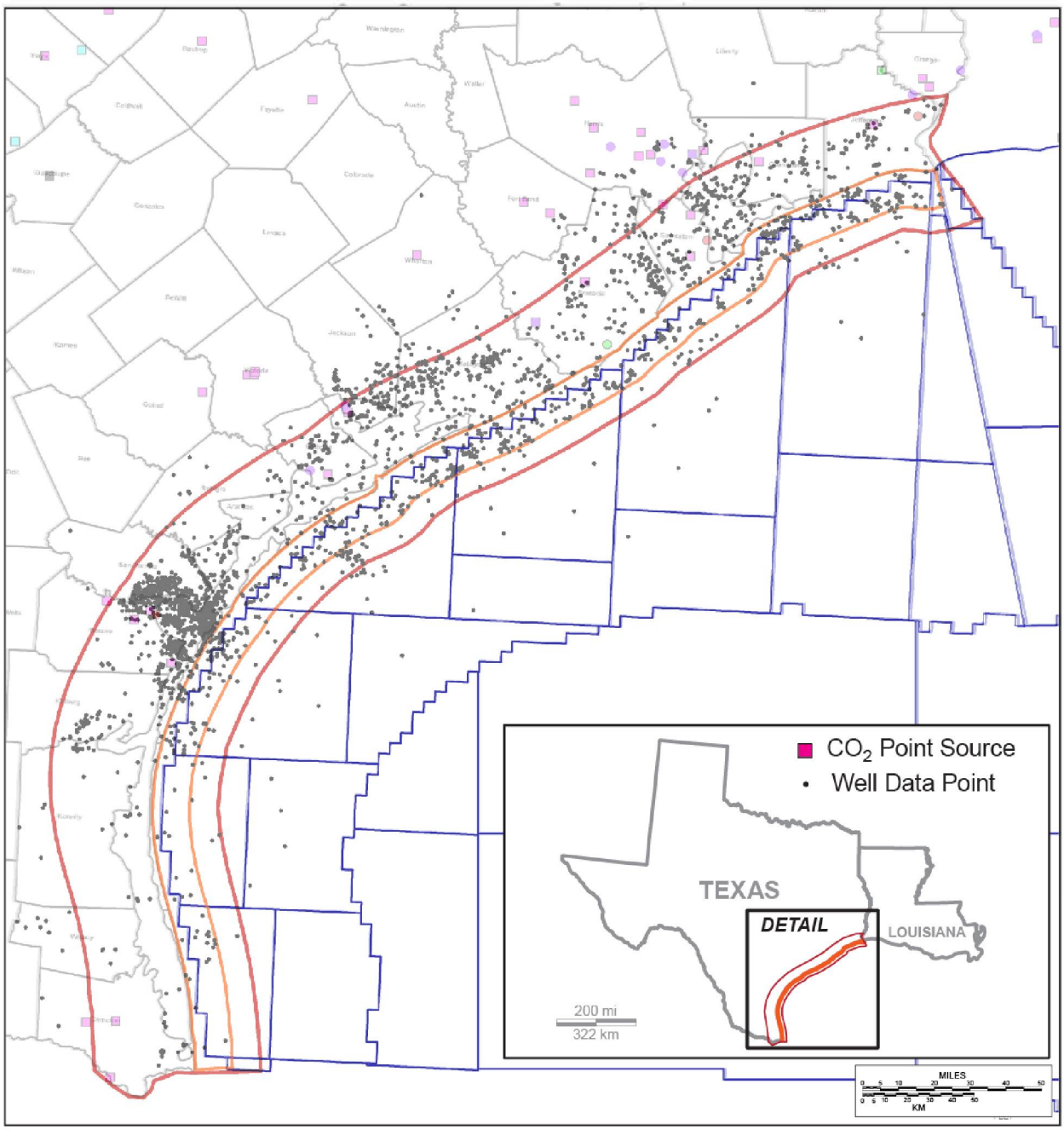

Figure 5.1. Location map showing study area and capacity estimate area geographic boundaries (dark red polygon), CO_2 point sources (magenta boxes), and outline of the offshore Texas State Waters (orange polygon). Black dots represent the 3,184 wells for which wireline log data, used for generating the regional static capacity estimate, were available.

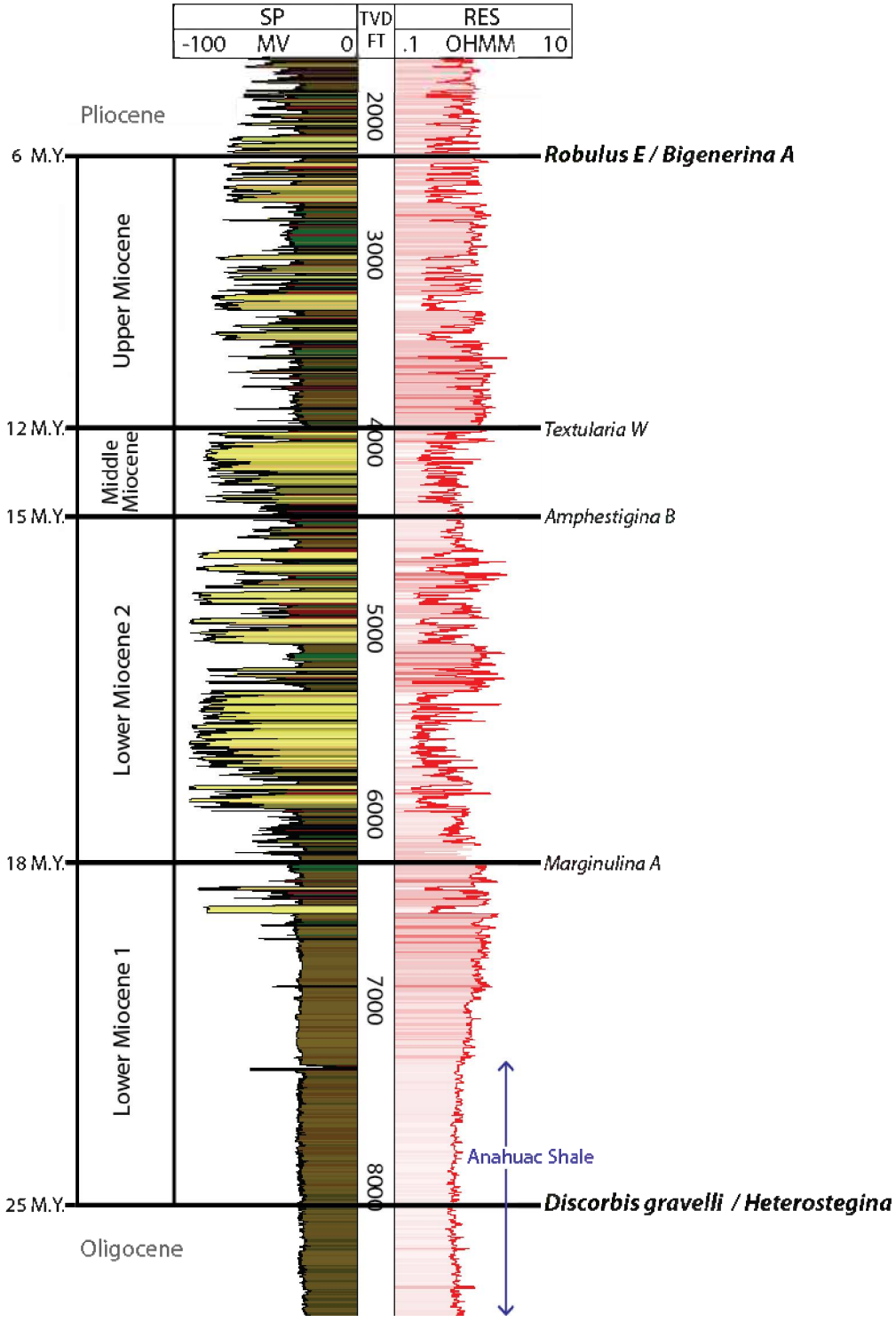

Figure 5.2. Type log of distal coastal and offshore Miocene interval showing major biostratigraphic tops used for regional interpretations, along with corresponding unit names (Galloway and others, 2000), paleontological markers, and geologic age. Spontaneous potential (SP) and deep resistivity (RES) curves

from Conquest Petroleum, State Tract #201, Brazoria Co., Texas. Modified from Wallace and others (2014).

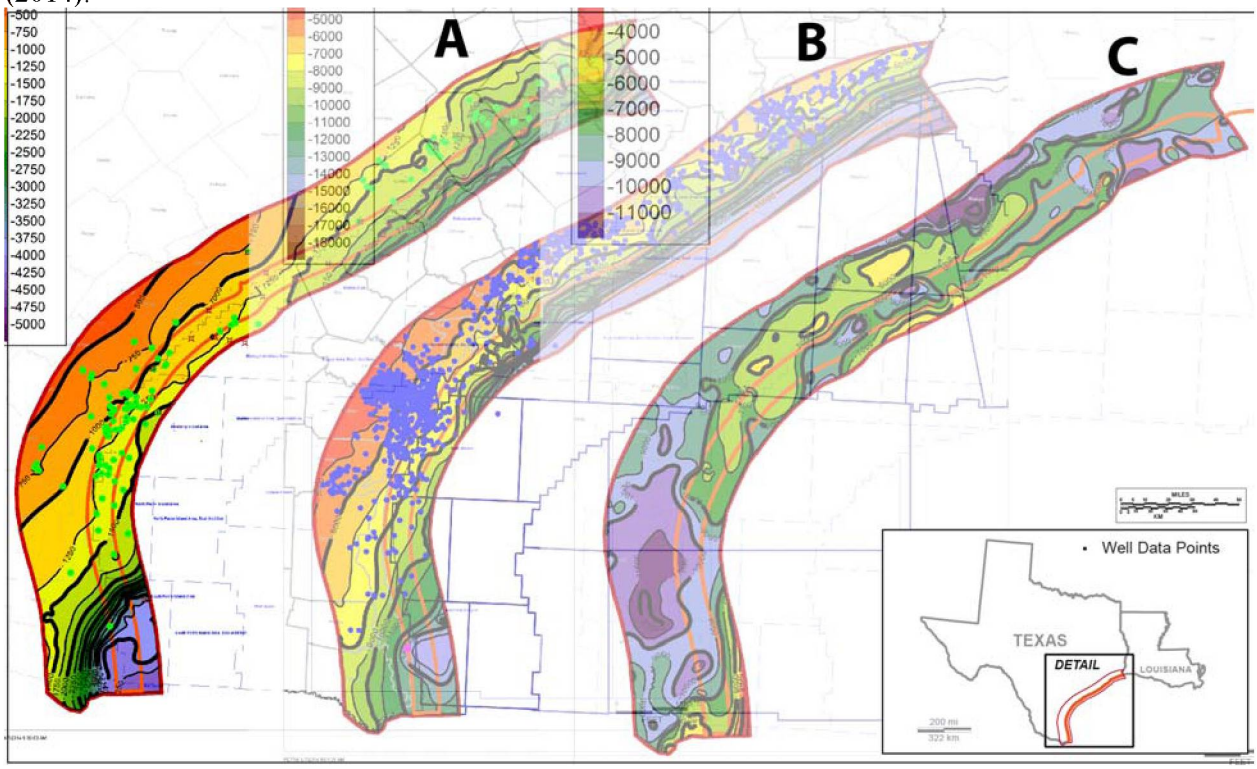

Figure 5.3. Structure maps (subsea true vertical depth: SSTVD) needed to define the Miocene interval in the study area. (A) Top of Miocene (*Bigenerina A* zone) made from 527 wells. (B) Base of Miocene, represented by the Anahuac maximum flooding surface made from 1,547 wells. (C) Top of overpressure, derived from Pitman (2011).

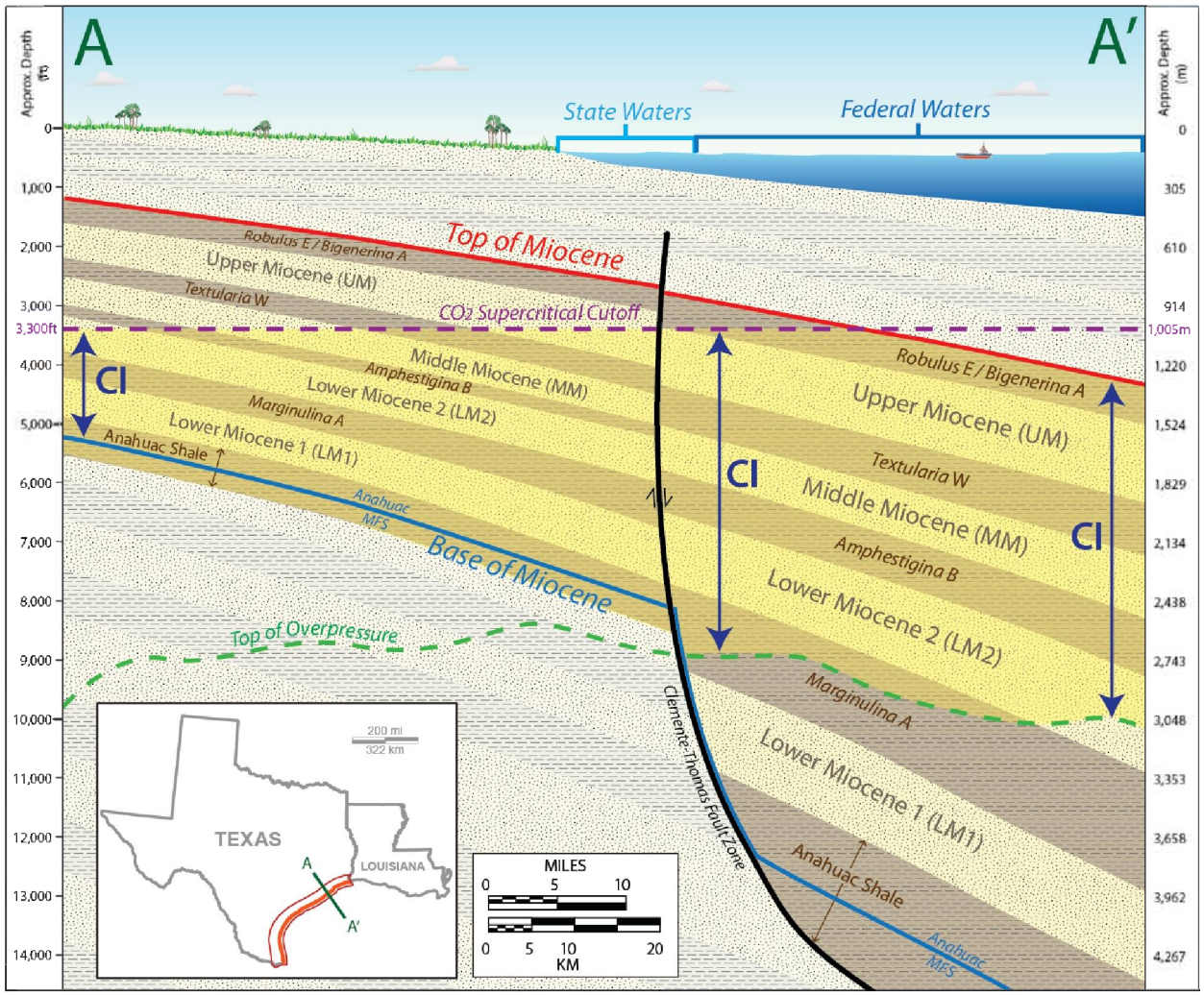

Figure 5.4. Schematic cross section showing the capacity interval (yellow) along with Miocene stratigraphy, with definitions from Galloway and others (2000). CI = Capacity Interval. The top of CI is defined as the top of either the Miocene or the CO_2 supercritical cutoff (3,300 ft, 1005 m), whichever is deeper. The base of CI is defined as either the base of the Miocene or the top of overpressure, whichever is shallower. Modified from Wallace and others (2014).

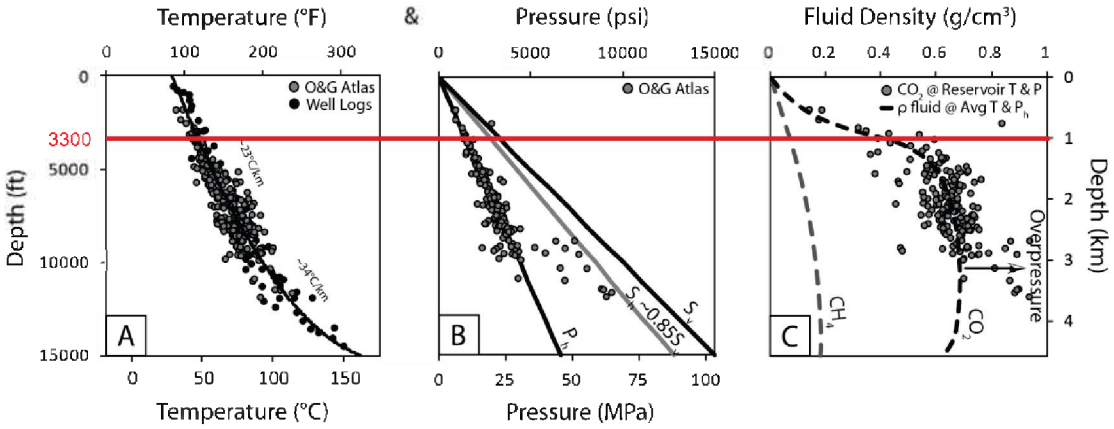

Figure 5.5. Charts for depth vs. temperature, pressure, and CO_2 fluid density, respectively, based on offshore Gulf of Mexico Miocene well data. Red line across all three charts represents the 3,300-foot upper depth limit for CO_2 supercritical behavior. Modified from Wallace and others (2014) after Nicholson (2012).

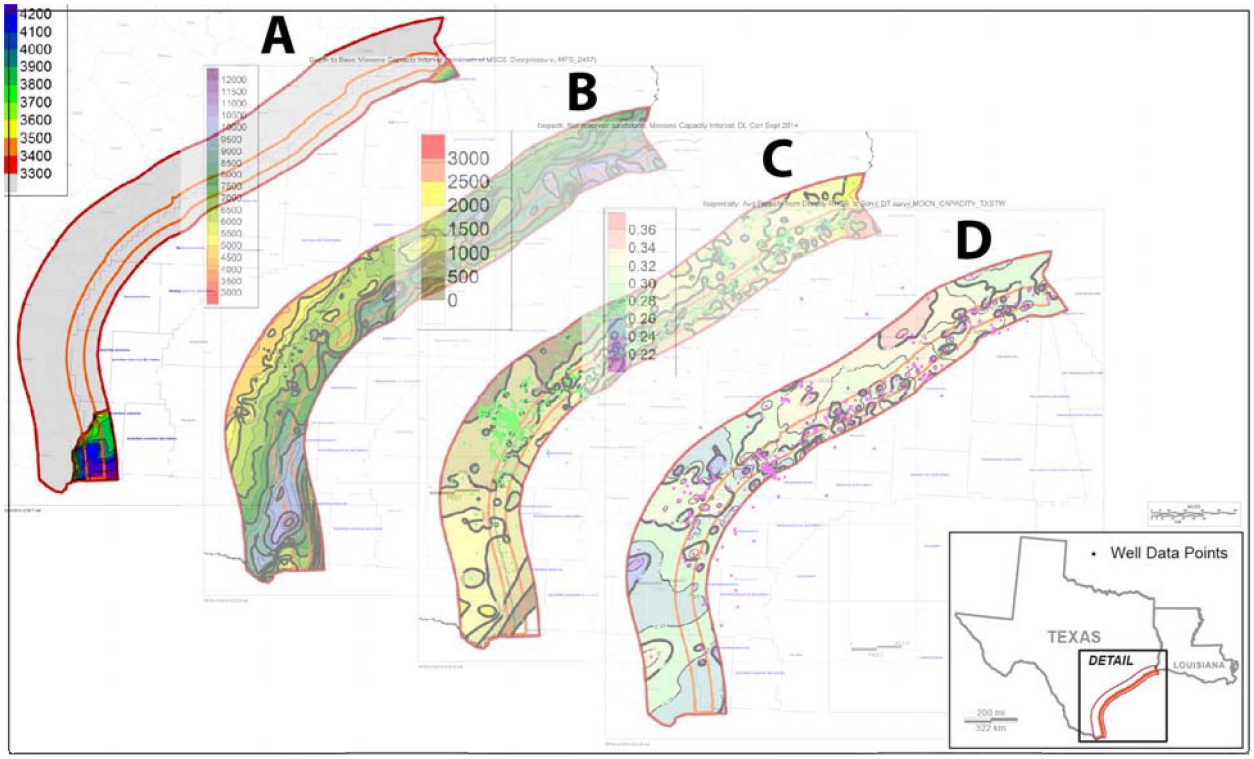

Figure 5.6. Input maps used to calculate net CO_2 capacity. (A) Depth (ft) to top of CI. (B) Depth (ft) to base of CI. (C) Net reservoir sandstone isopach (ft) of CI. (D) Average porosity isopach (dec) of CI.

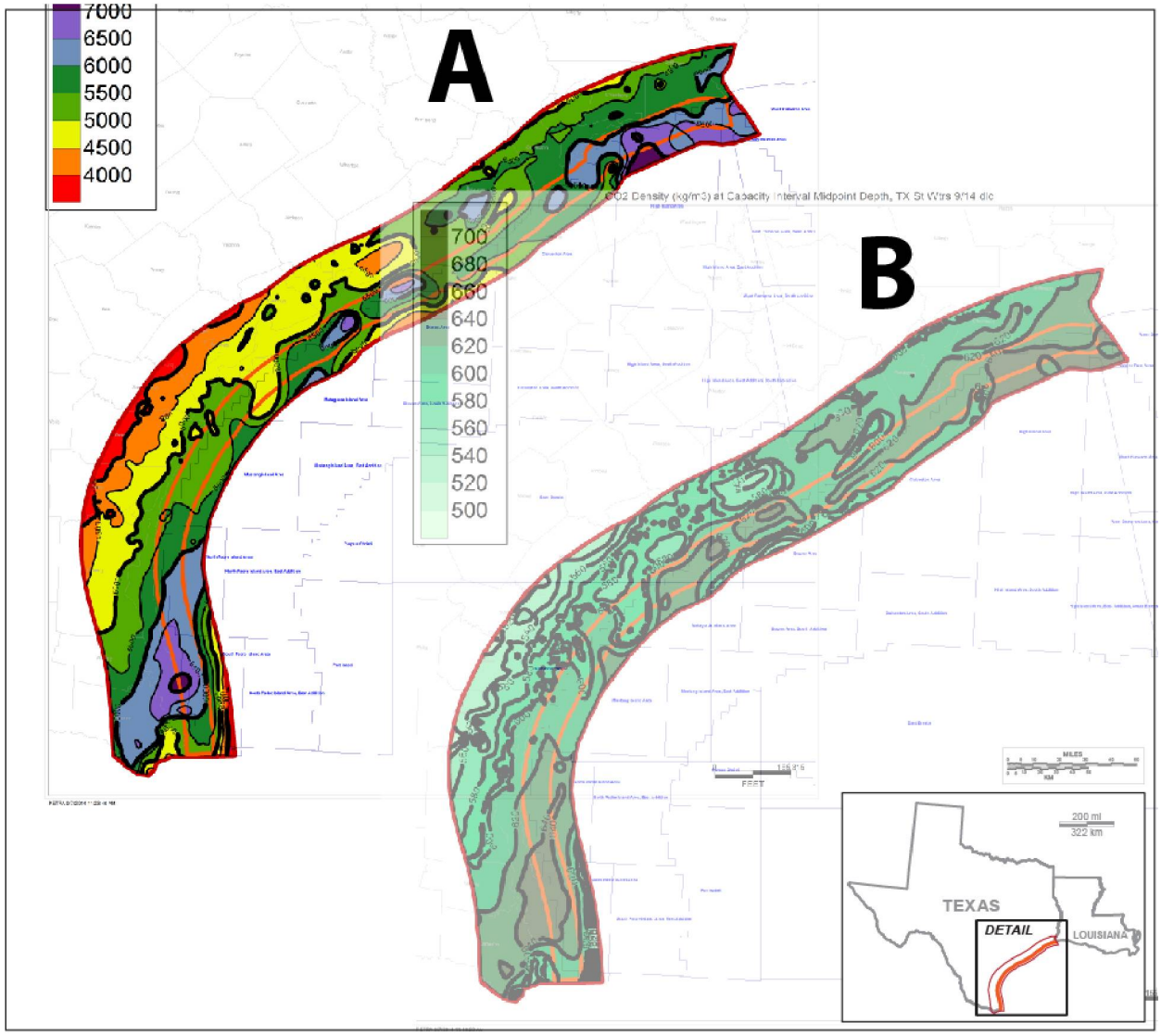

Figure 5.7. Output maps derived from the grid model calculation of CO_2 capacity. (A) Depth (ft) to midpoint of Miocene CI obtained by subtracting 3,300 ft from the depth to base of CI grid (fig. 5.6B). (B) CO_2 density (kg/m^3) of CI at midpoint depth of Miocene CI. Derived through the transform obtained for fluid density vs. depth shown in figure 5.4C.

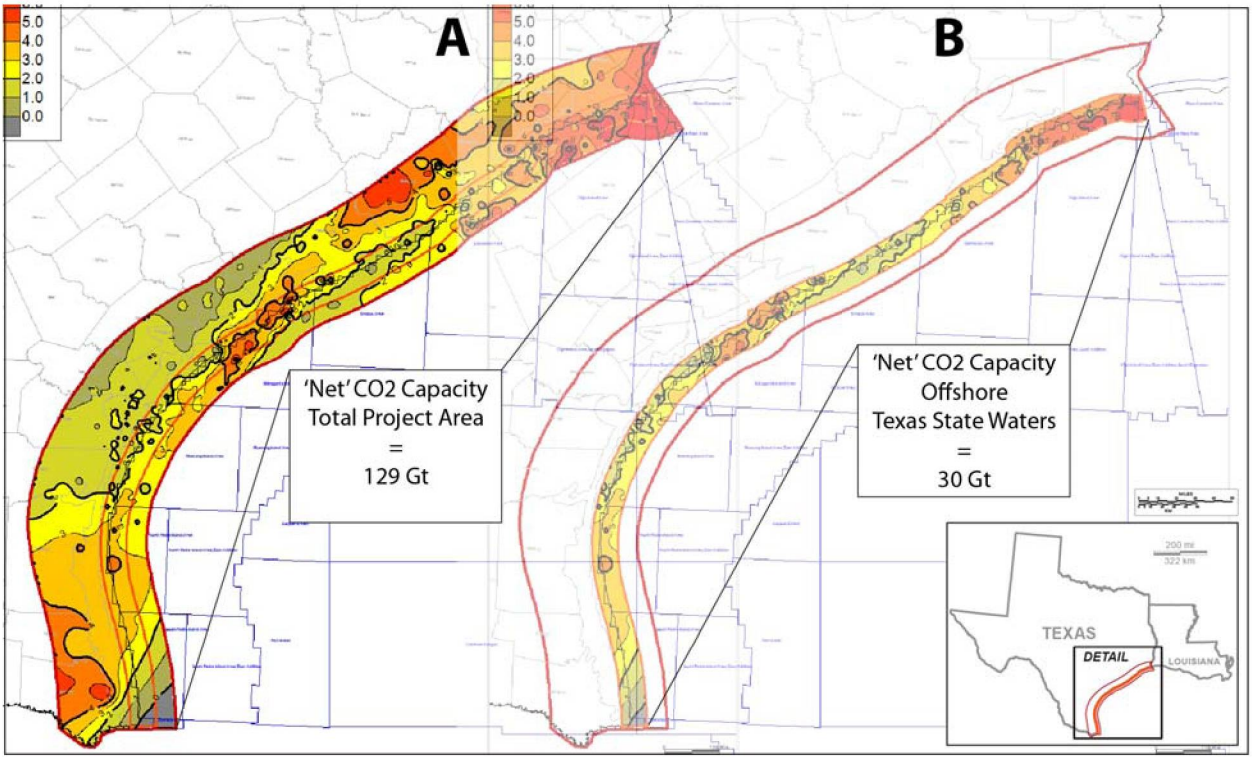

Figure 5.8. CO_2 isocapacity maps (kg/m^3) for (A) total study area, and (B) offshore Texas State Waters. Net capacity method of Wallace and others (2014) was utilized.

Chapter 6.1. Brazos Block 440-L Field

David L. Carr, Caleb Rhatigan, Ramon Trevino, Tip Meckel, Kerstan J. Wallace, Andrew J. Nicholson and Changbing Yang, Gulf Coast Carbon Center, Bureau of Economic Geology, The University of Texas at Austin, Austin, TX, USA

Introduction

An obvious place to look for CO_2 storage is where subsurface fluids have been trapped and "stored" naturally (i.e., known oil and gas reservoirs). The Brazos Block 440-L Field (fig. 6.1.1) has produced large volumes of natural gas (256 billion ft^3 gas equivalent, 1967–2010; fig. 6.1.2). According to the most recent available production data, the field now appears to be shut in (no longer producing). With a large, robust regional data set, we used 3D seismic, well logs, and micropaleontologic data to make a modified (Goodman and others, 2011) P_{50} static "net capacity" (Wallace and others, 2014) estimate for the lower Miocene *Marginulina ascensionensis* (Marg A) sandstone reservoirs that were the field's producing units in a 35.5 km^2 (13.7 mi^2, 8,768 ac; red polygon, fig. 6.1.1) footprint over the field. We also estimated net static capacity in the larger, surrounding study area (463 km^2, 179 mi^2, 114,575 ac; blue polygon outline, fig. 6.1.1). Based on this capacity estimate, proximity to multiple CO_2 sources and pipelines, and the availability of geological and engineering data/information on the Miocene subsurface in the offshore Texas Gulf of Mexico Basin, the Brazos Block 440-L Field has good potential as a sequestration target.

General Setting and Development History, Brazos Block 440-L Field

The Brazos 440-L Field (fig. 6.1.1) is located about 12 km (7.5 mi) off the shore of Matagorda Peninsula in Texas State Waters at depths of approximately 15–18 m (50–60 ft). The field was discovered by Shell in 1965 and produced from lower Miocene sandstone reservoirs beneath the *Marginulina ascensionensis* (Marg A) biozone mudrock interval. The productive Marg A reservoirs are

located at the apex of a compartmentalized rollover anticline located on the hanging wall of the Clemente-Tomas growth fault (Bradshaw and Watkins, 1994; McDonnell and others, 2009, 2010). We mapped a closed structure with approximately 122 m (400 ft) of relief within a 35.5 km^2 area (13.7 mi^2; 8,768 ac; red polygon, fig. 6.1.1). The field boundaries lie within a larger 466 km^2 area (179 mi^2; 114,575 ac; blue polygon, fig. 6.1.1) of study that provided structural and stratigraphic context for making the capacity estimate.

Figure 6.1.2 shows the field's gas and condensate ("oil") production history (Drillinginfo, Inc., data). 3D seismic data shot in 1995 clarified the complex faulting and compartmentalization in the field, which resulted in reserves growth during the mid- and late 1990's (Lane and Pace, 1998). No activity since 2010 has been reported by the Texas Railroad Commission or by commercial data providers, suggesting that the field is no longer economical and may no longer be of interest to oil and gas production companies.

Stratigraphy

The lower Miocene 1 (Galloway, 2005) Marg A reservoirs occur in the upper portion of a genetic sequence that was deposited from 22 to 20.5 MYPB (Fillon and others, 1997; Waterman, 2010; fig. 6.1.3). The bounding marine condensed-section shales contain Marg A (top) and *Siphonina davisi* (Siph D) (base) benthic foraminifera index fossils. The index zones were correlated into the Block 440-L Field mapping area from wells for which these paleo zones were identified, as well as from guidance provided by the type log of Lane and Pace (1998).

The lower Miocene 1 interval beneath the *Robulus chambersi* zone (Rob C; immediately above Marg A) thickens and thins dramatically, indicating that structural deformation occurred in the Block 440-L area prior to the time of Rob C. The overlying younger lower Miocene 2 (Galloway, 2005) sequences are underlain by the major transgressive-dominated Amph B. By comparison to sub–Rob C units, the Amph B sequence is more sand prone and more uniform in thickness across the

approximately 16 km (10 mi) width of the Texas State Waters in the Block 440-L area, indicating that it was deposited during a relatively more quiescent period in a more proximal shelf position. A series of sandstone reservoirs occurs within the Marg A genetic sequence. The sand bodies range up to 34 m (110 ft) thick, and the units are thicker in structural lows, indicating that deposition was penecontemporaneous with structural deformation. Likewise, porosity is slightly diminished in the structural lows (25−27%) and is typically better (28−32%) in the thinner (25−75 ft) productive sandstones on the structural highs. Spontaneous potential and gamma-ray log signatures suggest that individual sand packages exhibit "upward-coarsening and upward-thickening" successions. The Block 440-L Field occurs in a distal shelf setting, immediately landward of the Marg A shelf edge (Galloway and Ganey-Curry, 2008), which is essentially coincident with the Federal Outer Continental Shelf (OCS) boundary in the vicinity of the field. The productive hydrocarbon reservoirs at the Block 440-L Field are porous, permeable sandstones that cap progradational, shallowing-upward facies successions. These successions appear to be cyclic 4th-order, shelf and marginal-marine sequences that occur within a larger 3rd-order transgressive system tract. The uppermost 4th-order Marg A maximum flooding shales sealed hydrocarbons in underlying sandstone reservoirs.

Geologic Interpretations and Reservoir Architecture

The study area was examined using 3D seismic, well logs, and micropaleontology interpretations ("paleo picks") to build the structure, net reservoir sandstone, and average porosity maps needed to estimate CO_2 capacity. Well logs from approximately 170 wells in and around the study area were used to correlate the Marg A and Siph D maximum flooding surfaces in the Block 440-L Field study area. Figure 6.1.4 presents a dip-oriented structural cross section that illustrates some of the well-log correlations. The thick shale section above Marg A is the Amph B mudstone that represents a major 3rd-order transgression. The thick black line represents the Clemente-Tomas growth fault, which offsets the Marg A maximum flooding surface (MFS). Relatively few wells penetrated the base of the Marg A genetic

sequence (i.e., Siph D MFS, dark purple). However, the top of overpressure (sampled to wells from a grid made from Pitman's 2011 map) in the study area was shallower than Siph D in all wells in the study area. As such, the lack of base Marg A penetrations was not significant for capacity estimations; the top of overpressure represented the base of the Marg A capacity interval.

The seismic and well data were input into Landmark's OpenWorks® database and interpreted in the time domain using Geoprobe® and DecisionSpace® applications. More than 100 seismically resolvable faults were interpreted throughout the Miocene section. Horizons were interpreted on the zero crossings (+/-) of strong seismic reflections that we inferred to represent key stratigraphic surfaces. We picked two key seismic horizons pertinent to the Block 440-L Field Marg A capacity estimate throughout the study area:

1. Rob C biostratigraphic zone (represented by a condensed section); and
2. approximate top of Siph D biostratigraphic zone (condensed section), which serves as a proxy for the base of the Marg A reservoir zone.

The majority of the oil and gas production comes from reservoirs in the upper part of the Marg A MFS. The hydrocarbons were trapped in a faulted rollover anticline that can be observed in both well-log and seismic sections (figs. 6.1.4 and 6.1.5, respectively). The rollover anticline was set up by movement of the Clemente-Tomas growth fault, which strikes parallel to shore and approximately coincides with the north-northwestern margin of the seismic time-structure maps. Analysis of well logs indicates that the thickness of the Marg A unit increases by more than 600 m (2,000 ft), from 213 m (700 ft) near the top of the Block 440-L Field anticline to a measured maximum of 854 m (2,800 ft) on the proximal hanging wall of the Clemente-Tomas fault (figs. 6.1.4 and 6.1.5), demonstrating that Marg A deposition was penecontemporaneous with major fault movement.

Smaller-scale faulting was difficult to identify and map in the well-log data set, but the 3D seismic data enabled us to define and map numerous faults that compartmentalize the Block 440-L Field. Throw on the faults is on the order of 30−60 m (100−200 ft). It is likely that so-called subseismic faults

(typically with throw smaller than 10–15 m [30–50 ft]) are present; these could also locally complicate filling and trapping of CO_2 in the relatively thin (3–21 m; 10–70 ft) Marg A reservoir sandstones.

Synthesis of Seismic and Well-Log Interpretations

Structure Maps

In order to integrate the seismic interpretations with depth-domain well correlations, the 3D-seismic two-way time contours were imported into a Petra® (computer software) database. Inspection of the 3D-seismic vertical sections and horizon maps was also considered when making the depth-domain structure maps tied to well-log-based stratigraphic picks (frequently referred to as "tops" or "formation tops"). The Rob C MFS seismic time contours (fig. 6.1.6a) were used to guide the Marg A MFS depth-domain structure map (top capacity interval; fig. 6.1.8a). The Marg A MFS is approximately 20 milliseconds (ms) below the Rob C MFS, which provided the most easily traceable reflection near the Marg A MFS. Productive Marg A reservoirs occur in the middle-right part of the cross section from about 2,000 to 2,200 ms, where an anticlinal structure can be observed at the Marg A level but is most obvious at the base of Marg A. Similarly, the Siph D MFS seismic time contours (fig. 6.1.6b) were used to guide the Siph D MFS depth-domain structure map (fig. 6.1.7c).

Overpressure Map

Overpressure, a well-documented phenomenon, occurs throughout the Gulf of Mexico Basin. The USGS constructed a regional top overpressure structure map for the northwest Gulf of Mexico Basin and made its GIS files available for free download (Pitman, 2011). The map covers all of the onshore Texas and Louisiana Gulf of Mexico Basin and extends offshore to the present-day shelf edge, which is located at approximately the 200-m (656-ft) bathymetric contour. We extracted a small portion of this map to use in our capacity estimate (fig. 6.1.7c). In the study area, the depth to the Siph D MFS, which marks the base of the Marg A reservoir zone, (fig. 6.1.7b) was greater everywhere than it was in the USGS top

overpressure map. Thus, the USGS top overpressure map was designated to serve as the base of the Marg A capacity interval (fig. 6.1.8b).

Net Reservoir Sandstone Map

Net reservoir sandstone within the Marg A capacity interval was defined by spontaneous potential (SP) curves and (fewer) gamma ray (GR) curves where no SP was available. The SP curves were corrected for downhole drift and normalized to a range from -95 to -5. GR curves were normalized to a range from 0 to 180 API units. Net reservoir sandstone was defined as meeting an SP value of less than -40 normalized units or a GR value of less than 50 normalized units. SP or GR values satisfying these cutoffs were defined at 0.5 ft intervals (sampling density of LAS log curves) as net reservoir sandstone, and were summed in each well over the Marg A capacity interval (Marg A MFS to top overpressure) throughout the study area, and in some adjacent wells just the boundary, to ensure that accurate trends were captured. The summations of net reservoir of the Marg A capacity interval ranged from 0 to over 366 m (1,200 ft; fig. 6.1.8c) and decreased in the seaward direction because of (1) the steady rise of the top of overpressure (fig. 6.1.8b); and (2) a depositionally controlled (i.e., proximal-to-distal) decrease in sandstone content from the present-day coastline toward the Marg A paleo-shelf edge, which is coincident with the Federal OCS line (Galloway and Ganey-Curry, 2008).

Isoporosity Map

Porosity values were obtained from 26 wells with available sonic or density curves in and around the study area. The methodology for calculating porosity from sonic and density curves is detailed in Wallace and others. (2014). From the porosity curves, we calculated average porosity value for all porosity values within intervals that satisfied previously described net-reservoir criteria for the Marg A capacity interval for each well. The resulting isoporosity map shown in figure 6.1.8d is a geologically biased interpolation of the average porosity values for the 26 wells. Average porosity ranged from 0%,

where there was zero net-reservoir sandstone, to over 30% on the structural highs. The average porosity within net-reservoir sandstones can be observed to decrease slightly in structurally lower areas where the sands are thicker, implying that depositional winnowing occurred on the highs, including the Brazos Block 440-L Field.

Capacity Estimate, Brazos Block 440-L Field

A static CO_2 capacity estimate was made of the Marg A genetic sequence for three sections of the study area (fig. 6.1.10):

1. the entire study area (168.4 km^2; 65.0 mi^2);
2. the Brazos Block 440-L Field proper, defined by the closed -7600 ft (-2378 m) contour in figure 6.1.7A (35.5 km^2; 13.7 mi^2); and
3. the "2-Dome Arch," defined by the closed -7800 ft (-2378 m) contour in figure 6.1.7A (85.0 km^2; 32.8 mi^2).

Utilizing net-reservoir sandstone thickness and average porosity values (within intervals satisfying the defining cutoffs for net reservoir), we conducted a modified Goodman and others (2011) capacity calculation. The methodologies for both net-reservoir summations and capacity calculations are detailed in Wallace and others (2014) and Chapter 5 (this volume). The Wallace and others (2014) version of the volumetrics-based equation is summarized here:

$$G_{CO_{2net}} = A_t \, \mathbf{h_{net}} \, \varphi_{net} \, \rho \, E_{net} \qquad (1)$$

where,

A_t = Total area

$\mathbf{h_{net}}$ = Net-reservoir thickness

φ_{net} = Total porosity within net-reservoir thickness

ρ = CO_2 density at reservoir conditions

E_{net} = Storage efficiency factor.

Essentially, the Wallace and others (2014) modification used to calculate capacity substitutes net-reservoir sandstone thickness for gross thickness and utilizes an adjusted efficiency factor. Some details of the methodology we employed that are unique to the Block 440-L Field data set is included below.

Capacity Estimation Workflow

After the Marg A **capacity interval** was defined to be the Marg A MFS (top) and top overpressure (base; modified from Pitman, 2011), the pertinent data were utilized in a Petra® grid model written by Carr (2011) that calculates estimated CO_2 capacity using the above described modified Goodman and others (2011) method. The four input maps (grids) describing the Marg A capacity interval are presented in table 6.1.1.

Table 6.1.1. Explanation of input maps (grids) used in Carr (2011) Petra® grid model to calculate modified Goodman and others (2011) capacity estimate for Brazos Block 440-L Field

Eqn. 1 Variable Addressed	Comment	Description	Intermediate Grid	Final Input Grid
ρ	Depth maps needed as input to Nicholson (2012) TX Gulf Coast–specific CO_2 density transform coded into Carr (2011) Petra® grid model	Depth, top capacity interval	Subsea TVD structure map, Marg A MFS (fig. 6.1.7a)	Depth map, Marg A MFS (fig. 6.1.18a
ρ		Depth, base capacity interval	Subsea TVD structure map, top overpressure (modified from Pitman, 2011; fig. 6.1.7c)	Depth map, top overpressure (fig. 6.1.8b)
$\mathbf{h_{net}}$	Substitute net reservoir sandstone thickness for gross thickness compared to NETL-MIT original logic (Goodman and others, 2011)	Net-reservoir isopach	n/a	Net reservoir isopach map, Marg A capacity interval (fig. 6.1.8c)
φ_{tot}	n/a	Total porosity	0.045 (P_{50} value; Wallace and others, 2014)	Isoporosity map (average porosity of net reservoir), Marg A capacity interval

				(fig. 6.1.18d

Input constants used in the grid model are tabulated in table 6.1.2. Goodman and others (2011) presents a set of efficiency factors for use in saline aquifers of various lithologies and for probability values of P_{10}, P_{50}, or P_{90}, in which the storage efficiency factor, E_{saline}, ranges from 0.4 to 5.5%. For the capacity estimates herein, we have used 0.045, which is the median (or P_{50}) "E_{net}" value calculated by Wallace and others (2014).

Table 6.1.2. Explanation of constants input to Carr (2011) Petra® grid model to calculate modified Goodman and others (2011) capacity estimate for Brazos Block 440-L Field

Constant	Description	Value	Comment
SC_{DEP}	Supercritical CO_2 depth	3300 ft	Shallowest depth at which regional pressure/temperature gradients predict CO_2 will be in supercritical phase; limits top of capacity interval
G_{SZ}	Grid size	3280.84 ft	1 km^2 or 0.386 mi^2
E_{net}	Net-storage efficiency factor	0.045	E_{net} P_{50} (Wallace and others, 2014)
RHO_{shal}	CO_2 density	150 kg/m^3	Limits $RHOCO_2$ to constant above minimum expected depth
RHO_{deep}	CO_2 density	680 kg/m^3	Limits $RHOCO_2$ to constant below maximum expected depth

By this methodology and by using this workflow and computational tools, three output maps (grids) were generated for the study area; the outputs are described in table 6.1.3. We then obtained total capacity for given areas by integrating the net-capacity values per grid block over the study area, i.e., summing all the net-capacity values from the G_{CO_2} output grids.

Table 6.1.3. Explanation of outputs from Carr (2011) Petra® grid model to calculate modified Goodman and others (2011) capacity estimate for Brazos Block 440-L Field

Eqn. 1 Variable Addressed	Description	Intermediate Output Grid	Final Output Grid	Comment
ρ	Midpoint depth (ft) map of capacity interval	Midpoint depth (ft) map of capacity interval (fig. 6.1.9a)		Used to calculate CO_2 density; logic from Nicholson (2012) TX Gulf Coast–specific CO_2 density transform coded into Carr

				(2011) Petra® grid model
ρ	CO_2 density	CO_2 density map (kg/m^3) (fig. 6.1.9b)		Used to calculate capacity
$G_{CO_2}net$	CO_2 capacity (kg/m^3)	n/a	CO_2 capacity distribution per grid block ($tonnes/km^2$) of Marg A capacity interval (fig. 6.1.10)	"Net capacity" (Wallace and others, 2014)

Results

The P_{50} static "net capacity" for the 35.5 km^2 footprint of the Brazos Block 440-L Field area is 5.5 Mt of CO_2 (red polygon, fig. 6.1.1; fig. 6.10c). For the "2-Dome Arch," which is inclusive of the Brazos Block 440-L Field area, we calculate 13.8 Mt of CO_2 (fig. 6.10b). The entire study area contains an estimated 196 Mt of CO_2 storage (blue polygon, fig. 6.1.1; 463 km^2; fig. 6.10a). The majority of this CO_2 capacity is located in the west-northwest part of the study area, along the Clemente-Tomas growth fault where sand packages thicken and the overpressure is deep, both of which contribute to the large CO_2 storage potential there.

Sandstone reservoirs of the Brazos Block 440-L Field proper underlie the Marg A maximum flooding shale, which traps hydrocarbons on the field's anticlinal structure. Storage capacity is limited to 5.5 Mt of CO_2 by relatively thin reservoir sandstones and the shallow depth to top of overpressure (fig. 6.1.4). However, the Brazos Block 440-L Field proper would be a relatively low-risk site since it has definite 35.5-km^2 structural closure, demonstrated trapping capability, and a significant amount of well data to accurately characterize it. Although trapping capability is unproven in more than half the area, extending the potential Brazos Block 440-L Field site to include the "2-Dome Arch" closed structure (-7800-ft contour, fig. 6.1.7b) almost triples the capacity (13.8 Mt CO_2) under an 85-km^2 (32.8-mi^2) area.

The majority of the 196 Mt of CO_2 storage (blue polygon, fig. 6.1.1; 463 km^2; fig. 6.10a) is located in the west-northwest part of the study area, immediately adjacent to the Clemente-Tomas growth fault where thick, stacked sandstone reservoirs with large pore volumes are present above the top of

overpressure (fig. 6.1.4). However, mapping must be expanded to determine if structural closure(s) is/are present. If trapping is solely or partly dependent on the updip sealing capability of the Clemente-Tomas fault, then detailed fault-seal analysis would be required to prove this a large potential site since structural closure is not present. In general, CO_2 injection into a fault-closed trap would expose the operator to more risk than would a trap with four-way structural closure. Because of these risks and the follow-up work needed to address them, this area can be considered a lead rather than a potential site.

Both the Brazos Block 440-L Field and its extended area, the "2-Dome Arch," appear to have reasonable potential CO_2 sequestration sites. The larger northern lead area will need additional detailed geologic, geophysical, and engineering characterization to develop it for CO_2 sequestration. Nonetheless, this investigation highlights the potential for long-term CO_2 storage in Miocene sandstones of the Gulf of Mexico Basin.

References

Bradshaw, B. E., and Watkins, J. S., 1994, Growth-fault evolution in offshore Texas: Gulf Coast Association of Geological Societies Transactions 44, p. 103–110.

Carr, D. L., 2011, CO_2 capacity dlc.TXT: a computer program for use in Petra® software that calculates CO_2 capacity utilizing a modified Goodman and others (2011) capacity method: unpublished computer program, unnumbered.

Fillon, R. H., Lawless, P. N., Lytton, R. G., III, and others, 1997, Gulf of Mexico Cenozoic biostratigraphic and cycle charts, *in* Lawless, P. N., Fillon, R. H., and Lytton, R. G., III, eds., Gulf of Mexico Cenozoic biostratigraphic, lithostratigraphic, and sequence stratigraphic event chronology, Gulf Coast Association of Geological Societies (GCAGS) Transactions, v. 42, p. 271–282.

Galloway, W. E., 2005, Gulf of Mexico basin depositional record of Cenozoic North American drainage basin evolution: International Association of Sedimentologists Special Publication 35, p. 409–423.

Galloway, W. E., and Ganey-Curry, P. E., 2008, Gulf of Mexico Basin Depositional Synthesis (GBDS) Phase 6 Atlas, University of Texas Institute for Geophysics (UTIG), The University of Texas at Austin, 161 p.

Goodman, A., Hakala, A., Bromhal, G., Deel, D., Rodosta, T., Frailey, S. C., Small, M., Allene, D., Romanova, V., Fazioa, J., Huertaa, N., McIntyreb, D., Kutchkoa, B., and Guthriea, G., 2011, US DOE methodology for the development of geologic storage potential for carbon dioxide at the national and regional scale: International Journal of Greenhouse Gas Control, v. 5, p. 952–965.

Lane, R. F., and Pace, R. C., 1998, Brazos 440-L Field, Offshore Texas, p. 27–36: *in* 3-D Case Histories From the Gulf Coast Basin, A GCAGS Special Publication. Edited by J. L. Allen, T. S. Brown, C. J. John, and C. F. Lobo, 339 p.

McDonnell, A., Hudec, M. R., and Jackson, M. P. A., 2009, Distinguishing salt welds from shale detachments on the inner Texas shelf, western Gulf of Mexico: Basin Research, v. 21, p. 47–59.

McDonnell, A., Hudec, M. R., and Jackson, M. P. A., 2010, Origin of transverse folds in an extensional growth-fault setting: evidence from an extensive seismic volume in the western Gulf of Mexico: Marine and Petroleum Geology, v. 27, p. 1494–1507

Nicholson, A. J., 2012, Empirical analysis of fault seal capacity for CO_2 sequestration, lower Miocene, Texas Gulf Coast, The University of Texas at Austin, Master's Thesis, 78 p.

Pitman, J. K., 2011, Reservoirs and petroleum systems of the Gulf Coast: depth to top overpressure. American Association of Petroleum Geologists Datapages, GIS Open Files. Online, available at: http://www.datapages.com/Services/GISUDRIL/OpenFiles/ReservoirsandPetroleumSystemsoftheGulfCoast. aspx [March 1, 2013].

Wallace, K. J., Meckel, T. A., Carr, D. L., Treviño, R. H., and Yang, C., 2014, Regional CO_2 sequestration capacity assessment for the coastal and offshore Texas Miocene interval: greenhouse gases: Science and Technology, v. 4, p. 53–65.

Waterman, A. S., 2010, Biostratigraphic chart, Gulf of Mexico, Neogene, Paleo-Data, Inc., New Orleans, La.

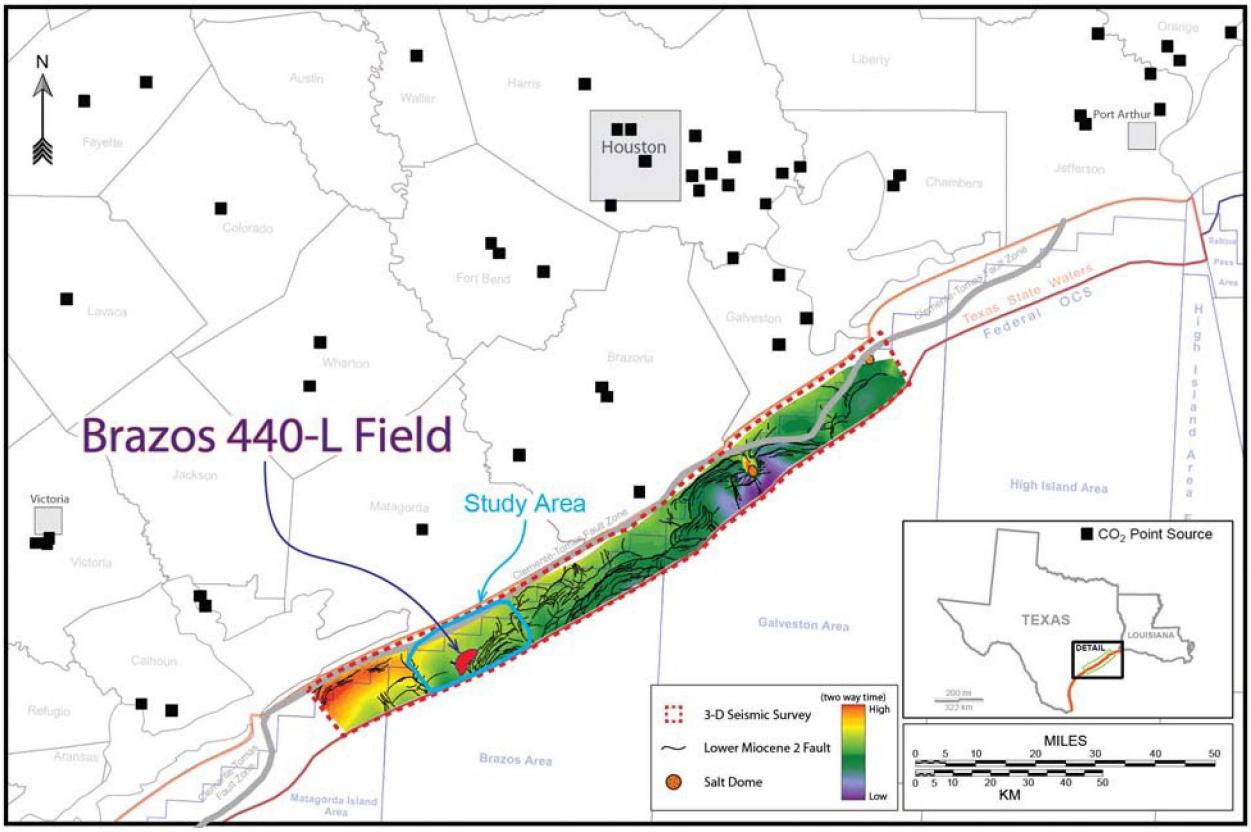

Figure 6.1.1. Location map showing Brazos Block 440-L Field (red polygon; area = 35.5 km^2, 13.7 mi^2, 8,768 ac) and surrounding study area (blue polygon outline; area = 463 km^2, 179 mi^2, 114,575 ac).

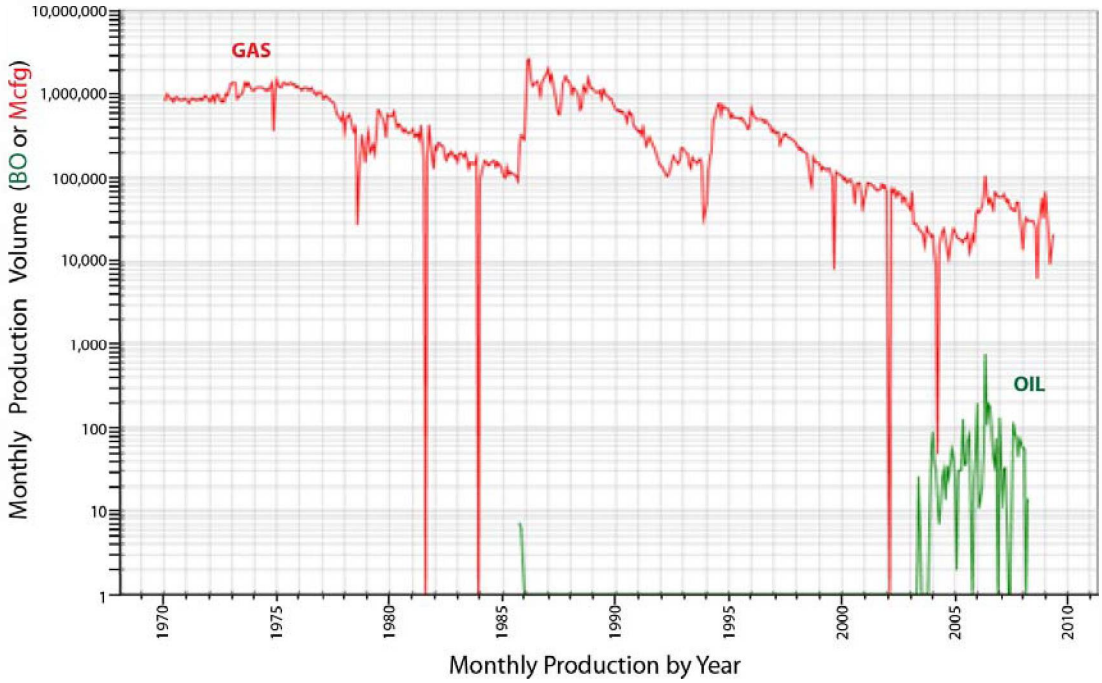

Figure 6.1.2. Production history of Brazos 440-L Field, 1970–2010, all wells in field combined. Source data from Drillinginfo, Inc.

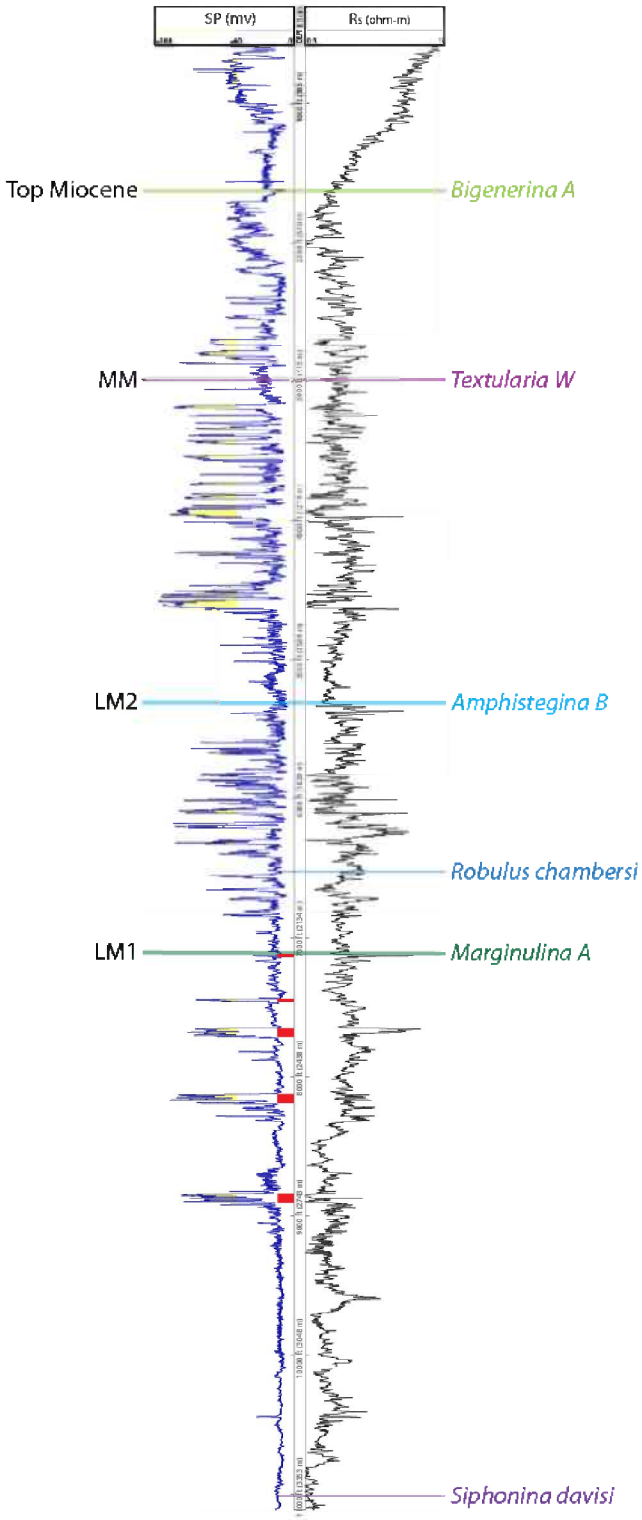

Figure 6.1.3. Type log for Brazos Block 440-L Field from Shell ST TR 440-L #1, API no. 42704000030000. Spontaneous potential (SP; blue) curve in left track, shallow resistivity (R_s; black) curve in right. Yellow-filled SP curve signifies permeable sandstone zones where SP < -40 mv. Key biostratigraphic zones are designated at right.

Galloway (2005) Miocene divisions are marked at left: LM1 = Lower Miocene 1, LM2 = Lower Miocene 2, MM = Middle Miocene.

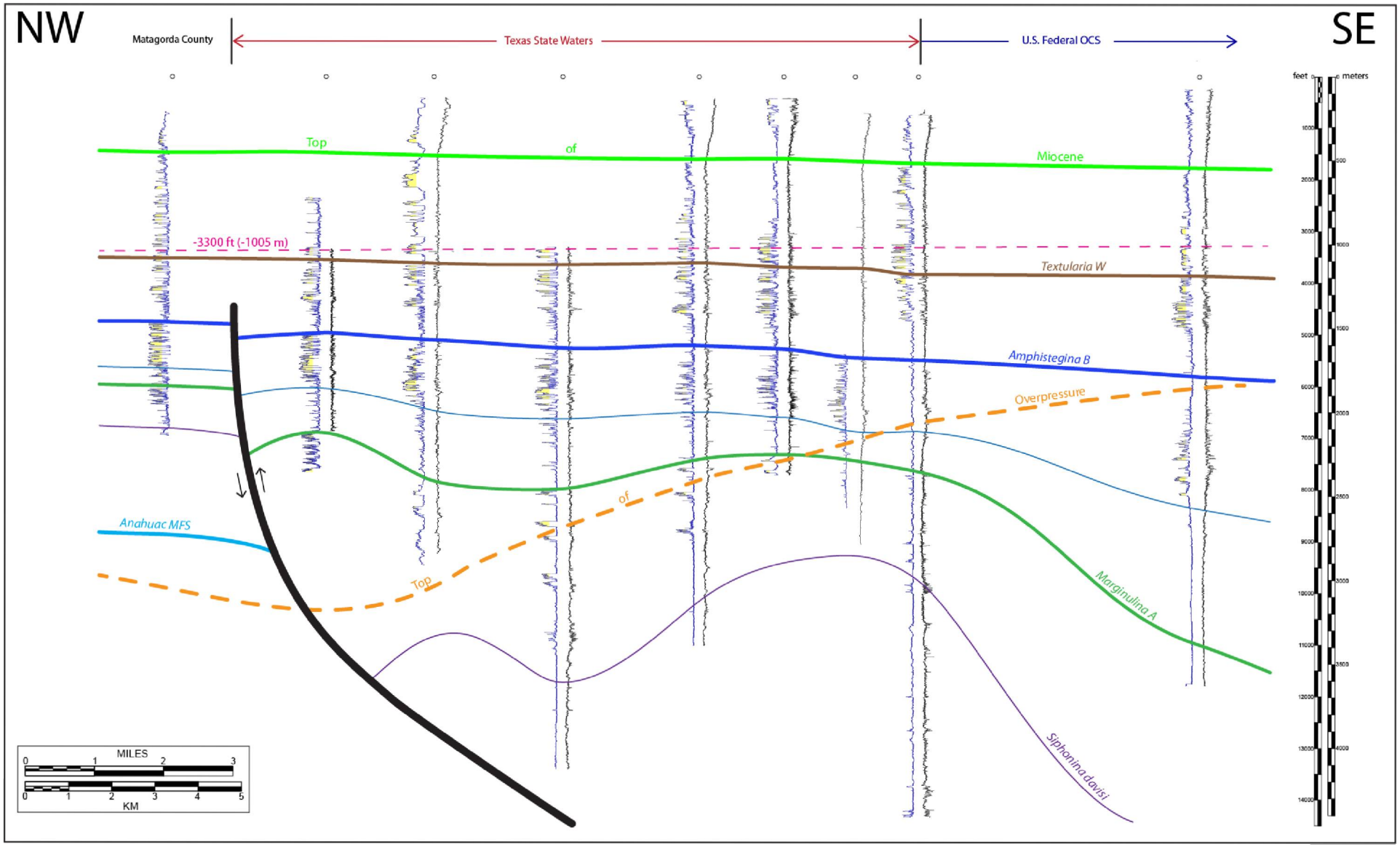

Figure 6.1.4. Dip-oriented structural cross section. Block 440-L Field lies in the middle-right part of the cross section, where an anticlinal structure can be observed at the Marg A MFS (green line). This cross section runs approximately parallel to the 3D seismic vertical section in figure 6.1.5. The line of cross section is shown on maps in figures 6.1.6–6.1.10.

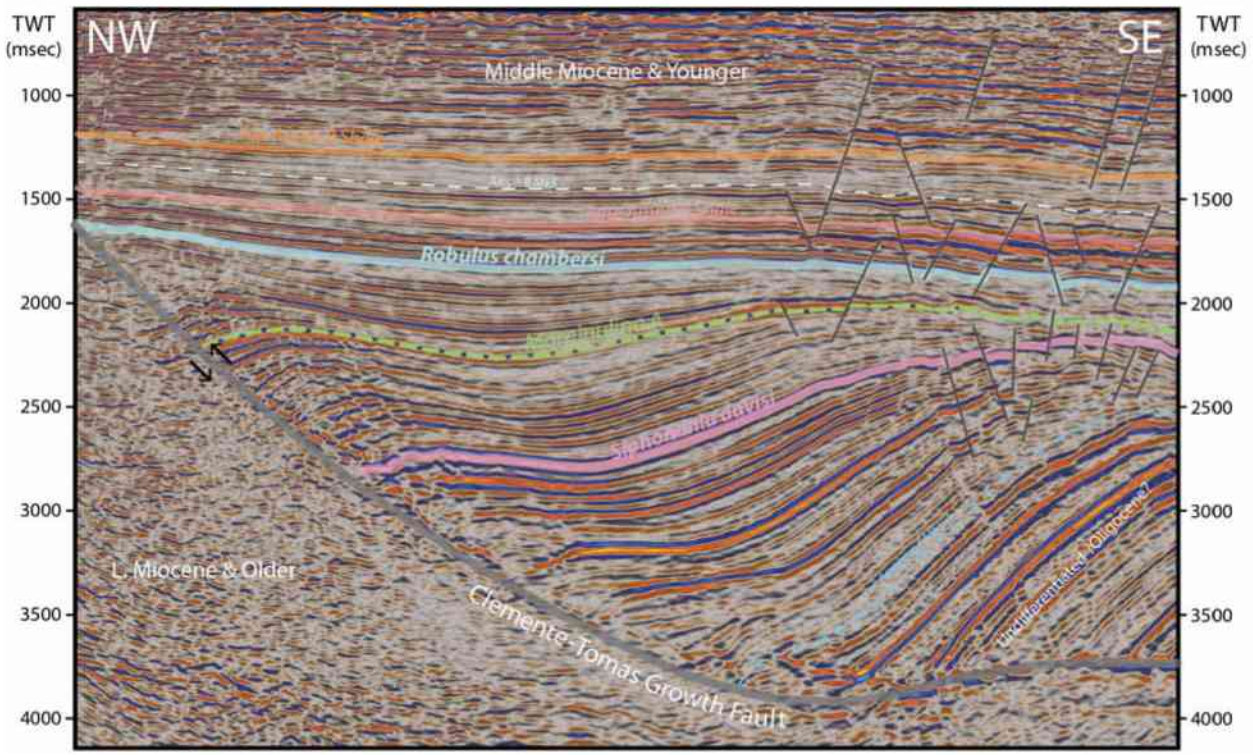

Figure 6.1.5. Dip-oriented vertical 3D seismic section and interpretation through Brazos Block 440-L Field. The vertical scale is in milliseconds (msec) of two-way time (TWT). The line of the section is shown in figures 6.1.6 and 6.1.7. The vertical seismic section runs approximately parallel to the well-log cross section in figure 6.1.4.

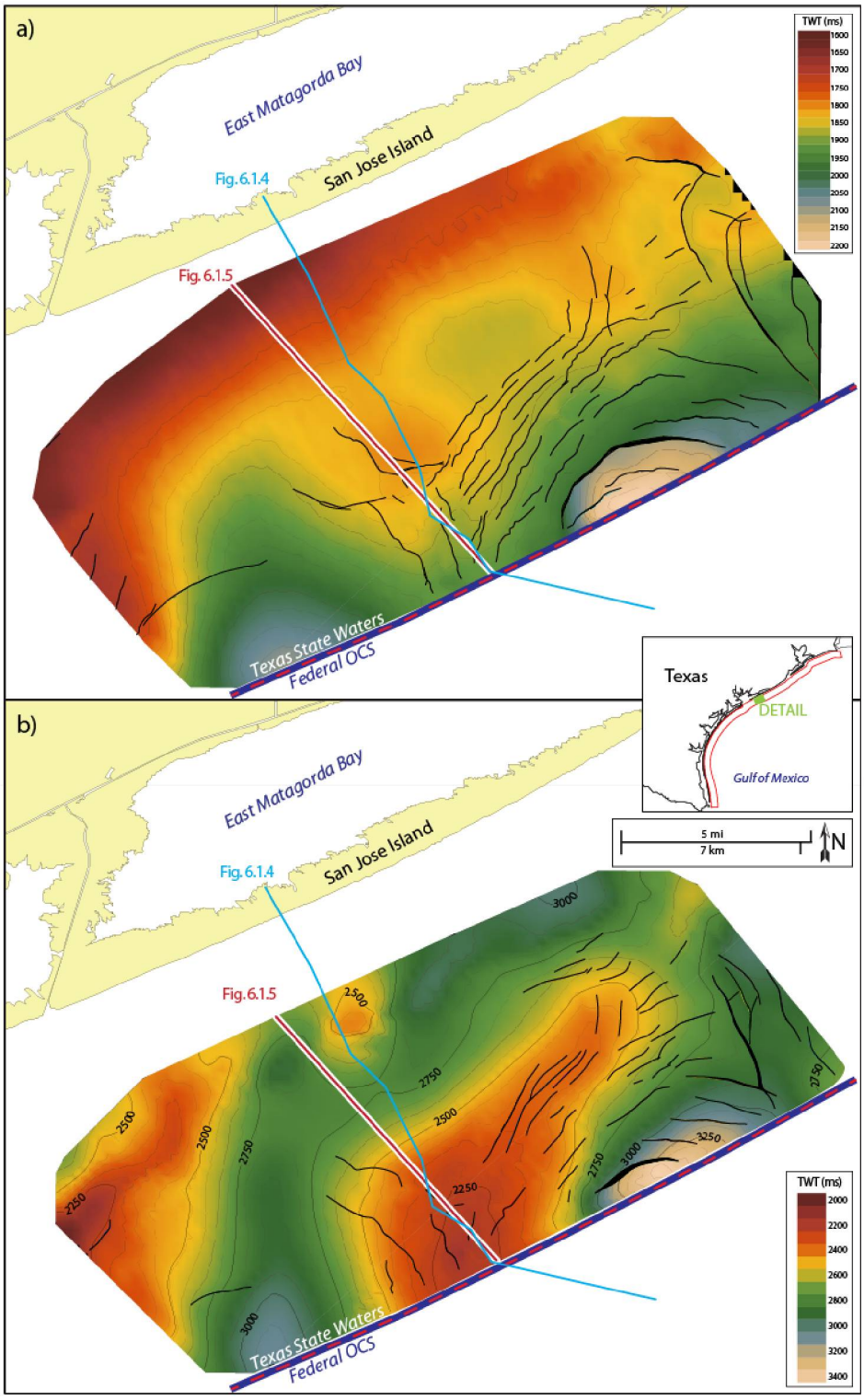

Figure 6.1.6. Seismic two-way time structure (ms) maps. (a) Horizon at the Rob C biostratigraphic zone (fig. 6.1.5). This stratigraphic surface provided the most easily traceable reflection near the Marg A MFS, which provides the seal of the reservoir interval at the Block 440-L Field. (b) Horizon at the Siph D biostratigraphic zone (fig. 6.1.5), which serves as the base of the Marg A unit. Note that the Siph D structural high is more pronounced and that its

peak is basinward of that of the Rob C.**8a**

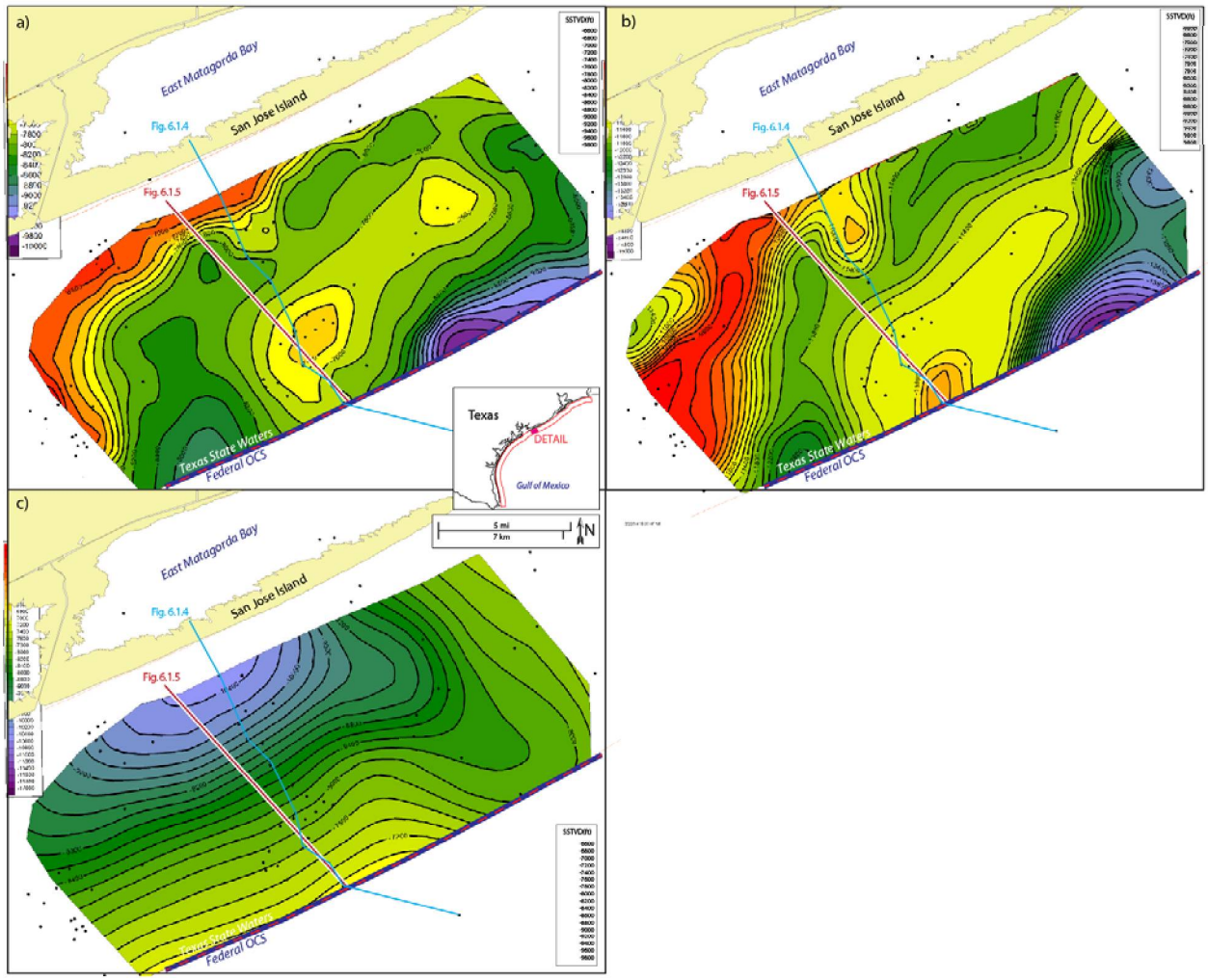

Figure 6.1.7. Subsea, true-vertical depth structure maps (ft) of key horizons. Lines of vertical seismic section (red; fig. 6.1.5) and cross section (blue; fig. 6.1.4) are shown. (a) Marg A MFS serves as the top of the capacity interval. Created using well control picks and guided by the Rob C MFS seismic time-structure map shown in figure 6.1.6A. (b) Siph D MFS, which serves as the base of the Marg A genetic sequence. (c) Top of overpressure, modified from Pitman (2011).

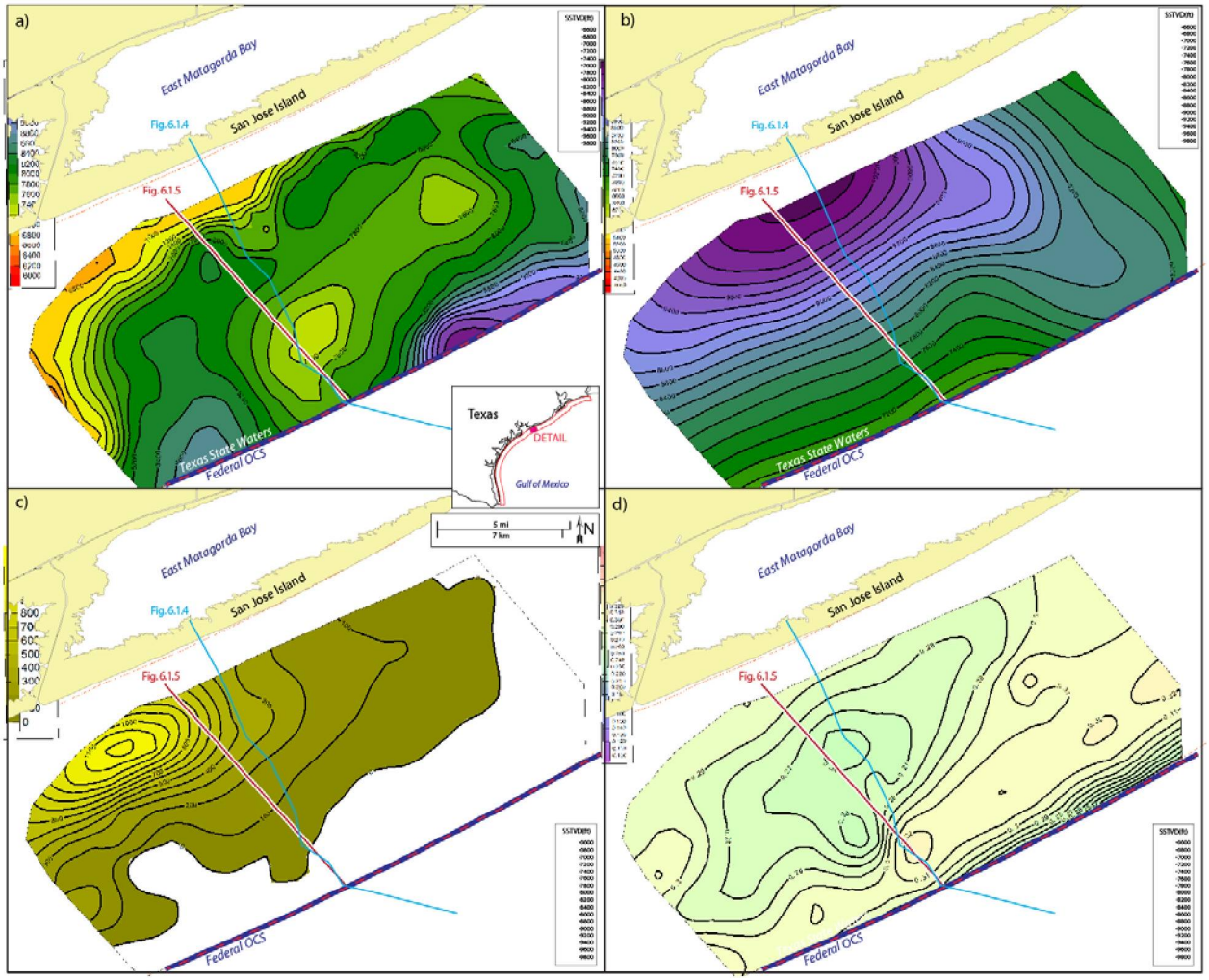

Figure 6.1.8. Input maps for capacity estimate. (a) Depth (ft) structure map, Marg A MFS, which serves as the top of the capacity interval. Subsea, true-vertical depth structure version of this map is shown in figure 6.1.7. (b) Depth (ft) map, top of overpressure (modified from Pitman, 2011), which serves as the base of the capacity interval. Subsea, true-vertical depth structure version of this map is shown in figure 6.1.7c. (c) Net sandstone reservoir isopach (ft) map. The areas without color indicate zero net sand. (d) Isoporosity map of study area. Yellow-shaded areas indicate greater isoporosity than green-shaded areas.

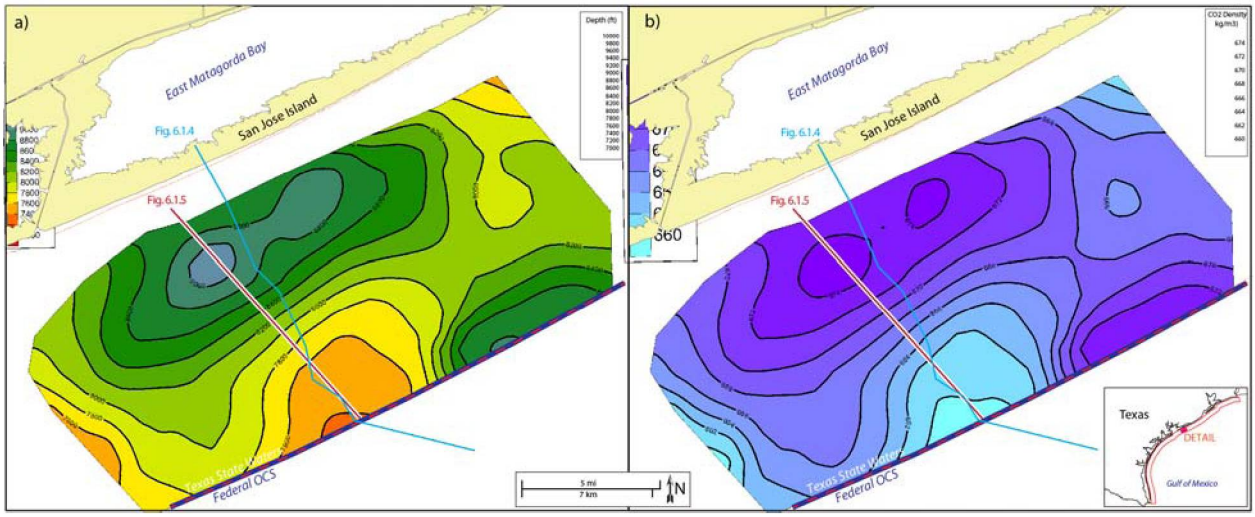

Figure 6.1.9. Intermediate output maps calculated by Carr (2011) Petra® capacity-estimate grid model. (a) Midpoint depth (ft) map of capacity interval, Marg A MFS to top overpressure. (b) CO_2 isodensity map (kg/m3) of capacity interval, Marg A MFS to top overpressure.

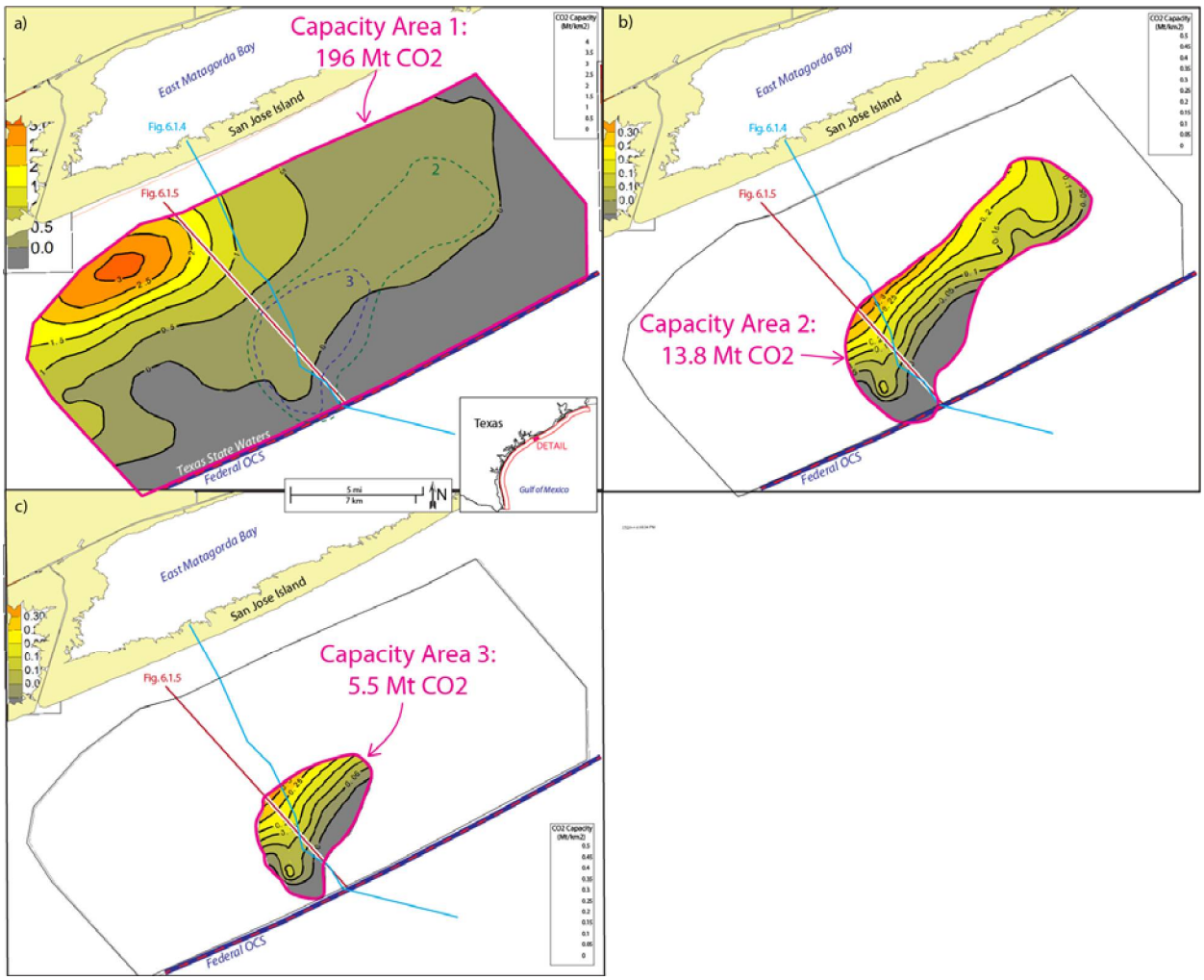

Figure 6.1.10. CO_2 capacity-distribution output maps calculated by Carr (2011) Petra® capacity-estimate grid model for capacity interval (Marg A MFS to top overpressure). (a) Entire study area. Polygons outlining capacity areas 2 (green) and 3 (blue) are shown in dashed lines. (b) "2-Dome Arch." (c) Block 440-L Field proper. Note that color-bar contour interval changes from 0.5 Mt/km^2 in (a) to 0.05 Mt/km^2 in (b) and (c).

Chapter 6.2. San Luis Pass Area

Kerstan J. Wallace, Ramon Trevino, Tip Meckel, David L. Carr, Caleb Rhatigan and Andrew J. Nicholson Gulf Coast Carbon Center, Bureau of Economic Geology, The University of Texas at Austin, Austin, TX, USA

Introduction

A seismically-defined Miocene saline aquifer east of Freeport, TX was analyzed for CO_2 storage capacity by generating a 3D fluid flow model. Three 3D fluid flow simulations were generated and run using CMG (Computer Modelling Group; Calgary, AB) modeling software package. In order to approximate a natural petroleum reservoir system and assess the amount of refinement needed to obtain an accurate CO_2 capacity estimate, the simulation scenarios increased in complexity from homogeneous to statistical heterogeneous and finally to seismic-based heterogeneous. The study area was selected based on an examination of the regional seismic time-structure horizon of the Lower Miocene 2 (LM2) (Figure 6.2.1), local well log interpretation (Figure 6.2.2) and lack of production data from study area wells, which all indicate that the area has encouraging structural closure (Figure 6.2.3), sufficient reservoir thickness (Figure 6.2.2), and is water saturated. Using Geoprobe® and Permedia®, the 26,496 acre field was mapped from seismic data, structurally analyzed, and used as a reservoir input for dynamic modeling. Through this exercise we hope to assess the potential outcome of a reservoir scale CO_2 injection project and identify the factors that influence the model results.

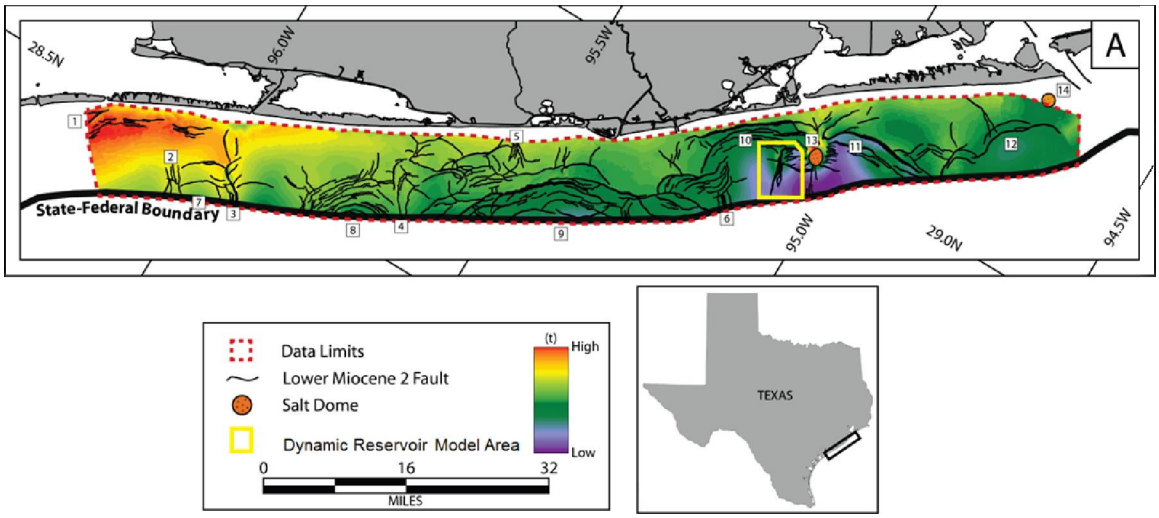

Figure 6.2.1: Time structure and faults of LM2 horizons (modified from Nicholson,2012). Yellow box indicates site selected for dynamic modeling.

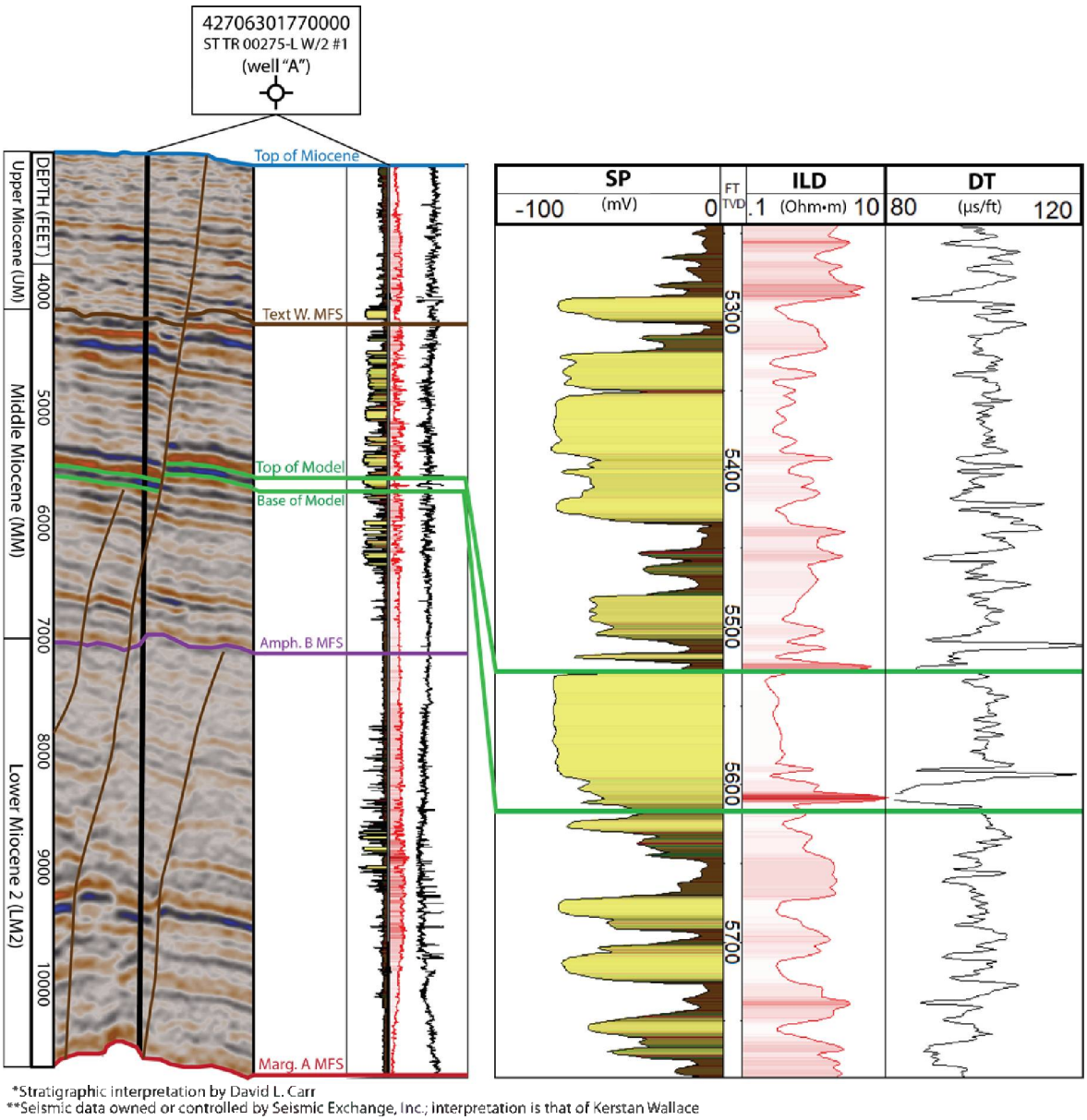

Figure 6.2.2: Seismic column and corresponding well log from well 42706301770000 (well A). Expanded log section shows reservoir interval. Location of well A is shown in figure 6.2.1 and 6.2.3.

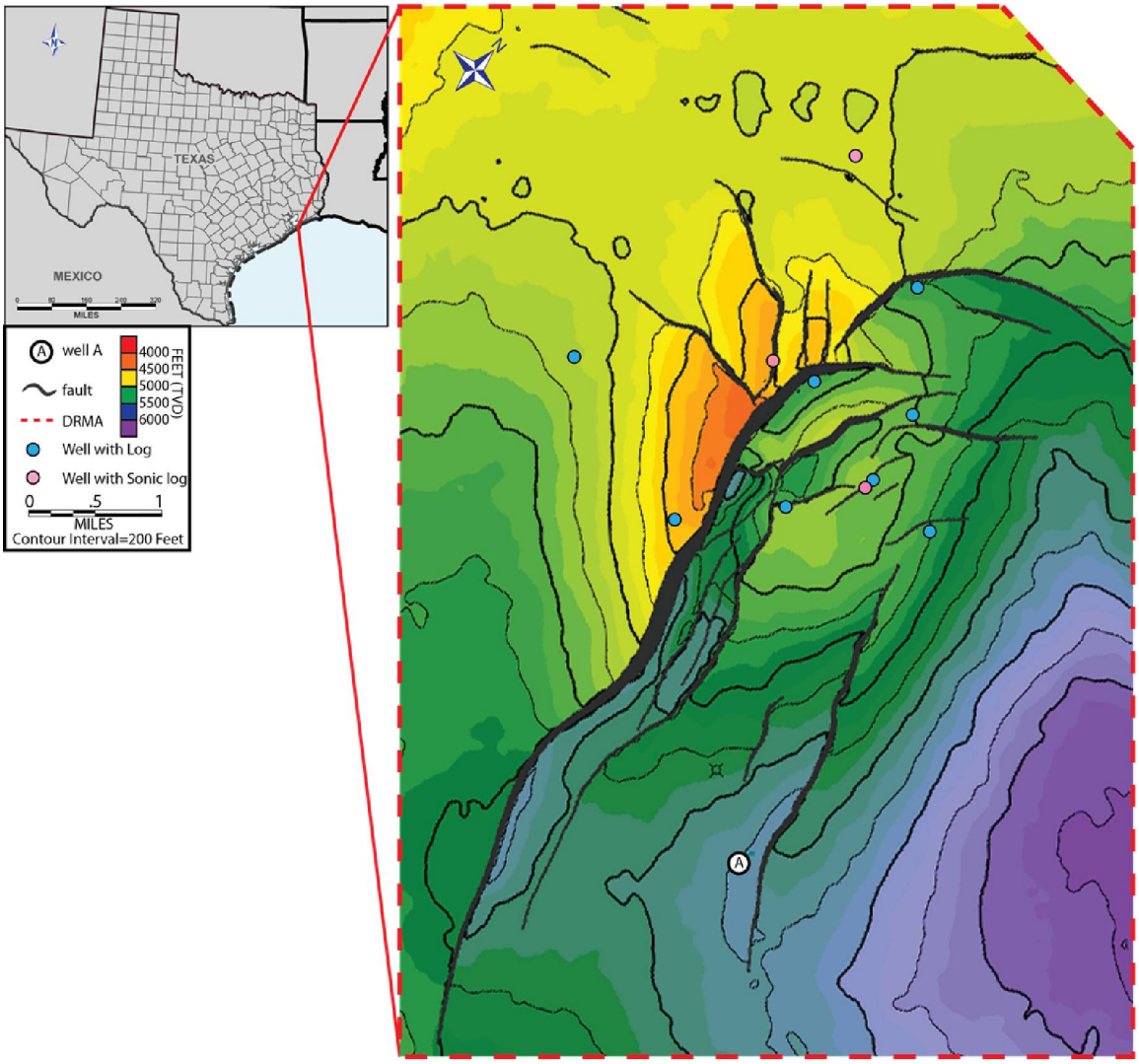

Figure 6.2.3: Structure map of the top of model interval. The location of the well A is shown along with the locations of wells with logs (blue). Wells with sonic logs (in addition to well A) are highlighted in pink.

Methodology

Selecting a reservoir depth interval within the model study area was based on seismic amplitude and continuity paired with SP, gamma ray, sonic, and resistivity curves examined through log-seismic ties. Figure 6.2.2 shows a log-seismic tie with stratigraphic interpretations for a key well in the model area, which we refer to as "well A" (API: 42706301770000). The selected reservoir lies above the Amph. B shale maximum flood surface, near a sequence boundary associated with the progradational, fluvio-deltaic, Middle Miocene (MM) depositional episode (figure 6.2.2). The model interval was mapped at a zero amplitude crossing above (+/-) and below (-/+) a reflection minimum. This reflection was chosen for its amplitude strength, continuity, and apparent tie to a thick sand package as measured in the low SP and gamma ray logs in intersecting wells. Faults were mapped in detail and used as barriers in subsequent 3D flow model analyses. Fault consideration was informed by prior work in the San Luis Pass area

(Nicholson, 2012). Figure 6.2.3 shows the resulting structure map of the top of the model interval. Using the upper and lower seismic horizons a grid mesh was generated in DecisionSpace®. A total of 288,781 grid blocks were created by using 10 evenly spaced layers between the two reservoir surfaces and a horizontal cell size of 200 x 200 feet. The vertical dimension at each cell location was determined by the thickness of the reservoir divided by 10 (number of layers) for an average grid cell thickness of 9.5 feet. Fault locations were stored in the grid mesh, and cells located within a fault gap were left null. The reservoir mesh was used for all subsequent simulations, only the properties within the grid cells were varied.

Three 3D flow model base case scenarios were considered in this study; (1) homogeneous, (2) statistical heterogeneous, and (3) seismic-based heterogeneous. These scenarios refer to the method by which permeability and porosity were applied to the model cells. For each of the three scenarios, eight additional variation cases were considered. These are: (1) high quality reservoir, (2) low quality reservoir, (3) open boundary conditions, (4) open fault transmissibility, (5) single injection well, (6) 15 injection wells, (7) optimized well placement, and (8) constant injection rate. Though the results for each scenario and variation case are presented here, we will focus primarily on the methods used to build the seismic-based heterogeneous base case, as it likely represents the most accurate model of the field based on observed data. For a more detailed description of the methods used to generate the homogeneous and statistical heterogeneous scenarios as well as the eight variation cases, see Wallace, 2013.

Many seismic attribute-to-log property relationships were examined in order to most accurately populate model cells with permeability and porosity. Unfortunately, the results of these comparisons for our dataset showed very weak to no correlation. The seismic-property to log-signature ties were likely unsuccessful for the following reasons: (1) time-depth conversion error at individual wells, (2) proximity of wells to faults, and (3) poor quality sonic log data.

Despite potential log-seismic issues, a seismic inversion of the amplitude depth volume from 4,500 to 6,000 feet was generated for the dynamic reservoir model area (DRMA) using Hampson-Russell Software Services and sonic logs from 4 wells. Though the resulting inversion volume appeared geologically reasonable, it did not show a strong correlation to most SP, gamma ray, or resistivity logs in the DRMA. Because the inversion volume was generated primarily with fault proximal sonic logs with no density curves, the potential error may be large.

Lacking confirmation from well log data, the seismic inversion volume was used as a hypothetical example of a seismically derived model population. The resulting inversion volume consisted of the impedance in a given unit. The impedance values were sampled to the reservoir mesh by averaging the values that fell within a 3D cell.

The geologic factors influencing impedance changes within a given interval are most likely related to changes in porosity or lithology. Porosity is most likely heterogeneous in the reservoir; however, the magnitude of the change is relatively small within a given lithology. Thus, we propose that changes in lithology primarily drive the changes observed in the impedance volume. To use this information in a way that allows for model population, a simple two facies sand-shale system was used, where values of impedance below 18,000 g/cc·ft/s were defined as shale and above as sand. Though more than two facies likely exist in the reservoir, they cannot be confidently resolved in the data due to ambiguity between porosity changes and lithology changes.

Porosity and permeability values were assigned to the sand facies by randomly populating values from the p40 to p60 range defined by the distribution of measurements recorded in 6,206 offshore Miocene reservoirs presented by Seni et al. 1997 . For a more detailed explanation of this process see Wallace, 2013. The shale facies was assigned porosity and permeability values of zero. Though in reality these shale facies will have non-zero porosity and permeability, these zones will effectively serve as impermeable baffles and assuming zero porosity/permeability was a reasonable simplification to enhance simulation speed. Permeability was defined as horizontally isotropic and vertically anisotropic (20% of horizontal permeability). Figure 6.2.4 shows statistically populated permeability for three of the ten layers in the seismic-based heterogeneous base case. Figure 6.2.5 presents the average permeability of all ten layers and includes the locations of the four model injection well sites.

The model was run for 100 years with the criteria that injection be terminated when pressure in the reservoir reaches 80% of lithostatic pressure. These pressure limits were determined for each injection well and are reported in table 6.2.1. Boundary conditions are assumed to be closed, meaning that pressure cannot equilibrate beyond the model edges. Additional inputs describing fluid transport and reservoir properties are listed in table 6.2.1 and described in detail in Wallace, 2012.

Table 6.2.1: Summary of inputs for homogeneous 3D flow model.

Summary of Homogeneous 3D Flow Model Base Case Inputs			
Parameter	**Property**	**Value**	**Source**
S_{wirr}	Irreducible Water Saturation	29%	6,206 Miocene reservoirs
Φ	Porosity	Seismic/statistically derived	6,206 Miocene reservoirs
T	Temperature	135.6° F (57.6° C)	11 log headers in DRMA
P_{init}	Initial Pressure	1,878-2,575 psi (12.9 -17.8 Mpa)	Hydrostatic gradient
Z	Depth	4,306-5,915 feet (1,312-1,803 meters)	Seismic mapping
h	Thickness	0-141 feet (0-43 meters)	Seismic mapping
κ	Permeability	Seismic/statistically derived	6,206 Miocene reservoirs
A	Area	26,496 acres (107 km^2)	Seismic mapping
k	Salinity	190,000 ppm	ILD and DT (well A)
n	Corey exponent (gas)	2	Zeidouni et al., 2009
λ	Mualem exponent	.457	Zeidouni et al., 2009
D	Duration	100 years	Assumption
P_{well1}	Pressure limit in well 1	3,510 psi (24.2 Mpa)	80% of lithostatic pressure
P_{well2}	Pressure limit in well 2	3,243 psi (22.4 Mpa)	80% of lithostatic pressure
P_{well3}	Pressure limit in well 3	3,107 psi (21.4 Mpa)	80% of lithostatic pressure
P_{well4}	Pressure limit in well 4	3,131 psi (21.6 Mpa)	80% of lithostatic pressure
Bound	Boundary Conditions	Closed	Assumption
Fault	Fault transmissibility	0	Assumption

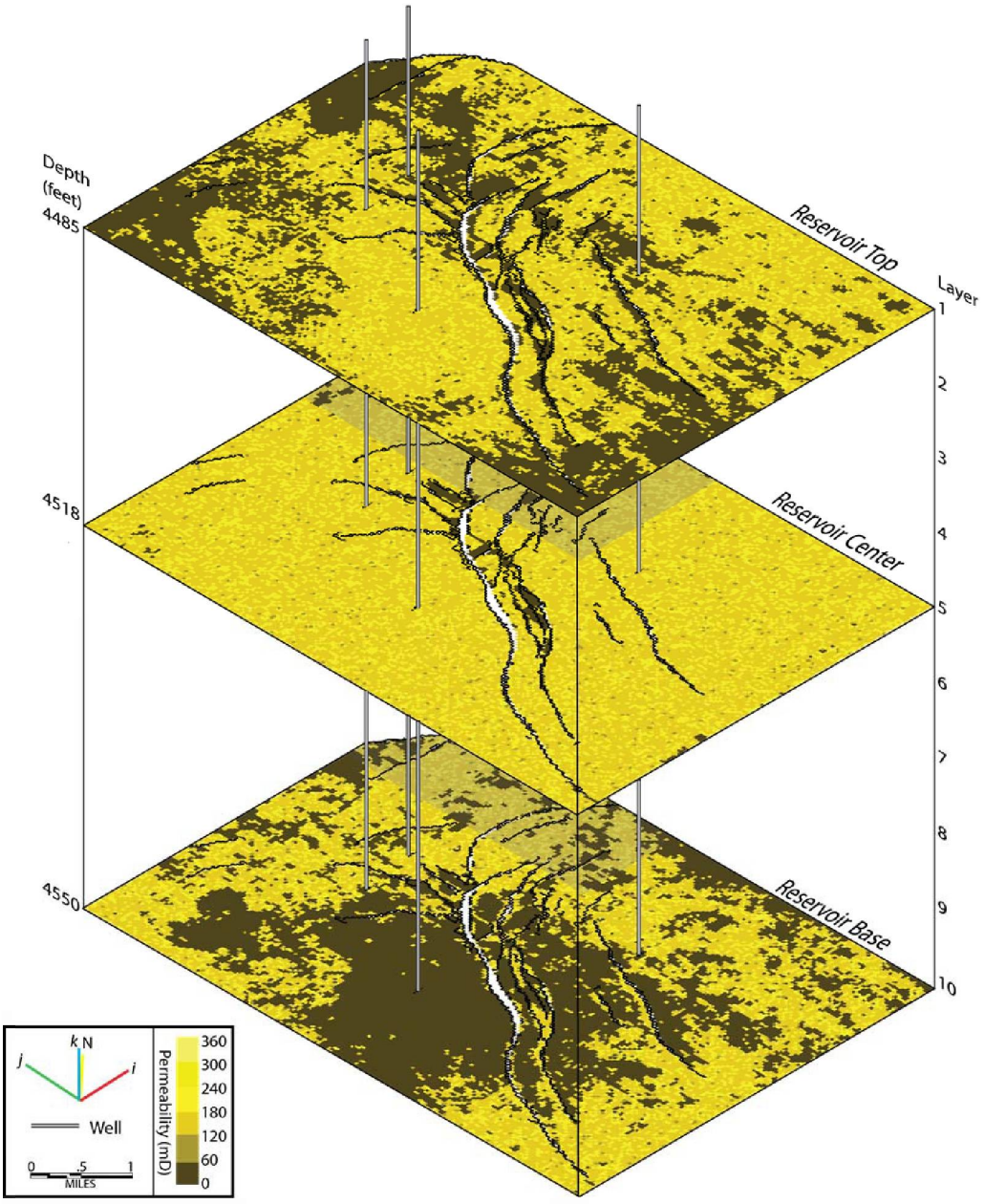

Figure 6.2.4: Layers 1, 5, and 10 colored by inversion and statistically populated permeability for the seismic-based heterogeneous base case model. Color scale is chosen to reflect lithology (brown=shale; yellow=sand). Locations of simulated injection wells are shown.

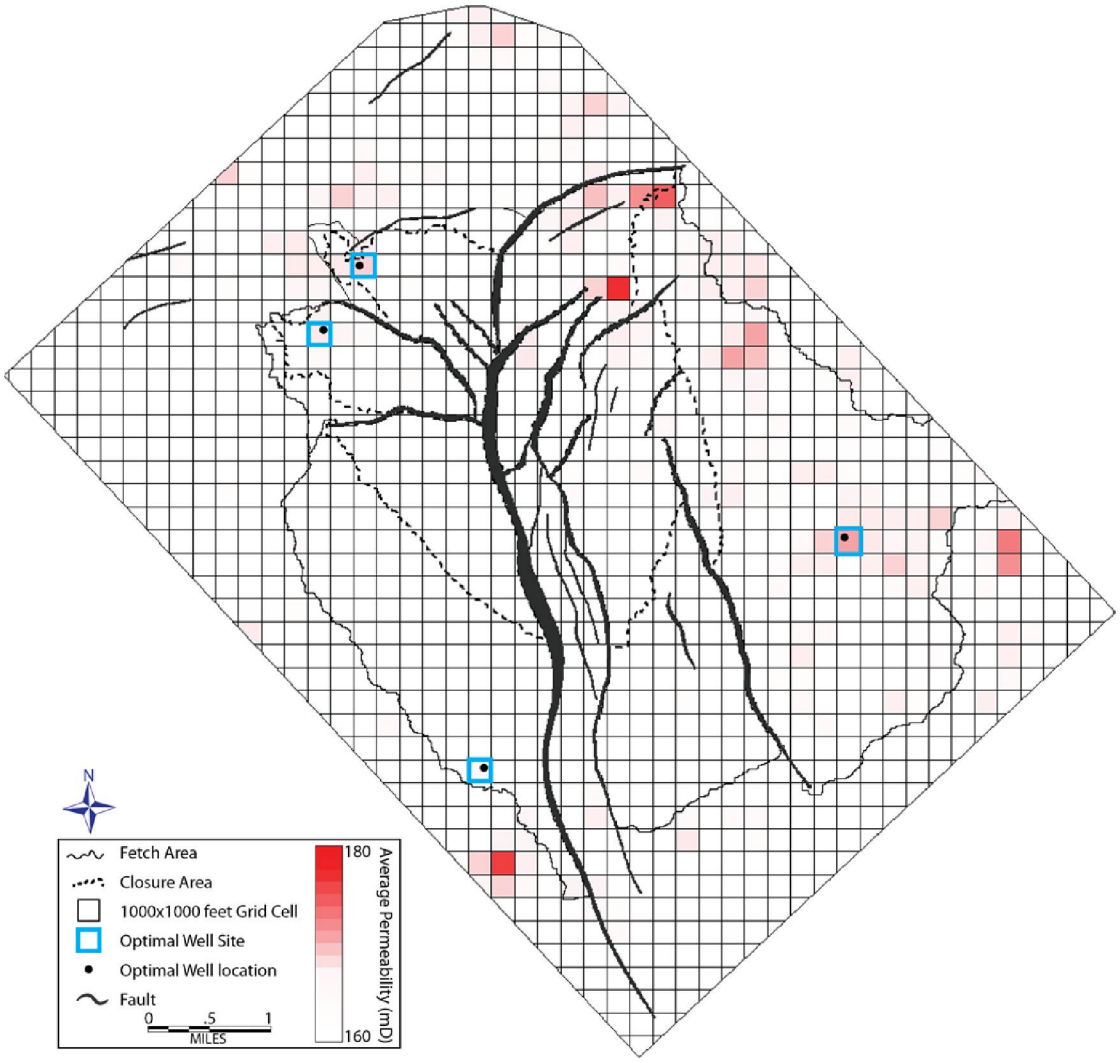

Figure 6.2.5: 10 layer average permeability of seismic-based heterogeneous model gridded with 1,000 x 1,000 feet (305 x 305 meter) cells. Optimal well sites are outlined in blue within which the optimal well locations are shown.

Results

Results from the seismic-based heterogeneous 3D fluid flow model scenario showed that the CO_2 capacity ranged from 3.1-5.7 Mt, excluding the open boundaries case (Table 6.2.2). The base case resulted in a capacity of 4.5 Mt. The seismic-based heterogeneous scenario resulted in the smallest storage capacity of the three scenarios in every variation case. The results of the seismic-based heterogeneous scenario showed a decrease in injected mass from the statistically heterogeneous scenario. This was likely due to the presence of minor impermeable baffles in the seismic-based heterogeneous scenario, which hindered fluid flow and reduced the available space for CO_2. Presence of baffles not only created locally sharper pressure increases, but also effectively diminished the size of the reservoir and caused pressure to rise more quickly in closed boundary cases. The CO_2 flow path was minimally affected

by random heterogeneity and was not significant enough to overcome the effects of high flow velocity from large injection rate or gravitational buoyancy effects. The open boundary case is considered to be unlikely because the actual connectivity of the reservoir is finite, but is treated as infinite under open boundary assumptions. This results in very large CO_2 plumes with minimal pressure build-up. When considering the makeup of rocks in nature, it is likely that subseismic heterogeneity will effectively compartmentalize reservoirs and prevent hydraulic connection over very large distances.

Table 6.2.2: Cumulative injection results for 27 model cases of the dynamic 3D flow model.

3D Flow Model Injected Mass Results (Mt)			
	Homogeneous	**Statistically Heterogeneous**	**Seismic-Based Heterogeneous**
Base Case	5.4	5.3	4.5
High Quality Reservoir	6.9	6.8	5.7
Low Quality Reservoir	***3.7***	***3.5***	***3.1***
Open Boundaries	***116.2***	***114.4***	***64.0***
Open Faults	5.6	5.3	4.6
1 Well	6.0	5.7	5.0
15 Wells	5.4	5.2	4.8
Optimized Array	5.4	5.3	4.9
Constant Rate Injection	4.8	5.1	4.5

Though the seismic-based heterogeneous scenario`s permeability was more varied than other 3D scenarios, it had a faster fill time than the statistical heterogeneous model. This was likely due to the slight decrease in reservoir pore volume from the presence of zero-porosity zones. Including these zones created a smaller reservoir that could be filled faster. The roughly 45% decrease from the homogeneous to seismic-based heterogeneous model highlights the influence these impermeable baffles present in natural systems. The presence of impermeable zones compartmentalized the reservoir and hindered pressure dissipation, causing capacity of the reservoir to decrease.

CO_2 storage capacity distribution results from the seismic-based heterogeneous base case model are shown in figure 6.2.6. Because porosity and permeability are not uniform and can contain zero values, a color scale is chosen to highlight impermeable zones with no porosity (white). Note that the plume is partially disrupted at the surface of the seismic-based heterogeneous scenario, where permeability is non-zero. In layers where the permeability profile is more continuous (figure 6.2.4) this effect is diminished.

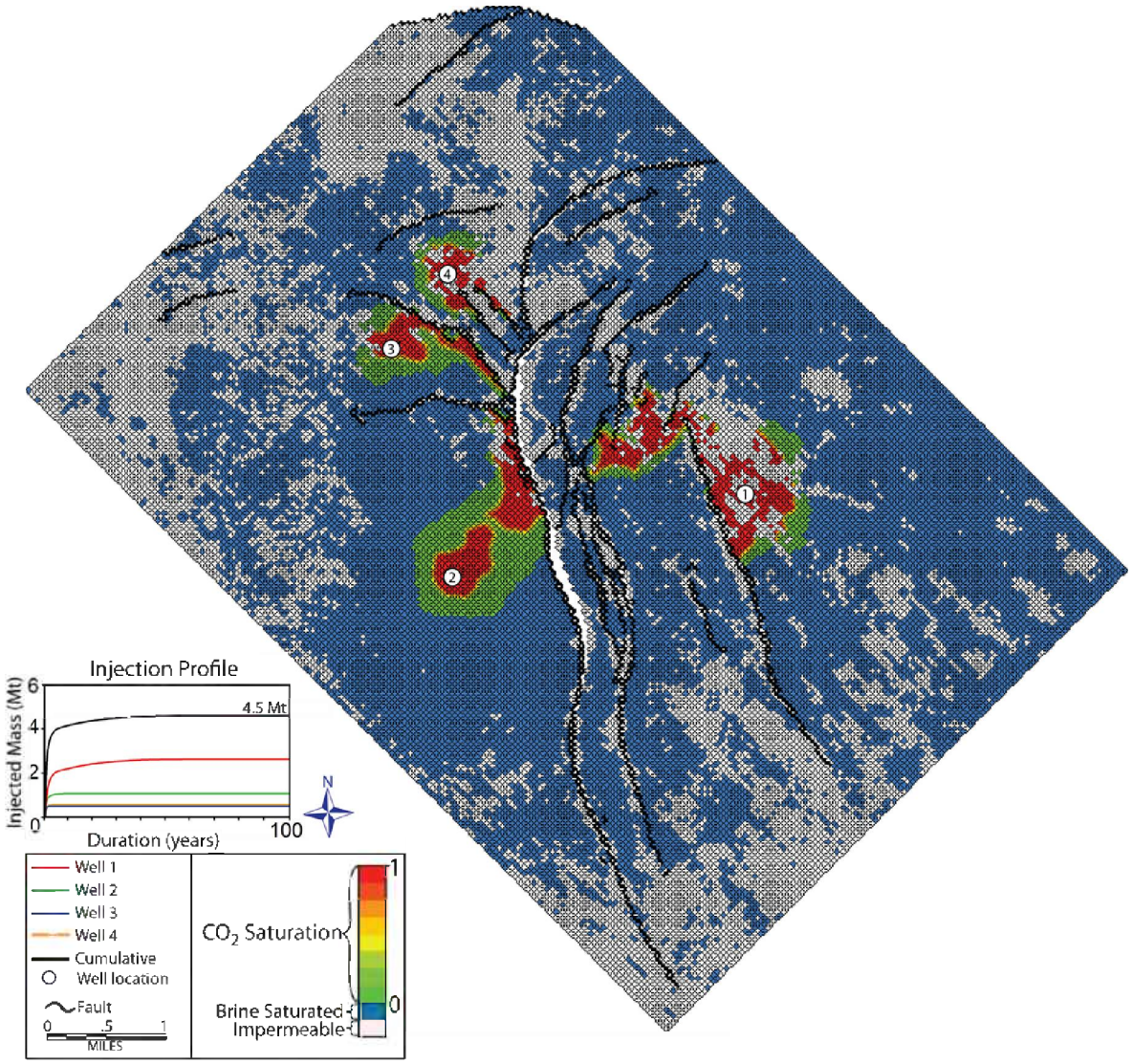

Figure 6.2.6: Final plume geometry at the top of the reservoir and injection profile for seismic-based heterogeneous scenario. Color scale is chosen to identify any impermeable zones, shown in white. CO_2 plume is indicated by the color spectrum from green to red.

Figure 6.2.7 shows the cumulative injection profile for the base cases of each of the three scenarios. The dotted vertical line indicates at which point no additional CO_2 could be injected without exceeding the reservoir pressure limit, which, in this case, is equivalent to the fill time. In each case, CO_2 injection falls off exponentially as the pressure limit is quickly reached and pressure dissipation becomes more difficult. Reservoir fill time for the seismic-based heterogeneous scenario base case was 57 years. Though the fill time was nearly six decades for the seismic-based heterogeneous scenario base-case, the majority of the capacity was filled within 25 years and approximately 85% of the total capacity was reached within the first five years. The total capacity of the seismic-based heterogeneous scenario was the smallest among the three base-case scenarios. However, all three exhibit similar fill rates throughout.

Conclusion

The use of 3D fluid flow simulations can greatly assist in assessing the potential storage capacity of a given reservoir. However, due to the complexity of geologic systems these simulations are simplified scenarios. The seismic-based heterogeneous scenario resulted in a capacity of 3.1-5.7 Mt for the Middle Miocene reservoir. Relative, to the other two scenarios, the reservoir had a reduced volume and permeability due to the presence of shale baffles throughout the interval. The presence of these baffles did not prevent CO_2 migration updip during injection to the top of each of the four closures. However, once injection ceased migration ended due to inability to overcome capillary pressure. In the seismic-based heterogeneous scenario, injection lasted for 57 years, at which time the reservoir pressure limit was reached, and pressure could no longer dissipate. The majority of CO_2 injection occurred in the first 25 years (Figure 6.2.7) as the volume of injected CO_2 experienced an exponential decay over time. These simulations illustrate the potential outcome of CO_2 injection in an offshore Miocene reservoir and highlight the effects of variable modeling parameters. As our confidence in this kind of modeling increases through field validation and additional data collection, we can begin to confidently estimate the feasibility of widespread carbon sequestration through geologic injection in the Gulf of Mexico.

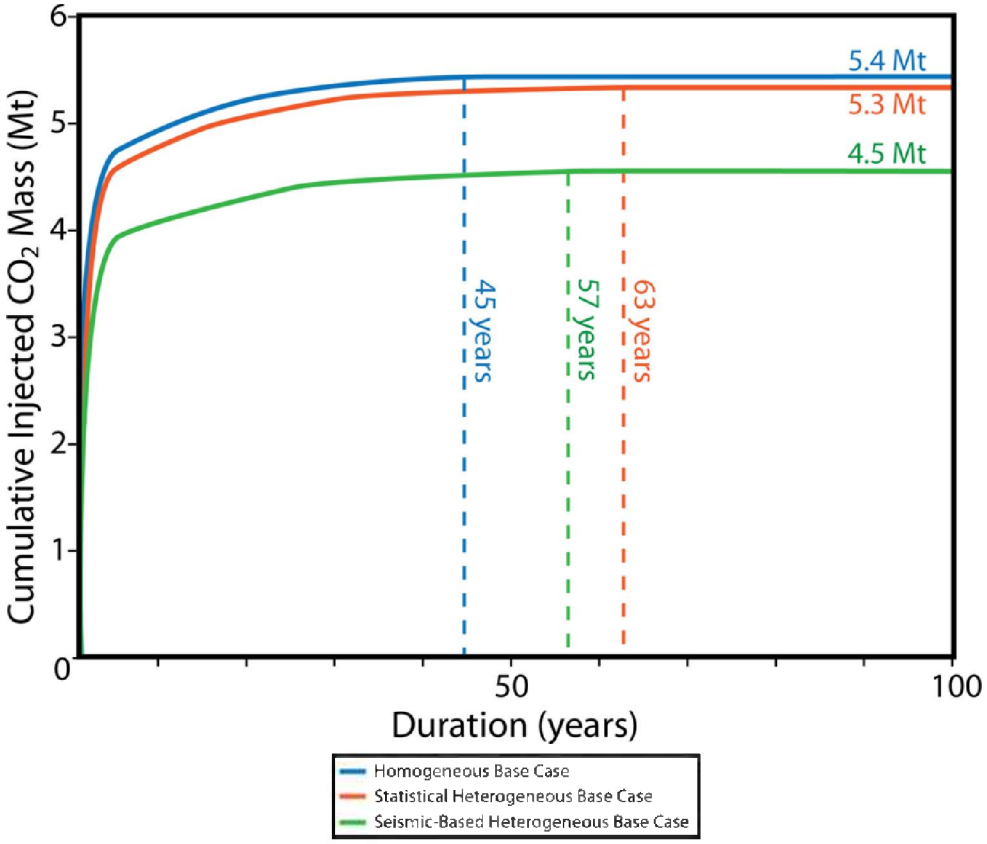

Figure 6.2.7: Cumulative injection vs. time of homogeneous, statistical heterogeneous and seismic-based heterogeneous base case models. Dotted vertical lines indicate time after which no additional CO2 is injected.

References

Nicholson, A.J., 2012. Empirical Analysis of Fault Seal Capacity for CO2 Sequestration, Lower Miocene, Texas Gulf Coast, Unpublished Masters Thesis. Geoscience. The University of Texas at Austin, pp. 88.

Seni, S.J., Hentz, T.F., Kaiser, W R., Wermund Jr., E.G., 1997. Atlas of Northern Gulf of Mexico Gas and Oil Reservoirs, 1. The University of Texas at Austin, Bureau of Economic Geology, Austin, Texas, 199 pp.

Wallace, K.J., 2013. Use of 3-Dimensional Dynamic Modeling of CO2 Injection for Comparison to Regional Static Capacity Assessments of Miocene Sandstone Reservoirs in the Texas State Waters, Gulf of Mexico, The University of Texas at Austin, Austin, 152 pp.

APPENDIX B

Risk Assessment:

CO_2-PENS Analysis

Final Report

Texas Submerged Lands CO_2 Sequestration Targets

Subcontract to Bureau of Economic Geology—The University of Texas-Austin
DE-FOA-0000033

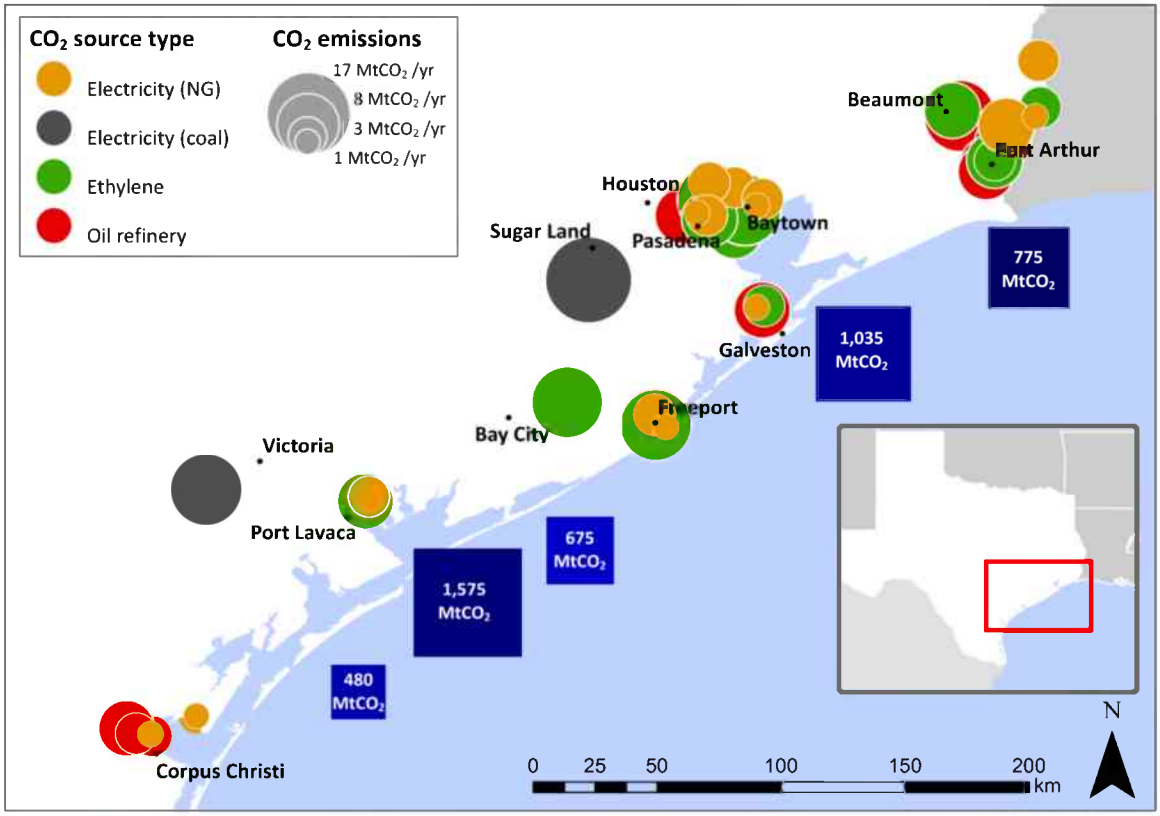

Authors

Bill Carey
Amy Jordan
Phil Stauffer
Richard Middleton

Los Alamos National Laboratory
Los Alamos, NM USA

September 30, 2011

1. Introduction

The potential for geologic storage of CO_2 in offshore settings is relatively undeveloped in the United States. In this project, the Bureau of Economic Geology at the University of Texas-Austin is leading a team that is assessing the suitability of Texas state waters (near-shore) in the Gulf of Mexico for CO_2 sequestration. The goals of the project include the development of an atlas of storage opportunities, a ranked list of prospective reservoirs with a 30 million tonne (MT) capacity, a detailed assessment of several of these targets, and a focused feasibility study of at least one site.

The potential storage reservoirs consist of Miocene deltaic sediments that include depleted oil and gas reservoirs as well as saline aquifers. The sequestration targets are sandstone units that are interbedded with low permeability/porosity shales. The sands have relatively small volumes and a sequestration reservoir encompasses a package containing a number of these sand units. The Los Alamos National Laboratory (LANL) team's role in the project was two-fold: the team assessed the capacity and injectivity of the sand units and the packages; and the team developed a cost-optimized model for connecting onshore CO_2 sources via pipelines to potential sequestration targets. Both of these efforts were conducted using LANL-developed risk assessment software that includes CO_2-PENS (Predicting Engineered Natural Systems) for reservoir studies and *simCCS* (spatial infrastructure model for carbon capture and sequestration [CCS]) for optimization of infrastructure and costs in CCS projects.

2. Capacity and Injectivity of Miocene Sediments in Texas State Waters

Geologic data for Miocene deltaic sediments were obtained from well data available in the Atlas of Northern Gulf of Mexico Gas and Oil Reservoirs ("Gulf Atlas"). These data were analyzed and used to conduct numerical modeling of capacity and injectivity using the LANL-developed Finite Element Heat and Mass transfer code (FEHM). The goals of the modeling effort were: (1) to quantify the injectivity and capacity of Miocene sands based on available geologic data; (2) to characterize the sensitivity of the results to uncertain geologic parameters and natural variability; and (3) to provide estimates of injectivity and capacity variability for the system-level modeling of the likely costs associated with regional carbon capture, transport and storage in offshore sequestration targets. The modeling methodology, results and conclusions are discussed below.

Computational Approach

All simulations were performed in a 3-D, radially symmetric domain. The modeling was conducted in three phases. In the first phase, the properties of individual sand units were investigated with a focus on the impact of differing boundary conditions

and the sensitivity of the results to individual geologic parameters. In the second phase, a conceptual model for the target reservoir was developed that consisted of a stacked set of eight closely spaced sandstone layers separated by low-permeability shale layers (a sand package). The injectivity and capacity of the package was investigated using data sampled randomly from varying geologic properties representative of the offshore Gulf of Mexico Miocene sandstones. Lastly, regional aggregates of packages were selected from the Gulf Atlas based on their proximity to carbon sources and potential for significant CO_2 storage. These regional reservoirs were modeled to determine injectivities and CO_2 storage capacities with results providing input to the spatial infrastructure analysis of regional carbon sequestration along the Gulf Coast.

The code used to perform the numerical modeling, FEHM, is a multi-phase fluid flow simulator for porous media (Zyvoloski 2007). The modeling was conducted on numerical grids generated from reservoir data obtained from the Gulf Atlas. In the grids, sandstone layer(s) were represented with a resolution of 15 nodes in the vertical direction (with thicknesses ranging from ~1 m to 30 m). Low-permeability layers bounding the sands (shales) were each 5 nodes thick. In the radial dimension, node spacing was less than 10 cm adjacent to the injection wellbore and grew with a geometric factor of 1.2 to the full extent of the reservoir.

For all simulations, the temperature gradient was based on a linear fit to the Gulf Atlas data:

$$T = D_S \times 0.0301 + 9.1327 \qquad \text{Equation (1)}$$

where T is temperature in degrees Celsius and D_S is depth below the seafloor in meters. Injection pressure was fixed at 70% of lithostatic pressure, a reasonable estimate of a safe overpressure of injection. Alternatively, we could have fixed the injection rate of CO_2 and allowed injection pressure to vary, but we have chosen to keep the pressure of injection fixed to represent reservoir limits based on the competence of the rock to withstand increased fluid pressures. Lithostatic pressure was based on a lithostatic gradient of 23 MPa/km estimated for offshore Gulf of Mexico formations (Bethke 1986).

A van Genuchten model for relative permeability and a Brooks-Corey model of capillary pressure (van Genuchten 1980, Brooks and Corey 1964) were used for all simulations. The parameters used are shown in Table 1, and are from Pruess and García (2002). This model was used within upper and lower cutoff boundaries of 0.01 for saturation, beyond which a linear interpolation is used for relative permeability and capillary pressure.

Table 1.
Relative permeability parameters used in the simulations (Pruess and García 2002)

Relative Permeability/Capillary Pressure Model Parameters	
Van Genuchten P_o	1.961E4 Pa
Van Genuchten m	0.457
Irreducible water saturation (for van Genuchten relative permeability)	0.3
Irreducible CO_2 saturation	0.05
Irreducible water saturation (for capillary pressure)	0.0

The modeling results use CO_2 injectivity and capacity as the dependent variables for recording the impact of varying independent geologic parameters (sand thickness, reservoir area, depth, porosity and permeability). Injectivity is defined as the CO_2 flow rate (in kg/s or $MtCO_2/yr$) at the point of injection. It is a primary variable of interest for determining the number of wells required to utilize a particular reservoir and the time for a reservoir to accept a certain quantity of CO_2. The other major variable of interest is the CO_2 storage capacity of a reservoir. Due to the buoyancy of CO_2 and resulting gravity segregation, the entirety of pore space in the reservoir is not available for CO_2 storage. If the size and porosity of a reservoir are known, maximum possible CO_2 capacity can be defined as (U.S. DOE 2008):

$$G_{CO2} = A_t\, h_g\, \varphi\, \rho\, E, \qquad \text{Equation (2)}$$

where G_{CO2} is the estimated mass of CO_2 that can be stored, A_t is the areal extent of the reservoir, h_g is reservoir thickness, φ is the average porosity, ρ is the average CO_2 density at the temperature and pressure of storage conditions, and E is a storage "efficiency" factor that represents the unavailability of parts of the reservoir to storage (the average fraction of pore volume within the total reservoir volume that cannot be occupied by CO_2).

Accurate estimates of E are difficult to obtain, either from field or numerical modeling studies, and the choice of E has a significant impact on the capacity result. In this study, we determine capacity as the mass of CO_2 injected at the time the CO_2 plume reaches the far edge boundary of the model. Some of the parameters that can affect the speed at which this boundary is reached include the relative permeability model and parameters; the choice of well casing properties for the model (cased versus open hole); permeability anisotropy; and geologic heterogeneity. The capacity values reported here should be considered rough estimates and highly dependent on the conceptual model of the simulation.

2.1 Boundary Conditions and Sensitivity to Geologic Parameters

Initial simulations were performed to test the model and evaluate the impact of various boundary conditions. For the boundary condition simulations, average reservoir properties for progradational-type Miocene plays were used from the Gulf Atlas (Table 2), with the exception of reservoir thickness, which was chosen as 8 m. For all scenarios, CO_2 was injected at the bottom of the reservoir from a 10-cm radius wellbore of porosity 0.1 and permeability 1 D. Injection pressure was 40 MPa, or approximately 70% of lithostatic pressure. A linear relationship for CO_2/brine relative permeability was used.

Four boundary conditions were considered:

(Case 1) Sealed reservoir, impermeable boundaries
(Case 2) Vertical fault boundary at far edge of reservoir with fixed hydrostatic pressure
(Case 3) Low-permeability upper and lower boundary layers (10^{-6} D), e.g. shale layers
(Case 4) Impermeable boundaries with a permeable well 1000 m from injection wellbore which allowed flow into the bottom of the well

Table 2.
Parameters used for modeling of reservoir boundary conditions

Reservoir Parameter	Method of Calculation	Value used in Models
Thickness	-	8 m
Length	Mean radius based on reservoir area	990 m
Depth below surface	Mean	2500 m
Porosity	Mean	0.28
Permeability	Geometric Mean	0.1 D

Figure 1 shows the attenuation of CO_2 injectivity over time as pressure builds up in the sealed reservoir of Case 1. Figure 2 shows the rate of CO_2 injection and CO_2 flow out of the fault zone for Case 2. Once the plume reaches the fault boundary, CO_2 escapes from the reservoir at rates that approach the injection rate. For Case 3, Figure 3 shows the fraction of CO_2 in the reservoir as well as the amount that migrates into the low-permeability bounding layers (shale) above and below the reservoir after 100 years. The corresponding injection rate for Case 3 is shown in Figure 4. The maximum injection into the lower shale layer is less than 0.5×10^{-3} kg/s (note that a small amount of CO_2 also flows out of the lower shale layer into the reservoir, but is not shown here), and the maximum injection rate into the upper shale is less than 2×10^{-3} kg/s. For Case 4, the CO_2 injection rate and the flow of CO_2 out of the leaky wellbore are shown in Figure 5. These results are similar to the leaking fault scenario (Figure 2), but the onset of leakage is delayed because flow occurs only from the bottom of the well.

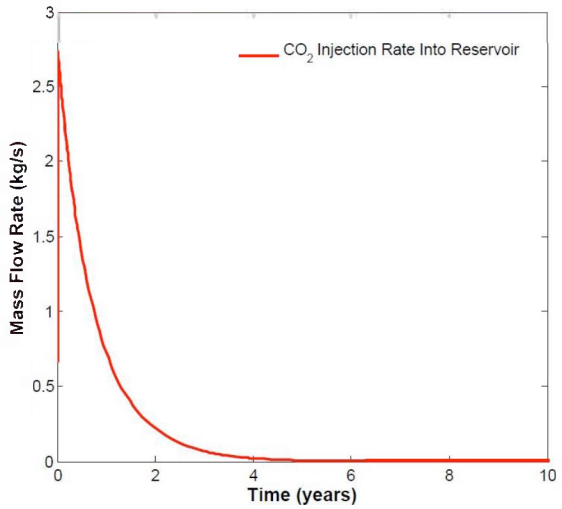

Figure 1: Case 1 CO_2 injection rate.

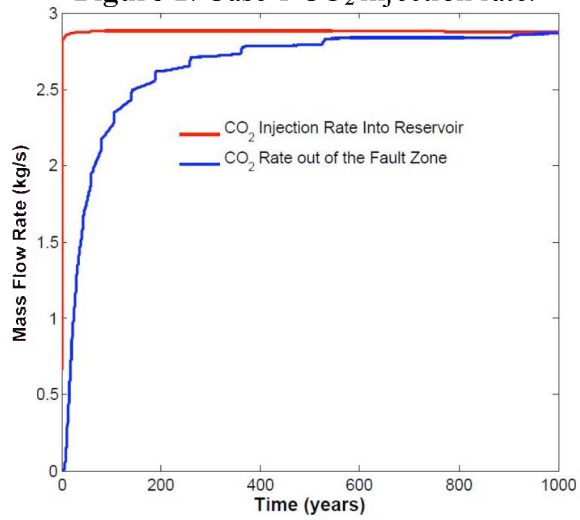

Figure 2: Case 2 CO_2 injection rate and flow out of the fault zone.

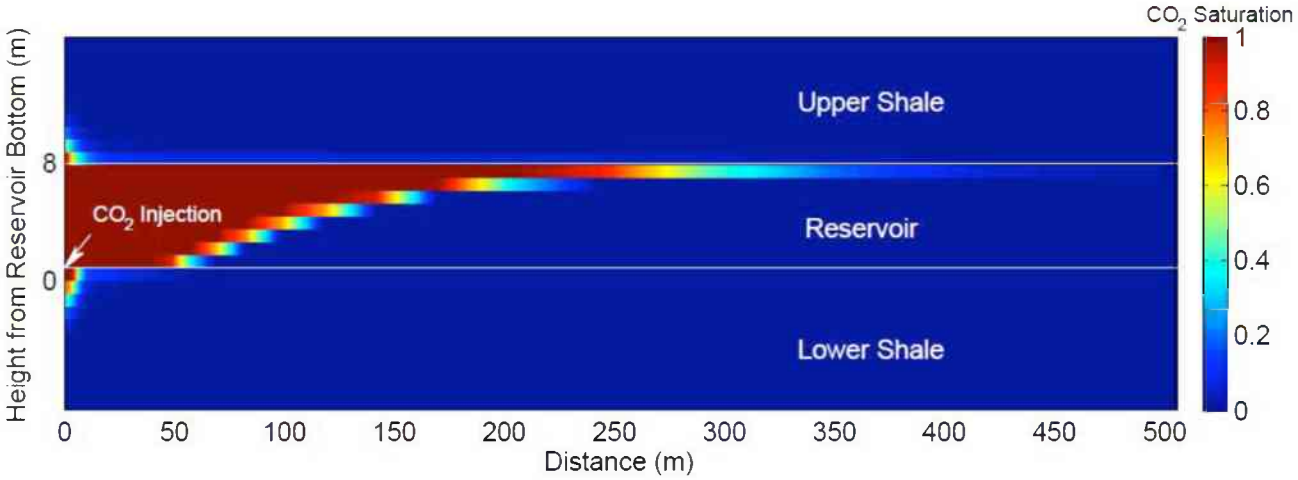

Figure 3: CO_2 saturation fraction for Case 3.

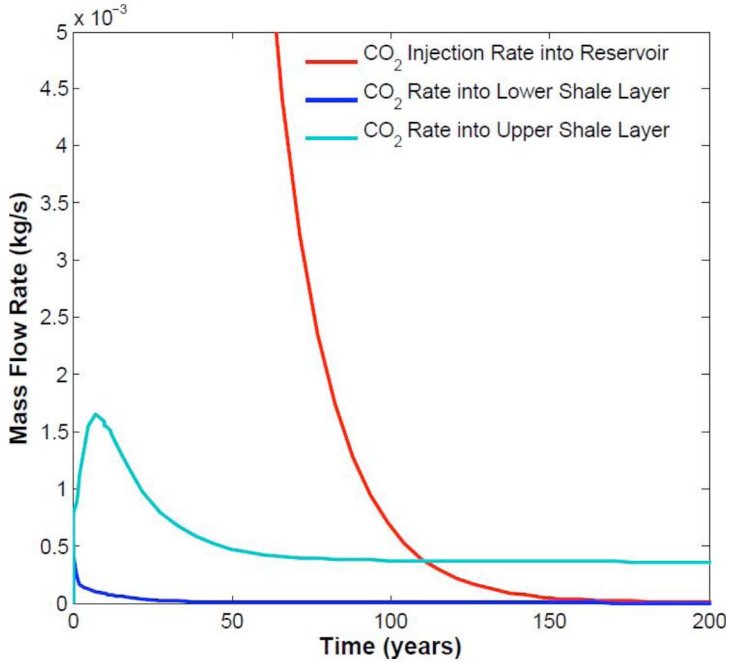

Figure 4: Case 3 CO_2 injection rate and flow into the upper and lower shale layers.

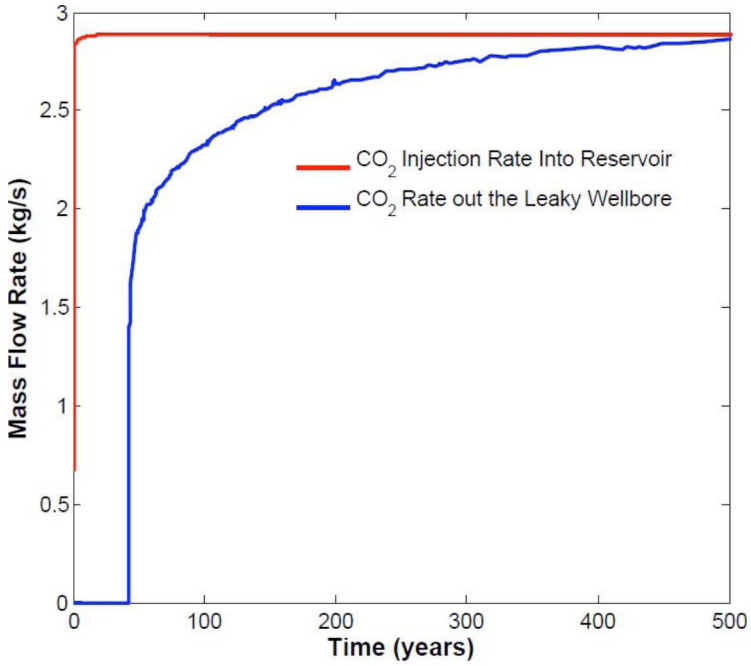

Figure 5: Case 4 CO_2 injection rate and flow out of the leaky wellbore.

Simulations involving the four different boundary conditions show that closed boundaries (Case 1) have poor injectivity due to rapidly rising pressure and are perhaps not realistic as we expect there to be some outlet for fluids. Simulations with semi-permeable, bounding shale layers (Case 3) accommodate some additional

CO_2 as CO_2 migrates into the shale but also perform as closed systems that pressurize as there is no fluid escape. Case 4 was modeled as a reservoir with a leaking well but also represents a reservoir with a spill point, whereby CO_2 can accumulate at the top of the reservoir and does not leak until it reaches the bottom of the well. Case 2 represents both a leaking fault as well as a permeable boundary for a sequestration site (e.g., the permit boundary). Both cases 2 and 4 have more realistic pressure histories as brine is allowed to migrate from the reservoir during CO_2 injection. We focused our subsequent studies on case 2.

A series of Monte Carlo simulations were performed to test the impacts of varying geologic properties on CO_2 injectivity and storage capacity of a reservoir. The boundary conditions were simulated as a high-permeability fault at the far-field with no flow allowed above and below the reservoir (case 2 above); however, one change to the model was the introduction of a wellbore casing, a low-permeability line of nodes along the wellbore except at the bottom node of the reservoir. Relative permeability and capillary pressure were modeled using van Genuchten and Brooks-Corey parameters, as described above. Reservoir sizes and other geologic parameter ranges were chosen to span the Gulf Atlas data for sand layer thickness, length, porosity, and permeability; depth was constrained between 800 m and 3660 m, based on the range of likely target depths for carbon sequestration. The "base case" parameters (i.e., the values used for the simulations in which those parameters were fixed) and range of variation are given in Table 3. Simulations were run until the CO_2 plume reached the far-edge fault boundary.

Table 3.

Base case and ranges of parameters used in basic Monte Carlo sensitivity studies.

	Thickness (m)	Length (m)	Depth (m)	Porosity	Permeability of reservoir (m^2)
Base Case	8	1500	2400	0.28	1×10^{-13}
Range	1 – 30	262 – 3900	800 – 3660	0.19 – 0.36	8.5×10^{-14} – 2×10^{-12}

Figure 6 shows the effect of uniformly varying five parameters (Table 3) individually on CO_2 injection rate and storage capacity. Figure 7 plots the time (in years) before the CO_2 plume reaches the far-edge fault. Note the change of y-axis scales between the different graphs in Figures 6 and 7. As expected, reservoir sizes (thickness and sand length scale) have the greatest effect on storage capacity. However, greater sand length scale has less of an effect on injectivity. Porosity and depth are also directly correlated with capacity (porosity has no effect on injection rate, but increased porosity slows the time to CO_2 breakthrough as additional pore volume is available to accept CO_2). Permeability has essentially no effect on capacity, as permeability increases injection rate and decreases time to breakthrough in proportion to each other.

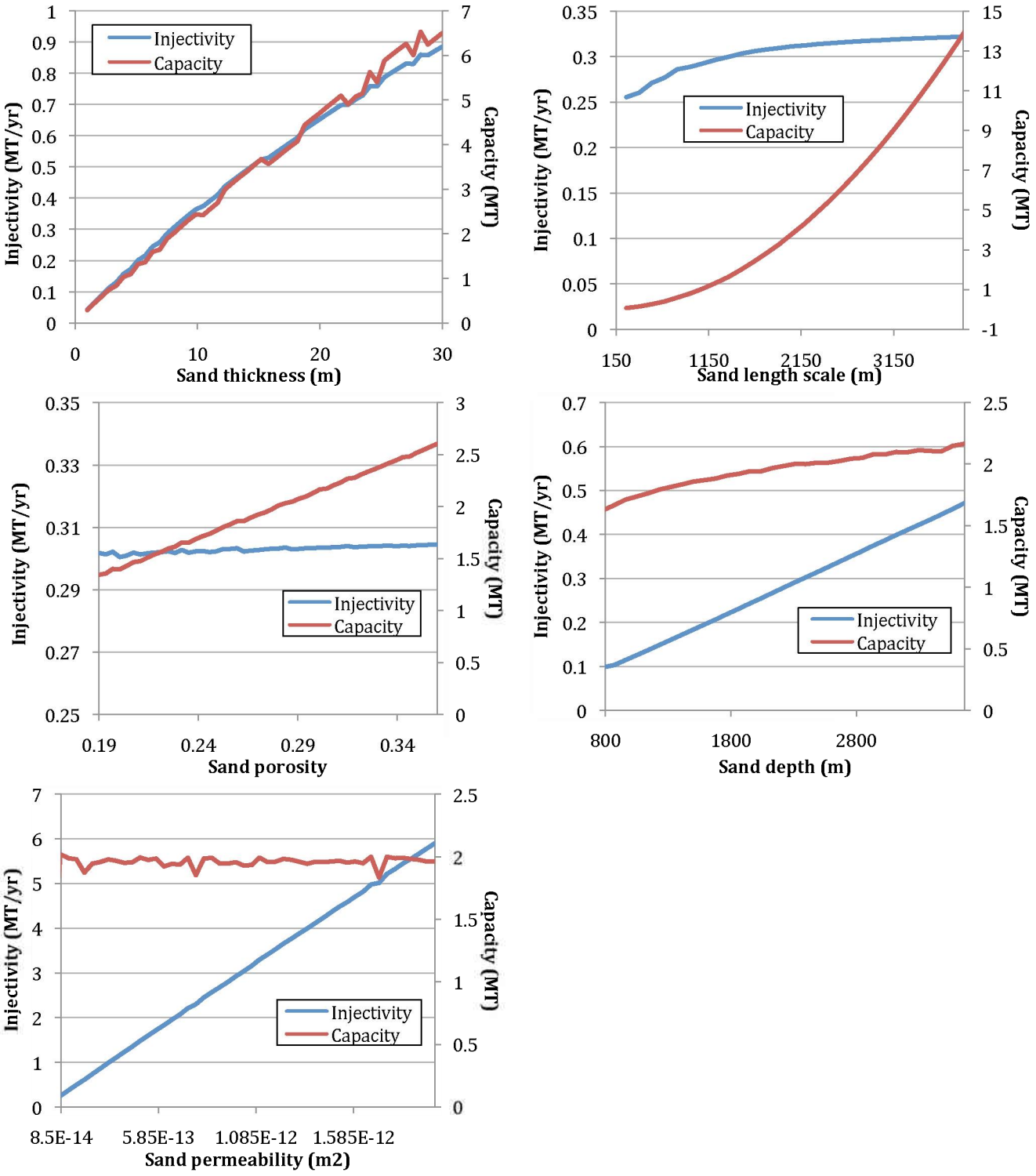

Figure 6. FEHM results for storage capacity and CO_2 injection rate for a single sandstone reservoir with properties spanning the range of values in the Gulf Atlas data set.

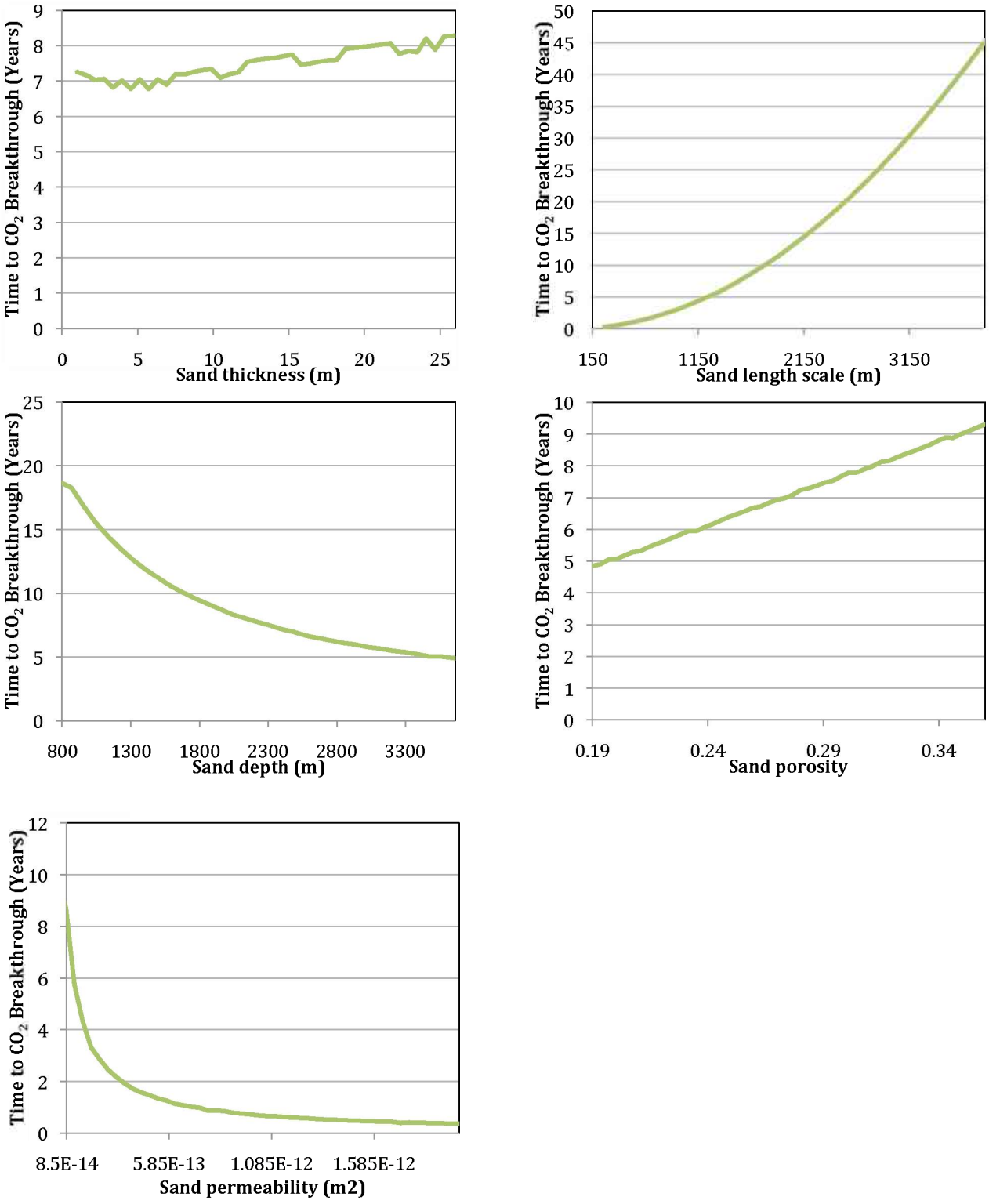

Figure 7. Time for CO_2 breakthrough at the far-edge fault boundary for a single sandstone reservoir with properties spanning the range of values in the Gulf Atlas data set.

Calculations made while varying individual properties do not capture interaction effects among the geologic parameters. In order to facilitate a study of interaction effects, probability distributions were developed based on the Gulf Atlas data for Miocene reservoirs. Rather than the discrete and limited Gulf Atlas data, the probability distributions are continuous and can be used to assign truly random values for the simulations. Latin hypercube sampling across multivariate parameter space was used to generate random data for the parameters, which were transformed to appropriate distributions for each parameter based on distributions observed in Gulf Atlas data. Relations between correlated variables (e.g. porosity and permeability, temperature/pressure and depth) were studied and reproduced in the generated data. FEHM runs using these generated distributions were compared to FEHM runs that used the real Gulf Atlas data for the reservoirs' geologic properties to validate the probability distributions.

Figure 8 compares data generated from the synthetic probability distribution with actual data for porosity and permeability. The probability distribution closely reproduces the center of gravity and range of observed values. A linear fit of the relationship between porosity and log (permeability) was determined. In subsequent modeling, porosity values were generated by Latin hypercube as described above, and permeability values were calculated using the linear fit from porosity values with an added term of normally distributed scatter.

Figure 9 compares cumulative distribution functions from the synthetic probability distributions with actual Gulf Atlas data. Note that pressures shown here are initial reservoir pressure from the Gulf Atlas (i.e., pressure upon discovery of the sand); pressures in the reservoir are assumed to be currently hydrostatic following development for oil and gas. Modeled pressures shown in Figure 9 are hydrostatic and therefore a poor fit to the data. Other parameters are well reproduced by the synthetic data.

As a final comparison, Figures 10 and 11 show CO_2 injectivity and capacity for (1) the synthetic probability distributions described above and (2) the actual Gulf Atlas submerged lands data fed directly into the model. Note that these are semi-log plots except for permeability, which is a log-log plot. The results show the fidelity between the synthetic and actual data. The much larger data set available from the synthetic distribution shows that the relationships between input geologic parameters and the resulting injectivity and capacity are less straightforward when all parameters are allowed to vary at once. However, correlations between permeability and injectivity, thickness and injectivity, length scale and capacity, and thickness and capacity are fairly strong. The ranges of injectivities and capacities seen in Figures 10 and 11 represent estimates of the ranges expected to be found in individual layers of the offshore Gulf of Mexico Miocene sandstones, as described by the Gulf Atlas data.

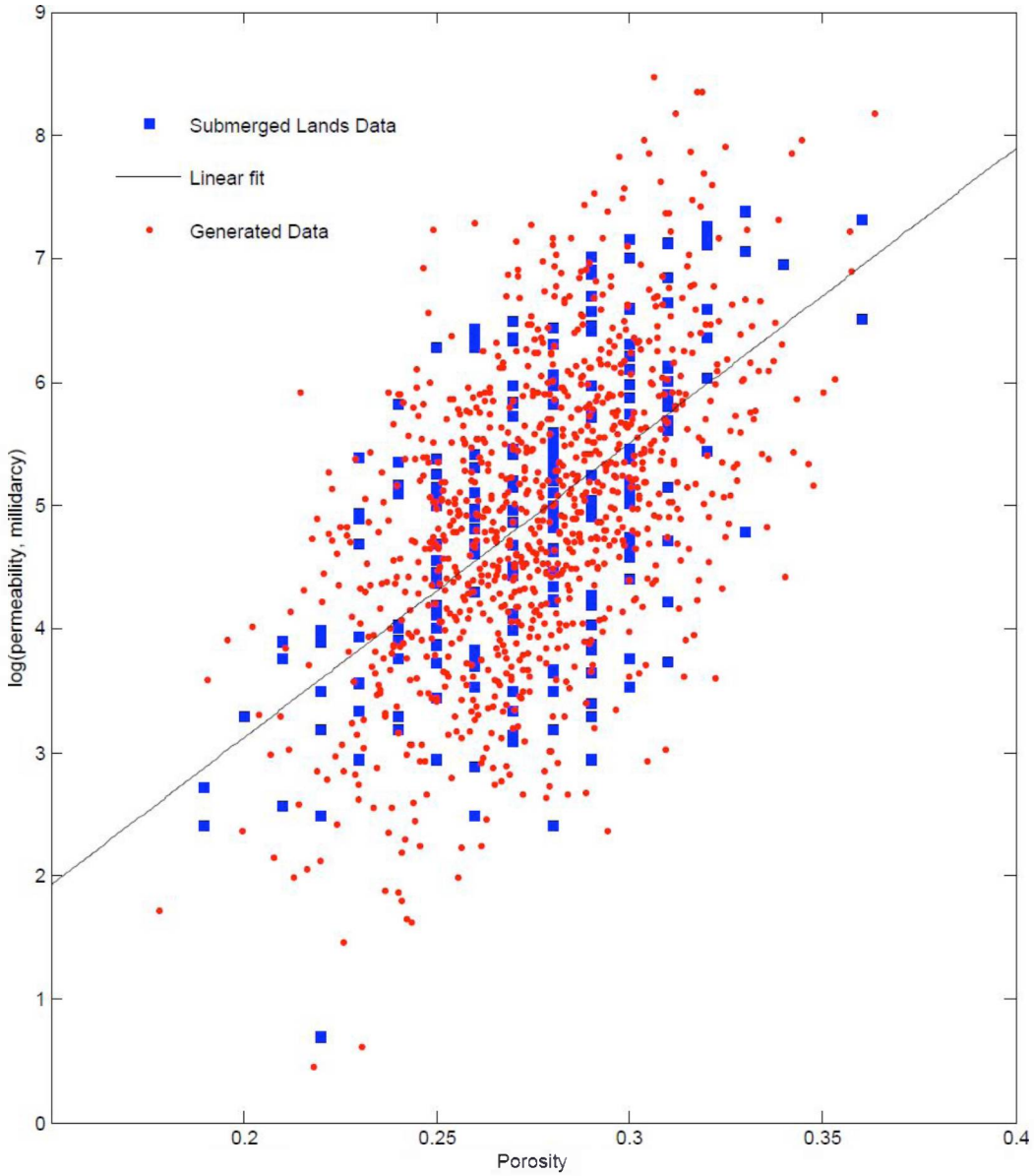

Figure 8: Gulf Atlas data (blue) and generated data for Monte Carlo simulations (red) – permeability and porosity.

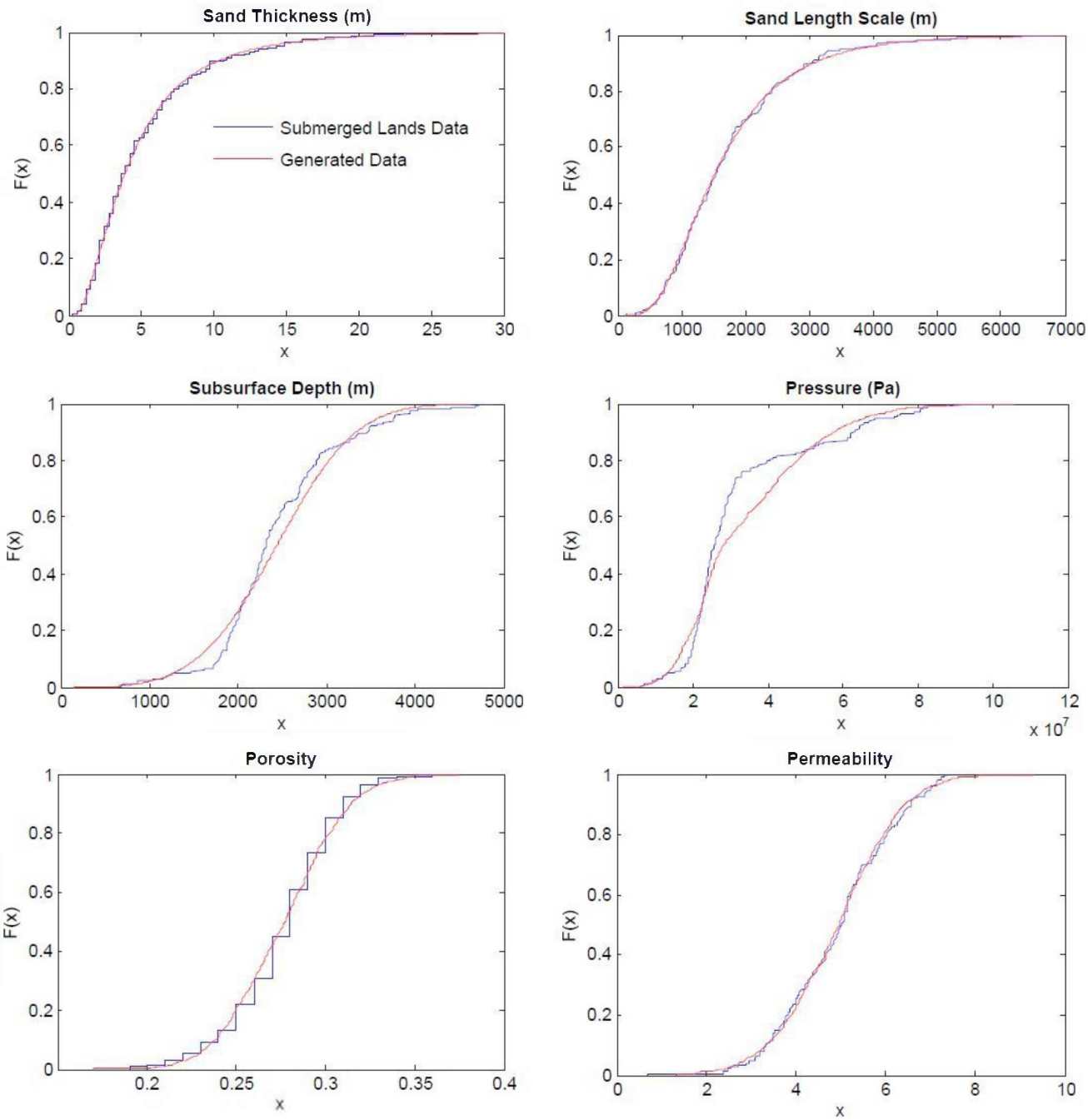

Figure 9: Empirical cumulative distribution functions for reservoir thickness, length, depth, pressure, porosity and permeability.

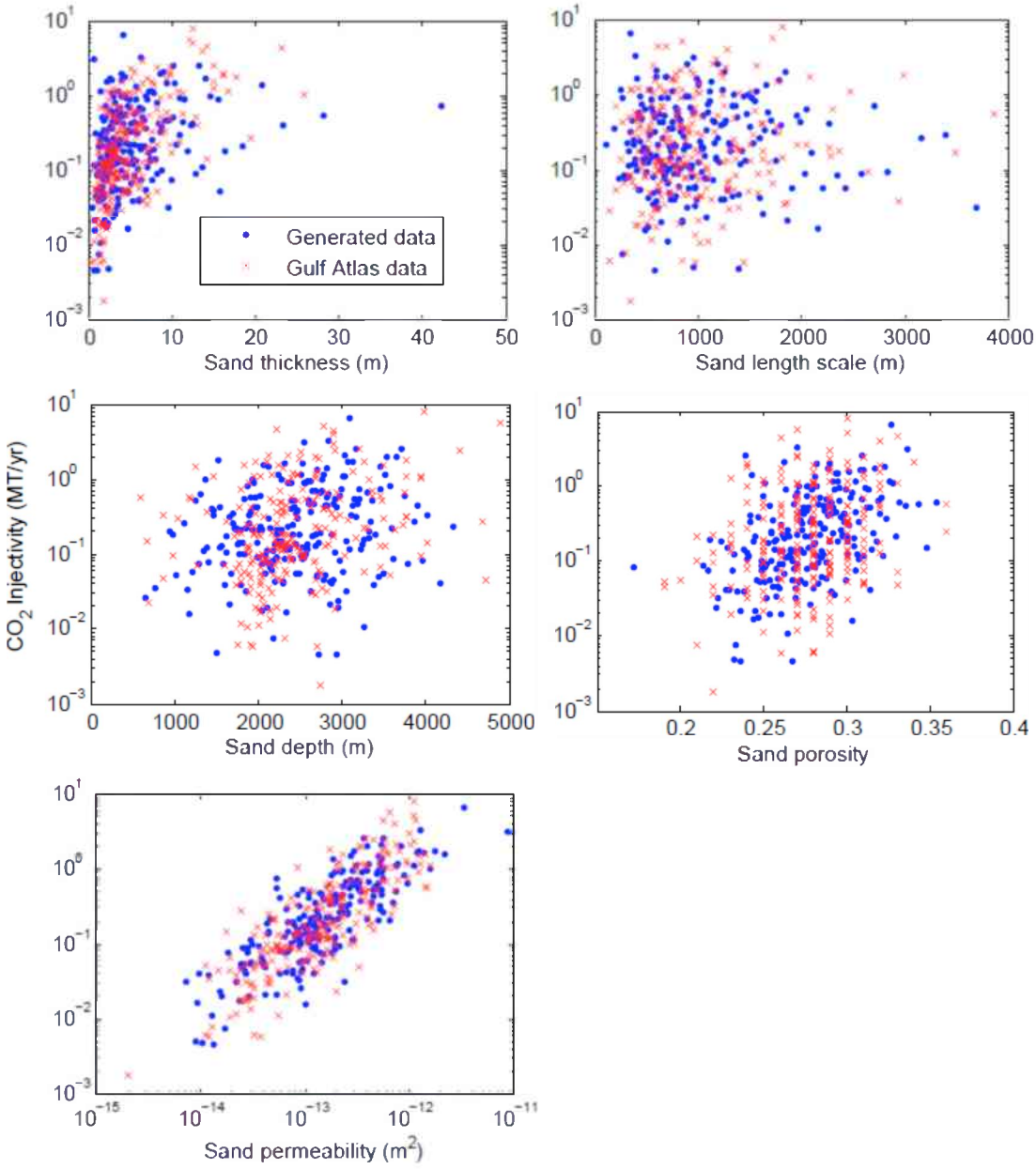

Figure 10. FEHM results for injectivity at the end of the simulation (the time CO_2 reaches the fault boundary). Each realization represents a single sandstone reservoir with properties as found in the Gulf Atlas data (red) or in the generated distributions (blue).

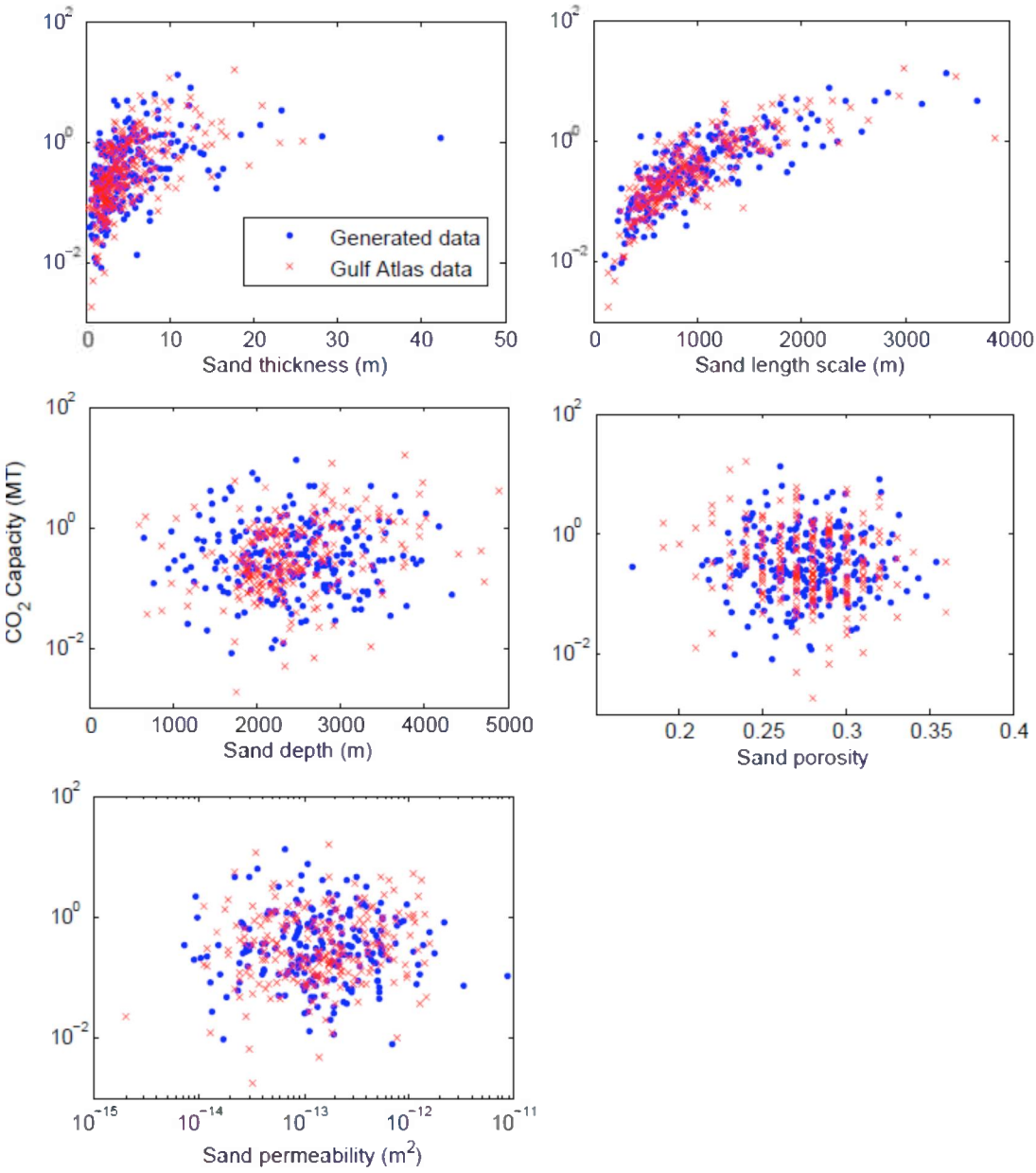

Figure 11. FEHM results for CO_2 capacity at the end of the simulation (the time CO_2 reaches the fault boundary). Each realization represents a single sandstone reservoir with properties as found in the Gulf Atlas data (red) or in the generated distributions (blue).

Analyses of the results from the first phase of modeling were used to check the validity of the model setup and to adjust boundary conditions before beginning the second phase, where a new conceptual model was implemented to test the impact of stacked sandstone layers as might be found in offshore Gulf of Mexico Miocene formations.

2.2 CO_2 Injectivity in Stacked Sandstone Reservoirs

Consideration of the geologic context of the Miocene deltaic sand reservoirs led to the development of a revised conceptual model. Rather than a single target sand, this consisted of a stack of multiple sands linked by a single wellbore. For this study, we considered a stack of eight sands intersected by an injection wellbore. CO_2 was injected at the bottom of the stack and allowed to fill in the sand layers, with the far-field boundary open to allow CO_2 and water flow. The results from the previous analysis of boundary conditions and probability distributions for geologic parameters were used for each of the stacked sands. Thus the eight sand layers could each have varying properties of thickness, porosity, and permeability, drawn from the probability distributions for the Gulf sandstones described above. Length and overall depth of the stack were also allowed to vary between realizations.

We did not model a low-permeability wellbore casing in these simulations; the high-permeability CO_2-filled wellbore (open hole) was simply in contact with the reservoirs and shales. The simulation was not stopped at the time the plume reached the far-edge boundary in the lowest reservoir, as the other sands would not have had time to reach their capacity.

A plot in "grid space" (i.e., not to scale) of CO_2 saturation after 10 years for one realization of the stacked sandstone reservoirs is shown in Figure 12. In this plot, the varying thicknesses of the reservoirs are not apparent because each reservoir contains the same number of nodes (in these simulations, the sands were all 8 nodes thick with varying map of actual thickness to node spacing). Regardless of its permeability or other properties, the closest reservoir to the injection node is expected to receive CO_2 at the highest flow rates because pressure gradients there will be steeper.

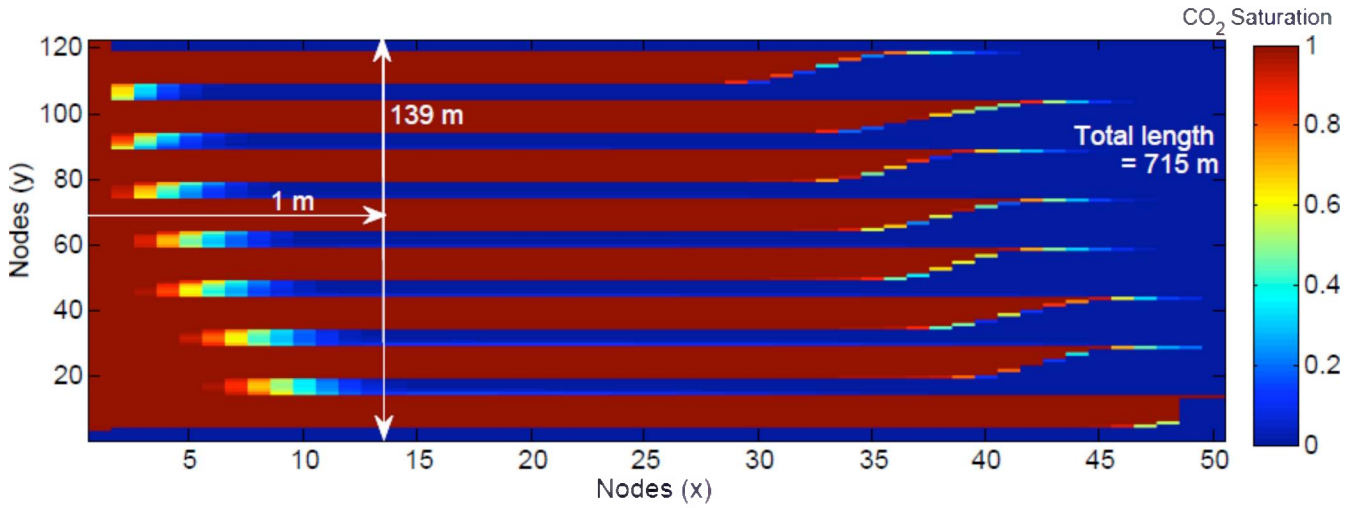

Figure 12. CO_2 saturation at t=10 years for one realization of a stack of eight sandstone layers, separated by 10 m shales, shown in grid space (not to scale). Node spacing is much smaller in the x dimension close to the wellbore.

For 20 realizations with thickness, porosity, and permeability varying between layers in a stack and between realizations, and with overall depth and length varying between realizations, CO_2 injection rate at 10 years is shown in Figure 13. Due to the lack of a wellbore casing, these injectivities generally exceed those seen in the individual reservoir simulations discussed above, with the exception of the high-permeability reservoir cases. Relationships between the parameters and injectivities are obscured due to averaging of properties across the layers, but the impact of depth on injectivity remains apparent.

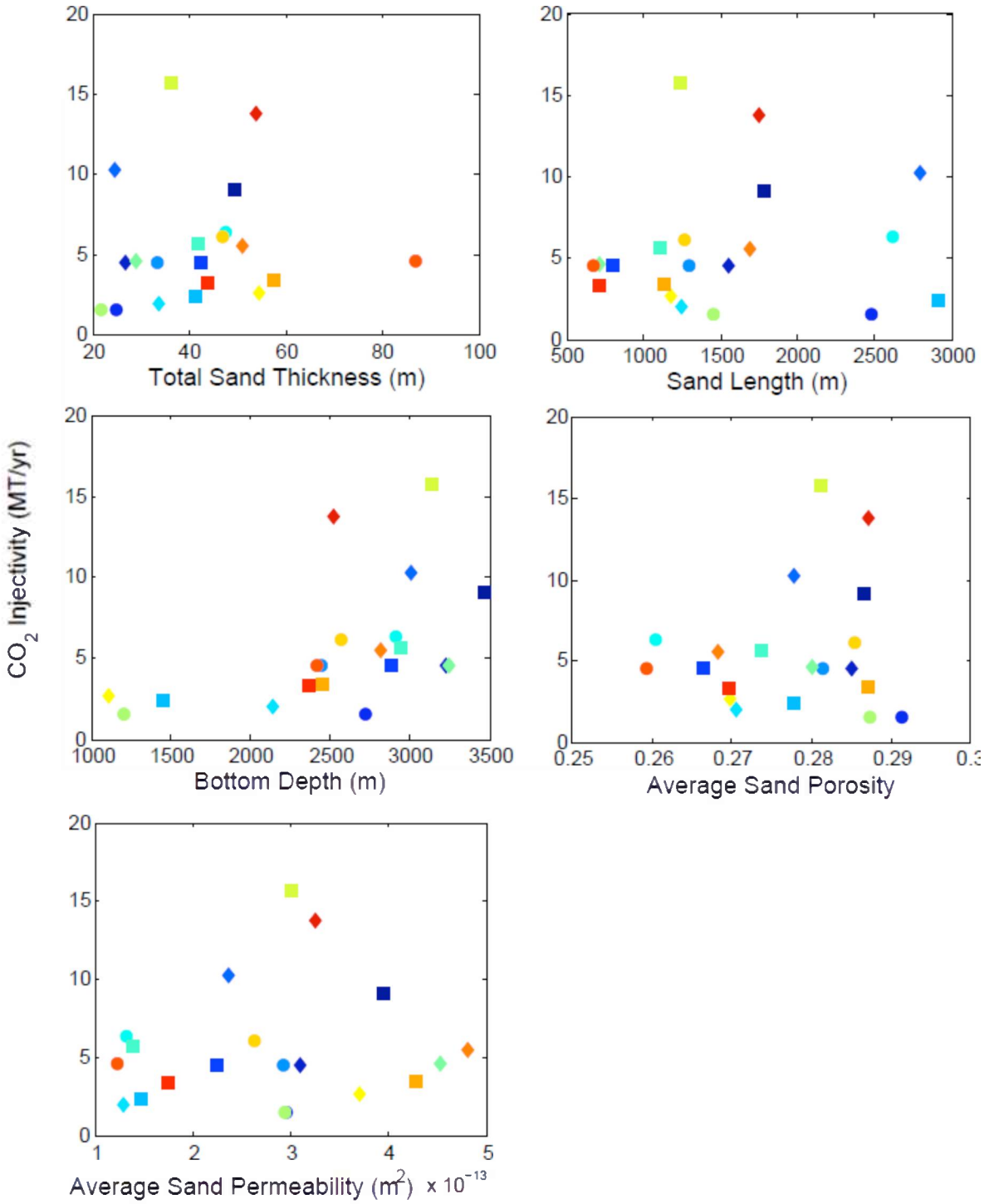

Figure 13. CO_2 injection rate at t=10 years for 20 realizations of the eight-layer stack of reservoirs. Injection continued after the plume reached the edge of the first reservoir. Since each sandsonte layer within each realization has a different permeability and porosity, average values for the realization are plotted here. Total sand thickness is the sum of the thicknesses of all eight sand layers in the simulation. Each unique symbol corresponds to a particular realization.

2.3 Analysis of CO_2 Injectivity and Capacity for Potential Gulf Coast CCS Sites

The final step of the capacity and injectivity analysis was to identify several geographic locations within the Texas state waters as potential sequestration targets. The results of the analysis were provided as input to the spatial infrastructure task (Section 3). Most of the available Gulf Atlas data are for federal waters that are adjacent to state waters. Thus, the available data do not provide a direct way of choosing suitable sequestration sites within state waters. In order to proceed, we used the existing near-state water data as a proxy for creating five sites as potential locations for CO_2 injection from carbon sources along the Gulf Coast of Texas (Figure 14). The five sites (red boxes in Figure 14) were identified through a combination of proximity to CO_2 sources (black dots) and areas that capture a large number of reservoirs from the database with high volumes. We expect that the geology in the state and federal waters is likely to be very similar and we have proceeded assuming that our reservoir property analyses apply to the state waters. The five sites are regions defined by a 15 by 15 mile square, and the reservoirs contained within each site were used for a study of injectivity and CO_2 storage capacity at this regional scale. The results were provided as input to the cost optimization model, as described in section 3.

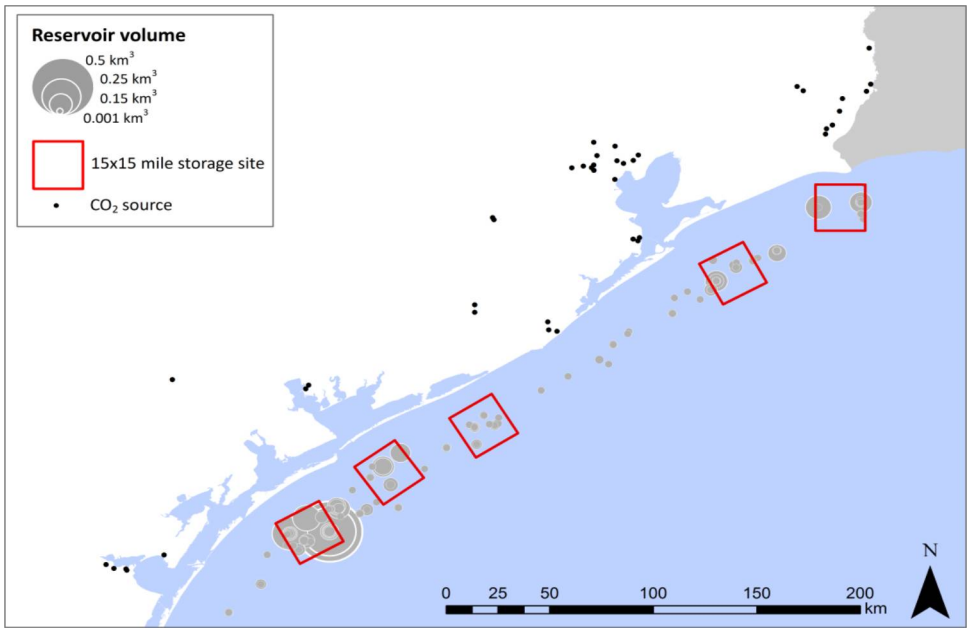

Figure 14. Map of the Texas Gulf Coast region showing the location of CO_2 sources (on-land) and the size and distribution of reservoirs obtained from the Gulf Atlas. Five geographically distributed regional sequestration sites were chosen for further study and are indicated as red boxes. The size of the symbol representing each reservoir corresponds to the reservoir volume.

In the Gulf Atlas data set, many of the potential sandstone reservoirs are stacked atop one another, each with unique properties of thickness, porosity, permeability and area. These occur at a much larger vertical separation compared to the closely spaced layers described in Section 2.2, which represent geologic variation at a finer scale. These sandstone reservoirs are likely to be accessible only through individual well operations. Nonetheless, these reservoirs were simulated in two ways: Type 1 were individual reservoirs, targeted for injection from separate wells with a low-permeability wellbore casing; and Type 2 were layers that were injected simultaneously, with no wellbore casing along the length of the high-permeability wellbore. Estimates of CO_2 storage capacity were determined for Type 1. Rates of injection determined using Type 2 are significantly higher due to the lack of a well casing, and they cannot be compared directly to injection rates for the individual reservoirs within a stack determined in the Type 1 simulations.

Results from Type 1 simulations are given in Tables 4 and 5. The total storage capacities and average injectivities based on the Gulf Atlas data for Sites 1–5 are given in Table 5, along with average reservoir depth, number of sands reported in the Gulf Atlas within that site, total volume of reservoirs, permeability, porosity, and E-factor (calculated from Equation 2 using the simulated mass of CO_2 in the reservoir at the time the plume reached the bounding fault). Site 1 has a total estimated storage capacity of 9.2 $MtCO_2$, with an average efficiency factor of 19% for the sands within its boundaries. Injectivities within Site 1 range from 0.05 $MtCO_2$/yr (for a low-permeability reservoir, k=24 mD) to 2.95 $MtCO_2$/yr, with an average of 0.89 $MtCO_2$/yr. Site 2 has an estimated capacity of 20.2 $MtCO_2$ for the 22 sandstone layers; it has the largest capacity of all the sites, with the second-highest average E-factor and the second-highest volume. Injectivities in Site 2 range from 0.006–2.56 $MtCO_2$/yr, with an average of 0.73 $MtCO_2$/yr. The capacity of Site 3 is estimated at 13.1 $MtCO_2$, with the most number of sands reported within the site in the Gulf Atlas, but the second-smallest volume and a low E-factor. Average injectivity is low at Site 3, at 0.13 $MtCO_2$/yr, with a maximum of 0.53 $MtCO_2$/yr. Site 4 has a total capacity of 13.3 $MtCO_2$, with an average injectivity of 1.29 $MtCO_2$/yr and a range of injectivities from 0.08–4.1 $MtCO_2$/yr. The site does not have many sands within it reported in the Gulf Atlas, but the sands have the highest average individual capacity, at 1.5 $MtCO_2$. Site 5 has a total capacity of 14.9 $MtCO_2$, an average injectivity of 0.7 $MtCO_2$/yr, and a range of injectivities from 0.03–5.08 $MtCO_2$/yr. A comparison of the average values and ranges for the five sites is shown in Figure 15.

Table 4. Capacity and injectivity of five regional (15 by 15 mile) sites, each with reservoirs characterized by Gulf Atlas well data.

Site	Well API Number	Subsea depth (m)	Area (m^2)	Thick-ness (m)	Porosity	Perme-ability (m^2)	CO_2 Density (kg/m^3)	Inject-ivity ($MtCO_2$/yr)	Capacity (MT)	E-factor (%)
1	427104001100	3,483.86	424,919.92	19.20	0.28	1.24E-13	727.15	1.01	0.36	21.87
1	427104001100	3,112.92	582,747.32	14.94	0.23	2.19E-13	732.30	1.27	0.28	19.26
1	427104001500	4,715.87	1,715,867.12	2.13	0.22	2.40E-14	734.91	0.05	0.12	20.81
1	427104001500	3,746.30	1,359,743.76	3.96	0.28	2.69E-13	732.76	0.67	0.21	19.41
1	427150002100	2,771.55	2,128,646.48	3.96	0.27	2.25E-13	739.18	0.41	0.31	18.23
1	427154000200	3,066.29	7,417,887.82	5.79	0.26	1.00E-13	734.63	0.28	1.39	16.92
1	427154000200	2,970.58	1,011,714.11	3.05	0.30	3.57E-13	740.34	0.55	0.13	18.70
1	427154000200	2,876.09	4,326,089.52	6.40	0.29	1.00E-12	732.68	2.95	1.06	17.96
1	427154000200	2,814.52	16,632,579.9	8.23	0.27	1.72E-13	728.94	0.65	4.79	17.79
1	427154000200	2,669.74	3,302,234.84	4.27	0.27	5.61E-13	738.87	1.04	0.50	17.83
2	427064003501	1,932.13	1,525,664.87	11.28	0.28	3.88E-13	739.85	1.13	0.58	16.40
2	427064009800	2,818.49	8,421,508.22	5.79	0.29	1.54E-13	736.35	0.40	1.71	16.37
2	427064009800	2,677.67	6,568,047.97	0.30	0.28	3.80E-14	760.15	0.01	0.05	12.46
2	427064009800	2,486.25	5,115,226.52	5.18	0.29	1.11E-12	738.00	2.30	0.98	17.35
2	427064009800	2,263.75	5,787,004.68	3.66	0.31	3.67E-13	745.82	0.48	0.79	16.23
2	427084001600	3,246.12	1,800,851.11	5.18	0.26	6.13E-13	733.41	1.66	0.33	18.62
2	427084001600	2,384.45	687,965.59	11.28	0.26	1.64E-13	738.76	0.57	0.27	17.82
2	427084002400	3,183.94	4,135,887.26	14.94	0.27	3.88E-13	725.77	2.56	2.14	17.72
2	427084002400	2,895.90	3,399,359.39	4.27	0.26	1.44E-13	737.52	0.30	0.51	18.25
2	427084002400	2,877.92	866,027.27	2.74	0.29	1.42E-13	742.78	0.19	0.09	18.45
2	427084002800	2,110.44	2,707,346.95	9.75	0.30	7.39E-13	738.71	2.10	0.88	14.98
2	427084003900	2,506.98	7,903,510.59	3.05	0.28	6.90E-14	743.83	0.09	0.84	16.67
2	427084003900	2,456.69	4,791,478.00	0.91	0.31	2.94E-13	754.71	0.12	0.20	19.60
2	427084003900	2,339.34	2,161,021.33	5.49	0.34	1.05E-12	741.02	2.03	0.48	16.20
2	427084003900	2,310.38	5,823,426.39	4.57	0.27	8.40E-14	743.76	0.14	0.87	16.27
2	427084003900	2,221.99	8,405,320.79	2.74	0.23	1.33E-13	748.46	0.13	0.71	17.78
2	427084003900	2,206.75	9,930,985.66	6.71	0.25	1.61E-13	738.64	0.37	1.95	15.83
2	427084003900	2,151.58	6,300,955.45	3.05	0.31	1.72E-13	747.78	0.19	0.78	17.47
2	427084003900	2,127.20	2,379,551.58	1.83	0.27	1.74E-13	752.89	0.11	0.16	18.08
2	427084003900	2,077.52	13,751,218.1	9.45	0.30	5.48E-13	733.54	1.68	4.56	15.93
2	427084003900	1,999.18	17,696,903.1	1.22	0.32	4.15E-13	757.27	0.17	0.92	17.65
2	427084003900	1,900.12	10,869,856.3	2.74	0.24	4.30E-14	747.83	0.03	0.33	6.11
2	427084003900	1,863.85	1,080,510.66	2.13	0.26	4.60E-14	756.95	0.03	0.08	17.52
3	427044002900	2,262.23	5,163,788.79	6.40	0.29	5.60E-14	737.22	0.13	1.18	16.74
3	427044002900	2,250.34	6,074,331.49	7.01	0.29	7.20E-14	737.33	0.18	1.56	17.19
3	427044002900	2,202.18	566,559.90	5.49	0.25	7.90E-14	745.21	0.14	0.09	16.35
3	427044002900	2,180.54	5,386,365.90	5.49	0.29	3.80E-14	741.04	0.07	0.63	9.99
3	427044002900	2,165.60	5,220,444.78	4.27	0.30	3.40E-14	742.21	0.05	0.46	9.30
3	427044002900	2,127.50	3,023,001.75	1.22	0.29	3.00E-14	756.24	0.01	0.12	15.40
3	427044002900	2,120.49	4,896,696.27	1.83	0.29	2.70E-14	750.82	0.02	0.16	8.25
3	427044002900	2,091.23	3,140,360.58	6.40	0.28	3.90E-14	741.74	0.08	0.71	17.12
3	427044002900	2,063.80	5,871,988.67	5.49	0.29	4.80E-14	741.96	0.08	0.76	10.95
3	427044002900	2,036.06	3,188,922.86	0.91	0.25	6.60E-14	762.44	0.02	0.10	18.80

Table 4, continued.

Site	Well API Number	Subsea depth (m)	Area (m^2)	Thick-ness (m)	Porosity	Perme-ability (m^2)	CO_2 Density (kg/m^3)	Inject-ivity ($MtCO_2$/yr)	Capacity (MT)	E-factor (%)
3	427044002900	2,005.58	3,103,938.88	0.91	0.27	1.29E-13	760.29	0.04	0.11	18.64
3	427044002900	1,999.49	4,042,809.57	1.22	0.25	9.50E-14	760.06	0.04	0.16	17.46
3	427044002900	1,984.25	3,779,763.90	2.13	0.25	5.50E-14	755.64	0.04	0.27	17.91
3	427044003400	2,113.79	2,820,658.93	3.05	0.30	4.98E-13	746.61	0.53	0.34	17.71
3	427044003400	2,108.30	2,452,394.99	5.49	0.26	4.30E-14	744.81	0.08	0.42	16.08
3	427044003400	2,026.01	776,996.43	4.57	0.27	5.90E-14	748.26	0.08	0.11	15.79
3	427044003400	1,992.48	5,329,709.91	3.96	0.27	2.30E-14	744.01	0.03	0.26	6.08
3	427044005200	2,017.17	7,968,260.30	2.13	0.31	6.80E-14	750.22	0.05	0.45	11.37
3	427044008500	2,211.02	2,415,973.28	3.96	0.29	5.60E-14	745.78	0.08	0.36	17.47
3	427044008600	2,325.01	10,355,905.5	4.27	0.28	8.70E-14	741.06	0.14	1.33	14.47
3	427044008600	2,206.75	2,347,176.72	3.96	0.28	3.30E-14	747.29	0.05	0.34	17.54
3	427044008600	2,103.12	10,675,607.2	2.13	0.29	4.60E-14	748.62	0.03	0.31	6.29
3	427044010300	1,893.11	1,651,117.42	2.13	0.31	1.11E-13	754.57	0.07	0.14	17.22
3	427044012700	4,005.68	2,804,471.50	14.33	0.26	1.80E-14	723.76	0.14	1.34	17.73
3	427044012700	3,453.69	339,935.94	8.53	0.26	1.22E-13	733.29	0.50	0.11	19.76
3	427044012701	3,738.98	797,230.72	8.84	0.28	6.80E-14	730.71	0.32	0.27	18.38
3	427044013400	2,250.95	1,343,556.33	7.01	0.23	1.90E-14	742.63	0.04	0.28	17.51
3	427044013400	2,192.43	2,092,224.77	1.83	0.23	2.80E-14	757.78	0.02	0.12	18.37
3	427044014000	3,707.89	1,400,212.32	10.97	0.26	4.40E-14	729.48	0.25	0.51	17.51
3	427044016900	2,031.80	1,991,053.36	0.91	0.29	3.01E-13	757.84	0.10	0.08	18.89
4	427033021800	2,823.67	1,412,352.89	7.92	0.25	4.10E-14	737.84	0.13	0.33	16.04
4	427033021800	2,637.74	3,816,185.61	3.66	0.24	5.00E-14	744.50	0.08	0.42	16.92
4	427033021800	2,498.75	1,242,384.92	4.57	0.27	5.40E-14	743.92	0.09	0.18	16.18
4	427033025800	2,453.64	400,638.79	10.67	0.28	3.38E-13	738.97	1.14	0.17	19.18
4	427034003200	2,764.54	8,255,587.10	13.11	0.26	7.40E-14	728.49	0.39	3.36	16.40
4	427034004300	2,782.52	13,334,391.9	9.75	0.23	5.10E-14	729.87	0.21	1.91	8.74
4	427034019500	2,667.30	4,730,775.16	16.15	0.24	3.37E-13	729.96	1.94	2.13	15.88
4	427034019500	2,458.21	1,942,491.08	9.75	0.32	5.76E-13	736.54	1.92	0.73	16.44
4	427034029400	4,873.14	9,372,519.47	12.19	0.27	6.55E-13	716.57	5.72	4.05	18.34
5	427034000300	2,786.48	6,106,706.34	2.44	0.24	2.70E-14	744.71	0.03	0.29	10.87
5	427034000300	2,625.24	4,455,588.92	12.80	0.25	1.09E-13	730.43	0.53	1.79	17.17
5	427034001200	1,240.54	1,323,322.05	2.44	0.30	1.50E-13	760.03	0.07	0.11	15.37
5	427034001200	1,225.30	9,914,798.23	6.40	0.31	1.25E-12	743.59	1.48	2.17	14.81
5	427034001200	1,168.91	570,606.76	4.57	0.29	7.19E-13	750.59	0.52	0.09	15.02
5	427034001200	1,005.84	10,020,016.5	4.27	0.30	4.45E-13	751.07	0.30	1.45	15.01
5	427034001200	955.55	1,388,071.75	2.44	0.31	2.71E-13	759.09	0.09	0.12	14.45
5	427034001200	842.77	910,542.70	1.22	0.31	3.31E-13	759.86	0.05	0.04	15.45
5	427034001200	838.20	4,208,730.68	3.66	0.30	7.21E-13	751.89	0.32	0.48	13.73
5	427034001300	2,756.31	2,306,708.16	12.50	0.30	1.09E-12	731.45	5.08	1.07	16.97
5	427034001300	2,666.09	2,318,848.73	16.76	0.26	2.01E-13	732.14	1.16	1.21	16.38
5	427034001300	2,534.72	2,986,580.04	7.32	0.28	1.90E-13	735.55	0.54	0.78	17.26
5	427034001800	1,705.97	27,227,250.0	6.40	0.27	2.20E-14	739.44	0.03	0.29	0.84
5	427034002200	2,892.86	7,822,573.46	9.75	0.27	5.78E-13	729.45	2.46	2.45	16.32

Table 4, continued.

Site	Well API Number	Subsea depth (m)	Area (m^2)	Thick-ness (m)	Porosity	Perme-ability (m^2)	CO_2 Density (kg/m^3)	Inject-ivity ($MtCO_2$/yr)	Capacity (MT)	E-factor (%)
5	427034002500	1,889.76	2,602,128.68	1.22	0.33	1.20E-13	760.40	0.05	0.14	17.57
5	427034002500	1,866.90	2,897,549.20	2.44	0.32	1.23E-12	752.08	0.87	0.28	16.43
5	427034002500	1,844.04	1,634,929.99	1.83	0.32	2.32E-13	754.81	0.13	0.13	17.57
5	427034002500	1,744.98	3,172,735.44	1.52	0.27	1.72E-13	759.10	0.07	0.17	16.77
5	427034002500	1,722.12	1,205,963.21	2.13	0.29	3.12E-13	753.32	0.18	0.10	17.42
5	427034012000	3,750.26	3,087,751.45	4.57	0.23	1.08E-13	733.20	0.30	0.42	17.65
5	427034024100	3,435.71	9,299,676.06	6.10	0.25	1.90E-14	729.00	0.06	0.59	5.69
5	427034040500	1,432.56	3,051,329.74	3.05	0.33	1.60E-12	751.24	1.07	0.38	16.49
5	427034040500	1,356.36	2,080,084.20	4.57	0.31	4.07E-13	749.33	0.37	0.33	15.15
5	427034040500	1,136.90	509,903.91	2.13	0.36	1.50E-12	757.03	0.56	0.05	16.36

Table 5.

Summary of storage capacity and injectivity for the five regional sites.

	CO_2 Storage Capacity (MT)	Number of Sands in the Gulf Atlas Within Site	Total Volume of Sands Within Site (m^3)	Average Injectivity ($MtCO_2$/yr)	Average E-factor in Equation (2) (%)
Site 1	9.2	10	2.59 E+08	0.89	19
Site 2	20.2	22	6.02 E+08	0.73	17
Site 3	13.1	30	4.48 E+08	0.13	15
Site 4	13.3	9	4.83 E+08	1.29	16
Site 5	14.9	23	6.55 E+08	0.70	15

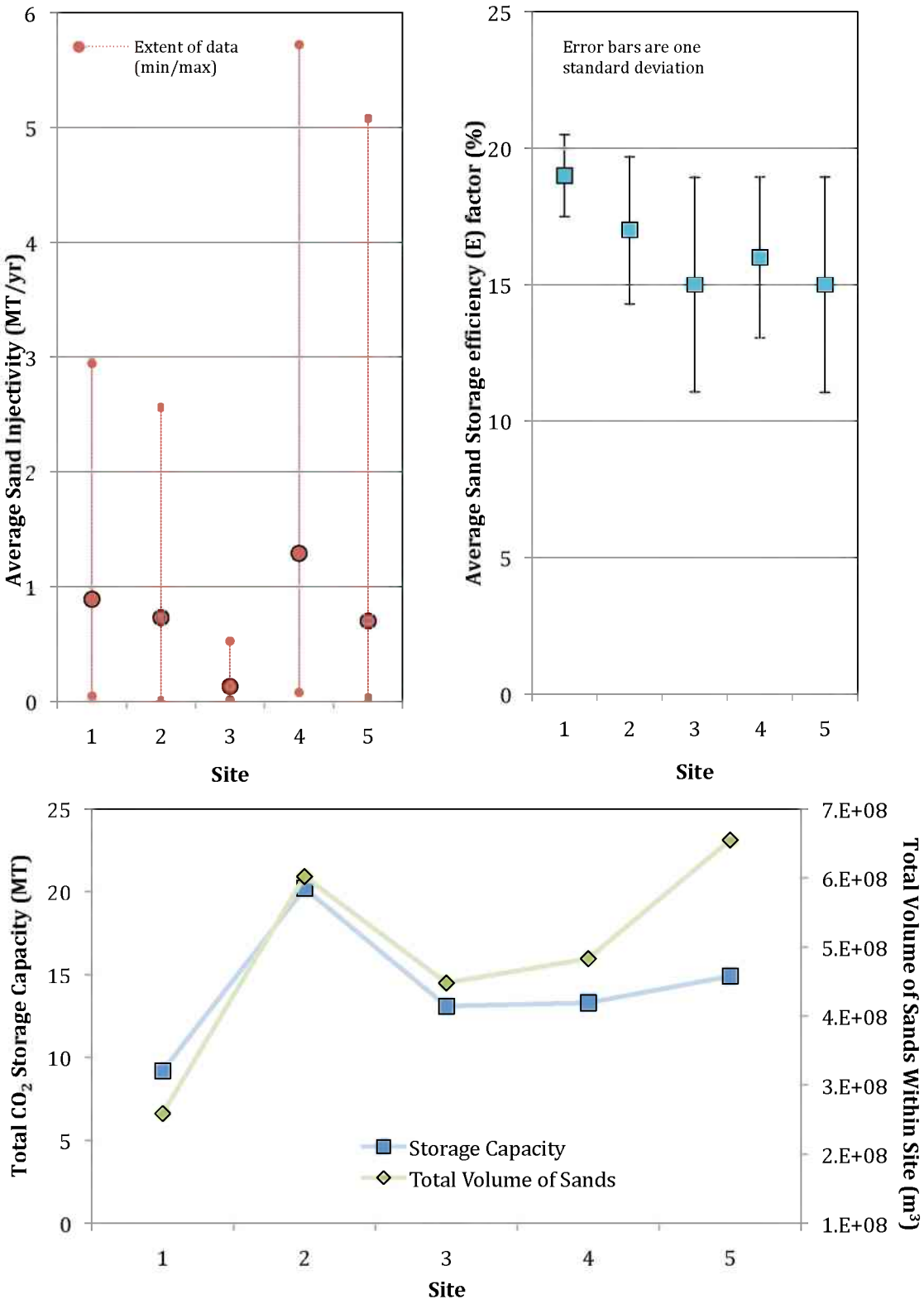

Figure 15. Injectivity, storage efficiency and capacity of the five regional sequestration sites.

The reservoir simulations show a high degree of correlation between the efficiency of storage (E-factor) and depth, with the exception of a cluster of low-permeability reservoirs that deviate from the trend (Figure 16). Thus, if the volume of a potential storage reservoir is known, together with its depth, porosity, and permeability, the E-factor may be estimated to provide an estimated storage capacity of CO_2.

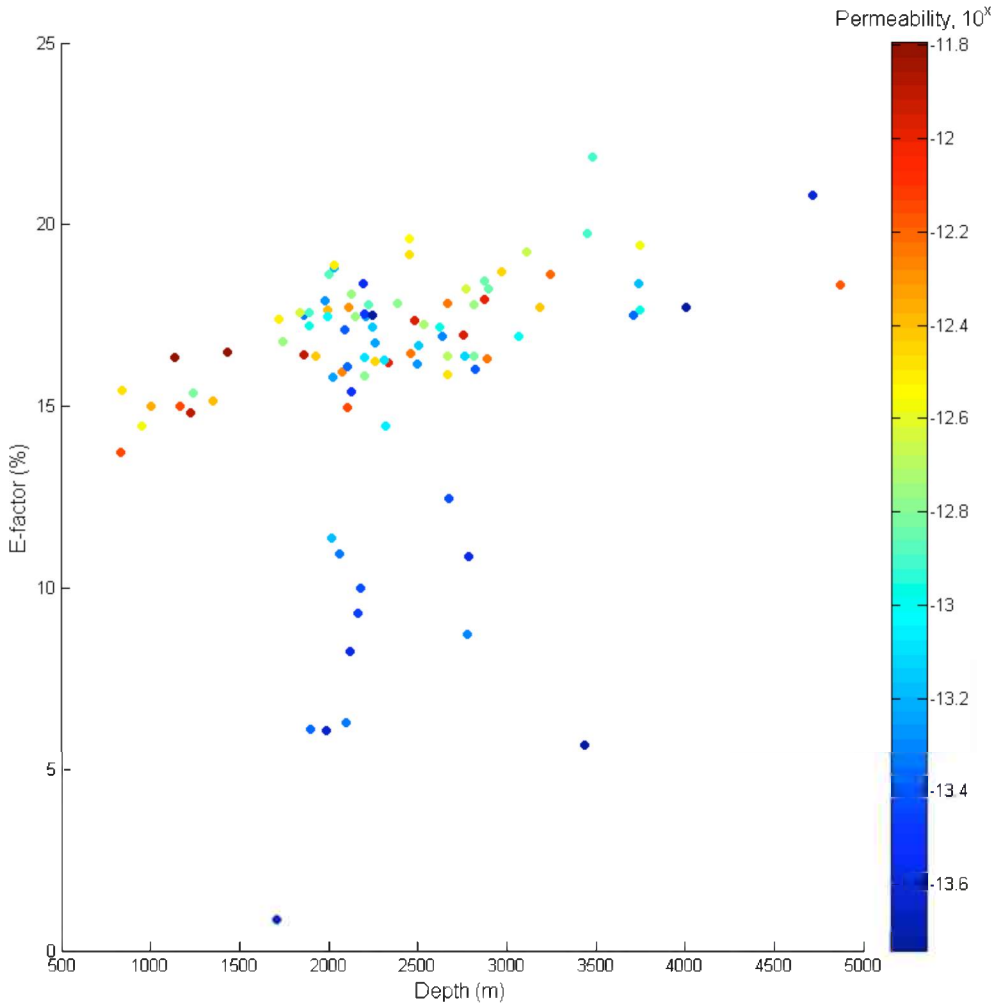

Figure 16. Storage efficiency factor (E-factor) versus depth for all of the simulated reservoirs located within the five regional sequestration sites.

Results for the Type 2 simulations (simultaneous injection into stacked reservoirs from a single well) are summarized in Table 6. These simulations involve injection into one or more layers without a wellbore casing. The lack of casing produces about a factor of 8 more injectivity for a single layer compared to cased intervals (Figure 17). However, simultaneous injection into multiple layers reduces the maximum possible rate of injection compared to injecting each layer individually, and is caused by lower pressures of CO_2 along the wellbore after the CO_2 encounters the first sandstone reservoir. For a given stack with multiple reservoirs, the injectivities for the whole stack range from about 0.6 to 9.2 times greater than the total injectivities calculated for each layer in the stack, with an average ratio of 3.9.

Table 6. Injectivity of wells from Type 2 simulations involving simultaneous injection into multiple layers from a single well.

Site #	Well API Number	Injectivity ($MtCO_2/yr$)	Number of reservoirs in stack
1	427104001100	9.714	2
1	427104001500	0.688	2
1	427150002100	3.529	1
1	427154000200	3.587	5
2	427064003501	9.189	1
2	427064009800	3.994	4
2	427084001600	14.135	2
2	427084002400	16.626	3
2	427084002800	14.242	1
2	427084003900	2.819	12
3	427044002900	3.281	13
3	427044003400	5.484	4
3	427044005200	0.376	1
3	427044008500	0.711	1
3	427044008600	1.507	3
3	427044010300	0.674	1
3	427044012700	1.773	2
3	427044012701	3.074	1
3	427044013400	0.584	2
3	427044014000	2.380	1
3	427044016900	0.834	1
4	427033021800	1.736	3
4	427033025800	10.698	1
4	427034003200	3.084	1
4	427034004300	1.570	1
4	427034019500	12.751	2
4	427034029400	30.467	1
5	427034000300	1.123	2
5	427034001200	2.605	7
5	427034001300	27.072	3
5	427034001800	0.183	1
5	427034002200	15.316	1
5	427034002500	3.745	5
5	427034012000	2.419	1
5	427034024100	0.486	1
5	427034040500	10.120	3

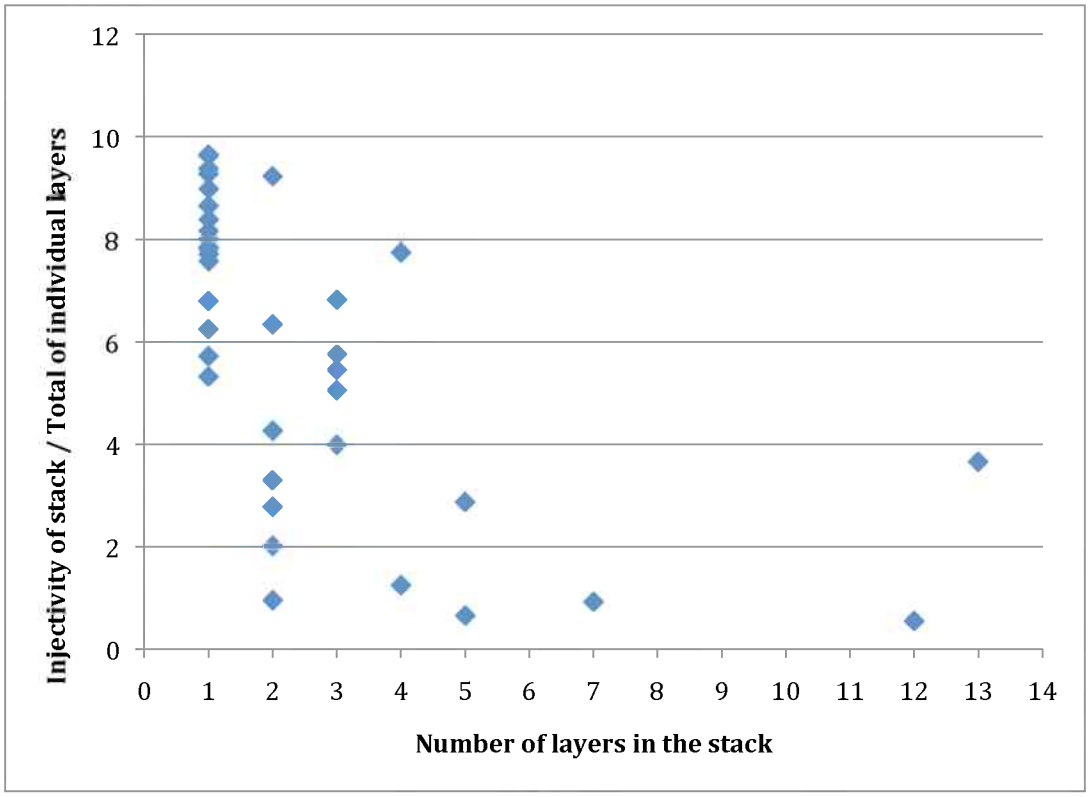

Figure 17. Ratio of the injectivity of a stack of reservoirs calculated using a single, uncased well (Type 2) compared to the total injectivity of the individual layers using a single, cased well (Type 1). The non-unity ratio for stacks with only one layer is due solely to the difference of the wellbore casing.

3. Spatial Infrastructure Analysis

3.1 CO_2 Management Overview

The Texas Gulf Coast region has many large industrial CO_2 sources and vast near-offshore CO_2 storage potential. Within 200 km of the Texas coast there are 45 individual industrial CO_2 sources, each emitting more than one million tonnes of CO_2 per year (>1 $MtCO_2$/yr); these sources include emissions from chemical processing plants (ethylene production), oil refineries, natural gas power plants, and coal-fired power plants (Figure 18). The 45 sources are spread out along roughly 400 km of Texas coast, and each source is within 115 km of its closest offshore reservoir. The 45 sources produce a CO_2 stream of 110.35 $MtCO_2$/yr (Table 7). The size of the CO_2 stream is greatest in ethylene production and decreases in the order of oil refining, natural gas, and coal-fired power plants. Capture costs range from as low as \$12.06/tCO_2 (an ethylene plant) through \$50.40/tCO_2 (a coal-fired power plant).

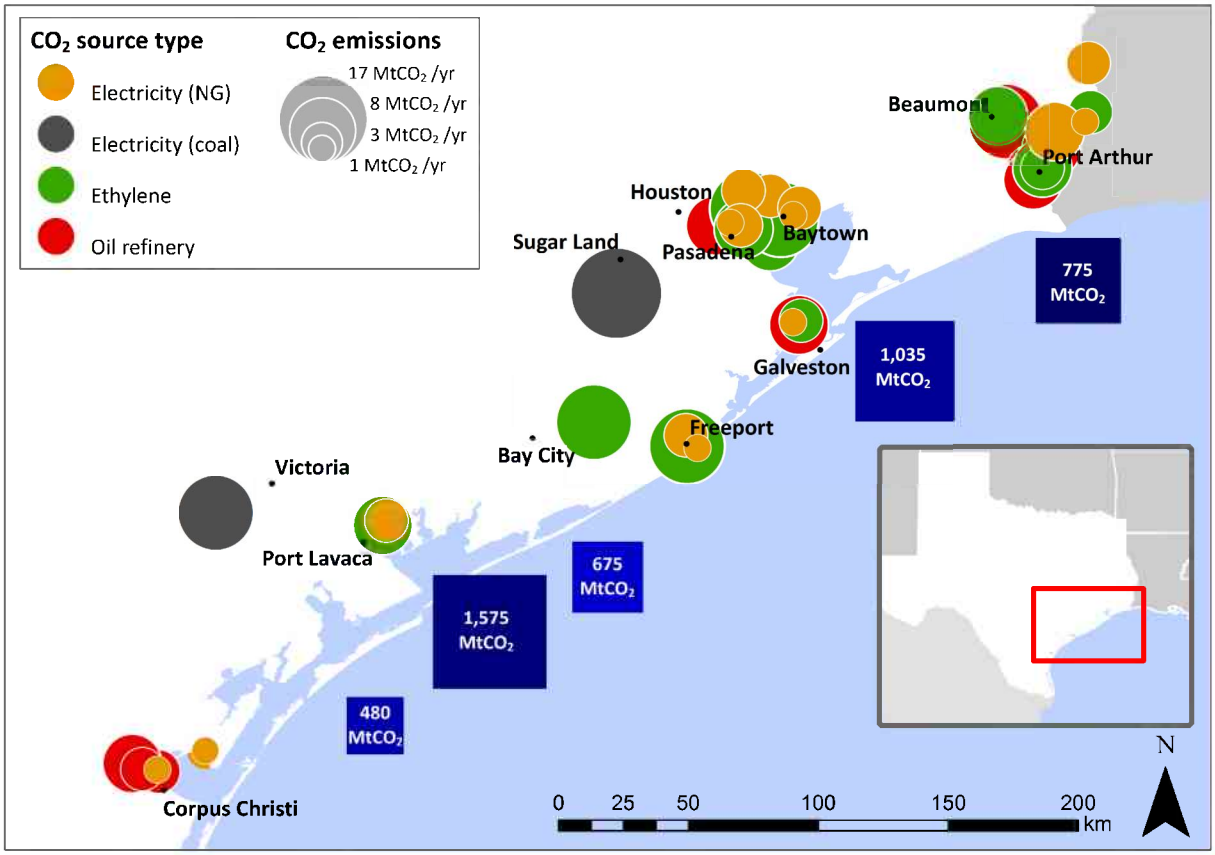

Figure 18: Overview of CO_2 industrial emissions and CO_2 storage potential in the Texas Gulf Coast region. The methodology for estimating regional storage capacities (blue squares) is described below.

Table 7: Emission and cost overview of industrial CO_2 sources

CO_2 source type	Number of sources	Capturable CO_2 (Mt CO_2/yr)	Capture cost ($/t$CO_2$)†	Reference for capture costs
Ethylene production	14	35.59	12.06 – 17.43	-
Oil refining	12	33.04	21.85 - 29.80	-
Power (natural gas)	17	21.03	34.12 – 45.53	-
Power (coal)	2	20.69	42.17 – 50.49	-
TOTAL	45	110.35	-	-

† Costs are illustrative of where each source is capturing its maximum rate of CO_2 production

While the sources are fixed, predefined offshore storage locations do not exist. In Section 2 of this report, we obtained the capacity and injectivity of Miocene deltaic sands in federal waters adjacent to potential targets in Texas state waters. We used these results to create Figure 14, which displays the location and volume of these oil and gas reservoirs (grey circles in Figure 14). Five 15 by 15 mile offshore regional storage sites were selected for detailed study for cost-optimization of the CO_2

capture-transport-storage system (Figure 18). The five regional sites were selected to be (a) spatially close to major CO_2 sources, (b) in areas that are well characterized in the Gulf Atlas database, and (c) areas that are likely to have significant CO_2 storage potential according to the database.

The regional offshore storage sites (225 square mile in area) were selected based on the assumption that several drilling rigs would be able to exploit such an area. Storage capacity and injectivity for the five sites was calculated using the following steps:

(1) Five storage sites were located based on proximity to CO_2 sources, data availability, and storage potential of each individual oil/gas reservoir in the Gulf Atlas (a limited sample of oil/gas reservoirs)

(2) Average values for each site were derived for injectivity, depth, thickness, porosity, density, and E-factor

(3) A representative number of sandstone layers within a stack was chosen for each site (see Table 8)

(4) Total storage capacity for each site was calculated by scaling up the average and representative reservoir values as if the reservoirs were spread across the entire 15 by 15 mile site

As an approximation, we estimated total capacity within each 15 by 15 mile site by extrapolating the identified reservoirs across the entire 225 square mile area. The results are shown in Figure 19. Note that these regional capacities are far larger than results from Section 2: the maximum site capacity is increased from 20 $MtCO_2$ (the summed capacity available from the sample data) to 1575 $MtCO_2$ (cf. data in Table 4 with Figure 18) based on our assumptions about the total extent of the geologic formations. The five offshore storage sites have a total CO_2 storage capacity of 4,540 $MtCO_2$, or just less than 91 $MtCO_2$/yr over 50 years (Table 8). Injection and storage costs for the five storage sites range between \$2.12 and \$5.32/tCO_2.

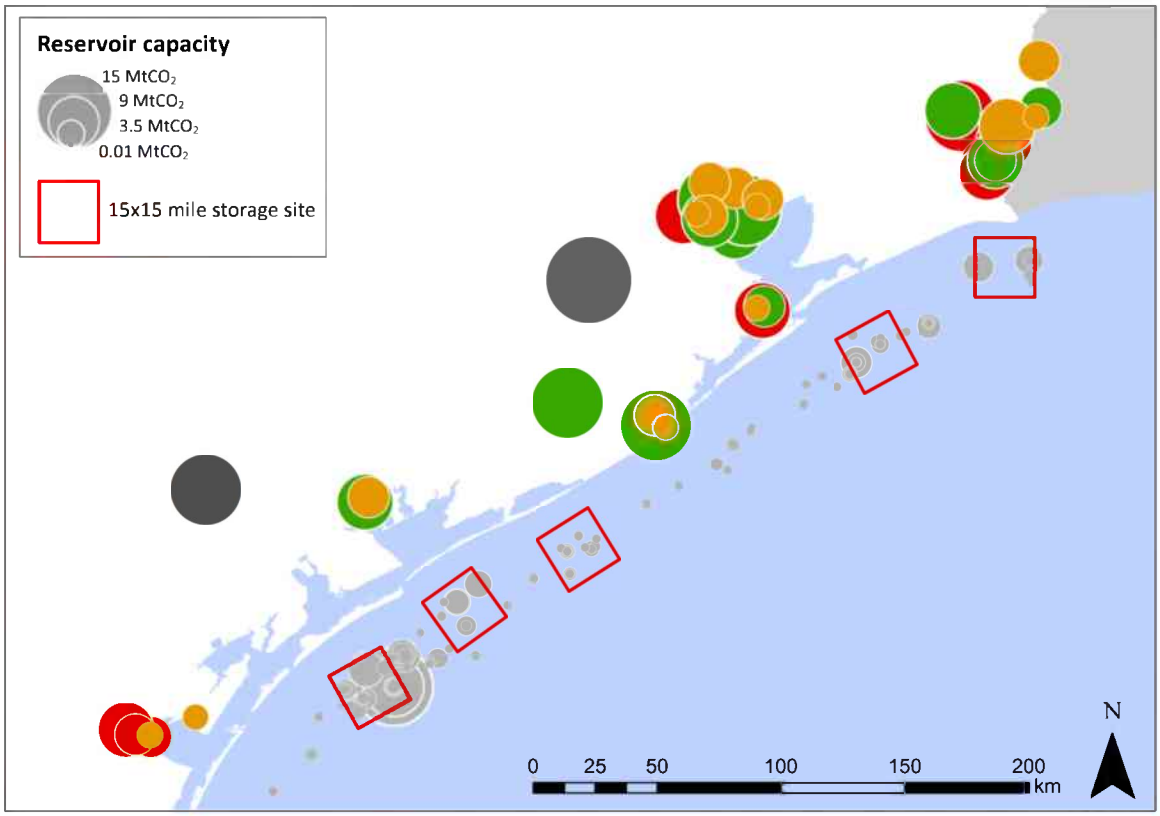

Figure 19. Map of the Texas Gulf Coast region showing the location of CO_2 sources (on-land) and the size and distribution of reservoirs obtained from the Gulf Atlas. Five geographically distributed regional sequestration sites were chosen for further study and are indicated as red boxes. The size of the symbol representing each reservoir corresponds to CO_2 storage capacity, as estimated by the maximum injection rate, capped at 1 MT/yr, and multiplied by 50 years.

Table 8: Overview of storage capacity and injection/storage costs

Site	Storage capacity ($MtCO_2$)	Well injectivity ($MtCO_2$/yr)‡	Injection/storage cost ($/t$CO_2$)†
1	775	0.661	2.19
2	1,035	0.449	2.27
3	675	0.113	5.32
4	1575	0.545	2.12
5	480	0.420	2.42
TOTAL	4,540	-	-

† Costs represent situation where each sink is injecting and storing at its maximum rate over 50 years.
‡ The injectivity for each reservoir in the Gulf Atlas database is assumed to not exceed 1 $MtCO_2$/yr, a representative upper bound for the injectivity of a single injection well.

In this study we analyze the infrastructure requirements to capture, transport, and store CO_2 emissions from the major industrial sources. We have selected to use *SimCCS*, an economic-engineering optimization model for CCS infrastructure. *SimCCS* has been applied to a range of problems including CO_2 policy analysis in California (Middleton and Bielicki, 2009), unconventional fossil fuel development (Keating et al., 2011), wind energy infrastructure (Phillips and Middleton, 2011), enhanced oil recovery (Middleton et al., 2011a), temporal deployment of CCS infrastructure (Middleton et al., 2011d), and the impacts of geologic uncertainty on CCS technology (Middleton et al., 2011b). *SimCCS* designs a geospatially realistic pipeline network while simultaneously considering where and how much CO_2 to capture and store.

3.2 Modeling and scenario assumptions

Many of the 45 industrial CO_2 sources are co-located within several kilometers. Consequently, for modeling purposes, the 45 sources have been grouped into 13 logical regions (see red circles in Figure 20). Figure 20 also illustrates the candidate network of pipelines—that is, a set of low-cost routes where new CO_2 pipelines would likely be built. The methodology for constructing the candidate pipeline network has been used in multiple previous studies and papers (e.g., Keating et al., 2011; Kuby et al., 2011a; Kuby et al., 2011b; Middleton and Bielicki, 2009; Middleton et al., 2011b; Middleton et al., 2011d), and the methodology is covered in greatest depth in Middleton et al. (2011c). Principally, these low-cost routes are identified using a shortest path algorithm run on a cost surface (see cost surface in Figure 20). The cost surface used in this study is modified for the Texas coastal from Middleton et al. (2011c), chiefly by including cost information for sensitive and protected coastal areas (dark areas immediately adjacent to the coast).

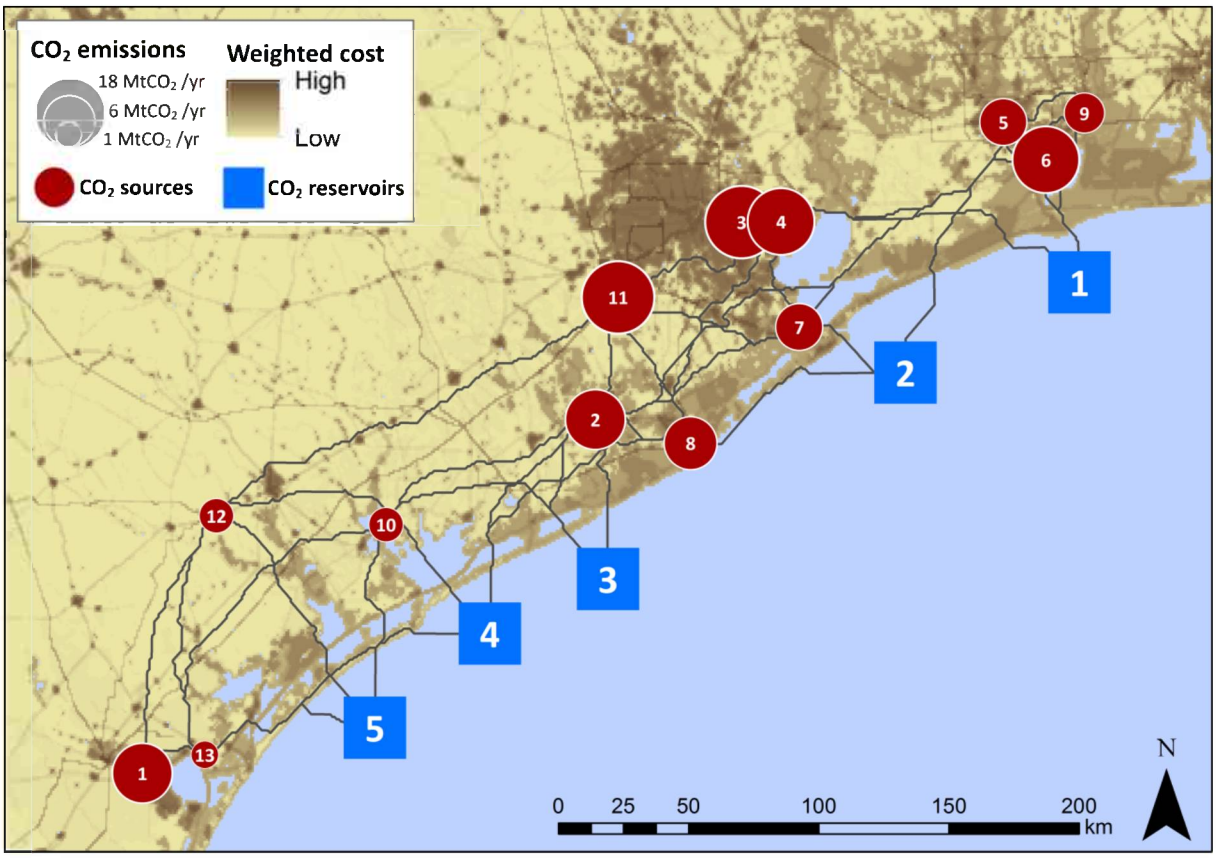

Figure 20: Candidate pipeline network, the 13 grouped CO_2 source sites, and the five CO_2 storage sites. The pipeline cost surface is shown as a shaded surface labeled "Weighted cost".

Costs for injecting and storing CO_2 in each of the five sites were derived using methods described in Middleton et al. (2011c). Injectivity is the principal driver for injection/storage costs because it controls the number of wells required to inject and store a given amount of CO_2. The variability in injection/storage costs can be seen in Figure 20 and Table 8.

For this study, we examine 18 different CO_2 management scenarios ranging from capturing-transporting-storing 5 $MtCO_2$/yr through 90 $MtCO_2$/yr over a 50 year period; 90 $MtCO_2$/yr is just short of the 50 year capacity of the five storage sites. All infrastructure costs are capitalized over the 50 year time period using a 10% interest rate. This gives a capital charge value, or capital recovery factor (CRF), of 0.1009.

Results and Discussion

Figure 21 illustrates the spatial layout of CCS infrastructure (capture, transport, and storage) for the eighteen CO_2 management scenarios employed in this study. Sources (red) and sinks (blue) are illustrated using pie charts; the area of each pie

chart is proportional to amount of CO_2 storage and supply, respectively. The dark red (sources) and blue (sinks) wedges in each pie chart are proportional to the amount of CO_2 captured and stored in each scenario. The candidate network (i.e., where pipelines could be built) is displayed as grey lines, while the actual pipelines built in each are illustrated as green lines. The width of each green line is proportional to pipeline diameter ranging from 4" (0.19 $MtCO_2$/yr) to 36" (54.46 $MtCO_2$/yr). For example, in the 5 $MtCO_2$/yr scenario, 1.93 $MtCO_2$/yr is captured from source #5 (S5) and transported to S6 in a 12" pipeline (3.25 $MtCO_2$/yr capacity). At S6, a further 3.07 $MtCO_2$/yr is captured (total of 5 $MtCO_2$/yr) and then transported for storage in reservoir 1, R1, in a 16" diameter pipeline (6.86 $MtCO_2$/yr capacity).

As the CO_2 target amount increases in each management scenario, more infrastructure—capture, transport, and storage—is required, which typically means more sources being retrofitted, more (and larger) pipelines, and more sinks coming online. However, the progression of infrastructure is somewhat non-intuitive. For instance, reservoir R1 is the only sink used in the 5 and 15 $MtCO_2$/yr scenarios, but is not used at all in the 10 $MtCO_2$/yr scenario. Similarly, sources S5 and S6 are used in the 5 and 15 $MtCO_2$/yr scenarios, but not in the intervening scenario. For the 25 $MtCO_2$/yr scenario, sources S3 and S4 contribute the largest amount of CO_2 and yet their closest sink, R2, is not employed. Instead, the cost savings from using R4 (it has the second highest injectivity) outweigh the costs to construct a much more extensive pipeline network.

There are clear patterns among the differing CO_2 management scenarios. For example, the pipeline network that emerges in the 20 $MtCO_2$/yr scenario is largely present in every subsequent scenario through 90 $MtCO_2$/yr. Reservoir R4 comes online in the 20 $MtCO_2$/yr scenario and is used in all following scenarios—for the 5 and 15 $MtCO_2$/yr scenarios, reservoir R1 is favorable because it is the second cheapest reservoir in the case study and is combined with a short pipeline distance (Table 8). Conversely, reservoir R3, the most expensive sink (due to low injectivity) is only used in two of the 18 scenarios.

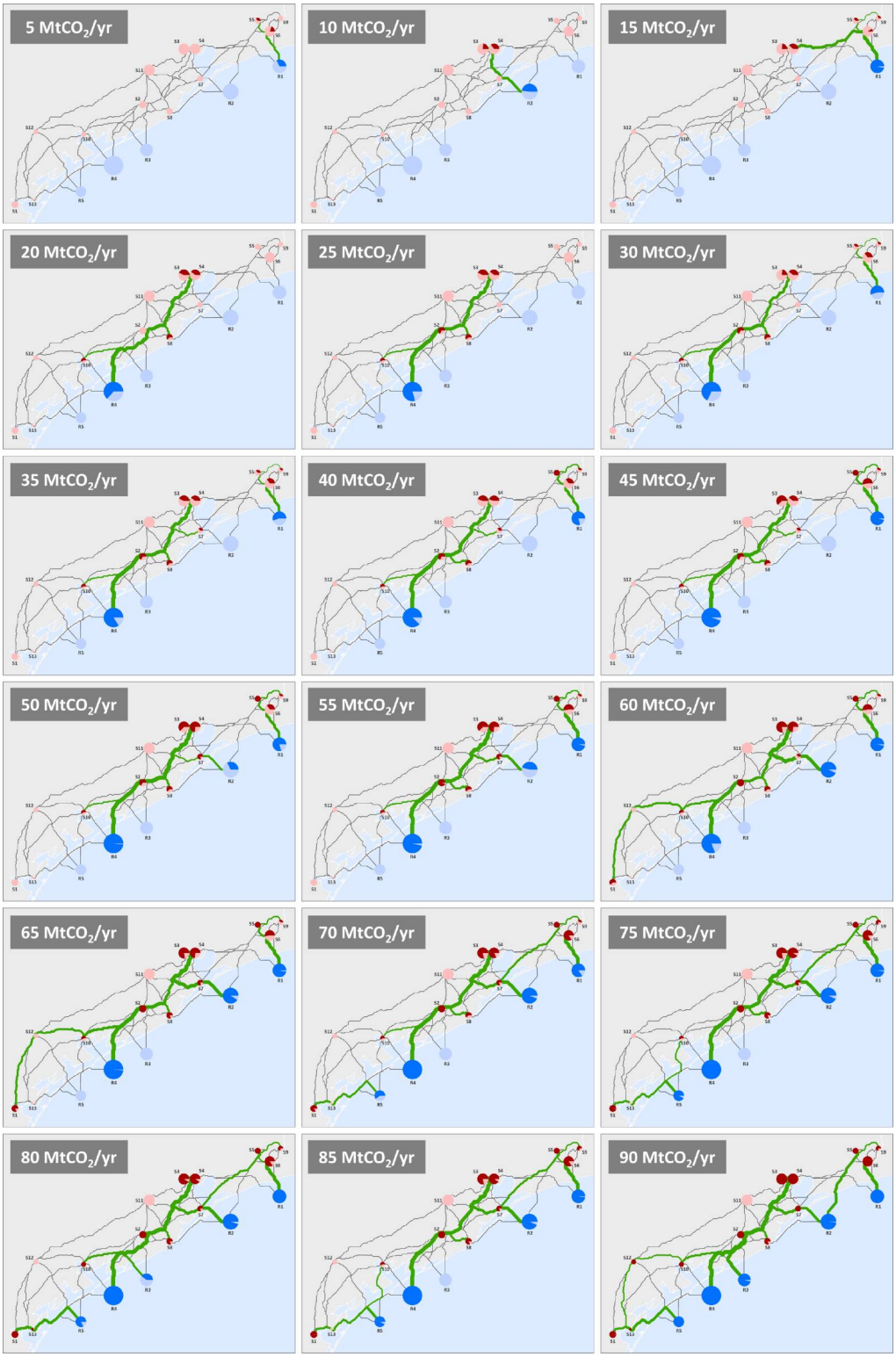

Figure 21: Infrastructure map for the eighteen CO_2 management scenarios.

The costs to manage CO_2 emissions can be broadly split into two phases. In the first scenario (5 $MtCO_2$/yr), CCS infrastructure costs start at \$20.21/tCO_2—\$13.52, \$3.82, and \$2.87/tCO_2 for capture, transport, and storage respectively (Figure 22). CCS costs gradually fall to \$18.66/tCO_2 for the 25 $MtCO_2$/yr scenario, a split of \$14.08, \$2.35, and \$2.23/tCO_2 for capture, transport, and storage. Even though capture costs have risen slightly, the model is able to deploy infrastructure with increasing economies of scale in the pipeline network (larger pipelines) and sinks (more CO_2 injected/stored for the same up front capital costs). Following this scenario, CCS costs steadily rise until reaching \$28.47/tCO_2 in the 90 $MtCO_2$/yr scenario. Costs rise because the model can no longer find significant economies of scale in the transport and storage sectors, and is forced to capture CO_2 from more expensive sources in order to meet the CO_2 targets.

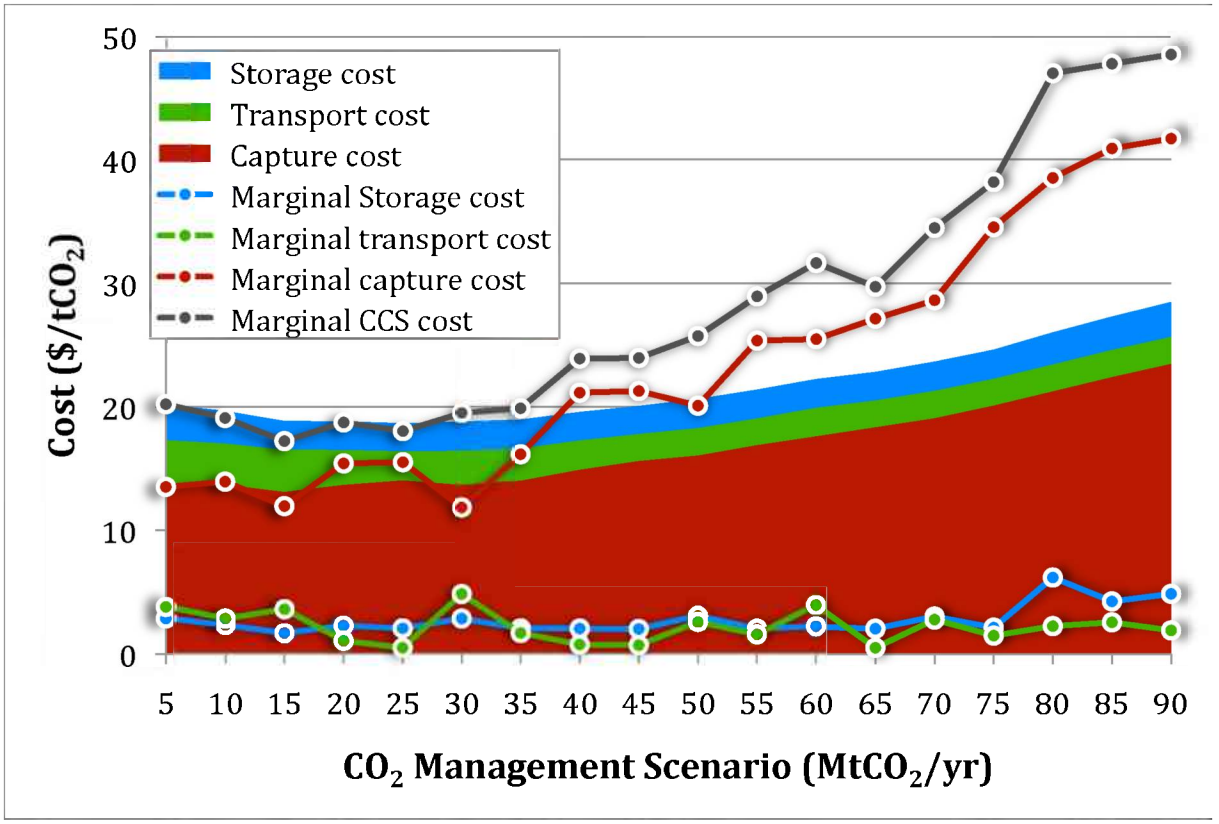

Figure 22: Cost to capture, transport and store CO_2 for the 18 CO_2 management scenarios. The stacked chart areas illustrate the unit costs (\$/tCO_2) to capture (red), transport (green), and store (blue) CO_2. Chart lines illustrate the marginal costs to capture, transport, and store CO_2—the grey line illustrates the total marginal cost to manage CO_2 emissions for each scenario.

Figure 22 also includes data for marginal costs, that is, the marginal cost to move from one CO_2 management scenario to the next higher CO_2 target. Marginal costs are important because they help stakeholders and policy makers understand where it makes sense to invest in managing a greater amount of CO_2. For example, marginal costs decline between the 60 and 65 $MtCO_2$/yr targets, suggesting that it is certainly

worth investing in infrastructure to capture, transport, and store the additional 5 $MtCO_2$/yr. In contrast, marginal costs see a large jump between the 35 and 40 $MtCO_2$/yr scenarios, suggesting that 35 $MtCO_2$/yr might be an ideal breakpoint for a "moderate" CCS scenario. In particular, it is worth examining the marginal costs for the pipeline network—in some cases (e.g., 25 and 65 $MtCO_2$/yr scenarios) the pipeline network can transport an additional 5 $MtCO_2$/yr by requiring exceedingly minor modification. When reservoir R3 comes online (the most expensive reservoir), the increase in the marginal cost of storage is notable; this trend is lost in the averaged values (i.e., colored areas in Figure 22). The total CCS management marginal costs rise particularly steeply for the 80 $MtCO_2$/yr scenario—not only does reservoir R3 have to come online, the model has to start capturing CO_2 from the coal-fired plants which have the most costly capture values (Table 8).

Unit transportation costs, as noted above, decrease in the early scenarios because greater amounts of CO_2 justify larger and larger pipelines. Once the pipeline network has started to build large pipelines (e.g. 30" and 36" pipelines), the benefit from economies of scale are lost; this occurs at about the 45 $MtCO_2$/yr scenario (see Figure 23). From this point, costs remain steady since the requirement to build longer and longer pipelines is balanced by greater amounts of CO_2 entering the transportation system. Network length, unsurprisingly, typically increases as more and more CO_2 is captured, transported, and stored. However, on two occasions (20 to 25 $MtCO_2$/yr and 60 to 65 $MtCO_2$/yr) the network length does not increase at all. These occasions match up with the marginal transport cost drops mentioned above. Even though the network length does not increase, the marginal costs are not necessarily zero since larger pipelines are required in parts of the pipeline network. Ultimately, the 90 $MtCO_2$/yr scenario requires a 1,012 km network of pipelines.

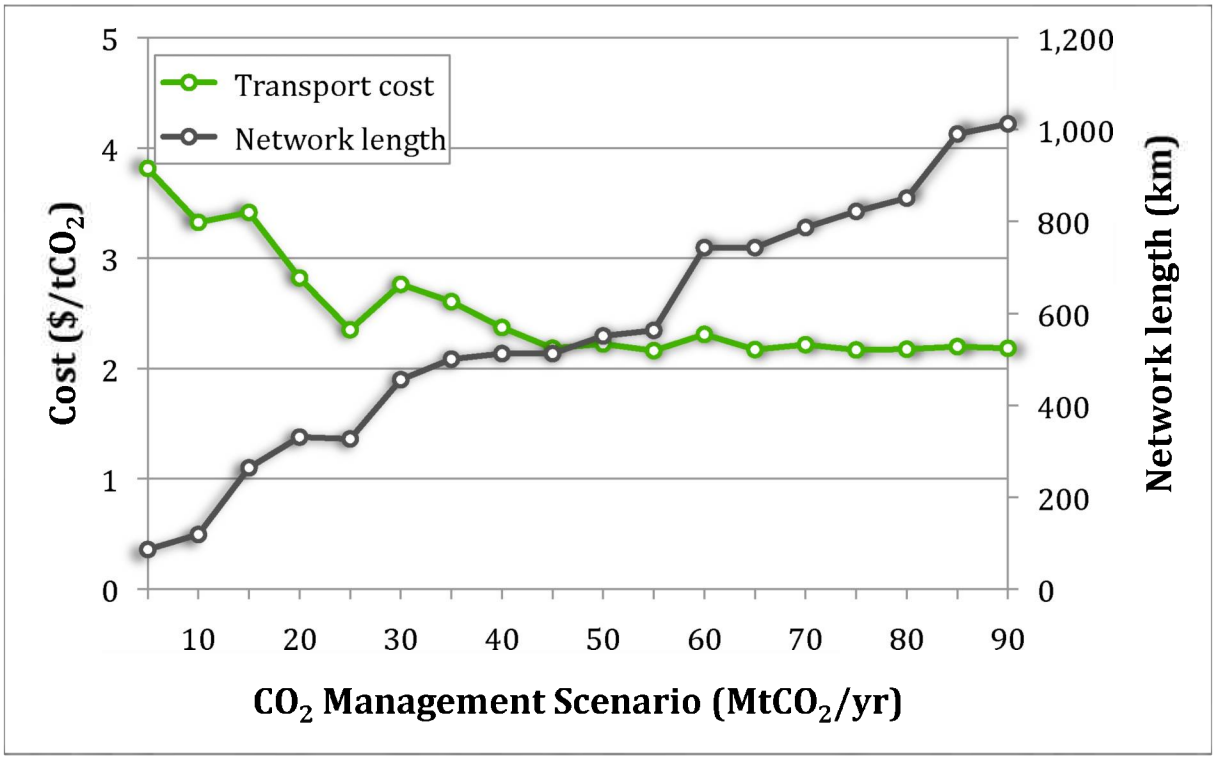

Figure 23: The cost of transporting CO_2 for the 18 CO_2 management scenarios, and the associated network length.

Overall, the CCS network infrastructure is largely driven by the capture costs. For example, the first scenarios (up to 35 $MtCO_2/yr$) consist of entirely ethylene plants since they are by far the cheapest sources (Figure 24). Ethylene production produces an almost pure stream of CO_2 and capture consists only of compression costs, as no separation costs are incurred. As the CO_2 management target is increased, the model has to capture from more expensive sources, which eventually means capturing CO_2 from the two coal-fired power plants.

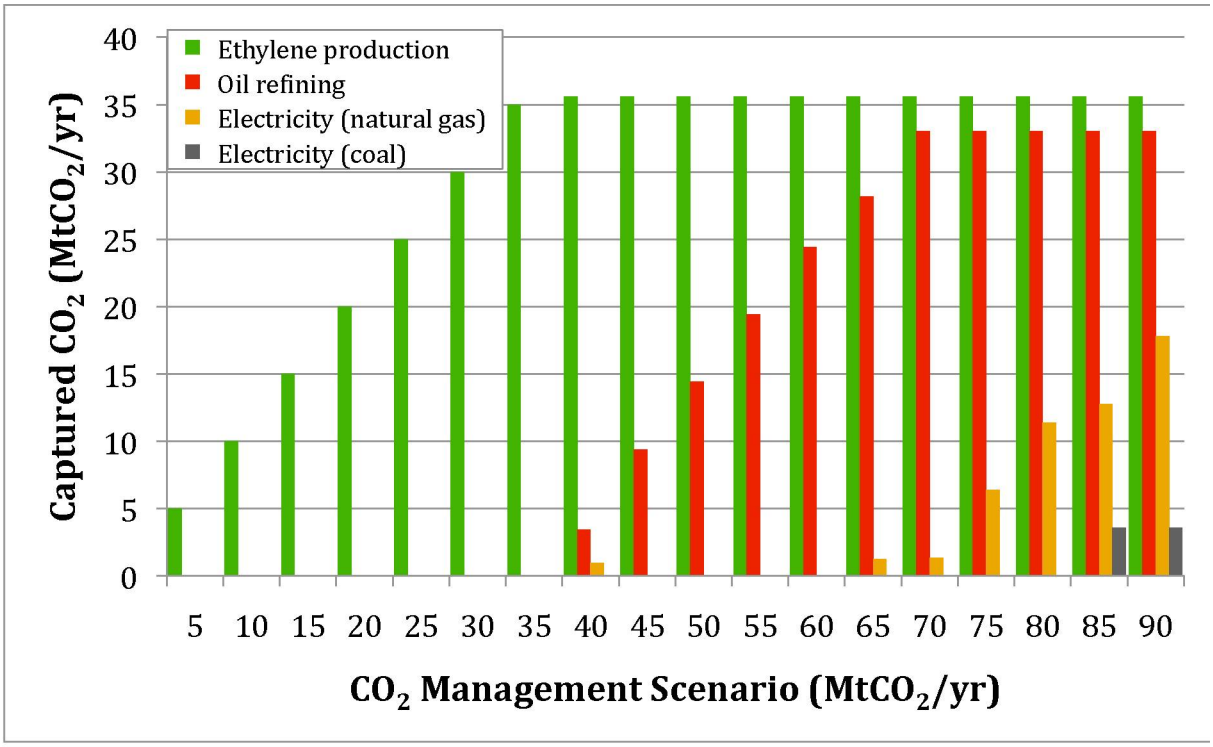

Figure 24: The distribution of industrial CO_2 sources utilized in the 18 CO_2 management scenarios.

4. Conclusions

CO_2 injectivity and capacity varies greatly across the range of reservoirs found below federal waters adjacent to Texas state waters in the Gulf of Mexico. CO_2 injection simulations were conducted for these reservoirs starting with simple explorations of the impact of boundary conditions to more complex scenarios involving independently varying parameters, stacked reservoirs, and finally regional collections of reservoirs. Capacity is mostly impacted by reservoir area and varies from 0.07–13.4 $MtCO_2$ for sands of length scale 262 m–3860 m. Stacked layers of sandstone, separated by low-permeability shales, can be expected to have higher total injectivity and capacity than single layers, but lower average injectivities for each layer.

Average storage efficiencies (E-factors) for the five regional sites ranged from 15% to 19%, far higher than the 1–4% assumed for saline formations in (U.S. DOE 2008) but consistent with findings in Doughty et al. (2001) for the Frio Formation in Texas (9.6% and 29.6% for 3-D and 1-D uniform simulations, respectively, with spill point determining when to evaluate capacity). These results are also consistent with Kopp et al. (2009), who report capacity estimates for simulations of saline aquifers under various temperature/pressure conditions and obtain results with equivalent E-factors ranging from 6%–17%. Geologic heterogeneity was not considered in our

simulations, but other numerical modeling studies (e.g., Doughty et al. 2001, Hovorka et al. 2004) have shown that it has the potential to increase storage capacity.

This study has demonstrated that the Texas Gulf Coast has significant CO_2 production and storage potential. Our results suggest that it is not unrealistic to expect to find sites with the potential to store 30 MT of CO_2, as proposed as a goal for this project. Although the five sites chosen in this study produced an estimated storage of a maximum of 20.2 MT (site 2), we do not expect the Gulf Atlas data to be comprehensive for all potential reservoirs within a given region. We estimated total capacity available in potential 15 by 15 mile squares by extrapolating the values for reservoirs in the Gulf Atlas database. Filling the gaps in the available data set will help further constrain the estimates presented here. Correlations developed in this study suggest that a combination of a volume estimate of the reservoir with a few other geologic parameters can be used to estimate E-factors and thus allow estimates of storage capacities for potential reservoirs.

The Gulf Coast region has up to a 35 $MtCO_2$/yr production from ethylene plants, which have low capture costs due to the production of a pure CO_2 stream. Consequently, this coastal region could jumpstart a large-scale sequestration industry by using CO_2 from ethylene production and selling the CO_2 to energy companies for enhanced oil and gas recovery—some estimates suggest that CO_2 is currently being purchased at ~$\$40/tCO_2$ due to elevated oil prices, a value high enough to pay for compression and transport of CO_2 to depleted oil and gas fields.

References

Bethke, C.M. (1986), Inverse hydrologic analysis of the distribution and origin of Gulf Coast-type geopressured zones, J. Geophys. Res., 91, 6535-6545.

Brooks, R. H., and A. T. Corey (1964), Hydraulic properties of porous media, Hydrol. Pap. 3, Colo. State Univ., Fort Collins.

Doughty, C., Pruess, K., Benson, S.M., Hovorka, S.D., Knox, P.R., and C.T. Green (2001), Capacity investigation of brine-bearing sands of the Frio Formation for geologic sequestration of CO2. Paper presented at first national conference on carbon sequestration, National Energy Technology Laboratory, Washington DC, 14–17 May 2001

Hovorka, S.D., Doughty, C., Benson, S.M., Pruess, K., and P.R. Knox (2004), The impact of geological heterogeneity on CO2 storage in brine formations: a case study from the Texas Gulf Coast, Geological Society, London, Special Publications 233, 147-163.

Keating, G.N., Middleton, R.S., Stauffer, P.H., Viswanathan, H.S., Letellier, B.C., Pasqualini, D., Pawar, R.J., Wolfsberg, A.V., 2011. Mesoscale Carbon Sequestration Site Screening and CCS Infrastructure Analysis. Environmental Science & Technology 45, 215-222.

Kopp, A., Probst, P., Class, H., Hurter, S., and R. Helmig (2009), Estimation of CO2 storage capacity coefficients in geologic formations, Energy Procedia, 1, 2863-2870.

Kuby, M.J., Bielicki, J.M., Middleton, R.S., 2011a. Optimal spatial deployment of CO_2 capture and storage given a price on carbon. International Regional Science Review 34, 285-305.

Kuby, M.J., Middleton, R.S., Bielicki, J.M., 2011b. Analysis of cost savings from networking pipelines in CCS infrastructure systems Energy Procedia 4, 2808-2815.

Middleton, R.S., Bielicki, J.M., 2009. A scalable infrastructure model for carbon capture and storage: *SimCCS*. Energy Policy 37, 1052-1060.

Middleton, R.S., Bielicki, J.M., Keating, G., N., Pawar, R.J., 2011a. Jumpstarting CCS using refinery CO_2 for enhanced oil recovery. Energy Procedia 4, 2185-2191.

Middleton, R.S., Keating, G.N., Stauffer, P.H., Viswanathan, H.S., Pawar, R.J., 2011b. Effects of geologic reservoir uncertainty on CCS infrastructure. International Journal of Greenhouse Gas Control. In review.

Middleton, R.S., Kuby, M.J., Bielicki, J.M., 2011c. Generating candidate networks for optimization: the CO_2 capture and storage optimization problem. Computers, Environment, and Urban Systems. In review.

Middleton, R.S., Wei, R., Kuby, M.J., Keating, G.N., Pawar, R.J., 2011d. A dynamic model for optimally phasing in CCS infrastructure. Environmental Modeling and Software In review.

Phillips, B.R., Middleton, R.S., 2011. *SimWIND*: A Geospatial Infrastructure Model for Optimizing Wind Power Generation and Transmission. Energy Policy, In Review.

Pruess, K., and J. García (2002), Multiphase flow dynamics during CO2 disposal into saline aquifers, Environ. Geol., 42, 282–295.

U.S. DOE (U.S. Department of Energy) (2008), Methodology for development of geologic storage estimates for carbon dioxide, Prepared for US Department of Energy National Energy Technology Laboratory Carbon Sequestration Program.

Van Genuchten, M.T. (1980), A closed-form equation for predicting the hydraulic conductivity of unsaturated soils. Soil Sci. Soc. Am. J., 44, 892–898.

Zyvoloski, G. A. (2007), FEHM: A control volume finite element code for simulating subsurface multi-phase multi-fluid heat and mass transfer. Los Alamos National Laboratory Report LAUR-07-3359, Los Alamos, NM.

APPENDIX C

Risk Assessment:

Identification of Environmental Risks

Specific to Offshore Settings

Key considerations for Selection & Development of Offshore Geologic Carbon Sequestration Projects Within Texas State Waters

---

Gulf of Mexico Miocene CO_2 Site Characterization Mega Transect:

Environmental Risks and Regulatory Considerations for Site Selection

December 2, 2014

Principal Authors:

Timothy O'Connor, Director, California Climate and Energy Initiative, Environmental Defense Fund

Scott Anderson, Senior Energy Advisor, Environmental Defense Fund

Daniel Carlin, Researcher, Environmental Defense Fund

Shanda Fisher, Researcher, Environmental Defense Fund

Final draft revised by Gulf Coast Carbon Center, Bureau of Economic Geology, The University of Texas at Austin

DISCLAIMER

Environmental Defense Fund (EDF) prepared this report to support the University of Texas Bureau of Economic Geology's Gulf of Mexico Miocene CO_2 Site Characterization Mega Transect project, related to identifying and choosing a suitable sequestration site or site(s), and as funded by the U.S. Department of Energy.

This report is intended to serve as a decision making tool for use when evaluating and selecting potential sites to develop the infrastructure and operations necessary to achieve geologic storage of carbon dioxide in the offshore environment of the Texas state waters. Although the document makes the case that CCS is a recognized and necessary tool for climate change mitigation, and development of offshore resources for CCS is likely key to that effort, this document is not meant to serve as a blanket recommendation for commercial scale development of CCS in the Texas state waters. Rather, prior to the development of any commercial scale CCS industry, in particular in the offshore environment, attention to, and coordination with existing and planned competing uses must be performed.

The views expressed herein are those of Environmental Defense Fund and not those of the Gulf Coast Carbon Center (GCCC), Bureau of Economic Geology (BEG), University of Texas or the Department of Energy, National Energy Technology Laboratory (NETL). Neither the United States Government nor any agency thereof, nor any of their employees, agents, contractors or volunteers makes any warranty, expressed or implied, or assumes any legal liability or responsibility for the accuracy, completeness, or usefulness of any information, finding, apparatus, product, or process disclosed, or represents that its use would not infringe privately owned rights.

As projects are developed or more information is collected, both in the Texas waters and beyond, the views and recommendations offered herein may be changed. As more information is developed, EDF reserves the right to update the findings, conclusions and recommendations of this paper in the future.

EXECUTIVE SUMMARY

Environmental Defense Fund (EDF) has prepared this analysis and recommendations as part of the Texas Bureau of Economic Geology's (BEG) evaluation of the suitability of geologic carbon sequestration projects within the offshore submerged lands inside the Texas state waters boundary. This analysis is part of BEG's larger research agenda associated with the Gulf of Mexico Miocene CO_2 Site Characterization Mega Transect project.

Global climate change is a serious threat to the health and well-being of the planet. The effects of climate change include increased global temperatures, increased extreme weather events, degraded air quality and sea level rise. Carbon capture and geologic sequestration (CCS)1 is one of many strategies that, if deployed correctly, can have a significant impact on reducing atmospheric concentrations of greenhouse gases (or at least the rate of their increase) that contribute to climate change. Examples that constitute correct deployment of CCS are well identified in the academic literature and from present day real-world operations. This combined experience with CCS suggests that with appropriate site selection, operational safeguards, and compliance with existing regulatory requirements and best practice methodology, long-term offshore sequestration can be performed safely and effectively and with manageable risk to the coastal environment.

Notwithstanding current experience however, CCS - perhaps particularly in the offshore environment - is not without risk. Accordingly, successful implementation will depend on the use of best industrial practices and safeguards by project developers and operators, and institutional capacity and integrity related to project oversight, precautionary management, monitoring, and adaptive management. For context, the BP Deepwater Horizon disaster appears to be attributable in large part to failures in both operational practices and institutional capacity and integrity – a result which must be avoided.

The purpose of this document is to assist BEG, prior to and during the process of selection of a geologic carbon sequestration site, to anticipate the environmental risks associated with long-term offshore carbon sequestration (including the processes required to do so) and to detail policy scenarios, recommendations and technical methods to avoid or minimize those risks. Issues and considerations associated with the site selection for carbon capture processes, the upstream component of CCS operations, are referred to only in passing, and are not a main point of reflection

1 This paper follows common practice and uses the term CCS interchangeably with the term "geologic carbon sequestration." Consideration of the carbon capture process at an emissions source is generally outside the scope of this research assignment.

for this report. Accordingly, this paper focuses on geologic carbon sequestration and the necessary infrastructure to achieve it, including pipelines and offshore platforms.

This report also makes recommendations for consideration during the project development and operations phase related to site-specific monitoring, verification, accounting and reporting (MVAR), and impact mitigation response planning. The authors reflect that the operational aspect of MVAR and impact mitigation response planning is outside the scope of the original task related to site selection. However, since the availability of particular MVAR strategies and mitigation responses to a particular site is necessarily considered during the site selection phase, those sections are included herein.

This report is divided into six main sections discussing considerations of CCS in the waters offshore of Texas with a final section describing ten key recommendations derived from EDF's research. Highlights from each section are summarized below.

In Section I, a brief introduction to the research assignment and paper is given.

In Section II, the report analyzes the environmental and economic attributes of the Texas coastal region, both offshore within the 10-mile state waters boundary and onshore in close proximity to the tidal zone. In general, the Texas coastal region is a series of connected ecosystems that are comprised of diverse flora and fauna and support a thriving tourism and fishing industry. In addition to bringing upwards of $48 billion of economic activity to the Texas economy every year, the coastal region supports a significant number of threatened and endangered species and overlays several aquifers which serve as an important drinking water source for 73 counties. Because of Texans' reliance on the coastal zone for tourism, fisheries, and drinking water, it is essential that this resource be protected for future generations.

In Section III, the report assesses lessons learned from offshore (and onshore) CCS operations ongoing in other parts of the world and draws conclusions related to the Offshore CCS in Texas. CCS off the coast of Texas could be the first of its kind not only in the Gulf, but also off the shores of the United States. As such, the skills and significant experience from both on and offshore oil and gas drilling operations, and onshore and offshore waste injection projects, are directly transferrable to undertaking a CCS project in Texas. For example, offshore projects, such as Statoil's Sleipner and Snovit CCS operations, can deliver valuable insight for implementing CCS in the Gulf. In addition, significant experience in onshore operations, both for oil extraction and CCS provide valuable examples.

In Section IV, the report evaluates the general benefits associated with offshore CCS as both a climate change mitigation tool and in comparison to onshore operations. In general, widespread deployment of CCS can have a near term and substantial impact on GHG levels impacting climate change. Although it has not been used widely, when compared to other methods to sequester CO_2 in the subsurface, offshore CCS project development may hold many benefits other locations do not. Potential benefits include improved public acceptance, reduced likelihood of human interaction with CO_2 leaks if they should occur, greater clarity over legal requirements and property rights, and improved leak detection capabilities.

In Section V, the report details the potential environmental and public health risks associated with offshore CCS projects. The pathways for these risks to become actual injury are also evaluated. These risks are identified both from existing project development experiences as well as from extrapolated experiences from offshore oil and gas development and operations. As discussed, with proper management and maintenance by the project developer and operator, much of these risks can be managed or minimized, but must be considered during the site selection and development phase. As discussed, the institutional capacity for oversight of project operations is also critical.

Sections VI and VII of the report encompass topics that were not part of EDF's project statement of work. Consequently, they and recommendations 5, 8 and 10 compose an appendix to the report and are not part of the report's main body.

In Section VI, the report details the existing legal and regulatory landscape for offshore CCS and installation of associated infrastructure for use in formulating policy recommendations related to site selection. Although more exhaustive accounts of legal and regulatory requirements may be found, this analysis presents the main body of regulatory restrictions associated with project development for protection of the offshore environment. As the discussion of regulatory requirements shows, while there is room for significant benefit from CCS operations in reducing greenhouse gas emissions, it is imperative that existing best management practices and regulatory requirements be followed in implementing CCS. Further, based on this set of regulatory requirements, it is apparent that much of the regulatory framework necessary to protect the offshore environment is currently in place.

In Section VII, this report takes the information presented and formulates ten key recommendations for use in siting and developing a project in the offshore environment of Texas. A summary of those recommendations is provided below. These recommendations are characterized both for use in the site selection phase of the research project associated with the Gulf of Mexico Miocene CO_2 Site Characterization Mega Transect, and also for use when considering larger-scale commercial deployment of geologic sequestration of CO_2 in the offshore environment. Where differences exist between the two uses for this report (informing the project as a research effort, and informing commercial deployment policies), the report identifies and discusses those differences.

KEY RECOMMENDATIONS

Recommendation 1: Any project for offshore CCS should be sited, designed and operated to avoid direct and significant impacts on human health or coastal natural resources (as defined by the Texas Natural Resources Code). To ensure adverse and / or unexpected environmental impacts are avoided, any offshore CCS project in Texas state waters must utilize the full range of precautions and safeguards available in all phases of the project timeline – including, but not limited to, site characterization, site selection, development, operation, monitoring, and closure. CCS site selection must evaluate whether the full range of precautions and safeguards are available at the target site or sites selected for development recommendation.

Recommendation 2**:** The siting of an initial project or projects to develop CCS in the offshore environment of the Texas coastal region must take a precautionary approach to prevent impacts on environmental attributes of concern. A precautionary approach should be used for offshore CCS deployment until such time as commercial scale deployment of CCS is achieved or a regulatory framework for managing offshore projects is adopted into law.

Recommendation 3: Prior to site selection, a proposed site must undergo a site specific evaluation of its potential to cause significant environmental impacts, including an evaluation of whether the full range of monitoring and mitigation techniques will be available to minimize impacts both at the point of injection and throughout the area of review / full zone of impact. Such a review should include a full characterization of potentially significant direct and indirect impacts prior to initiating development.

Recommendation 4: If the project must choose between two or more similar or equally situated sites for ensuring long term sequestration of injected CO_2, a formal risk assessment process which considers both 1) known conditions that might limit permanence and areas of uncertainty in characterization and 2) the consequences of both should be followed. A site with the smallest number of potentially transmissive pathways could also be the site for which there is less data. However, less data actually increases risk. Conditions that prevent the developer and regulator from listing all potential pathways does not eliminate them.

Recommendation 5 (see appendix): Regardless of regulatory applicability, strict application of the site characterization and control requirements of U.S. EPA UIC Class VI well regulations should be performed to ensure permanent retention of injected material is achieved. Future offshore geo-sequestration projects, should be sited and operated where the best geology and site characterization exists, and with strict application of U.S. EPA UIC Class VI requirements as required by law or as necessary to ensure permanent retention of injected material.

Recommendation 6: Distance from the shore, aquifers or areas of concern should be built into the determination of site suitability, though must not undermine the paramount need to have a site that represents the best geology for long-term sequestration.

Recommendation 7: All offshore CO_2 sequestration project sites should be evaluated for whether their proximity to existing infrastructure and right-of-ways would allow for re-use or co-location of new equipment so as to reduce the potential environmental footprint of any new project.

Recommendation 8 (see appendix): A CCS project should thoroughly evaluate several potential candidate sites for project development, allowing for critical evaluation of multiple locations and geologic characteristics by qualified experts prior to making a final determination. A complex system must have efficient redundancy to attain a stable operating condition. However requiring that every element has an idle backup is not good system engineering, because the backup requires major investment in both development and maintenance. In our society we save this for life-and death conditions like hospital generators, and it is not appropriate for atmospheric CO2 issues. Nonetheless, useful redundancies could include 1) combining sources and sinks via a pipeline network that provides redundancy, 2) developing a series of viable candidates during early characterization, so that sites with undesirable characteristics found during characterization can be dropped, and 3) phased build out so that untapped volumes are available if pressure increases in some more mature volumes; and 4) adequate redundancy and facilities to prepare for maintenance and contingencies, which would provide opportunities to take some parts of the project out of commission.

Recommendation 9: An up-front site characterization for project site selection must evaluate the set of monitoring and mitigation options available at a proposed project site prior to making the determination of its suitability. All offshore CO_2 sequestration projects should utilize an MVAR plan that is able to detect migration or leakage of CO_2 from the target confining zone early on in the formation of a non-conforming condition.

Recommendation 10 (see appendix): All offshore CO_2 sequestration projects should, prior to selecting a project site, evaluate the availability of contingency and remediation measures available at the site in the event an undesired impact is observed. A contingency and remediation plan should thereafter be finalized and published prior to commencement of the project.

TABLE OF CONTENTS

TABLE OF FIGURES

I. Introduction

EDF has prepared this analysis and recommendations as part of the Texas BEG's evaluation of the suitability of CCS projects within the offshore submerged lands inside the Texas state waters boundary. This analysis is part of BEG's larger research agenda associated with the Gulf of Mexico Miocene CO_2 Site Characterization Mega Transect project.

Today, offshore CCS projects exist in only a small set of locations around the world, though none yet in conjunction with a major power-generating facility. The most well known example of an offshore CCS project has been operating since 1996 and involves two facilities owned by Statoil of Norway: 1) a platform-based CCS facility at the Sleipner West natural gas field, roughly 155 miles off the Norwegian coast in the North Sea2, and 2) a similar project in the Snøhvit natural gas field in the Barents Sea. Major new offshore CCS operations are also in various stages of development in Western Australia, (Gorgon Gas Project at Barrows Island), off the coast of Brazil (Petrobras' Lula oil field), and in Western Norway (Mongstad refinery).3

Whereas offshore CCS has few project examples worldwide, onshore research, development and project operation is more prevalent, consisting of projects ranging in size from demonstration and pilot scale to much larger commercial sizes. According to the U.S DOE National Energy Technology Lab (NETL) CCS project database, there were about 250 onshore CCS projects in various stages of planning and development worldwide in the summer of 2011.4 Therefore, although currently operating offshore CCS examples provide a minimum level of guidance and assurances that CO_2 risks can be effectively managed offshore, significant onshore examples do provide much more insight.

Given the significant number of industrial CO_2 point sources near the Texas coast, a wealth of information and experience in oil extraction including enhanced oil recovery, and the proximity to potential sites for geologic sequestration (i.e. a close "source-sink match"), the region presents a significant opportunity to utilize CCS to achieve emissions reductions. CCS utilization though is not without risks, and should not be performed without adequate accounting for, and mitigation of those risks. In this document, EDF addresses what it sees as the principal environmental concerns with expanded CCS operations in Texas offshore

---

2 The Sleipner Project is perhaps the most well-known of any CCS project in the world due to its age and the amount of gas sequestered (roughly 1 $MMTCO_2E$/year since 1996).

3 The decision of whether to fund CCS at Mongstad has been delayed until 2016

4 U.S. Department of Energy, *NETL's Carbon Capture and Storage Database*, http://www.netl.doe.gov/technologies/carbon_seq/global/database/index.html (2011).

state waters, including public health issues, risks to flora, fauna, and ocean chemistry from development, operations and infrastructure. Evaluating historical examples and industry experience are central to this analytical effort.

In addition to evaluating potential environmental impacts and ways to minimize risks in the site selection phase, EDF's participation in this project involves an analysis of the applicability of current legal and regulatory frameworks within state, federal and international law that could impact offshore CCS operations in Texas state waters, and an evaluation of how these existing regulations present opportunities to protect against environmental harm. EDF also offers recommendations related to the site operations phase for context and future planning. Because this phase is beyond the scope of this focused project those recommendations are included as an appendix.

The conclusion made though this research assignment can generally be distilled down to the point that with appropriate site selection, operational safeguards, regulatory oversight, and compliance with existing regulatory requirements and best practice methodology, offshore CCS can be performed in Texas state waters safely and effectively, and with limited risk to the coastal environment and human population. Of course, this conclusion is built on the understanding that 1) meaningful opportunities for public participation will exist throughout the siting and environmental review process, and 2) rigorous independent regulatory oversight of project operations, including leak detection and leak mitigation, are present throughout the life of the project. To the extent that either or both of these mechanisms of participation and oversight break down, the risk of environmental harm increases and the stated conclusion may not hold.

In support of EDF's conclusion, ten discrete recommendations are made to manage and mitigate environmental risks from offshore CCS operations. In general, EDF's policy recommendations fit into the construct of ensuring rigorous site selection and characterization, followed by use of best in class monitoring and reporting practices to safeguard against environmental risks. The policy-related recommendations (5, 8 and 10) are not part of EDF's charge relative to the current project and as such are located in this report's appendix. Put more broadly, this policy framework can be thought of as promoting up front site selection work that 1) prevents problems from occurring, 2) creates mechanisms to identify problems if they arise, and 3) facilitates rapid response to problems if they should occur. Adopting these recommendations, in part or whole, are not trivial undertakings for project developers engaged in site selection. However, the application of the recommendations included in this document serve as the basis for EDF's finding that environmental risks can be effectively managed, and the recommendations therefore should be adopted in their entirety.

II. Environmental Attributes of The Texas Coastal region

Ecological Assets

The BEG Miocene CO_2 Site Characterization project focuses on the selection of potential CCS sites within state offshore lands, which extend three marine leagues, or about 10.35 miles from the Texas coast.5,6 The Texas coast is 367 linear miles long, running from Mexico to the Louisiana border.7 When counting barrier islands, bays, estuaries, and lagoons, the Texas coastline includes approximately 3,300 miles of shoreline and is characterized by a wide variety of ecosystems and economic activities. All together, the state waters a prospective area of approximately 6,400 square miles. (Figure 1)

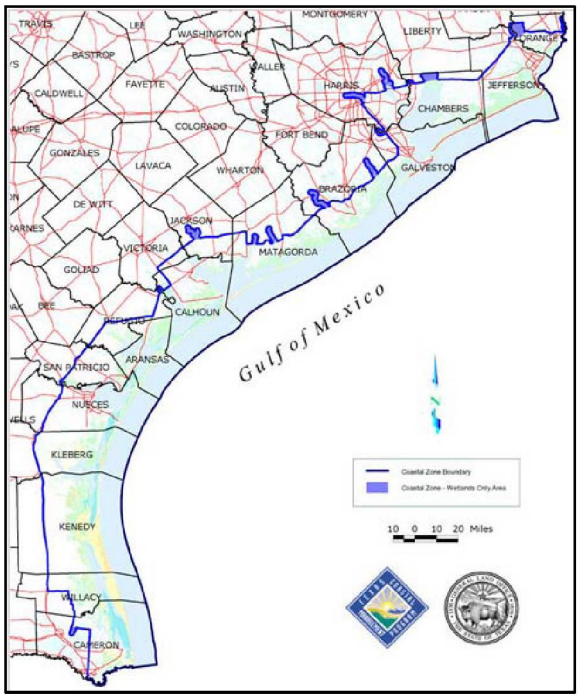

Figure 1 Texas Costal Zone

Source: Texas Parks and Wildlife

The coast plays a central role in the Texas economy, generating an estimated $48 billion in revenue through tourism, sport fishing, commercial fishing, and other economic activity at the coast's 16 ports.8 The coast's estimated $7.2 billion in annual tourism revenue comes in significant part from visitors to Texas' popular

5 J.T. Litynski et al., U.S. Department of Energy, *Carbon Capture and Sequestration: The U.S. Department of Energy's R&D Efforts to Characterize Opportunities for Deep Geologic Storage of Carbon Dioxide in Offshore Resources,* http://www.netl.doe.gov/technologies/carbon_seq/refshelf/project%20portfolio/2011/SelectedPubs/OTC-21987-PP%20-%20Litynski%20Offshore%20CCS%20Manuscript_Final.pdf (2011).

6 State Submerged Lands Act, 43 U.S.C. § 1331.

7 As discussed below, due to source-sink matching, suitability of injection formations and proximity to environmental attributes of concern, the upper third of the coast is the most likely site for an offshore CCS project in Texas state water.

8 Texas Ports Association, *Benefits: Texas Ports Stimulate Texas Economy*, http://www.texasports.org/benefits/

beaches, which are major destinations for bird-watching and fishing.9

In general, any existing environmental resource in the coastal zone may be impacted by expanded development and use of surface impoundments necessary to facilitate a CCS project. Examples of activities that have the potential to impact environmental resources include, but are not limited to, installation and operation of pipelines, floating and fixed platforms, floating and fixed vessel docking facilities, injection and extraction wells, as well as increased vehicle, vessel and aircraft traffic in and around the coastal zone. Additionally, accidental and intentional releases from storage sites, surface impoundments and vessels may also impact environmental resources in the coastal zone.

Determining whether a specific project or site for offshore CCS is likely to cause significant deleterious impacts on the environment is a highly fact-specific inquiry (explored in more detail in Section IV). Such an evaluation must not only take into account impacts from new development, but also the context of the ecosystem into which the project is performed. That individualized ecosystem evaluation however cannot fully be developed in a document such as this since it is highly fact specific to each and every development site and will require in depth site specific evaluations.

In a general sense, as detailed below, while the Gulf of Mexico near shore ecosystem remains fairly productive, it is also likely to, in places, be compromised with respect to overall resilience to new external stressors because of the cumulative impacts of many existing activities, some of which are resulting in large scale modification of the processes that maintain the ecosystem. These large scale drivers include flow and sediment modifications, nutrient input, habitat fragmentation, chronic oil pollution, the lingering effects of the BP Deepwater Horizon disaster, and regular hypoxic and anoxic events associated with mass marine mortality. The risks of any new project therefore, should be evaluated in the context of a compromised ecosystem that may not be very resilient to additional impact. Moreover, depending on the site, the surrounding ecosystem may already to be subject to high loadings of carbon in various forms - including chronic leakage from oil operations and organic carbon from mass mortality events and from nutrient-fueled algal blooms.

In addition to evaluating the ecosystem context for any development site, it is also important to evaluate the suitability of mitigation options available to a particular site to reduce the potential for impacts some mitigation options will be more readily available at some sites over others.

---

9 Oxford Economics, *Potential Impact of the Gulf Oil Spill on Tourism*, at 4, http://www.ustravel.org/sites/default/files/page/2009/11/Gulf_Oil_Spill_Analysis_Oxford_Economics_710.pdf

In the brief overview that follows, we attempt to characterize, at a macro-level, the types of environmental attributes that may be affected by offshore CCS developments in the study-region. This overview is not meant as a comprehensive set of findings on environmental impact potential, (as would be required to satisfy National Environmental Policy Act (NEPA) requirements). However, by providing a summary of the key issues that would need to be evaluated in a full site characterization process and Environmental Impact Statement (EIS) under NEPA, we attempt to offer a brief list of issues that should be considered by BEG when selecting a proposed site - prior to any NEPA requirements actually maturing.

1. Fauna

1. Amphibians

The shorelines, wetlands and brackish waters of the Texas coast are inhabited by a number of amphibians, including seven species of salamander, and several varieties of newts, frogs and toads. These include several endangered and threatened amphibians: the Houston toad is listed on both the Texas and U.S. Endangered Species list.10 Threatened amphibians include the Mexican tree frog, White Lipped frog, Sheep frog, and Mexican burrowing toad. Amphibian habitat is particularly fragile and susceptible to disturbance by development activity.

2. Reptiles

Eight species of sea turtles live along the shoreline, seven of which are threatened or endangered. These include the Kemp's Ridley sea turtle, the Atlantic Hawksbill sea turtle, the Leatherback sea turtle, and the Loggerhead sea turtle.11 Turtle nesting habitat is particularly fragile and susceptible to disturbance by development activity.

3. Fish

The Texas coastline can be thought of as comprising several comingled fisheries ecosystems, each influenced by the geomorphological formations nearby including bays, estuaries and barrier islands. (Figure 2)

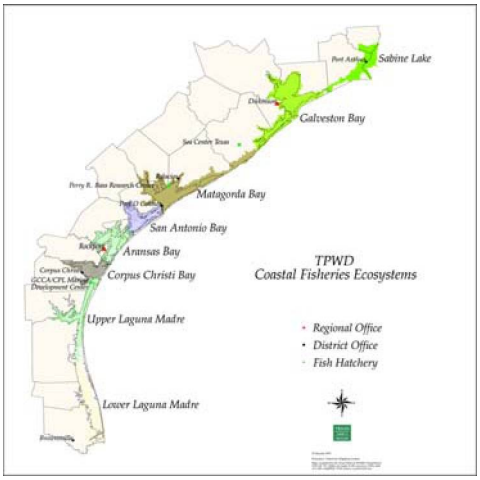

Figure 2: Texas Coastal Fisheries Ecosystems Source: Texas Parks and Wildlife

Open waters off the Texas coast, both within and outside the state waters boundary, are inhabited by more than 300 species of fish12 including sharks, rays, and many species sought after by commercial and sport fishermen such as Red snapper, Tarpon and Black drum. Of the fish that reside off the Texas coast, the Smalltooth sawfish

10 Texas Parks and Wildlife, *Endangered and Threatened Reptiles and Amphibians in Texas and the United States*, http://www.tpwd.state.tx.us/huntwild/wild/species/endang/animals/reptiles_amphibians/ (2009).

11 *Id.*

12 *Galveston Bay, Galveston & Gulf of Mexico*, http://www.ship468.org/seal/galveston.htm (2011).

is listed as a federally endangered species under the federal Endangered Species Act (ESA), while the Opossum pipefish, River goby, and Mexican goby are listed at the state level as threatened.13

4. Invertebrates

A number of invertebrates live in the coastal waters of Texas, including the Atlantic Bay scallop, lightning whelk, several species of crab, shrimp, beetles and spiders. Probably the most famous and economically important invertebrate in Texas waters is the oyster, American commercial oyster *Crassostrea virginica*, commonly referred to as the Eastern oyster, a highly commoditized invertebrate sought after by commercial fishermen. The American commercial oyster generally thrives in the bays and estuaries behind barrier islands separating the Texas mainland from the Gulf of Mexico.14 In particular, Galveston Bay is home to 60-70 percent of the oyster crop in the state.15 No coastal invertebrates are listed as threatened or endangered at this time.

5. Mammals

The Texas coastal zone and open water are home to several species of mammals, some of which are endangered or threatened. In fact, there are more endangered and threatened mammals in the Texas coastal zone than any other animal sub-group. There are two endangered land mammals that reside close to the coast, the Jaguarundi and the Ocelot, and three endangered marine mammals that are occasionally found in the coastal waters, the Finback whale, Humpback whale, and the West Indian manatee.16 Additionally, there are 10 threatened marine mammals that either reside in or pass through the Texas coastal waters, including the Black right whale, Sperm whale, Atlantic spotted dolphin, Gervais-beaked whale, Goose-beaked whale, Killer whale, Pygmy killer whale, Rough-toothed dolphin, and the Short finned pilot whale.17

6. Bird Life

---

13 Texas Parks and Wildlife, *Endangered and Threatened Fish in Texas and the United States*, http://www.tpwd.state.tx.us/huntwild/wild/species/endang/animals/fish/ (2011).

14 Texas Department of Agriculture, *About Texas oysters*, http://www.texasoysters.org/about.html (2011).

15 Texas Parks and Wildlife, *Endangered and Threatened Mammals in Texas and the United States*, http://www.tpwd.state.tx.us/huntwild/wild/species/endang/animals/mammals/ (2011).

16 *Id.*

17 *Id.*

Bird life is abundant throughout the coastal zone, particularly in one of Texas' six national wildlife refuges. Of the nature reserves in the coastal zone, the Aransas National Wildlife Refuge is the world's largest migration ground for Whooping cranes, a U.S. and State-listed endangered species.18 The area is also home to the state listed endangered Brown pelican, and three state listed threatened species of water birds: the Reddish egret, White-faced ibis, and Wood stork.19

18 Texas Parks and Wildlife, *Whooping crane (Grus americana)*, http://www.tpwd.state.tx.us/huntwild/wild/species/endang/animals/birds/whooper.phtml (2011).

19 Texas Parks and Wildlife, *Endangered and Threatened Birds in Texas and the United States,*

http://www.tpwd.state.tx.us/huntwild/wild/species/endang/animals/birds/ (2011).

2. FLORA

1. Wetlands

A large portion of the Texas coast is characterized by wetlands, which the Clean Water Act defines as "areas that are inundated or saturated by surface or groundwater at a frequency and duration sufficient to support, and that under normal circumstances do support, a prevalence of vegetation typically adapted for life in saturated soil conditions. Wetlands generally include swamps, marshes, bogs and similar areas."20 Wetlands provide a variety of critical ecosystem services, including water filtration, flood buffering, erosion control, and habitat for developing and mature wildlife. (Figure 3)

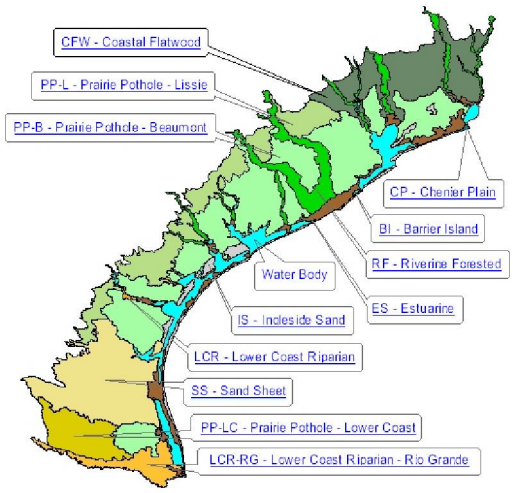

Figure 3: Seven major wetland categories for the Texas Gulf. Source: Jacob et. al., Texas Costal Wetlands Guidebook

Seven wetland areas are classified as either National Preserves or National Wildlife Refuges. As a nursery for fish, crab, and other shellfish, coastal near-shore wetlands support the commercial fishing industry throughout the Texas state waters which at the wholesale level is valued at more than $400 million annually and employs about 30,000 coastal residents. The total economic impact of saltwater sport fishing in Texas is almost $2 billion annually, employing about 25,000 coastal residents.21

Currently, the main threat to Texas' wetlands is from subsidence, hurricanes and resulting flooding. Together, these processes imbalance the freshwater/saltwater equilibrium and can result in wetland drowning (long term or permanent submersion). According to Jacobs et al., subsidence causes the land surface to drop, which can then become flooded if the surface is already very near to sea level.22 However, since CGS results in additional material sequestered below the surface, it is not expected to have a profound impact on

---

20 40 CFR § 230.3(t) http://water.epa.gov/lawsregs/guidance/wetlands/definitions.cfm (2009).

21 *Id.*

22 Although subsidence-induced flooding has drowned many wetlands, especially in and around large coastal cities such as Houston, and can be caused by multiple factors such as groundwater pumping, oil and minerals extraction, natural subsidence or surface removal, it is still unclear whether injection of new material, by itself, into the subsurface would have an appreciable impact on subsidence.

this phenomenon. Indeed, many consider a major possible effect of CO2 injection on land surface to be possibly offsetting subsidence.

2. Submerged Aquatic Vegetation

Submerged Aquatic Vegetation (SAV), which includes seaweeds and seagrasses, plays a central role in the Gulf of Mexico's offshore coastal ecosystem. These plants convert sunlight, water and nutrients into food for many fish, crustacean, invertebrate and bird species. In addition, they provide nursery grounds for many species sought after by commercial and recreational fishermen, such as shrimp, Black drum, Red snapper, Grouper, Spotted sea trout, Southern flounder, and others.23

Although abundant throughout the Gulf of Mexico, robust seagrass beds and their accompanying marine biodiversity only occur in two locations in the near-shore waters of Texas, covering roughly 37,000 acres: the Laguna Madre and the Copano-Aransas Bay complex. These are valuable, rare ecosystem resources that thrive due to a complex combination of environmental factors including temperature, water depth, turbidity, salinity, turbulence and substrate suitability.24 Seagrass conditions in these areas are fragile and can easily be disrupted by industrial activity or environmental damage.

1. GROUNDWATER ASSETS

Studies have shown there are no freshwater aquifers in the Texas offshore coastal area. (Figure 4) The onshore coastal zone does include significant freshwater aquifers that provide irrigation and drinking water for the nearly 73 counties of the Texas Gulf Coast region, and which are particularly critical for the Houston metro area.25

23 U.S. Coast Guard and Maritime Administration, *Final Environmental Impact Statement, Beacon Port Deepwater Port License Application*, at 3-32, Vol. 1 (Nov. 2006).

24 *Id.* at 3-32-33.

25 Texas Water Development Board. *Report 365: Aquifers of the Gulf Coast of Texas*, at 1 (Feb. 2006), see also http://www.twdb.state.tx.us/publications/reports/GroundWaterReports/GWReports/R365/R365_Composite.pdf.

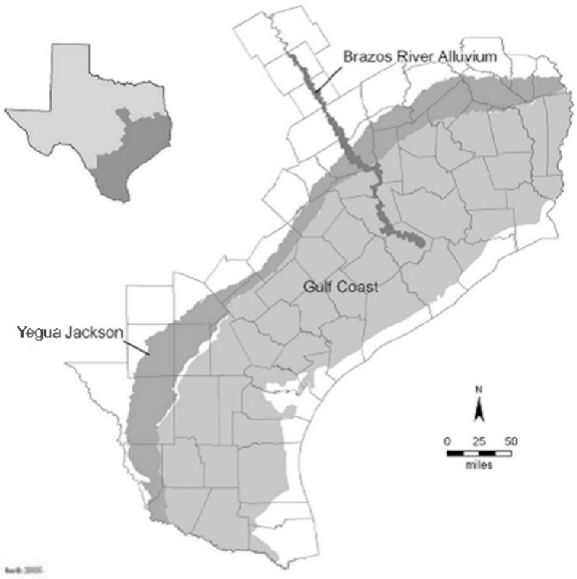

Figure 4: Locations of Major and Minor Aquifers in the Texas Coastal Area

The Texas Water Development Board has designated the Gulf Coast aquifer as a main aquifer, and the Yegua-Jackson Aquifer and the Brazos River Alluvium as minor aquifers. Altogether, these three aquifers serve a population of roughly 8 million Texans. Over 1.1 million acre-feet of groundwater from the Gulf Coast aquifer are used annually in Texas. The Gulf Coast aquifer extends over 430 miles from the Texas-Louisiana border in the northeast to Texas-Mexico border in the south.26

Groundwater quality in the Gulf Coast aquifer is generally of sufficient quality northeast of the San Antonio River but declines to the southwest due to increased chloride concentrations and saltwater encroachment near the coast. In addition, heavy pumpage has caused saltwater intrusion to occur along the coast as far north as Orange County.27

Much of the Gulf Coast region's freshwater resources are managed by 25 groundwater conservation districts. Following the passage of Texas House Bill 1763 (2005), as of 2010, all groundwater conservation districts are required to establish desired future conditions for the aquifers within their groundwater management area boundaries.28 Although not enforced or monitored by the Texas Water Development Board, groundwater conservation districts must ensure that their management plans are designed to meet the newly decided conditions.29

---

26 *Id*. at 81.

27 *Id*.

28 *Id.* at 173.

29 *Id.* at 16.

III. Operations and Events Important for Drawing Conclusions Related to Offshore CCS in Texas

Subsurface injection of gases onshore for disposal, enhanced oil recovery and / or sequestration has occurred across the globe for four decades. Additionally, injection of fluids and gases into the subsurface of the seabed (offshore) has also been ongoing at several sites across the globe since 1996. This offshore work has included CO_2 injection for the purpose of sequestration, fluid injection for disposal, and also for enhanced oil recovery. Finally, research of CO_2 emissions from natural CO_2 seeps and fissures located on the sea floor has also been ongoing for many years. Together, the body of information developed from these operations and research provide insight into the risk profile of the development and use of offshore CCS in submerged lands in Texas state waters.

The summation of this research and operational experience from onshore and offshore operations, and scientific research indicates that offshore CCS can be performed in the Texas offshore waters, at specified sites, without resulting in unmitigated leakage of CO_2 from the target confining zone and without causing significant environmental impacts on ecological assets of concern. However, given the direct record of offshore CCS operations and offshore CO_2 leakage research, albeit relatively brief, it has been demonstrated with sufficient clarity that offshore CCS projects in Texas should take certain precautions (as discussed in Section V).

1. On-Shore CCS Projects and Enhanced Oil Recovery with CO_2

There are approximately 250 onshore CCS projects in various stages of planning and development worldwide.[30][31] Across the globe, this proliferation and experience with CCS projects has matured the industry to the point that best practices standards have been generally identified and regulatory requirements have been developed for nearly every aspect of project monitoring, operation and reporting (including site characterization, selection, drilling and development, operation, closure and post-closure).[32]

Onshore CCS projects which do not use enhanced oil recovery (EOR) generally involve injection into either saline aquifers, depleted oil fields, coal seams, or other subsurface

---

30 NETL, http://www.netl.doe.gov/technologies/carbon_seq/global/database/index.html

31 Global CCS Institute 2011, *The global status of CCS: 2010*, Canberra http://cdn.globalccsinstitute.com/sites/default/files/publication_20110419_global-status-ccs.pdf (2011).

32 Forbes et al., *Guidelines for Carbon Dioxide Capture, Transport, and Storage*, World Resources Institute, http://pdf.wri.org/ccs_guidelines.pdf (2008).

structures. Of the various types of structure available, saline aquifer storage is generally thought of as providing the greatest opportunity for large scale CCS deployment.33

There are approximately 129 enhanced oil recovery projects using carbon dioxide (EOR CO_2) worldwide, with 114 of those located in the United States.34 In general, CO_2 is injected into an oil field through a number of injection wells drilled around a producing well and at a pressure equal to or above the minimum miscibility pressure (MMP). Once injected, the CO_2 and oil mix together and form a liquid that more easily flows to the production well. Pumping can also be enhanced by flooding CO_2 at a pressure below the MMP, swelling the oil and reducing its viscosity.35 (Figure 5)

33 Herzog, H., "*Carbon Dioxide Capture and Storage*," Chapter 13 in The Economics and Politics of Climate Change, http://sequestration.mit.edu/pdf/2009_CO_2_Capture_and_Storage_Ch13_book.pdf (2009).

34 Dooley et al., *CO_2-driven Enhanced Oil Recovery as a Stepping Stone to What?*, Pacific Northwest National Laboratory, U.S. Department of Energy (2010); (Citing Koottungal, L., *Special Report: EOR/Heavy Oil Survey: 2010 Worldwide EOR Survey*, Oil and Gas Journal (2010).

35 U.S. Department of Energy, *NETL EOR Factsheet*, http://www.netl.doe.gov/publications/factsheets/program/Prog053.pdf

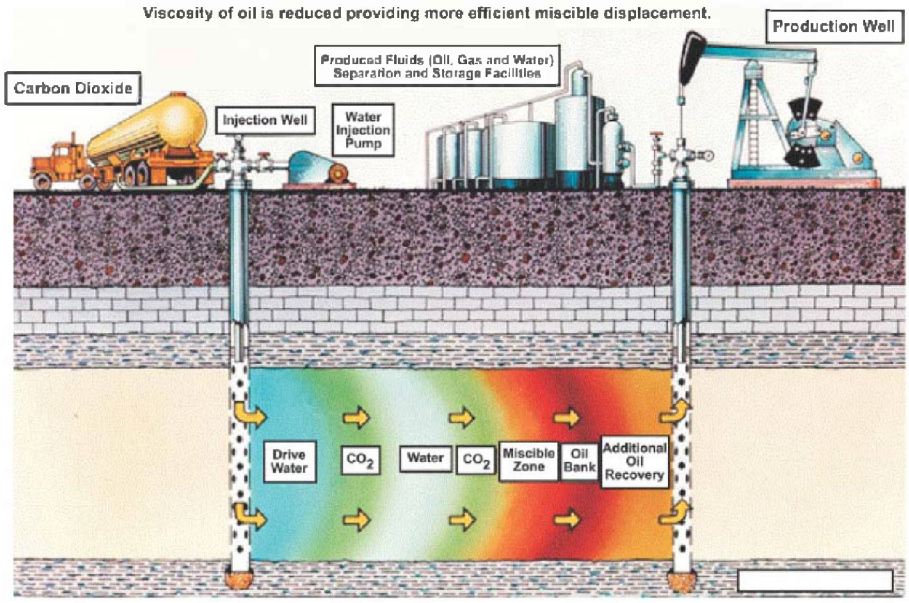

Figure 5: Simplified diagram of an onshore enhanced oil recovery with carbon dioxide operation. Source: U.S. DOE

Due to the large number and considerable degree of variability of standards and practices applicable to onshore CCS and EOR CO_2 operations, this paper does not attempt to characterize the full range of lessons learned and best practice standards developed. A more detailed discussion of requirements is included in Section VI (appendix) below. When taken together however, these site selection and operation standards support the claim by the Intergovernmental Panel on Climate Change (IPCC) that geologic storage sites that are well selected, designed and managed can trap CO_2 for millions of years and are likely to retain more than 99 percent of the injected CO_2 over more than 1,000 years.36 Accordingly, the history of onshore CCS and EOR CO_2 support the IPCC conclusion and the general conclusion of this paper that offshore CCS can be performed in a manner that 1) retains the CO_2 in the target injection zone and 2) does not cause adverse impacts on the offshore environment.

2. EXISTING OFFSHORE GEOLOGICAL CARBON SEQUESTRATION (CCS) PROJECTS

1. STATOIL – UTSIRA FORMATION (SLEIPNER PROJECT)

36 U.S. Department of Energy, *Carbon Dioxide Enhanced Oil Recovery Untapped Domestic Energy Supply*

and Long Term Carbon Storage Solution, National Energy Technology Laboratory http://www.netl.doe.gov/technologies/oil-gas/publications/EP/small_CO_2_eor_primer.pdf (2010).

The first, oldest, and most well known, and offshore CCS facility in the world is located at the Sleipner natural gas field in the North Sea, roughly 155 miles off the Norwegian coast.37 In the Sleipner gas field, carbon dioxide is injected into brine / saltwater within a sandstone formation approximately 2,600 ft (800 meters) below the sea floor and between 200 and 300 m thick.38 (Figure 6)

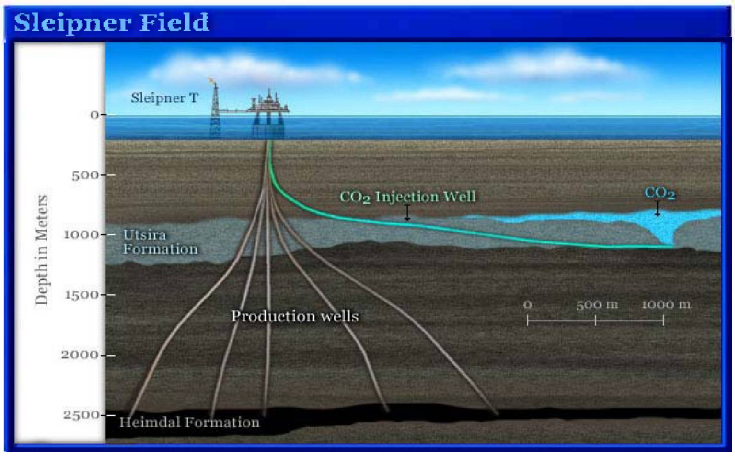

Figure 6: CCS infrastructure at the Sleipner natural gas field. Source: Schlumberger Excellence in Educational Development (SEED), Inc.)

The Sleipner project started in 1996 as a direct outgrowth of both Statoil's need to meet customer specifications for natural gas extracted from the Heimdal Formation (requiring decarbonization from 9% CO_2 content to 2.5%) and the Norwegian government's introduction of a $50/ton CO_2 tax in 1991.39 Conventional practice of natural gas purification would have involved venting produced CO_2 into the atmosphere. However, the CO_2 tax created a financial incentive for Statoil to look for opportunities to avoid releasing the CO_2 – and instead turned to CO_2 sequestration in a nearby geologic formation (the Utsira Formation).

To initiate the overall project, Statoil invested roughly $100 million on platform-based carbon capture technology, which captures the CO_2 during the natural gas processing phase using conventional amine scrubbing, and transports it via pipeline approximately

Figure 7: Sleipner A Platform. Source: Statoil

37 Bellona, *Factsheet: Security of CO_2 storage in Norway*, http://www.bellona.org/factsheets/1191928198.67

38 Id.

39 Statoil, *Annual Report*, http://www.statoil.com/AnnualReport2008/en/Sustainability/Climate/Pages/5-3-2-3_SleipnerCCS.aspx

650 feet (200 meters) to the sea floor. (Figure 7) From there, nearly pure CO_2 is injected to a depth of about 2,600 feet (800 meters) below the sea floor into the Utsira sandstone formation – a brine aquifer. The multiple (3) layers of impermeable caprock above the Utsira Formation extend upwards approximately to the sea floor surface.

Statoil has injected roughly 1 $MMTCO_2E$ per year into the Utsira Formation at Sleipner, equivalent to the annual CO_2 emissions of a 350 MW coal-fired power plant. So far, Statoil has reported no major CO_2 leaks. 40,41 Statoil has allowed and supported an extensive multinational, multi-decade monitoring project (SACS and following EU projects) to be conducted over the injection site. [42]

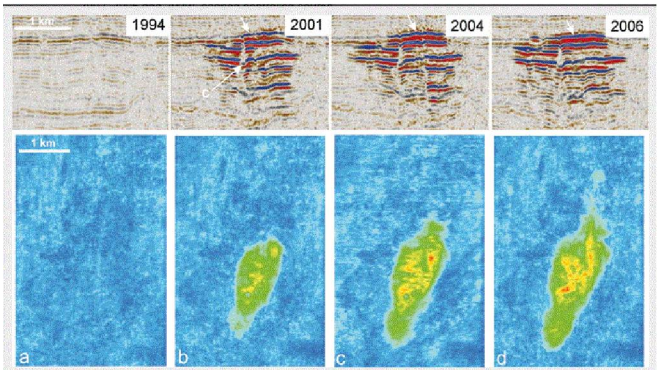

Figure 8: Time-lapse seismic images from Sleipner. Source: British Geological Survey

Research and time lapse plume monitoring similar to that shown (right) at the Sleipner site has shown that CO_2 migration from the point of injection has occurred to a lateral distance of approximately 1.6 miles (2 km), and with a vertical distance of approximately 250m.43,44 (Figure 8)

---

40 Eiken, et al., *Lessons learned from 14 years of CCS Operations: Sleipner, In Salah and Snøhvit.* 10th International Conference on Greenhouse Gas Technologies, 19-23 Sept. 2010, Amsterdam, Netherlands. www.sciencedirect.com (2010).

41 Statoil, *Annual Report*, http://www.statoil.com/AnnualReport2008/en/Sustainability/Climate/Pages/5-3-2-3_SleipnerCCS.aspx (2008).

42 Arts, R., Eiken, O., Chadwick, A., Zweigel, P., van der Meer, L., and Zinszner, B., 2004, Monitoring of CO2 injected at Sleipner using time-lapse seismic data: Energy, v. 29, no. 9–10, p. 1383-1392.

43 Rutqvist et al., *Coupled reservoir–geomechanical analysis of the potential for tensile and shear failure associated with CO_2 Injection in multilayered reservoir–caprock systems*, Int J Rock Mech Mining Sci, http://www.epa.gov/climatechange/emissions/downloads/LBNL3.pdf (2007).

44 Website British Geological Survey, http://www.bgs.ac.uk/science/CO_2/home.html

2. STATOIL – TUBÅEN FORMATION (SNØHVIT)

Similar to the Sleipner project, Statoil also operates a major offshore CCS facility at the Snøhvit gas field in the Barents Sea, approximately 87 miles from the Norwegian coast. Statoil began sequestering CO_2 at this site in April 2008, again as a byproduct from natural gas processing. Injection occurs to a depth of approximately 2,500m, and at a water column depth of approximately 330m.45

Statoil produces approximately 13,000 metric tons of liquefied natural gas annually from four sub-seabed wells within the Snøhvit gas field. After extraction, natural gas is transported via pipeline to the Melkoya processing facility, just off the coast of Hammerfest. At Melkoya, the CO_2 is separated via amine scrubbing and returned to the Snøhvit field via pipeline for injection into the Tubåen Formation. Although the Tubåen Formation is relatively thin (between 65m and 87 m thickness), Statoil estimates that at full capacity it will sequester 700,000 metric tons of CO_2 per year at the site.46

Figure 9: Snøhvit processing facility. Source: Statoil

Unlike the Sleipner project, the Snøhvit project requires no fixed or floating ocean surface impoundments at the point of injection.47 (Figure 9) This design allows for seabed facilities to be "over-trawlable", so that neither they nor fishing equipment will suffer any damage from coming into contact.

Although the Snøhvit facility's environmental record has been without recorded incident since operations began in 2008, the facility and accompanying injection has faced a series of extended maintenance shut-downs, largely due to its setting in the extreme climate of the Barents Sea. The facility was closed for nearly three months in 2009 to perform

---

45 Statoil, *Presentation CSLF Interactive Workshop*, Saudi Arabia, March 2011. P. Ringrose et al, *available at* http://www.cslforum.org/publications/documents/alkhobar2011/CO_2StoreProjectSleipnerandSn%C2%BFvitProjects_Session3.pdf (2011).

46 Statoil, *Annual Report* (2010). http://www.statoil.com/AnnualReport2010/en/sustainability/Health,Safety,ClimateAndTheEnvironment/Climate/CarbonCaptureAndStorage/Pages/OurCCSProjects.aspx

47 Statoil, http://www.statoil.com/en/ouroperations/explorationprod/ncs/snoehvit/pages/default.aspx

unspecified maintenance.48 From late 2010 to early 2011, the facility was closed to address leakage in the plant's cooling system.49 No leaks have been reported from this project.

48 UpstreamOnline.com, *Statoil Restarts Snohvit,* http://www.upstreamonline.com/live/article198246.ece. (2009).

49 McLoughlin, *Statoil says Snohvit LNG output to resume H_2 Jan*, Platt news service, http://www.platts.com/RSSFeedDetailedNews/RSSFeed/Oil/8362448 (2011).

3. PETROBRAS – LULA OIL FIELD

In September 2011, Brazil's Petrobras announced it had begun production at its Lula oil field, located roughly 185 miles from Rio de Janeiro. Currently the field is pumping about 30,000 barrels a day, with a projected maximum extraction rate of 100,000 barrels per day, 50 making it potentially one of the most productive fields in the Americas.

Brazil has a national greenhouse gas emissions reduction target of 33% to 36% below business as usual emissions by the year 2020. To boost production of the field and mitigate CO_2 emissions from produced gas, Petrobas will inject and retain some percent of the total emissions from the operations and reduce the project's overall GHG emissions.51 This mitigation consists of reinjection of CO_2 from produced gas into the field, and may be used to enhance oil recovery operations. Injection of produced gas into the field, including CO_2 likely began in April 2011.52 Sequestration of the emissions is also consistent with Petrobas' 2009-2013 Business Plan that called for avoiding voluntarily the emissions of 4.5 million tons of carbon dioxide equivalent (CO_2e) in 2013.53

4. OFFSHORE OIL EXTRACTION

Offshore oil extraction has been occurring in the United States since the turn of the 20th century, though practices have evolved to allow for deeper wells and greater water depths. Since many of the same types of operations and pieces of equipment are utilized in CCS operations as oil extraction operations, site impact prevention and mitigation applicable to installation of oil extraction infrastructure (oil platform siting, well drilling equipment, infrastructure installation and operation, etc.) are generally applicable to CCS operations.

Similarly, environmental impact reports prepared for the purpose of complying with the National Environmental Policy Act (NEPA) for new oil extraction operations can serve as valuable tools to assess the potential for environmental impacts associated with CCS surface impoundments, processing and transport equipment. Where possible, recommendations made in this paper draw information from EIR's (environmental impact reports) performed for siting of oil platforms in the near shore environment of Texas.

---

50 http://en.mercopress.com/2011/09/20/petrobras-begins-pumping-natural-gas-from-first-pre-salt-field-of-santos-basin

51 *Id.*

52 http://www.oilonline.com/default.asp?id=259&nid=19457&name=Lula+producing+on+commercial+basis

53 Petrobas, http://www.petrobras.com.br/rs2009/en/relatorio-de-sustentabilidade/meio-ambiente/mudanca-do-clima/

Although a strong correlation exists between the potential impacts from surface impoundments associated with oil extraction and offshore CCS, the differences associated with drilling for extraction of high pressure fluids (i.e. oil extraction) and drilling and operation for CO_2 injection urge caution in making direct correlation for the purposes of environmental impact evaluation from leaks.

5. Subsurface Injection of Non-CO_2 Liquids and Gases

1. Produced Water and Acid Gas Injection

In general, produced water and acid gases have been injected into the subsurface for decades and have resulted in the development of a large body of scientific understanding, industry literature and practices, and comprehensive regulations to prevent environmental damage. In fact, injection into underground formations represents the most common approach for onshore management of produced water.54 Additionally, in 2004 and 2005, there were over 60 different wells injecting acid gases (primarily consisting of hydrogen sulfide and carbon dioxide) across the United States, with the highest numbers in Wyoming and Texas.55

Stringent controls that have been developed by US EPA for protection of subsurface resources such as potable groundwater, and to prevent escape and migration from the target confining zone are discussed in Section VI (appendix) of this report. Together, this body of information and experience illustrates a long history with safe, long-term storage of subsurface injected high pressure materials. Additionally, this experience supports the conclusion that injection of pressurized CO_2 for the purpose of geologic sequestration can occur without deleterious impacts on the environment.

2. Statoil – Utsira Formation (Tordis gas field)

To date, only one example of problematic operations from offshore injection of produced water or acid gas exists. Although the Statoil project in the Tordis gas field does not entail CO_2 injection, it does involve the injection of high pressure fluids into the seabed

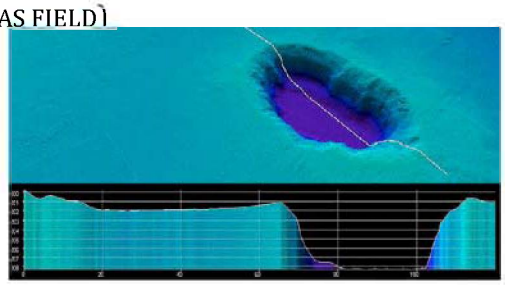

Figure 10: Illustration of the seabed crater near Tordis. The scale is in meters. Source: Statoil

54 U.S. Department of Energy, *Produced Water Management Technology Descriptions Fact Sheet - Underground Injection for Disposal,* http://www.netl.doe.gov/technologies/pwmis/techdesc/injectdisp/index.html

55 U.S. Department of Energy, *Acid Gas Injection in the United States,* Presentation at the Fifth Annual Conference on Carbon Capture & Sequestration (2010). http://www.netl.doe.gov/publications/proceedings/06/carbon-seq/Tech%20Session%20140.pdf

subsurface, and therefore is relevant for the purpose of identifying potentially undesirable impacts that may occur from seabed injection of high pressure fluids, namely CO_2.

The Tordis gas field is located approximately 180 miles (300 km) from the Sleipner project.56 In 2008, Statoil began injecting produced water into the Utsira formation at Tordis, at a depth that was expected to be roughly 1000m below the sea floor. However, due to poorer than expected injectivity of target reservoir that was not predicted in pre-operation geologic site characterization analyses, the fluid was not being injected into a target reservoir capable of handling the injection pressures and volumes.57

As a result of the geologic unsuitability for the injection operations, the Tordis project resulted in the Statoil operator over-pressuring the injection site and causing a direct fluid communication to the seabed which released between 48 m^3 and 175 m^3 of oil into the water column. (Figure 10) Follow-up investigation of the site revealed lack of a pressure monitoring regime capable of detecting the problems prior to the eventual total depressurization as well as lack of effective project management.58

3. RESEARCH OF CO_2 VENTS IN THE SEA FLOOR

A considerable amount of research has been performed on natural and induced seafloor vents and seeps. This research has yielded a range of outside-the-well detection methods that can be used to find out whether CO_2 is seeping into the water column, and also to calculate quantities and effects. However, no research has definitively characterized a fool proof single method for determining whether CO_2 is seeping from the seafloor into the water column over a large area and in all cases. Where applicable, this paper draws from the findings of that research to propose policy solutions in Section VII (Appendix) related to site selection, monitoring and operations for the express purpose of detecting and mitigating leaks of CO_2.

---

56 Statoil, *Tordis incident 2008,* http://www.statoil.com/en/OurOperations/ExplorationProd/ncs/tordis/Pages/TordisIncident2008.aspx (2009).

57 T. Eidvin and J. Øverland, *Faulty geology halts project,* NPD, http://www.npd.no/Global/Engelsk/3%20-%20Publications/Norwegian%20Continental%20Shelf/PDF/10%20faulty%20geology.pdf

58 Greenpeace, *Reality Check on Carbon Storage*, at 5 http://www.greenpeace.org/raw/content/international/press/reports/reality-check-on-carbon-storage.pdf. (2009).

Based on available literature, research on CO2 seeps, vents and discharges is ongoing or completed at the following sites:59

1. Norwegian offshore CO2 storage Sleipner;
2. Norwegian offshore CO2 storage Snøhvit;
3. B3 field in the Polish Baltic Sea;
4. Natural CO2 seeps off Italy (Panarea);
5. Natural CO2 seeps off Japan (Okinawa Trough);
6. Natural CO2 seeps off Germany (Salt dome Juist);
7. Natural CO2 seeps off Germany (Lake Kaach); and
8. Natural CO2 seeps off Norway (Jan Mayen).

59 European Commission, *Assessing the environmental risks of sub-seabed CO2 storage, http://www.ifm-geomar.de/index.php?id=537&L=1&tx_ttnews%5Btt_news%5D=742&tx_ttnews%5BbackPid%5D=8&cHash=0a2c58583e*

IV. General Benefits of Offshore Geologic Carbon Sequestration in Texas State Waters

Near-offshore CCS has some environmental and public health advantages compared to onshore geologic storage worth briefly noting before considering its environmental risks.

1. As Enumerated by the U.S. Department of Energy

Benefits of offshore CCS have been enumerated by the U.S Department of Energy as follows:60 (Figure 11)

Figure 11: U.S. Department of Energy
Enumerated Benefits of Offshore CCS

Offshore CCS is a promising technology due to several key advantages:

1. *Offshore storage provides additional CO_2 storage potential in the United States to supplement existing onshore capacity estimates.*
2. *The formation fluid in offshore sediments is typically similar to sea water in terms of chemistry and salinity with 30,000 to 40,000 ppm total dissolved solids (TDS)….*
3. *Locating sequestration sites away from heavily populated, onshore areas avoids the perception of storing waste material beneath a populated area. This also reduces the difficulty of establishing surface and mineral rights at candidate storage sites. …*
4. *Offshore storage reduces the risk to underground sources of drinking water (protected groundwater).*
5. *Establishing transport pipeline corridors or using existing infrastructure should be feasible based on already existing infrastructure for natural gas and oil.*
6. *Offshore CCS provides storage sites in the vicinity of heavily populated areas along U.S. coastlines (like the Northeast and California).*
7. *The overall economics of offshore CCS may be more favorable compared to onshore CCS, despite higher capital costs (for drilling rigs, well manifolds, etc.) typically associated with working in an offshore environment. This will be especially true if offshore storage projects prove relatively easy to permit, finance, and operate.*

Figure 11: US DOE Enumerated Benefits of Offshore CCS

60 J.T. Litynski et al., (2011); Citing extensively Schrag, D., *Storage of Carbon Dioxide in Offshore Sediments*. Science 325, 1658, DOE: 10.1126/science.1175770 (2009).

2. SEQUESTRATION OF GREENHOUSE GASES AND CLIMATE CHANGE MITIGATION

Global climate change is a serious threat to the health and well-being of the planet. The potential catastrophic effects of climate change are well documented and include increased global temperatures, increased extreme weather events, degraded air quality and sea level rise.61 Carbon capture and geologic sequestration is one of many strategies that, if deployed correctly, can have a significant impact on reducing atmospheric concentrations of greenhouse gases that contribute to climate change. Examples that constitute correct deployment of CCS are well identified in the academic literature and from present day real-world operations.

Although there may be roughly 250 research, development and / or deployment CCS projects world-wide at varying scales, mitigation of greenhouse gas pollution sufficient to combat climate change will require many more CCS sites. Rough estimates of CCS deployment needed to effectively reduce the emissions from the power sector (in combination with other emissions reduction measures) place the total number of project sites close to 3,500 projects as large as the Sleipner project62, and with coincident technological advancements to significantly reduce the overall cost of construction and operation of the facilities.

As identified by the U.S. Department of Energy, "the University of Texas at Austin (UT–Austin) will identify one or more CO_2 injection sites within Texas' offshore state lands that are suitable for the safe and permanent storage of 30 million metric tons of CO_2 from future large-scale commercial CCS operations (NETL, 2010c)." This deployment will serve as a measured starting point for a larger effort to tap into the vast geologic sequestration potential of the Gulf of Mexico, and prove the potential for offshore CCS projects elsewhere – a critical starting point for meaningful CCS in the United States.

3. REDUCED IMPACT TO HUMANS COMPARED TO OTHER CCS SITES ONSHORE

In general, and as identified by the U.S. DOE (above), storing CO_2 in offshore geologic formations makes it less likely the CO_2 will interact with humans, either through freshwater aquifers or direct atmospheric exposure. Although contamination of underground sources of drinking water (USDWs) is a significant concern when storing CO_2 in onshore sites, and is of particular focus within federal regulations for Underground

---

61 Cambridge University Press, *Contribution of Working Group II to the Fourth Assessment Report of the Intergovernmental Panel on Climate Change* (2007).

62 Pacala, Socolow, *Stabilization Wedges: Solving the Climate Problem for the Next 50 Years with Current Technologies*, Science, Vol. 305 (2004).

Injection Control (UIC) for Aquifer Protection, freshwater aquifers are much less prevalent under the ocean, and not observed in the area of review for this project.63

CO_2 stored in offshore formations is also 1) less impactful on the global atmosphere than releasing it directly from CO_2 sources, and 2) has far fewer chances of affecting humans (compared to onshore CCS) in the event of a storage leak to the atmosphere from the sequestration site.64 If CO_2 were to leak from an off-shore formation, CO_2 would either dissolve in the overlying water column or rise to the surface of the water and equilibrate with the atmosphere, away from human life. On land, a remote possibility exists that CO_2 could gather in low-lying topographic features and create a concentration that could present a dangerous condition for humans, animals, or plants. However, this scenario is highly unlikely because a leak would likely expel at slow rate and CO_2 dissipates quickly in the atmosphere,

Overall, reduced public health risks make offshore CCS advantageous both in terms of public safety and public acceptance. Whereas communities in Europe have vociferously opposed CCS operations being built near their homes, schools, and commercial districts,65 several surveys of community respondents have indicated less anxiety when the sequestration site is offshore.66 While some public concerns may remain, moving storage away from human communities should significantly narrow these objections.

4. Ability to Accurately Assess Existing Leakage Pathways

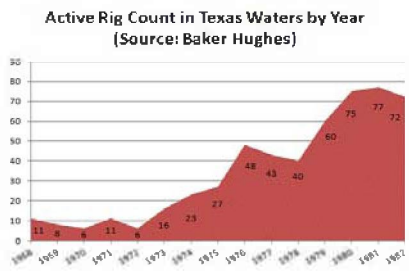

Figure 12: Rotary drilling rig count in Texas Waters by year (Source: Baker Hughes)

In general, the process of offshore oil drilling has not been occurring in Texas as long as onshore. The first offshore well was drilled in Texas in 1938, though oil was not discovered offshore until 1941.67 Offshore oil exploration and

63 On-shore groundwater contamination stemming from saltwater intrusion caused by a zone of elevated pressure at lateral extent of the injected CO_2 may occur in theory, though it has not been proven in practice.

64 Damen et al., *Health, Safety and Environmental Risks of Underground CO_2 Storage – Overview of Mechanisms and Current Knowledge,* 74 Climatic Change 289,298 (2006).

65 Van Noorden, *Buried Trouble: Protesters saying 'no to CO_2' are just one roadblock facing carbon sequestration*. 463 Nature 871 (2010).

66 IPCC, *Special Report on Carbon dioxide Capture and Storage*, at 257-258 (2005).

67 Owen, *Trek of the Oil Finders*, American Association of Petroleum Geologists, Memoir 6, p.800 (1975).

extraction in state waters ramped up significantly in the early to mid 1970's, increasing from six active rotary (drilling) rigs in 1970 to seventy seven active rotary rigs in 1981.68 (Figure 12)

In contrast, the first commercial onshore oil exploration and extraction began in Texas in 1866, at Melrose in Nacogdoches County.69 The proliferation of onshore production in Texas has significantly expanded since that time, with major discoveries and expansions occurring in 1900, 1930 and throughout the rest of the 20th century, including through modern day. Today, Texas has approximately 218,000 active oil and / or gas wells in operation.

As evidenced by data on offshore operations, the proliferation of offshore drilling in Texas waters is considered to be relatively young, with the major expansion occurring in the 1970's, well after the advent of modern record keeping requirements. Accordingly, well drilling operations and platform logs for offshore operations are expected to be of a much higher quality than onshore operations which may have been ongoing for 100 years or longer, surviving numerous transfers of ownership and quality of record keeping. As such, it is expected that any abandoned, plugged, orphaned or operational wells would be able to be easily found during a site survey or characterization for the purposes of CCS site selection.

Current and historical production wells can serve as migratory paths for the escape of injected CO_2 from a target reservoir, meaning the overall better awareness (and reduced number) of active or historic wells in the target confining zone, the lower the possibility that man-made leakage pathways exist. As such, it can be generally surmised that offshore operations are less likely to leak CO_2 in the offshore environment than their onshore counterparts.70

---

68 Rig count derived from historical data at BakerHughes, http://investor.shareholder.com/bhi/rig_counts/rigCountArchive.cfm?CategoryID=&SortOrder=FileDate%20Descending&Year=&PageNum=2

69 Texas State Comptroller of Public Accounts, http://www.window.state.tx.us/specialrpt/energy/nonrenewable/crude.php

70 Offshore geologic formations are generally intact, with far fewer wells than the onshore environment. See, e.g., Wilson et al., *Regulating the Ultimate Sink: Managing the Risks of Geologic CO_2 Storage*, Environmental Science & Technology, Vol. 38, No. 16 at 3479 (2003).

In addition to fewer man-made migratory pathways (active or historic wells) giving rise to less opportunities for leakage from the target confining zone, fewer pathways can also equate to a reduced need to monitor for leakage at suspect locations. In the onshore environment, active and abandoned wells are generally thought to be the location with the highest opportunity for leakage from the storage zone, and therefore demand significant monitoring and oversight. However, since offshore sites have a much more limited number of active or abandoned wells through the confining layer, less overall point specific monitoring may be needed, resulting in less costly project oversight.71

5. WIDE ARRAY OF LEAKAGE DETECTION STRATEGIES AND ANALYTICS AVAILABLE

Further, although the science of offshore leak detection is developing to this day, there is a suite of accepted analytical and technological techniques to ensure CO_2 sequestration effectiveness. These techniques are discussed in detail in Section VII below, and may include:

1. 3D and 4D seismic monitoring and plume migration mapping;
2. Sea floor surface mapping;
3. Injection condition monitoring;
4. Groundwater (aquifer) testing beyond the extent of the plume;
5. Seawater testing for pH, pCO_2 content, total CO_2 concentration, alkalinity, density and other characteristics;
6. Sediment testing for pH, pCO_2 content, alkalinity, density and other characteristics;
7. Biological testing and monitoring; and
8. Specialized Gas Leakage Systems for widely distributed low level leakage and for point source high level leakage through sonar observations, bubble observations, video capturing, gas sampling and gas flux quantification.

71 See, e.g., Solomon, Semere, *Carbon Dioxide Storage: Geological Security and Environmental Issues – Case Study on the Sleipner Gas field in Norway*, Bellona Foundation (2007).

V. Environmental and Public Health Risks From Offshore CCS

In general, risks from the development and operations of CCS project site can be summarized in three potential risk pathway categories as:

1. Risks associated with transport of CO_2 streams;
2. Risks associated with injection operations; and
3. Risks associated with sequestration of CO_2.

For each category of risk, this section evaluates sources of the risk, and then potential causes and impacts. If leakage or other disruption of the natural environment were to occur from a storage site, it could result in one or more of the following impacts:

1. Harm to human life;
2. Disruption to marine flora and fauna, both in the immediate coastal area and the greater Gulf of Mexico;
3. Harm to aquifers suitable for residential and / or agricultural purposes; or
4. Increased CO_2 emissions to the atmosphere.

Broadly speaking, the technological risks associated with offshore CCS are well-understood and moderate,[72] and find natural analogues to onshore EOR CO_2 operations.

In Texas, the oil and gas industry at large has decades of experience with oil extraction, CO_2 capture and pipeline infrastructure for use in enhanced oil recovery, and more recent experience globally with onshore and offshore CCS. The first CO_2-flood project in the world began in West Texas in the 1970s, in the Kelly-Snyder field in Scurry County. An estimated inventory of CO2 purchase and injected over the project lifecycle is 55 million tons. A significant amount of CO_2 has been extracted with produced oil, separated and reinjected, however this inventory is approximate because record-keeping was not designed for greenhouse gas accounting. No systematic assessment of permanence of storage has been conducted over the life of the project. However, a study of groundwater over the SACROC field conducted from 2006 to 2009[73] found no evidence of CO2 leakage into the Dockum aquifer, suggesting that permanence has been good (at the sensitivity of this monitoring method).

---

72 See, e.g., Heinrich et. al., *Environmental Assessment of Geologic Storage of CO_2,* Laboratory for Energy and the Environment, Massachusetts Institute of Technology at 1 (2003); Wilson et. al., *Regulating the Ultimate Sink* at 3476.

[73] Romanak, K. D., Smyth, R. C., Yang, C., Hovorka, S. D., Rearick, M., and Lu, J., 2012, Sensitivity of groundwater systems to CO2: application of a site-specific analysis of carbonate monitoring parameters at the SACROC CO2-enhanced oil field: International Journal of Greenhouse Gas Control, v. 5, no. 1, p. 142–152

Performing CO_2 sequestration in the near-offshore environment presents a close analog to the established practice of onshore CCS, including transportation and pipeline protocols, siting requirements, well construction and injection techniques, and monitoring regimes. In that sense, near-offshore CCS should be seen as presenting no major new technological challenges or need for "experimental" techniques.

1. RISK PATHWAYS - GENERALLY

1. RISKS FROM TRANSPORT OF CO_2

1. PIPELINE LEAKS AND BREAKS

Although ship-bound transportation is potentially an option for CO_2 transmission from point sources to offshore storage sites, CO_2 pipelines are likely to be the more economically feasible technology. There are analogs for these pipelines, both in the practice of enhanced oil recovery and wastewater disposal, which offer some baselines for understanding its safety and environmental risk profile. Overall, CO_2 pipelines are a low-risk transportation technology with a relatively strong safety record.

Roughly 4,000 miles of CO_2 pipelines were in use in the U.S. as of 2010.74 The U.S. Department of Transportation Pipeline and Hazardous Material Safety Administration (PHMSA) collects statistics on pipeline-related incidents. From 1986-2008 there were 12 incidents of CO_2 pipeline ruptures in 3,500 miles of pipeline, and no human injuries or fatalities reported.75 It is important to note that 3,500 miles of pipeline is a relatively small sample size, especially compared to 500,000 miles of natural gas (a potentially explosive material) and hazardous liquid pipelines.76 Consequently, one study ranked CO_2 pipelines as safer than natural gas or hazardous liquid pipelines.77

Marine pipelines have similarly low incident rates. Although dragging ship anchors do cause some failures, such events only occur in shallow water (less than 50 m) and at low frequency. Very rarely do ships sink on to pipelines, or do objects fall on to them. Pipelines

74 Bliss et. al. *A Policy, Legal, and Regulatory Evaluation of the Feasibility of a National Pipeline Infrastructure for the Transport and Storage of Carbon Dioxide*, IOGCC at 14 (2010).

75 *Id.* at 23.

76 Folger & Parformak, *Carbon Dioxide (CO_2) Pipelines for Carbon Sequestration: Emerging Policy Issues* Congressional Research Service at 5 (2007).

77 Davison & Gale, *Transmission of CO_2—safety and economic considerations.* Energy Vol. 20., 1319, 1322 (2004).

of 400 mm diameter and larger have been found to be safe from damage caused by fishing gear, but smaller pipelines are generally trenched to protect them.78

2. CORROSION INDUCED LEAKS AND BREAKS

A commonly-discussed source of CO_2 release is a gradual leak due to corrosion of a pipeline or well. The risks of corrosion can be greater or smaller depending on the storage method used, and the environment within which the pipeline is located.

Storing CO_2 in deep saline aquifers is one of the options available to the Texas offshore environment. In contrast to oil fields, saline aquifers are even more ubiquitous in offshore state lands, though they generally are thought to have no other current commercial value than for storage purposes, though protection as an existing of future gas resources might be a consideration. Since CO_2 can dissolve into the brine and eventually form carbonic minerals, brine formations are commonly accepted as the most secure form of CO_2 trapping. Additionally, since the dissolution of CO_2 into the brine increases its density by about 1%, the CO_2-saturated brine tends to sink to the bottom of the injection formation, rather than buoying upwards.79 Accordingly, brine injection is thought of as a high quality candidate for CO_2 injection.

However, mixing CO_2 with brine water can potentially create two types of corrosion that may interfere with storage integrity and capacity. CO_2 in contact with water forms carbonic acid (H_2CO_3), a weak acid that can interact with surrounding minerals in various ways. First, the acidification of the pore water reduces the amount of CO_2 that can be dissolved into the formation as a whole. Further, the CO_2-rich water may react with minerals in the reservoir rock or cap rock matrix or with the primary pore fluid. Importantly, the resultant weak acid may also react with borehole cements and steels. Such reactions may cause either mineral dissolution or potential breakdown of the rock (or cement) matrix or mineral precipitation and plugging of the pore system (and thus, reduction in permeability).80 Accordingly, deep saline aquifer wells and equipment are generally designed to be protected against corrosive forces. UIC well integrity and construction protocol address these issues in detail, which will be explored further in Section VI.

There is a greater risk of corrosion if a captured CO_2 stream is not pure. An unpurified CO_2 waste stream from a power generating plant may contain sulfur dioxide (SO_2), nitrogen

---

78 *IPCC Special Report on Carbon dioxide Capture and Storage* at 188.

79 J.T. Litynski et al., (2011).

80 Solomon, S., *Carbon Dioxide Storage: Geological Security and Environmental Issues – Case Study on the Sleipner Gas field in Norway*. Bellona Foundation (2007); Id et al., *CO_2 Leakage Through Existing Wells: Current Technology and Regulations, in Proceedings of the Eight International Conference on Greenhouse Gas Control Technologies* (2006).

oxide (NOx), as well as trace heavy metals including lead, mercury and cadmium.81 However the purity of the CO2 stream sent to storage depends on the capture process, and the link between flue gas and captured stream is complex. So, the environmental risk is dependent on injection-stream composition. When combined with water in a saline aquifer, SO_2 forms highly corrosive sulfuric acid, which can corrode surrounding materials, including carbonates, potentially augmenting pre-existing leakage pathways. 82 However, this is not relevant to Miocene formations offshore, which are siliciclastics. Allowing injection of mixed streams underground requires less scrubbing at the plant level and reduces capture costs. However, permitting the disposal of non-CO_2 components alters the risk profile of geological storage as well as the regulatory and legal responses. Matching of capture stream to pipeline and well construction and subsurface rock-water interactions should be assessed to determine the correct risk for the system.

3. RISKS FROM INJECTION OF CO_2

1. OVER-INJECTION, FRACTURING AND INDUCED SEISMICITY

As with onshore CCS or EOR CO_2, use of excessive injection pressure, combined with improper site selection or incorrect modeling, could theoretically cause instability or leakage at an offshore storage site through fracturing or induced seismicity.

Instances of induced seismicity have been recorded in the context of waste disposal wells and injection into oil fields. In the 1960s, for example, the U.S. Army Corps of Engineers found that a series of earthquakes near Denver was caused by injection well disposal at the Rocky Mountain Arsenal; one tremor measured 5.5 on the Richter scale.83 Similar seismic activity has been recorded in both Texas and Arkansas. In general, deep well injection only triggers activity in a seismically unstable area, or when it occurs directly into faulted rock,

81 U.S. Environmental Protection Agency Website, http://www.epa.gov/cleanenergy/energy-and-you/affect/air-emissions.html (2007).

82 IEA Energy Technology Essentials - CO_2 Capture & Storage, http://www.iea.org/techno/essentials1.pdf (2006).

83 Osborne, P., *Technical Program Overview: Underground Injection Control Regulations*, U.S. EPA (2001).

rather than causing an earthquake in a seismically stable area.84 Given the stable seismology of offshore state lands in Texas, induced seismicity would be highly unlikely.85

Fractures caused by over-injection of the seabed, such as occurred at the Tordis gas field, would similarly be unlikely, as long as operators followed commonly adopted business practices and performed the extensive site characterization required under EPA's Underground Injection Control (UIC) program.86 The details of this program and its applicability to offshore CCS are discussed in Section VI below. However, it is sufficient to note here that the UIC requirements can (and in most circumstances do) apply to offshore CCS, and will require an operator to perform extensive borehole sampling, mapping, and seismic surveys in order to ensure the selected site comprises a "Confining zone(s) free of transmissive faults or fractures and of sufficient areal extent and integrity to contain the injected carbon dioxide stream and displaced formation fluids and allow injection at proposed maximum pressures and volumes without initiating or propagating fractures in the confining zone(s)."87

With proper attention to and enforcement of these and other siting and monitoring protocols already in use for other subsurface injection activities, the risk of fracture or induced seismicity at a Texas coastal offshore storage site is expected to be low.

4. RISKS FROM SEQUESTRATION OF CO_2

1. LEAKAGE FROM THE CONFINING ZONE TO THE SEAFLOOR SURFACE OR WATER COLUMN

A significant amount of discussion in this document is dedicated to the description of the potential impacts of CO_2 migration away from the target confining zone for CO_2 sequestration. If injected CO_2 does not remain in the target confining geologic structure, it is likely that some injected CO_2 would move laterally and vertically away from the point of injection, opening the door for some of the impacts described below to occur. Moreover, through anticipated plume migration, the zone of influence of a particular project may also elicit undesired impacts if improper attention to time variant plume migration occurs. However, the risk of such impacts occurring can be almost entirely removed by proper site

84 Wesson & Nicholson, *Earthquake Hazard Associated with Deep Well Injection.* U.S. Geological Survey. Open-File Report 87-331 (1987).

85 U.S. Department of Energy, Sminchak, et al., *Issues Related to Seismic Activity Induced by the Injection of CO_2 in Deep Saline Aquifers.* http://www.netl.doe.gov/publications/proceedings/01/carbon_seq/p37.pdf

86 *See* Greenpeace, *Reality Check on Carbon Storage* at 5 (2009).

87 U.S. CFR § 146.83(a)(2)

selection, attention to established UIC rules, CO_2 monitoring and modeling, accounting and verification.
Put simply, due to the physical properties of high pressure CO_2, if it is injected into the subsurface without proper safeguards, leakage from the confining zone to the surface or to lateral geologic structures is possible. In the offshore environment, this would include dissolution into the water column and eventual equilibrium with the atmosphere. As discussed above, leakage of CO_2 into sediments and the water column may result in adverse effects on Gulf benthic organisms, especially those residing in an already low oxygen/high CO_2 environment.

2. GROUNDWATER INTERACTION

A primary concern with onshore geologic storage is the potential of groundwater contamination. In the event of a leak, stored CO_2 or dissolved solids could migrate from a sub-aquifer disposal well, move upward or laterally through leakage pathways and contaminate an underground source of drinking water (USDWs).

Groundwater contamination is less of a concern, though not impossible, with sub-seabed CCS. Although there are no significant aquifer resources in the offshore environment, the Texas coastal environment does include significant freshwater resources in the onshore area near the Gulf coast.88 Accordingly, groundwater contamination may occur by two main pathways: saltwater intrusion, or injected / displaced fluid interaction.

Saltwater intrusion - Once an aquifer's freshwater is depleted through utilization of the water (not related to the CCS site operations), an up-dip migration of the fresh-salt water interface, or saltwater intrusion, may occur.89 (Figure 13) This has occurred to some extent along the coastal region, and could be exacerbated by further overdrawing of the Gulf Coast aquifer. In this circumstance, salt water begins contaminating the freshwater aquifer. Given the severe drought conditions throughout the state in recent years, this may represent a real concern as aquifers are depleted further.90 Additionally, salt-water intrusion may be accelerated if the project injection forms a zone of high pressure behind the salt-water interface, providing an extra push for an up-dip occurrence and further contamination of the freshwater aquifer resource.

---

88 Texas Water Development Board, *Report 345: Aquifers of Texas,* at 8 (1995).

89 *Id.* at 14.

90 Betsy Blaney, *Drought-stricken Texas declared natural disaster area,* Associated Press (Jun. 29, 2011), http://www.star-telegram.com/2011/06/28/3186526/drought-stricken-texas-declared.html.

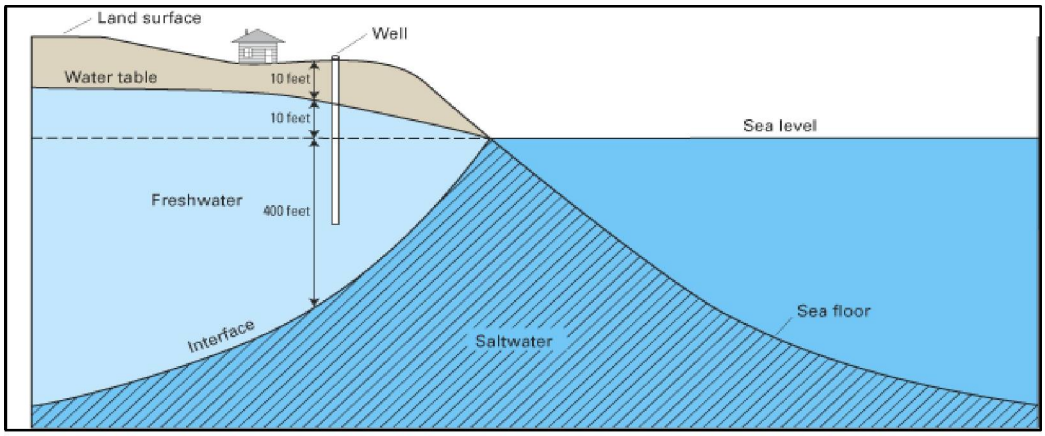

Figure 13: Simplified Diagram, Coastal Zone Freshwater-Saltwater Interface.

Injected fluid or displaced fluid interaction - As CO_2 is injected in the offshore environment, both injected material and displaced fluids (material that used to occupy the area where the injected material is now located) can migrate away from the confining zone. Such a migration could be accelerated by natural underground fluid flows existing prior to the injection, or if CO_2 is dispersed as finger-like migration rather than as a general zone of elevated CO_2.91 The size and extent of the plume, including fingering of flow and plume heterogeneity, depend on a number of factors associated with the target injection formation characteristics and injection operations.92,93

A third pathway, albeit much less likely to occur on a widespread scale, includes leaked CO_2 dissolving rock and material from abandoned petroleum wells, causing toxic compounds such as benzene, phenols, and polyaromatic hydrocarbons to leach and migrate into fresh water sources.94 Such a series of events would require both interaction with petroleum producing sites and interaction with freshwater resources, presumably in that order and prior to discovery of the migration so as to avoid any mitigation – and is therefore rather remote.

---

91 Solomon, S., at 27-28, 30-31. (2007).

92 Gasda et al. *Significance Of Dipping Angle On CO_2 Plume Migration In Deep Saline Aquifers,* http://conferences.dtu.dk/fedora/objects/CMWR-XVI:16063/datastreams/PDF/content?contribId=63&sessionId=3&resId=0&materialId=paper&confId=a051

93 Siln et al., *A Modeling of Buoyant Gas Plume Migration,*

http://www.osti.gov/bridge/servlets/purl/948573-wuGEvp/948573.pdf

94 Kharaka et al., *Changes in the chemistry of shallow groundwater related to the 2008 injection of CO_2 at the ZERT field site, Bozeman, Montana*, Environmental Earth Science at 274 (2010).

Careful management of coastal aquifers, and siting of injection wells at a sufficient distance to avoid groundwater interaction will help minimize, but would not likely eliminate, such risks.

3. CATASTROPHIC RELEASE OF CO_2

There are well-known examples of natural CO_2 venting systems, particularly volcanic formations that can sometimes produce sudden eruptions. When these releases occur in confined topographies in proximity to populated areas, they can be dangerous. Perhaps the best-known CO_2-related incident was the limnic eruption at Lake Nyos in Cameroon in 1986, which released enormous volumes of CO_2, resulting in the death of 1,746 people and thousands of animals.95 However, there are now serious questions as to whether or not CO_2 or CO (carbon monoxide) was the culprit. [96] Regardless, limnic eruption is an inappropriate analogy to sub-seabed geologic sequestration, particularly in the Texas offshore coastal environment.

The cause of the release at Lake Nyos was a combination of unusual (though not unique) factors, in particular the lack of natural turnover in the lake above a dormant volcano, which led to the gradual build-up of gas and catastrophic release.97 In contrast, ocean systems are not subject to the same process. Natural ocean currents provide constant circulation of CO_2, such that even if gas were to escape into the water column, it would be diffused before it could build up to significant pressures. The Texas coastal sites under consideration for CO_2 storage are subject to the kinds of natural flows and currents that would prevent any such catastrophic eruption from occurring, even if leakage were to occur. Accordingly, the Lake Nyos example is not applicable for the purpose of considering where to site a CCS project in offshore Texas state waters because it does not present a viable risk for the sequestration of CO_2 in the offshore environment. It's important however to quantify the process in order to provide assurance that the mixing is adequate to overcome stratification. Anoxic conditions that create the dead zone discussed later in this document indicate that stratification does exist in water mass under study.

5. POTENTIAL IMPACTS FROM OFFSHORE CCS IN TEXAS STATE WATERS SPECIFICALLY

1. POTENTIAL IMPACTS ON HUMANS

---

95 Benson, et al., *Lessons Learned from Natural and Industrial Analogues for Storage of Carbon Dioxide in Deep Geological Formations*, Earth Sciences Division, E.O. Lawrence Berkeley National Laboratory at 57, http://www.netl.doe.gov/technologies/carbon_seq/refshelf/reg-issues/Lessons%20Learned%20From%20Analogs%20-%20LANL.pdf.

96 Duncan, I., 2013, Suicide by Catalytic Converter and Deaths at Lake Nyos; Is Carbon Monoxide the Toxic Agent? Implications for Leakage Risks from CO2 Pipelines: Energy Procedia, v. 37, no. 0, p. 7696-7701.

97 Heinrich, et al. (2003).

Given that CO_2 storage will likely take place under the sea bed at a distance of several miles from inhabited areas, the primary vector for direct human impact is through an on-land pipeline leak. In low concentrations, CO_2 is not toxic to humans. However, CO_2 causes significant physiological effects at concentrations over 3% and will produce fatalities above 10%.98 Given that CO_2 generally disperses in air quickly and effectively at the point of release, this risk of CO_2 directly impacting humans is minimal. Examples of humans in close proximity to high volumes of naturally released CO_2, such as that released from Crystal Geyser, demonstrate the remote possibility of this occurring.

Groundwater interaction is another possible vector for human impact, though the likelihood of such an impact can be mitigated by attention to stringent regulations and precautions in the siting phase. As described above, CO_2 could potentially contaminate an aquifer if it migrates into the Gulf Coast aquifer, or displaces other materials into the aquifer. Texas' current groundwater monitoring regime involves annual monitoring and sampling roughly 2,000 wells across the state's 30 major and minor aquifers for contamination.99 If significant CO_2 storage operations take place in the offshore region, increased sampling frequency may be desirable for wells in the Gulf Coast aquifer—particularly when aquifer levels are low—in order to quickly detect any intrusion of contaminants. However, given the extensive nature of the existing testing regime for water quality and aquifer protection, it is unlikely that the current groundwater program will miss an impact if it were to occur.

As discussed above, the possibility of a massive CO_2 release from the seabed causing deleterious impacts to humans, similar to what happened when the CO_2-laden cold bottom water of Lake Nyos turned over, is extremely remote. If CO_2 were to be emitted from the subsurface and into the water column, local ocean currents and wave action would likely cause mixing of affected ocean water prior to any damage occurring – though passing emissions to the atmosphere would be likely.

2. Potential Impacts on Aquatic Life (General)

Data illustrating the impacts of offshore CCS on marine life are limited, due to the difficulty of obtaining permission for in-situ experiments,100 and the absence of any known CO_2 leakage from an existing offshore CCS installation.

---

98 Occupational Safety & Health Admin., *Carbon Dioxide*

http://www.osha.gov/dts/chemicalsampling/data/CH_225400.html. (2001). As a basis of comparison, the atmospheric concentration of CO_2 in the year 2000 was 0.0368% (368 parts per million).

99 Texas Water Development Board, *Groundwater Monitoring Section Activities*, http://www.twdb.state.tx.us/GwRD/HEMON/GMSA.asp

100 Proposed small-scale studies of ocean CO_2 sequestration (i.e. injecting CO_2 directly into the water) were derailed by public opposition in Hawaii and Norway in 2000-01. *IPCC Special Report on Carbon dioxide Capture and Storage* at 285 (2005).

However, a variety of studies have sought to simulate the localized impacts of leakage from a sub-seabed CO_2 storage well on various aquatic species.101 Other studies have assessed the regional impacts of ocean acidification from natural systems and anthropogenic CO_2. These studies provide both 1) examples of acute, localized impacts on stationary animals exposed to elevated CO_2 conditions and 2) an analog to the remote prospect of a massive, widespread leakage of CO_2 sufficient to change the regional pH of the Texas Gulf Coast region in a short time span.102 A review of these studies provides insight into the potential ecosystem impacts, both moderate and worst-case scenario, of leakage from offshore storage wells.

In general, elevated CO_2 levels and lowered pH can cause two primary impacts on marine fauna: 1) decreased calcification, and 2) disturbance of acid-base regulation, which affects metabolism, reproduction and other levels of activity.103 Decreased calcification is more of a dispersed, medium- to long-term threat to aquatic life and is already present in many aquatic zones worldwide due to ocean acidification—imposing a particular risk to the survival of tropical coral reefs and calcifying organisms such as mussels, shrimp, and plankton.104 The addition of CO2 into areas already affected by acidification would be expected to exacerbate these adverse impacts.

Disturbance of acid-base regulation, on the other hand, typically requires much higher concentrations of pCO_2, sufficient to produce hypercapnia. This level of exposure is only likely to result from contact with a plume of CO_2 vented from a storage well or natural seep.

3. Potential Impacts on Fauna

As detailed in Part II, the Texas coastal zone includes a variety of aquatic fauna, ranging from phytoplankton, to fish, crabs, cetaceans, and birds. The effect of contact with CO_2 leaked locally into the water column will vary significantly depending on the animal group, age, and level of exposure. (Figure 14)

---

101 *See, e.g.*, Fabry et al., *Impacts of ocean acidification on marine fauna and ecosystem processes.* ICES Journal of Marine Science, 65: 414–43 (2008); Seibel & Walsh, *Biological Impacts of deep-sea carbon dioxide injection inferred from indices of physiological performance.* 206 *Journal of Experimental Biology* 641-50 (2003).

102 *See, e.g.*, Denman et al., *Potential impacts of future ocean acidification on marine ecosystems and fisheries: current knowledge and recommendations for future research.*" 68 ICES Journal of Marine Science 1019-29 (2011); Seaubien et al., *Potential Hazards of CO_2 Leakage in Storage Systems – Learning From Natural Systems.* Greenhouse Gas Control Technologies, Volume I

103 Fabry et al. at 414 (2008).

104 *Id.*

Arthropods	Description	CO_2 System Parameter	Sensitivity	Reference
Acartia steueri	Copepod	0.2-1%CO_2,	Decrease in egg hatching success; increase in nauplius mortality rate	Kurihara et al. (2004)
Acartia erythraea	Copepod	~2000–10 000 ppmv		
Copepods	Pacific, deep vs. shallow	~860–22 000 ppmv CO_2	Increasing mortality with increasing CO_2 concentration and duration of exposure	Watanabe et al. (2006)
		pH < 7.6	Mortality increased with increasing exposure time and decreasing pH	Yamada and Ikeda (1999)
Euphausia pacifica	Krill			
Paraeuchaeta elongata	Mesopelagic copepod			Metzger et al. (2007)
			Reduced thermal tolerance, aerobic scope	
Conchoecia sp.	Ostracod	1% CO_2, ~10 000 ppmv		
Cancer pagurus 1	Crab			

Figure 14: Effect of hypercapnia on various arthropod species, including the edible crab Cancer pagurus. 105

Significant species for the Texas offshore ecosystem and economy include crab, shrimp, and several variety of finfish (e.g. Red snapper, Amberjack, Yellowfin tuna) and Menhaden, which is caught for use as protein in animal feeds and as a source of Omega-3 oils for human consumption.106 Below, we perform a detailed evaluation of the potential impacts on four types of aquatic fauna important to Texas (crab, shrimp, fish and stationary bivalves), and which also serve to represent a broad cross section of species types. The evaluation also discusses the impact of cumulative CO_2 loading in the offshore environment and the proliferation of dead zones. This examination is meant to illustrate the types of adverse impacts that may occur if leakage from CO_2 sequestration sites is allowed to occur and provides the basis by which the policy recommendations in Section VII are made.

1. Potential Impacts on Crab

Figure 15: *Necora puber*; Source: sealifebase.org

At least four studies have examined the tolerance of various crab species to elevated pCO_2.107

105 Fabry et al. at 423 (2008).

106 Mattei, *Fishing for Dollars*. Texas Parks & Wildlife Magazine (2008).

107 Truchot, JP., *Mechanisms of compensation of blood respiratory acid-base disturbances in the shore crab Carcinus maenas (L)*. 201 J Exp Zool 407-416 (1979); Cameron, JN. *Compensation of hypercapnic acidosis in the aquatic blue crab, Callinectes sapidus: the predominance of external sea water over carapace carbonate as the proton sink*. 114 J Exp Biol 197-206 (1985); Cameron & Iwama, *Compensation of progressive hypercapnia in channel catfish and blue crabs*. 57 J Exp Biol 673-80 (1987); Metzger et al., *Influence of elevated CO_2*

Perhaps most germane to the present analysis was a study examining the Velvet Swimming crab's (*Necora puber*)108 resistance to pH levels ranging from 6.05 to 7.96 over a period of 16 days, intended to simulate both short-term, localized CO_2 leakage, and medium- term, chronic exposure through ocean acidification.109

In particular, the Spicer study found that crabs were able to compensate for certain degrees of hypercapnia through an increase in bicarbonate, generally derived from both the environment and through dissolution of their shells. However, compensation was possible only within limited temporal and pH ranges, beyond which the crabs experienced uncompensated acidosis and in some cases mortality.

At the lowest pH level tested, 6.05, mortality occurred widely within the sample populations after 24 hours of exposure, and reached 100% within 4-5 days. Meanwhile, at pH 6.74, the animals took 10 days to show a significant change in haemolymph (the crab's blood-like circulatory fluid) pCO_2. This change was compensated for temporarily by a rise in haemolymph pH, before mortality began occurring around the 14-day mark. At pH level 7.31, compensation also occurred but with no effect on mortality. However, the time scale of the experiments was too short to note potential impacts, even at higher pH levels, of exoskeleton dissolution on predator-prey interaction.110

To put these results in perspective, the business-as-usual scenario for ocean acidification predicts global ocean pH will reach 7.5 by 2100,111 (down from a current open-water average of pH 7.9-8.3).112If *Necora puber* is representative of other Gulf crab species, such as the Blue crab (*Callinectes sapidus*) and Florida stone crab (*menippe mercenaria*), these results suggest fairly high resistance of crabs to foreseeable drops in pH due to general ocean acidification. However, since marine organisms can vary dramatically in physiological and ecological characteristics it is not necessarily safe to assume that all crabs will react in a similar fashion to changes in pH and CO_2 levels. Accordingly, additional

---

concentrations on thermal tolerance of the edible crab, Cancer pagurus. Journal of Thermal Biology 144-51 (2007); Spicer et al., *Influence of CO_2-related seawater acidification on extracellular acid-base balance in the velvet swimming crab Necora puber*, Marine Biology, 1117-25 (2007).

108 Large crab native to the coastal area of England, the North Sea and the Mediterranean.

109 Spicer et al., at 1117.

110 *Id.* at 1123.

111 *Id.*

112 *Intergovernmental Panel on Climate Change Fourth Assessment Report* at 405 (2007).

research may be needed to evaluate the full range of potential impact of crab species due to chronic low level CO_2 exposure resulting in pH modification.

As far as acute exposures in a confined water column, i.e. to pH levels in the pH 6-7 range, results show that *Necora puber* can experience significant die-off within 1-2 days. This suggests that a significant localized leak could very quickly have deleterious effects in the zone that receives leakage. However, the impact would lessen significantly as the CO_2 disperses from the storage site into the greater aquatic zone and the average pH change is diluted.

The second study of crab response to pCO_2 changes focused more on long-term impacts of ocean acidification, and the combined effect of CO_2 concentration and temperature variations on the distribution of crab populations.113 The study found that under hypercapnic conditions (10,000 ppm of CO_2), the test species, *Cancer pagarus*, was far less able to adjust its metabolic processes under elevated temperatures than in normal CO_2 conditions (normocapnia). This impaired metabolism meant the crab had less energy for feeding, reproduction and survival. In extrapolation, such results indicate that as ocean CO_2 levels increase, this species (and likely other crabs) will be able to inhabit an increasingly limited range, based on what combination of temperature and pCO_2 it can tolerate.

Currently, *Cancer pagarus* inhabits water in the North Sea in a thermal range between 4° and 15° C. Above that temperature, sample specimens in normocapnia were able to maintain metabolic systems up to 18-19°, whereas specimens in hypercapnic conditions (i.e. 1% CO_2, or 10,000 ppm) began experiencing metabolic impairment at 12-13°.114

These results suggest another long-term threat to crab from increased CO_2 concentration includes reduced tolerance to sea temperature changes. Higher ambient temperatures may interact with higher CO_2 concentrations (lower pH) to reduce the capacity of crabs to respond to additional impacts (such as increased CO_2 levels resulting from CCS leakage).

2. Potential Impacts on Shrimp

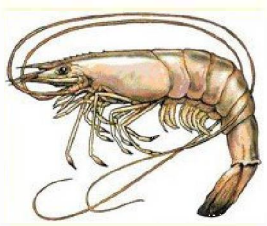

Figure 16: Brown Shrimp; Source: 21food.com

The Brown shrimp (*Farfantepenaeus aztecus*), White shrimp (*Litopenaeus setiferus*), and Pink shrimp (*Farfantepenaeus duorarum*) are the cornerstone of the Texas commercial shrimp fishery, with Texas commercial shrimp landings averaging 74% brown shrimp and pink shrimp,

113 R. Metzger et al. (2007).

114 *Id.* at 149.

25% white shrimp, and 1% "other" species.115 The 1% "other" species consist of seabobs (*Xiphopenaeus kroyeri*), Roughback shrimp (*Trachypenaeus sp.*), Royal Red shrimp (*Hymenopenaeus robustus*), and Rock shrimp (*Sicyonia brevirostris*).116

The most extensive study to date on shrimp and CO_2 exposure appears to be conducted through the Institute for East China Sea Research at Nagasaki University in Japan, where several studies have been conducted on the common Indo-West Pacific rocky-shore shrimp (*Palaemon pacificus)*, among other species.117 Two studies are worth noting; one focused on the impact of two levels of CO_2 exposure on *Palaemon pacificus*,118 while the other focused specifically on the impact of heightened CO_2 on the development stages of *Palaemon pacificus*.119

In the study with two levels of CO_2 exposure, the shrimps were reared in seawater equilibrated with air containing 1,000 ppmv (parts per million by volume, seawater pH 7.89 ± 0.05) of CO_2 for 15 weeks or 1,900 ppmv (pH 7.64 ± 0.09) CO_2 for 30 weeks.120 Experimental conditions were identical between the two experiments except for the CO_2 concentration. 121

---

115 Texas Parks and Wildlife. *Executive Summary: Texas Shrimp Fishery. A report to the Governor and the 77th Legislature of Texas*, at 30 (2002).

116 *Id.*

117 See, Nagasaki University's Academic Output SITE: NAOSITE is the Nagasaki University's Institutional Repository, Institute for East China Sea Research. http://naosite.lb.nagasaki-u.ac.jp/dspace/handle/10069/20066

118 Kurihara, et al. *Long-term effects of predicted future seawater CO_2 conditions on the survival and growth of the marine shrimp Palaemon pacificus.* Journal of Experimental Marine Biology and Ecology, 367(1), pp.41-46 (2008).

119 Kurihara, H. *Effects of CO_2-driven ocean acidification on the early developmental stages of invertebrates.* Marine Ecology Progress Series 373:275-84, http://www.int-res.com/articles/theme/m373p275.pdf. (2008).

120 Kurihara et al., Ishimatsu et al., *Coastal Marine Animals in High CO_2, Acidified Oceans: Impacts on Early Development, Growth and Reproduction*. Institute for East China Sea Research, Nagasaki University.

121 Ishimatsu, et al.
http://intellagence.eu.com/psi2009/output_directory/cd1/Data/articles/000283.pdf

The results of this study suggest that shrimp could be lethally affected by exposure to seawater equilibrated with the CO_2 concentrations of 1,000 ppmv and 1,900 ppmv, because survival was significantly suppressed in both experimental groups compared to the respective controls. 122 The 1,000 ppmv shrimp group started to die after 18 weeks and had a final survival rate of 55% (9 of 20 individuals died) as compared to 90% (2 of 20 individuals died, 1 died due to handling error) in the control group. The 1,900 ppmv shrimp group started to die in 7 weeks with an exception of one specimen, which had died in 13 days. The final survival rates were 65% (7 of 20 individuals died) for the 1,900 ppmv group and 95% (1 of 20 individuals died) in the control group.

The growth rates of each group were also measured. The growth rate was unaffected in the 1,000 ppmv experiment group, but was significantly reduced in the 1,900 ppmv experiment group compared to the control. Due to the difference in initial size between the 1,000 ppmv (10 mm) and 1,900 ppmv (20 mm) shrimp groups, the authors of the study caution against comparing them.123 Instead, they direct attention to the important role long-term exposure CO_2 appears to play in the survival rates of *Palaemon pacificus*.

A separate study by the same group of authors focused on the impacts of CO_2 on the development stages of *Palaemon pacificus*. The study found no significant effects on planktonic larval stages where hatched embryos were cultured until settlement stage under 2000 µatm pCO_2 seawater (pH 7.6).124 However, the CO_2-treated metamorphosing and settling juveniles were significantly smaller than in the control suggesting that settlement state was the most severely affected by pCO_2. 125

If the Indo-West Pacific rocky-shore shrimp (*Palaemon pacificus)* is a proper indicator for how the brown shrimp, white shrimp, and pink shrimp will be impacted by a potential CO_2 leak from a CCS site in the Gulf of Mexico, it appears that the shrimp population may be able to withstand a short duration of increased CO_2 exposure. Clearly, the longer the duration of exposure and the concentration, the greater the potential harm to the population.

---

122 *Id.*

123 *Id.*

124 Kurihara, H. (2008).

125 *Id.* at 279, 281.

3. Potential Impacts on Fish, Squid and Marine air breathers

Fish and squid are, in general, less likely to be negatively impacted to elevated levels of CO_2 in the water column due to their mobility, though such mobility is likely markedly less in early life stages. However, fish and squid physiology is an important factor in overall impact.

Adult fish appear better adapted to fluctuations in CO_2 levels than squid, likely due to their low metabolic rate, presence of red blood cells to carry oxygen, existence of a venous oxygen reserve, tight epithelia, and efficient acid-base regulations. Tests on shallow-water fish have shown short-term tolerance among adult fish of pCO_2 of 50,000-70,000 ppm. Juveniles are more sensitive to acute CO_2 stress, and are subject to mortality at 13,000-28,000 ppm.126 In Texas, many fish such as Red drum (*Sciaenops ocellatus)* are spawned in or near gulf-bay passes, and are hatched close to shore. Over time, as fish mature through the larval and juvenile stages, they are generally found in bays and estuaries during early life, extending out into the gulf only at mild distances. For Red drum, studies indicate a maximum distance of 12 mile from the shore for juvenile fish, extending upwards of 70 miles from shore for adults.127 Accordingly, like Red drum, while some fish may be very mobile in certain life stages (as adults), many species are tied to certain habitat types for completion of other life stages (i.e. larval and juvenile) making them more vulnerable to local impacts. Such impacts may be exacerbated if the species is in a vulnerable life stage (i.e. larval or juvenile) while experiencing elevated CO_2 conditions.

Similar to fish species, squid are also present in the Gulf Coast waters, though squid tend to be more highly sensitive to fluctuations in pH because they do not have red blood cells, which play an important role in regulating blood pH. Acute CO_2 exposure in squid causes acidification of the blood, which blocks oxygen uptake and binding at the gills, and reduces the amount of oxygen carried in the blood. This limits body function and at high concentrations could cause death.128

Diving marine air breathers such as turtles, dolphins and whales would also not likely be affected directly by acidification caused by a leak from a CCS operation, because they possess higher pCO_2 values in their body fluids than water breathers and gas exchange is minimized during diving. Such animals could still be affected by impacts of acidification on the ocean food chain.129

---

126 *Id.*

127 Davis, *Red Drum, Biology and History*, Southern Regional Aquaculture Center, available at https://srac.tamu.edu/index.cfm/event/getFactSheet/whichfactsheet/59/ (1990).

128 *IPCC Special Report on Carbon dioxide Capture and Storage* at 303 (2005).

129 *Id.* at 304.

4. Potential Impacts on Stationary Mollusks

The dangers of localized or regional acidification are different, but even more acute for organisms that are 1) stationary and 2) depend on calcification for the formation of their exoskeletons, such as pteropods130, oysters, mussels, and coral.131 The calcification process that forms shells and exoskeletons is impaired as ocean pH decreases, and at certain levels is impaired altogether.

Either sudden or gradual leakage of CO_2 could have significant impacts on these organisms, and potentially broader ecosystem implications. One study, for example, found that a CO_2 induced reduction of water pH to 7.3 (seawater is typically between 7.5 and 8.4) caused a 55% reduction in growth of Mediterranean mussels.132

Figure 17: Commercial oyster; Source: Oyster.us

In Texas, the prevalence oysters and mussels in bays and estuaries is well documented, as is the widespread importance of these resources on the local economy. Although CO_2 impacts on Texas specific mollusks has not been studied, analogous studies demonstrate a significant impact may occur if CO_2 leaks into the geographies where these species are present in high numbers – in particular in bays and estuaries – landward of the Texas barrier islands.

5. Potential Impacts through Exacerbation and Proliferation of Cumulative Impacts and Dead Zones

The ocean environment, including the near shore environment, in the Gulf of Mexico is threatened by a combination of conditions related to

---

130 These small sea snails are particularly critical for many ocean ecosystems, because they represent an important source of food for fish, seals and whales. The calcification process involved in building their shells is highly vulnerable to increases in ocean acidity. National Research Council of the National Academies. *Ocean Acidification: Starting With the Science*. National Academies (2011).

131 Seibel & Walsh. *Potential Impacts of CO_2 Injection on Deep-Sea Biota*. 294 Science at 391 (2001).

132 Michaelidis et al., *Effects of long-term moderate hypercapnia on acid-base balance and growth rate in marine mussels (Mytilus galloprovincialis)* Marine Ecology Progress Series, 293: 109-18.

increasing carbon dioxide and decreasing oxygen concentrations caused by urban and agricultural run-off and pollution.133 (Figure 18)
These "dead zones" represent an area with very low or nearly zero concentration of dissolved oxygen and are typically found at or near the ocean floor. The dead (or anoxic) zone is created through a waste cycling process where phytoplankton produce organic material (waste) at the ocean surface which then sinks to the bottom (benthic zone) where it is broken down by bacteria. Bacteria use oxygen and give off carbon dioxide during this process, causing the anoxic condition. 134

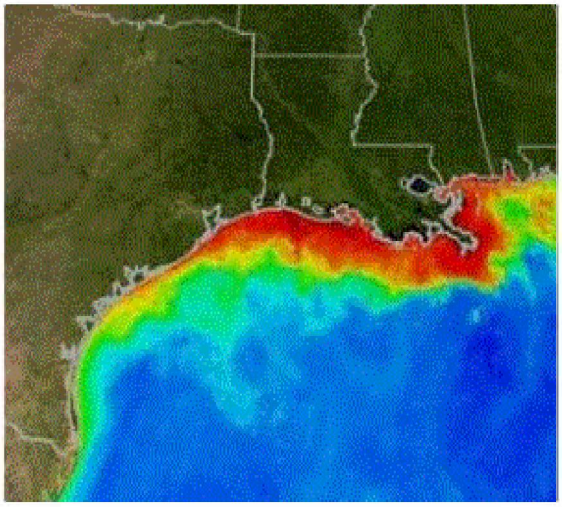

Figure 18: Gulf of Mexico Dead Zone Source: NASA/Goddard Space Flight Center Scientific Visualization Studio

As identified in the discussion in the sections above, increased CO_2 can be harmful to aquatic life. In the event that anoxic conditions are formed through urban or agricultural pollution and a dead zone is formed in whole or part within Texas state waters, the adding-on of CO_2 from leaking CCS operations could be especially problematic, resulting in a larger impact than if the leakage were to occur in a pristine ecosystem. Accordingly, the cumulative impact of CCS leakage and the proliferation of anoxic conditions through dead zone formation should be considered another potential mechanism of damage to flora or fauna stemming from CCS operations. Anoxic conditions mean that mixing is not effective at the times of formation of the dead zone. At that time at least the bottom waters might accumulate concentrations of CO2 higher than would be present in a mixed water body. It also might indicate that the ecosystem is equilibrated to intermittent high CO2 emissions and biologic risk from leakage is therefore reduced compared with more mixed ecosystems. More study is warranted; although such a study is beyond the scope of the current project.

A. General Recommendations for Project Site Selection

The research and analysis outlined in Sections II-VI has examined the potential risks inherent in offshore CCS in the Texas coastal region, and the existing laws that regulate those potential risks. Based on this review, we conclude, as others have concluded about

---

133 ScienceDaily, *Ocean Dead Zones Likely To Expand: Increasing Carbon Dioxide And Decreasing Oxygen Make It Harder For Deep-Sea Animals To Breath* (2009). http://www.sciencedaily.com/releases/2009/04/090417161506.htm

134 NASA. *Science Focus: Dead Zones*. http://disc.sci.gsfc.nasa.gov/oceancolor/additional/science-focus/ocean-color/dead_zones.shtml (2010).

geologic storage generally, that an offshore CCS project in Texas can be done safely and responsibly if existing laws, best operational and management practices, and newly adopted UIC class VI regulations are applied and complied in a precautionary manner. However, we also emphasize the large risks posed by failure of governmental oversight, as has been documented at other large infrastructure projects, must also be closely watched and managed.

Currently, there are only a few CCS projects thus far in the offshore environment, and only a handful of operational commercial scale CCS projects in the onshore environment (not including enhanced oil recovery without CCS). Accordingly, offshore development of CCS and the associated mechanisms for leak detection must still be considered an emerging area of technological development - regardless of the ability to analogize experience in the onshore environment. Therefore, to manage risk and protect the environmental health of the Texas offshore environment, at the heart of this set of recommendations for siting

> **Recommendation 1:** Any project for offshore CCS should be sited, designed and operated to avoid direct and significant impacts on human health or coastal natural resources (as defined by the Texas Natural Resources Code). To ensure adverse and / or unexpected environmental impacts are avoided, any offshore CCS project in Texas state waters must utilize the full range of precautions and safeguards available in all phases of the project timeline – including, but not limited to, site characterization, site selection, development, operation, monitoring, and closure. CCS site selection must evaluate whether the full range of precautions and safeguards are available at the target site.

policy is:

Although offshore CCS is a relatively new area of development, as discussed above, the strong experience and applicability of existing injection and storage techniques used in the onshore environment, coupled with a long history of characterizing risks and vulnerabilities of the aquatic environment, can be generally thought of as meaning that offshore CCS presents few unknown risks generally. However, knowing whether a risk exists is not the same as saying no risk exists. On the contrary, empirical evidence shows, and discussed above, that CCS development in the Texas water does carry risks, albeit manageable. Such risks include both acute and chronic risks to flora and fauna stemming from CO_2 release, migration or other related activity; as well as cumulative risks related to the reduced resilience of the Gulf from existing human activities (i.e. large scale

hydrological and sediment modifications, existing networks of underwater pipelines and drilling platforms, inputs of nutrients, large-scale anoxic events, etc,).

To fully mitigate the full slate of known risks, a coherent technical framework for project site selection specifically tailored to take into account the range of conditions in the offshore environment is necessary. Additionally, since an offshore CCS project in Texas state waters will likely be the first of its kind in the United States, and possibly the world (taking into account site differences between the Texas environment and that of the currently operating projects), strict adherence to best management practices and use of conservative (precautionary) assumptions throughout the project site selection, development and operations phase is critically important. Such practices must also be paired with exceptionally robust institutions of high integrity capable of handling an innovative project like this.

Recommendation 2: The siting of an initial project or projects to develop CCS in the offshore environment of the Texas coastal region must take a precautionary approach to prevent impacts on environmental attributes of concern. A precautionary approach should be used for offshore CCS deployment until such time as commercial scale deployment of CCS is achieved or a regulatory framework specific to managing offshore projects is adopted into law.

In the context of offshore CCS project development for the BEG project, use of the precautionary principle should be thought of as an obligation to avoid causing harm in the project site selection phase as a foundational canon. In practice, use of the principle would mean avoiding or mitigating conditions that are potentially harmful to the offshore environment (i.e. avoid choosing sites that have not been fully evaluated, or mitigating any leak as opposed to only leaks of a certain size, etc.) even if there is not absolute scientific proof that the particular action would actually cause harm. The principle is at its strongest if the potential harm is irreversible. Historically, the precautionary principle has been used to require manufacturers to supply enough information to conclude that new and existing chemicals are safe and don't endanger public health or the environment.

What follows are suggestions and recommendations for key policies and practices that should be considered throughout the entire project timeline for an offshore CCS project in Texas state waters. Many of these recommendations are built upon an application of the precautionary principle in practice. Although the express purpose of this overall research

agenda is to assist the process of site selection ongoing at BEG, this research may also be helpful as an exploratory document resulting in specific recommendations for further discussion in other parts of the project development process. Accordingly, this set of recommendations will, at times, extend beyond the scope of being purely associated with site selection and speak to the offshore CCS endeavor in general. The intent of this document in that regard, and the analysis involved, is for consideration in the context of further discussions related to developing offshore resources for CCS.

These recommendations are meant to complement compliance with existing regulations, in order to mitigate or reduce the potential for public health or environmental impacts from offshore CCS. The recommendations are organized, at a high level, based on their applicability in the overall project development timeline, as identified below, and divided into four general phases: 1) site characterization and selection, 2) permitting / planning, 3) development / operation and 4) closure. This classification is made for the purposes of organization of this document and do not necessarily reflect how industrial operators or site developers engage in planning.

Since the task of this research project is to assist the selection of a sequestration site, the bulk of recommendations included herein refer to that phase (Phase 1) of the project development timeline. Additionally, to the extent that choices made during the site selection process affect the suitability of mechanisms to reduce potential environmental impact during other phases, that issue is noted and discussed. Phases 2 and 3 are discussed in less detail, and Phase 4 is evaluated least.

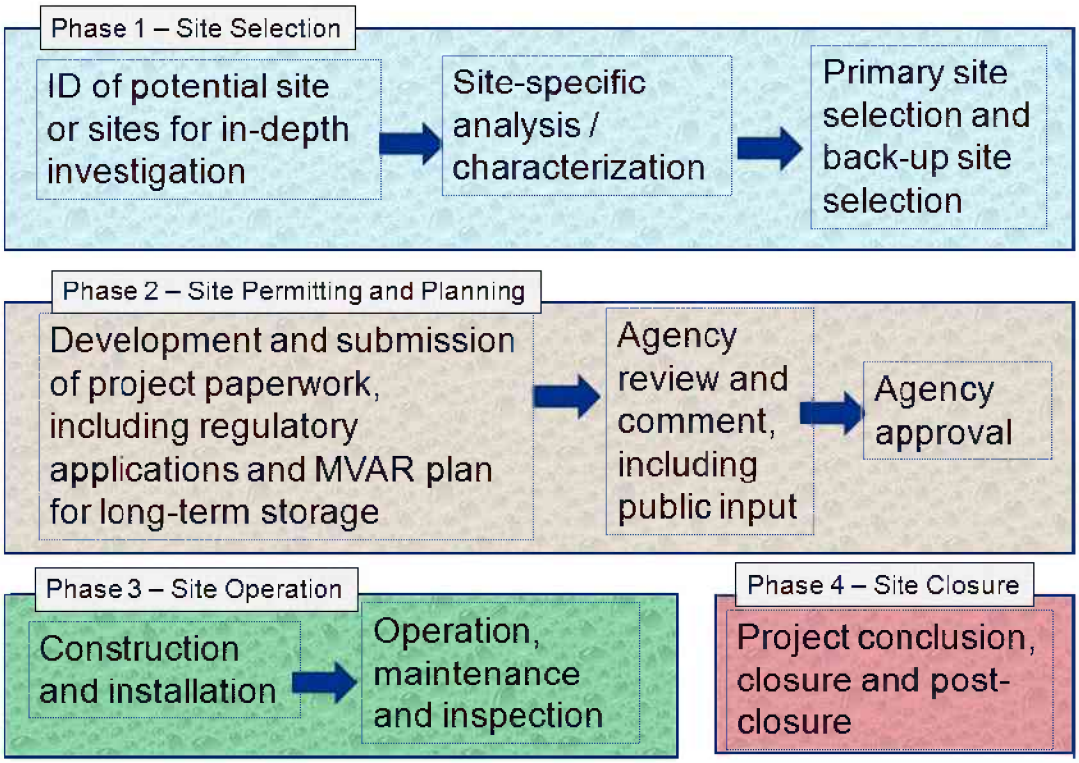

Figure 19: Simplified Project Development Timeline

6. PHASE I – SITE SELECTION

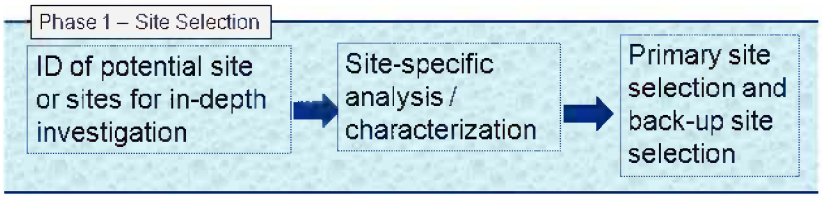

1. IDENTIFICATION OF PROSPECTIVE SITES

At the outset, examination of potential storage sites for offshore CCS development will require an in-depth evaluation of a range of factors, including, but not limited to, suitability for containing injected material over geologic time periods, potential for adverse environmental impact from development and operation, costs and project economics. As the site assessment phase is performed, evaluating coarse indicators to assess site suitability may be helpful for narrowing down the universe of available project sites to a few select sites worthy of additional, more in-depth evaluation.

As a starting point, an initial evaluation of potential project sites in Texas waters should look to the following factors as coarse indicators of site suitability. Some, but possibly not all, of these factors will be relevant for evaluation of projects further offshore, though that is beyond the main focus of the research assignment. Final selection of the project site is discussed after this discussion.

1. COARSE INDICATORS OF SUITABLE SEQUESTRATION SITES

Source-sink match - A site's proximity to point sources of CO_2 generation provides shorter piping runs, which can reduce environmental impact and the risk of being struck by ships. Shorter distances also provide greater ease of maintenance and inspection. Accordingly, sites with a strong source-sink match should be evaluated closely for suitability. This should nonetheless be balanced with the need to ensure a buffer zone between the storage site and resources of concern such as onshore aquifers or sensitive habitat.

Isolation from human activities - Facilities should be sited to avoid shipping lanes, which pose the risk of pipeline damage, and interference with economically valuable activities in the coastal area such as commercial and recreational fishing, water sports, boat cruises and

others. This minimizes the economic impact of offshore CCS on the coastal zone. Siting facilities away from human activity will also significantly reduce the risk that a leak, if it were to occur, would cause harm to humans. Accordingly, sites with less proximity to human operations should be considered preferential.

Proximity to existing infrastructure and pipelines - Piggybacking on existing infrastructure can produce lower ecosystem impacts compared to new construction.135 Further, coordinating pipeline corridors with existing equipment can also help.136 Accordingly, sites with close proximity to developed infrastructures and pipeline corridors should be considered preferential.

Depth of water column - In general, shallower-depth seafloor installations are easier to develop and maintain than greater depth, though increasing experience and technological capabilities have significantly closed the gap. However, since there is little experience implementing the comprehensive monitoring framework systems necessary to ensure CO_2 sequestration offshore, it is highly likely that the shallower systems will be much less costly to monitor and maintain for CO_2 sequestration at the outset. Additionally, due to the decreased ocean pressures associated with decreased water column, a larger availability of monitoring tools may be available to project operators in shallower installations. Furthermore, if leakage were to occur, shallower sites are more likely to be impacted by wind and wave action which would therefore lead to greater dispersion of leaked CO_2 into the ocean water, leading to potentially less overall impact on aquatic species of concern before the leak could be remedied. Accordingly, for the BEG research project, sites where the sea floor is located at a shallow depth should be considered preferential.

Presence of preferential geologic features in the injection zone - As a threshold matter, sites with unfit geologic structures for sequestration cannot be used for CCS, and should not be considered. However, certain geologic features can serve a coarse indicators that one project site might be preferable to another. Such indicators and preferential features include high storage volume potential, deeper confining zone, large confining layer thickness, absence of transmissive faults or fractures near the zone of influence, small numbers of active or abandoned wells in the confining area, lack of freshwater aquifers near the lateral border of the CO_2 plume's zone of influence, high distance from resources

135 J.T. Litynski et al., (2011),

136 International Energy Agency, *Carbon Capture and Storage: Model Regulatory Framework*, at 31(2010), http://www.iea.org/ccs/legal/model_framework.pdf

defined by the Texas Coastal Management Plan as critical areas,137 and lack of obstacles to using the full range of MVR provisions for leakage detection and site analysis.

2. IN DEPTH SITE SPECIFIC ANALYSIS AND CHARACTERIZATION

Regardless of the use of coarse indicators to narrow down potential project sites, rigorous application of site analysis and characterization must be performed prior to ultimate site selection, and completed in concert with opportunities for public participation.

> **Recommendation 3**: Prior to site selection, a proposed site must undergo a site specific evaluation of its potential to cause significant environmental impacts, including an evaluation of whether the full range of monitoring and mitigation techniques will be available to minimize impacts both at the point of injection and throughout the area of review / full zone of impact. Such a review should include a full characterization of potentially significant direct and indirect impacts prior to initiating development.

Site analysis will need to encompass, but should not be limited to:

1. Geologic, hydrogeologic, and geomechanical site assessment - A thorough evaluation of a site's geologic suitability for permanent sequestration is critical. As discussed in Section VI above, the UIC Class VI regulations governing geologic sequestration (GS) require a comprehensive set of tests and surveys, which should serve as a model for any GS site characterization, including in the offshore environment.

2. Ecosystem assessment - Documentation of the potentially affected flora, fauna, and water resources in the area of review (AoR), based on the full range of site activities, including the cumulative impacts of those activities with respect to existing conditions to provide an assessment of how a proposed project may add to or synergize impacts.

137 33 Tex. Nat. Res. Code 203.3(8) defines "critical area" as a coastal wetland, an oyster reef, a hard substrate reef, submerged aquatic vegetation, or a tidal sand or mud flat.

3. Upfront assessment of monitoring options - Whether natural or man-made surface or subsurface features would prevent or enable the use of the full range of project monitoring and mitigation options known or available to project site operators. The full slate of monitoring options that must be considered for offshore CCS projects is included in the discussion of Phase 2 (Recommendation 9) below.

For an initial project in Texas state waters, a comprehensive environmental impact assessment must occur, taking into account the full range of site features which may affect the impact of the project on the offshore environment. This includes performing a review of both direct and indirect impacts, and evaluating the likelihood of those impacts occurring based on the project design. If a significant environmental impact is likely to occur at a project site, based on the project design and as determined by the site specific evaluation, then the project must be redesigned or another site selected to prevent those direct and significant impacts from occurring. Any mitigation techniques used to prevent impacts must be performed on-site to prevent those impacts from occurring rather than ameliorating impacts after they occur.

Although we believe that offshore CCS can be done safely and responsibly, it is critical that agencies take into account the environmental assets in the full geographic extent of the area of review, including flora and fauna, and perform an alternatives analysis to identify the least-impactful option for a project. This is important not only to minimize environmental harm, but also to provide the public with a complete set of facts regarding offshore CCS projects, and a robust process through which to make their concerns and suggestions heard. This level of accountability will build public confidence in offshore CCS and encourage stronger safety measures.

This recommendation pertains to the project or projects to be developed pursuant to the BEG Gulf of Mexico Miocene CO_2 Site Characterization Mega Transect project. Environmental impact assessments as thorough as that presented here may or may not be required under Federal or State regulations for individual projects outside this study - and should be applied according to the law. Applicability in this project is derived from the application of the precautionary principle as described above.

4. PRIMARY SITE SELECTION

1. DEVELOPMENT OF THE SEQUESTRATION SITE WITH MOST SUITABLE GEOLOGY AND RETENTION INTEGRITY

A bedrock principle associated with CO_2 sequestration is that operations should not occur if the target geology is not sufficient to sequester the injected material for the desired time period. In some cases though, such as in choosing between one or more sequestration

sites, the issue may be more a matter of degree than a clear marker of non-suitability. One site may be considered better than another even though both might be able to sequester the requisite volume of material. Accordingly, in these situations, a site with the best characteristics should be chosen.

Recommendation 4: If the project must choose between two or more similar or equally situated sites for ensuring long term sequestration of injected CO_2, a formal risk assessment process which considers both 1) known conditions that might limit permanence and areas of uncertainty in characterization and 2) the consequences of both should be followed. A site with the smallest number of potentially transmissive pathways could also be the site for which there is less data. However, less data actually increases risk. Conditions that prevent the developer and regulator from listing all potential pathways does not eliminate them.

2. Application of US EPA Class VI siting rules

At the national level, the current mechanism for ground water protection from permanent CO_2 sequestration is the recently enacted US EPA UIC Class VI regulation, described in detail above in Section VI. In particular, Class VI requires that:

1. Chosen geologic systems must comprise "a confining zone free of transmissive faults or fractures" to protect underground sources of drinking water;138

2. The injection zone(s) be of sufficient areal extent, thickness, porosity, and permeability to receive the total anticipated volume of the carbon dioxide stream;139

3. An operator must identify all penetrations, including abandoned wells, that may penetrate the confining zone, and provide a description of each well's

138 40 CFR §146.83(a)(2)

139 40 CFR §146.83(a)(1)

type, construction, date drilled, location, depth, record of plugging and/or completion, and determine which abandoned wells have been plugged in a manner to prevent the movement of CO_2 and fluids into USDW, including using CO_2 compatible materials. If a well has not been properly plugged, the operator must take corrective action to ensure the well does not permit the leakage of CO_2 from the confining zone;[140]

4. The confining zone must have sufficient integrity to allow injection at maximum proposed pressure without initiating or propagating fractures; and[141]

5. Operator must use all available data and modeling to predict the extent of the CO_2 plume over the lifetime of the project.[142]

Although freshwater resources are not likely to come into contact with the injected material at the project site selected by BEG, Class VI rules are strong enough so as to ensure a basic general atmospheric protection and to ensure injected CO_2 remains trapped in the geologic feature into which it was injected.

> **Recommendation 6**: Distance from the shore, aquifers or areas of concern should be built into the determination of site suitability, though must not undermine the paramount need to have a site that represents the best geology for long-term sequestration.

As mentioned, although a good deal of information is documented relating to the lateral migration associated with existing CO_2 injection projects, there continues to be some uncertainty related to the full extent of migration possible from a CO_2 injection site. In Texas, modeling indicates that injected CO_2 plume migration in the Frio sandstone formation may reach 320 km^2 for a commercial sized 30-year injection project entailing

140 49 CFR § 146.84

141 *Id.*

142 *Id.*

emissions from an 800 MW power plant.143 This aspect of storage is being evaluated as part of a current research project conducted by the UT BEG.

Accordingly, and in part based on the uncertainty that still exists related to plume migration, the application of the precautionary principle in project siting should result in site selection that places injection as far away from resources of concern as possible within the state waters. In particular, locating storage sites farther from shore reduces risks of contaminating the Gulf Coast aquifer (or other aquifers), sensitive coastal habitat or human population through saltwater intrusion, CO_2 migration, or displaced fluids. Although aquifer protection may be inherently built into the siting program by other recommendations, or by up-front requirements to place sequestration offshore, away from bays and estuaries, the added protection of maximizing distance from resources of concern, for a first mover project, is advisable.

In most cases, application of this recommendation will mean the project should be located as close as possible to the 10.3 mile state waters boundary as possible, and seaward of any barrier islands. Of course, the ultimate choice of a primary injection site will necessarily be based on a number of factors - with the first and foremost factor undoubtedly being whether the site contains geologic conditions suitable for retaining the CO_2 in the subsurface over geologically and climatologically relevant timescales (greater than 1,000 years). However, as this document is focused on avoiding environmental impact, Recommendation 6 (above) should also be implemented during site selection as a rule.

1. UTILIZATION OF EXISTING INFRASTRUCTURE

As described above and shown in the figures below, (Figures 22 and 23) the offshore area within Texas state waters has already undergone significant development for oil and gas extraction. According to well logs, this work began in earnest in the mid 1970's and has continued through modern day, though most oil exploration and production has shifted to deeper water, and deeper geologic formations located further offshore.

As a result of the historic oil and gas development in Texas waters, significant existing infrastructure, (i.e. wells, pipelines and rigs) remain. Well density manuscripts for the offshore environment show that the upper coast is more developed than the lower or middle coast, though maps indicate numerous areas up and down the Texas coastal region in close proximity (within 1 - 10 miles) of a wide array of existing equipment capable of being co-located with equipment necessary to perform CCS. To the extent that existing infrastructure is suitable and usable for reuse or co-location with new equipment, it should actually be reused or co-located be as a general rule of thumb. Similar treatment should be

143 Gresham et al., *Implications of Compensating Property Owners for Geologic Sequestration of CO_2*

Environ. Sci. Technol, 44, 2897–2903 (2010).

given to existing and developed rights-of-way that have already undergone environmental review.

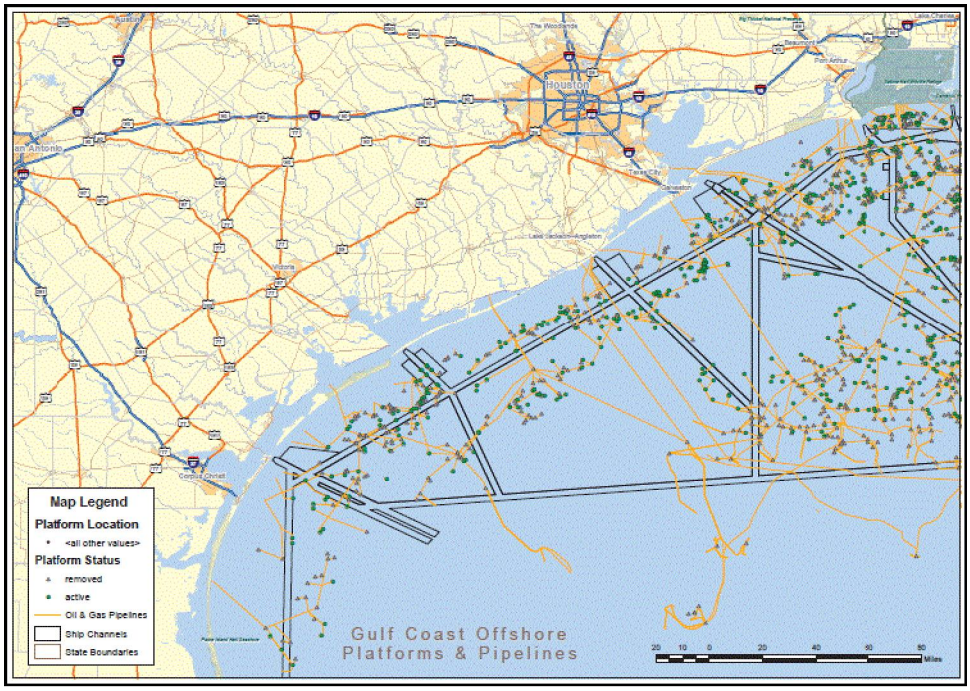

Figure 20: Existing Oil Infrastructure near Galveston, Texas (2009)

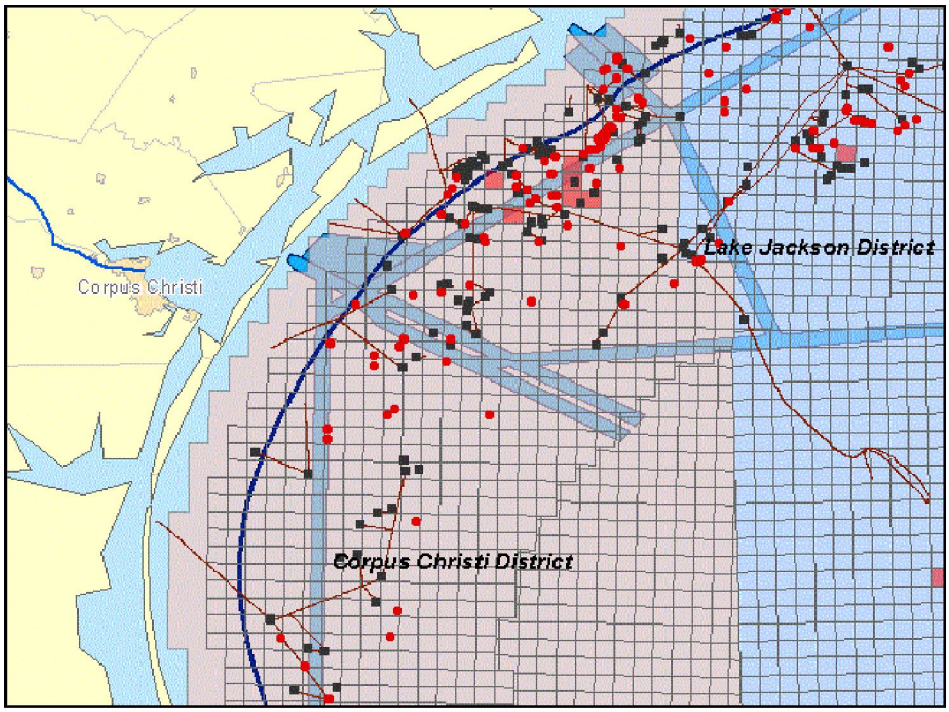

Figure 21: Existing Oil Infrastructure near Corpus Christi, Texas (2006)

Recommendation 9: An up-front site characterization for project site selection must evaluate the set of monitoring and mitigation options available at a proposed project site prior to making the determination of its suitability. All offshore CO_2 sequestration projects should utilize an MVAR plan that is able to detect migration or leakage of CO_2 from the target confining zone early on in the formation of a non-conforming condition.

6. REVIEW OF MULTIPLE PROJECT SITES AND SELECTION OF A BACK-UP

The process of choosing a site for CO_2 sequestration in the Texas offshore environment is complex and time consuming, requiring the evaluation of geological appropriateness in combination with several other factors as previously described and recommended. The ultimate decision on which proposed site or sites should be pursued for further in-depth analysis leading to site selection should therefore be subject to review and inquiry by qualified experts prior to becoming final. However, requiring that every element have an idle backup is not good system engineering, because the backup requires major investment in both development and maintenance. In our society we require such redundancy only for life-and death conditions like hospital generators, and such is therefore not appropriate for atmospheric CO_2 issues. More useful redundancies might be 1) combining sources and sinks via a pipeline network that provides redundancy, 2) developing a series of viable candidates during early characterization, so that sites with undesirable characteristics found during characterization can be dropped, and 3) phased build out so that untapped reservoir volumes are available if pressure increases in more mature reservoirs; and 4) adequate redundancy and facilities to prepare for maintenance and contingencies, which would provide opportunities to take some parts of the project out of commission.

As described in the prior sections, coastal water resources and biological systems, both onshore and offshore, could be impacted if CO_2 leakage from storage sites occurs. Therefore, it is crucial that monitoring and testing be performed frequently enough to quickly detect any such leaks or CO_2 migration away from the target confining zone. At present, the Texas Water Development Board monitors roughly 2,000 wells on an annual basis for water quality and contamination. 144 While this may seem like a large amount of

144 Texas Water Development Board, Groundwater Monitoring Section Activities, http://www.twdb.state.tx.us/GWRD/HEMON/GMSA.asp (2011).

monitoring at first glance, this frequency is insufficient, by itself, to exist as an adequate total monitoring regime for coastal monitoring in areas that could be impacted by leaks from nearby CCS project sites.

An adequate MVAR plan to detect CO_2 migration and leaks will need to include a baseline evaluation of the project site prior to the start of the project, be rigorous and frequent enough to provide deep early detection of non-conformance conditions, and include periodic observations and testing of groundwater, seawater, sediment and biological resources.

EPA's guidance to link a monitoring program closely to the site-specific risks is an essential element to robust monitoring. A prescriptive all-encompassing monitoring program should not be laid out until information about site-specific risks is reviewed. This is true for offshore sites as it is for onshore sites. Nonetheless, BEG considers the pressure response (in the subsurface) of injection to be orders of magnitude more sensitive than any kind of geochemical approach in documenting conformance and nonconformance of a system to injection. Any seafloor or water column monitoring must be shown to be able to separate a leakage signal from other types of ambient variability; if it's not sensitive it is not worthwhile regardless of how much money is invested. The expectation of high quality monitoring that EPA requires onshore should be matched (or possibly exceeded) offshore. as characterization data mature it is essential to revisit the issue of robust monitoring via risk assessment.

1. Specialized Gas Leakage System

Probably one of the most important and publically visible aspects of an MVAR program for offshore CCS is detection of leakage of CO_2 using specialized gas leakage detection equipment. Such systems are not generally used in the onshore environment since they are either only relevant to the aquatic environment or are so new as to have not been widely considered. Rather, most of the information associated with offshore leak detection from specialized equipment discussed below is based on research and development in the scientific community – and is therefore still an emerging field.

Whatever system is used to detect CO_2 leakage from the target confining reservoir, it must be able to perform two functions – 1) detect widely distributed low level leakage throughout the area of review and 2) detect point source high level leakage within the full area of review, and with targeted focus at points most likely to result in leakage. At the heart of these two functions may exist different types of equipment and leak detection

practices. Examples of equipment and practices associated with both functions are identified below. (Figures 23 and 24) However, due to the cost and accuracy associated with utilizing these leakage detection systems, it will likely be up to the discretion of the project operator to establish the proper leakage detection regime using specialized equipment. If certain types of equipment are not used, the project developer should identify the reason why, and should be able to demonstrate that the MVAR as designed will achieve the same level of accuracy in leak detection as the specialized practice not chosen.

Evaluation of sea floor surface leaks from an offshore CCS project could include the following:

1. Sonar observations, including, but not limited to, sidescan sonar, multibeam echosounder, sediment echosounders, and hydroacoustical monitoring able to cover large surface areas;145

1. Visible bubble observations using submersibles, boats and / or divers;

2. Video capturing (in the event that an anomaly or bubbling is detected);

3. Gas sampling (in the event that an anomaly of bubbling is detected);

4. Gas flux quantification (in the event that an anomaly or bubbling is detected).

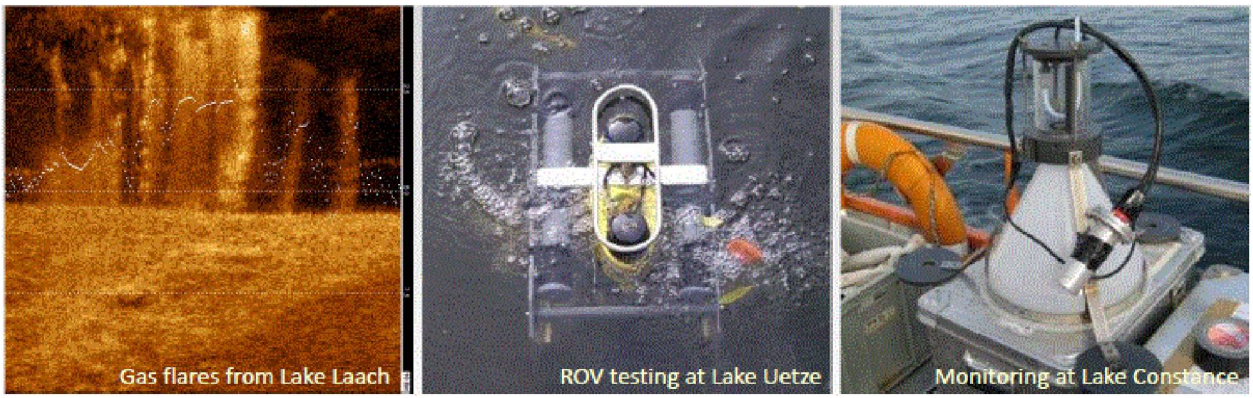

Figure 22: Offshore leakage detection methodologies being developed at research sites

145 Moeller, *Integrated Monitoring Research at Natural CO2 Vents: Lake Laach (Germany)*, Presentation for the 6th CO_2Geo Net Open Forum, Venice, May 9-11, 2011, http://www.co2geonet.com/UserFiles/file/Open%20Forum%202011/PDF-presentations/2-03_Moeller.pdf

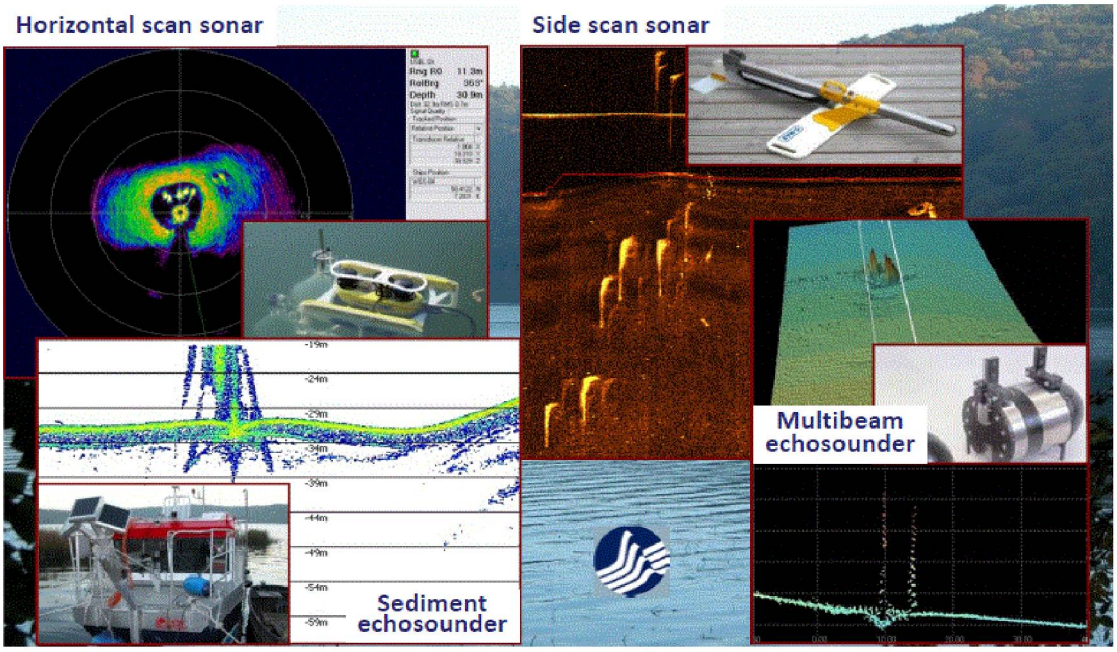

Figure 23: Offshore leakage detection methodologies using sonar Source: Moehller (2011)

APPENDIX

As a discussion of legal and regulatory issues was not part of EDF's Statement of Work, the following is not included in the body of the report. However, the legal and regulatory section may be useful to some readers and is therefore, included in this appendix. In addition, GCCC does not attempt to influence policy. Rather, the GCCC conducts scientific research whose results can then be used by policy makers to inform their policy decisions. All policy-related opinions or recommendations are solely those of EDF and do not necessarily reflect the views of the GCCC, BEG, the University of Texas at Austin or the DOE NETL. Consequently, in addition to the sections below, recommendations 5, 8 and 10 are included in this appendix and not in the body of the report.

VI. Existing Legal and Regulatory Landscape for Offshore CCS and Installation of Associated Infrastructure

As currently being documented by the Interstate Oil and Gas Compact Commission (IOGCC) and formerly by a number of legal and regulatory scholars, geologic CO_2 storage in offshore lands is likely subject to a variety of existing state and federal jurisdictions and corresponding laws governing transport, injection, storage, monitoring, and long-term liability of CO_2. (Note: This document does not address regulations concerning closure and plugging of wells nor property rights associated with captured CO_2). The applicability of these legal and regulatory systems and changes depends on whether the CCS project is located within a state boundary (i.e. within the 10.3 mile line from the Texas coast), or whether they are in the open ocean.

The vast majority of the techniques and technologies involved in offshore CCS are identical to those used in onshore CCS, and are thus subject to established regulations. Therefore, the legal and regulatory framework for offshore CCS is hardly a blank slate. However, given the relative novelty of offshore CCS in the U.S., the exact overlay of agencies and jurisdictions is not completely established, and further regulations and amendments to existing regulations are likely to emerge.

This section identifies laws relevant to environmental regulation that will be components of the offshore CCS framework and how they will likely apply. For the purpose of this paper, only the legal and regulatory aspects that apply to Texas state waters are examined.

1. PIPELINES

1. JURISDICTIONS

The jurisdictions of note include the General Land Office (right of way on public land) and the Railroad Commission Pipeline Safety Division (HLPSA monitoring and enforcement).

Pipelines are the most economical, and thus most likely, mode of transporting high volumes of CO_2 to an offshore injection and sequestration site. The U.S. oil and gas industry currently operates more than 4,000 miles of CO_2 pipelines nationwide for CCS and enhanced oil recovery.146 The Department of Transportation's Pipeline Hazardous Material Safety Agency (PHMSA)147 oversees these operations and sets regulations under the Hazardous Liquid Pipeline Safety Act of 1979 (HLPSA).148 In many states, including Texas, PHMSA delegates monitoring and enforcement authority to state agencies.

In Texas, the Pipeline Safety Division of the Texas Railroad Commission (RRC) has authority over "the intrastate pipeline transportation of hazardous liquids or carbon dioxide and all intrastate pipeline facilities as provided in 49 U.S.C. §§60101, *et seq.;* and Texas Natural Resources Code, §117.011 and §117.012."149 Pipelines crossing federal waters are subject to a different set of jurisdictions, including Bureau of Ocean Management (BOEM), the Federal Energy Regulatory Commission (FERC), and potentially the U.S. Coast Guard, but the present analysis focuses on state waters only, making those jurisdictions inapplicable.

---

146 Carbon Sequestration Leadership Forum, siting: Interstate Oil and Gas Compact Commission, *A Policy, Legal and Regulatory Evaluation of the Feasibility of a National Pipeline Infrastructure for the Transport and Storage of CO_2* (2010).

147 One of 10 agencies within the DOT, PHMSA was created in 2004 under the Norman Y. Mineta Research and Special Programs Improvement Act (P.L. 108-426) of 2004, which was signed into law by President Bush on November 20, 2004.

148 49 U.S.C. 60102(i)

149 16 Tex. Admin. Code §8.1(C).

While some commentators have proposed amending federal regulations to facilitate the construction of CO_2 pipelines, for example by issuing federal permits exempt from state eminent domain restrictions, this document will not comment on the potential merits of such proposals.150 Rather, the analysis below seeks to characterize the existing law and its implications for offshore CCS in Texas.

2. REGULATORY AUTHORITY

In Texas, the Department of Transportation's Pipeline Hazardous Material Safety Agency (PHMSA) delegates primary HLPSA responsibility for safety of intrastate CO_2 pipelines to the Pipeline Safety Division of the RRC. Under this delegated authority, RRC adopts minimum federal standards and makes an annual certification to the Office of Pipeline Safety at PHMSA.151 The regulation also includes reporting requirements, integrity assessment and management plans, notification requirements, and periodic inspections.152 In addition, the Texas Administrative Code includes a subchapter that outlines provisions applicable to hazardous liquids and CO_2 pipelines only. This section includes reporting requirements, corrosion control measures, and public education measures.153

3. RIGHT OF WAY OVER PUBLIC LANDS

The General Land Office (GLO) has authority to grant right of way and easements on public lands "for any purpose, under any terms, and for any term that the commissioner deems to be in the best interest of the state."154 This includes easements for pipelines running over onshore and offshore state lands. However, the GLO is generally required to avoid impacting areas designated part of the Coastal Barrier Resources System (CBRS).155 This

150 Sean McCoy, ed. *Policy Brief: Regulating Carbon Dioxide Pipelines for the Purpose of Transporting Carbon Dioxide to Geologic Sequestration Sites* Carnegie Mellon University at 2. (2009).

151 Nordhaus and Pitlick, *Carbon Dioxide Pipeline Regulation,* 86 Energy Law Journal Vol. 30:85 (2008).

152 16 Tex. Admin. Code § 8.1-8.315

153 *Id.*

154 31 Tex. Admin. Code § 13.12

155 31 Tex. Admin. Code § 13. 19

includes islands located immediately on the coastline such as Galveston Island and Matagorda Island, among others.156 Requests for pipeline easements running through these areas would presumably be disfavored by the GLO.

4. SITING & EMINENT DOMAIN

In Texas, pipeline operators can choose to become private carriers or common carriers, as defined by the Texas Natural Resources Code.157 A common carrier, (a carrier that "owns, operates, or manages, wholly or partially, pipelines for the transportation of carbon dioxide or hydrogen in whatever form to or for the public for hire") has the statutory right of eminent domain, which allows them to "enter on and condemn the land, rights-of-way, easements, and property of any person or corporation necessary for the construction, maintenance, or operation of the common carrier pipeline." However, for the purposes of offshore sequestration of CO_2 questions about eminent domain are not relevant.

Unlike federal pipeline permitting, Texas does not require CO_2 pipeline operators to obtain a certificate of need and public convenience before the power of eminent domain is granted, which expedites the permitting process.158 Siting is not performed by the state, but by the pipeline operator, which has the authority to decide the route a pipeline takes.159 The Safety Division of the RRC oversees pipeline construction and grants permits for operations of intrastate hazardous liquids pipelines.

As mentioned above, the GLO has primary authority for granting pipeline access over public lands, and would take into consideration environmental resources potentially impacted by pipeline passage. Indeed, the GLO must act consistently with the goals of the Coastal Management Plan.160 In addition to avoiding siting a pipeline in proximity to a

156 See John H. Chafee Official Coastal Barrier Resources System online database for full list of CBRS areas: http://projects.dewberry.com/FWS/CBRS%20Maps/Forms/AllItems1.aspx

157 3 Tex. Nat. Res. Code Ann. § 111.002

158 Nordhaus at 97

159 *Id.*

160 31 Tex. Admin. Code § 16.2

CBRS-designated area, GLO would likely avoid granting right of way through any other significant environmental asset onshore or along the coast.

5. SAFETY AND REPORTING STANDARDS

As mentioned, the Pipeline Safety Division of the RRC adopts minimum safety and reporting standards from HLPA. This involves annual reporting by operators to RRC, immediate reporting of any accidents, following of basic best practices around pipeline corrosion, as well as public notice requirements for pipelines sited within 1,000 feet of a school.

6. DRILLING, INJECTION & STORAGE

1. JURISDICTION

The jurisdictions of note regarding drilling, injection, and storage include the U.S. EPA, Texas RRC Injection & Storage Division, TCEQ and Texas GLO.

The primary regulatory framework for CO_2 injection and storage in the U.S. is the UIC program within the federal Safe Drinking Water Act (SDWA). While the federal UIC program is administered and supervised by U.S. EPA, states can apply for primacy of UIC responsibility within their state, as is the case in Texas. Responsibility for UIC in Texas is shared between the RRC and the TCEQ.161

Until December 2010, the federal UIC program included five classes of wells, each with different safety and materials requirements, including Class II, which concerns CO_2 injection for enhanced oil recovery or non-permanent storage.162 On December 30, 2010, U.S. EPA adopted final rules (first issued in July 2008) creating a new Class VI well type governing injection and geologic storage of anthropogenic CO_2.163 The rule thereafter became effective on September 7, 2011.164

Classes	Use	Inventory
Class II	Inject brines and other fluids associated with oil and gas production, and hydrocarbons for storage.	151,000 wells

161 University of Texas, *Injection and Geologic Storage Regulation of Anthropogenic Carbon Dioxide: A Preliminary Joint Report by The Texas Gen. Land Office, RRC, TCEQ, In Consultation with The Bureau of Economic Geology, Jackson School of Geosciences, The University of Texas at Austin.*
http://www.rrc.state.tx.us/forms/reports/notices/SB1387-FinalReport.pdf (2010)

162 U.S. EPA UIC website, available at http://water.epa.gov/type/groundwater/uic/wells.cfm

163 Id.

164 56982 Federal Register / Vol. 76, No. 179 / Thursday, September 15, 2011, available at http://www.gpo.gov/fdsys/pkg/FR-2011-09-15/pdf/2011-23662.pdf

Class VI	Inject Carbon Dioxide (CO_2) for long term storage, also known as Geologic Sequestration of CO_2	6-10 commercial wells expected to come online by 2016.

Figure 24: UIC well classes governing CO_2 injection and storage.165

Prior to EPA issuing the final Class VI rules, Texas had developed its own rules governing storage of anthropogenic CO_2 pursuant to SB 1387 (2009), which directed the General Land Office, in consultation with several other state agencies,166 to develop geologic sequestration rules consistent with future EPA regulations.167 In late 2010, RRC adopted rules governing geologic sequestration, largely modeled on the UIC Class VI regulations. However, significant differences exist between state and federal rules that may need to be reconciled prior to RRC obtaining primacy.

With regard to the differences between the 2010 Texas rules and the Class VI UIC rules, one major difference exists in the area of "Minimum criteria for siting." In the Class VI regulations, chosen geologic systems must comprise "a confining zone free of transmissive faults or fractures" to protect underground sources of drinking water.168 The RRC rules, meanwhile, only require that an applicant for a storage permit identify "the location, orientation, and properties of known or suspected transmissive faults or fractures that may transect the confining zone within the area of review and [determine] that such faults or fractures would not compromise containment."169 Additionally, the minimum siting criteria under Class VI also require, "[a]n injection zone(s) of sufficient areal extent, thickness, porosity, and permeability to receive the total anticipated volume of the carbon dioxide stream."170 In comparison, the RRC rules contain no such requirement, meaning that an applicant need not prove that a selected site has sufficient capacity to contain the volume of CO_2 proposed to be injected. However, in making a comparison of Class VI and RRC accounting rules, it is important to consider that the RRC credit rules are additives to

165 U.S. EPA UIC website: http://water.epa.gov/type/groundwater/uic/wells.cfm)

166 RRC, TCEQ and the Bureau of Economic Geology, Jackson School of Geosciences, University of Texas at Austin.

167 S.B. 1387 Sec. 27.048(a)

168 40 CFR § 146.83(a)(2)

169 16 Tex. Admin. Code 5.203(c)(2)(C)

170 40 CFR §146.83(a)(1)

all other existing RRC rules, including many injection rules. For example, the capacity of the injection zone in Railroad Commission context would probably be dealt with through maximum allowable surface injection pressure limitations, which may actually be *more* rigorous.

In order to obtain primacy, the Texas RRC must show that the state programs meet EPA's minimum federal requirements for UIC programs, including construction, operating, monitoring and testing, reporting, and closure requirements for well owners or operators.171 However, it is unclear whether the absence of a USDW in the state of Texas submerged lands obviates the need for or applicability of UIC program rules in those areas.

2. CLASS II VS. CLASS VI

Assuming the standards set by EPA are included in the final Texas regulations, the Class VI regulations will likely apply to geologic sequestration of CO_2 in brine aquifers, and set a significantly higher bar than Class II in terms of siting, wellbore, and monitoring requirements. Examples of elements required by Class VI but not Class II include, but are not limited to, the following: 172

3. The target site must include an injection zone with sufficient properties to receive the total anticipated volume of CO_2.
4. The confining zone must have sufficient integrity to allow injection at maximum proposed pressure without initiating or propagating fractures.
5. Operator must use all available data and modeling to predict the extent of the CO_2 plume over the lifetime of the project.

6. SITE SELECTION AND WELLBORE REQUIREMENTS

171 40 CFR § 145

172 40 CFR Part 146, Subpart H.

Class VI regulations include extensive specifications for site selection and wellbore construction. Without listing all of these elements, it is worth noting some key safeguards against environmental risk included in the regulations:

- **Identifying potential leakage pathways:** An operator must identify all penetrations, including abandoned wells, that may penetrate the confining zone, and provide a description of each well's type, construction, date drilled, location, depth, record of plugging and/or completion, and determine which abandoned wells have been plugged in a manner to prevent the movement of CO_2 and fluids into USDW, including using CO_2 compatible materials. If a well has not been properly plugged, the operator must take corrective action to ensure the well does not permit the leakage of CO_2 from the confining zone.[173] In the offshore environment, there should be fewer abandoned wells than onshore, but this measure is still vitally important in order to close off potential leakage pathways from the confining zone.
- **Stringent corrosion-resistance materials requirements:** All materials used for casing, cementing, tubing and packer must be compatible with fluids that they may come in contact, and meet or exceed standards for those materials by API, ASTM, or others. This includes ensuring the materials can resist corrosion from CO_2 and formation fluids, as well as all internal and external pressure predicted at the site.[174] This requirement is critical, as carbonic acid and other corrosive fluids may come into contact with well materials at various times in the project's lifetime and could create leakage pathways if sufficiently corrosion-resistant materials are not used.
- **Mechanical Integrity Testing:** Prior to injection, the well operator must conduct a series of tests designed to demonstrate the internal and external mechanical integrity of injection wells, which may include:

    i. A pressure test with liquid or gas;

    ii. A tracer survey such as oxygen activation logging;

    iii. A temperature or noise log;

    iv. A casing inspection log; or

173 49 CFR § 146.84

174 49 CFR § 146.86

v. Any alternative methods that provide equivalent or better information and that are required by and/or approved of by the Director.175

Extensive mechanical integrity testing prior to injection is crucial to ensuring suitability of a site, and can identify problems preemptively rather than waiting for a blowout or fracturing of casing once storage operations are underway.

7. TEXAS COMMISSION ON ENVIRONMENTAL QUALITY INVOLVEMENT

Although the Texas RRC would likely have authority over permitting of geologic sequestration projects in the offshore zone, the TCEQ has jurisdiction over injection of carbon dioxide into a zone "below the base of usable quality water…and that is not productive of oil, gas, or geothermal resources."176 While the offshore area is not believed to contain usable water, if EPA or the Texas Water Board were to find otherwise, TCEQ would have jurisdiction under this provision of the Texas Water Code.

Additionally, RRC may not issue a permit for geologic sequestration projects until the applicant has submitted a letter from the TCEQ stating that the storage project will not "injure any freshwater strata in that area" and that "the formation or stratum to be used for the geologic storage facility is not freshwater sand."177 Thus, even where storage is not done beneath an underground source of drinking water, TCEQ must provide certification that no underground sources of drinking water will be affected (using a methodology outlined in the Texas Water Code).178 This shared responsibility between RRC and TCEQ ensures that RRC permitting complies with groundwater protection under the SDWA. As stated before, this discussion may be a inapplicable for the overwhelming majority of Texas submerged lands, but it is included here for the sake of completeness.

8. MONITORING, TESTING, ACCOUNTING AND REPORTING

175 49 CFR § 146.87(a)(4)

176 Tex. Water Code § 27.022

177 Tex. Water Code § 27.046

178 *Id.*

1. JURISDICTION

In general, the jurisdictions of note include the U.S. EPA; RRC Injection & Storage Division (primacy currently undetermined). A discussion of the interplay between these jurisdictions and the primacy application process is included above.

2. MONITORING & TESTING

Unique among UIC classes, Class VI requires that applicants submit, along with their permit application, a "testing and monitoring plan" that includes a variety of measures. Key measures include:

1. Regular chemical and physical analysis of the carbon dioxide stream;
2. Installation and use, except during well workovers, of continuous recording devices to monitor injection pressure, rate, and volume; the pressure on the annulus between the tubing and the long string casing; and the annulus fluid volume added;
3. Quarterly corrosion monitoring of the well materials for loss of mass, thickness, cracking, pitting, and other signs of corrosion;
4. Periodic monitoring of the ground water quality and geochemical changes above the confining zone(s) that may be a result of carbon dioxide movement through the confining zone(s) or additional identified zones; and
5. Testing and monitoring to track the extent of the carbon dioxide plume and the presence or absence of elevated pressure. 179

A robust testing and monitoring program is critical for ensuring that a storage site is effective at containing the injectate, and that the plume is behaving as predicted. The current RRC rules effectively require the same minimum elements outlined above.180 In addition to including these minimum elements, under the UIC regulations—but not current

17949 CFR § 146.90

180 16 Tex. Admin. Code § 5.203(j)

RRC rules—every five years an operator must review its program and submit a revised testing and monitoring program to the program administrator, or explain why no changes to its program are necessary.181

Overlapping with the UIC regulations in this area is another EPA-issued regulation, on mandatory reporting of greenhouse gases (GHGs) at CO_2 injection and storage sites.182 The purpose of the mandatory reporting rule is to establish a reliable recording regime,183 as well as to monitor efficacy of carbon capture and storage projects. Whereas the UIC program operates under the authority of the Safe Drinking Water Act, the GHG regulations operate under authority of the Clean Air Act.

The 40 CFR part 98 subpart RR rule, pertaining to CO_2 storage, includes its own monitoring, reporting and verification (MRV) requirements for CO_2 storage projects (the accounting component of the rule is discussed separately below). While a UIC Class VI permit may satisfy some parts of the subpart RR rule's MRV requirement, the applicant must include additional information outlining how monitoring will achieve detection and quantification of CO_2 in the event surface leakage occurs.184

The Subpart RR MRV plan requirements include five main components: 185

1. Delineation of the maximum monitoring area (MMA) and the active monitoring area (AMA);

181 49 CFR § 146.90(j)

182 Mandatory Reporting of Greenhouse Gases: Injection and Geologic Sequestration of Carbon Dioxide; Final Rule, 40 CFR Parts 72, 78, and 98

183 For example, if a storage site is injecting 1 $MMTCO_2E$ per year, but leaking 20% of that volume due to improper storage methods, the operator should not be credited for the full amount injected.

184 75 Fed. Reg. 230 at 75063

185 40 CFR § 98.448(a)(1)-(5)

2. Identification and evaluation of the potential surface leakage pathways and an assessment of the likelihood, magnitude, and timing, of surface leakage of CO_2 through these pathways in the MMA;

3. A strategy for detecting and quantifying any surface leakage of CO_2 in the event leakage occurs;

4. An approach for establishing the expected baselines for monitoring CO_2 surface leakage; and

5. A summary of considerations made to calculate site-specific variables for the mass balance equation.

Again, some overlap exists between these components and the elements of the "testing and monitoring" plan required by UIC Class VI. While both are concerned with detecting leakages from the storage site, the Subpart RR MRV requirements focus more on quantifying the leakages through baseline and post-leak measurements for accounting purposes.

Research and Development: Of note, subpart RR exempts research and development (R&D) projects from reporting if they meet the eligibility requirements. If so, they report instead under Subpart UU, which requires reporting mass of CO_2 received, and does not require reporting CO_2 injected or leaked.186 Exempt projects include those that "investigate or will investigate practices, monitoring techniques, or injection verification, or if it is engaged in other applied research that focuses on enabling safe and effective long-term containment of a CO_2 stream in subsurface geologic formations, including research and injection tests conducted as a precursor to a larger more permanent long-term storage operation."187 A pilot offshore CCS may qualify for this exemption to the extent that is characterized as evaluating the potential for more extensive storage in the offshore environment.

6. ACCOUNTING

Central to the U.S. EPA Subpart RR GHG reporting rule is a methodology for measuring net sequestration of GHGs at the storage site. The rule calculates this net amount using a "mass

186 40 CFR § 98.472

187 40 CFR § 98.440(d)

balance" equation, which subtracts leakage measured from various points in the well and injection site (e.g. between the flow meter and the injection wellhead; between the production wellhead and the flow meter, etc.) from the total volume of CO_2 injected into the well or a group of wells to reach a final total:

$$CO_2 = CO_{2I} - CO_{2P} - CO_{2E} - CO_{2FI} - CO_{2FP} \quad \text{(Equation RR-11)}$$

Where:

CO_2 = Total annual CO_2 mass sequestered in subsurface geologic formations (metric tons) at the facility in the reporting year. CO_2I = Total annual CO_2 mass injected (metric tons) in the well or group of wells covered by this source category in the reporting year.

CO_{2P} = Total annual CO_2 mass produced (metric tons) in the reporting year.

CO_{2E} = Total annual CO_2 mass emitted (metric tons) by surface leakage in the reporting year.

CO_{2FI} = Total annual CO_2 mass emitted (metric tons) as equipment leakage or vented emissions from equipment located on the surface between the flow meter used to measure injection quantity and the injection wellhead, for which a calculation procedure is provided in subpart W of this part.

CO_{2FP} = Total annual CO_2 mass emitted (metric tons) as equipment leakage or vented emissions from equipment located on the surface between the production wellhead and the flow meter used to measure production quantity, for which a calculation procedure is provided in subpart W of this part.

This final amount indicates how much sequestration a project should be credited for in a given year.

7. Long-Term Liability and Financial Responsibility

1. JURISDICTION

The agency with primary responsibility for long term liability from a project site located in the Texas coastal region will be the Texas RRC as it implements the U.S. EPA Class VI UIC regulation.

2. EXISTING REGULATORY LANDSCAPE

In addition to placing requirements on site operation and development, the UIC Class VI regulations also address the question of long-term responsibility for monitoring and maintenance of a storage site after closure has occurred.

The UIC Class VI regulation requires that an owner or operator must conduct monitoring as specified in the Director-approved Post-Injection Site Care (PISC) and site closure plan following the end of injection, until the owner or operator can demonstrate to the Director that the geologic sequestration project no longer poses a danger to underground sources of drinking water.188 Once an owner or operator has met all regulatory requirements under part 146 for Class VI wells and the Director has approved site closure pursuant to requirements at § 146.93, the owner or operator will generally no longer be subject to enforcement under section 1423 of SDWA for noncompliance with UIC regulatory requirements. However, an owner or operator may be held liable for regulatory noncompliance under certain circumstances even after site closure for violating § 144.12 of the UIC rule, such as where the owner or operator provided erroneous data to support approval of site closure.

Additionally, an owner or operator may always be subject to administration jurisdiction if the Administrator deems necessary to protect the health of persons under section 1431 of the SDWA after site closure – for example if there is fluid migration that causes or threatens imminent and substantial endangerment to an underground sources of drinking water. For example, the Administrator may issue a SDWA section 1431 order if a well presents an imminent and substantial endangerment to the health of persons, and the State and local authorities have not acted to protect the health of such persons. The order may include commencing a civil action for appropriate relief. If the owner or operator fails to comply with the order, they may be subject to a civil penalty for each day in which such violation

188 http://www.federalregister.gov/articles/2010/12/10/2010-29954/federal-requirements-under-the-underground-injection-control-uic-program-for-carbon-dioxide-co2#p-601

occurs or failure to comply continues. Furthermore, after site closure, an owner or operator may, depending on the fact scenario, remain liable under tort and other remedies, or under other Statutes including, but not limited to, Clean Air Act, 42 U.S.C. §§ 7401–7671; CERCLA, 42 U.S.C. § 9601–9675; and RCRA, 42 U.S.C. 6901–6992.

3. WILDLIFE & COASTAL ZONE MANAGEMENT AND PROTECTION

1. JURISDICTION

The agencies of record for jurisdiction are the Texas Coastal Coordination Council (CCC) in concert with the Texas RRC, TCEQ; Texas Parks and Wildlife Department (TPWD); National Marine Fisheries Service (NMFS).

2. EXISTING REGULATORY LANDSCAPE

Development activity in the Texas coastal zone is subject to laws protecting the coastal environment. This includes the federal Coastal Zone Management Act of 1972 (CZMA),189 which authorizes states to create their own Coastal Management Plans (CMPs), making them eligible for federal grants for coastal improvement and restoration projects.

The Texas CCC, part of the Texas GLO, manages Texas' CMP,190 administering federal grants and ensuring various agency actions affecting the Texas coastal zone are consistent with the goals and policies of the CMP.191 This includes RRC permitting within the coastal zone.192

---

189 16 U.S.C. § 1451

190 Tex Nat. Res. Code § 33.203(22)

191 Texas General Land Office website

http://www.glo.texas.gov/what-we-do/caring-for-the-coast/grants-funding/cmp/index.html

192 31 Tex. Admin. Code § 505.11(a)(3)

Under RRC rules, the RRC is required to determine if a proposed permitted activity will have a "direct and significant impact" on any coastal natural resource area (CNRA).193 If the RRC determines that a proposed activity in the coastal zone will not have a direct and significant impact on any CNRA, then the RRC must issue a specific written determination.

In addition to the CZMA, development in the Texas coast zone may also implicate the Federal Endangered Species Act and Magnuson-Stevens Fishery Conservation and Management Act for the purpose of protecting wildlife and critical habitat.
The 1996 amendments (known as the "Sustainable Fisheries Act") to the Magnuson-Stevens Fishery Conservation and Management Act of 1976 require federal and state agencies to consult with the National Marine Fisheries Service (NMFS) and local Fisheries Management Council (FMC)194 before approving any activity that may adversely affect the habitat of a fishery resource in the development area, including essential fish habitat.195 Essential fish habitat can include coastal areas, oceans, and rivers used by anadromous fish (i.e. living in the ocean but migrating upstream in freshwater rivers for breeding). If it is determined that the activity would adversely affect essential fish habitat, the FMC and NMFS will recommend measures to the agency for conserving the habitat. Although the Act does not require the federal or state agencies to carry out the measures, if a federal agency elects not to follow the recommendation, it will be required to explain in writing their reasons for not following the recommendations.196

3. PUBLIC REVIEW AND COMMENT

A myriad of regulations and administrative requirements establish a wide array of public review and comment procedures for development projects located in the Texas coastal zone and state waters.

Safe Drinking Water Act Rules: Under RRC rules, Texas has adopted the central public notice and comment provisions of the SDWA, requiring an applicant to provide notice to both the

193 16 Tex. Admin. Code § 3.8(j) A coastal natural resource area is a coastal barrier, coastal historic area, coastal preserve, coastal shore area, coastal wetland, critical dune area, critical erosion area, gulf beach, hard substrate reef, oyster reef, submerged land, special hazard area, submerged aquatic vegetation, tidal sand or mud flat, water in the open Gulf of Mexico, or water under tidal influence, as these terms are defined in §33.203 of the Texas Natural Resources Code.

194 The FMC for Texas is the Gulf of Mexico Fishery Management Council; http://www.gulfcouncil.org/

195 16 U.S.C. § 1855(b)(3) (2009). "Essential fish habitat" refers to the waters and substrate necessary to fish protected under the Magnuson-Stevens Act "for spawning, breeding, feeding or growth to maturity."

196 16 U.S.C. § 1854(b)(4)(B)

general public and to specific individuals when a permit application is filed with the RRC.197 First, a copy must be made available to the public with the County Clerk at the courthouse of each county where the storage facility is to be located, or at another equivalent public office. The applicant also must provide an electronic copy of the complete application for access on the Railroad Commission website.

Additionally, under the RRC rules, general notice must be made through a local newspaper of general circulation, and specific notice given to adjoining or overlying owners and leaseholders of land and mineral rights, as well as: the clerk of the county or counties where the proposed storage facility is located; the city clerk or other appropriate city official where the proposed storage facility is located within city limits; and any other class of persons that the director determines should receive notice of the application.198

If RRC receives a protest from one of the specific individuals who were notified of the application, the commission cannot administratively approve the application. It must then schedule a hearing, notifying all affected persons, local governments, and other persons who express, in writing, an interest in the application.199 Administrative hearings are open to the public and allow opponents to the application to present evidence, but hearings do not otherwise include time for public comment. If no protest to the application is received, RRC may administratively approve the application.200

School Land Board Rules: When an application for geologic sequestration concerns use of state land, the School Land Board's (SLB) public review process would apply.201 The SLB usually meets twice a month and publishes notice of any meeting and action under consideration in the Texas Register. Time is allotted at the end of every meeting for public comment, giving the opportunity for any public member to provide input on any matter where SLB approval is sought, including whether a tract of land is permitted for geologic storage. Following SLB's determination of which tracts are suitable, the public or staff may nominate any or all of the tracts for inclusion in an upcoming lease sale. Notice of the lease sale will be published, giving the public an opportunity comment on the proposed lease at any SLB meeting up to and including the day bids are opened.202 The public may at any

197 16 Tex. Admin. Code § 5.204

198 16 Tex. Admin. Code § 5.204(b)(1)-(2)

199 16 Tex. Admin. Code § 5.204(c)(1)

200 16 Tex. Admin. Code § 5.204(c)(2)

201 University of Texas (2010).

202 *Id.* at 52.

time during the life of the lease request to be placed on the SLB agenda to discuss on-going operations and to request SLB action on their concerns.

National Environmental Policy Act Rules: The SDWA UIC permits are ostensibly exempt from performing an Environmental Impact Statement (EIS) under section 101(2)(C) and an alternatives analysis under section 101(2)(E) of NEPA under a functional equivalence analysis. See *Western Nebraska Resources Council* v. *U.S. EPA,* 943 F.2d 867, 871–72 (8th Cir. 1991) and EPA Associate General Counsel Opinion (August 20, 1979).203 However, this determination could potentially change if federal funding is involved in an offshore CCS project. This document will not speculate as to the applicability of NEPA requirements, which is a highly fact-specific determination. However, the question of environmental review is discussed in more detail in Section VII.

VII. Policy recommendations for environmental risk reduction during site selection

Recommendation 5: Regardless of regulatory applicability, strict application of the site characterization and control requirements of U.S. EPA UIC Class VI well regulations should be performed to ensure permanent retention of injected material is achieved. Future offshore geo-sequestration projects should be sited and operated where the best geology and site characterization exists, and with strict application of U.S. EPA UIC Class VI requirements as required by law or as necessary to ensure permanent retention of injected material.

203 75 Fed. Reg. 237 at 77236

1. CONSIDERATION OF BRINE AQUIFER INJECTION

One of the benefits of the Gulf of Mexico Miocene CO_2 Site Characterization Mega Transect Project is that by facilitating the future siting and development of a commercial scale CCS project in Texas waters, it could help set the stage for other carbon sequestration in the subsurface. As identified by U.S. DOE, the sites with the largest sequestration potential in the Gulf, and elsewhere, are brine formations. Accordingly, although it is not a recommendation made in this paper since our focus (as covered in Recommendation 4) is to ensure the development of the best available site, we recommend the site selection process, at a minimum, place focus on the suitability of brine formations as suitable sequestration sites.

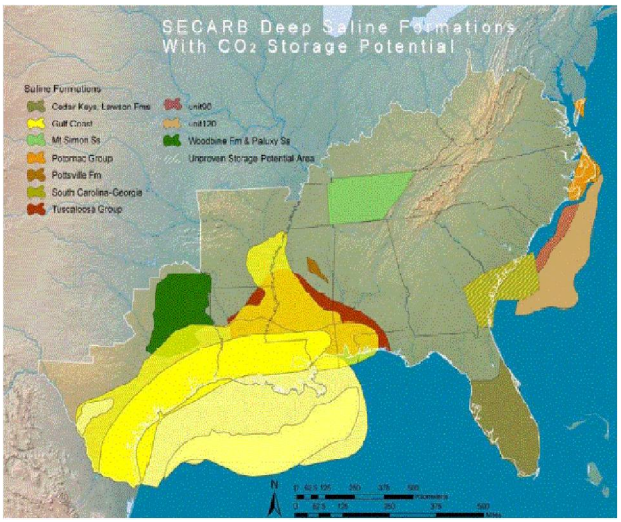

Figure 24: SECARB Brine Formation Map. Source U.S. DOE

2. DEVELOPMENT AWAY FROM ASSETS OF CONCERN

Although there are benefits to locating storage sites closer to sources of CO_2, or to shoreline resources (i.e. shorter piping runs, more convenient monitoring and inspection, etc.) the risk to human health, onshore aquifers and critical ecological assets on the coastline is reduced by locating CO_2 storage sites further from resources of concern yet still within the 10.3-mile state water boundary. Furthermore, requiring that no groundwater aquifers or coastal natural resource areas be located within and above the area of review (full zone of impact, including zones of elevated pressure or displaced fluid migration), the project site selection takes into account uncertainty that exists associated with predicting plume migration extent.

Recommendation 8: A CCS project should thoroughly evaluate several potential candidate sites for project development, allowing for critical evaluation of multiple locations and geologic characteristics by qualified experts prior to making a final determination. A complex system must have efficient redundancy to attain a stable operating condition. However requiring that every element has an idle backup is not good system engineering, because the backup requires major investment in both development and maintenance. In our society we save this for life-and death conditions like hospital generators, and it is not appropriate for atmospheric CO2 issues. Nonetheless, useful redundancies could include 1) combining sources and sinks via a pipeline network that provides redundancy, 2) developing a series of viable candidates during early characterization, so that sites with undesirable characteristics found during characterization can be dropped, and 3) phased build out so that untapped volumes are available if pressure increases in some more mature volumes; and 4) adequate redundancy and facilities to prepare for maintenance and contingencies, which would provide opportunities to take some parts of the project out of commission.

4. PHASE 2 – SITE PERMITTING AND PLANNING

As noted above, the key aims of the research project end at site identification and characterization. Accordingly, Phases 2, 3 and 4 discussed below are somewhat beyond the study scope. However, due to the importance of performing offshore CCS in a manner that mitigates the risk to the human population and the offshore environment, this paper goes into some detail and makes two initial recommendations related to the phases after site selection.

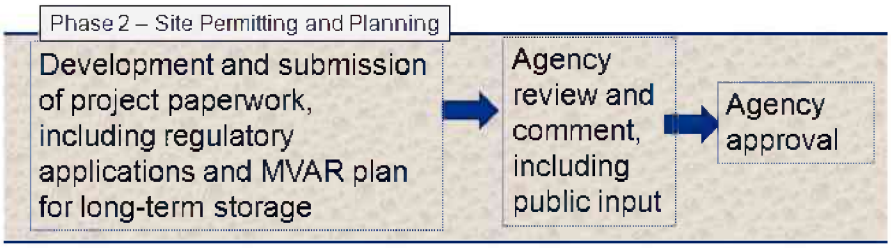

1. DEVELOPING A MONITORING, VERIFICATION, ACCOUNTING AND REPORTING PLAN

In Recommendation 3 (above), this paper states that an up-front site characterization for project site selection must evaluate the set of monitoring options available at a proposed project site prior to making the determination of its suitability. In this evaluation is the inquisition of whether natural or man-made features (surface or subsurface) would prevent or enable the use of the full range of project monitoring and mitigation options

known or available to project site operators. In this section, the suite of monitoring tools is discussed.

To determine whether the full range of monitoring mechanisms are available at a project site, an evaluation of the extent of monitoring that should be pursued must first be performed. At the heart of any site specific monitoring, verification, accounting and reporting (MVAR) plan is making sure project operators are aware of the conditions and location of injected CO_2 when it is in the subsurface. The MVAR plan must be comprehensive enough to detect widespread low level releases as well as high concentration single point leaks, and include contingency procedures (mitigation procedures) to be implemented in the event that a problem or leak is discovered. Such a plan is also necessarily coupled with a detailed site characterization and site operation procedure that informs operators of what practices they must follow to operate the overall injection project without leakage or accident.

Although many of the conditions and practices associated with site monitoring on-shore may be the same as that in the offshore environment, certain important aspects are different and require special attention. In particular, downhole inspections cannot be performed in the offshore environment as they can on land, nor can surface leak detection using portable, hand-held instrumentation. Additionally, if a leakage from a confining zone on land occurred, wind or other conditions may disperse the leaking CO_2. However, in the ocean, a leak presents the risk of localized ocean acidification that has the potential to lead to changes in biologic systems.

Recommendation 10: All offshore CO_2 sequestration projects should, prior to selecting a project site, evaluate the availability of contingency and remediation measures available at the site in the event an undesired impact is observed. A contingency and remediation plan should thereafter be finalized and published prior to commencement of the project.

2. RELEASE MITIGATION AND PLANNING

In the event that a developed CCS site does not operate as designed, or that CO_2 is discovered to be leaking from the target confining zone, the operator must respond quickly to prevent damage to the Texas coastal environment. Accordingly, prior to any injection, the project operator will need to have a contingency plan for mitigation of problems that may be observed. Such a plan is as important (for the assurance of CO_2 sequestration) as a site specific MVAR plan. Mitigation plans should include a provision to immediately cease injection if leakage from the target confining zone is observed.

At the core of any mitigation plan must be methods to determine the extent of the plumes non-conformance with expected behavioral models and expectations, including identifying size of any transmissive pathways and leaks, the cause of the leak, and the method to stop the leak. For the purpose of this document, we reference the full range of leak detection methodologies discussed above as critical components of any mitigation plans because the size, extent and characteristics of a leak will be a determining factor for understanding the likely impact on the offshore environment. Of course, a project developer must develop a mitigation plan that incorporates all three aspects, and potentially others as needed.

3. PHASE 3 – SITE OPERATION

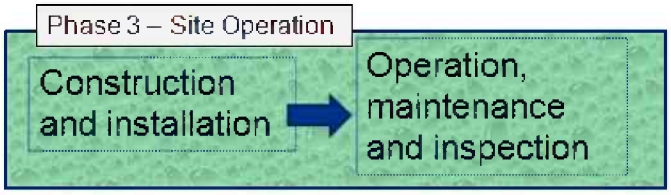

Perhaps the most effective way to prevent unwanted environmental impacts from an offshore CCS project is to create a comprehensive development plan that takes into account all of the protections and best business practices available, and observe the site with rigorous governmental oversight.

Included in a site development and operations plan should, at a minimum, be all the necessary parameters associated with site construction, installation, operation, maintenance and inspection. For example, development plans should identify and require conformance with best practice standards regarding well design, materials selection, installation, operation, and maintenance in the offshore environment. Additionally, development plans should include injection pressure and flow rate guidance.

By following established guidelines built from the site specific development plan and the site specific MVAR plan, including guidelines associated with contingency planning, project operators and developers will have a course of action predetermined to minimize undesired impacts and prevent project delays.

With reference to governmental oversight, as a threshold manner full cooperation with governmental officials prior to, and during, the development and operation of a project site will be necessary. Additionally, institutional capacity and integrity for rigorous governmental oversight should be thoroughly evaluated on a periodic basis, including the nature of the relationships between oversight bodies and project personnel. Finally, critical reviews of institutional performance should inform whether correction action is needed and to ensure regulators remain informed yet unbiased.

4. PHASE 4 - SITE CLOSURE AND POST-CLOSURE

The purpose of this document was to examine the environmental risks and regulatory considerations associated with offshore CCS in Texas coastal waters. In this report, methods and opportunities to minimize the potential environmental impact of CCS associated with leakage of CO_2 and infrastructure installation was discussed. Site closure and post-closure are critical aspects of an environmental protection regime, but are likely to be well into the future and based on project dynamics observed during the development and operations phase. Accordingly, site closure and post-closure are outside the bounds of this project at this time and are not discussed further.

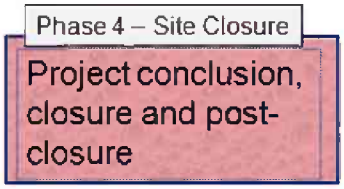

APPENDIX D

Well Bore Management

BUREAU OF ECONOMIC GEOLOGY

TEXAS OFFSHORE MIOCENE PROJECT

TASK 11

BOREHOLE MANAGEMENT PLAN

October 2013

Sandia Technologies, LLC

6731 Theall Road Houston, Texas 77066 USA

Tel: (832) 286-0471 Fax: (832) 286-0477 www.sandiatech.com

BUREAU OF ECONOMIC GEOLOGY

TEXAS OFFSHORE MIOCENE PROJECT

TASK 11 – BOREHOLE MANAGEMENT PLAN

TABLE OF CONTENTS

TABLES

FIGURES

APPENDICES

1.0 SUMMARY

Carbon Dioxide injection wells are regulated by the US Environmental Protection Agency (EPA) under 40 CFR 146 Subpart H (Criteria and Standards Applicable to Class VI Wells). Class VI injection wells are referred to as Geologic Sequestration wells. Under 40 CFR 146.84 (Area of Review and Corrective Action), the Area of Review is defined as the region surrounding the Geologic Sequestration project where underground sources of drinking water (USDW) may be endangered by injection activities. The owner/operator will 1) identify all artificial penetrations that penetrate the confining zone and determine whether they have been plugged so as they do not provide conduits for fluid movement and 2) provide required descriptive information for each artificial penetration. The evaluation of the artificial penetrations should include whether materials of construction are compatible with the carbon dioxide stream. By completing this evaluation, the owner/operator will identify wells that require corrective action prior to Geologic Sequestration injection activities.

This document outlines a Wellbore Management Plan for locating and evaluating artificial penetrations in a Geologic Sequestration project area subject to UIC Class VI regulations. The document presents the Wellbore Management Plan, explaining the series of steps that should be completed to ensure adequate review and evaluation of artificial penetrations. It then presents the results of the implementation of the Wellbore Management Plan in the Gulf of Mexico Miocene CO2 Site Characterization Mega Transect project's San Luis Pass Dome area to determine if any well can serve as a conduit for the movement of borehole fluids to USDWs. As an Injection Zone and operating conditions have yet to be determined for this project, the modeling element of the Wellbore Management Plan cannot be demonstrated in the San Luis Pass Dome area.

The San Luis Pass Dome study area is approximately 292 square miles and contains wells drilled in the offshore area under the control of the State of Texas (Texas waters) and the United States (Federal waters). The Wellbore Management Plan process identified 62 wells: 37 located in Texas waters and 25 located in Federal waters. These

wells are listed in Table 11-1. The majority of information for wells was compiled from records maintained by the Texas Railroad Commission and the Bureau of Ocean Energy Management.

2.0 INTRODUCTION

A map of the study area was provided by the BEG (Bureau of Economic Geology) Gulf of Mexico Miocene CO2 Site Characterization Mega Transect project (Figure 11-1). When fluid is injected into a subsurface geologic formation (e.g., CO_2 during a carbon geosequestration operation), pressure within the injection interval will increase. Pressure increase will be greatest at the injection well, and will decrease with distance away from the well. Due to the driving force supplied by the increase in formation pressure during injection, artificial penetrations within the resulting injectate plume have the potential to convey fluid out of the injection interval, and potentially into an USDW. In an unplugged borehole, this driving force is opposed by the flow resistance of the material residing in the borehole. Fluid movement cannot begin until the pressure in the injection interval has increased beyond the critical threshold value necessary to overcome the flow resistance of the borehole material. As long as the pressure buildup in the injection interval is less than the threshold value, the artificial penetration cannot serve as a conduit for injectate or formation brines. Therefore, the artificial penetration as abandoned is safe, and no corrective action is necessary.

After injection operations cease, the pressure buildup within the injection interval will decrease to a value approaching the original formation pressure. This occurs at a relatively rapid rate and reaches background formation pressure within years. Upon pressure stabilization in the injection interval, the injectate plume will be in hydrostatic equilibrium with surrounding formation brines. Consequently, no driving force capable of conveying fluid or formation brines out of the Injection Interval and Injection Zone will be present. Therefore, even if the resulting plume, pushed by natural hydrogeologic or geochemical processes, encounters a mud-filled artificial penetration, the only process available to transport constituents out of the Injection Zone is molecular diffusion.

BUREAU OF ECONOMIC GEOLOGY
Scott W. Tinker, Director
JOHN A. and KATHERINE G. JACKSON SCHOOL OF GEOSCIENCES
The University of Texas at Austin

Offshore Miocene CO2 Repository

Texas -- Gulf of Mexico Basin

Initial Data Transfer to Sandia Tech

POSTED WELL DATA

ATTRIBUTE MAP

Any Digital Log IS PRESENT [38]
Any Raster Log IS PRESENT [75]

WELL SYMBOLS

- Abandoned Well
- Dry Hole, With Show of Gas
- Dry Hole, With Show of Oil
- Dry Hole
- Gas Well
- Location Only
- Oil Well
- Plugged & Abandoned Gas Well
- Drilling Well
- Temporarily Abandoned

By: David L. Carr & Jordan-Leigh Taylor

MAP PROJECTION

NAD27 / UTM zone 15N
North American Datum 1927 (NAD27)
XY IN US FEET

Blue Marble Projection Details
Datum: North American Datum 1927 (NAD27)
Ellipsoid: Clarke 1866
Projection: Transverse Mercator
Central Meridian: -93.0000000
False Easting: 500000.00 Meter (m)
False Northing: 0.00 Meter (m)
Latitude Of Origin: 0.0000000
Scale Factor: 0.99960000
EPSG: 26715

May 23, 2012

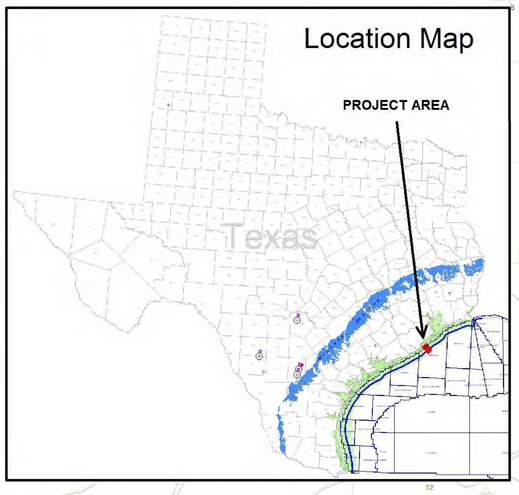

Figure 11-1 - Map of the Well Bore Management Plan study area is shown within the red polygon, with the blue line representing the boundary between State of Texas offshore waters jurisdiction and Federal Offshore Continental Shelf (OCS) jurisdiction. Note that wells, respectively, fall under one or the other jurisdiction.

Also, wells within a defined Area of Review that do not penetrate the Injection Zone and/or Injection Interval or where the Injection Interval is absent due to geologic conditions (i.e., pinchout, truncation, sealed faults) cannot provide a conduit or pathway for fluid migration.

3.0 WELLBORE MANAGEMENT PLAN PROTOCOL

Per EPA's Class VI UIC regulations, the Area of Review is defined as the area surrounding the Geologic Sequestration project where USDWs may be endangered by injection activities (40 CFR 146.84(a)). An artificial penetration is considered a potential compromise to a USDW when it has the potential to convey fluid from an injection interval into the USDW (Non-Endangerment Standard). Regulation requires identification and evaluation of artificial penetrations to ensure that abandoned boreholes will not provide a pathway for injection-induced movement of fluids into a USDW.

A process to identify and evaluate artificial penetrations follows. The process focuses on evaluation of artificial penetrations against the Non-Endangerment Standard. The process can be augmented to evaluate artificial penetrations against other standards and/or regulations if required. See Figure 11-2 for a visual representation of the process described in the following subsections (Section 3.1 to 3.7).

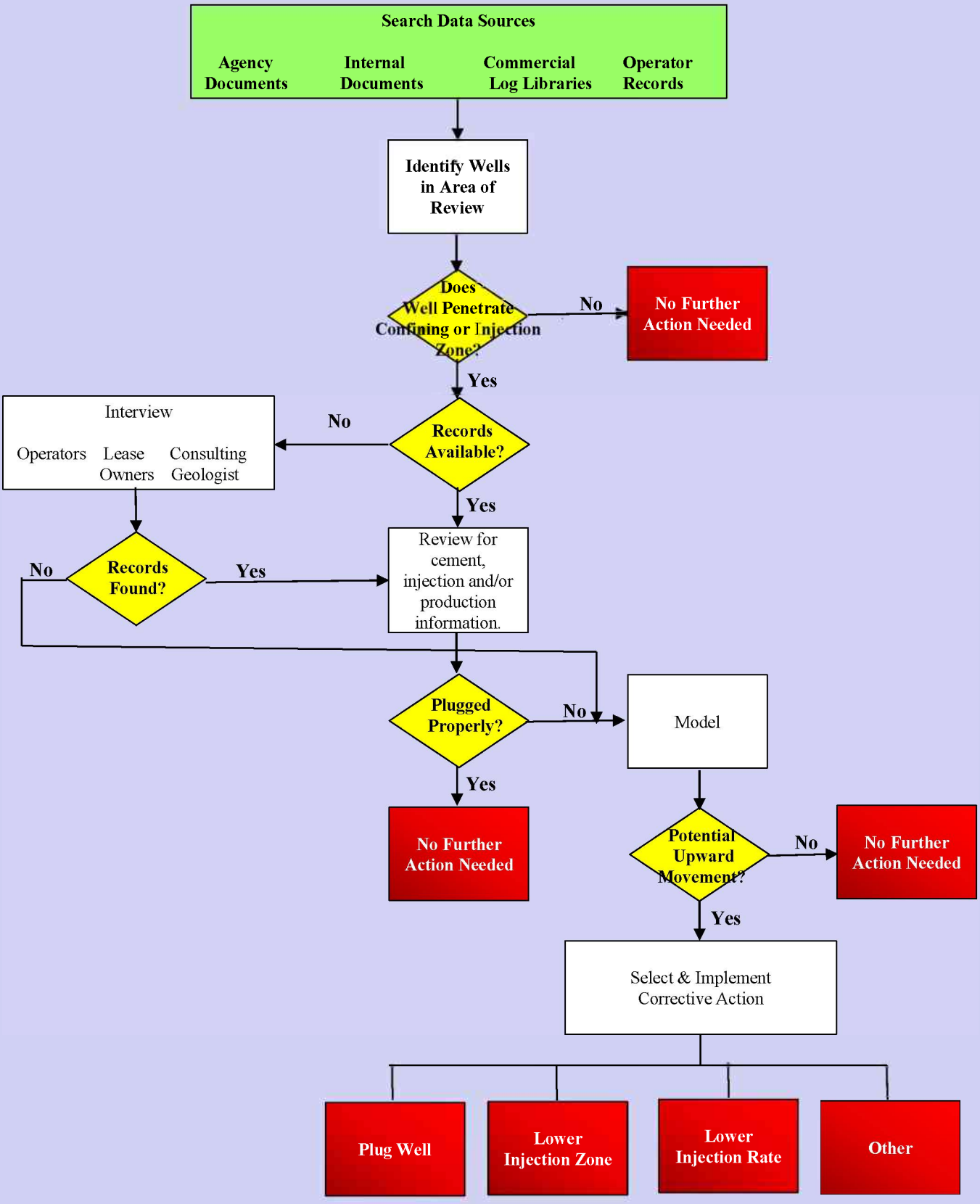

Figure 11-2

Flow diagram representing the process of identifying and evaluating artificial penetrations (i.e., abandoned boreholes to ensure that they do not provide a pathway for injection-induced movement of fluids into a USDW.

3.1 WELL IDENTIFICATION

A specific and consistent methodology should be used to identify all artificial penetrations in the Area of Review, with the overall goal being to establish a general background on all the artificial penetrations. Several data sources are available to locate pertinent information regarding each artificial penetration, among these are the following.

1. Revised or updated base maps (i.e., Tobin Surveys, Inc., Geomap, Inc.) to identify wells drilled within the Area of Review.
2. The Texas Railroad Commission's off-shore area base maps with reference to the county that borders the Texas waters. Use these to initially identify and establish a background on the wells in the Area of Review.
3. State agency files and State libraries to obtain descriptive well documentation such as well records and geophysical well logs.
4. Commercial log regional libraries to obtain well logs and scout tickets applicable to each identified well.
5. University research institutes and geologic data repositories for a variety of information.
6. The Bureau of Ocean Energy Management for wells located in Federal offshore areas to obtain well records and geophysical well logs.
7. State water regulatory agencies and groundwater conservation districts for information on location and descriptive information of potable water wells.

Where discrepancies exist among data sources, the form data from regulatory agencies should be considered the most accurate since it was directly reported from the well operator. The following discussion is a synopsis of the procedures used to procure well records and regulatory agency form data.

3.2 RESEARCH PROCEDURES FOR THE TEXAS RAILROAD COMMISSION

The Texas Railroad Commission is a mature agency, and its well record filing system is cumbersome due to system changes implemented by incoming agency directors throughout its history. Major restructuring of the data set resulted when efforts were undertaken to provide records digitally and on-line. The following discussion on file searches and research procedures outlines the steps that must be taken in order to retrieve oil and gas well records, including researching each well within the area of interest.

3.2.1 Maps

Before the data retrieval process can begin, it is necessary to know the operator, lease name, county, and name of the land survey in which the well is located This information is normally found on commercially prepared oil and gas base maps or other plats and survey maps. The Texas Railroad Commission maintains two types of maps (county and field) for use by researchers to determine this information, including approximate drilling date and field name.

County maps are also produced by commercial firms, who obtained the data to build commercially available base maps. The data used is often generated from scout tickets and completion data provided by well operators and the Texas Railroad Commission. The Texas Railroad Commission purchases these maps and utilizes them as base maps on which they plot information filed by oil and gas operators. Plotting is now performed on a digital base map, which allows revisions, corrections, and changes in the status of existing wells to be made, as well as including notes or linking factual material on new wells to the new data point on the map.

Field maps are prepared by Texas Railroad Commission personnel from these commercial base maps. Field maps are prepared when there is a high density of wells in an area of interest, and it is necessary to expand the scale of the map so that all wells can be properly identified and regulated by agency personnel. All data including survey name, fee name, acreage and configuration of tracts of land, operator name, and well

location are taken from the county map and transposed onto the field map. Once the field map is prepared, any wells drilled, deepened, plugged back, or plugged in the area encompassed are spotted on this map.

The research should utilize county and field maps (digital, paper, on-line) which are on file with the Texas Railroad Commission as well as other available commercial oil and gas base maps. The information found on these various base maps is used to integrate and proceed to the next step of the well record research process.

3.2.2 Microfilm Records

All records filed with the Texas Railroad Commission prior to 1973 are stored on microfiche and microfilm. Many have been converted to portable document format (PDF) files for on-line access. Records in some Texas Railroad Commission districts are filmed through 1980.

Microfiche and microfilm records are organized in several different systems, such as operator and lease name, or district, field, and operator name, or district, field, and lease number. Within these systems, a large number of exceptions to the filing procedures result in file sub-systems.

The standard film sets available are the following.

a. Unit Cards
b. Well Records-Folders Rolls
c. Well Records-Runs 20-30 and A-I
d. Well Records-Major Runs
e. Well Records-Old Warehouse Film
f. Well Records-K, L, M Runs
g. Potential Film
h. Wildcat And Suspense Film
i. Well Record Files
j. Suspense Files

Each is discussed individually below.

3.2.2.1 Unit Cards

Unit cards are microfiche records. These are for well records filed with the Texas Railroad Commission prior to 1962. Unit cards are filed sequentially by operator number; the operator number was assigned by the Texas Railroad Commission when the operator filed the required organization report with the agency. The operator number can be referenced in either the county book or the county microfiche. A county book is maintained for each county within the state. Within the county book, the information is organized alphabetically by lease name with cross references to the operator name and operator number. The county microfiche was added to the Texas Railroad Commission filing system when the agency took the county books, reorganized the leases into alphabetical order, and microfilmed the information. Unintentional omissions were made when the county book listings were reorganized. Therefore, although the county books are not organized as neatly as the county microfiche, they are the original system and are the more accurate of the two systems.

For the first half of the 20th century, the Texas Railroad Commission maintained organization ledgers, and operator numbers can be obtained from these. The ledgers are grouped into five sets which correspond to various time periods from the 1920s to the 1960s. The ledgers list only operator names, addresses, and the assigned operator numbers. The ledgers are used as a last resort, since they do not indicate lease names and often list multiple operators with the same name.

Once the operator name is matched to a lease name and an operator number is identified, the unit card, if available, is pulled. The lease names are filed alphabetically within each operator number. Since there are exceptions to the filing system, if the desired information is not available or only partially available on the unit card, then the researcher must proceed to the next set of microfilm.

3.2.2.2 Well Records-Folders Rolls

Duplicate copies of unit cards, which sometimes contain information that was not included in the initial filming of the unit cards, are referenced on the folder rolls. The folder rolls are organized by operator number and folder number which appear on the unit card jacket. Some folder rolls do not have a given folder number, but only an operator number. These rolls are called "add-on rolls" and also contain records not included in the initial filming of the unit cards.

3.2.2.3 Well Records-Runs 20 to 30 and A to I

These rolls are organized by operator number and by a specific time periods. These rolls encompass a period from 1945 to 1960 and commonly have three to five rolls for a specific year and operator number. When information is not available on the unit cards or well records-folder rolls, these are the next set of film to be researched for records.

3.2.2.4 Well Records-Major Runs

Well Records-Major Runs is a special film set that contains only records filed by major operators. These rolls are organized by operator and then alphabetically by lease name. It should be noted that there are very few unit cards for major companies and that, if any information were filed on a lease or well, it would be found on this set of film. It should also be noted that major operators, even in the early years of the oil industry, were prudent about filing completions and plugs for wells which they operated.

3.2.2.5 Well Records-Old Warehouse Film

This set of film contains well records filed from 1919 to 1939 and represents some of the earliest information filed with the Texas Railroad Commission. The film set consists of five rolls, with three rolls organized numerically by operator number and two rolls organized alphabetically by operator name.

3.2.2.6 Well Records - K, L, and M Film

In March 1966, the Texas Railroad Commission instituted a new filing system. However, before the system could be fully implemented, many well records which were filed during this transition period were placed onto the K, L, and M film. The K Run covers portions of records filed from 1963 to 1964, the L Run covers portions of records filed from 1964 to 1965, and the M Run covers portions of records filed from 1965 to March 1966. The K, L, and M film is organized by operator number, with leases listed alphabetically under the operator number.

3.2.2.7 Potential Film

In March of 1966, the Texas Railroad Commission filing system was converted to the potential filing system, which is used today. This film contains records of all wells that produced oil and/or gas and were placed in a designated oil or gas field. This film is organized by Texas Railroad Commission District, field name, and oil lease number or gas well identification number.

3.2.2.8 Wildcat and Suspense Film

This film contains records of all wells with applications to drill in wildcat fields or new leases in designated fields that were on leases that did not have a previously assigned lease identification number because there was no producing well on the lease in the field. This film is organized by district, county, and/or American Petroleum Institute (API) number. The API numbering system has been in effect since April 1966. The numbers have been stored within the Texas Railroad Commission computer system as well as being noted on all forms filed for the well. The system allows information to be retrieved by computer showing drilling status, operator, lease name, oil lease number or gas identification number, and field name. It is an efficient system and allows quick and accurate retrieval of data filed since 1978.

3.2.2.9 Well Record Files

These are hard copy files of data not yet placed on microfilm. These files are organized by district, field name, and oil lease number or gas identification number. The files contain the most recent data processed by the Texas Railroad Commission's Central Records Department. Inside these folders are references to data that have been placed onto potential film.

3.2.2.10 Suspense Files

These files contain the most recent information to be filed with the Central Records Department. This is the holding area for information to be placed into existing well record files or to have new oil lease or gas identification files prepared. The information is filed by district and API number. To obtain API numbers assigned to these records, it is necessary to search suspense cards that are filed by district, county, and alphabetically by lease name. Records that have not been placed in suspense files are usually found within the Map Department where they are held until data are placed on the county or field maps.

The aforementioned record sets are the primary file systems utilized to access records from the Texas Railroad Commission. In retrieving information from the Texas Railroad Commission, the researcher often has to examine every file system available in search of a particular piece of information.

3.3.3 Digital Records of Files

These Texas Railroad Commission's long-term plan is to convert all paper copies of oil and gas well records to digital format (PDF) to allow ease of access, search and use with the agency's website and GIS map-based search engine. There are inherent errors in field maps and records have been converted to digital format without full knowledge of specific field details; therefore, a detailed search of agency's paper files and maps, with assistance from trained personnel can also be undertaken to solve well spot and record discrepancies.

3.3 RESEARCH PROCEDUES FOR THE BUREAU OF OCEAN ENERGY MANAGEMENT

To retrieve well data from the Bureau of Ocean Energy Management, the researcher should have the field name, area name, block number, operator, and lease name in which the well is located. That information is normally found on commercially prepared oil and gas base maps or other plats and survey maps. The Bureau of Ocean Energy Management maintains a database with information on all wells drilled in Federal Waters and it is filed primarily by area (i.e., Brazoria, Pensacola, Ewing Bank).

A search for records drilled in Federal waters begins at the Bureau of Ocean Energy Management website to see if the information needed is available. Interactive maps for Federal waters are available on the website, and Bureau of Ocean Energy Management Reading Rooms can be visited to see if documentation is filed there. The most effective manner of obtaining records from the Bureau of Ocean Energy Management is to file a Freedom of Information Act request.

A request is made by sending a written letter or electronic mail, citing that the request is made under the Freedom of Information Act. Reasonably describe the records you are requesting. State the category of your request for fee purposes (i.e. Commercial, Media, Educational, or All Others). Authorize fees up to the maximum amount you are willing to pay; fees for manpower to pull records is published on the Bureau of Ocean Energy Management website. A fee waiver may be requested, but commercial requests typically do not qualify for the waiver. Specify the format in which you want your response (hard copy, diskette, magnetic tape, etc.). Provide an address and telephone number for a contact person (researcher). Submit the request to either the location where the records are housed (if you know this information) or to the Freedom of Information Act Officer listed on the Bureau of Ocean Energy Management website.

Separate Freedom of Information Act requests will likely have to be made for different types of data. For example, one request will cover well records (forms), and a second request will cover geophysical well logs.

3.4 EVALUATION PROCEDURE FOR ARTIFICIAL PENETRATIONS

3.4.1 Well Type

Once identified, the artificial penetrations should be divided into abandoned and active wells. An abandoned well is one where use has been permanently discontinued, or it is in such disrepair that it cannot be used for its intended purpose. These types of wells include dry holes, abandoned production (oil and gas) wells, and injection wells. An active well is one that is currently operating, including production wells, and injection (saltwater disposal, enhanced recovery or other) wells, or wells which are temporarily shut-in. Some temporarily shut-in wells will be subject to annual integrity testing.

3.4.2 Well Status

Each artificial penetration (active/abandoned) will be evaluated as to the adequacy of construction and plugging to determine the potential of the penetration to convey fluid from an Injection Interval and Injection Zone into the identified USDWs (Non-Endangerment. Where construction or plugging does not eliminate potential concerns, wells will be evaluated or modeled to determine compliance with the Non-Endangerment standard. In cases where the Geologic Sequestration project has an Injection Depth Waiver, a USDW may not always be located above the Injection Interval and/or Injection Zone.

3.4.3 Confining and Injection Intervals and Zone Penetration

The site characterization of the Geologic Sequestration project area will identify and describe the extent of the Confining Zone, Injection Zone, and Injection Interval. It will also provide petrophysical characteristics and formation fluid characteristics. Based on this information, each artificial penetration will be evaluated to determine if it penetrates these intervals and zones. Only those wells that penetrate the Injection Interval and its overlying confining beds could have the direct potential to convey fluid from the Injection Interval to an overlying USDW. Available geophysical well logs for the artificial penetrations within the defined Area of Review should then be correlated to

determine which of the wells actually penetrate the Confining/Injection Zone, Injection Zone, and Injection Interval. Wells that do not penetrate these intervals are not potential avenues for fluid movement and are not considered artificial penetrations; therefore, they do not need further evaluation.

3.4.4 Rock Types

In evaluating whether an artificial penetration can convey fluids to a USDW, consideration must be given to the type of rock present in the Injection Interval, Injection Zone, and Confining Zone. Unconsolidated rock formations such as the geologically young shales of the Gulf Coast contain expanding clays and exhibit plastic properties which result in natural closure of man-made boreholes (Johnston et al., 1979), (Davis, 1986), and (Clark, et al., 1992). Drilling engineers also report that the geologically young and unconsolidated sediments of the Gulf Coast tend to slough and swell, and an uncased borehole will commonly squeeze shut within a matter of hours, resulting in natural borehole closure (Johnston and Knape, 1986). Agency Information Consultants, 1987, examined improperly plugged abandoned wells in a large number of Texas oil and gas fields located in consolidated and unconsolidated sediments, and documented natural borehole closure as a mechanism that prevents upward fluid movement in unconsolidated sediments (Clark et al., 1987).

Borehole closure has also been verified in the routine experience of field engineers and/or petroleum consultants who encounter difficulty in keeping boreholes open while drilling and running casing and sometimes find boreholes closed when re-entry is attempted for plugging.

3.4.5 Drilling Methods and the Mud Column

The artificial penetrations should also be classified by their drilling methods (i.e., rotary, cable, etc.). Because boreholes tend to close in unconsolidated rock formations such as the geologically young sands and hydrated shales of the Gulf Coastal Plain (Clark, 1991), rotary drilling has been the preferred drilling method.

Generally, drilling mud is balanced to control caving sand and sloughing shales from entering the borehole. Rotary drilled dry holes without plugging records can be assumed to be mud-filled as a minimum condition because there is no economic value to recovering drilling mud prior to abandonment (Johnston and Knape, 1986). An exception to this is if a well is drilled with polymer- or oil-based muds whose recovery is economically feasible; however, the borehole is typically filled with a less expensive bentonite mud during extraction of the higher value mud. Mud characteristics (density, viscosity, type, and pH) can generally be obtained from geophysical well logs, regulatory agency forms, and operator records when available.

Texas Railroad Commission regulations (16 TAC 3.14) require 9.5 ppg mud be placed in the borehole in all areas not occupied by a cement plug. This requirement has been in effect for several decades. Federal regulations require that fluid be left in the borehole in the intervals between plugs but do not specify a weight, instead, it requires that the mud be dense enough to exert a hydrostatic pressure that is greater than the formation pressures in the intervals.

Drilling mud's hydrostatic pressure and other physical characteristics make it an effective barrier to vertical fluid movement. The two more important mud properties relevant to vertical fluid movement in improperly constructed and/or improperly abandoned wells are mud weight and gel strength. Generally, mud weight is increased as drilling depths increase so that the mud column will overbalance the encountered formation pressures. Weight is often increased by increasing the salinity of the mud and/or adding insoluble solids (i.e., barite). The drilling mud column will commonly overbalance formation pressures by 200 to 400 psi (Pierce, 1989).

Mud plugs can provide an effective barrier to vertical fluid flow in the abandoned wellbore. The permeability of the mud plug is less than that of the surrounding sand formations which, in combination with the hydrostatic head of an overbalanced mud column, is sufficient to counterbalance increased formation pressure due to injection and creates an effective barrier to vertical fluid flow. These factors, combined with borehole

closure, will minimize the chance of encountering a truly open conduit in an artificial penetration that was drilled in unconsolidated regions.

Rotary drilled dry holes with protection and/or production casing strings should be reviewed for perforations because a well that has been production tested by perforating usually has the drilling mud replaced with a water cushion.

3.5 EVALUATION METHODOLOGY FOR NON-ENDANGERMENT

3.5.1 Plugging

Texas Railroad Commission rule 16 TAC 3.14 establishes plugging requirements for abandoned wells. The rule (a.k.a. Statewide Rule 14) requires that all formations bearing fresh water, oil, gas, or geothermal resources be protected with type-specific cement plugs and mud-laden fluid. Uncemented areas in the abandoned wellbore must be filled with a mud-laden fluid weighing at least 9.5 lb/gal (ppg). The weight of fluid left in the borehole is obtained from the Texas Railroad Commission well records for the artificial penetration, normally Form W-3.

Setting depths for cement plugs are dependent upon the construction of the well and the geologic environment. Wells abandoned with only surface casing should be plugged across the base of the lowermost USDW regardless of casing depth. When insufficient surface casing is set to protect all USDWs and such strata are exposed to the open wellbore, a cement plug must be placed across each productive horizon and useable quality water strata.

When sufficient surface casing has been set to protect all USDWs, a cement plug must be set across the surface casing shoe. If surface casing has been set deeper than 200 ft below the base of the deepest USDW, an additional cement plug must be placed within the surface casing across the base of the deepest USDW.

For wells abandoned with protection and/or production casing that have been cemented through all USDW strata, all productive horizons must have cement plugs placed inside the casing and cement plugs centered opposite the base of the lowermost USDW. For wells abandoned with protection and/or production casing set back to surface, the casing must be perforated at the depths required to protect all productive horizons and the lowermost USDW with cement placed outside of the casing by squeeze cementing.

For purpose of evaluations in this document, any well that is plugged in accordance with State and/or Federal cementing requirements or wells that are plugged across the diameter of the borehole between the Injection Interval and lowermost USDW are not considered a potential threat to an USDW. These wells then need no further evaluation for purposes of demonstrating compliance with the "Non-Endangerment" standard.

3.5.2 Wells Requiring Additional Evaluation

Additional consideration should be given to wells not properly plugged with cement to determine if they require additional evaluation through modeling. These wells can be categorized for items specific to the geology of the study area. Items to consider include the following:

1) wells that are not deep enough to penetrate the Injection Interval; or
2) wells that are geologically separated from the active injection interval. Separation may be due to sealing faults, formation pinchouts, facies changes, or other factors.

These additional evaluation sub-criteria are discussed in the following subsections. If modeling is required to show the likelihood of vertical movement of borehole fluids, the modeling process in Section 3.6 of this document should be followed.

3.5.2.1 Well Depth

Wells that do not penetrate the Injection Interval cannot provide a conduit for fluid movement and therefore do not require further evaluation. These wells are considered safe as abandoned for that particular Injection Interval. The same evaluation must be performed for each individual Injection Interval to be used in the Geologic Sequestration project.

3.5.2.2 Wells Geologically Separated from Injection Interval

Artificial penetrations can be separated from the Injection Interval by faulting, stratigraphic pinchouts, and/or facies change. If separation is due to faulting, a determination must be made as to whether the faults act as a seal to fluid migration. This evaluation must take into consideration the structural elements presented in the site characterization and any historical production and/or test data to support the sealing capacity of the fault(s).

If separation from the Injection Interval is due to stratigraphic pinchouts and/or facies change. The characteristics of the surrounding sediments and formation pressures must be evaluated to determine if those formation conditions will prevent fluid movement from the Injection Interval. The basic question that should be answered is whether the formations are in pressure communication and whether the pressure in the Injection Interval is sufficiently high to transfer fluids to the surrounding sediments. Geophysical testing, including well logs, may provide information on testing. If pressure communication is not present or if the pressure in the Injection Interval is insufficient to transfer fluid to the surrounding formation, the artificial penetration is considered safe as abandoned.

3.5.3 Well Construction

For the purpose of this Wellbore Management Plan protocol, a properly constructed well is defined as one in which the annulus between the borehole and a casing string has been effectively sealed by cement across and/or above the correlated injection interval(s), thereby preventing vertical fluid movement. Wells that were drilled into or through the injection interval and abandoned with protection and/or production casing left in the hole could potentially provide a pathway for fluid movement. If cement was not circulated to a depth above the correlated injection interval, only drilling fluid would provide the same resistance to vertical fluid movement as a mud plug in the wellbore. Therefore, the depth at which casing was set, depth at which casings were severed, and placement of cement plugs should be documented and compared to the depth of the Injection Interval, Injection Zone, and Confining Zone.

3.5.4 Incomplete Records

Most data on the artificial penetrations in the Area of Review will be obtained from State and Federal records kept on file at each specific agency. Other records can be obtained from operators and companies. In most cases for wells that were spotted on Texas Railroad Commission Oil Field maps, or identified as having been drilled, documentation will support that the wells were adequately plugged. In the event documentation is not complete, or inconclusive, these wells should be evaluated or modeled for possible vertical fluid movement utilizing the known data. In the event that no documentation is available, a negative certification letter can be obtained from the Texas Railroad Commission after their personnel review all available records from 1919 and onward; the negative certification indicates that no record of a well or forms exist. The negative certification letter means that no records were found, not that a well was not drilled; however, it is highly unlikely that a well was drilled and no records filed, especially for wells drilled after the 1940s. It is unclear if the Bureau of Ocean Energy Management will provide a similar document.

3.6 MODELING ARTIFICIAL PENETRATIONS FOR NON-ENDANGERMENT

Wells that are improperly completed, improperly abandoned, or for which no records are available and that penetrate the Confining Zone, Injection Zone and/or Injection Interval can be mathematically evaluated or modeled to determine if increases in formation pressure due to injection operations may initiate vertical movement of borehole fluids. [Note: The Injection Interval is a 'sub-set' of the Injection Zone. The Injection Zone usually contains numerous sand and shale sequences. The Injection Interval can be a single sand layer within the Injection Zone. It may also be a finite number of intervals within the Injection Zone for which the operator obtains permission to complete the well to afford flexibility.] The wells are evaluated by comparing a model-predicted pressure increase with a conservatively-calculated allowable pressure buildup (static column pressure plus minimum gel strength) at each well, using well specific information (mud weight, borehole diameter, sand depth, etc.). In cases where information is not available, conservative assumptions can be made in the model calculations based on nearby drilling practices. Assumptions that are valid for this process are summarized below:

a) For calculating pressure due to gel strength, in cases where the borehole diameter (bit size) across the injection interval sands is unknown, the surface casing diameter is used as the bit size. This is conservative since the actual bit diameter *must* be less than the outer diameter of the surface casing string;

b) For calculating pressure due to gel strength, a conservative ultimate gel strength of 20-lb/100 ft^2 is used. This is conservative as studies and well reentries indicate that with time, the gel strength of mud may be at least an order of magnitude higher (Pierce, 1989);

c) For calculating the static mud column pressure, in cases where the weight of the mud in contact with the injection intervals cannot be found or otherwise conservatively determined (i.e., no well log header information or operator with no other wells in the area), the minimum drilling mud weight from nearby offset wells is used.

d) To be extremely conservative in calculating the static column pressure, a fallback of 50 feet in the mud column is assumed in the calculations. This is very conservative as Texas Railroad Commission regulations require that all uncemented intervals in a well be filled with mud. Additionally, mud to surface is required to support the surface plug; otherwise, the plug would not set properly and would fall down the hole.

A set of calculations that can be used in the modeling analysis is presented below.

A static fluid column exerts pressure. The pressures acting on the static fluid column (pressure due to injection plus original formation pressure) must exceed the static fluid column pressure, before fluid movement may start.

In this case, for upward fluid movement to begin, original formation pressure (P_f) plus the pressure due to injection (P_i) must be greater than the static fluid column pressure:

$$P_f + P_i > P_s \quad (3)$$

Where:

P_f = original formation pressure (psi)
P_i = formation pressure increase due to injection (psi)
P_s = static fluid column pressure (psi)

In other words, pressure increase due to injection must be greater than static fluid column pressure minus original formation pressure:

$$P_i > P_s - P_f \quad (4)$$

Static fluid column pressure is calculated using the equation:

$$P_s = 0.052 \times h \times M \quad (5)$$

Where:

P_S = pressure of static mud column (psi)
h = depth to the injection reservoir (feet)
M = fluid weight (lb/gal)

where 0.052 converts pressure in psig to pressure in psi. To be more conservative, a fallback of 50 feet in the height of the mud column is assumed for the calculation of the static fluid column pressure.

In an artificial penetration filled with a column of drilling mud, the gel strength of the mud must also be considered. In this case, for upward fluid movement to begin, original formation pressure (P_f) plus the pressure due to injection (P_i) must be greater than the static fluid column pressure plus the mud gel strength. This relationship is based on a balance of forces (Davis, 1986):

$$P_f + P_i > P_S + P_g \quad (6)$$

Where:

P_f = original formation pressure (psi)
P_i = formation pressure increase due to injection (psi)
P_S = static fluid column pressure (psi)
P_g = gel strength pressure (psi)

Therefore, pressure increase due to injection must be greater than static fluid column pressure minus original formation pressure:

$$P_i > P_S + P_g - P_f \quad (7)$$

The pressure due to gel strength (G) in an open borehole can be calculated from the following equation:

$$P_g = \frac{0.00333 \times G \times h}{d} \quad (8)$$

Where:

P_g = pressure due to gel strength (psi)
G = gel strength (lb/100 ft^2)
d = borehole diameter (inches)
h = depth to the injection reservoir (feet)

where 0.00333 is the conversion factor, such that P_g is in psi.

For a hypothetical open borehole, the added resistance due to gel strength for a mud with a very conservative ultimate gel strength of 20-lb/100 ft^2 in a 10-inch borehole is approximately 6.7 psi for every 1,000 feet of depth.

For a cased hole, pressure due to gel strength (G) can be calculated from:

$$P_g = \frac{0.00333 \times G \times h}{d_b - d_c} \quad (9)$$

Where:

P_g = pressure due to gel strength (psi)
G = gel strength (lb/100 ft^2)
d_b = borehole diameter (inches)
d_c = outside casing diameter (inches)
h = depth to the injection reservoir (feet)

For a hypothetical cased borehole, the added resistance due to gel strength for a mud with a conservative ultimate gel strength of 20-lb/100 ft^2 in a 10-inch borehole with seven-inch casing is approximately 22 psi for every 1,000 feet of depth.

As the above calculations show, gel strength provides a significant additional resistance to fluid movement due to injection. Additional conservatism is added due to borehole rugosity, which can increase the contribution in pressure from gel strength by a factor of three to five. Using the above formulas for an open borehole and a cased borehole, the average measured gel strength from the Nora Schulze No. 2 well (267-lb/100 ft^2) (Pierce, 1989) and a factor of three contribution in gel strength due to borehole rugosity, the added resistance due to gel strength could reasonably be expected to be 266 psi per 1,000 feet of depth in an open borehole and 889 psi per 1,000 feet of depth in a cased well.

For purposes of calculating a conservative pressure due to gel strength, use the drill bit diameter plus a one-inch washout factor. In cases where the bit diameter is unknown, use the external diameter of the surface casing string, plus a one-inch washout factor. In cases where neither the bit diameter nor the diameter of the surface casing string was available, use the external diameter of the largest surface casing string plus a one-inch washout factor in the calculation of the threshold pressure due to gel strength. As a further degree of conservatism, use a fallback of 50 feet in the mud column height in determining the pressure due to gel strength.

The general results of the calculations can be summarized in a form similar to what is shown below to quickly show parameters used and pressure comparison. Since these are wells for which information is lacking, worst-case assumption should be made.

Modeling Demonstration - Injection Interval Sands

Injection Interval	**Mud Weight (ppg)**	**Borehole Diameter (in)**	**Original Press. Gradient (psi/ft)**	**Top of Injection Interval (ft)**	**Allowable Pressure Increase COI (psi)**	**Model Pressure** at a given year **(psi)**
Sample Interval 1	9.5	12.5	0.4519	2708	103	72

$$\text{Max DP} = [\ 0.052*(h-50)*M+\{(0.00333*G*(h-50))\ /(d_b-d_c)\}\ ] - P_{grad} * h$$

Where:

h = depth, ft
M = mud weight, lb/gal
G = gel strength, 20 lb/100 ft2
d_b = borehole diameter, inches
d_c = cased hole outside diameter, inches (if not cased, use 0)
P_{grad} = initial pressure gradient, psia/ft

The worst case parameters are defined as follows:

- The minimum mud weight = *The minimum mud weight found in the well; if data is unavailable for the specific well, the lowest mud weight from nearby wells. In the example, the weight was 9.5 #/gal*
- Maximum borehole diameter = *The maximum borehole diameter determined for the well. In the example, this was 12.5".*
- Shallowest depth of injection interval = *The shallowest occurrence of the Injection Interval in the Area of Review or study area. In the example case, this was 2708 feet.*

Based on the results, a statement can be made as to whether corrective action is required for any of the artificial penetrations located in the Area of Review or study area.

3.7 CORRECTIVE ACTION PLAN

Wells that do not meet the Non-Endangerment modeling or evaluation criteria are labeled or considered "potential problem wells" and could require corrective action.

Should potential problem wells be identified, and should vertical fluid movement be calculated, then the following actions are recommended to address the problem well. (See Figure 11-2.)

1. Search for private or other offset records to more fully describe the condition of the well.
2. Determine if lowering the injection rate of the injection well to reduce head pressure will alleviate the condition at the artificial penetration and require no further action.
3. Determine if recompleting the injection well at a greater depth will allow the potential problem well to tolerate a higher pressure without fluid movement.
4. Recomplete the injection well in a deeper interval/reservoir than the potential problem well penetrates.
5. Increase the density of the injected waste to prevent vertical fluid movement.
6. Locate and re-enter the well to properly plug it.

A corrective action plan will be required upon filing a permit application for a Class VI injection well.

4.0 WELLBORE MANAGEMENT PLAN IMPLEMENTATION IN THE SAN LUIS PASS DOME AREA

4.1 DETERMINATION OF THE AREA OF REVIEW

The Area of Review for a Geologic Sequestration project is defined as that area surrounding the project where an USDW may be endangered by injection activities. The Area of Review is determined by modeling injection into the target injection interval. As the operating conditions and Injection Zone and/or Interval are not defined, the areal extent of the pressure influence cannot be determined for the San Luis Pass Dome Area. Therefore, the assumption was made that all wells in the study area are within the Area of Review and collected information was reviewed for each one.

4.2 RECORDS SEARCH FOR ARTIFICIAL PENETRATIONS

A map of the study area was provided by the BEG Gulf of Mexico Miocene CO2 Site Characterization Mega Transect project (Figure 11-1). A record search was conducted by D-B Associates of Austin, Texas for the wells located in the study area. Files were searched at the Texas Railroad Commission and Bureau of Ocean Energy Management as outlined in the Wellbore Management Plan Protocol in Section 3 above. Records at the Texas Railroad Commission were searched via electronic and physical databases. Bureau of Ocean Energy Management records were obtained via Freedom of Information Act requests.

The search resulted in the identification of 37 wells in Texas waters and 25 wells in Federal waters. All wells identified were evaluated to determine their potential impact to an USDW. Several wells had incomplete records.

4.3 EVALUATION OF ARTIFICIAL PENETRATIONS

4.3.1 Well Type and Status

The record search identified 62 artificial penetrations (Table 11-1) in the San Luis Pass Dome study area. Of these wells, 37 are located in Texas water and 25 are located in Federal waters. A summary of the well type are shown in the table below.

Jurisdiction	Producing	P&A	Not Drilled	Total
Federal Waters	5	18	2	25
Texas Waters	1	36	-	37
Total	6	54	2	62

Because the Area of Review has not yet been defined, all wells were evaluated as to the adequacy of construction and/or plugging per the Wellbore Management Plan Protocol (Section 3 above).

4.3.2 Penetration of Confining Zone, Injection Interval, and Injection Zone

The operating conditions, Confining Zone, Injection Zone, and Injection Interval were not yet identified for the Gulf of Mexico Miocene CO2 Site Characterization Mega Transect project. Therefore, it was assumed that all wells drilled in the study area will penetrate these intervals and all were evaluated for adequacy of plugging and/or completion to prevent movement from the Injection Interval to USDWs.

4.3.3 Rock Types

Rock formations in the Gulf of Mexico Basin have varied over its developmental history ranging from non-marine deposits of the Eagle Mills (Late Triassic – Early Jurassic) to evaporites (Middle Jurassic) and fine grained deltaic sediments (Late Triassic to Current Time). The deposits of the Miocene are marked by an abrupt decrease in the amount of sediment entering the Rio Grande Embayment (south of the study area) and an increase in the rate of sediment supply in southeast Texas, Louisiana, and Mississippi. Since then, maximum depositional centers were controlled by the Mississippi River and are located in offshore Louisiana and Texas.

The geologic formations in the study area appear typical of deposits of the Gulf Coast. They are fine grained, relatively unconsolidated, and relatively easy to drill through as is indicated by the spud and plug/completion dates on Table 11-1. The shale in the formations often behave in a plastic manner due to clay content. These properties lead to the self-sealing of penetrations whether they be natural (faults, fractures) or artificial (borehole closure).

4.3.4 Drilling Methods and the Mud Column

Based on data available, the wells in the study area were drilled using rotary methods and conventional casing programs. The records shows that the average drilling mud weight for the wells in the San Luis Pass Dome study area is 12.3 pounds per gallon (ppg). The minimum drilling mud weight reported is 8.7 ppg used in USA-1 (drilled in 1983) in the upper 1,000 ft of the borehole. The maximum drilling mud weight reported is 18.1 ppg in TX-21 (drilled in 1965) at a depth of 9,408 ft.

For plugging and abandonment operations, the average mud weight used and left in the borehole in the San Luis Pass Dome study area is 12.5 ppg. The minimum mud weight is estimated at 9 ppg in TX-9 (drilled in 1966). The maximum plugging mud weight reported is 17.7 ppg in TX-37 (drilled 1981).

4.4 EVALUATION FOR NON-ENDANGERMENT OF USDWs

As noted in the Wellbore Management Plan Protocol (Section 3), a well that is plugged across the diameter of the borehole between the Injection Interval and lowermost USDW is not considered a potential threat to an USDW. Both State and Federal regulations for plugging wells require that cement plugs be placed so as to isolate / protect USDWs from borehole fluid influx, vertical migration of hydrocarbons, and/or saline water.

For wells drilled in Texas, including Texas waters, operators are required to report the deepest occurrence of fresh water on Texas Railroad Commission Form W-3 (Plugging Record). A review of the records for the wells in the San Luis Pass Dome study area indicate that fresh water was reported in three wells at depths of 800 ft and 1,200 ft. The remaining records report that no fresh water was encountered, that the question was not applicable, or no information was provided.

Additionally, geophysical well logs for the wells in the San Luis Pass Dome study area were examined for the occurrence of fresh water, using 3 ohm-meters as the cut-off indicating a potentially useable USDW (10,000 ppm). Of the wells that were logged above 3,000 ft KB, several indicate a potential occurrence of a USDW above 1,300 ft. No evidence of fresh water was seen below this depth. See Table 11-2 for a summary of wells whose geophysical logs indicated the presence of a potential USDW or reported fresh water on the well records.

4.4.1 Plugging

To determine if a well was properly plugged to protect USDWs the following assumptions were used for the San Luis Pass Dome study area.

1. Fresh water occurs as deep as 1,300 ft throughout the entire study area. This is a conservative assumption because the majority of well records did not indicate fresh water at all, and the majority of wells were not logged shallow enough to support the assumption.

2. The depth of the Injection Interval will be at 4,000 ft or deeper.

Given these two assumption, 17 wells are considered to pose potential risk to USDWs. The wells are considered risks because 1) cement plugs were not placed between 1,300 ft and 4,000 ft, 2) there was not enough information to determine whether a plug was placed between these two depths, or 3) the status of the well could not be determined. The wells considered a potential risk to the USDW are shown in Table 11-3.

Well records show that 98% of the plugged wells in the study area have a cement plug placed between the seafloor and 1,000 ft. Seventy-seven percent (74%) of the plugged wells have cement plugs placed between 2,000 and 4,000 ft. See Table 11-4 for a summary of cement plug placement.

4.4.2 Wells Requiring Additional Evaluation

At this time, no wells were identified as requiring further evaluation for issues other than potential endangerment of USDWs. This may change when site characterization of the Area of Review is completed.

4.4.3 Well Construction

A properly constructed well is defined as one in which the annulus between the borehole and a casing string has been effectively sealed by cement across and/or above the correlated injection interval(s), preventing vertical fluid movement. Wells that were drilled into or through the injection interval and abandoned with protection and/or production casing left in the hole could potentially provide a pathway for fluid movement. If cement was not circulated to a depth above the correlated injection interval, only drilling fluid would provide the same resistance to vertical fluid movement as a mud plug in the wellbore.

For the wells in the San Luis Pass Dome study area, well records show that typical casing design and cementing programs were followed. Records generally indicate that cement was circulated through the annulus to a point above the top of the casing string. Upon abandonment protection casing was generally left in place through at least 4,000 ft and often through deeper levels. Based on this, the wells would be deemed adequately constructed.

The remaining issue that cannot be assessed at this time is how the materials of construction of the wells currently in the study area will tolerate carbon dioxide. Generally, neither Portland Cement nor carbon steel (typical for most wells in the study area) tolerate carbonic acid well.

4.4.4 Incomplete Records

Records reviewed indicate that seven wells have incomplete records in that the records provided were insufficient to fully evaluate well's status and/or construction configuration. Issues with the records are summarized in Table 11-5.

4.5 MODELING ARTIFICAL PENETRATIONS FOR NON-ENDANGERMENT

Modeling of artificial penetrations was not performed for the San Luis Pass Dome study area as the Injection Interval, Injection Zone, Confining Zones, and operational conditions have not yet been defined. Modeling performed should follow the procedure outlined in Section 3.6 of the Wellbore Management Plan Protocol (above).

4.6 CORRECTIVE ACTION PLAN

Based on review of records and geophysical logs for wells located in the San Luis Pass Dome study area and the assumptions made for USDW and Injection Interval depth, the 17 wells listed on Table 11-3 will require corrective action. Corrective action implemented for each well should be tailored for each specific well. The initial corrective action recommended is to attempt to obtain additional information on the well either from the regulatory agency files, commercial sources, or the well operators themselves.

REFERENCES

Agency Information Consultants, 1987, Survey of Proper Plugging Hearings for Fluid Migration from Unplugged or Improperly Plugged Wells in the Texas Railroad Commission Districts 02, 03, 04, 07B, 07C, and 09: Prepared for DuPont: Austin, Texas.

Clark, J. E., M. R. Howard, and D. K. Sparks, 1987, Factors that can Cause Abandoned Wells to Leak as Verified by Case Histories from Class II injection, Texas Railroad Commission files: International Symposium on Subsurface Injection of Oil field Brines, Underground Injection Practices Council, New Orleans, Louisiana, pp. 166-223.

Clark, J. E., R.E. McGowen, P.W. Papadeas, and D. K. Sparks, 1992, Borehole Closure Paper, DuPont Borehole Closure Well, Orangefield, Texas, Groundwater Protection Council Meeting.

Davis, K. E., 1986, Factors Affecting the Area of Review for Hazardous Waste Disposal Wells: Proceedings of the International Symposium on Subsurface Injection of Liquid Wastes, New Orleans, National Water Well Association, Dublin, Ohio, pp. 148-194.

Johnston, O. C. and C. J. Green, 1979, Investigation of Artificial Penetrations in the Vicinity of Subsurface Disposal Wells: Texas Department of Water Resources.

Johnston, O. C., and B. Knape, 1986, Pressure Effects of the Static Mud Column in Abandoned Wells: Texas Water Commission LP86-06, p. 106.

Klotzman, M., 1986, Petroleum Consultant, Concerning Plugging Abandoned Wells near Victoria, Texas: personal communication.

Meers, B., 1986, Petroleum Consultant, Concerning Plugging Abandoned Wells on the Gulf Coastal Plain: personal communication.

Pierce, M. S., 1989, Long-term properties of clay, water-based drilling fluids: Proceedings of the International Symposium on Class I & II Injection Well Technology, Dallas, Texas, Underground Injection Practices Council Research Foundation, pp. 115-132.

TABLES

Table 11-1
San Luis Pass Dome
Well Listing and Information Summary

Map ID No.	API No.	Operator	Lease and Well No.	Latitude	Longitude	Vertical / Deviated	Ground Level	Kelly Bushing	Well Spud Date	Status	Date Plugged	Well Total Depth (feet)	P&A Mud Weight (ppg)	Logging Mud Weight (ppg)	Cement Plug Depth (feet)	Casing Size (inch)	Casing Depth (feet)	Casing Cut Off (feet)	Hole Size (inch)	Deepest Fresh Water (feet)	Properly Plugged* (Yes / No)	Note
TX-1	42-605-30156	Santa Fe Energy Oper. Part., L.P.	State Tract 315-S No. 1	29 03' 13.741" x=3,250,255.81	95 05' 09.164" y=464,680.00	Vertical	MSL	88	08/17/90	P&A	08/27/90	7,985	14.7	13.8 14.7	15 - 116 3,475	24 16 10 3/4	276 755 3,600	136 141 146	Driven 20 14 3/4	Forms: 500	Yes	
TX-2	42-605-30017	Rutherford Oil Cor (Dow Chem.)	State Tract 315-S No. 1	29 03' 13.975" x=3,252,535.81	95 04' 43.449" y=464,780.00	Deviated	MSL	67	08/26/73	P&A	09/13/73	1973=7,677	1973=13.8	15.8	140 - 240 3,290 - 3,590	26 16 10 3/4	245 603 3,482	N/A 20 20	Driven 22 15	Forms: Depth not provided	Yes	
							MSL	25				1977=12,000	N/A	13.1		10 3/4 7	3,461 10,859	20 20?	N/A 9 7/8			
TX-3	42-706-00018	Humble Oil and Refining Company	State Tract 247-L No. 3	x=3,256,235.81	y=458,400.00	Vertical	MSL	63	10/18/56	P&A	11/16/56	6,852	N/A	10 @ 2,500 10.2 @ 5,204 10.3 @ 6,025 11.5 @ 6,598 14 @ 6,853	375 - 175 2,140 - 2,340 2,286 - 2,400 6,500 - 6,800	36 13 3/8 9 5/8	164 482 2,465	84 84 86	Driven 12 1/4	Forms: Depth not provided. Log: None.	Yes	
TX-4	42-706-00113	Shell Oil Company	State Tract 247-L (SE) No. 2	--	--	Vertical	MSL	82	04/16/67	P&A	05/08/67	9,833	10.5	N/A	130 - 280 2,850 - 3,100 6,000 - 6,300 7,800 - 8,000	48 16 10 3/4	215 523 3,000	0 0 0	Driven	Forms: Depth not provided	Yes	Former well name: State Tract 247-L (SW) No. 2. No well logs located.
TX-5	42-706-30129	Shell Oil Company	State Trct 75934 (Block 247-L SW) No. 4	29.03046 4700' FNL, 5800' FSL of SW/4	-95.05588	Vertical	MSL	70	08/27/78	P&A	09/15/78	5,548	9.7	11.5	275 - 475 2,920 - 2,975 3,412 - 3,680	48 16 10 3/4	217 514 3,024	137 200 258	Driven 20 13 1/2	Forms: note "N/A"	Yes	
TX-6	42-706-30004	Shell Oil Company	State Tract 247-L (SW) No.3			Vertical	MSL	75.7	03/29/69	P&A	03/29/69	6,289	11	9.1 @ 5,728 9.5 @ 6,083 11 @ 6,289	300 - 500 2,900 - 3,150	16 10 3/4	507 3,001	137 137		Forms: note "None"	Yes	
TX-7	42-706-00096	Shell Oil Company	State Tract 247-L (SW) No. 1	--	--	Vertical	MSL	81.5	06/08/69	P&A	06/08/69	7,400 PBTD 5,715	10	N/A	132 - 352	48 16 10 3/4 7 5/8	208 505 3,003 5,802	80 108 108 108	Driven	Forms: Depth not provided	No	No well log available.
TX-8	42-706-30238	Gryphon Exploration Company	State Tract 246-L No. 1	N 29 01' 30.7476" x=3,272,716.79	W 95 00' 59.9173" y=456,031.02	Vertical	MSL	98	09/09/04	P&A	10/27/04	13,100	17.4	11.5 @ 11,000 17.4 @ 13,124	294 - 494 3,955 - 4,155 10,715 - 10,915	18 5/8 13 3/8 9 5/8	815 4,115 11,000	188 188 188	22 17 1/2 12 1/4	Forms: note "None"	Yes	
TX-9	42-706-00099	Shell Oil Company	State Tract 247-L (SE) No. 1	29.02219	-95.01220	Vertical	MSL	84	06/13/66	P&A	06/23/66	5,838	9 estimated	N/A	230 - 280 2,900 - 3,000	48 16 10 3/4	200 512 3,006	0 0 0	Driven	Forms: Depth not provided	Yes	P&A borehole fluid is logging mud; weight not available.
TX-10	42-706-00019	Humble Oil and Refining Company	State Tract 247-L No. 1	700' W of E line SW/4, 3200' N of S line SW/4	--	Vertical	MSL	61	08/12/56	P&A	09/26/56	6,702	10.3 estimated	9.8 @ 500 10.5 @ 3,000 10 @ 3,604 10 @ 4,400 10.3 @ 4,572	175 - 275 2,615 - 2,715 2,715 4,100 - 4,580	36 20 13 3/8	180 487 2,811	89 89 89	Driven 12 1/4 12 1/4	Forms: Depth not provided Log: 1,300	Yes	P&A borehole fluid is mud; weight not available.
TX-11	42-706-30128	Shell Oil Company	State Tract 75934 (Block 247-L (SW)) No. 5	29.02265	-95.05563	Vertical	MSL	70	09/17/78	P&A	09/30/78	5,978	9.5	9.3 @ 3010 12.4 @ 5,977	275 - 475 2,918 - 2,970 5,250 - 5,470	16 10 3/4	510 3,000	200 375	20 13 1/2	Forms: note "N/A" Log: 1200	Yes	
TX-12	42-706-30067	Union Texas Petroleum Corporation	State Lease 69010 (Block 246-L (SW)) No. 1	x=3,271,975.81	y=451,907	Vertical	MSL	47.6	08/23/74	P&A	10/19/74	9,954	12.8	9.5 @ 3,000 12 @ 9,060 12.1 @ 9,954	125 - 235 2,834 - 3,175	30 16 10 3/4	263 608 3,000	106 106 106	Driven N/A 14 3/4	Forms: note "None" Log: None	Yes	
TX-13	42-706-00020	Shell Oil Company	State Tract 249 No. 1	820' S of N line, 3911' E of W line	--	Vertical	MSL	59	03/26/55	P&A	04/29/55	7,629	13.7 estimated	10.4 @ 2,034 10.4 @ 5,534 12.1 @ 6,696 13 @ 7,359 13.7 @ 7,629	 1,900 - 2,085 4,125 - 4,325	48 20 13 3/8 9 5/8	170 410 2,008 4,273	115 115 115 2,010	Driven	Forms: Depth not provided Log: 800	Yes	

All depth in Measured Depth unless otherwise noted.
* If Injection Interval / Zone is 4,000' or deeper.
N/A = Not Available

Table 11-1
San Luis Pass Dome
Well Listing and Information Summary

Map ID No.	API No.	Operator	Lease and Well No.	Latitude	Longitude	Vertical / Deviated	Ground Level	Kelly Bushing	Well Spud Date	Status	Date Plugged	Well Total Depth (feet)	P&A Mud Weight (ppg)	Logging Mud Weight (ppg)	Cement Plug Depth (feet)	Casing Size (inch)	Casing Depth (feet)	Casing Cut Off (feet)	Hole Size (inch)	Deepest Fresh Water (feet)	Properly Plugged* (Yes / No)	Note
TX-14	42-706-30109	Monsanto Company	State Tract 248-L (NW) No. 1	29 00' 23.1013" x=3,238,945.01	95 07' 23.1013" y=447,060.00	N/A	MSL	74	N/A	P&A	04/26/77	9,050	11.5 estimated	10.8 @ 8,529 11.5 @ 8,900 11.5 @ 9,050	N/A	10 3/4	3,040	N/A	9-7/8 estimated	Forms: note "N/A"	No	Incomplete Records
TX-15	42-706-30049	The Cherryville Corp	State Tract 248-L (NW) No. 1	29 00' 9.343" x=3,244,195.01	99 06' 24.628" y=445,440.00	Vertical	MSL	68.7	01/20/70	P&A	02/03/70	8,872	11.8	11.8 @ 8,872	114 - 185 2,880 - 3,080	30 16 10 3/4	144 524 2,010	84 84 0 estimated	Driven 15	500 est	Yes	Former API Number: 42-704-30034.
TX-16	42-706-30003	Shell Oil Company	State Tract 249-L (NW) No. 2			Vertical	MSL	70 estimated	04/14/69	P&A	04/28/69	9,104	11.5		370 - 570 2,895 - 3,145 8,148 - 8,448	48 16 10 3/4	197 535 3,025	137 142 147	Driven	Forms: note "None"	Yes	No well log available.
TX-17	42-706-00118	Shell Oil Company	State Tract 248-L (SE) No. 2	28 58' 36.286" x=3,248,333.81	95 05' 40.802" y=438,600.00	Vertical	MSL	81.8	05/11/67	P&A	05/22/67	9,572	11.6	9.9 @ 8,627 10.2 @ 9,014 10.4 @ 9,319 11.5 @ 9,572	325 - 375 1,925 - 2,075 9,236 - 9,490	48 16 10 3/4	159 515 2,026	0 0 0	Driven	Forms: Depth not provided	Yes	
TX-18	42-706-30110	Monsanto Company	State Tract 248-L (SW/4) No. 1	28 59' 15.5652" x=3,243,895.61	95 06' 29.8931" y=440,400.00	Vertical	MSL		04/10/77	P&A	04/26/77	8,627	11.5	N/A	42 - 150 2,882 - 2,990	16 10 3/4	617 3,040	0 0	22 14 3/4	Forms: 1200	Yes	No log available.
TX-19	42-706-00088	Shell Oil Company	State Tract 248-L (SW) No. 1	--	--	Vertical	MSL	81 estimated	05/18/66	P&A	05/29/66	8,509	10.7	9.6 @ 3,010 10.6 @ 7,050 10.7 @ 7,617 10.7 @ 7,695	60' Below Mudline 2,950	18 16 10 3/4	160 501 3,010	0 0 0	Driven 13 1/2	Forms: Depth not provided Log: 1200	Yes	
TX-20	42-706-30174	Inexco	State Lease 248-L No. 1	28 59' 7.152 X=3,242,395.81	95 06' 47.112" Y=439,500.00	Vertical	MSL	82	02/12/82	P&A	03/06/82	9,122	13.3	13.3	175 - 525 950 - 1,050 2,408 - 2,880 3,150 - 3,450	20 10 3/8	1,009 3,491	0 0	26 17 1/2	Forms: note "None"	Yes	
TX-21	42-706-00085	Shell Oil Company	State Tract 248-L (SE) No. 1	--	--	Deviated	MSL	78	12/05/65	N/A	01/22/66	9,850	18.1	11.4 @ 8,208 in ST 11.4 @ 8,386 in ST 11.5 @ 8,476 in ST 18.1 @ 9,408 in ST	N/A	48 20 13 3/8 9 5/8	215 512 2,989 8,476	0 0 0 0	Driven 12 1/4	Forms: Depth not provided	No	Incomplete Records. Drilling suspended 1/22/1966; Statewide Rule 14(B)(2) requested..
TX-22	42-059-30007	Shell Oil Company	State Tract 248-L (SE) No. 3	--	--	Deviated	MSL	47.7	04/12/69	P&A	04/12/69	8,958	10.5	10.5	340 - 540 2,900 - 3,200	48 16 10 3/4	161 538 3,000	83 84 83	Driven	Forms: note "None"	Yes	API Number 42-706-30005 shown on well log.
TX-23	42-706-30081	Union Texas Petroleum Corporation	State Lease 69012 (Block 249-L (SE)) No. 1	28 59' 05.493" x=3,265,275.81	95 02' 30" y=440,100.00	Deviated	MSL	56	06/26/75	P&A	08/11/75	10,153	17	10.1	125 - 225 2,800 - 3,200 8,900 - 9,000	30 16 10 3/4 7	222 610 3,010 9,173	17 17 17 3,000	Driven 14 3/4 9 7/8	Forms: note "None"	Yes	
TX-24	42-706-30225	Samedan Oil Corp. - Offshore Div	S. L. 98156 No. 1 (State Tract 249-L)	SL 28 58" 50.814" x=3,269,250.77 BHL x=3,267,611.81	SL 95 01' 45.165" y=438,751.46 BHL y=438,091.00	Deviated	MSL	99	03/01/00	P&A	11/09/04	13,400	11.6	12.8 @ 10,435 17.6 @ 11,649 17.8 @ 13,400	190 500 1,300 3,560 4,300 9,966 11,385	30 20 13 3/8 9 5/8 7 5/8 liner 5 1/2 liner 2 7/8	319 818 4,480 10,400 10,066 - 11,645 11,377 - 13,300 12,744	183 185 185 610 Not Applicable Not Applicable 3,400	Driven 26 17 1/2 12 1/4 8 1/2 6 1/2 12 1/4	Forms: Depth not provided	Yes	

All depth in Measured Depth unless otherwise noted.
* If Injection Interval / Zone is 4,000' or deeper.
N/A = Not Available

Table 11-1
San Luis Pass Dome
Well Listing and Information Summary

Map ID No.	API No.	Operator	Lease and Well No.	Latitude	Longitude	Vertical / Deviated	Ground Level	Kelly Bushing	Well Spud Date	Status	Date Plugged	Well Total Depth (feet)	P&A Mud Weight (ppg)	Logging Mud Weight (ppg)	Cement Plug Depth (feet)	Casing Size (inch)	Casing Depth (feet)	Casing Cut Off (feet)	Hole Size (inch)	Deepest Fresh Water (feet)	Properly Plugged* (Yes / No)	Note
TX-25	42-706-30221	Samedan Oil Corp. - Offshore Div	S. L. 98157 (Block 250-L) No. 1 Sidetrack	SL 28 58' 37.207" N x=3,270,938.90 BHL 28 58' 34.84" x= 3,270,995.81	SL 95 01' 26.672" W y=437,433.90 BHL 95 01' 26.19" y=436,995.00	Deviated	MSL	149	06/01/00	P&A	05/18/10	13,463 MD (plugged back to 13,028 MD)	N/A	17.6	11,740 - 11,940 9,931 - 10,465 266 - 393 1,800 - 10,146 6,750 - 10,146 9,938 - 9,984 9,966 - 10,145	30 20 13 3/8 9 5/8 7 5/8 5 1/5 liner 3 1/2 liner 2 7/8	297 795 4,511 10,778 10,285 7,492 - 10,790 10,181 - 13,400 10,181	0 28 26 334 344 0 0 2,050	Driven 26 17 1/2 17 1/2 9 5/8 6 1/2 5	Forms: Depth not provided	No	Original vertical hole abandoned. Details shown on well schematic.
TX-26	42-706-30130	Union Texas Petroleum Corporation	STL 69012; Galveston Block 249-L No. 2	26 58' 35.324" x=3,266,747.38	95 02' 14.045" y=436,899.18	Vertical	MSL	82	04/11/78	P&A	05/11/78	11,000	9.2 - 11.2	9.5 @ 3,020 11 @ ,9244 10.9 @ 9,898 13.4 @ 10,864	176 - 196 2,651 - 2,760 10,100 - 10,500	30 16 10 3/4	270 605 3,018	150 150 150	Driven 22 1/2 14 3/4	Form: note "None" Log: None	Yes	
TX-27	42-706-30207	Seagull Energy E&P Inc.	State Tract 276-L (NE) No. 1	-95.08595	28.9679	N/A	MSL	N/A	N/A	N/A	N/A	N/A	N/A	N/A	N/A	N/A	N/A	N/A	N/A	forms: note "N/A"	No	Incomplete Records. No information other than 10/23/87 application to drill (Form W-1).
TX-28	42-706-00021	The Ohio Oil Company	State of Texas Lease No. 31708 (Block 248) No. 1	N 28 58' 40"	95 05' 54"	Vertical	MSL	50	10/03/49	P&A	03/14/49	8,888	N/A	N/A	347 - 147 2,436 - 2,021 3,427 - 2,874	24 18 5/8 13 3/8 9 5/8	190 401 2,874 7,969	0 0 0 0	Driven N/A N/A N/A	Forms: Depth not provided	Yes	PA& borehole fluid is mud; weight N/A.
TX-29	42-706-30108	Monsano Company	State Tract 248-L (SE/4) No. 1	28 58' 51.3058" x=3,248,435.81	95 05' 39.6614" y=438,100.00	Vertical	MSL	92	09/06/77	P&A	09/20/77	8,230	11.7	11.7 @ 8,230	225 - 325 2,900 - 2,950	16 10 3/4	516 2,997	0 0	22 14 3/4	Forms: 800	Yes	
TX-30	42-706-30249	Contango Operators Incorporated	State Tract 277-L No. 1	28 58' 15.4262" x=3,236,845.81	95 07' 51.6771" y=434,100.00	Vertical	MSL	100	09/26/10	P&A	11/12/10	14,005	17.2	17.2 @ 14,005	250 - 400 225 - 425 4,400 - 4,600 9,350 - 9,550 12,686 - 13,086	18 5/8 13 3/8 9 5/8 7 5/8 liner	800 4,500 10,000 9654 - 12883	26 28 30 0	22 17 1/2 12 1/4 8 1/2	Forms: note "None"	No	
TX-31	42-605-30169	Manti Operating Company	State Tract 341 No. 1	SL 28 59' 36.5"N x=3,218,403 BHL 28 59' 21.5"N x=3,221,303	SL 95 11' 17.2"W y=441,588 BHL 95 10' 45.0"W y=440,167	Deviated	MSL	127	N/A	Oil / Gas	Not Applicable	9,500	Not Applicable	N/A	Not Applicable	20 9 5/8 5 1/2 2 7/8 2 7/8	389 3,520 9,500 7,621 6,449	Not Applicable Not Applicable Not Applicable Not Applicable Not Applicable	Driven 12 1/4 8 3/4	Forms: Depth not provided	Not Applicable	
TX-32	42-605-30130	Rutherford Oil Co.	State Tract 349-S No. 1	SL 28 58' 29.206 x=3,221,738.18	SL 95 10' 41.270 y=434, 984.51	Deviated	MSL	88	04/07/81	P&A	04/22/81	9,619	10.3	12 @ 9,619	160 - 320 2,830 - 3,103	30 16 10 3/4	300 615 3,003	157 158 159	Driven 22 14 1/2	Forms: note "N/A"	Yes	
TX-33	42-605-30166	Samedan Oil Corp. - Offshore Div	S. L. 98166 No. 1 (State Tract 349-S)	SL 28 58' 22.060" x=3,221,755.81 BHL x=3,221,755.81	SL 95 10'.41.337" y=434,263.00 BHL y=431,749.00	Deviated Planned	MSL	N/A	N/A	N/A	N/A	N/A	N/A	N/A	N/A	N/A	N/A	N/A	N/A	N/A	No	Inicomplete Records. Abandoned location.
TX-34	42-605-30158	Samedan Oil Corp. - Offshore Div	State Tract 349-S No. 1	x=3,221,855.01	y=432,900.00	Vertical Planned	MSL	N/A	N/A	N/A	N/A	N/A	N/A	N/A	Not Applicable	N/A	N/A	N/A	N/A	N/A	No	Incomplete Records. Abandoned location.
TX-35	42-706-30112	Monsanto Company	State Tract 276-L (NW/4) No. 1	28 57' 59.8266" x=3,243,995.81	95 06' 31.8333" y=432,750.00	Vertical	MSL	89	08/10/77	P&A	08/25/77	8,708	10.8	10.5 @ 8,708	159 - 270 3,108 - 3,408	16 10 3/4	524 3,456	0 0	22 1/2 14 3/4	Forms: 800	Yes	
TX-36	42-706-30206	Seagull Energy E&P Inc.	State Tract 276-L (SE) No. 1	28 57' 01.230" x=3,251,988.94	95 05' 03.823" y=427,095.67	Vertical	MSL	N/A	12/05/87	P&A	12/22/87	9,900	9.5	N/A	200 - 300 3,360 - 3,500	30 16 10 3/4	225 872 3,434	157 178 190	Driven 20 14 3/4	Forms: note "N/A"	Yes	

All depth in Measured Depth unless otherwise noted.
* If Injection Interval / Zone is 4,000' or deeper.
N/A = Not Available

Table 11-1
San Luis Pass Dome
Well Listing and Information Summary

Map ID No.	API No.	Operator	Lease and Well No.	Latitude	Longitude	Vertical / Deviated	Ground Level	Kelly Bushing	Well Spud Date	Status	Date Plugged	Well Total Depth (feet)	P&A Mud Weight (ppg)	Logging Mud Weight (ppg)	Cement Plug Depth (feet)	Casing Size (inch)	Casing Depth (feet)	Casing Cut Off (feet)	Hole Size (inch)	Deepest Fresh Water (feet)	Properly Plugged* (Yes / No)	Note
TX-37	42-706-30177	MTS Limited Partnership (Mesa Petroleum)	State Tract 275-L (W/2) #1	28 56' 48" x=3,255.162.81	95 04' 29" y=425,835.00	Vertical	MSL	88	09/11/81	P&A	11/23/81	14,100	17.7	9.3 @ 4,027 13.5 @ 10,185 16.9 @ 11,781 17.7 @ 14,100	257 - 400 9,590 - 9,950 11,198 - 11,237 11,590 - 11,740	30 20 13 3/8 9 5/8 7 5/8	142 605 3,794 10,162 9,303 - 11,760	20 20 20 20 20	Driven 26 17 1/2 12 1/4 8	Forms: note "None"	Yes	Well name amended from State Tract 275L (SW) No. 1.
USA-1	42-706-40094	Tenneco Oil Company	OCS-G-4565 GA-303 No. 1	28 50' 44.969" x=3,265,525.81	95 02' 45.820" y=389,530.00	Vertical	MSL	79	02/22/83	P&A	04/03/83	11,426	16.6 estimated	8.7 @ 841 9.4 @ 4,512 13.5 @ 7,587 16.6 @ 11,050	280	30 20 13 3/8 9 5/8	301 837 4,512 7,560	162 162 232 240	Driven 26 17 1/2 12 1/4	BOEM notes state "None Expected"	No	
USA-2	42-706-40395	Burlington Resources Offshore Inc	OCS-G-4565 GA-303 No. 5	28 52' 14.82" x=3,258,721.31	95 03' 58.950" y=398,380.33	Vertical	MSL	91	03/16/97	Shut-In	Not Applicable	7,000	9.3	9.9 @ 7,000	None	30 16 10 3/4 7 5/8 2 7/8 #4 Liner	316 805 2,526 7,000 5,480 5,666 - 5,711	Not Applicable	Driven 20 13 1/2 9 7/8 6 7/8 6 7/8	Forms: Depth not provided	N/A	
USA-3	42-706-40217	Tenneco Oil Company	OCS-G-4565 GA-303 No. 3	28 52' 25.630" X=3,260,135.81	95 03' 42.617" Y=399,520.00	Vertical	MSL	100 estimated	Permit Cancelled 11/2/89	N/A	N/A	N/A	N/A	N/A	N/A	N/A	N/A	N/A	Not Available	BOEM notes state "None Expected"	Not Applicable	Permit cancelled; see form dated 11/2/89.
USA-4	42-706-40459	W & T Offshore, Inc.	OCS-G-4565 GA-303 No. 7	SL 28 52' 46.126" N x=3,259,213.00 BHL 28 52' 32.634" N x=3,262,617.81	SL 95 03' 52.219" W y=401,560.00 BHL 95 03' 14.413" W y=400,311.44	Deviated	MSL	100	10/18/06	Gas	Not Applicable	10,230 MD 8,827 TVD	Not Applicable	10.40	9,684 - 10,184 (kick off point)	48 16 10 3/4 7 5/8	365 1,030 MD 4,010 MD 9,936 MD	Not Applicable Not Applicable Not Applicable Not Applicable	Driven 20 14 3/4 9 7/8	Forms: Depth not provided	N/A	
USA-5	42-706-40390	Burlington Resources Offshore Inc (W&T Offshore, Inc.)	G-4565 GA-303 No. 4	28 2' 44.147" x=3,262,475.81	95 03' 15.570" y=401,470.00	Vertical	MSL	140 est	09/02/96		11/03/96	9,350	N/A	12.5 @ 9224	9,100 - 9,102	30 16 10 3/4 7 5/8 5 2 3/8 2 3/8	360 738 3,539 8,320 8273 - 9350 7,927 8,258	Not Applicable Not Applicable Not Applicable Not Applicable Not Applicable Not Applicable Not Applicable	Driven 20 13 1/2 9 7/8 6 1/2	Forms: Depth not provided	Not Applicable	
			B001				MSL	140	12/20/04	Temporarily Abandoned	Status Date 3/27/07	9,350	N/A		8,248 8,257 9,076 - 9,086	30 16 10 3/4 7 5/8 #5 Liner 2 3/8	360 738 3,539 8,320 8273 - 9350 7,927		Driven 20 13 1/2 9 7/8 6 1/2 4 8/29		N/A	
			B001D				MSL	140					N/A	11 @ 9320		30 16 10 3/4 7 5/8 2 3/8 4 1/2	360 738 3,539 8,320 7,927 8,273 - 8,258		Driven 20 13 1/2 9 7/8 4 8/29 6 13/17		N/A	

All depth in Measured Depth unless otherwise noted.
* If Injection Interval / Zone is 4,000' or deeper.
N/A = Not Available

Table 11-1
San Luis Pass Dome
Well Listing and Information Summary

Map ID No.	API No.	Operator	Lease and Well No.	Latitude	Longitude	Vertical / Deviated	Ground Level	Kelly Bushing	Well Spud Date	Status	Date Plugged	Well Total Depth (feet)	P&A Mud Weight (ppg)	Logging Mud Weight (ppg)	Cement Plug Depth (feet)	Casing Size (inch)	Casing Depth (feet)	Casing Cut Off (feet)	Hole Size (inch)	Deepest Fresh Water (feet)	Properly Plugged* (Yes / No)	Note
USA-6	42-706-40398	Burlington Resources Offshore Inc (W&T Offshore, Inc.)	G-4565 GA-303 No. 6	SL 28 52' 48.967" x=3,267,854.81 BHL x=3,267,372.81	SL 95 02' 14.841" y=402,139.00 BHL y=400,259.00	Deviated	MSL	139	04/16/97	Gas		10,330 PBTD 9394	N/A	16.2 @ 10331		26	353		Driven		N/A	
																20	800		24			
																13 3/8	4,010		17			
																9 5/8	7,917		12 1/4			
																7	7,509 - 10,330		8 1/2			
			G-4565 GA-303 No. A-2			Deviated	MSL	140				10,330 PBTD 9,394	N/A		8,550 - 8,600	26	353		24		N/A	Two Kelly Bushing elevations reported: 140' (1976 completion) and 90' (2/6/2001 Sundry Notice).
															8,620 - 8,690	13 3/8	4,010		17			
																9 5/8	7,917 MD		12 1/4			
																2 7/8 tubing	8,931					
																#7 liner	7,490 - 10,331		8 1/2			
																#4 liner	9,038 - 9,106					
			G-4565 GA-303 No. A-2D			Deviated	MSL						N/A		8,736 - 8,738	26	353				N/A	
															8,878 - 8,898	20	800		24			
															9,850 - 9,854	13 3/8	4,010		17			
																9 5/8	7,917		12 1/4			
																7" liner	7,509 - 10,331		8 1/2			
																4" liner	8,759 - 8,794					
																2 7/8	7,387					
USA-7	47-706-40100-S2	Burlington Resources Offshore Inc	OCS-G-4565 GA-303 No. A-1A	28 52' 48.772" x=3,267,875.81	95 02' 14.612" y=402,120.00	Deviated	MSL	93	09/03/85	Temporarily Abandoned	Status Date 9/2/2006	10,140 PBTD 8,120	16.2	N/A	7,260 - 7,425	30	314	Not Applicable	Driven			Subordinate API numbers assigned: S1, S2, S3, and S4. Previous operators: Tenneco, W&T Offshore, Inc., and Pennzoil. Original Kelly Bushing 100'; subsequent Kelly Bushing elevations area 85' (1985), 93', and 90'.
															7,548 - 7,568	16	1,021	Not Applicable	20			
															7,880 - 7,900	10 3/4	3,460	Not Applicable	14 3/4	Forms: Depth not provided	No	
															8,100 - 8,120	7 5/8	8,528	Not Applicable	9 7/8			
															8,227 - 8,237							
USA-8	42-706-40201	Seagull Energy E&P Inc.	OCS-G-9042 GA-302 No. 1			Deviated	MSL	132	03/19/88	P&A	05/13/88	10,036 PBTD 7,113	13.8		307	30	354	221	Driven	Forms: Depth not provided	No	
																16	757	223	20			
																10 3/4	4,572	224	14 3/4			
																7 5/8	7,387	4,479	9 7/8			
USA-9	42-706-40310	Rutherford Oil Corporation	OCS-G-9042 GA-302 No. 2	28 52' 59.181" x=3,275,175.81	95 00' 52.042" y=403,420.00	Vertical	MSL	90	10/14/91	P&A	12/01/91	10,290	16.4		200 - 400	30	320	168	Driven	Forms: Depth not provided	No	
															4,342 - 4,600	18 5/8	771	168	22			
															7,230 - 7,533	13 3/8	4,490	168	17 1/4			
																9 5/8	7,433	168	12 1/4			
USA-10	42-706-40207	Seagull Energy E&P Inc.	OCS-G-9038 GA-281 No. 1			Vertical	MSL	93	10/16/89	P&A	11/05/89	8,570	9.5 estimated	9.5	309 - 469	48	300	179	Driven	Forms: Depth not provided	Yes	
															3,400 - 3,450	16	785	179	22			
															7,444 - 7,772	10 3/4	3,502	180	13 1/2			
USA-11	42-706-40133	Mobil Producing Texas & New Mexico Inc.	OCS-G-7243 GA-282G No. 1	28 54' 26.48"N x=3,272,775.81	95 01' 15.68W y=412,160.00	Vertical	MSL	92	07/08/86	P&A	07/31/86	9,500	12.3	11 @ 9075 12 @ 9500	180 - 475	20	313	175	Driven	Forms: Depth not provided	Yes	
															3,863 - 3,933	13 3/8	1,075	189	17 1/2			
															3,933 - 4,120	9 5/8	4,002	189	12 1/4			
															6,900 - 7,200							
USA-12	42-706-40402	Seagull Energy E&P Inc.	G15747 GA-282 No. 1	28 55' 12.484"N x=3,276,879.38	95 00' 27.694"W y=416,948.70	Deviated	MSL	100	06/14/97	P&A	08/24/97	16,500.00	17.6	14.2 @ 10,550	263 - 563	30	311	181	Driven	Forms: Depth not provided	Yes	
														17.6 @ 12,679	3,832 - 4,645	20	213 - 745		24			
														17.6 @ 15,400	10,015 - 10,424	13 3/8	4,499	183	17 1/2			
														17.6 @ 16,500	12,466 - 12, 896	9 5/8	4,200 - 10,520	4,200	12 1/4			
															12,466 - 12,591	7 5/8	10,224 - 12,678		8.5			
USA-13	42-706-40303	Seagull Energy E&P Inc.	OCSG-7243 GA-282G No. 2	28 55' 12.179"N x=3,284,208.60	94 59' 05.178"W y=417,168.90	Vertical	MSL	96	06/05/91	P&A	07/19/91	10,003	16.1	12.9 @ 8,448	195 - 250	24	320	175	24	Forms: Depth not provided	Yes	
														15.8 @ 10,003	309 - 609	16	819	175	20			
															600 - 1,960	10 3/4	3,828	175	13.5			
															7,250 - 7,398	7 5/8	8,346	257	9 7/8			
															8,190 - 8,290							
															8,290 - 8,590							

All depth in Measured Depth unless otherwise noted.
* If Injection Interval / Zone is 4,000' or deeper.
N/A = Not Available

Table 11-1
San Luis Pass Dome
Well Listing and Information Summary

Map ID No.	API No.	Operator	Lease and Well No.	Latitude	Longitude	Vertical / Deviated	Ground Level	Kelly Bushing	Well Spud Date	Status	Date Plugged	Well Total Depth (feet)	P&A Mud Weight (ppg)	Logging Mud Weight (ppg)	Cement Plug Depth (feet)	Casing Size (inch)	Casing Depth (feet)	Casing Cut Off (feet)	Hole Size (inch)	Deepest Fresh Water (feet)	Properly Plugged* (Yes / No)	Note
USA-14	42-706-40280	Seagull Energy E&P Inc.	OCS-G 9037 GA-273 No. 2			Deviated	MSL	93	09/27/90	P&A	11/05/90	11,534	11.6 estimated	11.6 @ 10,876	204 - 704 4,210 - 4,501	48 16 10 3/4	405 810 4,501	0 0 192	Driven 22 13.5	Forms: Depth not provided	No	
USA-15	42-706-40299	Seagull Energy E&P Inc.	OCS-G 9037 GA-273 No. 4	28 56' 07.756"N x=3,286,936.40	94 58' 32.288"W y=422,878.90	Deviated	MSL	97	07/28/92	P&A	08/20/92	9,655	10.5	10.5 @ 9,655	192 - 271 312 - 612 3,791 - 4,091 7,300 - 7,600	24 16 10 3/4	285 713 3,991 246	178 228 246	Driven 20 13 1/2	Forms: Depth not provided	Yes	
USA-16	42-706-40199	Seagull Energy E&P Inc.	OCS-G 9037 GA-273 No. 1	Not Applicable	Not Applicable	Not Applicable	MSL	Not Applicable	Not Applicable	Not Applicable	Not Applicable	Not Applicable	Not Applicable	Not Applicable	Not Applicable	Not Applicable	Not Applicable	Not Applicable	Not Applicable	Not Applicable	Not Applicable	Incomplete Records. Operator requested cancellation of permit on 11/17/1989
USA-17	42-706-40271	Seagull Energy E&P Inc.	OCS-G 9037 GA-273 No. 1	28 56' 27.487"N x=3,291,921.46	94 57' 35.371" y=425,044.71	Vertical	MSL	93	07/19/90	P&A	08/23/06	11,000 PBTD 10,411	11.9 estimated	11.5 @ 8,818 11.4 @ 10,050 11.9 @ 11,000	280 - 480 338 - 538 1,700 - 2,000 5,500 - 6,000 7,400 - 7,750 9,203 - 9,230 7,817	48 30 16 10 3/4 7 5/8 5 1/2 2 3/8	295 354 805 3,515 6,032 10,500 7,828	169 169 169 169 169 169 1,000	Driven Driven 22 13 1/2 9 7/8 6 3/4	Forms: Depth not provided	Yes	Subordinate API numbers: S01, S02, and S03 for production zone changes.
USA-18	42-706-40331	Seagull Energy E&P Inc.	OCS-G-9037 GA-273 No. 5	N 28' 55' 55"	W 94 57' 25"	Deviated	MSL	94	01/29/93	P&A	12/22/06	9,756 PBTD 8,537	11.5	11.7 @ 9,750	280 - 480 1,700 - 2,000 5,700 - 6,200 8,000 8,537 - 9,756	24 16 10 3/4 7 5/8 5 1/2 liner 2 7/8 tubing	296 706 3,735 6,543 6,140 - 9,750 8,368	169 169 169 169	24 20 13.5 9 7/8	Forms: Depth not provided	Yes	Subordinate API numbers: S01 and S02.
USA-19	42-706-40295	Seagull Energy E&P Inc.	OCS-G-9037 GA-273 No. 3	BHL 28 55' 46.695" x=3290604.026000	BHL 94 57' 51.809 y=420877.038000	Deviated	MSL	96.5	05/01/91	P&A	12/31/06	10,960 PBTD 9,985	N/A	12.5 @ 9365 14.1 @ 10404 14.7 @ 10964	283 - 483 1,700 - 2,000 5,500 - 6,000 9,985 - 10,960	48 16 10 3/4 7 5/8 5 1/2 2 3/8	325 797 4,402 9,287 8,853 - 10,073 8,091	N/A 174 174 174 Not Cut 1,000	Driven 21 13 1/2 9 7/8 6 3/4	Forms: Depth not provided	Yes	API number discrepancy on well log: 402915. Subordinate API number: S01.
USA-20	42-706-40344	Seagull Energy E&P Inc.	OCS-G-9037 GA-273 No. B-1	28 55' 50.822	94 54' 54.611	Deviated	MSL	96	12/04/93	N/A	N/A	8,448	N/A	10.9 @ 8297	N/A	10 3/4	3,057	N/A	N/A	N/A	No	Information recovered from well logs. No well records located. Logs refer to Well No. 6.
USA-21	42-706-40352	Seagull Energy E&P Inc.	OCS-G-9039 GA-283 No. B-2	Incomplete Record	Incomplete Records	Deviated	MSL	105	07/21/94	N/A	N/A	8,815	10.6 estimated	10.7 @ 8804	N/A	10 3/4	4,154	N/A	N/A	N/A	No	Information recovered from well logs. No well records located.
			OCS-G-9039 GA-283 No. B-2 Sidetrack 1			Deviated	MSL		08/08/94			8,621		10.6 @ 8621	N/A	10 3/4	4,154	N/A	N/A	N/A	No	
USA-22	42-706-40198	Seagull Energy E&P Inc.	OCS-G-9039 GA-283 No. 1	28 55' 05.569" x=3,291,030.95	94 57' 48.616" y=416,735.86	Vertical	MSL	87	01/28/88	P&A	02/28/88	10,200	15.4	15.4	250 - 400 3,110 - 3,260 8076 - 8089	30 16 10 3/4 7 5/8	321 816 3,296 8,185	175 180 185 3,200	Driven 20 14 3/4 9 7/8	Forms: Depth not provided	Yes	
USA-23	42-706-40345	Seagull Energy E&P Inc.	OCS-G-9039 GA-283 No. 5	28 55'31.485"N x=3,297,252.4	94 56' 37.540"W y=419,570.1	Vertical	MSL	97	11/24/93	P&A	12/06/93	7,513	11.2		220 - 450 3,350 - 3,600 6,690 - 6,920	24 16 10 3/4	305 724 3,471	180 0 282	Driven 20 13 1/2	Forms: Depth not provided	Yes	
USA-24	42-706-40333	Seagull Energy E&P Inc.	OCS-G-9039 GA-283 No. 4 / A-4	SL 28 55' 10.997"N x=3,299,156.82 BHL 28 54' 54.17N	SL 94 56' 16.903"W y=417,565.80 BHL 94 56' 16.26"W	Deviated	MSL	98	03/28/93	P&A	10/17/03	7,400 PBTD 7,242	10.5		240 - 500 6,675 - 6,975 7,146 - 7,154 7,170 - 7,198 7,214 - 7,222 7,710 - 7,198	48 Caisson 24 16 10 3/4 7 5/8 3 1/2	325 321 750 2,975 7,400	210 210 N/A 210 210 514	Driven Driven 20 13 1/2 9 7/8	Forms: Depth not provided	No	Well number amended to A-4 on 11/12/93. Subsequent API number: S01

All depth in Measured Depth unless otherwise noted.
* If Injection Interval / Zone is 4,000' or deeper.
N/A = Not Available

Table 11-1
San Luis Pass Dome
Well Listing and Information Summary

Map ID No.	API No.	Operator	Lease and Well No.	Latitude	Longitude	Vertical / Deviated	Ground Level	Kelly Bushing	Well Spud Date	Status	Date Plugged	Well Total Depth (feet)	P&A Mud Weight (ppg)	Logging Mud Weight (ppg)	Cement Plug Depth (feet)	Casing Size (inch)	Casing Depth (feet)	Casing Cut Off (feet)	Hole Size (inch)	Deepest Fresh Water (feet)	Properly Plugged* (Yes / No)	Note
USA-25	42-706-40286	Seagull Energy E&P Inc. (Ocean Energy)	OCS-G-9039 GA-283 No. 2 / A-2	28 55' 10.989"N x=3,229,164.30	94 56' 16.819"W y=417,565.30	Vertical	MSL	94	03/10/91	P&A	10/17/03	9,737 PBTD 7,625	10.8		251 - 404	30 16 10 3/4 7 5/8 2 7/8	320 805 3,801 7,767 6,781	154 179 174 194 424	Driven 21 14 3/4 9 7/8	Forms: Depth not provided	No	Well number amended to A-2 on 11/12/93. Subsequent API numbers: S01

All depth in Measured Depth unless otherwise noted.
* If Injection Interval / Zone is 4,000' or deeper.
N/A = Not Available

Table 11-2
Depth of Potential USDW

Well ID No.	USDW Depth (feet KB)	Source
TX-1	500	W-3
TX-10	1,300	Log
TX-11	1,200	Log
TX-13	800	Log
TX-15	500	W-3
TX-18	1,200	W-3
TX-19	1,200	Log

Table 11-3
San Luis Pass Dome
Wells that Potentially Endanger an USDW

Map ID No.	API No.	Operator	Lease and Well No.	Status	Cement Plug Depth (feet)	Properly Plugged?* (Yes / No)	Reason Well Failed Evaluation
TX-7	42-06-00096	Shell Oil Company	State Tract 247-L (SW) No. 1	P&A	132 - 352	No	No plug between 1300' & 4000'
TX-14	42-706-30109	Monsanto Company	State Tract 248-L (NW) No. 1	P&A	Not Available	No	Incomplete records
TX-21	42-706-00085	Shell Oil Company	State Tract 248-L (SE) No. 1		Not Available	No	Incomplete records
TX-25	42-706-30221	Samedan Oil Corp. - Offshore Div	S. L. 98157 (Block 250L) No. 1	P&A	**Original** 9,931 - 10,465 10,470 10,740 - 11,940 10,810 - 10,890 MD **Sidetrack** 266 - 393 1800 - 10 146 6750 - 10146 9938 - 9984 9966 - 10145	No	No plug between 1300' & 4000'
TX-27	42-706-30207	Seagull Energy E&P Inc.	State Tract 276-L (NE) No. 1	Not Available	Not Available	No	Incomplete records
TX-30	42-706-30249	Contango Operators Incorporated	State Tract 277-L #1	P&A	250 - 400 225 - 425 4400 - 4600 9350 - 9550 12686 - 13086	No	No plug between 1300' & 4000'
TX-33	42-605-30166	Samedan Oil Corp. - Offshore Div	S. L. 98166 No. 1 (State Tract 349S)	Not Available	Not Available	No	Incomplete records
TX-34	42-605-30158	Samedan Oil Corp. - Offshore Div	State Tract 349-S No. 1	Not Available	Not Available	No	Incomplete records

* Assumes USDW at 1300' and Injection Zone / Interval below 4000'

Table 11-3
San Luis Pass Dome
Wells that Potentially Endanger an USDW

Map ID No.	API No.	Operator	Lease and Well No.	Status	Cement Plug Depth (feet)	Properly Plugged?* (Yes / No)	Reason Well Failed Evaluation
USA-1	42-706-40094	Tenneco Oil Company	OCS-G-4565 GA-303 No. 1	P&A	280	No	No plug between 1300' & 4000'
USA-7	42-706-40100	Burlington Resources Offshore Inc	OCS-G-4565 GA-303 No. A-1A	TA	7,260 - 7,425 7,548 - 7,568 7,880 - 7,900 8,100 - 8,120 8,227 - 8,237	No	Incomplete records.
USA-8	42-706-40201	Seagull Energy E&P Inc.	OCS-G-9042 GA-302 No. 1	P&A	307	No	No plug between 1300' & 4000'
USA-9	42-706-40310	Rutherford Oil Corporation	OCS-G-9042 GA-302 No. 2	P&A	200-400 4342-4600 7230-7533	No	No plug between 1300' & 4000'
USA-14	42-706-40280	Seagull Energy E&P Inc.	OCS-G 9037 GA-273 No. 2	P&A	204 - 704 4,210 - 4,501	No	No plug between 1300' & 4000'
USA-20	42-706-40344	Seagull Energy E&P Inc.	OCS-G-9037 GA-273 No. B-1	Not Available	Not Available	No	Incomplete Records
USA-21	42-706-40352	Seagull Energy E&P Inc.	OCS-G-9039 GA-283 No. B-2	Not Available	Not Available	No	Incomplete records

* Assumes USDW at 1300' and Injection Zone / Interval below 4000'

Table 11-3
San Luis Pass Dome
Wells that Potentially Endanger an USDW

Map ID No.	API No.	Operator	Lease and Well No.	Status	Cement Plug Depth (feet)	Properly Plugged?* (Yes / No)	Reason Well Failed Evaluation
USA-24	42-706-40333	Seagull Energy E&P Inc.	OCS-G-9039 GA-283 No. 4	P&A	240 - 500 6,675 - 6,975 7,146 - 7,154 7,170 - 7,198 7,214 - 7,222 7,710 - 7,198	No	No plug between 1300' & 4000'
USA-25	42-706-40286	Seagull Energy E&P Inc. (Ocean Energy)	OCS-G-9039 GA-283 No. 2 / A-2	P&A	251 - 404	No	No plug between 1300' & 4000'

* Assumes USDW at 1300' and Injection Zone / Interval below 4000'

Table 11-4

Distribution of Cement Plug Placement

Depth Range (feet)	Texas Waters % of 31 Wells	USA Waters % of 15 Wells	Total % of 46 Wells
0 - 1000	97%	100%	98%
1,000 - 2,000	13%	20%	15%
2,000 - 3,000	61%	0%	41%
3,000 - 4,000	29%	40%	33%
4,000 - 5,000	13%	13%	13%
5,000 - 6,000	3%	20%	9%
6,000 - 7,000	10%	27%	15%
7,000 - 8,000	3%	40%	15%
8,000 - 9,000	6%	13%	9%
9,000 - 10,000	19%	7%	15%
10,000 - 11,000	10%	7%	9%
11,000 - 12,000	10%	0%	7%
12,000 - 13,000	3%	7%	4%
13,000 - 14,000	0%	0%	0%

Table 11-5

Wells with Incomplete Records

Map ID No. & Name	API No.	Records Summary
TX-14 Monsanto Company State Tract 248-L (NW) No. 1	42-706-30109	Application to drill (Form W-1) to 9,000 ft filed in 03/1977.
TX-21 Shell Oil Company State Tract 248L (SE) No. 1	42-706-00085	Drilled to 9,850 ft; plugged back to 8,376 ft. Operations suspended on 01/22/1966 and request for extension filed.
TX-27 Seagull Energy E&P Inc. State Tract 276-L (NE) No. 1	42-706-30207	Application to drill (Form W-1) to 9,200 ft in 10/19987. Permit expired in 10/1988. Well operator on record not located.
TX-33 Samedan Oil Corp. S. L. 98166 No. 1 (State Tract 349-S)	42-605-30166	Application to drill (Form W-1) to 12,000 ft filed on 03/16/2000. Railroad Commission modified API number on 03/20/2000.
TX-34 Samedan Oil Corp. - Offshore State Tract 349-S No. 1	42-605-30158	Application to drill (Form W-1) to 11,900 ft filed on 12/20/1991.
USA-20 Seagull Energy E&P Inc. OCS-G-9037 GA-273 No. B-1	.42-706-40344	No records available from the Bureau of Energy Management. Geophysical well logs were located. Well status is unknown.
USA-21 Seagull Energy E&P Inc. OCS-G-9030 GA-283 No. B-2	42-706-40352	Application to drill (Form W-1) to 9,200 ft filed in 10/1987 and permit expired in 10/1988. No other records were found. The well operator listed on the permit application was not located.